

INFORMATION TO USERS

This manuscript has been reproduced from the microfilm master. UMI films the text directly from the original or copy submitted. Thus, some thesis and dissertation copies are in typewriter face, while others may be from any type of computer printer.

The quality of this reproduction is dependent upon the quality of the copy submitted. Broken or indistinct print, colored or poor quality illustrations and photographs, print bleedthrough, substandard margins, and improper alignment can adversely affect reproduction.

In the unlikely event that the author did not send UMI a complete manuscript and there are missing pages, these will be noted. Also, if unauthorized copyright material had to be removed, a note will indicate the deletion.

Oversize materials (e.g., maps, drawings, charts) are reproduced by sectioning the original, beginning at the upper left-hand corner and continuing from left to right in equal sections with small overlaps. Each original is also photographed in one exposure and is included in reduced form at the back of the book.

Photographs included in the original manuscript have been reproduced xerographically in this copy. Higher quality 6" x 9" black and white photographic prints are available for any photographs or illustrations appearing in this copy for an additional charge. Contact UMI directly to order.

UMI[®]

Bell & Howell Information and Learning
300 North Zeeb Road, Ann Arbor, MI 48106-1346 USA
800-521-0600

University of Alberta

**Two Dimensional Vertically Averaged and Moment
Equations for Shallow Free Surface Flows**

by

Haitham Kamal GHAMRY ©

A thesis submitted to the

Faculty of Graduate Studies and Research

in partial fulfillment of the requirements for the degree of

Doctor of Philosophy

in

Water Resources Engineering

Department of Civil and Environmental Engineering

Edmonton, Alberta

Spring, 1999



National Library
of Canada

Acquisitions and
Bibliographic Services

395 Wellington Street
Ottawa ON K1A 0N4
Canada

Bibliothèque nationale
du Canada

Acquisitions et
services bibliographiques

395, rue Wellington
Ottawa ON K1A 0N4
Canada

Your file Votre référence

Our file Notre référence

The author has granted a non-exclusive licence allowing the National Library of Canada to reproduce, loan, distribute or sell copies of this thesis in microform, paper or electronic formats.

The author retains ownership of the copyright in this thesis. Neither the thesis nor substantial extracts from it may be printed or otherwise reproduced without the author's permission.

L'auteur a accordé une licence non exclusive permettant à la Bibliothèque nationale du Canada de reproduire, prêter, distribuer ou vendre des copies de cette thèse sous la forme de microfiche/film, de reproduction sur papier ou sur format électronique.

L'auteur conserve la propriété du droit d'auteur qui protège cette thèse. Ni la thèse ni des extraits substantiels de celle-ci ne doivent être imprimés ou autrement reproduits sans son autorisation.

0-612-39531-6

University of Alberta
Library Release Form

Name of Author: Haitham Kamal Ghamry
Title of Thesis: Two Dimensional Vertically Averaged
and Moment Equations for Shallow
Free Surface Flows
Degree: Doctor of Philosophy
Year this Degree Granted: 1999

Permission is hereby granted to the University of Alberta library to reproduce single copies of this thesis and to lend or sell such copies for private, scholarly, or scientific research purposes only.


The author reserves all other publication and other rights in association with the copyright in the thesis, and except as herein before provided, neither the thesis nor any substantial portion thereof may be printed or otherwise reproduced in any material form whatever without the author's prior written permission.

Haitham K. Ghamry
T. Blench Hydraulics Lab
University of Alberta
Edmonton, Alberta,
Canada T6G 2N4

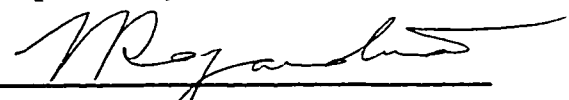
Date: Feb 5, 1999

University of Alberta
Faculty of Graduate Studies and Research

The undersigned certify that they have read, and recommend to the Faculty of Graduate Studies and Research for acceptance, a thesis entitled **"Two Dimensional Vertically Averaged and Moment Equations for Shallow Free Surface Flows"** submitted by **Haitham Kamal Ghamry** in partial fulfillment of the requirements for the degree of **Doctor of Philosophy in Water Resources Engineering**.



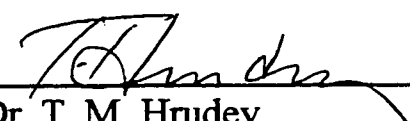
Dr. P. M. Steffler
(Supervisor)



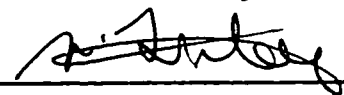
Dr. N. Rajaratnam



Dr. F. E. Hicks



Dr. T. M. Hruday



Dr. W. Finlay

Professeur J. L. Robert
(External Examiner) *72/1*

Date: Feb 4, 1999

بِسْمِ اللَّهِ الرَّحْمَنِ الرَّحِيمِ
أَوَلَمْ يَرِ الَّذِينَ كَفَرُوا أَنَّ السَّمَاوَاتِ
وَالْأَرْضَ كَانَتَا رَتْقًا فَفَتَقْنَاهُمَا وَجَعَلْنَا مِنَ الْمَاءِ
كُلَّ شَيْءٍ حَيٍّ أَفَلَا يُؤْمِنُونَ .

(سورة الأنبياء — آية ٣٠)

In the Name of Allah the Most Gracious, the Most Merciful

*"Do not those who disbelieve see that the
heavens and the earth were joined together.
then We (God Almighty) tore them asunder?
And We made of water every living thing.
Will they not then believe?"*

The Quran, 21:30

Abstract

The classical depth averaged de St. Venant equations, which are used for most of the computational models in open channels, are based on the fundamental assumptions of uniform velocity and hydrostatic pressure distributions. The depth averaging process used to derive de St. Venant equations neglects flow details over the vertical dimension to reduce computational effort. Thus, they are limited in their applicability to cases where vertical details are not of importance. Alternative two-dimensional vertically averaged and moment equations are developed to account for problems where more vertical details are significant and essential. These problems include flow cases with non-uniform velocity and non-hydrostatic pressure distributions.

The vertically averaged equations are derived by vertically integrating the fundamental three dimensional Reynolds equations, whereas the new moment equations required to solve for the extra degrees of freedom are derived by a moment weighted residual method from the same Reynolds equations. The equations are derived in a general way that can suit different shapes of velocity as well as pressure distributions. The derivation of the two-dimensional vertically- averaged and moment equations is presented in detail.

The implicit Petrov-Galerkin finite element scheme is applied in this study. Triangular elements with linear basis functions are used for all variables.

The vertically averaged and moment equations model is used to analyze a wide variety of hydraulic problems involved in open channel flow. These problems include flow in channel transitions with rapid contraction and/or expansion and flow in curved channels with different degrees of curvature. Linear and quadratic distribution shapes are proposed for the horizontal velocity components. In addition, quadratic vertical velocity and pressure distribution shapes are considered in these simulations.

The numerical model developed in this study is applied to two sets of experimental data. Computed values for water surface profile, depth averaged longitudinal and transverse velocities across the channel width and vertical profiles of longitudinal and transverse velocities are compared to the observed experimental data. For the rapidly varied flow simulations, the proposed model simulates the observed water surface profile slightly better than the conventional de St. Venant model. For the curved open channel simulations, this study recommends the replacement of the standard conventional de St. Venant model by the proposed model in terms of depth or vertically averaged modeling. This should be true for large-scale models where the generated numerical meshes are not very fine. This study also recommends that very fine finite element meshes, in which the numerical discretizations are of the order of the flow depth, be used when a high degree of accuracy of the predicted secondary flows near the channel walls is sought.

The present vertically averaged and moment model is found to be efficient, robust and converges to the correct solutions in a 2-D setting.

Acknowledgements

First and foremost I am thankful to Allah the Almighty for His continuous Grace and Mercy.

I wish to acknowledge the valuable advice and continuous support provided by my supervisor Prof. Peter Steffler. His keen interest and understanding of the topic was inspiring and led to many fruitful discussions. My special thanks are due to his time and effort in reviewing this thesis and advising on the application of the model.

My thanks are also due to Professor Rajaratnam for his valuable advice and encouragement during my work on the thesis.

I wish to extend my thanks to Professeur J. L. Robert, my external examiner, for his time and effort in reading this thesis thoroughly and making many helpful comments and suggestions.

Thanks are also extended to Mr. Perry Fedun and Mr. Sheldon Lovell for their technical support.

I would like to acknowledge the financial support provided by the Natural Sciences and Engineering Research Council of Canada through an operating grant to my supervisor.

I wish to extend a warm thank you to my mother, father, aunt, sister, brothers Nael, and Wa'el, twin brother Waleed and nieces Merhan and Haidy for their support and encouragement throughout the course of this study.

Table of Contents

Chapter 1	Introduction	1
References.....		6
Chapter 2	Derivation of the Two Dimensional Vertically Averaged and Moment Equations	8
2.1	Introduction.....	8
2.2	Derivation of the Vertically Averaged and Moment Equation Model.....	13
2.3	Vertically Averaged and Moment Linear and Quadratic Models.....	30
2.4	Steady Uniform Flow Solution.....	37
2.5	Numerical Solution of the Equations.....	39
2.5.1	Finite element formulation.....	39
2.5.2	Treatment of boundary conditions.....	44
2.5.3	Time discretization.....	44
2.5.4	Solution of the non-linear equations.....	46
2.5.4.1	Transient solution.....	46
2.5.4.2	Steady state solution.....	47
2.5.5	The mesh generation.....	49
2.5.6	The finite element code.....	50
2.6	A Preliminary Numerical Test.....	50
	A symmetric bed profile test.....	51
2.7	Summary	52

2.8	References.....	53
-----	-----------------	----

Chapter 3 Rapidly Varied Flow 67

3.1	Introduction.....	67
3.1.1	Rapid transitions.....	68
3.1.2	Free overfalls.....	70
3.1.3	Hydraulic jump.....	71
3.1.4	Unsteady rapid flow.....	71
3.2	Applications.....	74
3.2.1	Ippen and Dawson's (1951) experiment.....	75
3.2.2	Ye and McCorquodale's (1997) experiment.....	77
3.3	Comparison of Computational Effort.....	78
3.4	Summary and Conclusions.....	79
3.5	References.....	80

Chapter 4 Curved Channel Flows 95

4.1	Introduction.....	95
4.2	Experimental Verifications and Comparisons.....	106
4.2.1	Experimental Errors.....	107
4.2.2	DeVriend's (1976) Experiment.....	109
4.2.3	DeVriend's (1980) Experiment.....	113
4.2.4	Steffler's (1984) Experiment.....	118
4.2.5	Rozovskii's (1961) Experiment.....	123

4.2.6	Chang's (1971) Experiment.....	128
4.3	Effect of Numerical Discretization on the Accuracy of the Results.....	131
4.4	A Field Test Case.....	133
4.5	Summary and Conclusions.....	135
4.6	References.....	139
 Chapter 5 Summary and Conclusions		304
	Recommendations.....	309
 Appendix A Model Development		311
	References.....	375
 Appendix B List of the Integral Constants in the Derived Equations		377
 Appendix C Evaluation of the Square Root of the Convection Matrix		381
 Appendix D List of the Integral Constant Values in the Derived Linear and Quadratic Models		383

List of Figures

Figure 2.1	Definition sketch.....	57
Figure 2.2	Assumed general longitudinal velocity distribution	58
Figure 2.3	Assumed general transverse velocity distribution	58
Figure 2.4	Assumed general vertical velocity distribution	59
Figure 2.5	Assumed general pressure distribution	59
Figure 2.6	Assumed linear longitudinal velocity distribution	60
Figure 2.7	Assumed linear transverse velocity distribution.....	60
Figure 2.8	Assumed quadratic longitudinal velocity distribution.....	61
Figure 2.9	Assumed quadratic transverse velocity distribution.....	61
Figure 2.10	Assumed quadratic vertical velocity distribution	62
Figure 2.11	Assumed quadratic pressure distribution	62
Figure 2.12	The comparison between different assumed velocity distributions for the case of uniform flow for $C_* = 10$	63
Figure 2.13	Finite element mesh for Sivakumaran et al.'s (1983) experiment.....	64
Figure 2.14	The comparison of water surface profiles for Sivakumaran et al.'s (1983)	65
Figure 2.15	The comparison of bed pressure profiles for Sivakumaran et al.'s (1983).....	66
Figure 3.1	The layout of Ippen and Dawson's (1951) experiment.....	85
Figure 3.2	Finite element mesh for Ippen and Dawson's (1951) experiment.....	86

Figure 3.3	Measured depth contours (adapted from Ippen and Dawson, 1951)	87
Figure 3.4	Numerical prediction of depth contours for Ippen and Dawson's (1951) experiment (VAM model).....	87
Figure 3.5	Numerical prediction of depth contours for Ippen and Dawson's (1951) experiment (VA or Standard de St. Venant model).....	87
Figure 3.6	The layout of Ye and McCorquodale's (1997) experiment.....	88
Figure 3.7	Finite element mesh for Ye and McCorquodale's (1997) experiment.....	89
Figure 3.8	Comparison of cross channel averaged surface elevation for Ye and McCorquodale's (1997) experiment	90
Figure 3.9	The comparison of longitudinal velocity distribution across the flume for Ye and McCorquodale's (1997) at cross-section 1.....	91
Figure 3.10	The comparison of longitudinal velocity distribution across the flume for Ye and McCorquodale's (1997) at cross-section 2.....	91
Figure 3.11	The comparison of longitudinal velocity distribution across the flume for Ye and McCorquodale's (1997) at cross-section 3.....	92
Figure 3.12	The comparison of longitudinal velocity distribution across the flume for Ye and McCorquodale's (1997) at cross-section 4.....	92
Figure 3.13	The comparison of longitudinal velocity distribution across the flume for Ye and McCorquodale's (1997) at cross-section 5.....	93
Figure 3.14	The comparison of longitudinal velocity distribution across the flume for Ye and McCorquodale's (1997) at cross-section 6.....	93

Figure 3.15	The comparison of longitudinal velocity distribution across the flume for Ye and McCorquodale's (1997) at cross-section 7.....	94
Figure 4.1	The layout of DeVriend's (1976) experiment.....	143
Figure 4.2	Finite element mesh for DeVriend's (1976) experiment.....	144
Figure 4.3	The comparison of the longitudinal velocity distribution across the flume for DeVriend (1976) at cross-section 0 degrees.....	145
Figure 4.4	The comparison of the longitudinal velocity distribution across the flume for DeVriend (1976) at cross-section 30 degrees.....	145
Figure 4.5	The comparison of the longitudinal velocity distribution across the flume for DeVriend (1976) at cross-section 60 degrees.....	146
Figure 4.6	The comparison of the longitudinal velocity distribution across the flume for DeVriend (1976) at cross-section 90 degrees.....	146
Figure 4.7	The comparison of the longitudinal velocity distribution across the flume for DeVriend (1976) at cross-section 120 degrees.....	147
Figure 4.8	The comparison of the longitudinal velocity distribution across the flume for DeVriend (1976) at cross-section 150 degrees.....	147
Figure 4.9	The comparison of the longitudinal velocity distribution across the flume for DeVriend (1976) at cross-section 180 degrees.....	148
Figure 4.10	Numerical prediction of surface velocity distribution for DeVriend's (1976) experiment (VAM model).....	149
Figure 4.11	Numerical prediction of mean velocity distribution for DeVriend's (1976) experiment (VAM model).....	150

Figure 4.12	Numerical prediction of bed velocity distribution for DeVriend's (1976) experiment (VAM model).....	151
Figure 4.13	Numerical prediction of mean velocity distribution for DeVriend's (1976) experiment (VA model).....	152
Figure 4.14	Numerical prediction of mean velocity contours for DeVriend's (1976) experiment (VAM model)	153
Figure 4.15	Numerical prediction of mean velocity contours for DeVriend's (1976) experiment (VA model)	154
Figure 4.16	Numerical prediction of water surface elevation contours for DeVriend's (1976) experiment (VAM model)	155
Figure 4.17	The comparison of applying 5x5 VAM against 10x10 VAM models for longitudinal velocity distribution across the flume for DeVriend's (1976) at cross-section 30 degrees	156
Figure 4.18	The comparison of applying 5x5 VAM against 10x10 VAM models for longitudinal velocity distribution across the flume for DeVriend's (1976) at cross-section 90 degrees	156
Figure 4.19	The comparison of applying 5x5 VAM against 10x10 VAM models for longitudinal velocity distribution across the flume for DeVriend's (1976) at cross-section 180 degrees	157
Figure 4.20	The layout of DeVriend's (1980) experiment (adapted from DeVriend, 1980).....	158
Figure 4.21	Cross-sections geometry of DeVriend's (1980) experiment (adapted	

	from DeVriend, 1980)	159
Figure 4.22	Depth contours and characteristics of DeVriend's (1980) experiment (adapted from DeVriend, 1980).....	159
Figure 4.23	Finite element mesh for DeVriend's (1980) experiment	160
Figure 4.24	The comparison of the longitudinal velocity distribution across the flume for DeVriend (1980) at cross-section A_1	161
Figure 4.25	The comparison of the longitudinal velocity distribution across the flume for DeVriend (1980) at cross-section A_2	161
Figure 4.26	The comparison of the longitudinal velocity distribution across the flume for DeVriend (1980) at cross-section B_0	162
Figure 4.27	The comparison of the longitudinal velocity distribution across the flume for DeVriend (1980) at cross-section B_1	162
Figure 4.28	The comparison of the longitudinal velocity distribution across the flume for DeVriend (1980) at cross-section C_0	163
Figure 4.29	The comparison of the longitudinal velocity distribution across the flume for DeVriend (1980) at cross-section C_1	163
Figure 4.30	The comparison of the longitudinal velocity distribution across the flume for DeVriend (1980) at cross-section D_0	164
Figure 4.31	The comparison of the longitudinal velocity distribution across the flume for DeVriend (1980) at cross-section D_1	164
Figure 4.32	The comparison of the longitudinal velocity distribution across the flume for DeVriend (1980) at cross-section E_0	165

Figure 4.33	The comparison of the transverse surface velocity distribution across the flume for DeVriend (1980) at cross-section A_1	166
Figure 4.34	The comparison of the transverse surface velocity distribution across the flume for DeVriend (1980) at cross-section A_2	166
Figure 4.35	The comparison of the transverse surface velocity distribution across the flume for DeVriend (1980) at cross-section B_0	167
Figure 4.36	The comparison of the transverse surface velocity distribution across the flume for DeVriend (1980) at cross-section B_1	167
Figure 4.37	The comparison of the transverse surface velocity distribution across the flume for DeVriend (1980) at cross-section C_0	168
Figure 4.38	The comparison of the transverse surface velocity distribution across the flume for DeVriend (1980) at cross-section C_1	168
Figure 4.39	The comparison of the transverse surface velocity distribution across the flume for DeVriend (1980) at cross-section D_0	169
Figure 4.40	The comparison of the transverse surface velocity distribution across the flume for DeVriend (1980) at cross-section D_1	169
Figure 4.41	The comparison of the transverse surface velocity distribution across the flume for DeVriend (1980) at cross-section E_0	170
Figure 4.42	Numerical prediction of surface velocity distribution for DeVriend's (1980) experiment (VAM model)	171
Figure 4.43	Numerical prediction of mean velocity distribution for DeVriend's (1980) experiment (VAM model)	172

Figure 4.44	Numerical prediction of bed velocity distribution for DeVriend's (1980) experiment (VAM model)	173
Figure 4.45	Numerical prediction of mean velocity distribution for DeVriend's (1980) experiment (VA model)	174
Figure 4.46	The comparison of applying 5x5 VAM against 10x10 VAM models for longitudinal velocity distribution across the flume for DeVriend's (1980) at cross-section B ₁	175
Figure 4.47	The comparison of applying 5x5 VAM against 10x10 VAM models for longitudinal velocity distribution across the flume for DeVriend's (1980) at cross-section C ₀	175
Figure 4.48	The comparison of applying 5x5 VAM against 10x10 VAM models for longitudinal velocity distribution across the flume for DeVriend's (1980) at cross-section C ₁	176
Figure 4.49	The comparison of applying 5x5 VAM against 10x10 VAM models for transverse velocity distribution across the flume for DeVriend's (1980) at cross-section B ₁	176
Figure 4.50	The comparison of applying 5x5 VAM against 10x10 VAM models for transverse velocity distribution across the flume for DeVriend's (1980) at cross-section C ₀	177
Figure 4.51	The layout of Steffler's (1984) experiment	178
Figure 4.52	Finite element mesh for Steffler's (1984) experiment	179

Figure 4.53	The comparison of surface elevation across the flume for Steffler's (1984) run 1 at cross-section 0 degrees	180
Figure 4.54	The comparison of surface elevation across the flume for Steffler's (1984) run 1 at cross-section 90 degrees	180
Figure 4.55	The comparison of surface elevation across the flume for Steffler's (1984) run 1 at cross-section 180 degrees.....	181
Figure 4.56	The comparison of surface elevation across the flume for Steffler's (1984) run 1 at cross-section 270 degrees.....	181
Figure 4.57	The comparison of longitudinal velocity distribution across the flume for Steffler's (1984) run 1 at cross-section 0 degrees.....	182
Figure 4.58	The comparison of longitudinal velocity distribution across the flume for Steffler's (1984) run 1 at cross-section 90 degrees	182
Figure 4.59	The comparison of longitudinal velocity distribution across the flume for Steffler's (1984) run 1 at cross-section 180 degrees	183
Figure 4.60	The comparison of longitudinal velocity distribution across the flume for Steffler's (1984) run 1 at cross-section 270 degrees	183
Figure 4.61	The comparison of longitudinal velocity profile for Steffler's (1984) run 1 at cross-section 0 degrees and $y/b = -1$	184
Figure 4.62	The comparison of longitudinal velocity profile for Steffler's (1984) run 1 at cross-section 0 degrees and $y/b = -0.5$	184
Figure 4.63	The comparison of longitudinal velocity profile for Steffler's (1984) run 1 at cross-section 0 degrees and $y/b = 0$	185

Figure 4.64	The comparison of longitudinal velocity profile for Steffler's (1984) run 1 at cross-section 0 degrees and $y/b = 0.5$	185
Figure 4.65	The comparison of longitudinal velocity profile for Steffler's (1984) run 1 at cross-section 0 degrees and $y/b = 1$	186
Figure 4.66	The comparison of longitudinal velocity profile for Steffler's (1984) run 1 at cross-section 90 degrees and $y/b = -1$	187
Figure 4.67	The comparison of longitudinal velocity profile for Steffler's (1984) run 1 at cross-section 90 degrees and $y/b = -0.5$	187
Figure 4.68	The comparison of longitudinal velocity profile for Steffler's (1984) run 1 at cross-section 90 degrees and $y/b = 0$	188
Figure 4.69	The comparison of longitudinal velocity profile for Steffler's (1984) run 1 at cross-section 90 degrees and $y/b = 0.5$	188
Figure 4.70	The comparison of longitudinal velocity profile for Steffler's (1984) run 1 at cross-section 90 degrees and $y/b = 1$	189
Figure 4.71	The comparison of longitudinal velocity profile for Steffler's (1984) run 1 at cross-section 180 degrees and $y/b = -1$	190
Figure 4.72	The comparison of longitudinal velocity profile for Steffler's (1984) run 1 at cross-section 180 degrees and $y/b = -0.5$	190
Figure 4.73	The comparison of longitudinal velocity profile for Steffler's (1984) run 1 at cross-section 180 degrees and $y/b = 0$	191
Figure 4.74	The comparison of longitudinal velocity profile for Steffler's (1984) run 1 at cross-section 180 degrees and $y/b = 0.5$	191

Figure 4.75	The comparison of longitudinal velocity profile for Steffler's (1984) run 1 at cross-section 180 degrees and $y/b = 1$	192
Figure 4.76	The comparison of longitudinal velocity profile for Steffler's (1984) run 1 at cross-section 270 degrees and $y/b = -1$	193
Figure 4.77	The comparison of longitudinal velocity profile for Steffler's (1984) run 1 at cross-section 270 degrees and $y/b = -0.5$	193
Figure 4.78	The comparison of longitudinal velocity profile for Steffler's (1984) run 1 at cross-section 270 degrees and $y/b = 0$	194
Figure 4.79	The comparison of longitudinal velocity profile for Steffler's (1984) run 1 at cross-section 270 degrees and $y/b = 0.5$	194
Figure 4.80	The comparison of longitudinal velocity profile for Steffler's (1984) run 1 at cross-section 270 degrees and $y/b = 1$	195
Figure 4.81	The comparison of transverse surface velocity distribution across the flume for Steffler's (1984) run 1 at cross-section 0 degrees	196
Figure 4.82	The comparison of transverse surface velocity distribution across the flume for Steffler's (1984) run 1 at cross-section 90 degrees	196
Figure 4.83	The comparison of transverse surface velocity distribution across the flume for Steffler's (1984) run 1 at cross-section 180 degrees ...	197
Figure 4.84	The comparison of transverse surface velocity distribution across the flume for Steffler's (1984) run 1 at cross-section 270 degrees...	197
Figure 4.85	The comparison of transverse velocity profile for Steffler's (1984) run 1 at cross-section 0 degrees and $y/b = -1$	198

Figure 4.86	The comparison of transverse velocity profile for Steffler's (1984) run 1 at cross-section 0 degrees and $y/b = -0.5$	198
Figure 4.87	The comparison of transverse velocity profile for Steffler's (1984) run 1 at cross-section 0 degrees and $y/b = 0$	199
Figure 4.88	The comparison of transverse velocity profile for Steffler's (1984) run 1 at cross-section 0 degrees and $y/b = 0.5$	199
Figure 4.89	The comparison of transverse velocity profile for Steffler's (1984) run 1 at cross-section 0 degrees and $y/b = 1$	200
Figure 4.90	The comparison of transverse velocity profile for Steffler's (1984) run 1 at cross-section 90 degrees and $y/b = -1$	201
Figure 4.91	The comparison of transverse velocity profile for Steffler's (1984) run 1 at cross-section 90 degrees and $y/b = -0.5$	201
Figure 4.92	The comparison of transverse velocity profile for Steffler's (1984) run 1 at cross-section 90 degrees and $y/b = 0$	202
Figure 4.93	The comparison of transverse velocity profile for Steffler's (1984) run 1 at cross-section 90 degrees and $y/b = 0.5$	202
Figure 4.94	The comparison of transverse velocity profile for Steffler's (1984) run 1 at cross-section 90 degrees and $y/b = 1$	203
Figure 4.95	The comparison of transverse velocity profile for Steffler's (1984) run 1 at cross-section 180 degrees and $y/b = -1$	204
Figure 4.96	The comparison of transverse velocity profile for Steffler's (1984) run 1 at cross-section 180 degrees and $y/b = -0.5$	204

Figure 4.97	The comparison of transverse velocity profile for Steffler's (1984) run 1 at cross-section 180 degrees and $y/b = 0$	205
Figure 4.98	The comparison of transverse velocity profile for Steffler's (1984) run 1 at cross-section 180 degrees and $y/b = 0.5$	205
Figure 4.99	The comparison of transverse velocity profile for Steffler's (1984) run 1 at cross-section 180 degrees and $y/b = 1$	206
Figure 4.100	The comparison of transverse velocity profile for Steffler's (1984) run 1 at cross-section 270 degrees and $y/b = -1$	207
Figure 4.101	The comparison of transverse velocity profile for Steffler's (1984) run 1 at cross-section 270 degrees and $y/b = -0.5$	207
Figure 4.102	The comparison of transverse velocity profile for Steffler's (1984) run 1 at cross-section 270 degrees and $y/b = 0$	208
Figure 4.103	The comparison of transverse velocity profile for Steffler's (1984) run 1 at cross-section 270 degrees and $y/b = 0.5$	208
Figure 4.104	The comparison of transverse velocity profile for Steffler's (1984) run 1 at cross-section 270 degrees and $y/b = 1$	209
Figure 4.105	Numerical prediction of surface velocity distribution for Steffler's (1984) experiment (VAM model)	210
Figure 4.106	Numerical prediction of mean velocity distribution for Steffler's (1984) experiment (VAM model)	211
Figure 4.107	Numerical prediction of bed velocity distribution for Steffler's (1984) experiment (VAM model)	212

Figure 4.108	Numerical prediction of mean velocity distribution for Steffler's (1984) experiment (VA model)	213
Figure 4.109	Numerical prediction of mean velocity contours for Steffler's (1984) experiment (VAM model)	214
Figure 4.110	Numerical prediction of mean velocity contours for Steffler's (1984) experiment (VA model)	215
Figure 4.111	The comparison of applying 5x5 VAM against 10x10 VAM models for transverse velocity distribution across the flume for Steffler's (1984) run 1 at cross-section 180 degrees	216
Figure 4.112	The comparison of applying 5x5 VAM against 10x10 VAM models for transverse velocity distribution across the flume for Steffler's (1984) run 1 at cross-section 180 degrees	216
Figure 4.113	The comparison of applying 5x5 VAM against 10x10 VAM models for longitudinal velocity profile for Steffler's (1984) run 1 at cross-section 180 degrees and $y/b = -0.4$	217
Figure 4.114	The comparison of applying 5x5 VAM against 10x10 VAM models for longitudinal velocity profile for Steffler's (1984) run 1 at cross-section 180 degrees and $y/b = 0$	217
Figure 4.115	The comparison of applying 5x5 VAM against 10x10 VAM models for transverse velocity profile for Steffler's (1984) run 1 at cross-section 180 degrees and $y/b = -0.8$	218

Figure 4.116	The comparison of applying 5x5 VAM against 10x10 VAM models for transverse velocity profile for Steffler's (1984) run 1 at cross- section 180 degrees and $y/b = 0.8$	218
Figure 4.117	The comparison of of applying 5x5 VAM against 10x10 VAM models for longitudinal velocity distribution across the flume for Steffler's (1984) run 1 at cross-section 270 degrees	219
Figure 4.118	The comparison of of applying 5x5 VAM against 10x10 VAM models for transverse velocity distribution across the flume for Steffler's (1984) run 1 at cross-section 270 degrees	219
Figure 4.119	The comparison of applying 5x5 VAM against 10x10 VAM models for longitudinal velocity profile for Steffler's (1984) run 1 at cross- section 270 degrees and $y/b = -0.4$	220
Figure 4.120	The comparison of applying 5x5 VAM against 10x10 VAM models for longitudinal velocity profile for Steffler's (1984) run 1 at cross- section 270 degrees and $y/b = 0$	220
Figure 4.121	The comparison of applying 5x5 VAM against 10x10 VAM models for transverse velocity profile for Steffler's (1984) run 1 at cross- section 270 degrees and $y/b = -0.8$	221
Figure 4.122	The comparison of applying 5x5 VAM against 10x10 VAM models for transverse velocity profile for Steffler's (1984) run 1 at cross- section 270 degrees and $y/b = 0.8$	221
Figure 4.123	The layout of Rozovskii's (1961) experiment	222

Figure 4.124	Finite element mesh for Rozovskii's (1961) experiment	223
Figure 4.125	The comparison of surface elevation for Rozovskii's (1961) run 1 along the left side of the channel	224
Figure 4.126	The comparison of surface elevation for Rozovskii's (1961) run 1 along the center line of the channel	224
Figure 4.127	The comparison of surface elevation for Rozovskii's (1961) run 1 along the right side of the channel	225
Figure 4.128	The comparison of longitudinal velocity distribution across the flume for Rozovskii's (1961) run 1 at cross-section 1	226
Figure 4.129	The comparison of longitudinal velocity distribution across the flume for Rozovskii's (1961) run 1 at cross-section 2	226
Figure 4.130	The comparison of longitudinal velocity distribution across the flume for Rozovskii's (1961) run 1 at cross-section 3	227
Figure 4.131	The comparison of longitudinal velocity distribution across the flume for Rozovskii's (1961) run 1 at cross-section 5	227
Figure 4.132	The comparison of longitudinal velocity distribution across the flume for Rozovskii's (1961) run 1 at cross-section 6	228
Figure 4.133	The comparison of longitudinal velocity distribution across the flume for Rozovskii's (1961) run 1 at cross-section 9	228
Figure 4.134	The comparison of longitudinal velocity distribution across the flume for Rozovskii's (1961) run 1 at cross-section 10	229
Figure 4.135	The comparison of longitudinal velocity distribution across the flume for Rozovskii's (1961) run 1 at cross-section 11	229

Figure 4.136	The comparison of longitudinal velocity distribution across the flume for Rozovskii's (1961) run 1 at cross-section 12	230
Figure 4.137	The comparison of longitudinal velocity distribution across the flume for Rozovskii's (1961) run 1 at cross-section 13	230
Figure 4.138	The comparison of longitudinal velocity profile for Rozovskii's (1961) run 1 at cross-section 3 and $y/b = -1$	231
Figure 4.139	The comparison of longitudinal velocity profile for Rozovskii's (1961) run 1 at cross-section 3 and $y/b = -0.5$	231
Figure 4.140	The comparison of longitudinal velocity profile for Rozovskii's (1961) run 1 at cross-section 3 and $y/b = 0$	232
Figure 4.141	The comparison of longitudinal velocity profile for Rozovskii's (1961) run 1 at cross-section 3 and $y/b = 0.5$	232
Figure 4.142	The comparison of longitudinal velocity profile for Rozovskii's (1961) run 1 at cross-section 3 and $y/b = 1$	233
Figure 4.143	The comparison of longitudinal velocity profile for Rozovskii's (1961) run 1 at cross-section 3 and $y/b = -0.5$	234
Figure 4.144	The comparison of longitudinal velocity profile for Rozovskii's (1961) run 1 at cross-section 3 and $y/b = -0.25$	234
Figure 4.145	The comparison of longitudinal velocity profile for Rozovskii's (1961) run 1 at cross-section 3 and $y/b = 0$	235
Figure 4.146	The comparison of longitudinal velocity profile for Rozovskii's (1961) run 1 at cross-section 3 and $y/b = 0.25$	235

Figure 4.147	The comparison of longitudinal velocity profile for Rozovskii's (1961) run 1 at cross-section 3 and $y/b = 0.5$	236
Figure 4.148	The comparison of longitudinal velocity profile for Rozovskii's (1961) run 1 at cross-section 3 and $y/b = 0.75$	236
Figure 4.149	The comparison of longitudinal velocity profile for Rozovskii's (1961) run 1 at cross-section 3 and $y/b = 1$	237
Figure 4.150	The comparison of longitudinal velocity profile for Rozovskii's (1961) run 1 at cross-section 8 and $y/b = -0.5$	238
Figure 4.151	The comparison of longitudinal velocity profile for Rozovskii's (1961) run 1 at cross-section 8 and $y/b = 0$	238
Figure 4.152	The comparison of longitudinal velocity profile for Rozovskii's (1961) run 1 at cross-section 8 and $y/b = 0.5$	239
Figure 4.153	The comparison of longitudinal velocity profile for Rozovskii's (1961) run 1 at cross-section 8 and $y/b = 1$	239
Figure 4.154	The comparison of longitudinal velocity profile for Rozovskii's (1961) run 1 at cross-section 12 and $y/b = -1$	240
Figure 4.155	The comparison of longitudinal velocity profile for Rozovskii's (1961) run 1 at cross-section 12 and $y/b = -0.5$	240
Figure 4.156	The comparison of longitudinal velocity profile for Rozovskii's (1961) run 1 at cross-section 12 and $y/b = 0$	241
Figure 4.157	The comparison of longitudinal velocity profile for Rozovskii's (1961) run 1 at cross-section 12 and $y/b = 0.5$	241

Figure 4.158	The comparison of longitudinal velocity profile for Rozovskii's (1961) run 1 at cross-section 12 and $y/b = 1$	242
Figure 4.159	The comparison of transverse velocity profile for Rozovskii's (1961) run 1 at cross-section 3 and $y/b = -1$	243
Figure 4.160	The comparison of transverse velocity profile for Rozovskii's (1961) run 1 at cross-section 3 and $y/b = -0.5$	243
Figure 4.161	The comparison of transverse velocity profile for Rozovskii's (1961) run 1 at cross-section 3 and $y/b = 0$	244
Figure 4.162	The comparison of transverse velocity profile for Rozovskii's (1961) run 1 at cross-section 3 and $y/b = 0.5$	244
Figure 4.163	The comparison of transverse velocity profile for Rozovskii's (1961) run 1 at cross-section 3 and $y/b = 1$	245
Figure 4.164	The comparison of transverse velocity profile for Rozovskii's (1961) run 1 at cross-section 6 and $y/b = -1$	246
Figure 4.165	The comparison of transverse velocity profile for Rozovskii's (1961) run 1 at cross-section 6 and $y/b = -0.75$	246
Figure 4.166	The comparison of transverse velocity profile for Rozovskii's (1961) run 1 at cross-section 6 and $y/b = -0.5$	247
Figure 4.167	The comparison of transverse velocity profile for Rozovskii's (1961) run 1 at cross-section 6 and $y/b = -0.25$	247
Figure 4.168	The comparison of transverse velocity profile for Rozovskii's (1961) run 1 at cross-section 6 and $y/b = 0$	248

Figure 4.169	The comparison of transverse velocity profile for Rozovskii's (1961) run 1 at cross-section 6 and $y/b = 0.25$	248
Figure 4.170	The comparison of transverse velocity profile for Rozovskii's (1961) run 1 at cross-section 6 and $y/b = 0.5$	249
Figure 4.171	The comparison of transverse velocity profile for Rozovskii's (1961) run 1 at cross-section 6 and $y/b = 0.75$	249
Figure 4.172	The comparison of transverse velocity profile for Rozovskii's (1961) run 1 at cross-section 6 and $y/b = 1$	250
Figure 4.173	The comparison of transverse velocity profile for Rozovskii's (1961) run 1 at cross-section 8 and $y/b = -1$	261
Figure 4.174	The comparison of transverse velocity profile for Rozovskii's (1961) run 1 at cross-section 8 and $y/b = -0.5$	251
Figure 4.175	The comparison of transverse velocity profile for Rozovskii's (1961) run 1 at cross-section 8 and $y/b = 0$	252
Figure 4.176	The comparison of transverse velocity profile for Rozovskii's (1961) run 1 at cross-section 8 and $y/b = 0.5$	252
Figure 4.177	The comparison of transverse velocity profile for Rozovskii's (1961) run 1 at cross-section 8 and $y/b = 1$	253
Figure 4.178	Numerical prediction of surface velocity distribution for Rozovskii's (1961) experiment (VAM model)	254
Figure 4.179	Numerical prediction of mean velocity distribution for Rozovskii's (1961) experiment (VAM model)	255

Figure 4.180	Numerical prediction of bed velocity distribution for Rozovskii's (1961) experiment (VAM model)	256
Figure 4.181	Numerical prediction of mean velocity distribution for Rozovskii's (1961) experiment (VA model)	257
Figure 4.182	Numerical prediction of mean velocity contours for Rozovskii's (1961) experiment (VAM model)	258
Figure 4.183	Numerical prediction of mean velocity contours for Rozovskii's (1961) experiment (VA model)	259
Figure 4.184	Numerical prediction of water surface elevation contours for Rozovskii's (1961) experiment (VAM model)	260
Figure 4.185	The layout of Chang's (1971) experiment	261
Figure 4.186	Finite element mesh for Chang's (1971) experiment	262
Figure 4.187	The comparison of longitudinal velocity distribution across the flume for Chang (1971) at cross-section 1	263
Figure 4.188	The comparison of longitudinal velocity distribution across the flume for Chang (1971) at cross-section 3	263
Figure 4.189	The comparison of longitudinal velocity distribution across the flume for Chang (1971) at cross-section 5	264
Figure 4.190	The comparison of longitudinal velocity distribution across the flume for Chang (1971) at cross-section 7	264
Figure 4.191	The comparison of longitudinal velocity distribution across the flume for Chang (1971) at cross-section 9	265

Figure 4.192	The comparison of longitudinal velocity distribution across the flume for Chang (1971) at cross-section 11	265
Figure 4.193	The comparison of longitudinal velocity distribution across the flume for Chang (1971) at cross-section 13	266
Figure 4.194	Numerical prediction of surface velocity distribution for Chang's (1971) experiment (VAM model)	267
Figure 4.195	Numerical prediction of mean velocity distribution for Chang's (1971) experiment (VAM model)	268
Figure 4.196	Numerical prediction of bed velocity distribution for Chang's (1971) experiment (VAM model)	269
Figure 4.197	Numerical prediction of mean velocity distribution for Chang's (1971) experiment (VA model)	270
Figure 4.198	Numerical prediction of mean velocity contours for Chang's (1971) experiment (VAM model)	271
Figure 4.199	Numerical prediction of mean velocity contours for Chang's (1971) experiment (VA model)	272
Figure 4.200	The comparison of applying 5x5 VAM against 10x10 VAM models for longitudinal velocity distribution across the flume for Chang's (1971) at cross-section 7	273
Figure 4.201	The comparison of applying 5x5 VAM against 10x10 VAM models for longitudinal velocity distribution across the flume for Chang's (1971) at cross-section 9	273

Figure 4.202	Refined generated finite element mesh for DeVriend's (1976) experiment.....	274
Figure 4.203	Refined generated finite element mesh for Steffler's (1984) experiment	275
Figure 4.204	Refined generated finite element mesh for Chang's (1971) experiment	276
Figure 4.205	The comparison of the longitudinal velocity distribution across the flume for DeVriend (1976) at cross-section 30 degrees for two different generated finite element meshes.....	277
Figure 4.206	The comparison of the longitudinal velocity distribution across the flume for DeVriend (1976) at cross-section 120 degrees for two different generated finite element meshes.....	277
Figure 4.207	The comparison of the longitudinal velocity distribution across the flume for DeVriend (1976) at cross-section 150 degrees for two different generated finite element meshes.....	278
Figure 4.208	The comparison of the longitudinal velocity distribution across the flume for DeVriend (1976) at cross-section 180 degrees for two different generated finite element meshes.....	278
Figure 4.209	The comparison of longitudinal velocity distribution across the flume for Steffler's (1984) run 1 at cross-section 0 degrees for two different generated finite element meshes.....	279

Figure 4.210	The comparison of longitudinal velocity distribution across the flume for Steffler's (1984) run 1 at cross-section 90 degrees for two different generated finite element meshes.....	279
Figure 4.211	The comparison of longitudinal velocity distribution across the flume for Steffler's (1984) run 1 at cross-section 180 degrees for two different generated finite element meshes.....	280
Figure 4.212	The comparison of longitudinal velocity distribution across the flume for Steffler's (1984) run 1 at cross-section 270 degrees for two different generated finite element meshes.....	280
Figure 4.213	The comparison of longitudinal velocity distribution across the flume for Chang (1971) at cross-section 1 for two different generated finite element meshes.....	281
Figure 4.214	The comparison of longitudinal velocity distribution across the flume for Chang (1971) at cross-section 5 for two different generated finite element meshes.....	281
Figure 4.215	The comparison of longitudinal velocity distribution across the flume for Chang (1971) at cross-section 9 for two different generated finite element meshes.....	282
Figure 4.216	The comparison of longitudinal velocity distribution across the flume for Chang (1971) at cross-section 11 for two different generated finite element meshes.....	282

Figure 4.217	The comparison of longitudinal velocity profile for Steffler's (1984) run 1 at cross-section 0 degrees and $y/b = -0.8$ for two different generated finite element meshes.....	283
Figure 4.218	The comparison of longitudinal velocity profile for Steffler's (1984) run 1 at cross-section 0 degrees and $y/b = 0.8$ for two different generated finite element meshes.....	283
Figure 4.219	The comparison of longitudinal velocity profile for Steffler's (1984) run 1 at cross-section 90 degrees and $y/b = -0.8$ for two different generated finite element meshes.....	284
Figure 4.220	The comparison of longitudinal velocity profile for Steffler's (1984) run 1 at cross-section 90 degrees and $y/b = 0.8$ for two different generated finite element meshes.....	284
Figure 4.221	The comparison of longitudinal velocity profile for Steffler's (1984) run 1 at cross-section 180 degrees and $y/b = -0.8$ for two different generated finite element meshes.....	285
Figure 4.222	The comparison of longitudinal velocity profile for Steffler's (1984) run 1 at cross-section 180 degrees and $y/b = 0.8$ for two different generated finite element meshes.....	285
Figure 4.223	The comparison of longitudinal velocity profile for Steffler's (1984) run 1 at cross-section 270 degrees and $y/b = -0.8$ for two different generated finite element meshes.....	286

Figure 4.224	The comparison of longitudinal velocity profile for Steffler's (1984) run 1 at cross-section 270 degrees and $y/b = 0.8$ for two different generated finite element meshes.....	286
Figure 4.225	The comparison of transverse velocity profile for Steffler's (1984) run 1 at cross-section 0 degrees and $y/b = -0.8$ for two different generated finite element meshes.....	287
Figure 4.226	The comparison of transverse velocity profile for Steffler's (1984) run 1 at cross-section 0 degrees and $y/b = 0.8$ for two different generated finite element meshes.....	287
Figure 4.227	The comparison of transverse velocity profile for Steffler's (1984) run 1 at cross-section 90 degrees and $y/b = -0.8$ for two different generated finite element meshes.....	288
Figure 4.228	The comparison of transverse velocity profile for Steffler's (1984) run 1 at cross-section 90 degrees and $y/b = 0.8$ for two different generated finite element meshes.....	288
Figure 4.229	The comparison of transverse velocity profile for Steffler's (1984) run 1 at cross-section 180 degrees and $y/b = -0.8$ for two different generated finite element meshes.....	289
Figure 4.230	The comparison of transverse velocity profile for Steffler's (1984) run 1 at cross-section 180 degrees and $y/b = 0.8$ for two different generated finite element meshes.....	289

Figure 4.231	The comparison of transverse velocity profile for Steffler's (1984) run 1 at cross-section 270 degrees and $y/b = -0.8$ for two different generated finite element meshes.....	290
Figure 4.232	The comparison of transverse velocity profile for Steffler's (1984) run 1 at cross-section 270 degrees and $y/b = 0.8$ for two different generated finite element meshes.....	290
Figure 4.233	The comparison of extra non-hydrostatic pressure head (h_1) distribution across the flume for Steffler's (1984) run 1 at cross-section 180 degrees for two different generated finite element meshes.....	291
Figure 4.234	The comparison of extra non-hydrostatic pressure head (h_2) distribution across the flume for Steffler's (1984) run 1 at cross-section 180 degrees for two different generated finite element meshes.....	291
Figure 4.235	The comparison of average vertical velocity distribution across the flume for Steffler's (1984) run 1 at cross-section 180 degrees for two different generated finite element meshes.....	292
Figure 4.236	The comparison of applying VAM 5- against 10-equation models for longitudinal velocity profile for Steffler's (1984) run 1 at cross-section 180 degrees and $y/b = -0.8$ for the finer finite element mesh	293
Figure 4.237	The comparison of applying VAM 5- against 10-equation models for longitudinal velocity profile for Steffler's (1984) run 1 at cross-	

	section 180 degrees and $y/b = 0.8$ for the finer finite element mesh	293
Figure 4.238	The comparison of applying VAM 5- against 10-equation models for longitudinal velocity profile for Steffler's (1984) run 1 at cross-section 270 degrees and $y/b = -0.8$ for the finer finite element mesh	294
Figure 4.239	The comparison of applying VAM 5- against 10-equation models for longitudinal velocity profile for Steffler's (1984) run 1 at cross-section 270 degrees and $y/b = 0.8$ for the finer finite element mesh	294
Figure 4.240	The comparison of applying VAM 5- against 10-equation models for transverse velocity profile for Steffler's (1984) run 1 at cross-section 180 degrees and $y/b = -0.8$ for the finer finite element mesh	295
Figure 4.241	The comparison of applying VAM 5- against 10-equation models for transverse velocity profile for Steffler's (1984) run 1 at cross-section 180 degrees and $y/b = 0.8$ for the finer finite element mesh	295
Figure 4.242	The comparison of applying VAM 5- against 10-equation models for transverse velocity profile for Steffler's (1984) run 1 at cross-section 270 degrees and $y/b = -0.8$ for the finer finite element mesh	296

Figure 4.243	The comparison of applying VAM 5- against 10-equation models for transverse velocity profile for Steffler's (1984) run 1 at cross- section 270 degrees and $y/b = 0.8$ for the finer finite element mesh	296
Figure 4.244	Location of the study reach of the river Dommel (adapted from De Vriend and Geldof, 1983).....	297
Figure 4.245	Contour map of bed level in central part of the study reach of the river Dommel (adapted from De Vriend and Geldof, 1983)	298
Figure 4.246	Finite element mesh for the study reach of the river Dommel.....	299
Figure 4.247	The comparison of longitudinal velocity distribution across the river Dommel at cross-section 19.....	300
Figure 4.248	The comparison of longitudinal velocity distribution across the river Dommel at cross-section 21.....	300
Figure 4.249	The comparison of longitudinal velocity distribution across the river Dommel at cross-section 24.....	301
Figure 4.250	The comparison of longitudinal velocity distribution across the river Dommel at cross-section 26.....	301
Figure 4.251	The comparison of longitudinal velocity distribution across the river Dommel at cross-section 31.....	302
Figure 4.252	The comparison of longitudinal velocity distribution across the river Dommel at cross-section 33.....	302

Figure 4.253 The comparison of longitudinal velocity distribution across the
river Dommel at cross-section 35.....303

Figure 4.254 The comparison of longitudinal velocity distribution across the
river Dommel at cross-section 37.....303

List of Symbols

e	=	natural logarithmic constant = $\text{Exp}(1) = 2.71828$;
g	=	acceleration due to gravity;
h	=	depth of flow measured vertically;
h_1	=	bed pressure head in excess of hydrostatic pressure head;
h_2	=	mid-depth pressure head in excess of the average of pressure heads at the bed and surface;
i, j	=	tensor indices;
i_1, \dots, i_{68}	=	integral constants;
k_s	=	effective roughness height;
n_x	=	the x -component of the unit normal vector n .
n_y	=	the y -component of the unit normal vector n .
p	=	pressure;
p_1	=	bed pressure in excess of hydrostatic pressure;
p_2	=	mid-depth pressure in excess of the average of pressure at the bed and surface;
q_x	=	discharge per unit width of the channel in x -direction;
q_y	=	discharge per unit width of the channel in y -direction;
R_c	=	radius of the centerline of the curved flume;
$2b$	=	width of the flume;
t	=	time;
u	=	longitudinal velocity;

u_o	=	vertically averaged longitudinal velocity;
u_l	=	velocity at the surface in excess of the mean u_o ;
u_*	=	shear velocity;
v	=	transverse velocity;
v_o	=	vertically averaged transverse velocity;
v_l	=	velocity at the surface in excess of the mean v_o ;
w	=	vertical velocity;
w_b	=	vertical velocity at the bed;
\bar{w}	=	$1/2 w_b + 2/3 w_2 + 1/2 w_h$;
$\overline{w^2}$	=	$\bar{w}^2 + \frac{w_b^2}{12} + \frac{w_h^2}{12} - \frac{w_b w_h}{6} + \frac{1}{20} (2\bar{w} - w_b - w_h)^2$;
w_h	=	vertical velocity at the surface;
w_2	=	mid-depth vertical velocity in excess of the average of the vertical velocity at the bed and surface;
x	=	horizontal coordinate;
y	=	transverse coordinate;
z	=	vertical coordinate;
z_b	=	bed elevation;
\bar{z}	=	mid-depth elevation;
A	=	the area of the applied finite element;
C	=	Chezy coefficient;
C_1, \dots, C_{10}	=	constants;
C_*	=	dimensionless Chezy coefficient;

F	=	a weighted residual function;
N_e	=	number of nodes per element;
NS	=	total number of shape functions;
N_u	=	total number of unknowns;
Q	=	total discharge;
S_{fx}	=	friction slope in x -direction;
S_{fy}	=	friction slope in y -direction;
S_{ox}	=	bed slope in x -direction;
S_{oy}	=	bed slope in y -direction;
V	=	velocity;
VA	=	vertically averaged;
VAM	=	vertically averaged and moment;
V_n	=	transverse velocity along the normal (n -axis) to the s -axis;
V_s	=	longitudinal velocity along s -axis;
\mathbf{A}_x	=	the advection matrix in x -direction of the continuity, momentum in x -direction and momentum in y -direction equations respectively
	=	$\frac{\partial \mathbf{F}_x}{\partial \phi}$;
\mathbf{A}_y	=	the advection matrix in y -direction of the continuity, momentum in x -direction and momentum in y -direction equations respectively
	=	$\frac{\partial \mathbf{F}_y}{\partial \phi}$;
$\hat{\mathbf{B}}$	=	a matrix of weight functions;
\mathbf{B}	=	a matrix of test functions;

\mathbf{F}_x	=	a vector of x -derivative parts of the equations;
\mathbf{F}_y	=	a vector of y -derivative parts of the equations;
\mathbf{G}	=	a vector of non-derivative parts of the equations;
\mathbf{J}	=	Jacobian matrix;
\mathbf{q}_n	=	vector of normal discharge per unit width;
\mathbf{R}	=	Residual vector;
\mathbf{W}_x	=	upwinding matrix in x -direction;
\mathbf{W}_y	=	upwinding matrix in y -direction;
ψ	=	a vector of temporal parts of the equations;
ϕ	=	vector of unknown variables at each node;
$\tilde{\phi}$	=	trial function;
Φ	=	vector of nodal values of the unknown;
$\delta\Phi$	=	correction to the assumed guesses;
$f_1(\eta), g_1(\eta)$	=	functions defining the longitudinal velocity distribution shape;
$f_2(\eta), g_2(\eta)$	=	functions defining the transverse velocity distribution shape;
$f_3(\eta), g_3(\eta), H_3(\eta)$	=	functions defining the vertical velocity distribution shape;
$f_4(\eta), g_4(\eta)$	=	functions defining the pressure distribution shape;
Δx	=	discretization in the x -direction;
Δt	=	time increment;
Δy	=	discretization in the y -direction;
ν_h	=	eddy viscosity in x - y direction;

ν_z	=	eddy viscosity in z-direction;
η	=	non-dimensional vertical coordinate;
ε	=	the error norm;
ε_g	=	a user specified goal relative change of all the variables;
Γ	=	the boundary domain;
ω	=	upwinding parameter;
Ω	=	the solution domain;
λ	=	wavelength;
ρ	=	density;
θ	=	implicitness factor;
$\sigma_x = \tau_{xx}$	=	total turbulent normal stress in x-direction;
$\sigma_y = \tau_{yy}$	=	total turbulent normal stress in y-direction;
$\sigma_z = \tau_{zz}$	=	total turbulent normal stress in z-direction;
$\bar{\sigma}_x = \bar{\tau}_{xx}$	=	vertically averaged total turbulent normal stress in x-direction;
$\bar{\sigma}_y = \bar{\tau}_{yy}$	=	vertically averaged total turbulent normal stress in y-direction;
$\bar{\sigma}_z = \bar{\tau}_{zz}$	=	vertically averaged total turbulent normal stress in z-direction;
$\tau_{xy} = \tau_{yx}$	=	total turbulent shear stress in x-y plane;
$\tau_{xz} = \tau_{zx}$	=	total turbulent shear stress in x-z plane;
$\tau_{yz} = \tau_{zy}$	=	total turbulent shear stress in y-z plane;
$\bar{\tau}_{xy} = \bar{\tau}_{yx}$	=	vertically averaged total turbulent shear stress in x-y plane;
$\bar{\tau}_{xz} = \bar{\tau}_{zx}$	=	vertically averaged total turbulent shear stress in x-z plane;

$\bar{\tau}_{yz} = \bar{\tau}_{zy} =$ vertically averaged total turbulent shear stress in y - z plane;

τ_{xb} = bed shear stress in x - z plane;

τ_{yb} = bed shear stress in y - z plane;

Chapter 1

Introduction

Most open-channel computational models are based on the conventional depth averaged de St. Venant equations. The derivation of the de St. Venant equations is normally based on the assumptions of uniform velocity and hydrostatic pressure distributions. Other distributions may be used but must be pre-specified with respect to both magnitude and shape. The depth averaging process used to derive de St. Venant equations sacrifices flow details over the vertical dimension for simplicity and substantially reduced computational effort. Thus, they are limited to cases with horizontal length scales much greater than the channel depth (very shallow flows, with wavelength to depth ratio in excess of about 20 (Henderson, 1966)).

Loss of vertical distribution information makes consideration of secondary flows limited as in case of river meandering and channel bends. With only the mean velocity and depth available from the de St. Venant equations, uniform flow bed shear relationships are used even for cases which involve highly non-uniform velocity. As a result, the de St. Venant equations are inapplicable for modeling flow situations that involve non-hydrostatic pressure and/or non-uniform velocity distributions and with length scales close to channel depth (Steffler and Jin, 1993). These flow situations include: bed form growth and migration, rapidly varied flows in hydraulic structures, sudden contractions and expansions. These are important practical problems and require relatively accurate solutions.

A number of approaches have been proposed in the past to model short length scale flow problems. Most of these attempts were based on the assumption that the flow could be approximated as potential flow. In such cases, the vertical velocities and non-hydrostatic pressure distributions were used to predict the flow field characteristics. Another approach is to use the Boussinesq equations. The Boussinesq equations represent the next higher level of approximation compared to the traditional de St. Venant equations as they assume linear vertical velocity and non-hydrostatic linear pressure distributions (Henderson, 1966). These equations are applicable for moderately shallow flows with wavelength to depth ratio of about six (Steffler and Jin, 1993).

A further alternative in this area was the introduction of the vertically averaged and moment equations by Steffler and Jin (1993). They assumed linear longitudinal velocity distribution, and quadratic vertical and pressure distributions. They derived the equations for the one-dimensional case. In their approach, the plane Reynolds equations were vertically averaged and the moment equations were derived by vertically integrating the same Reynolds equations having been multiplied by the vertical coordinate. They showed that their equations are valid up to a wavelength to depth ratio of about one.

Application of a 3-D model would overcome all of the above limitations. However, the additional non-linearity caused by the free surface, the much greater

computational effort required and the difficulty in finding a suitable numerical scheme are the limiting factors.

In this study, a new set of two-dimensional vertically averaged and moment (termed VAM) equations model is developed. This development could be considered as the extension to the one- dimensional vertically averaged and moment equations introduced by Steffler and Jin (1993). Alternatively, it could be represented as a quasi three-dimensional model where more vertical details are included, without extending to the full three- dimensional Navier Stokes equations.

The VAM equations are derived by vertically averaging or integrating the three-dimensional Reynolds equations after multiplying them by the vertical coordinate. This derivation is equivalent to the first moment about the mid-depth of the channel. Vertical distributions for the velocities as well as the pressure are considered in general form to derive the equations as generally as possible.

The VAM equations are discretized and modeled using a hybrid Petrov-Galerkin and Bubnov-Galerkin finite element scheme. The Characteristic Dissipative Petrov-Galerkin finite element scheme recently used by Ghanem et al. (1995) is employed to upwind the continuity, horizontal momentum and moment of horizontal momentum equations. The rest of the equations are modeled using the Bubnov-Galerkin finite element scheme.

Triangular elements with linear basis functions for all variables are used. The time derivatives are approximated using a weighted-implicit finite difference formulation. For the resulting implicit set of non-linear algebraic equations a Newton-Raphson technique is used to advance the solution to the next time. Transient and steady state solution methods are used to solve the system of obtained non-linear equations.

Generated meshes with generally uniformly distributed elements are used in this study. When it is necessary, a non-uniform discretization is used so that elements are concentrated in areas where gradients are large, while fewer elements are used in areas where the flow is more uniform. This allows for optimization of computational effort. An existing finite element code (Ghanem et. al, 1995) is modified to suit the new set of developed equations. The new code (R2D_VAM) is written in standard C language.

The developed general VAM equations are adapted to allow for the use of definite pre-assumed distribution shapes of velocities and pressure for comparison and convenience purposes. Two different sets of horizontal velocity distributions, linear and quadratic, while quadratic vertical velocity and pressure distributions are considered.

The details of the derivation of the VAM equations and the analysis of the numerical methods applied are presented in chapter two.

As a first test, the proposed VAM model is tested for the uniform steady state case. Then, a one-dimensional laboratory scale test is carried out to check if the developed equations are derived and coded correctly. These tests are carried out in chapter two.

In chapter three, the proposed VAM model is investigated for simulating rapidly varied flow transitions with relatively small wavelength to depth ratios of about seven where non-hydrostatic pressure and non-uniform velocity distributions might be expected to be significant. The main goal is to see if there is an improvement of the proposed model over the conventional de Saint Venant model in simulating flows with such transitions. Two channel laboratory scale experimental tests are selected for validation and comparison purposes. These experiments include: flow through a rapid contraction and flow through sudden contraction and expansion interconnected with a throat section with parallel side walls. Comparisons of numerical predictions and the corresponding experimental results are presented.

In chapter four, the proposed VAM model is investigated for modeling curved open channel flows. The proposed model is tested for simulation of the secondary flow variation in curved channels and the effects of the secondary flow on the depth-averaged flow field. Evaluation of the sensitivity of the results to different approximations of the pre-assumed velocity and pressure distribution shapes is carried out. Comparison between different approximations of the pre-assumed velocity and pressure distribution shapes in terms of computational effort and time necessary for simulation is also presented. Finally, comparison between different

approximations of the numerical discretization of the generated applied finite element meshes in terms of degree of accuracy attained, computational effort and time necessary for simulation is carried out.

Five curved channel laboratory scale experimental tests are selected for validation and comparison purposes. These experiments include: flow in a 180° channel bend with mild curvature, flow in a 90° channel bend with a very irregular cross section, flow in a 270° channel bend, flow in a 180° channel bend with very strong curvature, and flow in two reversing 90° channel bends respectively. In addition, a field case is chosen to test the ability of the proposed model to simulate real situation flows. Comparisons of various numerical predictions and the corresponding experimental results are presented.

The summary, major conclusions and recommendations for future work follow in chapter five. The full details of the numerical scheme applied are provided in appendix A.

References

Ghanem, A., Steffler, P. M., Hicks, F. E. and Katopodis, 1995. "Two-Dimensional Finite Element Modeling of Flow in Aquatic Habitats". Water resources Engineering Report No. 95-S1, Department of Civil Engineering, University of Alberta.

Henderson, F. M., 1966. "Open Channel Flow". Book, The Mcmillan Company, New York.

Steffler, P. M. and Jin, Y. C., (1993). "Depth averaged and Moment Equations for Moderately Shallow Free Surface Flow." Journal of Hydraulic Research, IAHR, Vol. 31, No. 1, pp. 5-17.

Chapter 2

Derivation of the Two Dimensional Vertically Averaged and Moment Equations

2.1 Introduction

Most of the computational models in open channel flow problems use the classical depth averaged de St. Venant equations which can be written in the form (Liggett, 1974):

$$\frac{\partial h}{\partial t} + \frac{\partial q_x}{\partial x} + \frac{\partial q_y}{\partial y} = 0 \dots\dots\dots(2.1)$$

$$\frac{\partial q_x}{\partial t} + \frac{\partial u_o q_x}{\partial x} + \frac{\partial v_o q_x}{\partial y} + \frac{g}{2} \frac{\partial h^2}{\partial x} = gh(S_{ox} - S_{fx}) \dots\dots\dots(2.2)$$

$$\frac{\partial q_y}{\partial t} + \frac{\partial u_o q_y}{\partial x} + \frac{\partial v_o q_y}{\partial y} + \frac{g}{2} \frac{\partial h^2}{\partial y} = gh(S_{oy} - S_{fy}) \dots\dots\dots(2.3)$$

Where h is the depth of flow; q_x is the flow discharge in longitudinal direction per unit width; q_y is the flow discharge in transverse direction per unit width; u_o is the depth averaged longitudinal velocity; v_o is the depth averaged transverse velocity; S_{fx} is the friction slope in x-direction; S_{fy} is the friction slope in y-direction; S_{ox} is the bed slope in x-direction; S_{oy} is the bed slope in y-direction; g is the acceleration due to gravity; t is the time; and x and y are the Cartesian coordinates in the horizontal plane.

Equation (2.1) is the continuity equation, while equations (2.2) and (2.3) are the x and y -direction momentum equations, respectively. Together with appropriate initial and boundary conditions, de St. Venant equations define a 'model' for two-dimensional flow in open channels solving for three dependent variables: " h ", " q_x " and " q_y ".

The derivation of de St. Venant equations is based on the assumptions of uniform velocity and hydrostatic pressure distributions. The depth averaging process used to derive de St. Venant equations sacrifices flow details over the vertical dimension for simplicity and substantially reduced computational effort. Thus, they are valid only for horizontal length scales much greater than the channel depth (very shallow flows, with wavelength to depth ratio in excess of about 20 (Henderson, 1966)). Loss of vertical distribution information limits consideration of secondary flows as in case of meandering rivers. In addition, with only the mean velocity and depth available from the de St. Venant equations, only uniform flow bed shear relationships are used even for cases which involve highly non-uniform velocity. Developing pressure gradients may cause considerable local difference effects.

As a result, the previous equations are inapplicable for modeling flow situations that involve non-uniform velocity and/or non-hydrostatic pressure distributions and with length scales close to channel depth (Steffler and Jin, 1993a). These flow situations include: rapidly varied flows in hydraulic structures, sudden contractions and expansions, and flow over bed form and around alluvial channel which may result in

scour and erosion. These are important problems and require relatively accurate solutions in open channel hydraulics.

A number of attempts or approaches have been proposed in the past to model short length scale flow problems. Most of these attempts were based on the assumption that the flow could be approximated as potential flow in which vertical velocities and non-hydrostatic pressure distributions were used to predict the flow field characteristics. A prediction of potential flow field over dunes and antidunes was provided by Kennedy (1963). Boussinesq equations, which assume linear vertical velocity and non-hydrostatic linear pressure distributions, represent the next level of approximation compared to the de St. Venant equations (Henderson, 1966). These equations are applicable for moderately shallow flows with wavelength to depth ratio of about six (Steffler and Jin, 1993a). Dressler (1978) introduced a bed curvilinear coordinate system into the Euler equations to come up with more general depth averaged equations.

Application of a 3-D model would overcome all of the above limitations. However, due to the additional non-linearity caused by the free surface; the much greater computational effort required and the difficulty in finding a suitable numerical scheme and mesh or grid generation system, the application of 3-D model is not an easy task or alternative. An attempt to apply a three-dimensional model was carried out by Shimuzi et al. (1990). They found that a three-dimensional model gave better results than a two-dimensional depth averaged model including secondary flows for

predicting flow fields for a curved channel bed topography problem. Odgaard et al. (1998) developed a three-dimensional model for simulating flow through natural river reaches. The model solved the Reynolds averaged Navier Stokes equations. The $k-\varepsilon$ turbulence closure model was used in their model. Calculations were carried out for flow through a 4-km stretch of Columbia River downstream of the Wanapum Dam. Comparisons of computed mean velocity profiles with field measurements were presented.

Steffler and Jin (1993a) introduced a further alternative in this area to recover more vertical details. They developed a new set of vertically averaged and moment equations. They derived the equations for the case of one-dimensional model in which they assumed a linear longitudinal velocity distribution, and quadratic vertical and pressure distributions. In their approach, the vertical plane Reynolds equations were vertically averaged and the moment equations were derived by vertically integrating the same Reynolds equations having been multiplied by the vertical coordinate. Three extra equations were developed which allowed specification of three further flow parameters due to their assumed flow distributions. Successful numerical applications for that model were carried out by Khan (1995). He applied the model to cases with rapidly varied changes, e.g. free overfalls, smooth transition from a horizontal to a very steep bed, flow over curved beds and a hydraulic jump.

Naef (1996) extended the same model, depth-averaged and moment equations, derived by Steffler and Jin (1993a) for the 1-D case, to a 2-D model. The turbulent

stresses were neglected. The model was verified for partial dam-break problems. A fairly reasonable agreement was obtained.

Jin and Li (1996) improved the two-dimensional depth-averaged model derived by Steffler and Jin (1993b) to account for the effects of non-hydrostatic pressure distribution. The non-hydrostatic pressure distribution was added to the z-direction momentum equation and assumed to be linearly decreasing from the bed up to the surface. Thus the pressure-effect terms were modified in both the moment of momentum and momentum equations. The resulting set of one-dimensional nonlinear equations was solved by a finite element Galerkin method. The model was verified for uniform open-channel flow over dunes, free surface flow over a sill and flow through a rectangular free overfall.

The objectives of this study are as follows:

1. To derive and establish a 2-D vertically averaged and moment free surface flow model in which more vertical details concerning velocity and pressure distributions can be recovered.
2. To derive the new set of equations as generally as possible to be able to accommodate different kinds of distribution shapes assumed for velocities as well as pressure.

The derivation of the new equations could be considered as the extension to the one-dimensional vertically averaged and moment equations introduced by Steffler and Jin (1993a). Alternatively, it could be represented as a quasi three-dimensional model where more vertical details are accounted for, without extending to the full three-dimensional Navier Stokes equations.

2.2 Derivation of the Vertically Averaged and Moment Equation Model

The vertically averaged and moment equations can be derived by applying the conventional laws of mass, momentum and moment of momentum conservation to a prismatic vertical water column bounded by the bed from the bottom and the free water surface from the top (Van Rijn, 1990). Alternatively, they can be derived by vertically integrating the full three-dimensional Reynolds equations after being multiplied by the vertical coordinate (Steffler and Jin, 1993a). Herein, the latter approach is chosen.

With reference to the definition sketch shown in Figure 2.1, the x - y direction forming the horizontal frame while the z direction forming the vertical coordinate, the fundamental full three-dimensional Reynolds equations read:

$$\frac{\partial u}{\partial x} + \frac{\partial v}{\partial y} + \frac{\partial w}{\partial z} = 0 \dots\dots\dots(2.4)$$

$$\frac{\partial u}{\partial t} + \frac{\partial u^2}{\partial x} + \frac{\partial uv}{\partial y} + \frac{\partial uw}{\partial z} = -\frac{1}{\rho} \frac{\partial p}{\partial x} + \frac{1}{\rho} \left(\frac{\partial \sigma_x}{\partial x} + \frac{\partial \tau_{xy}}{\partial y} + \frac{\partial \tau_{xz}}{\partial z} \right) \dots\dots\dots(2.5)$$

$$\frac{\partial v}{\partial t} + \frac{\partial vu}{\partial x} + \frac{\partial v^2}{\partial y} + \frac{\partial vw}{\partial z} = -\frac{1}{\rho} \frac{\partial p}{\partial y} + \frac{1}{\rho} \left(\frac{\partial \tau_{yx}}{\partial x} + \frac{\partial \sigma_y}{\partial y} + \frac{\partial \tau_{yz}}{\partial z} \right) \dots\dots\dots(2.6)$$

$$\frac{\partial w}{\partial t} + \frac{\partial wu}{\partial x} + \frac{\partial wv}{\partial y} + \frac{\partial w^2}{\partial z} = -\frac{1}{\rho} \frac{\partial p}{\partial z} + \frac{1}{\rho} \left(\frac{\partial \tau_{xz}}{\partial x} + \frac{\partial \tau_{zy}}{\partial y} + \frac{\partial \sigma_z}{\partial z} \right) \dots\dots\dots(2.7)$$

Where u is the longitudinal velocity, v is the transverse velocity, w is the vertical velocity, τ is the total turbulent shear stress, σ is the total turbulent normal stress, p is the pressure, and ρ is the density of water. Equation (2.4) represents the continuity equation, equation (2.5) represents the horizontal momentum equation, equation (2.6) represents the transverse momentum equation, and equation (2.7) represents the vertical momentum equation.

The vertically averaged equations (termed VA) are derived by vertically integrating the above three-dimensional Reynolds equations over the vertical from the bed level up to the surface. This can be explained as follows:

$$\int_{z_b}^{z_b+h} \left(\frac{\partial u}{\partial x} + \frac{\partial v}{\partial y} + \frac{\partial w}{\partial z} \right) dz = 0 \dots\dots\dots(2.8)$$

$$\int_{z_b}^{z_b+h} \left(\frac{\partial u}{\partial t} + \frac{\partial u^2}{\partial x} + \frac{\partial uv}{\partial y} + \frac{\partial uw}{\partial z} \right) dz = \int_{z_b}^{z_b+h} \left(-\frac{1}{\rho} \frac{\partial p}{\partial x} + \frac{1}{\rho} \left(\frac{\partial \sigma_x}{\partial x} + \frac{\partial \tau_{xy}}{\partial y} + \frac{\partial \tau_{xz}}{\partial z} \right) \right) dz \dots\dots\dots(2.9)$$

$$\int_{z_b}^{z_b+h} \left(\frac{\partial v}{\partial t} + \frac{\partial vu}{\partial x} + \frac{\partial v^2}{\partial y} + \frac{\partial vw}{\partial z} \right) dz = \int_{z_b}^{z_b+h} \left(-\frac{1}{\rho} \frac{\partial p}{\partial y} + \frac{1}{\rho} \left(\frac{\partial \tau_{yx}}{\partial x} + \frac{\partial \sigma_y}{\partial y} + \frac{\partial \tau_{yz}}{\partial z} \right) \right) dz \dots\dots(2.10)$$

$$\int_{z_b}^{z_b+h} \left(\frac{\partial w}{\partial t} + \frac{\partial wu}{\partial x} + \frac{\partial wv}{\partial y} + \frac{\partial w^2}{\partial z} \right) dz = \int_{z_b}^{z_b+h} \left(-\frac{1}{\rho} \frac{\partial p}{\partial z} + \frac{1}{\rho} \left(\frac{\partial \tau_{zx}}{\partial x} + \frac{\partial \tau_{zy}}{\partial y} + \frac{\partial \sigma_z}{\partial z} \right) \right) dz \dots\dots(2.11)$$

Where z_b is the bed elevation. Vertical distributions for the velocities as well as the pressure are required to perform the above integrations. Herein, the distributions are treated as general functions to derive the equations as generally as possible.

The following distributions are assumed for the horizontal velocity components (Figures 2.2-2.3):

$$u = u_o f_1(\eta) + u_l g_1(\eta) \dots\dots\dots(2.12)$$

$$v = v_o f_2(\eta) + v_l g_2(\eta) \dots\dots\dots(2.13)$$

Where $f_1(\eta)$, $g_1(\eta)$, $f_2(\eta)$ and $g_2(\eta)$ are functions defining the distribution shapes of the horizontal velocity components. In both cases $\int_0^1 g_1(\eta) d\eta = \int_0^1 g_2(\eta) d\eta = 0$ and

$$\int_0^1 f_1(\eta) d\eta = \int_0^1 f_2(\eta) d\eta = 1 \text{ so that } u_o \text{ and } v_o \text{ are the depth averaged velocity}$$

components. In addition, $g_1(\eta=1) = g_2(\eta=1) = 1$. As a result, u_l and v_l can be

interpreted as the velocities at the water surface in excess of the means u_o and v_o respectively.

It should be mentioned that the assumption of $\int_0^1 g_1(\eta) d\eta = \int_0^1 g_2(\eta) d\eta = 0$ implies that

there is no net transverse transport of fluid in the channel. That is to say that the rate at which fluid is transported outward over the upper half of the profile equals the rate at which fluid moves inward over the lower half.

The non-dimensional vertical coordinate η is defined as:

$$\eta = (z - z_b)/h \dots \dots \dots (2.14)$$

The following distribution of vertical velocity is considered (Figure 2.4):

$$w = w_b f_3(\eta) + w_2 g_3(\eta) + w_h H_3(\eta) \dots \dots \dots (2.15)$$

Where $f_3(\eta)$, $g_3(\eta)$ and $H_3(\eta)$ are functions defining the distribution shape of the vertical velocity, w_b is the vertical velocity at the bed, w_h is the vertical velocity at the surface and w_2 is the mid-depth vertical velocity in excess of the average of vertical velocities at the surface and bed.

The vertical velocity at the bed, w_b , is given by the following kinematic bed boundary condition:

$$w_b = (u_o - C_1 u_1) \frac{\partial z_b}{\partial x} + (v_o - C_1 v_1) \frac{\partial z_b}{\partial y} \dots\dots\dots(2.16)$$

This condition assumes that the bed stays fixed with time and the flow is parallel to the bed. C_1 is a constant that depends on the pre-assumed distribution shapes of the horizontal velocity components.

The surface vertical velocity w_h is given by the following kinematic surface condition:

$$w_h = \frac{\partial h}{\partial t} + (u_o + u_1) \frac{\partial}{\partial x} (h + z_b) + (v_o + v_1) \frac{\partial}{\partial y} (h + z_b) \dots\dots\dots(2.17)$$

The following pressure distribution is considered (Figure 2.5):

$$p = \rho g h f_4(\eta) + p_1 f_4(\eta) + p_2 g_4(\eta) \dots\dots\dots(2.18)$$

Where $f_4(\eta)$ and $g_4(\eta)$ are functions defining the different distribution shapes of the pressure, p_1 is the pressure intensity in excess of the hydrostatic at bed and p_2 is the mid-depth pressure in excess of the average of pressures at the bed and surface.

The water surface dynamic conditions are given by $p_h = \tau_h = \sigma_h = 0.0$ which assume that the pressure is atmospheric and turbulent shear and normal stresses at the surface are negligible (Steffler and Jin, 1993a).

Having inserted the previous proposed distributions into equations (2.8)-(2.11), applied the aforementioned kinematic and boundary conditions, made the use of Liebig's rule, we are left with four vertically averaged equations. These equations may be written and described as:

The vertically averaged continuity equation is:

$$\frac{\partial h}{\partial t} + \frac{\partial}{\partial x}(q_x i_1 + u_1 h i_2) + \frac{\partial}{\partial y}(q_y i_3 + v_1 h i_4) = 0 \dots\dots\dots(2.19)$$

The vertically averaged momentum equation in the x-direction is:

$$\begin{aligned} & \frac{\partial}{\partial t}(q_x i_1 + u_1 h i_2) + \frac{\partial}{\partial x} \left(\frac{q_x^2}{h} i_5 + q_x u_1 i_6 + u_1^2 h i_7 + g h^2 i_{30} \right) \\ & + \frac{\partial}{\partial y} \left(\frac{q_x q_y}{h} i_{11} + q_x v_1 i_{12} + u_1 q_y i_{13} + u_1 v_1 h i_{14} \right) + \frac{\partial}{\partial x} \left(\frac{p_1 h i_{30}}{\rho} + \frac{p_2 h i_{31}}{\rho} - \frac{h \bar{\sigma}_x}{\rho} \right) \dots (2.20) \\ & + \frac{\partial}{\partial y} \left(\frac{-h \bar{\tau}_{xy}}{\rho} \right) + \frac{1}{\rho} \left\{ (\rho g h + p_1) \frac{\partial z_b}{\partial x} + \tau_{x_b} \right\} = 0 \end{aligned}$$

The vertically averaged momentum equation in the y-direction is:

$$\begin{aligned}
& \frac{\partial}{\partial t} (q_y i_3 + v_1 h i_4) + \frac{\partial}{\partial x} \left(\frac{q_x q_y}{h} i_{11} + q_x v_1 i_{12} + u_1 q_y i_{13} + u_1 v_1 h i_{14} \right) \\
& + \frac{\partial}{\partial y} \left(\frac{q_y^2}{h} i_8 + q_y v_1 i_9 + v_1^2 h i_{10} + g h^2 i_{30} \right) + \frac{\partial}{\partial y} \left(\frac{p_1 h i_{30}}{\rho} + \frac{p_2 h i_{31}}{\rho} - \frac{h \bar{\sigma}_y}{\rho} \right) \dots \dots \dots (2.21) \\
& + \frac{\partial}{\partial x} \left(\frac{-h \bar{\tau}_{yx}}{\rho} \right) + \frac{1}{\rho} \left\{ (\rho g h + p_1) \frac{\partial z_b}{\partial y} + \tau_{yz_b} \right\} = 0
\end{aligned}$$

The vertically averaged momentum equation in the z-direction is:

$$\begin{aligned}
& \frac{\partial}{\partial t} (w_b h i_{15} + w_2 h i_{16} + w_h h i_{17}) \\
& + \frac{\partial}{\partial x} [w_b (q_x i_{18} + u_1 h i_{19}) + w_2 (q_x i_{20} + u_1 h i_{21}) + w_h (q_x i_{22} + u_1 h i_{23})] \\
& \dots \dots \dots (2.22) \\
& + \frac{\partial}{\partial y} [w_b (q_y i_{24} + v_1 h i_{25}) + w_2 (q_y i_{26} + v_1 h i_{27}) + w_h (q_y i_{28} + v_1 h i_{29})] \\
& + \frac{\partial}{\partial x} \left(\frac{-h \bar{\tau}_x}{\rho} \right) + \frac{\partial}{\partial y} \left(\frac{-h \bar{\tau}_y}{\rho} \right) - \frac{1}{\rho} \left\{ p_1 + \tau_{yz_b} \frac{\partial z_b}{\partial y} + \tau_{xz_b} \frac{\partial z_b}{\partial x} \right\} = 0
\end{aligned}$$

Where i 's represent integral constants and are given in Appendix B.

Four further equations are required to close the above system of equations provided that all turbulent stresses are modeled by relating them to flow parameters. Basically, the additional required equations (vertically averaged and moment equations, termed VAM) are models for the four additional flow parameters u_I , v_I , p_2 and w_2 . These equations are derived by vertically averaged or integrating the same four Reynolds equations after they have been multiplied by a weighting function $F = 2(z - \bar{z})/h$, \bar{z} being the vertical coordinate at the middle of the channel and is equal to $z_b + h/2$. This derivation is equivalent to the first moment about the mid-depth of the channel. This can be done as follows:

$$\frac{2}{h} \int_{z_b}^{z_b+h} (z - \bar{z}) \left(\frac{\partial u}{\partial x} + \frac{\partial v}{\partial y} + \frac{\partial w}{\partial z} \right) dz = 0 \dots\dots\dots(2.23)$$

$$\begin{aligned} & \frac{2}{h} \int_{z_b}^{z_b+h} (z - \bar{z}) \left(\frac{\partial u}{\partial t} + \frac{\partial u^2}{\partial x} + \frac{\partial uv}{\partial y} + \frac{\partial uw}{\partial z} \right) dz \\ &= \dots\dots\dots(2.24) \\ & \frac{2}{h} \int_{z_b}^{z_b+h} (z - \bar{z}) \left(-\frac{1}{\rho} \frac{\partial p}{\partial x} + \frac{1}{\rho} \left(\frac{\partial \sigma_x}{\partial x} + \frac{\partial \tau_{xy}}{\partial y} + \frac{\partial \tau_{xz}}{\partial z} \right) \right) dz \end{aligned}$$

$$\begin{aligned}
& \frac{2}{h} \int_{z_b}^{z_b+h} (z - \bar{z}) \left(\frac{\partial v}{\partial t} + \frac{\partial vu}{\partial x} + \frac{\partial v^2}{\partial y} + \frac{\partial vw}{\partial z} \right) dz \\
& = \dots\dots\dots(2.25) \\
& \frac{2}{h} \int_{z_b}^{z_b+h} (z - \bar{z}) \left(-\frac{1}{\rho} \frac{\partial p}{\partial y} + \frac{1}{\rho} \left(\frac{\partial \tau_{yx}}{\partial x} + \frac{\partial \sigma_y}{\partial y} + \frac{\partial \tau_{yz}}{\partial z} \right) \right) dz
\end{aligned}$$

$$\begin{aligned}
& \frac{2}{h} \int_{z_b}^{z_b+h} (z - \bar{z}) \left(\frac{\partial w}{\partial t} + \frac{\partial wu}{\partial x} + \frac{\partial wv}{\partial y} + \frac{\partial w^2}{\partial z} \right) dz \\
& = \dots\dots\dots(2.26) \\
& \frac{2}{h} \int_{z_b}^{z_b+h} (z - \bar{z}) \left(-\frac{1}{\rho} \frac{\partial p}{\partial z} + \frac{1}{\rho} \left(\frac{\partial \tau_{zx}}{\partial x} + \frac{\partial \tau_{zy}}{\partial y} + \frac{\partial \sigma_z}{\partial z} \right) \right) dz
\end{aligned}$$

Having integrated, we are left with four further equations. These equations may be written and described as follows:

The moment of continuity equation is:

$$\begin{aligned}
& \frac{\partial}{\partial t} \left(\frac{h^2}{4} \right) + \frac{\partial}{\partial x} [q_x(h.i_{32} + z_b.i_1) + u_1 h(h.i_{33} + z_b.i_2)] + \frac{\partial}{\partial y} [q_y(h.i_{34} + z_b.i_3) + v_1 h(h.i_{35} + z_b.i_4)] \\
& - \bar{z} \left[\frac{\partial}{\partial x} (q_x.i_1 + u_1 h.i_2) + \frac{\partial}{\partial y} (q_y.i_3 + v_1 h.i_4) \right] - (w_b h.i_{15} + w_2 h.i_{16} + w_h h.i_{17}) = 0 \\
& \dots\dots\dots(2.27)
\end{aligned}$$

The moment of momentum equation in the x-direction is:

$$\begin{aligned}
& \frac{\partial}{\partial t} [q_x (h i_{32} + z_b i_1) + u_1 h (h i_{33} + z_b i_2)] \\
& + \frac{\partial}{\partial x} \left[\frac{q_x^2}{h} (h i_{36} + z_b i_5) + q_x u_1 (h i_{37} + z_b i_6) + u_1^2 h (h i_{38} + z_b i_7) \right] \\
& + \frac{\partial}{\partial y} \left[\frac{q_x q_y}{h} (h i_{44} + z_b i_{11}) + q_x v_1 (h i_{46} + z_b i_{12}) + q_y u_1 (h i_{45} + z_b i_{13}) + v_1 u_1 h (h i_{47} + z_b i_{14}) \right] \\
& + \frac{\partial}{\partial x} \left[g h^2 (h i_{39} + z_b i_{30}) + \frac{p_1 h (h i_{39} + z_b i_{30})}{\rho} + \frac{p_2 h (h i_{40} + z_b i_{31})}{\rho} \right] \\
& - \bar{z} \left[\frac{\partial}{\partial t} (q_x i_1 + u_1 h i_2) + \frac{\partial}{\partial x} \left(\frac{q_x^2}{h} i_5 + q_x u_1 h i_6 + u_1^2 h i_7 \right) \right. \\
& \quad \left. + \frac{\partial}{\partial y} \left(\frac{q_x q_y}{h} i_{11} + q_x v_1 i_{12} + q_y u_1 i_{13} + v_1 u_1 h i_{14} \right) \right] \\
& - [w_b (q_x i_{18} + u_1 h i_{19}) + w_2 (q_x i_{20} + u_1 h i_{21}) + w_h (q_x i_{22} + u_1 h i_{23})] \\
& \dots\dots\dots(2.28) \\
& + \frac{1}{\rho} \left\{ \rho g \left[-\bar{z} \frac{\partial h^2 i_{30}}{\partial x} - \frac{h^2}{2} \frac{\partial z_b}{\partial x} \right] - \bar{z} \frac{\partial p_1 h i_{30}}{\partial x} - \frac{p_1 h}{2} \frac{\partial z_b}{\partial x} \right. \\
& \quad \left. - \bar{z} \frac{\partial p_2 h i_{31}}{\partial x} - h \bar{\sigma}_x \frac{\partial \bar{z}}{\partial x} - h \bar{\tau}_{xy} \frac{\partial \bar{z}}{\partial y} - \frac{h}{2} \tau_{xz} + h \bar{\tau}_{xz} \right\} = 0
\end{aligned}$$

The moment of momentum equation in the y -direction is:

$$\begin{aligned}
& \frac{\partial}{\partial t} [q_y (h i_{34} + z_b i_3) + v_1 h (h i_{35} + z_b i_4)] \\
& + \frac{\partial}{\partial x} \left[\frac{q_x q_y}{h} (h i_{44} + z_b i_{11}) + q_x v_1 (h i_{46} + z_b i_{12}) \right. \\
& \quad \left. + q_y u_1 (h i_{45} + z_b i_{13}) + v_1 u_1 h (h i_{47} + z_b i_{14}) \right] \\
& + \frac{\partial}{\partial y} \left[\frac{q_x^2}{h} (h i_{41} + z_b i_8) + q_y v_1 (h i_{42} + z_b i_9) + v_1^2 h (h i_{43} + z_b i_{10}) \right] \\
& + \frac{\partial}{\partial y} \left[g h^2 (h i_{39} + z_b i_{30}) + \frac{p_1 h (h i_{39} + z_b i_{30})}{\rho} + \frac{p_2 h (h i_{40} + z_b i_{31})}{\rho} \right] \\
& - \bar{z} \left[\frac{\partial}{\partial t} (q_y i_3 + v_1 h i_4) + \frac{\partial}{\partial x} \left(\frac{q_x q_y}{h} i_{11} + q_x v_1 i_{12} + q_y u_1 i_{13} + v_1 u_1 h i_{14} \right) \right. \\
& \quad \left. + \frac{\partial}{\partial y} \left(\frac{q_y^2}{h} i_8 + q_y v_1 i_9 + v_1^2 h i_{10} \right) \right] \\
& - [w_b (q_y i_{24} + v_1 h i_{25}) + w_2 (q_y i_{26} + v_1 h i_{27}) + w_h (q_y i_{28} + v_1 h i_{29})] \\
& + \frac{1}{\rho} \left\{ \rho g \left[-\bar{z} \frac{\partial h^2 i_{30}}{\partial y} - \frac{h^2}{2} \frac{\partial z_b}{\partial y} \right] - \bar{z} \frac{\partial p_1 h i_{30}}{\partial y} - \frac{p_1 h}{2} \frac{\partial z_b}{\partial y} \right. \\
& \quad \left. - \bar{z} \frac{\partial p_2 h i_{31}}{\partial y} - h \bar{\sigma}_y \frac{\partial \bar{z}}{\partial y} - h \bar{\tau}_{yx} \frac{\partial \bar{z}}{\partial x} - \frac{h}{2} \tau_{yz} + h \bar{\tau}_{yz} \right\} = 0 \quad \dots\dots\dots(2.29)
\end{aligned}$$

The moment of momentum equation in the z -direction is:

$$\begin{aligned}
& \frac{\partial}{\partial t} [w_b h(hi_{48} + z_b i_{15}) + w_2 h(hi_{49} + z_b i_{16}) + w_h h(hi_{50} + z_b i_{17})] \\
& + \frac{\partial}{\partial x} \left\{ \begin{aligned} & w_b [q_x(hi_{51} + z_b i_{18}) + u_1 h(hi_{54} + z_b i_{19})] \\ & + w_2 [q_x(hi_{52} + z_b i_{20}) + u_1 h(hi_{55} + z_b i_{21})] \\ & + w_h [q_x(hi_{53} + z_b i_{22}) + u_1 h(hi_{56} + z_b i_{23})] \end{aligned} \right\} \\
& + \frac{\partial}{\partial y} \left\{ \begin{aligned} & w_b [q_y(hi_{57} + z_b i_{24}) + v_1 h(hi_{60} + z_b i_{25})] \\ & + w_2 [q_y(hi_{58} + z_b i_{26}) + v_1 h(hi_{61} + z_b i_{27})] \\ & + w_h [q_y(hi_{59} + z_b i_{28}) + v_1 h(hi_{62} + z_b i_{29})] \end{aligned} \right\} \\
& - \bar{z} \left\{ \begin{aligned} & \frac{\partial}{\partial t} (w_b hi_{15} + w_2 hi_{16} + w_h hi_{17}) \\ & + \frac{\partial}{\partial x} [w_b (q_x i_{18} + u_1 hi_{19}) + w_2 (q_x i_{20} + u_1 hi_{21}) + w_h (q_x i_{22} + u_1 hi_{23})] \\ & + \frac{\partial}{\partial y} [w_b (q_y i_{24} + v_1 hi_{25}) + w_2 (q_y i_{26} + v_1 hi_{27}) + w_h (q_y i_{28} + v_1 hi_{29})] \end{aligned} \right\} \\
& - (w_b^2 hi_{63} + w_b w_2 hi_{64} + w_b w_h hi_{65} + w_2^2 hi_{66} + w_2 w_h hi_{67} + w_h^2 hi_{68}) \dots\dots\dots(2.30) \\
& + \frac{1}{\rho} \left\{ \begin{aligned} & -h\bar{\tau}_x \frac{\partial \bar{z}}{\partial x} - h\bar{\tau}_y \frac{\partial \bar{z}}{\partial y} + \left(\frac{h}{2} - hi_{30} \right) (\rho gh + p_1) - p_2 hi_{31} \\ & + \frac{h}{2} \left[\tau_{yz} \frac{\partial z_b}{\partial y} + \tau_{xb} \frac{\partial z_b}{\partial x} \right] + h\bar{\sigma}_z \end{aligned} \right\} = 0
\end{aligned}$$

The vertically averaged total turbulent shear and normal stresses appearing in equations (2.19)-(2.22) and (2.27)-(2.30) are approximated (assuming laminar stresses are negligible) according to the Boussinesq model as follows:

$$\bar{\sigma}_x = \bar{\tau}_{xx} = \frac{1}{h} \int_{z_b}^{z_b+h} \tau_{xx} = 2\rho\nu_h \frac{\partial u_o}{\partial x} \dots\dots\dots(2.31)$$

$$\bar{\sigma}_y = \bar{\tau}_{yy} = \frac{1}{h} \int_{z_b}^{z_b+h} \tau_{yy} = 2\rho\nu_h \frac{\partial v_o}{\partial y} \dots\dots\dots(2.32)$$

$$\bar{\sigma}_z = \bar{\tau}_{zz} = \frac{1}{h} \int_{z_b}^{z_b+h} \tau_{zz} = 2\rho\nu_z \frac{\partial \bar{w}}{\partial z} = 2\rho\nu_z \frac{w_h - w_b}{h} \dots\dots\dots(2.33)$$

$$\bar{\tau}_{xy} = \bar{\tau}_{yx} = \frac{1}{h} \int_{z_b}^{z_b+h} \tau_{yx} = \rho\nu_h \left(\frac{\partial u_o}{\partial y} + \frac{\partial v_o}{\partial x} \right) \dots\dots\dots(2.34)$$

$$\bar{\tau}_{xz} = \bar{\tau}_{zx} = \frac{1}{h} \int_{z_b}^{z_b+h} \tau_{zx} = \rho\nu_z \left(\frac{\partial \bar{u}}{\partial z} + \frac{\partial \bar{w}}{\partial x} \right) = \rho\nu_z \left(\frac{C_2 u_1}{h} + \frac{\partial \bar{w}}{\partial x} \right) \dots\dots\dots(2.35)$$

$$\bar{\tau}_{yz} = \bar{\tau}_{zy} = \frac{1}{h} \int_{z_b}^{z_b+h} \tau_{yz} = \rho\nu_z \left(\frac{\partial \bar{v}}{\partial z} + \frac{\partial \bar{w}}{\partial y} \right) = \rho\nu_z \left(\frac{C_2 v_1}{h} + \frac{\partial \bar{w}}{\partial y} \right) \dots\dots\dots(2.36)$$

Where C_2 is a constant that depends on the pre-assumed distribution shapes of the horizontal velocity components; $\bar{w} = i_{15} w_b + i_{16} w_2 + i_{17} w_h$; ν_h is the vertically averaged turbulent exchange coefficient or eddy viscosity in the horizontal direction (x-y plane); and ν_z is the vertically averaged turbulent eddy viscosity in the vertical direction. For simplicity, the case of bed-dominated turbulence is assumed and values of the order of $\nu_h = 0.5 u_* h$ and $\nu_z = 0.07 u_* h$ are used (Fisher et al., 1979). u_* is the shear velocity and is defined as:

$$u_* = \sqrt{\left(\frac{\tau_{bx}}{\rho}\right)^2 + \left(\frac{\tau_{by}}{\rho}\right)^2} \dots\dots\dots(2.37)$$

It should be mentioned, herein, that the present proposed models for turbulent shear stresses represent the simplest models available. More sophisticated models are possible and their incorporation may be an interesting topic for further research.

The bed shear stresses, appearing in equations (2.19)-(2.22) and (2.27)-(2.30), are approximated according to:

$$\tau_{x_b} = \frac{\rho}{C_*^2} u_o \sqrt{u_o^2 + v_o^2 + \bar{w}^2} \dots\dots\dots(2.38)$$

$$\tau_{y_b} = \frac{\rho}{C_*^2} v_o \sqrt{u_o^2 + v_o^2 + \bar{w}^2} \dots\dots\dots(2.39)$$

C_* is the dimensionless Chezy Coefficient and is related to the effective roughness height, k_s , through:

$$C_* = 5.75 \log \left(12 \frac{h}{k_s} \right) \dots \dots \dots (2.40)$$

For small depth to roughness ratios ($h/k_s < e/12$), e being the natural logarithmic constant and equal to 2.71828, equation (2.40) is replaced by:

$$C_* = \frac{30}{e} \left(\frac{h}{k_s} \right) \dots \dots \dots (2.41)$$

This equation gives a smooth, continuous, non-negative relation for any depth of flow. This is necessary for numerical solution in very shallow areas where the velocity is essentially negligible.

The mathematical character of this set of equations has not yet been studied, and as a result, definitive boundary and initial condition requirements have not established. For practical purposes, the following approach to boundary conditions seems to work: the continuity and horizontal momentum equations are essentially the shallow water equations and use the appropriate set of boundary conditions for sub- and supercritical inflow, outflow and no flow cases. For the case of subcritical flow, a given total flow is specified at the upstream cross-section as an inflow boundary, whereas a fixed water surface elevation is specified at the downstream cross-section

as an outflow boundary. For case of supercritical flow, both the flow and the water surface elevation are given at the upstream cross-section as inflow conditions, whereas no conditions are applied at the outflow boundary. A no cross-flow condition is specified at any vertical wall boundaries.

The equations of moment of horizontal momentum appear to have the characteristic of transport equations. As a result, values for the velocities in excess of the means at the surface, u_I and v_I , are given at the upstream cross-section for inflow boundary case, whereas they are left free at the outflow boundary case. It is found that assuming constant definite values other than zero for u_I and v_I at the inflow boundary does not affect the output results. This arises from the fact that the upstream boundary is placed far enough upstream of the domain of interest such that different constant values assigned to u_I and v_I does not affect the solution in the domain of interest. For the sake of simplicity, u_I and v_I are assumed to be zero as boundary conditions at the upstream boundary. At the walls, a slip velocity condition is specified for u_I and v_I . That means the velocities in excess of the means at the surface, u_I and v_I , may have a component parallel to the wall, but not perpendicular to the wall.

In the rest of the equations, the primary dependent variable being evaluated is not differentiated with respect to the spatial coordinates. As a result, the variables: \bar{w} or w_2 , w_b , w_h , p_1 , and p_2 are left free at all boundaries.

At time $t = 0$, all variables are defined to have initial values at each point of the domain of interest. Having defined the initial values of the variables and specified the boundary conditions, we are left with a closed system that defines a 'model' for 2-D or a quasi 3-D flow in open channels (equations (2.16)-(2.17), (2.19)-(2.22) and (2.27)-(2.30)). This model solves for " w_b ", " w_h ", " h ", " q_x ", " q_y ", " p_1 or h_1 ", " \bar{w} or w_2 ", " u_1 ", " v_1 ", and " p_2 or h_2 " dependent variables respectively. h_1 is the pressure head in excess of the hydrostatic at the bed and is equal to $p_1/\rho g$. h_2 is the mid-depth pressure head in excess of the average of pressure heads at the bed and surface and is equal to $p_2/\rho g$.

Essentially, equation (2.16) solves for " w_b ", equation (2.17) solves for " w_h ", equation (2.19) solves for " h ", equation (2.20) solves for " q_x ", equation (2.21) solves for " q_y ", equation (2.22) solves for " p_1 or h_1 ", equation (2.27) solves for " \bar{w} " or " w_2 ", equation (2.28) solves for " u_1 ", equation (2.29) solves for " v_1 " and equation (2.30) solves for " p_2 or h_2 ". This results in a ten-equation by a ten-unknown (10 x 10) model.

If a hydrostatic pressure distribution is assumed, h_1 and h_2 are set to zero, their corresponding equations ((2.22) and (2.30)) are eliminated, and substitution for the vertical velocities included in equations (2.19)-(2.21) and (2.28)-(2.29) from equations (2.16), (2.17) and (2.27) this will result in a reduced set of 5 equations in 5 unknowns.

If we even go further and force u_1 and v_1 to zero and eliminate their corresponding equations ((2.28)-(2.29)), then we'll be left with the traditional de St. Venant equations. These equations are used in most of the applications of this study as to compare their results with those of the proposed VAM equations. It should be mentioned that the code has been written in such a way to accommodate 10, 5 or 3 equation models.

2.3 Vertically Averaged and Moment Linear and Quadratic Models

For convenience and comparison purposes, the developed equations ((2.19)-(2.22) and (2.27)-(2.30)) are adapted to allow for the use of linear or quadratic distribution shapes of horizontal velocity components. This is carried out in the following sections.

Two different sets of horizontal velocity distributions, linear and quadratic, are considered. The linear horizontal velocity distributions read (Figure 2.6-2.7):

$$u = u_o + u_1(2\eta-1) \dots\dots\dots (2.42)$$

$$v = v_o + v_1(2\eta-1) \dots\dots\dots (2.43)$$

In both cases $\int_0^1 g_1(\eta) d\eta = \int_0^1 g_2(\eta) d\eta = 0$, $g_1(\eta=1) = g_2(\eta=1) = 1$ and

$$\int_0^1 f_1(\eta) d\eta = \int_0^1 f_2(\eta) d\eta = 1.$$

The quadratic horizontal velocity distributions read (Figure 2.8-2.9):

$$u = u_o + u_i(-2+6\eta-3\eta^2) \dots\dots\dots(2.44)$$

$$v = v_o + v_i(-2+6\eta-3\eta^2) \dots\dots\dots(2.45)$$

The assumed quadratic horizontal velocity distributions are found to be physically reasonable as compared to a Reynolds model and also consistent with the applied Boussinesq turbulence models. For the case of steady and uniform flow (assuming a one-dimensional flow in the x-direction), equation (2.5) is reduced to:

$$\frac{\partial p}{\partial x} = \frac{\partial \tau_{xz}}{\partial z} \dots\dots\dots(2.46)$$

Substitution of $\tau_{xz} = \rho\nu_z \frac{\partial u}{\partial z}$ into equation (2.46) and assuming; a constant pressure gradient, $\frac{\partial p}{\partial x}$, along the x-direction; constant density, ρ ; and constant eddy viscosity ν_z ; results in:

$$\frac{\partial^2 u}{\partial z^2} = constant \dots\dots\dots(2.47)$$

Integrating equation (2.47) yields the following quadratic distribution:

$$u(z) = a_o + a_1 z + a_2 z^2 \dots\dots\dots(2.48)$$

or

$$u(\eta) = u_o + u_1(b_o + b_1\eta + b_2\eta^2) \dots\dots\dots(2.49)$$

Where a_o , a_1 , a_2 , b_o , b_1 and b_2 are constant coefficients, $u_o \neq u_o(\eta)$ and $u_1 \neq u_1(\eta)$.

The following three conditions are applied to solve for the constant coefficients b_o , b_1 and b_2 :

$$\int_0^1 g_1(\eta) d\eta = 0 \dots\dots\dots(2.50)$$

$$g_1(\eta = 1) = 1 \dots\dots\dots(2.51)$$

$$g_1'(\eta = 1) = 0 \dots\dots\dots(2.52)$$

The first condition (equation (2.50)) implies that there is no net transverse transport of fluid in the channel. The second condition (equation (2.51)) implies that u_1 can be interpreted as the velocity at the water surface in excess of the mean u_o . The third condition (equation (2.52)) implies that at the water surface the dynamic shear stress

τ_{xz} vanishes. Applying these three conditions results in $b_1 = -2$, $b_2 = 6$ and $b_3 = -3$ respectively.

A quadratic vertical velocity distribution is considered (Figure 2.10). This distribution reads:

$$w = w_b(1-\eta) + w_2 4\eta(1-\eta) + w_h \eta \dots \dots \dots (2.53)$$

A quadratic pressure distribution is also considered (Figure 2.11). This distribution reads:

$$p = \rho g (h+h_p)(1-\eta) + \rho g h_2 4\eta(1-\eta) \dots \dots \dots (2.54)$$

Making the use of the above distribution shapes into equations (2.16)-(2.17), (2.19)-(2.22) and (2.27)-(2.30) results in:

$$w_b = (u_o - C_1 u_1) \frac{\partial z_b}{\partial x} + (v_o - C_1 v_1) \frac{\partial z_b}{\partial y} \dots \dots \dots (2.55)$$

$$w_h = \frac{\partial h}{\partial t} + (u_o + u_1) \frac{\partial}{\partial x} (h + z_b) + (v_o + v_1) \frac{\partial}{\partial y} (h + z_b) \dots \dots \dots (2.56)$$

$$\frac{\partial h}{\partial t} + \frac{\partial q_x}{\partial x} + \frac{\partial q_y}{\partial y} = 0 \dots \dots \dots (2.57)$$

$$\frac{\partial q_x}{\partial t} + \frac{\partial}{\partial x} \left(\frac{q_x^2}{h} \right) + \frac{\partial}{\partial y} \left(\frac{q_x q_y}{h} \right) + C_3 \left(\frac{\partial h u_1^2}{\partial x} + \frac{\partial h u_1 v_1}{\partial y} \right) + gh \frac{\partial}{\partial x} (h + z_b) + \frac{g}{2} \frac{\partial h h_1}{\partial x} \dots (2.58)$$

$$+ \frac{2g}{3} \frac{\partial h h_2}{\partial x} + gh_1 \frac{\partial z_b}{\partial x} - \frac{1}{\rho} \frac{\partial h \bar{\sigma}_x}{\partial x} - \frac{1}{\rho} \frac{\partial h \bar{\tau}_{xy}}{\partial y} + \frac{1}{\rho} \tau_{x_b} = 0$$

$$\frac{\partial q_y}{\partial t} + \frac{\partial}{\partial x} \left(\frac{q_y q_x}{h} \right) + \frac{\partial}{\partial y} \left(\frac{q_y^2}{h} \right) + C_3 \left(\frac{\partial h v_1^2}{\partial y} + \frac{\partial h u_1 v_1}{\partial x} \right) + gh \frac{\partial}{\partial y} (h + z_b) + \frac{g}{2} \frac{\partial h h_1}{\partial y} \dots (2.59)$$

$$+ \frac{2g}{3} \frac{\partial h h_2}{\partial y} + gh_1 \frac{\partial z_b}{\partial y} - \frac{1}{\rho} \frac{\partial h \bar{\sigma}_y}{\partial y} - \frac{1}{\rho} \frac{\partial h \bar{\tau}_{yx}}{\partial x} + \frac{1}{\rho} \tau_{y_b} = 0$$

$$\frac{\partial h \bar{w}}{\partial t} + \frac{\partial}{\partial x} \left[\bar{w} q_x + C_4 \left(-\frac{u_1 h}{10} (3w_b - \bar{w} - 2w_b) \right) \right] + \frac{\partial}{\partial y} \left[\bar{w} q_y + C_4 \left(-\frac{v_1 h}{10} (3w_b - \bar{w} - 2w_b) \right) \right]$$

$$- \frac{1}{6} \frac{\partial}{\partial x} [h u_1 (w_b - w_h)] - \frac{1}{6} \frac{\partial}{\partial y} [h v_1 (w_b - w_h)] - \frac{1}{\rho} \frac{\partial h \bar{\tau}_x}{\partial x} - \frac{1}{\rho} \frac{\partial h \bar{\tau}_{xy}}{\partial y}$$

$$- gh_1 - \frac{1}{\rho} \tau_{y_b} \frac{\partial z_b}{\partial y} - \frac{1}{\rho} \tau_{x_b} \frac{\partial z_b}{\partial x} = 0$$

$$\dots (2.60)$$

$$\frac{1}{4} \frac{\partial h^2}{\partial t} + C_5 \left(\frac{\partial h^2 u_1}{\partial x} + \frac{\partial h^2 v_1}{\partial y} \right) + q_x \frac{\partial \bar{z}}{\partial x} + q_y \frac{\partial \bar{z}}{\partial y} - h \bar{w} = 0 \dots\dots\dots(2.61)$$

$$\begin{aligned} & \frac{\partial u_1}{\partial t} + \frac{\partial}{\partial x} \left(\frac{q_x u_1}{h} \right) + v_1 \frac{\partial}{\partial y} \left(\frac{q_x}{h} \right) + \frac{q_y}{h} \frac{\partial u_1}{\partial y} \\ & + C_6 \left(\begin{aligned} & -\frac{9}{10} u_1 \frac{\partial u_1}{\partial x} - \frac{1}{2} u_1 \frac{\partial v_1}{\partial y} - \frac{2}{5} v_1 \frac{\partial u_1}{\partial y} + \frac{4u_1^2}{h} \frac{\partial}{\partial x} \left(-\frac{h}{20} + \frac{3}{10} z_b \right) \\ & + \frac{4u_1 v_1}{h} \frac{\partial}{\partial y} \left(-\frac{h}{20} + \frac{3}{10} z_b \right) \end{aligned} \right) \dots\dots\dots(2.62) \end{aligned}$$

$$+ C_7 \left(\frac{gh_1}{3h} \frac{\partial h}{\partial x} - \frac{g}{3} \frac{\partial h_1}{\partial x} + \frac{8gh_2}{3h} \frac{\partial \bar{z}}{\partial x} - \frac{4\bar{\sigma}_x}{h\rho} \frac{\partial \bar{z}}{\partial x} - \frac{4\bar{\tau}_{xy}}{h\rho} \frac{\partial \bar{z}}{\partial y} + \frac{4\bar{\tau}_{xz}}{h\rho} - \frac{2}{h\rho} \tau_{xz_b} \right) = 0$$

$$\begin{aligned} & \frac{\partial v_1}{\partial t} + \frac{\partial}{\partial y} \left(\frac{q_y v_1}{h} \right) + u_1 \frac{\partial}{\partial x} \left(\frac{q_y}{h} \right) + \frac{q_x}{h} \frac{\partial v_1}{\partial x} \\ & + C_6 \left(\begin{aligned} & -\frac{9}{10} v_1 \frac{\partial v_1}{\partial y} - \frac{1}{2} v_1 \frac{\partial u_1}{\partial x} - \frac{2}{5} u_1 \frac{\partial v_1}{\partial x} + \frac{4v_1^2}{h} \frac{\partial}{\partial y} \left(-\frac{h}{20} + \frac{3}{10} z_b \right) \\ & + \frac{4u_1 v_1}{h} \frac{\partial}{\partial x} \left(-\frac{h}{20} + \frac{3}{10} z_b \right) \end{aligned} \right) \dots\dots\dots(2.63) \end{aligned}$$

$$+ C_7 \left(\frac{gh_1}{3h} \frac{\partial h}{\partial y} - \frac{g}{3} \frac{\partial h_1}{\partial y} + \frac{8gh_2}{3h} \frac{\partial \bar{z}}{\partial y} - \frac{4\bar{\sigma}_y}{h\rho} \frac{\partial \bar{z}}{\partial y} - \frac{4\bar{\tau}_{yx}}{h\rho} \frac{\partial \bar{z}}{\partial x} + \frac{4\bar{\tau}_{yz}}{h\rho} - \frac{2}{h\rho} \tau_{yz_b} \right) = 0$$

$$\begin{aligned}
& \frac{\bar{w}}{4} \frac{\partial h^2}{\partial t} - \frac{\partial}{\partial t} \left[\frac{h^2}{12} (w_b - w_h) \right] - h \overline{w^2} + \left[q_x \bar{w} + C_8 \left(-\frac{h u_1}{6} (w_b - w_h) \right) \right. \\
& \quad \left. + C_9 \left(-\frac{h u_1}{10} (-\bar{w} + 3w_b - 2w_h) \right) \right] \frac{\partial \bar{z}}{\partial x} \\
& + \left[q_y \bar{w} + C_8 \left(-\frac{h v_1}{6} (w_b - w_h) \right) \right. \\
& \quad \left. + C_9 \left(-\frac{h v_1}{10} (-\bar{w} + 3w_b - 2w_h) \right) \right] \frac{\partial \bar{z}}{\partial y} - \frac{\partial}{\partial x} \left[\frac{h q_x}{12} (w_b - w_h) \right] - \frac{\partial}{\partial y} \left[\frac{h q_y}{12} (w_b - w_h) \right] \\
& \dots \\
& + \frac{\partial}{\partial x} \left[\frac{h^2 u_1}{10} C_{10} \left(\frac{3}{2} \bar{w} + \frac{w_b}{2} + \frac{w_h}{2} \right) \right] + \frac{\partial}{\partial y} \left[\frac{h^2 v_1}{10} C_{10} \left(\frac{3}{2} \bar{w} + \frac{w_b}{2} + \frac{w_h}{2} \right) \right] \\
& - \frac{h}{\rho} \left(\bar{\tau}_x \frac{\partial \bar{z}}{\partial x} + \bar{\tau}_y \frac{\partial \bar{z}}{\partial y} - \bar{\sigma}_x \right) + \frac{h}{2\rho} \tau_{y_b} \frac{\partial z_b}{\partial y} + \frac{h}{2\rho} \tau_{x_b} \frac{\partial z_b}{\partial x} - \frac{2g}{3} h_2 = 0
\end{aligned}$$

.....(2.64)

The average vertical velocity, \bar{w} , and the mean square vertical velocity, $\overline{w^2}$, are given by:

$$\bar{w} = \frac{1}{2} w_b + \frac{2}{3} w_2 + \frac{1}{2} w_h \dots \dots \dots (2.65)$$

$$\overline{w^2} = \bar{w}^2 + \frac{w_b^2}{12} + \frac{w_h^2}{12} - \frac{w_b w_h}{6} + \frac{1}{20} (2\bar{w} - w_b - w_h)^2 \dots \dots \dots (2.66)$$

The above set of equations ((2.55)-(2.64)) is termed in this study as VAM linear or quadratic model.

The values of the constants $C_1, C_2, C_3, C_4, C_5, C_6, C_7, C_8, C_9$ and C_{10} for the VAM linear read 1, 2, 1/3, 0, 1/6, 0, 3/2, 1, 0 and 2/3 respectively, while for the VAM quadratic read 2, 3, 4/5, 1, 1/4, 1, 1, 0, 1 and 1 respectively. The values of the integral constants i 's are listed in Appendix D. It should be mentioned that the derived equations for the VAM linear model ((2.55)-(2.64)) are identical to those obtained by Naef (1996).

2.4 Steady Uniform Flow Solution

A comparison between the different approximations of the pre-assumed velocity shapes for the case of steady uniform flow in the x -direction is made. Since all derivatives vanish, the moment of momentum equations in the x - direction reduces to:

$$C_7 \left(\frac{4\bar{\tau}_x}{h\rho} - \frac{2}{h\rho} \tau_{xb} \right) = 0 \dots\dots\dots(2.67)$$

Making use of equations (2.35) and (2.38) in equation (2.67), neglecting \bar{w} (for small bed slopes), results in:

$$2\nu_z \left(\frac{C_2 u_1}{h} \right) = \frac{u_o^2}{C_*^2} \dots\dots\dots(2.68)$$

The depth averaged eddy viscosity ν_z can be estimated from uniform flow considerations as follows:

$$\nu_z = 0.07 u_* h = 0.07 \frac{u_o}{C_*} h \dots\dots\dots(2.69)$$

Using this value in equation (2.68) and combining (2.68)-(2.69) results in:

$$0.14 C_2 u_1 = \frac{u_o}{C_*} \dots\dots\dots(2.70)$$

For the VAM linear and quadratic models respectively, equation (2.70) may be written as:

$$u_1 = 3.571 \frac{u_o}{C_*} \dots\dots\dots(2.71)$$

$$u_1 = 2.381 \frac{u_o}{C_*} \dots\dots\dots(2.72)$$

Making use of equations (2.71) and (2.72) in equations (2.42) and (2.44) respectively results in:

$$\frac{u}{u_o} = 1 + \frac{3.571}{C_*} (2\eta - 1) \dots\dots\dots(2.73)$$

$$\frac{u}{u_o} = 1 + \frac{2.381}{C_*}(-2 + 6\eta - 3\eta^2) \dots\dots\dots(2.74)$$

Figure 2.12 shows a comparison of the well-known logarithmic, predicted linear (represented by equation (2.73)), and quadratic (represented by equation (2.74)) velocity profiles for $C_* = 10$. It can be easily seen that the proposed VAM linear and quadratic models offer a significant improvement over the simple depth averaged model ($u = u_o$). The slope of the predicted linear profile seems to approximately match the average of the logarithmic one, whereas the quadratic profile seems to closely match the surface velocity of the logarithmic profile. This indicates that the VAM quadratic model may be more accurate than the VAM linear model.

2.5 Numerical Solution of the Equations

The finite element method is used for this study as it readily facilitates efficient definition of the regular features common to natural channels and rivers. In addition, non-uniform discretization may be used so that few elements are located in areas where the flow is more uniform, while more elements are located in areas where large gradients are anticipated. This allows for optimization of computational effort necessary for simulation (Hicks and Steffler, 1990).

2.5.1 Finite element formulation

The vertically averaged and moment equations are discretized and modeled using a hybrid Petrov-Galerkin and Bubnov-Galerkin finite element scheme. The vertically averaged continuity, longitudinal and transverse momentum, and moment of

longitudinal and transverse momentum equations are upwinded using the two-dimensional Characteristic Dissipative Galerkin finite element scheme recently used by Ghanem et al. (1995). This scheme has the ability of providing selective artificial dissipation for shock capturing and modeling both progressive and regressive waves accurately (Hicks and Steffler, 1990, 1992 and Ghanem et al., 1995). The rest of the equations are modeled using the Bubnov-Galerkin finite element scheme. This may be briefly explained as follows:

Equations (2.16)-(2.17), (2.19)-(2.22) and (2.27)-(2.30) or equations (2.55)-(2.64) can be written in the following conservative form:

$$\frac{\partial \psi(\phi)}{\partial t} + \frac{\partial \mathbf{F}_x(\phi)}{\partial x} + \frac{\partial \mathbf{F}_y(\phi)}{\partial y} + \mathbf{G}(\phi) = 0 \dots\dots\dots(2.75)$$

Where bold letters represent vectors and matrices. ϕ represents a $N_u \times 1$ vector, N_u being the number of unknown variables. For example ϕ is equal to $(h, q_x, q_y, u_1, v_1, \bar{w}, w_b, w_h, h_1, h_2)^T$ for the 10-equation model ($N_u = 10$). $\psi(\phi)$ represents the time-variation vector. $\mathbf{F}_x(\phi)$ and $\mathbf{F}_y(\phi)$ represent the flux vectors in the x - and y -directions respectively. $\mathbf{G}(\phi)$ represents the sink and/or source vector. Ω is the solution domain.

Equations (2.75) represents the actual conservative form of equations (2.19)-(2.21) or equations (2.57)-(2.59). As a result, the ψ and ϕ vectors are identical and \mathbf{F}_x and \mathbf{F}_y represent the fluxes. Equations (2.62)-(2.63) originally represented the conservation

of the angular momentum but they still can be written in the form of equation (2.75). The rest of the equations ((2.16)-(2.17), (2.22), (2.27) and (2.30)) or equations (2.55)-(2.56), (2.60)-(2.61) and (2.64) can also be written in the form of equation (2.75) for the sake of convenience.

The application of the Petrov-Galerkin (Streamline Upwind) finite element scheme to equations (2.19)-(2.21) or equations (2.57)-(2.59) in the form of equation (2.75) results in the following weak statement equation:

$$\int_{\Omega} \hat{\mathbf{B}} \left(\frac{\partial \psi(\tilde{\phi})}{\partial t} + \frac{\partial \mathbf{F}_x(\tilde{\phi})}{\partial x} + \frac{\partial \mathbf{F}_y(\tilde{\phi})}{\partial y} + \mathbf{G}(\tilde{\phi}) \right) d\Omega = 0 \dots\dots\dots(2.76)$$

Where:

$$\hat{\mathbf{B}} = \mathbf{B} + \omega \Delta x \mathbf{W}_x \frac{\partial \mathbf{B}}{\partial x} + \omega \Delta y \mathbf{W}_y \frac{\partial \mathbf{B}}{\partial y} \dots\dots\dots(2.77)$$

$\hat{\mathbf{B}}$ is the matrix of test functions and is of size $(N_u \times NS) \times N_u$, NS being the total number of shape functions. \mathbf{B} is the matrix of basis functions and is of size $(N_u \times NS) \times N_u$. In this study, triangular elements with linear basis functions for all variables are used.

ω is an upwinding coefficient set equal to 0.5 for this study. \mathbf{W}_x and \mathbf{W}_y are the upwinding matrix coefficients in x and y directions respectively which control both

the amount and the direction of the numerical diffusion. The upwinding matrices, \mathbf{W}_x and \mathbf{W}_y , are calculated according to Hughes and Mallet (1986a and 1986b) and Hughes et al. (1986), these are:

$$\mathbf{W}_x = \mathbf{A}_x \left(\sqrt{\mathbf{A}_x^2 + \mathbf{A}_y^2} \right)^{-1} \dots\dots\dots(2.78)$$

$$\mathbf{W}_y = \mathbf{A}_y \left(\sqrt{\mathbf{A}_x^2 + \mathbf{A}_y^2} \right)^{-1} \dots\dots\dots(2.79)$$

Where \mathbf{A}_x and \mathbf{A}_y are the advection matrices of (2.19)-(2.21) or (2.57)-(2.59) system of equations in x and y directions respectively. The inverse of the matrix $\left(\sqrt{\mathbf{A}_x^2 + \mathbf{A}_y^2} \right)$ is calculated numerically using Hoger and Carlson's (1984) method. Hoger and Carlson pointed out that by applying the Cayley-Hamilton theorem, the inverse of a square matrix can be obtained directly without recourse to the eigenvalues of the matrix. They added that this should be true when the underlying vector space has dimensions less than five. $\Delta x = \Delta y = \frac{\sqrt{A}}{2}$ is used, A being the element area (Ghanem et al., 1995).

The approximation, $\tilde{\Phi}$, to the unknown vector is defined as:

$$\tilde{\Phi} = \mathbf{B}^T \Phi \dots\dots\dots(2.80)$$

where Φ is the nodal-value vector of the unknowns and is of length $(N_u \times NS) \times 1$.

The application of the Bubnov-Galerkin Scheme to the rest of the equations ((2.16)-(2.17), (2.22) and (2.27)-(2.30)) or equations (2.55)-(2.56) and (2.60)-(2.64) in the form of equation (2.75) results in the following weak statement equation:

$$\int_{\Omega} \mathbf{B} \left(\frac{\partial \psi(\tilde{\phi})}{\partial t} + \frac{\partial \mathbf{F}_x(\tilde{\phi})}{\partial x} + \frac{\partial \mathbf{F}_y(\tilde{\phi})}{\partial y} + \mathbf{G}(\tilde{\phi}) \right) d\Omega = 0 \dots\dots\dots(2.81)$$

Integrating equation (2.76) by parts results in:

$$\begin{aligned} & \int_{\Omega} \left(\mathbf{B} + \omega \Delta x \mathbf{W}_x(\tilde{\phi}) \frac{\partial \mathbf{B}}{\partial x} + \omega \Delta y \mathbf{W}_y(\tilde{\phi}) \frac{\partial \mathbf{B}}{\partial y} \right) \frac{\partial \psi(\tilde{\phi})}{\partial t} d\Omega \\ & - \int_{\Omega} \left(\mathbf{F}_x(\tilde{\phi}) \frac{\partial \mathbf{B}}{\partial x} + \mathbf{F}_y(\tilde{\phi}) \frac{\partial \mathbf{B}}{\partial y} \right) d\Omega + \int_{\Omega} \mathbf{B} \left(\frac{\partial \mathbf{F}_x(\tilde{\phi})}{\partial x} + \frac{\partial \mathbf{F}_y(\tilde{\phi})}{\partial y} + \mathbf{G}(\tilde{\phi}) \right) d\Omega \\ & \dots\dots\dots(2.82) \\ & + \int_{\Omega} \left(\omega \Delta x \mathbf{W}_x(\tilde{\phi}) \frac{\partial \mathbf{B}}{\partial x} + \omega \Delta y \mathbf{W}_y(\tilde{\phi}) \frac{\partial \mathbf{B}}{\partial y} \right) \left(\frac{\partial \mathbf{F}_x(\tilde{\phi})}{\partial x} + \frac{\partial \mathbf{F}_y(\tilde{\phi})}{\partial y} + \mathbf{G}(\tilde{\phi}) \right) d\Omega \\ & + \int_{\Gamma} \mathbf{B} \left[\mathbf{F}_x(\tilde{\phi}) n_x + \mathbf{F}_y(\tilde{\phi}) n_y \right] d\Gamma = 0 \end{aligned}$$

The same expression with $\omega = 0$ is obtained on integrating equation (2.81) by parts.

Γ is the boundary domain. n_x and n_y are the x and y components of the unit normal vector n .

2.5.2 Treatment of boundary conditions

The boundary integral in equation (2.82) represents natural convective fluxes across the boundaries. This provides an accurate and easy means for specifying boundary conditions. For example, the boundary integral term for the continuity equation is

$\int_{\Gamma} -\mathbf{B}(\mathbf{q} \cdot \mathbf{n}) d\Gamma$. To specify a no-flow boundary condition (wall condition), \mathbf{q}_n

($=\mathbf{q} \cdot \mathbf{n}$) is set equal to zero, and the term is simply not computed. In addition, specified boundary conditions are implemented directly by specifying given values in that term. For example, for an inflow boundary \mathbf{q}_n has a specified distribution and the integral term is evaluated and the contributions summed to the appropriate residuals. For an outflow boundary \mathbf{q}_n has an unknown value and thus the integral boundary term is treated as an unknown term in the equations.

2.5.3 Time discretization

The time derivatives are approximated using a weighted-implicit finite difference formulation. As a result, equation (2.82) becomes:

$$\int_{\Omega} \left\{ \theta \left(\mathbf{B} + \omega \Delta x \mathbf{W}_x(\tilde{\phi}) \frac{\partial \mathbf{B}}{\partial x} + \omega \Delta y \mathbf{W}_y(\tilde{\phi}) \frac{\partial \mathbf{B}}{\partial y} \right)^{n+1} + (1-\theta) \left(\mathbf{B} + \omega \Delta x \mathbf{W}_x(\tilde{\phi}) \frac{\partial \mathbf{B}}{\partial x} + \omega \Delta y \mathbf{W}_y(\tilde{\phi}) \frac{\partial \mathbf{B}}{\partial y} \right)^n \right\} \frac{[\psi(\tilde{\phi})^{n+1} - \psi(\tilde{\phi})^n]}{\Delta t} d\Omega$$

$$\begin{aligned}
& \left. \begin{aligned}
& - \int_{\Omega} \left(\mathbf{F}_x(\tilde{\phi}) \frac{\partial \mathbf{B}}{\partial x} + \mathbf{F}_y(\tilde{\phi}) \frac{\partial \mathbf{B}}{\partial y} \right) d\Omega + \int_{\Omega} \mathbf{B} \left(\frac{\partial \mathbf{F}_x(\tilde{\phi})}{\partial x} + \frac{\partial \mathbf{F}_y(\tilde{\phi})}{\partial y} + \mathbf{G}(\tilde{\phi}) \right) d\Omega \\
& + \theta \left\{ + \int_{\Omega} \left(\omega \Delta x \mathbf{W}_x(\tilde{\phi}) \frac{\partial \mathbf{B}}{\partial x} + \omega \Delta y \mathbf{W}_y(\tilde{\phi}) \frac{\partial \mathbf{B}}{\partial y} \right) \left(\frac{\partial \mathbf{F}_x(\tilde{\phi})}{\partial x} + \frac{\partial \mathbf{F}_y(\tilde{\phi})}{\partial y} + \mathbf{G}(\tilde{\phi}) \right) d\Omega \right. \\
& \quad \left. + \int_{\Gamma} \mathbf{B} [\mathbf{F}_x(\tilde{\phi}) n_x + \mathbf{F}_y(\tilde{\phi}) n_y] d\Gamma \right\}
\end{aligned} \right\}^{n+1} \\
& + (1-\theta) \left\{ + \int_{\Omega} \left(\omega \Delta x \mathbf{W}_x(\tilde{\phi}) \frac{\partial \mathbf{B}}{\partial x} + \omega \Delta y \mathbf{W}_y(\tilde{\phi}) \frac{\partial \mathbf{B}}{\partial y} \right) \left(\frac{\partial \mathbf{F}_x(\tilde{\phi})}{\partial x} + \frac{\partial \mathbf{F}_y(\tilde{\phi})}{\partial y} + \mathbf{G}(\tilde{\phi}) \right) d\Omega \right. \\
& \quad \left. + \int_{\Gamma} \mathbf{B} [\mathbf{F}_x(\tilde{\phi}) n_x + \mathbf{F}_y(\tilde{\phi}) n_y] d\Gamma \right\}^n = 0
\end{aligned}$$

.....(2.83)

Where superscript n refers to evaluation of the quantity at the n^{th} time step (assumed known) and $n+1$ represents evaluation at a time Δt later (generally unknown). θ is the implicitness factor.

2.5.4 Solution of the non-linear equations

Equations (2.83) may be generally represented by:

$$\mathbf{R} = 0 \dots\dots\dots(2.84)$$

\mathbf{R} represents the vector of the residuals and is of length $(N_u \times NS) \times 1$. \mathbf{R} actually represents an implicit set of non-linear algebraic equations. An iterative technique is thus necessary to solve this system of non-linear equations. This may be explained as follows:

Two methods are used to solve the resulting system of non-linear equations. These methods are the transient and steady state methods.

2.5.4.1 Transient solution

The objective of the transient solution method is to get the correct distributions of the flow at a certain time or to actually follow the time history of the flow. For the resulting implicit set of non-linear algebraic equations, a Newton-Raphson technique, where the derivatives are evaluated analytically where possible, is used to advance the solution to the next time level. The corrections vector necessary to update the variables after each iteration, $\delta\Phi$, is obtained from:

$$\mathbf{J}^{n+1,m} \delta\Phi^{n+1,m} = -\mathbf{R}^{n+1,m} \dots\dots\dots(2.85)$$

Where the superscript m refers to evaluation of the quantity at the m^{th} iteration. \mathbf{J} is the Jacobian matrix of size $(N_u \times NS) \times (N_u \times NS)$ and is given by:

$$\mathbf{J}^{n+1,m} = \left[\frac{\partial \mathbf{R}}{\partial \Phi} \right]^{n+1,m} \dots\dots\dots (2.86)$$

As a result, the system of equations represented by equation (2.85) becomes linear in $\delta\Phi^{n+1,m}$. A LU decomposition matrix solver, with a skyline matrix storage for the Jacobian \mathbf{J} , is employed to solve this system of linear equations to obtain $\delta\Phi^{n+1}$. After each iteration, the values of the variables are updated through:

$$\Phi^{n+1,m+1} = \Phi^{n+1,m} + \delta\Phi^{n+1,m} \dots\dots\dots (2.87)$$

Where the superscript $m+1$ refers to evaluation of the quantity at the $m+1^{\text{th}}$ iteration.

Finally, when the error norm $\varepsilon^{n+1,m} = \left(\sqrt{\frac{\sum (\delta\Phi)^2}{\sum \Phi^2}} \right)^{n+1,m}$ is \leq a user specified tolerance

(typically 10^{-6}), the solution proceeds to the next time step.

2.5.4.2 Steady state solution

The objective is to reach the final steady state with as few calculations as possible while remaining stable under any flow circumstances. To control convergence, the steady state is found to be essentially simulated as unsteady and with one iteration per time step. The starting guess for the solution at the next time step is the solution at the

end of the previous time step. The equations are solved with $\theta = 1$ (fully implicit). To speed the process to final completion an acceleration procedure is used. This may be explained as follows:

The time increment is increased according to:

$$\Delta t^{n+1} = \Delta t^n \frac{\varepsilon_g}{\varepsilon^{n+1,1}} \dots\dots\dots(2.88)$$

Where ε_g is a user-specified goal relative change of all the variables and $\varepsilon^{n+1,1}$ is the

error norm and is equal to $\left(\sqrt{\frac{\sum (\delta\Phi)^2}{\sum \Phi^2}} \right)^{n+1,1}$. Typically a value of ε_g of the order of

0.1 is used. After each time step, the values of the variables are updated through:

$$\Phi^{n+1,1} = \Phi^{n,1} + \delta\Phi^{n+1,1} \dots\dots\dots(2.89)$$

As the solution progresses toward steady state, usually the overall rate of change $\varepsilon / \Delta t$ decreases and longer time steps are possible. The progress toward a final steady state may not be uniform. The program logic proceeds as follows. At the end of each time step the overall relative change ε is calculated and compared to the goal change ε_g . If the actual change is less than 1.25 times the goal change ε_g , then the current iteration is accepted and the increment for the next time step is then calculated according to equation (2.88). If the actual change is greater than 1.25 times the goal

change ε_g , then the current iteration is rejected and a new time increment is calculated as half of the result of equation (2.88) and the iteration is retried. This process may repeat a few times until a small enough time step is achieved to allow the solution to progress.

In most cases, the time step eventually becomes large and the solution converges quickly to steady state. At each successful iteration, the overall change ε and the net outflow discharge ($q_n = q_x \Delta y - q_y \Delta x$) are printed on the screen as indicators of how close the solution is to a final steady state. When the net outflow discharge indicates a constant value and the overall change approaches zero (typical value of the order of 10^{-6} is used), the solution is considered to be steady state. More details are found in Steffler (1997a).

2.5.5 The mesh generation

An automatic mesh generation program R2D_Mesh (Steffler, 1997b) is used to aid in the generation of appropriate two-dimensional triangular meshes. A finite element mesh is defined interactively and graphically by the user by placing nodes individually or in pattern coverages. The mesh is then generated on the basis of a boundary constrained Delauney triangulated irregular network including breaklines (Steffler, 1997b). As a result, the meshes generated are limited to linear triangular elements.

2.5.6 The finite element code

The code used (R2D_VAM) is written in standard C language and executes on any system which supports direct 32-bit addressing. Versions for Windows 95 and various Unix systems are compiled. In general, fast floating point performance and large memory (at least 80 MB) spaces are required. The R2D_VAM program is based on existing code (Ghanem et. al, 1995). The element matrix calculations are replaced. In addition, the input-output commands and file formats are adapted to accommodate the increased number of variables suggested by the proposed model.

It should be mentioned that more details regarding the model development and the numerical solution of the derived equations are presented in Appendix A.

2.6 A Preliminary Numerical Test

A preliminary numerical test is carried out in this section to check if the equations are derived and coded correctly. A one-dimensional channel laboratory scale experimental test is selected for this purpose.

The finite element grid is designed to be fine enough to meet the requirements of reasonable accuracy as well as execution time. The R2D_VAM program is run till a steady state solution is obtained. The VAM linear model (the 10-equation model) and the VA model (the 3-equation model) are used in this simulation.

A symmetric bed profile test

The proposed model is compared and tested with the experimental results obtained by Sivakumaran et al. (1983). They performed experiments in a horizontal flume 0.915 m long, 0.65 m high and 0.3 m wide. The flume had symmetric and asymmetric bed profiles. The symmetric profile was shaped according to a normal distribution and was 0.2 m high and 0.12 m long.

The upstream undisturbed depth was measured at 0.16 m from the leading edge of the profile. Different discharges were used.

Measurements of water surface and bed pressure profiles were plotted. The experiment with a discharge of $0.11197 \text{ m}^2/\text{s}$ and a symmetric bed profile is selected in this study.

The simulation is performed using a finite element mesh composed of 4467 triangular elements and 2399 nodes (Figure 2.13). The mesh is designed such that additional nodes are added to the parts of the flume where high velocity variations are expected.

The boundary conditions are specified as subcritical inflow, supercritical outflow and no-flow across the vertical side walls. The boundary conditions specified at the inflow section at the entrance on the left are total discharge = $0.033591 \text{ m}^3/\text{s}$, $u_I = 0.0$, and $v_I = 0.0$. No boundary condition applied at the outflow section on the right. Initial

values for the depth h are assumed while the rest of the variables ($q_x, q_y, u_I, v_I, \bar{w}, w_b, w_h, h_I$ and h_2) are set to zero.

The results are shown in Figures 2.14-2.15. Figure 2.14 compares the experimental and numerically water surface profiles for the symmetric bed profile. Figure 2.15 compares the experimental and numerically bed pressure profiles for the symmetric bed profile.

It can be clearly seen from Figures 2.14-2.15 that the proposed VAM model predicts the water surface and bed pressure profiles very well. It can also be noticed from Figures 2.14-2.15 that the VAM model behaves better than the VA model.

2.7 Summary

A full two-dimensional (2-D) frame-work model, in which more vertical details are recovered, is established. The new equations, vertically averaged and moment equations, are derived by a moment weighted residual method from the fundamental three-dimensional (3-D) Reynolds equations. The equations are developed in their general case that accommodate different distribution shapes of velocities and pressure.

The developed general equations are adapted, for convenience and comparison purposes, to allow for the use of linear or quadratic distributions of horizontal velocity components.

The vertically averaged and moment equations are discretized and modeled using a hybrid Petrov-Galerkin and Bubnov-Galerkin finite element schemes. The vertically averaged continuity, longitudinal and transverse momentum, and moment of longitudinal and transverse momentum equations are upwinded using a two-dimensional Characteristic-Dissipative Galerkin finite element scheme. The rest of the equations are modeled using the Bubnov-Galerkin finite element scheme.

Triangular elements with linear basis functions for all variables are used. The time derivatives are approximated using a weighted-implicit finite difference formulation. For the resulting implicit set of non-linear algebraic equations a Newton-Raphson technique is used to advance the solution to the next time level and to reach a steady state solution as well.

The proposed model is tested for a uniform steady state case. A preliminary numerical one-dimensional test shows that the derivation and the coding of the proposed equations are correctly done.

2.8 References

Dressler, R. F. (1978), "New Nonlinear Shallow-flow Equations with Curvature."
Journal of Hydraulic Research, IAHR, Vol. 16, No. 3, pp. 205-222.

- Fischer et al. (1979), "Mixing in Inland and Coastal Waters." Book, Academic Press.
- Ghanem, A., Steffler, P. M., Hicks, F. E. and Katopodis (1995), "Two-Dimensional Finite Element Modeling of Flow in Aquatic Habitats". Water resources Engineering Report No. 95-S1, Department of Civil Engineering, University of Alberta.
- Henderson, F. M. (1966), "Open Channel Flow". Book, The Mcmillan Company, New York.
- Hicks, F. E. and Steffler, P. M. (1990), "Finite Element Modeling of Open Channel Flow." Department of Civil Engineering, University of Alberta, Technical Report (WRE 90-6).
- Hicks, F. E. and Steffler, P. M. (1992), "Characteristic Dissipative Galerkin Scheme for Open-Channel Flow." Journal of Hydraulic Engineering. ASCE, Vol. 118, No. 2, pp. 337-352.
- Hoger, A. and Carlson, D. E. (1984), "Determination of the stretch and rotation in the polar decomposition of the deformation gradient." Quarterly of Applied Mathematics, Vol. 42, No. 1, pp. 113-117.
- Hughes, T. J. R. and Mallet, M. (1986a), "A new finite element formulation for computational fluid dynamics: III. The generalized streamline operator for multidimensional advective-diffusive systems." Computer Methods in Applied Mechanics and Engineering, Vol. 58, pp. 305-328.

- Hughes, T. J. R. and Mallet, M. (1986b), "A new finite element formulation for computational fluid dynamics: IV. A discontinuity-capturing operator for multidimensional advective-diffusive systems." *Computer Methods in Applied Mechanics and Engineering*, Vol. 58, pp. 329-336.
- Hughes, T. J. R., Mallet, M. and Mizukami, A. (1986), "A new finite element formulation for computational fluid dynamics: II. Beyond SUPG." *Computer Methods in Applied Mechanics and Engineering*, Vol. 54, pp. 341-355.
- Jin, Yee-Chung and Li, Baozhu (1996), "The Use of a One-dimensional Depth-averaged Moment of Momentum Equation for the Nonhydrostatic Pressure Condition." *Canadian Journal of Civil Engineering*, Vol. 23, pp. 150-156.
- Kennedy, J. F. (1963), "The Mechanics of Sediment Ripples, Dunes and Antidunes in Erodible Bed Channels." *Journal of Fluid Mechanics*, Vol. 16, Part 4, pp. 521-544.
- Khan, A. (1995), "Modeling Rapidly Varied Open Channel Flows". PhD Thesis, Water Resources Engineering, Department of Civil Engineering, University of Alberta.
- Liggett, J. A. (1974), "Equations of Unsteady Flow." *Unsteady Flow in Open Channels*, ed. Mahmood K. and Yevjevich V., Vol. 1, pp. 29-62.
- Naef, Daniel R. (1996), "Extension of the 2-dimensional Shallow Water Approach Using Moment Equations." *Proceedings of Hydroinformatics '96*, 2nd international conference, Zurich, Switzerland

- Odgaard, A. Jacob, Sinha, Sanjiv K. and Sotiropoulos, Fotis (1998), "Three-dimensional Numerical Model for Flow through Natural Rivers." *Journal of Hydraulic Engineering*, ASCE, Vol. 124, No. 1, pp. 13-24.
- Shimuzi, Y., Yamaguchi, H. and Itakura, T. (1990), "Three-dimensional Computation of Flow and Bed Deformation." *Journal of Hydraulic Engineering*, ASCE, Vol. 116, No. 9, pp. 1090-1108.
- Sivakumaran, N. S., Tingsanchali, T., and Hosking, R. J. (1983), "Steady Shallow Flow over Curved Beds." *Journal of Fluid Mechanics*, Vol. 128, March, pp. 469-487.
- Steffler, P. M. (1997a), "cdg2d depth averaged hydrodynamic model reference manual." Civil Engineering Department, University of Alberta, Edmonton, Canada.
- Steffler, P. M. (1997b), "CDGMESH- A windows based mesh generation program for two dimensional depth averaged finite element hydrodynamic modeling." Civil Engineering Department, University of Alberta, Edmonton, Canada.
- Steffler, P. M. and Jin, Y. C. (1993a), "Depth averaged and Moment Equations for Moderately Shallow Free Surface Flow." *Journal of Hydraulic Research*, IAHR, Vol. 31, No. 1, pp. 5-17.
- Steffler, P. M. and Jin, Y. C. (1993b), "Predicting Flow in Curved Open Channel by Depth-Averaged Method." *Journal of Hydraulic Engineering*, ASCE, Vol. 119, No. 1, January, pp. 109-124.
- Van Rijn, L. C. (1990), "Principles of Fluid Flow and Surface in Rivers, Estuaries, Seas and Oceans." Aqua Publications, Amsterdam, The Netherlands.

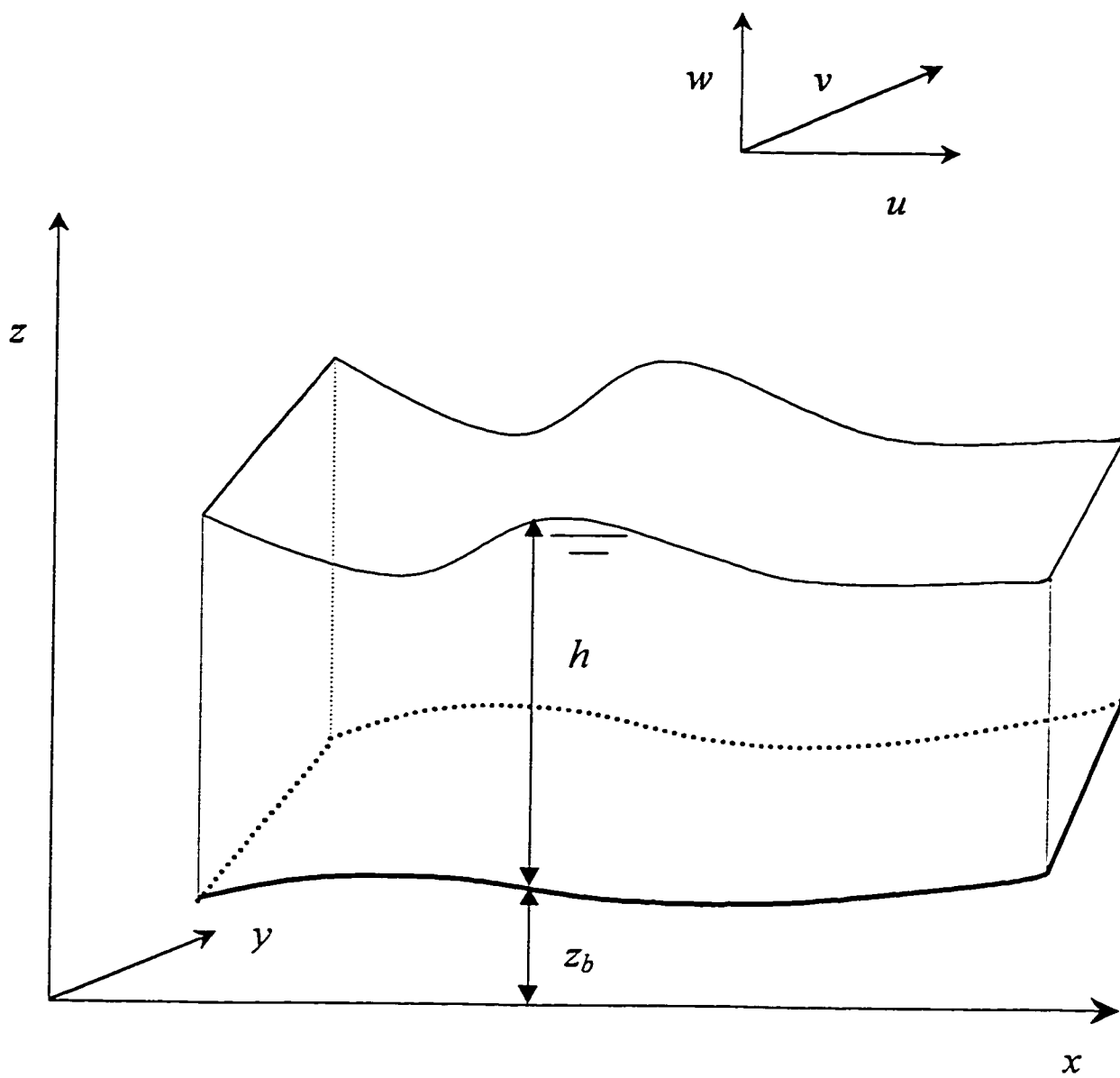


Figure 2.1 Definition sketch

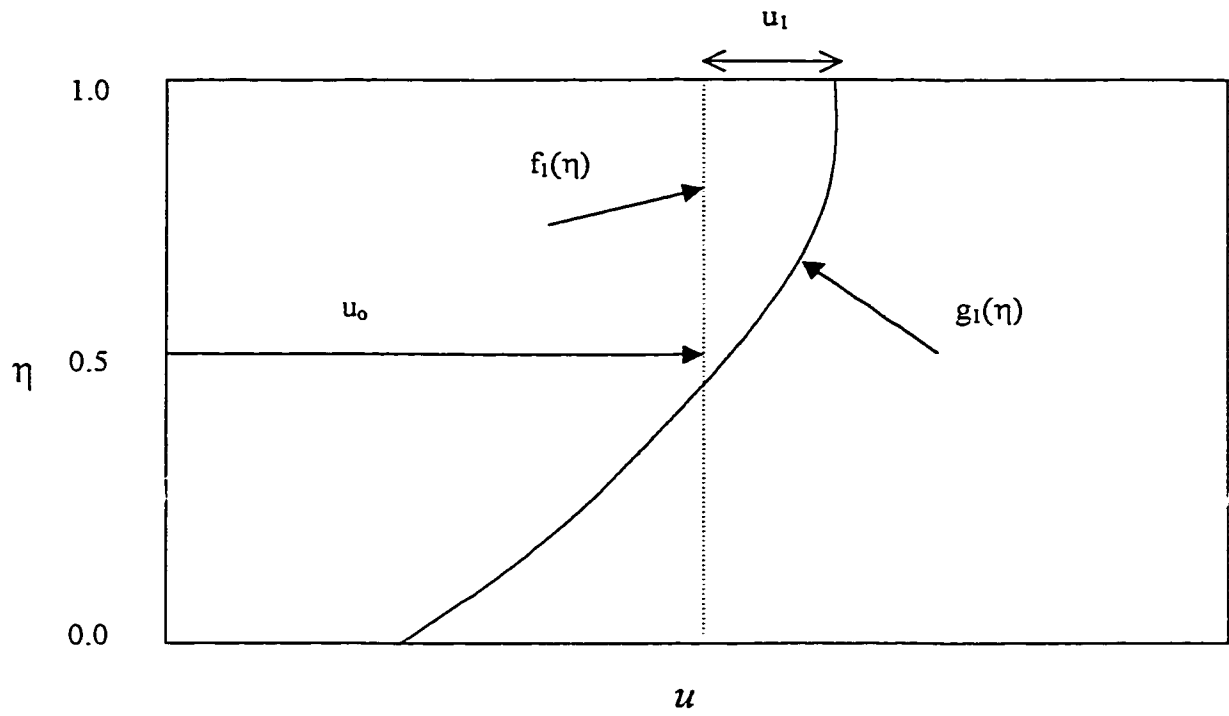


Figure 2.2 Assumed general longitudinal velocity distribution

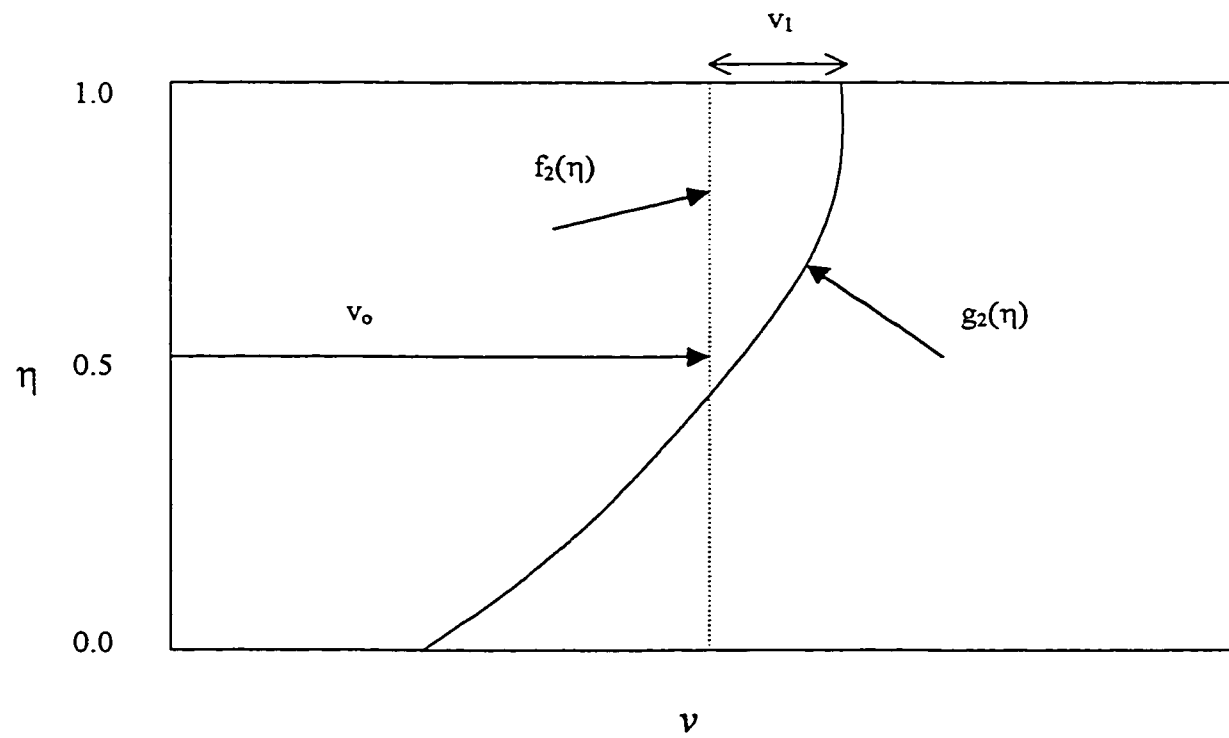


Figure 2.3 Assumed general transverse velocity distribution

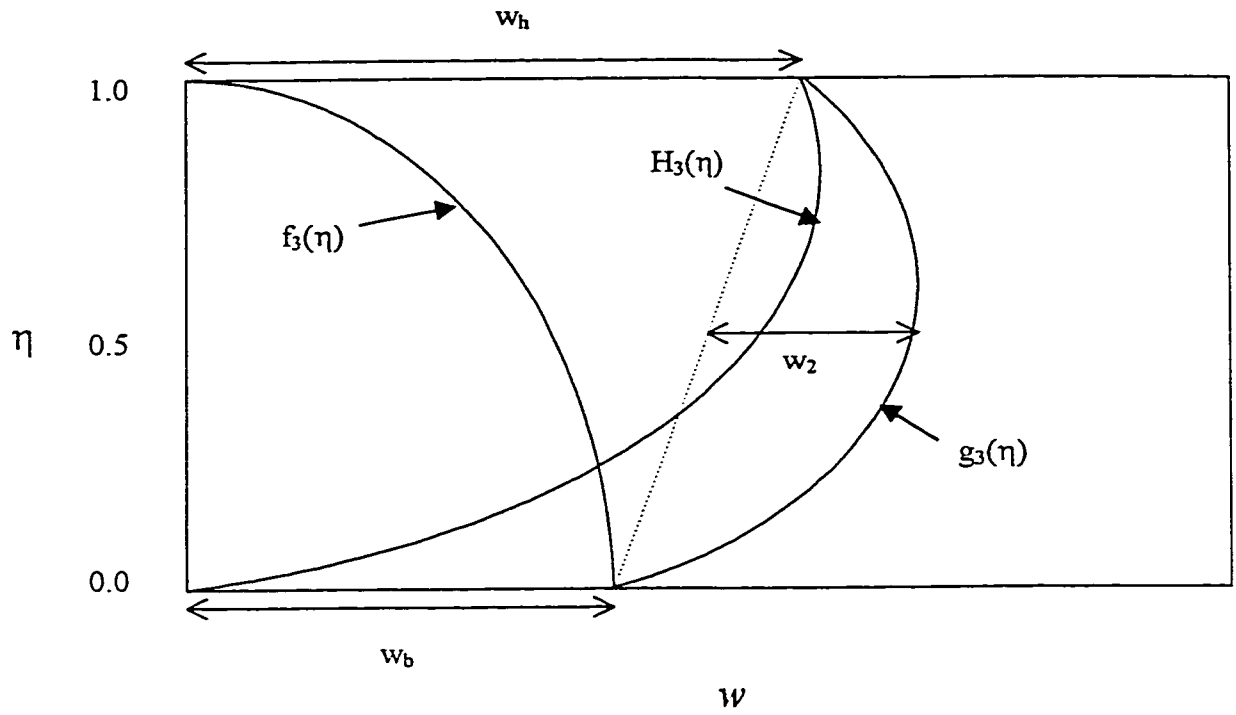


Figure 2.4 Assumed general vertical velocity distribution

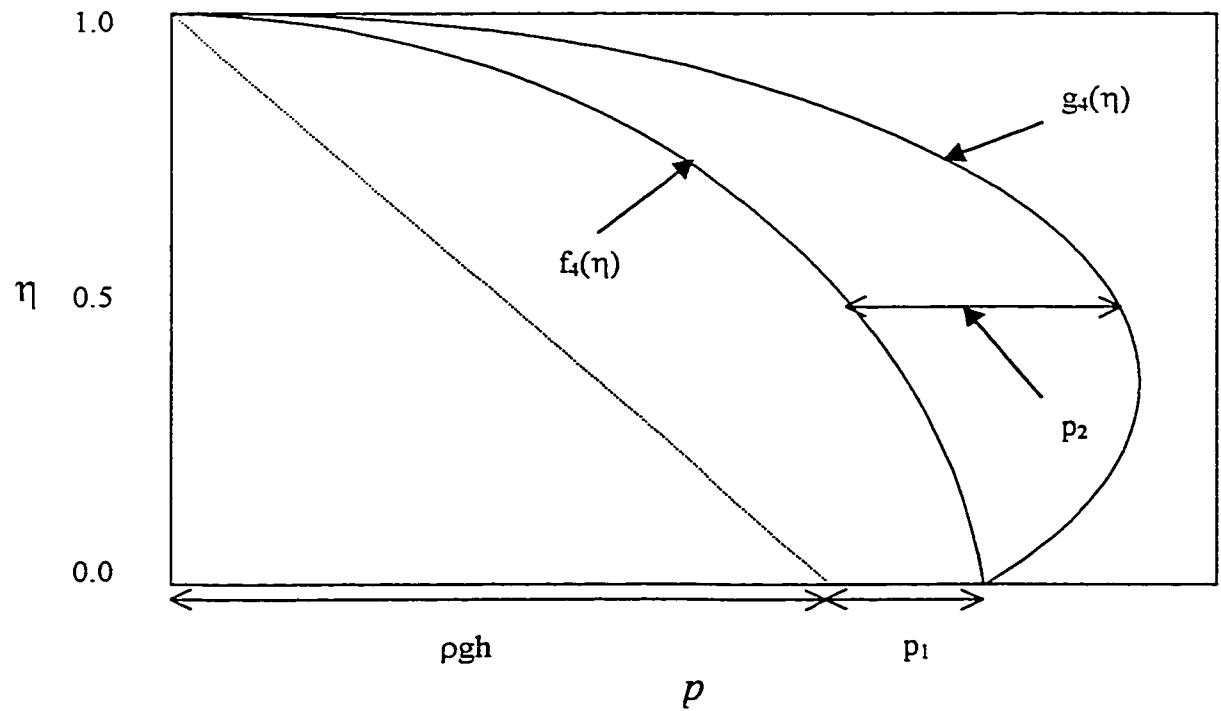


Figure 2.5 Assumed general pressure distribution

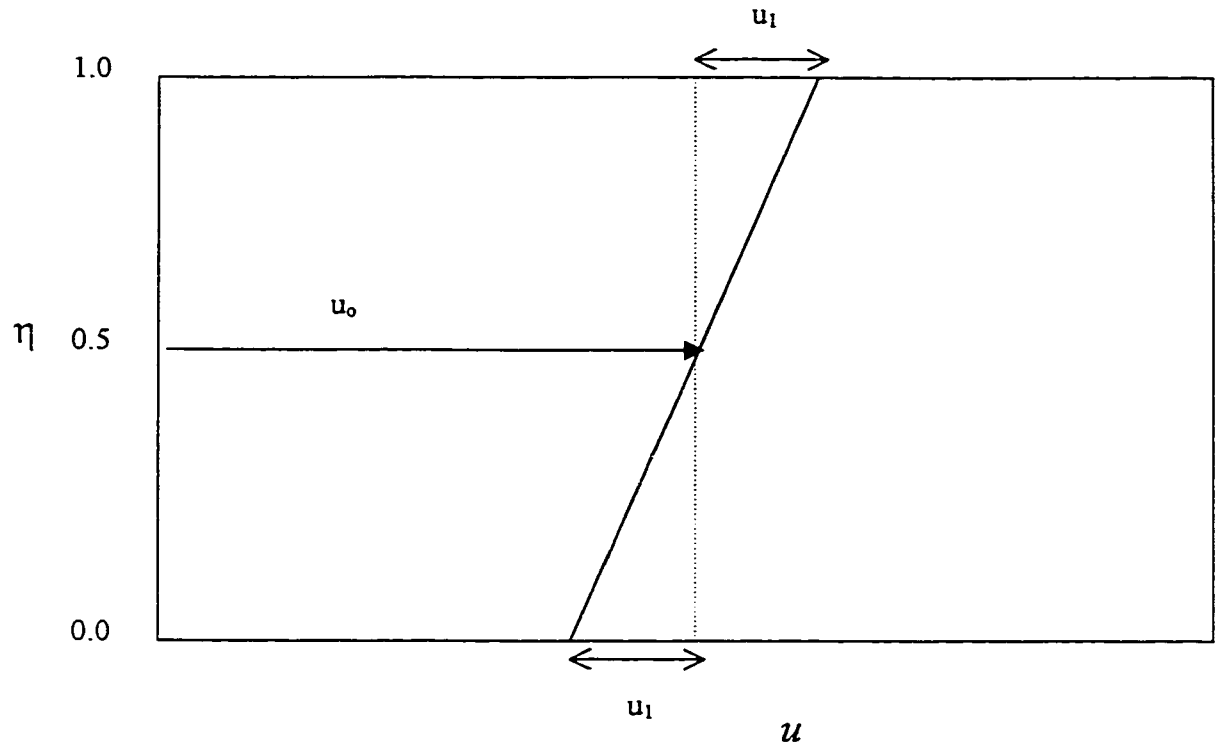


Figure 2.6 Assumed linear longitudinal velocity distribution

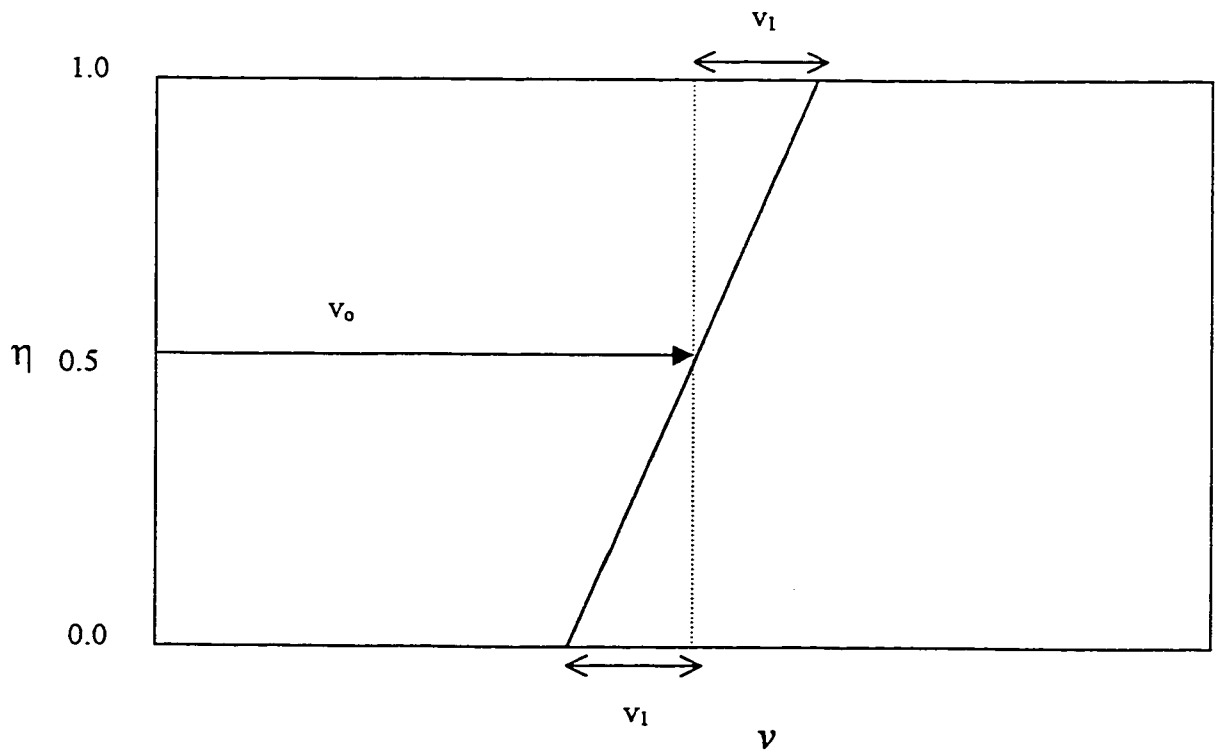


Figure 2.7 Assumed linear transverse velocity distribution

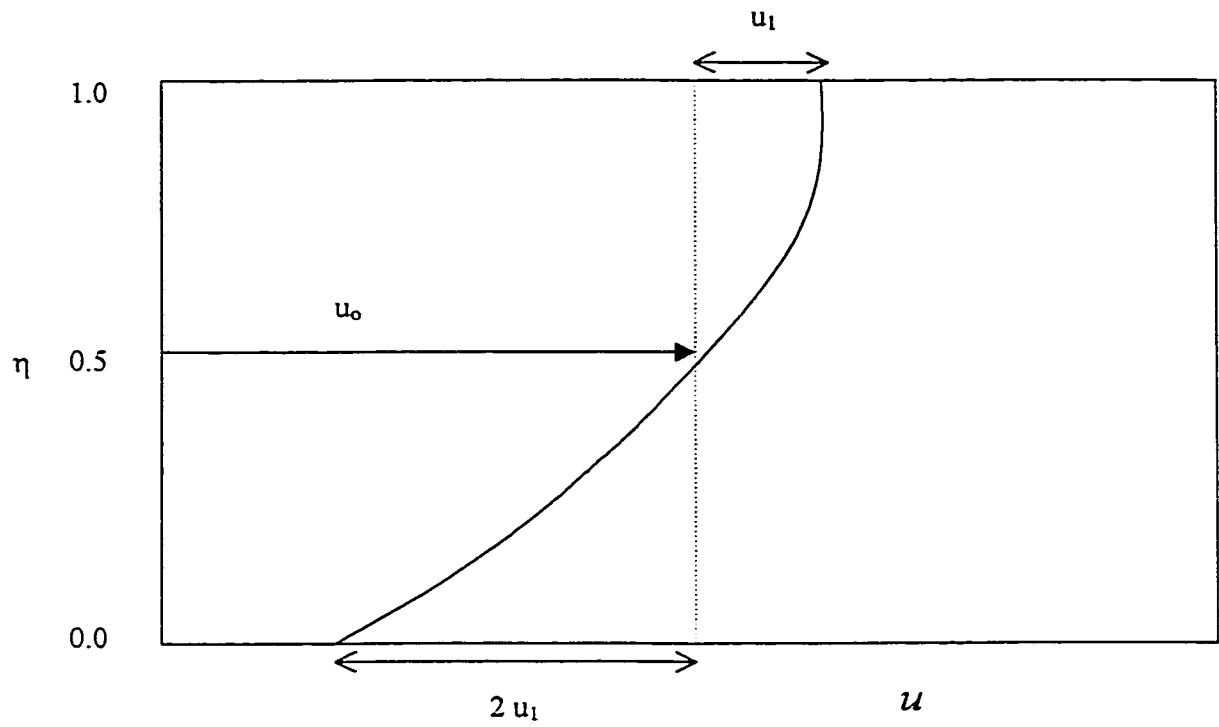


Figure 2.8 Assumed quadratic longitudinal velocity distribution

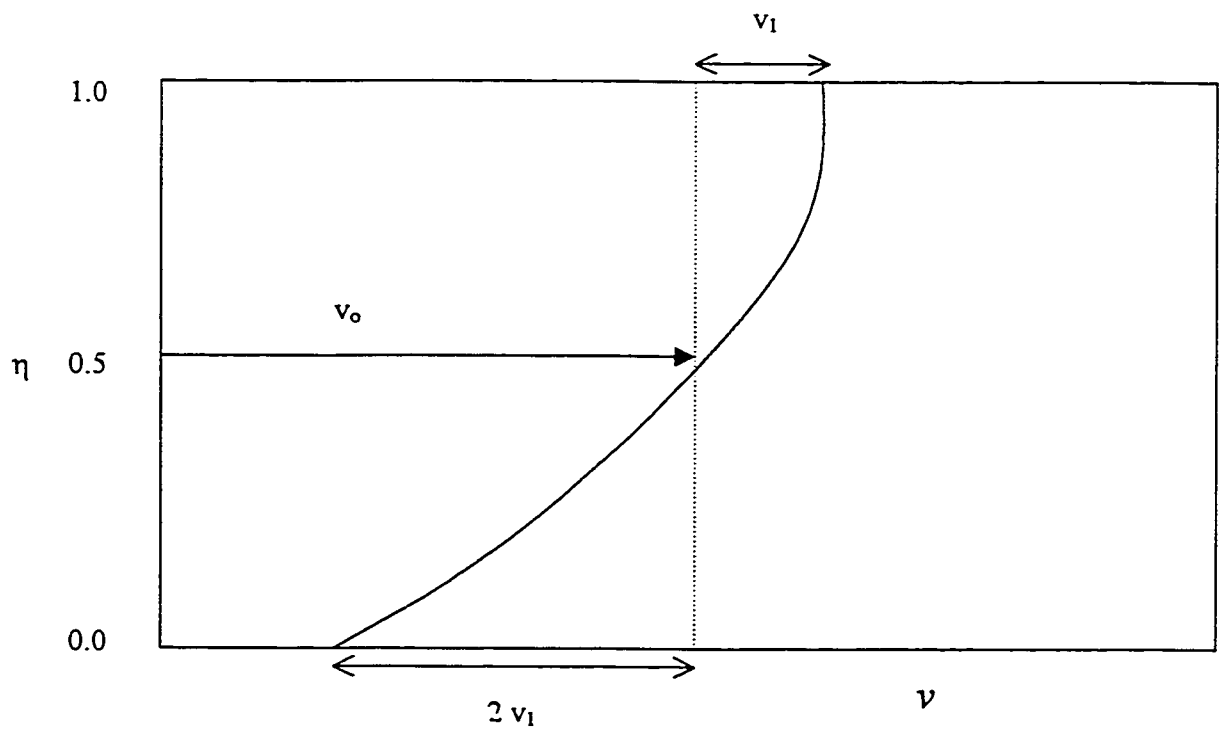


Figure 2.9 Assumed quadratic transverse velocity distribution

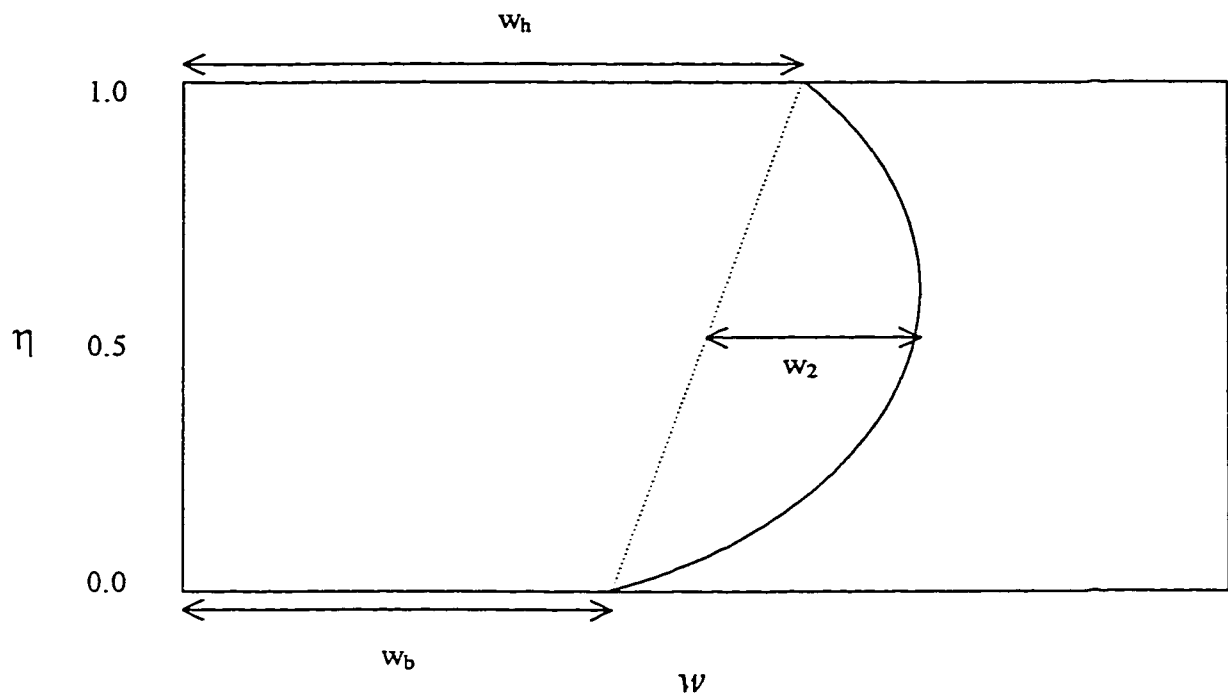


Figure 2.10 Assumed quadratic vertical velocity distribution

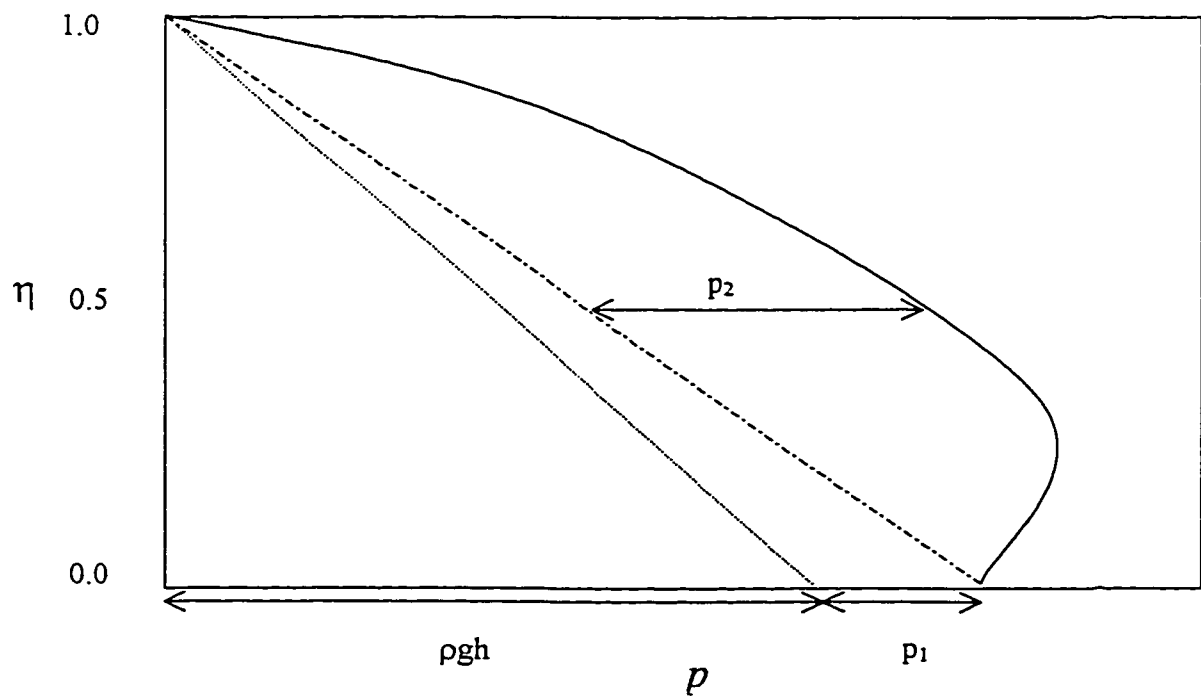


Figure 2.11 Assumed quadratic pressure distribution

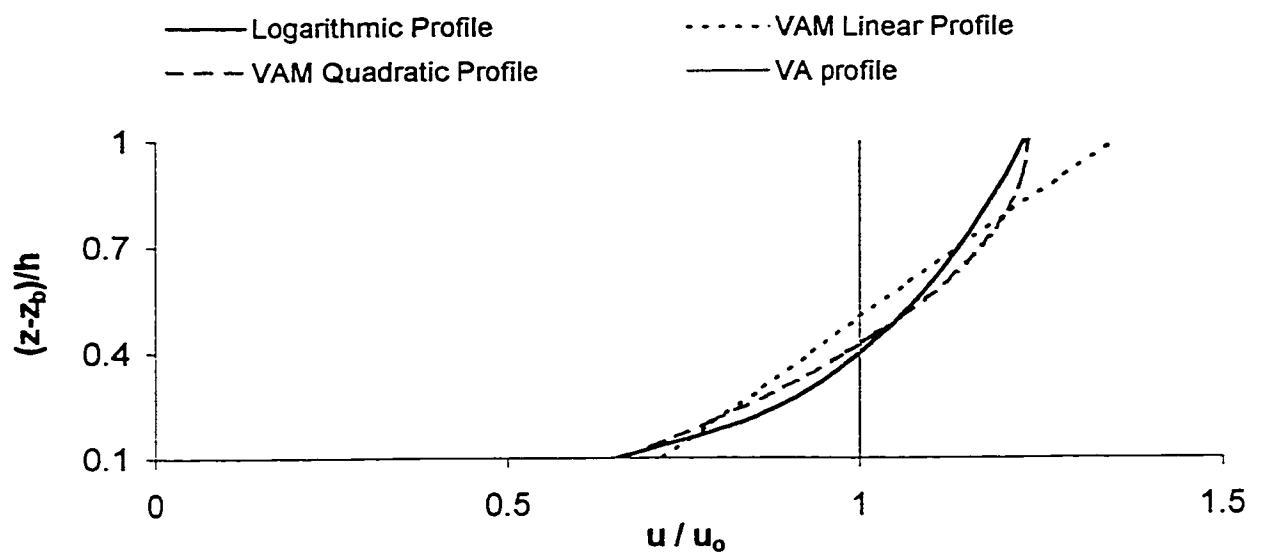


Figure 2.12 The comparison between different assumed velocity distributions for the case of steady uniform flow for $C_s = 10$

Distance
0.1 m

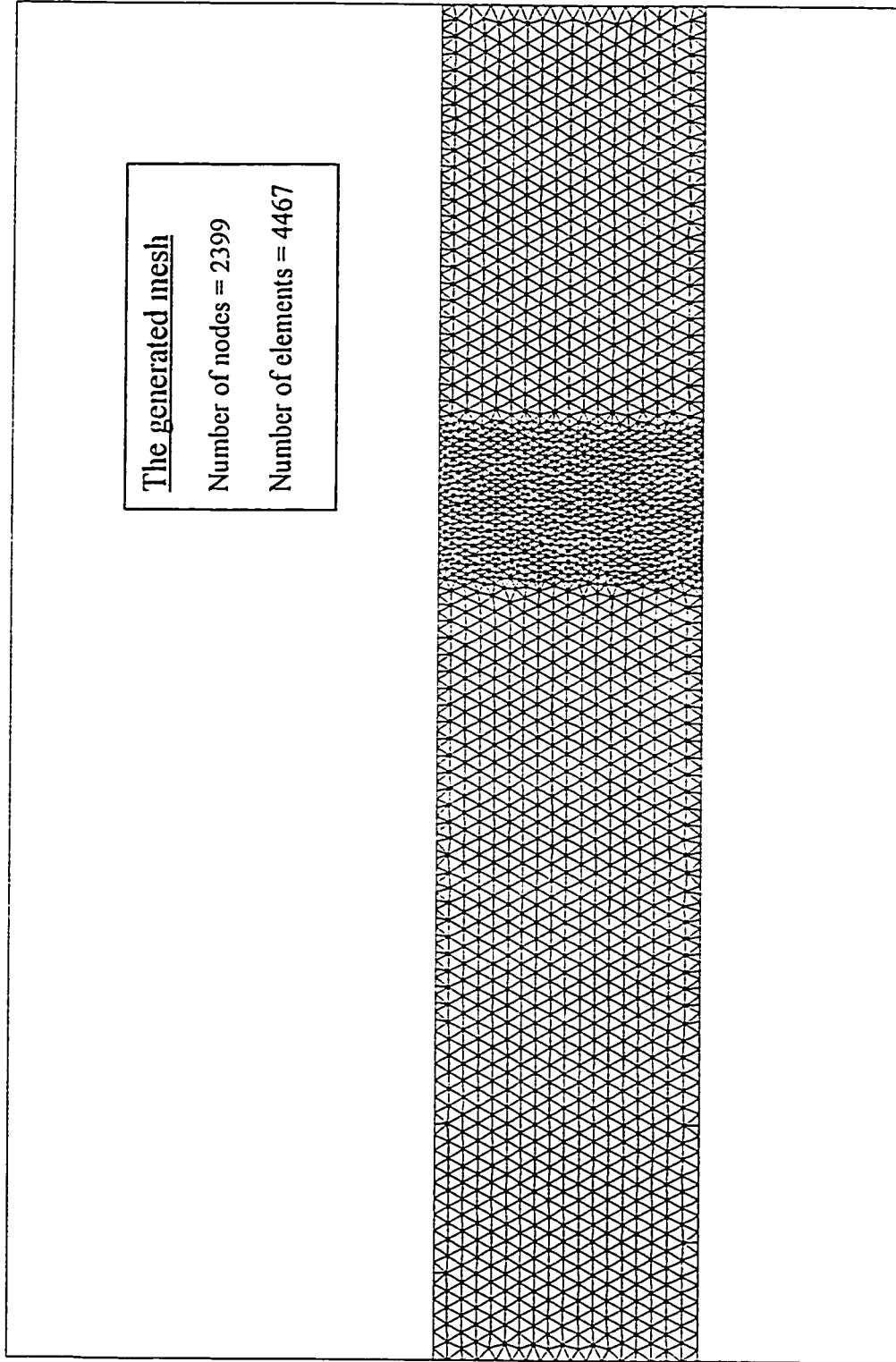


Figure 2.13 Finite element mesh for Sivakumaran et al.'s (1983) experiment

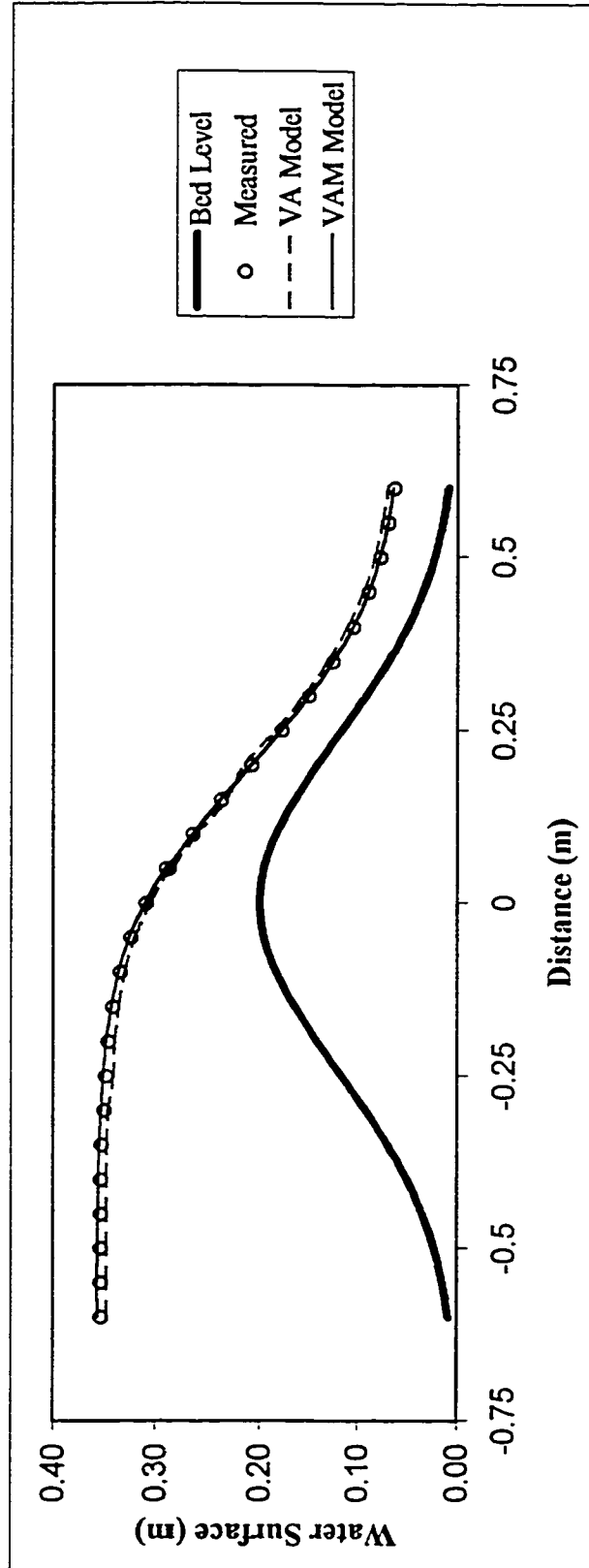


Figure 2.14 The comparison of water surface profiles for Sivakumaran et al.'s (1983)

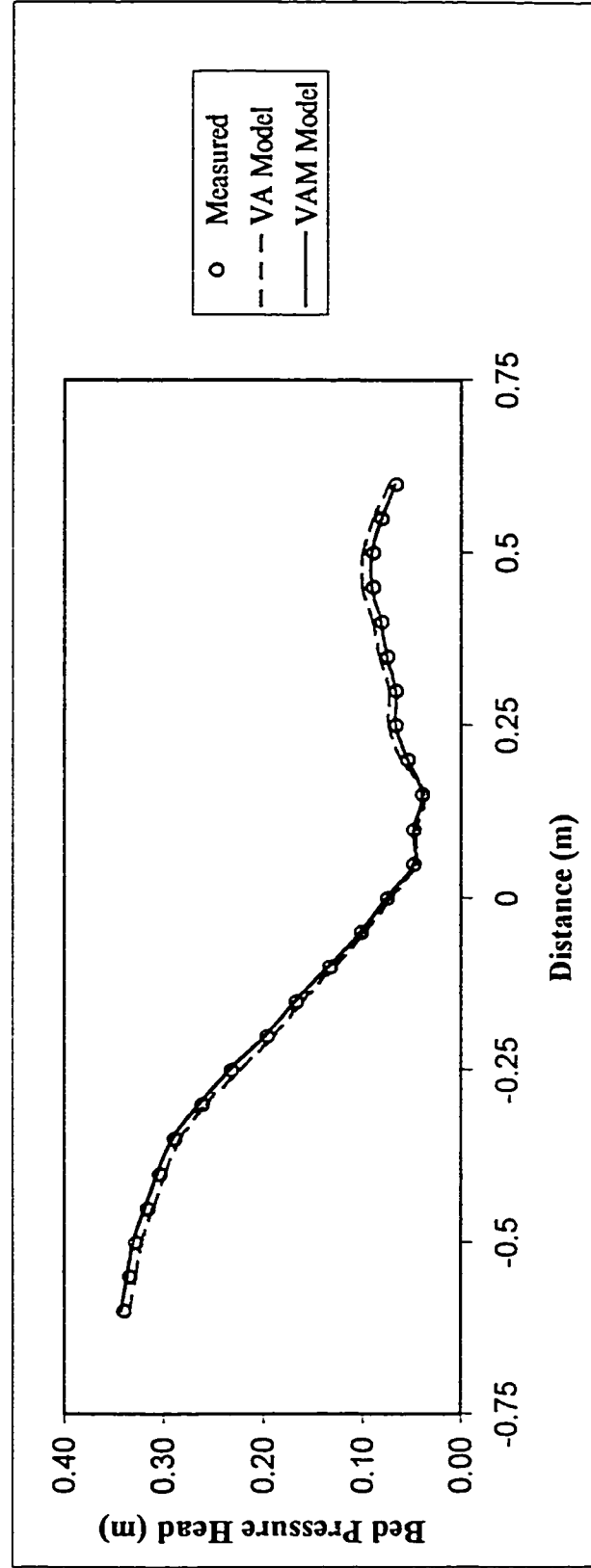


Figure 2.15 The comparison of bed pressure profiles for Sivakumaran et al.'s (1983)

Chapter 3

Rapidly Varied Flow

3.1 Introduction

The flow of water in an open channel is classified as rapidly varied if the depth of flow changes rapidly or abruptly over a relatively short distance; examples are the hydraulic jump and the rapidly varied transitions. Rapidly varied flow may have streamline curvature such that the pressure distribution can no longer be assumed to be hydrostatic and the velocity distribution can not be assumed to be uniform. The rapid variation in flow regime often occurs in a comparatively short distance and thus the boundary friction is relatively small and in most cases is insignificant (Chow, 1959).

Rapidly varied flow encompasses many different applications in open channel hydraulics. These applications include: flow through bridge contractions, design of channel transitions, abrupt rises and drops, rapid operation of flow control structures, catastrophic failure of a dam and so forth (French, 1985). Therefore, an accurate description and understanding of the rapidly varying flow regime is highly important. Most of the literature addresses specific topics, for example different kinds of hydraulic jumps or rapid transitions. A brief review of rapidly varied flow problems, mainly transitions, is considered in this chapter.

3.1.1 Rapid transitions

Open channel transitions are commonly used in structures between canals and flumes and between canals and tunnels to reduce energy losses. They are also used in some critical flow measuring devices (Chow 1959). The design of channel transitions has received the attention of hydraulic engineers for a long time and has been formulated into a number of suggestions and procedures (Ippen and Dawson, 1951).

Rapidly varied transitions, such as rapid contractions or expansions of the flow in a horizontal or vertical plane, typically involve flows with high curvature of the streamlines. The length of these transitions is relatively small. As a result, nonuniform velocity and non-hydrostatic pressure distributions may have an effect. In addition, the bed shear stress may be no longer attributed to the corresponding uniform flow conditions. Determining the depth of flow is complicated in such transitions because of the boundary features of these transitions. These boundary features in supercritical flow cause disturbances that can result in a significant increase in the local flow depth. As a result, an accurate description and understanding of the rapidly varying flow regime in such transitions is highly desirable.

The presence of transitions in high velocity channels can cause the flow to choke, to form a hydraulic jump or to produce a series of standing waves. Complex wave patterns due to multiple reflections of the boundary and their subsequent interactions with one another are possible. These flow disturbances complicate the structure

design. In addition, both sub- and supercritical flows are more likely to be present when the standing waves interact with one another. That makes the analyses even more complicated. A three dimensional model would be able to model these rapidly varied flow situations satisfactorily. However, the computational effort involved and the difficulties in defining the geometry and treating the boundary conditions are usually the limiting factors (Berger and Stockstill, 1995).

Studies considering supercritical flow passing through transitions have been conducted by several researchers. Among them, Rouse et al. (1951) and Ippen and Dawson (1951) made noteworthy analytical and experimental studies of supercritical flow in transitions. Herbish and Walsh (1972) tested the suitability of the method of characteristics, as developed by Bagge and Herbich (1967), for predicting the form of supercritical flow passing through a rectangular expansion. The angle of the expansion was larger than 5° . They recommended that the method of characteristics be redeveloped with the friction term included to provide a proper check of its suitability for predicting supercritical flow.

Pandolfi (1975) and Rajar and Centina (1983) solved the two-dimensional steady flow equations numerically to simulate the supercritical flow in transitions. Fennema and Chaudhry (1990) used two-dimensional finite difference to simulate mixed sub- and supercritical flows in transitions. They recommended that extreme care should be taken on including the side wall boundaries. Bhallamudi (1992) used two-

dimensional, depth-averaged, unsteady flow equations in a transformed coordinate system to analyze flows in channel expansions and contractions.

Berger and Stockstill (1995) applied a two-dimensional finite-element model to simulate a supercritical flow passing through a contraction. The model utilized a characteristic based Petrov-Galerkin method and a shock-detection mechanism. Rahman and Chaudhry (1997) used a two-dimensional, second-order accurate finite difference scheme to simulate supercritical flow passing through a contraction. An adaptive grid system, instead of a fixed grid system, was used for a better resolution of the flow properties. Hydrostatic pressure and uniform velocity distributions were assumed in their approach.

3.1.2 Free overfalls

Rouse (1936, 1943) experimentally studied the end depth of a horizontal rectangular free overfall. Rajaratnam et al. (1976) conducted a detailed experimental study in the upstream portion of a rectangular free over fall for various bed slopes. They measured pressure, velocity and shear stress distributions. In addition, they studied the effect of bed roughness on the velocity, pressure and shear stress distributions at the brink.

Clarke (1965) used a two-dimensional potential flow to solve for the surface profile upstream of a rectangular free overfall and the boundaries of the free jet. Moayeri (1970) applied potential flow theory with numerical integration to solve for the free rectangular overfall. Hager (1983) used an analytical approach using an extended

Bernoulli equation to solve for the free rectangular overfall. Marchi (1993) obtained an analytical solution for the potential flow and used it to solve for the free rectangular overfall. Montes (1992) obtained a solution for the free rectangular overfall problem after solving the potential flow equations numerically.

3.1.3 Hydraulic jump

McCorquodale and Khalifa (1983) used the two dimensional Reynolds equations to solve the hydraulic jump problem. Their approach was based on integrating the Reynolds equations. Gharangik and Chaudhry (1991) applied a one-dimensional unsteady, rapidly varied flow finite-difference numerical technique with an explicit artificial viscosity to study the hydraulic jump problem. Hicks and Steffler (1992) used a finite element Petrov Galerkin scheme to analyze the hydraulic jump phenomena. Garcia-Navarro et al. (1994) applied a finite difference numerical technique with flux limiters to calculate the length and the location of a hydraulic jump. Younus and Chaudhry (1994) incorporated the k - ϵ model in their numerical model to calculate the hydraulic jump length. They showed that the length was found to be mainly governed by the artificial viscosity or the numerical diffusion coefficients applied.

3.1.4 Unsteady rapid flow

Vide (1992) made a review on the classification of rapidly varied unsteady flow from continuity and momentum principles. Non-dimensional equations, in a purely algebraic way, were proposed for analyzing the combinations of super- or subcritical

regimes in a one-dimensional surge. Uniform velocity and hydrostatic pressure distributions were assumed. The friction and weight forces were neglected. Chanson (1997) made a review on several near-critical flow situations. These flows included: undular surges, undular hydraulic jumps and undular flow above a broad-crested weir

Most of the previous computational models used to model rapidly varied flow situations were based on the depth or vertically averaged classical de Saint Venant equations due to their efficiency and reasonable accuracy. These equations are based on the fundamental assumptions of uniform velocity and hydrostatic pressure distribution conditions. As a result, these equations are applicable for flows in which large width-to-depth ratios exist and the vertical variation in the mean flow quantities, due to strong vertical mixing induced by the bottom shear stresses, is not significant (Henderson, 1966). Yen (1973) showed that correction factors or coefficients could be applied, on using these equations, for velocity or pressure distributions to account for cases where non-uniform velocity and non-hydrostatic pressure distributions are significant. He added that these distributions should be established a priori to evaluate such correction coefficients, though.

Another set of equations that have been used to model rapidly varied flow is the Boussinesq equations. These equations represent the next higher level of approximation compared to de St. Venant equations as they assume linear vertical velocity and linear non-hydrostatic pressure distributions. They are thus applicable for moderately shallow water flows with wavelength to depth ratios of about six

(Steffler and Jin, 1993). Abbott (1979) noted that it is necessary to employ third- or higher-order accurate methods to solve the Boussinesq equations numerically. Montes (1994) pointed out that these equations are limited to problems with mild slopes, though.

A further alternative in terms of depth or vertically averaged modeling was introduced by Steffler and Jin (1993). Therein, more vertical details are incorporated in their one-dimensional model compared to the classical de St. Venant model. Moment equations were developed by vertically integrating the plane Reynolds equations having multiplied by the vertical coordinate. The extra equations allow solution of the extra degrees of freedom introduced by the extra vertical parameters. A linear longitudinal velocity and quadratic vertical velocity and pressure distributions were assumed. The equations were then rewritten in terms of the parameters of these distributions.

Steffler and Jin showed that the new equations are applicable for flows with wavelength to depth ratios as small as one. They added that the assumed longitudinal velocity distribution may allow for direct and better representation of bed shear stress in non-uniform flow. The method suffers, however, from the crudeness and arbitrariness of the assumed distributions. The long and complex equations that result are difficult to derive and model correctly. Khan (1995) applied this method to some one-dimensional rapidly varied flow problems successfully.

This study uses the proposed model, vertically averaged and moment model derived in chapter 2, with assumed linear distributions of horizontal velocity components and quadratic vertical velocity and pressure distributions (the VAM linear model). The model is used to simulate the flow passing through transitions.

The main objectives of this study are as follows:

1. To test the proposed model for simulating rapidly varied flow transitions with relatively small wavelength to depth ratios ($\lambda/h \approx 7$, λ being the wavelength) where non-hydrostatic pressure and non-uniform velocity distributions might be expected to be significant.
2. To see if there is an improvement of the proposed model over the conventional de St. Venant model in simulating flows with such transitions.

The hybrid Petrov-Galerkin and Bubnov-Galerkin finite element schemes, mentioned earlier, are used in the simulation. Two channel laboratory scale experimental tests are selected for validation and comparison purposes.

3.2 Applications

Comparisons of the model predictions are made with the experimental results obtained by Ippen and Dawson (1951) and Parshall (1926). These two channels are selected as they have transitions with relatively small wavelength to depth ratios

($\lambda/h \approx 7$) where non-hydrostatic pressure and non-uniform velocity distributions might be expected to be significant. As a result, a noticeable difference between the proposed model and the conventional de St. Venant model could be anticipated.

In both cases, the finite element grids are designed to be fine enough to meet the requirements of reasonable accuracy as well as execution time. The program is run till a steady state solution is obtained. The 10 and 3 equation models are used in these simulations.

3.2.1 Ippen and Dawson's (1951) experiment

The numerical model is compared and tested with the flume results reported in Ippen and Dawson (1951). The channel had a straight entry length and then contracted from 2 ft (0.6096 m) to 1 ft (0.3048 m) wide in a length of 4.78 ft (1.457 m), i.e., an angle of 6° on each side. The channel had a rectangular cross section. The layout of this channel is shown in Figure 3.1.

The test is performed for an approach Froude number of 4, with a total discharge of 1.44 ft³/s (0.0408 m³/s), an upstream depth of 0.1 ft (0.03048 m) and a velocity of 7.15 ft/s (2.19 m/s).

The simulation is performed using a finite element mesh composed of 3623 triangular elements and 1954 nodes (Figure 3.2). The mesh is designed such that additional nodes are added to the contracted part (the transition part) of the flume to

accommodate the expected high velocity gradients in this area. Conversely, fewer nodes are placed in the straight parts of the flume as less velocity variation is to be expected in these areas.

The boundary conditions are specified as supercritical inflow at left side, supercritical outflow at the right side and no-flow across the vertical side walls. The boundary conditions specified at the inflow section are total discharge = $0.0408 \text{ m}^3/\text{s}$, flow depth = 0.0305 m , $u_I = 0.0$ and $v_I = 0.0$. The initial conditions are prescribed as $h = 0.0305 \text{ m}$, $q_x = 0.0408 \text{ m}^2/\text{s}$ and the rest of the variables (q_y , u_I , v_I , \bar{w} , w_b , w_h , h_I and h_2) are set to zero. The program is run till a steady state solution is obtained.

The results are shown in Figures 3.3-3.5. Figure 3.3 shows the measured depth contours obtained by Ippen and Dawson. Figure 3.4 shows the simulated depth contours obtained by the proposed VAM model, while Figure 3.5 shows the simulated depth contours obtained by the VA model (de St. Venant model).

It can be seen from Figures 3.3-3.4 that the overall quality of the simulated solution compares reasonably well with the measured values. In addition, the VAM model seems to behave almost the same as the VA model (see Figures 3.3-3.5).

3.2.2 Ye and McCorquodale's (1997) experiment

The flume results of Ye and McCorquodale (1997) are invoked to test the ability of the model to simulate the near critical flow conditions. The experiment was conducted at the University of Windsor in a Parshall flume. The Parshall flume, which was developed by Parshall (1926), is considered one of the most widely installed open channel devices for field flow measurements. The flume consisted of a contracting section with a flat floor to create the critical depth; a throat section with parallel side walls and a sloping bed in which supercritical flow occurs; and a diverging section with an adverse sloping bed. The flume had a rectangular cross section. The layout of the flume is shown in Figure 3.6. The flow discharge was equal to $0.0145 \text{ m}^3/\text{s}$.

The simulation is performed using a finite element mesh composed of 2485 triangular elements and 1383 nodes (Figure 3.7). Additional nodes are added to the part of the flume in the vicinity of critical flow where velocity gradients are expected to be high. Conversely, fewer nodes are placed in the other parts of the flume where less velocity gradients are expected.

The boundary conditions are specified as subcritical inflow, supercritical outflow and no-flow across the side vertical walls. The boundary conditions specified at the inflow section are total discharge = $0.0145 \text{ m}^3/\text{s}$, $u_I = 0.0$, and $v_I = 0.0$. Initial values for the depth h are assumed while the rest of the variables (q_x , q_y , u_I , v_I , \bar{w} , w_b , w_h , h_I and h_2) are set to zero. The program is run till a steady state solution is obtained.

The results are shown in Figures 3.8-3.15. Figure 3.8 compares the experimental and numerically predicted cross channel averaged water surface elevation. Figures 3.9-3.15 compare the experimental and numerically predicted depth averaged longitudinal velocity distributions across the flume at different cross sections.

It can be clearly seen from Figure 3.8 that the proposed VAM model simulates favorably the cross channel averaged water surface elevation. In addition, the proposed model seems to predict the flow better than the traditional de St. Venant model (VA model) in the vicinity of the critical flow section.

It can be noticed from Figures 3.9-3.15 that the agreement with the experimental results is generally good. The model seems to underestimate the results particularly near the walls at some cross sections (cross sections 2, 3, 4 and 7). In addition, the VAM and VA models seem to behave almost the same.

As a result, the overall quality of the VAM simulated solutions compare well with the measured values and the VAM model seem to predict the flow better than the VA model.

3.3 Comparison of Computational Effort

For both the transition and the Parshall flume, a comparison between the VAM 10-equation and the conventional 3-equation de St. Venant (VA) models in terms of

computational effort and time necessary for simulation is made. It is found that the time required for the VAM 10-equation model to converge to a final steady state solution is approximately four times larger than that of the VA model. The memory allocated for the VAM 10-equation model is found to be eleven times larger than that of the VA model, though.

3.4 Summary and Conclusions

The proposed model with assumed linear distributions of horizontal velocity components and quadratic vertical velocity and pressure distributions (the VAM linear model) is used in this study. The 3-equation and 10-equation models are used in the simulation. The finite element hybrid Petrov-Galerkin and Bubnov-Galerkin schemes are used.

The obtained derived equations are investigated for modeling rapidly varied flow transitions with relatively small wavelength to depth ratios ($\lambda/h \approx 7$) where non-hydrostatic pressure and non-uniform velocity distributions might be expected to be significant. Two experimental hydraulic problems, from the literature, are selected.

A comparison between the VAM 10-equation and the conventional 3-equation de St. Venant (VA) models in terms of computational effort and time necessary for simulation is made.

The conclusions of this study are stated as follows:

1. Generally, a satisfactory agreement is obtained between the numerical predictions and the experimental measured data. The obtained results show that slightly improved water surface profile details are gained by the proposed model compared to the conventional depth or vertically averaged de St. Venant model.
2. This study suggests that the test cases considered don't contain wavelength short enough to show the significance of the non-hydrostatic and non-uniform effects.
3. It is found that the time required for the VAM 10-equation model to converge to a final steady state solution is approximately four times larger than that of the traditional de St. Venant model (the 3-equation VA model). In addition, the memory allocated for VAM 10-equation model is found to be eleven times larger than that of the VA 3-equation model.

3.5 References

- Abbott, M. B. (1979), "Computational hydraulics: elements of the theory of free surface flows." Pitman Publishing Limited, London, United Kingdom.
- Bagge, G. and Herbich, J. B. (1967), "Transitions of supercritical open-channel flow." Journal of the Hydraulics Division, ASCE, Vol. 93, No. HY5, Proc. Paper 5417, Sep., pp. 23-41.

- Berger, R. C. and Stockstill, R. L. (1995), "Finite-element model for high-velocity channels." *Journal of Hydraulic Engineering*. ASCE, Vol. 121, No. 10, Oct., pp. 710-716.
- Bhallamudi, TY and Chaudhry, M. Hanif (1992), "Computation of flows in open-channel transitions." *Journal of Hydraulic Research*, IAHR, Vol. 30, No. 1, pp. 77-93.
- Chanson, H. (1997), "Free-surface flows with near-critical flow conditions." *Can. J. Civ. Eng.* 23: 1272-1284.
- Chow, Ven Te (1959), "Open-channel hydraulics." Book, The McGraw-Hill Company, New York.
- Clarke, N. S. (1965), "On two-dimensional inviscid flow in a waterfall." *Journal of Fluid Mechanics*, Vol. 22, Part 2, 359-369.
- Fennema, Robert J. and Chaudhry, M. Hanif (1990), "Explicit methods for 2-D transient free-surface flows." *Journal of Hydraulic Engineering*. ASCE, Vol. 116, No. 8, Aug., pp. 1013-1034.
- French, Richard H. (1985), "Open-channel hydraulics." Book, The McGraw-Hill Company, New York.
- Garcia-Navarro, P., Priestley, A. and Alcrudo, F. (1994), "An implicit method for water flow modeling in channels and pipes." *Journal of Hydraulic Research*, IAHR, Vol. 32, No. 5, pp. 721-742.
- Gharangik, Araz M. and Chaudhry, M. Hanif (1991), "Numerical simulation of hydraulic jump." *Journal of Hydraulic Engineering*. ASCE, Vol. 117, No. 9, Sep., pp. 1195-1211.

- Hager, W. H. (1983), "Hydraulics of plane free overfall." *Journal of Hydraulic Engineering*. ASCE, Vol. 109, No. 12, Dec., pp. 1683-1697.
- Henderson, F. M. (1966), "Open Channel Flow." Book, The Mcmillan Company, New York.
- Herbish, John B. and Walsh, Peter (1972), "Supercritical flow in rectangular expansions." *Journal of the Hydraulics Division*, ASCE, Vol. 98, No. HY9, Sep., pp. 1691-1700.
- Hicks, F. E. and Steffler, P. M., 1992. "Characteristic Dissipative Galerkin Scheme for Open-Channel Flow." *Journal of Hydraulic Engineering*. ASCE, Vol. 118, No. 2, pp. 337-352.
- Ippen, A. T. and Dawson, J. H., 1951. "Design of Channel Contractions." *Transactions of the American Society of Civil Engineers*, Vol. 116, pp. 341-355.
- Khan, A. (1995), "Modeling Rapidly Varied Open Channel Flows." PhD Thesis, Water Resources Engineering, Department of Civil Engineering, University of Alberta.
- Marchi, Enrico (1993), "On the free overfall." *Journal of Hydraulic Research*, IAHR, Vol. 31, No. 6, pp. 777-790.
- McCorquodale, J. A. and Khalifa, A. (1983), "Internal flow in hydraulic jumps." *Journal of Hydraulic Engineering*. ASCE, Vol. 109, No. 5, May, pp. 684-701.
- Moayeri, M., Strelkoff, Th. (1970), "Pattern of potential flow in a free overfall." *Journal of the Hydraulics Division*, ASCE, Vol. 96, No. HY4, April, pp. 879-901.

- Montes, J. S. (1992), "A potential flow solution for the free overfall." Proc. Instn Civ. Engrs Wat., Marit. & Energy, 96, Dec., 259-266.
- Montes, J. S. (1994), "Potential-flow solution to 2D transition from mild to steep slope." Journal of Hydraulic Engineering. ASCE, Vol. 120, No. 5, May, pp. 601-621.
- Pandolfi, M. (1975), "Numerical experiments on free surface water motion with bores." Proc. 4th Int. Conf. on Numerical Methods in Fluid Dynamics, Lecture Notes in Physics No. 35, Springer-Verlag, pp. 304-312.
- Parshall, R. L. (1926), "The improved Venturi flume." Trans. ASCE, ASCE, 89, pp. 841-880.
- Rahman, Mizanur and Chaudhry, M. Hanif (1997), "Computation of flow in open-channel transitions." Journal of Hydraulic Research, IAHR, Vol. 35, No. 2, pp. 243-256.
- Rajar, R. and Centina, M. (1983), "Two-dimensional dam-break floww in steep curved channels." Proc. XX Congress of IAHR, Inter. Assoc. for Hydr. Res., Vol. II, pp. 571-579.
- Rajaratnam, N., Muralidhar, D. and Beltaos, S. (1976), "Roughness effects on rectangular free overfall." Journal of the Hydraulics Division, ASCE, Vol. 102, No. HY5, May, pp. 599-614.
- Rouse, H. (1936), "Discharge characteristics of the free overfall." Civil Engineering, Vol. 6, No. 4, 257-260.
- Rouse, H. (1943), "Discussion to energy loss at the base of free overfall." Transaction ASCE, Vol. 108, 1383-1387.

- Rouse, H., Bhoota, B. V. and Hsu, E. V. (1951), "Design of channels expansions." Symposium on High-Velocity Flow in Open Channels, Trans. Amer. Soc. Civ. Engrs., Vol. 116, pp. 347-363.
- Steffler, P. M. and Jin, Y. C., (1993), "Depth averaged and Moment Equations for Moderately Shallow Free Surface Flow." Journal of Hydraulic Research, IAHR, Vol. 31, No. 1, pp. 5-17.
- Vide, P. Martin (1992), "Open channel surges and roll waves from momentum principle." Journal of Hydraulic Research, IAHR, Vol. 30, No. 2, pp. 183-196.
- Ye, J. and McCorquodale, J. A. (1997), "Depth-averaged hydrodynamic model in curvilinear collacted grid." Journal of Hydraulic Engineering, ASCE, 123(5), 380-388.
- Yen, B. C. (1973), "Open channel flow equations revisited." J. Eng. Mech. Div., ASCE, Vol. 99, No. EM5, pp. 979-1009.
- Younus, M. and Chaudhry, M. Hanif (1994), "A deoth averaged $k-\varepsilon$ model for the computation of free surface flow." Journal of Hydraulic Research, IAHR, Vol. 32, No. 3, pp. 415-444.

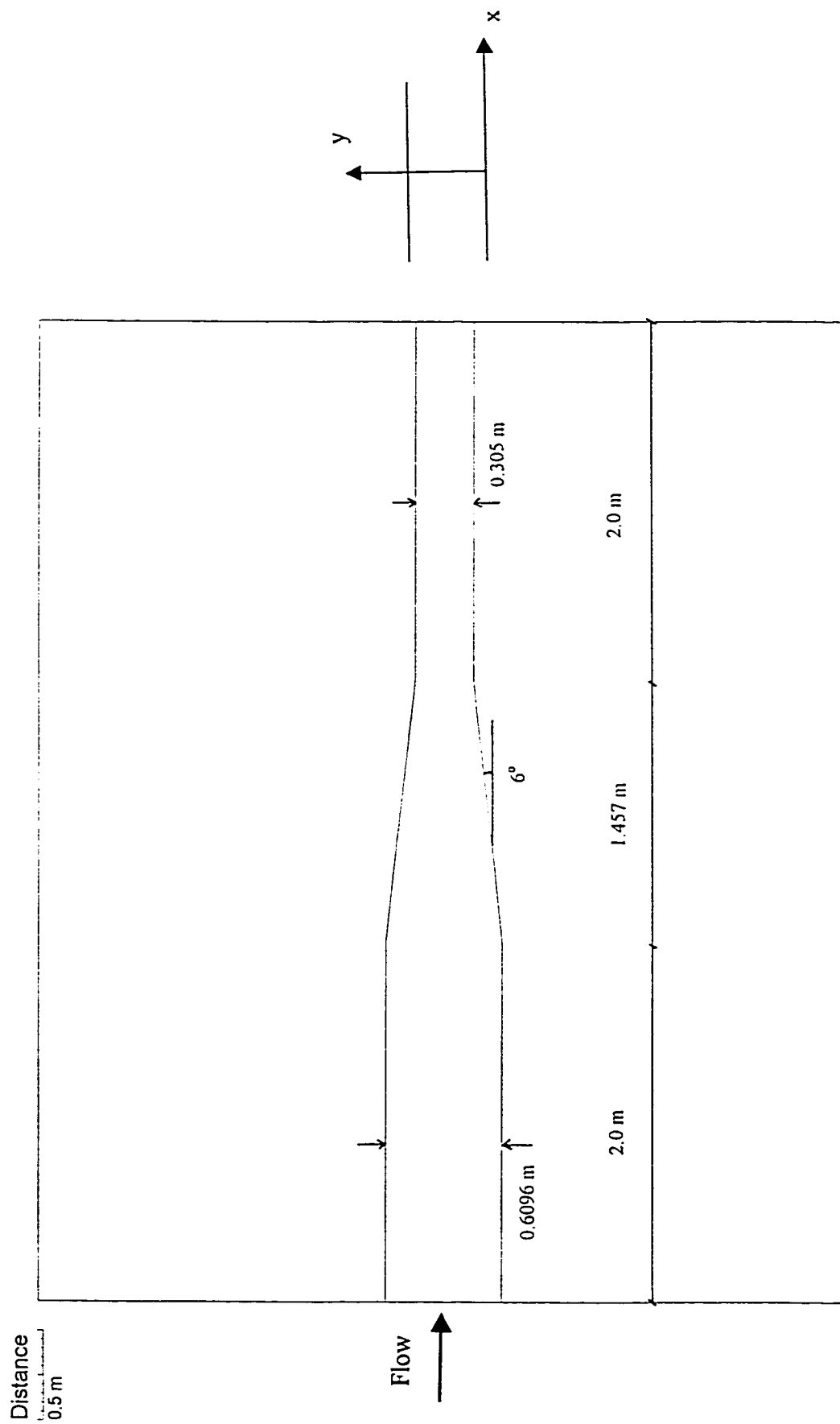
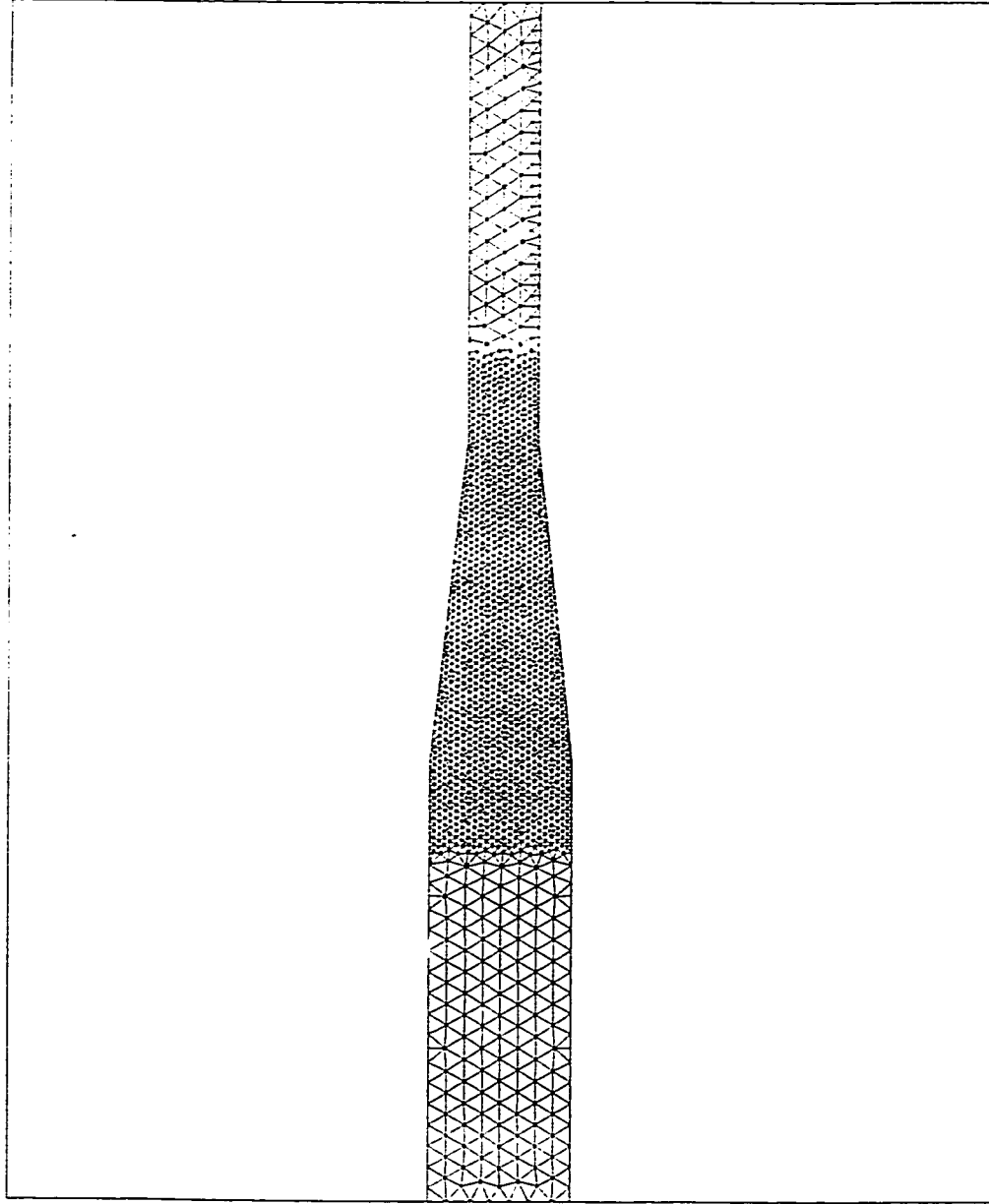


Figure 3.1 The layout of Ippen and Dawson's (1951) experiment

Distance
0.5 m



The generated mesh

Number of nodes = 1954

Number of elements = 3623

Figure 3.2 Finite element mesh for Ippen and Dawson's (1951) experiment

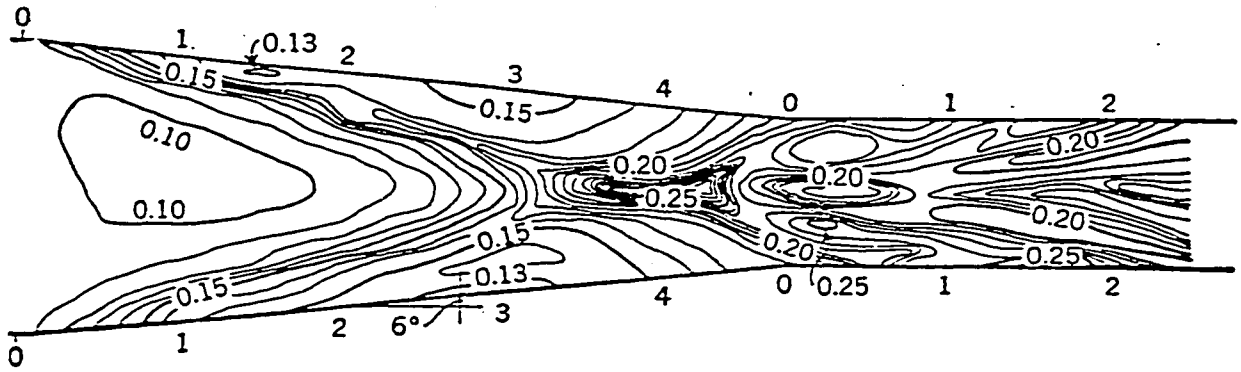


Figure 3.3 Measured depth contours (adapted from Ippen and Dawson, 1951)

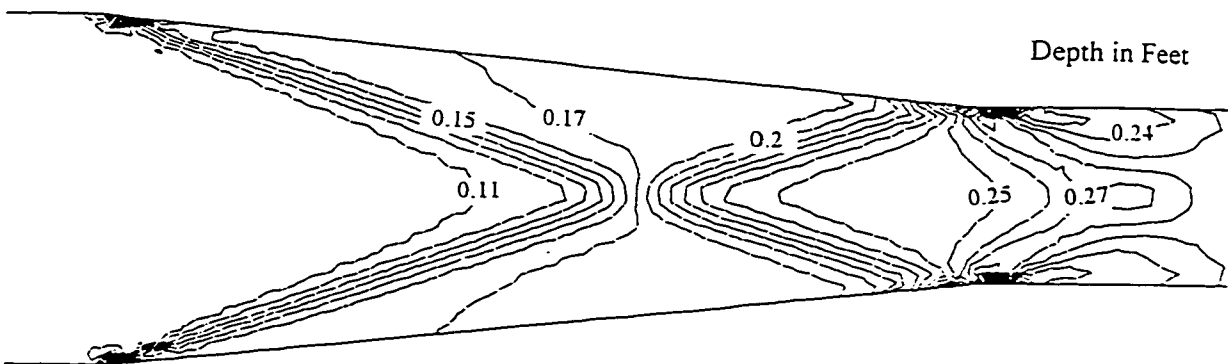


Figure 3.4 Numerical prediction of depth contours for Ippen and Dawson's (1951) experiment (VAM model)

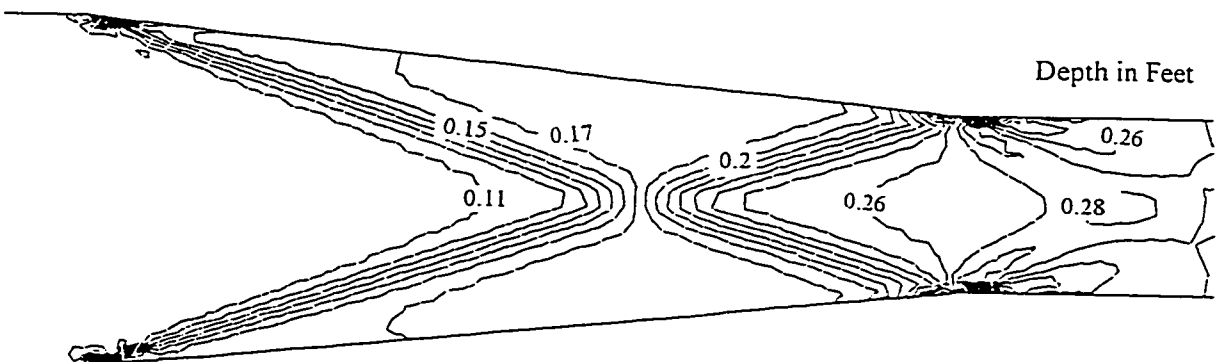


Figure 3.5 Numerical prediction of depth contours for Ippen and Dawson's (1951) experiment (VA or Standard De St. Venant model)

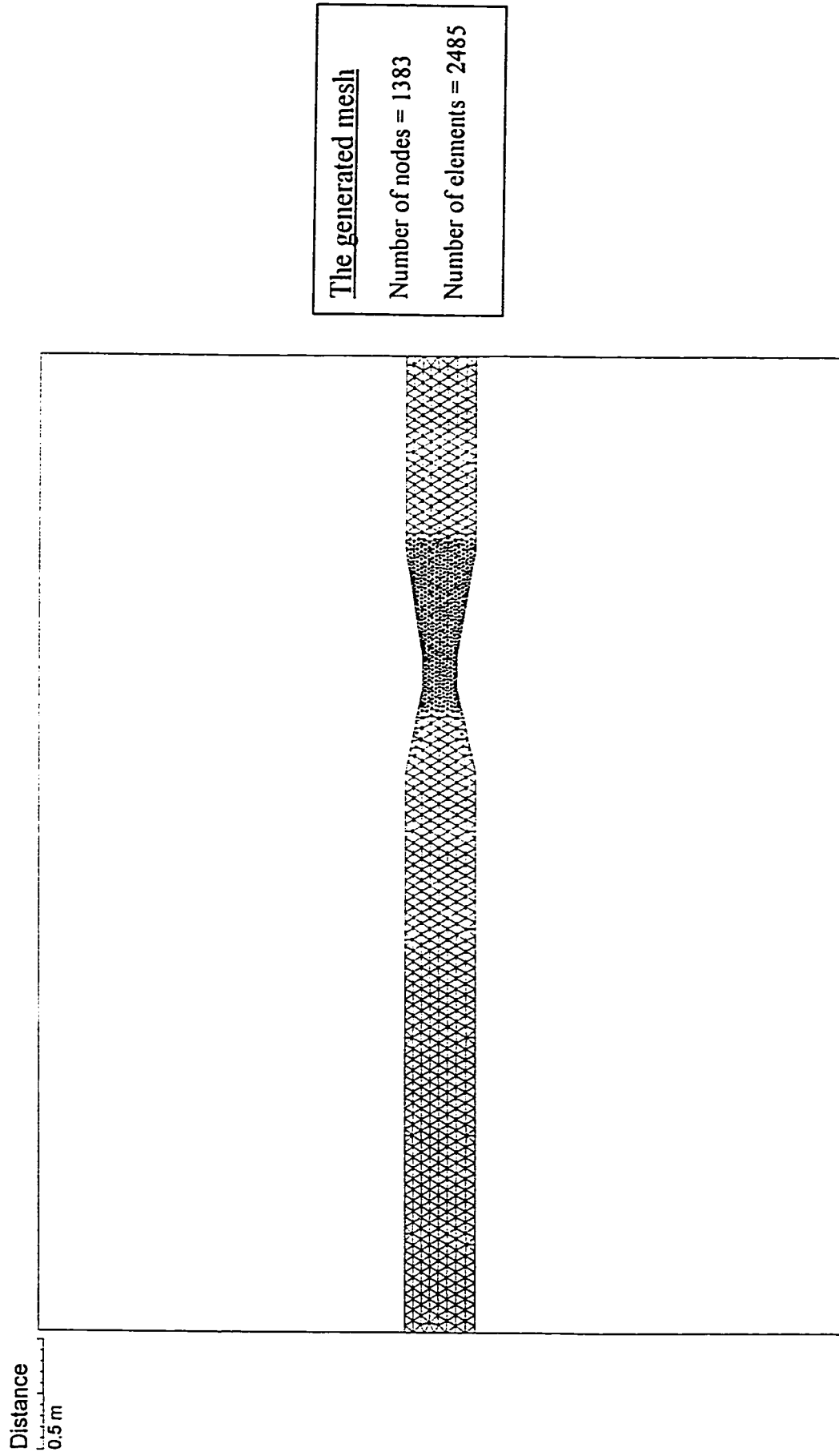


Figure 3.7 Finite element mesh for Ye and McCorquodale's (1997) experiment

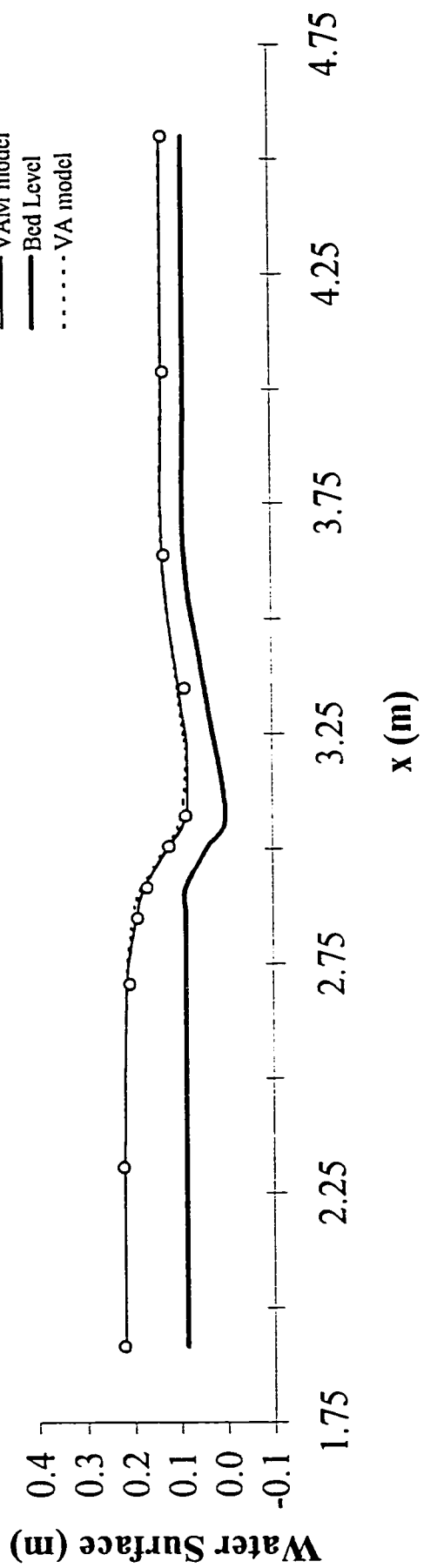


Figure 3.8 Comparison of cross channel averaged surface elevation for Ye and McCorquodale's (1997) experiment

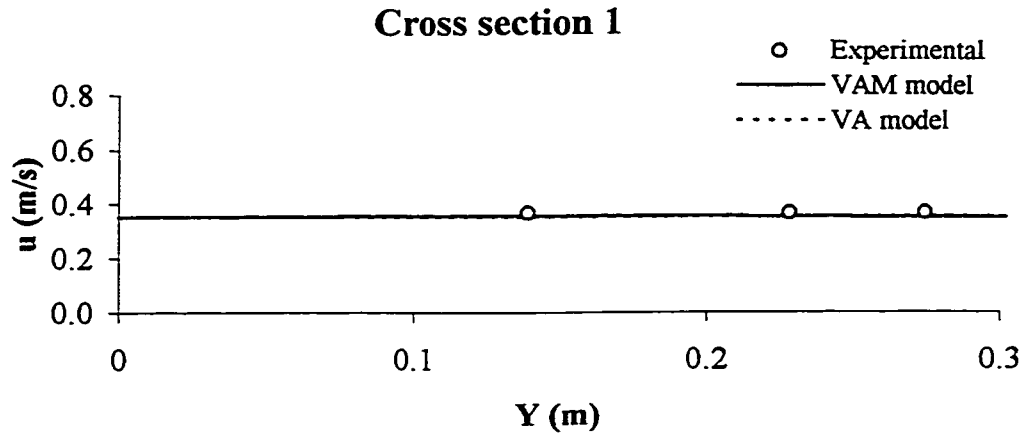


Figure 3.9 The comparison of longitudinal velocity distribution across the flume for Ye and McCorquodale's (1997) at cross-section 1

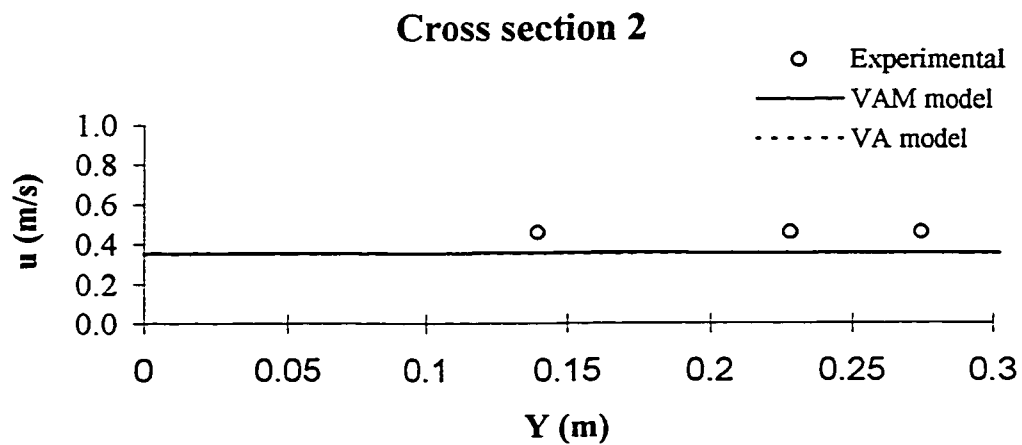


Figure 3.10 The comparison of longitudinal velocity distribution across the flume for Ye and McCorquodale's (1997) at cross-section 2

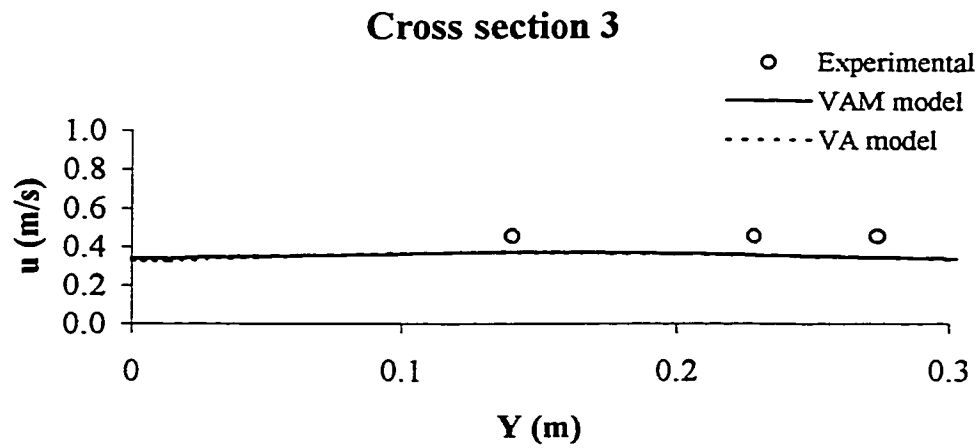


Figure 3.11 The comparison of longitudinal velocity distribution across the flume for Ye and McCorquodale's (1997) at cross-section 3

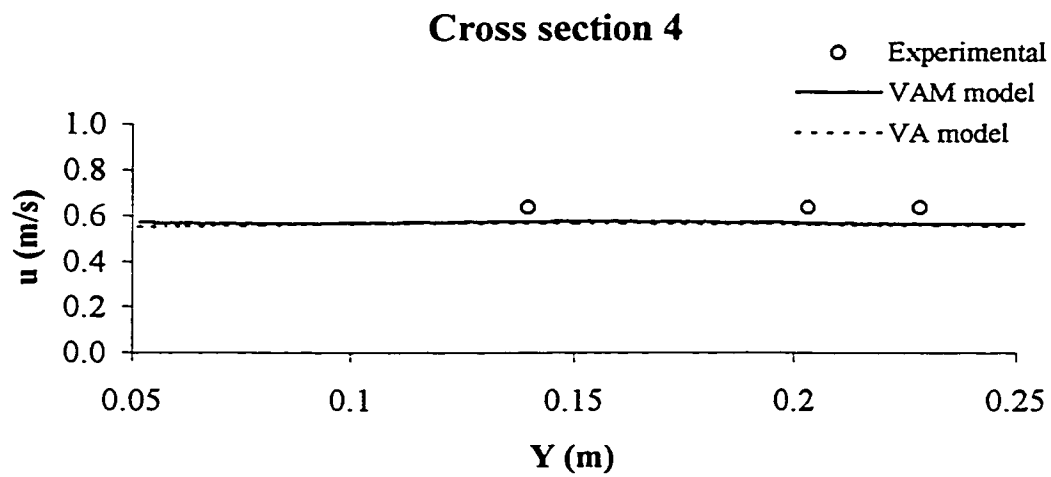


Figure 3.12 The comparison of longitudinal velocity distribution across the flume for Ye and McCorquodale's (1997) at cross-section 4

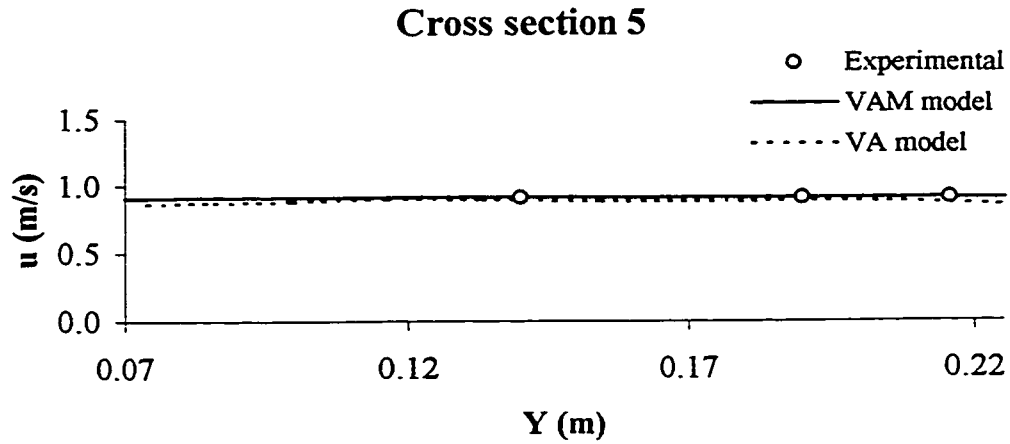


Figure 3.13 The comparison of longitudinal velocity distribution across the flume for Ye and McCorquodale's (1997) at cross-section 5

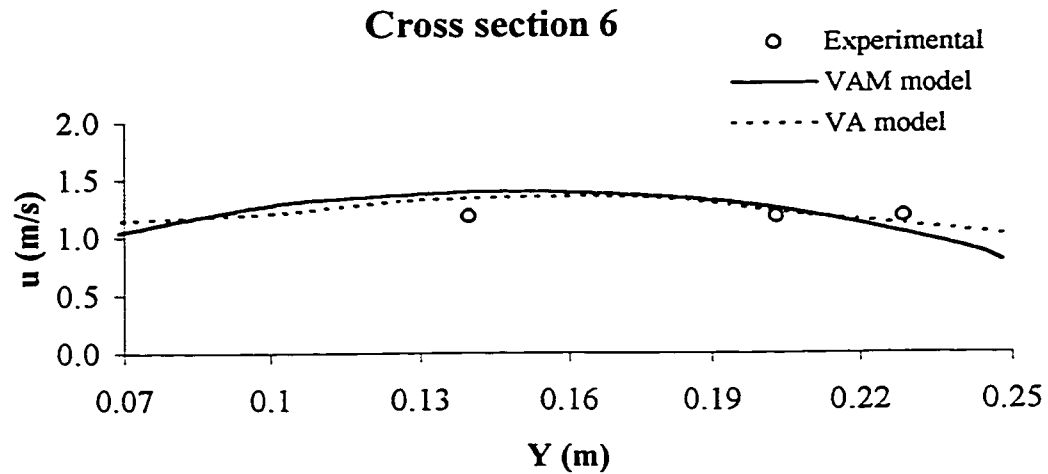


Figure 3.14 The comparison of longitudinal velocity distribution across the flume for Ye and McCorquodale's (1997) at cross-section 6

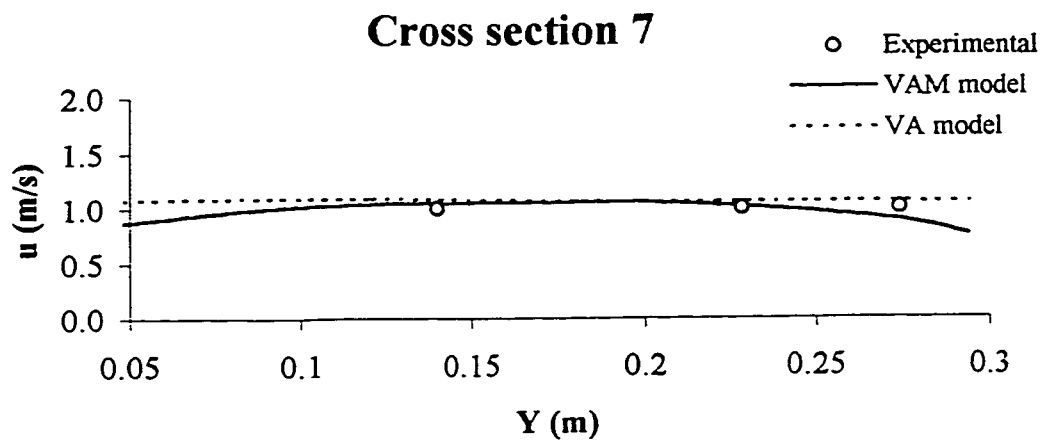


Figure 3.15 The comparison of longitudinal velocity distribution across the flume for Ye and McCorquodale's (1997) at cross-section 7

Chapter 4

Curved Channel Flows

4.1 Introduction

The smooth sinuous or curvature pattern of a natural stream has attracted the interests of both geologists and engineers. As noticed by Leopold and Wolman (1960), it is almost impossible to find a straight stream with length longer than ten channel widths. The engineering importance of channel curvature stems largely from the fact that they affect the flow of water in open channels or streams in many ways. These effects include super-elevation, secondary flows, redistribution of longitudinal velocities, migration of meanders, bank erosion and shifting, bed migration and bed scour in mobile boundary channels.

Many experimental and mathematical studies have been carried out to give an attempt to a clear understanding of the flow characteristics in curved open channels or river bends. Rozovskii (1957) was among the pioneers who conducted a series of experiments on a tight 180° bend of rectangular cross section with straight inlet and outlet reaches. The channel was considered strongly curved and exhibited 3-D flow characteristics ($R_c/2b = 1$), R_c and $2b$ being the radius of curvature to the centerline of the flume and the flume width respectively. As a result, strong secondary velocities were produced. He measured velocity profiles near the channel walls, with the maximum velocity occurring below the water surface. Rozovskii obtained and presented results for depth average tangential velocities, surface elevation contours

and vertical distributions of tangential and transverse velocity components. By performing an order of magnitude analysis, he derived a solution for transverse velocity for turbulent flow.

Ippen and Drinker (1962) investigated and described the distributions and the magnitudes of boundary shear stresses in the curved reaches of smooth trapezoidal channels. That was carried out under conditions of subcritical flow. A series of experimental tests was conducted in a 60°-curved channel to determine the effects of variation in discharge and bend geometry on the shear pattern. Ippen and Drinker found that the locations of the shear maxima were generally found associated with the course of the filament of highest velocity and with the zones of local accelerated motion. Thus, at lower curvatures, the increased stresses are found along the outer bank, in the downstream portion of the curve, while at large curvatures, high shear appears near the inside bank in the curve and near the outside bank below the curve exit. In addition, the relative shear patterns were found to be not greatly modified by variations in depth and velocity at the entrance section but rather by the channel geometry. They also demonstrated the importance of boundary shear stress patterns with respect to the ultimate understanding of erosion and deposition processes in channel curves.

Yen (1965) utilized an indirect way to determine the eddy viscosity field based on the assumption of a logarithmic or power-law vertical distribution of the tangential

velocity (Leschziner and Rodi 1979). He found an approximate solution for the development and the decay of the secondary circulation.

Engelund (1974) described briefly the theory of helical flow in circular bends. The theory was developed for the case of steady fully developed uniform channel in a wide rectangular channel. Only the middle part of the channel, where the vertical velocity components are negligible, was considered in the theory. A constant eddy-viscosity model, a slip velocity condition at the wall, small bank slopes, a quadratic velocity distribution along the depth described by the defect law and a hydrostatic pressure distribution were assumed. The theory was then extended and applied to a more complicated problem of flow in meander bends with movable bed.

De Vriend (1976) developed a mathematical model to describe 3-D flow features in bends. That model, however, seems not to behave well in case of dealing with strongly curved bends. Kupiers and Vreugdenhil (1973) applied a depth-averaged model to account for axial flow features. As the model was based on a depth averaged process, it completely didn't account for secondary flows or in other words the transverse motion (Leschziner and Rodi 1979).

Kalkwijk and DeVriend (1980) developed a mathematical model based on dealing with curvilinear coordinate system for steady flows in shallow rivers with gradual depth changes and moderate curvatures. They explained that accounting for the convective influence of the secondary flow on the main flow is essential to a

mathematical model of curved flow. Kalkwijk and DeVriend used the depth-averaged method to simplify the 3-D curved channel problems into 2-D problems. They believed that by depth averaging the complete 3-D incompressible flow equations (having included the convective influence of secondary flow), a more convenient and appropriate approach would be developed other than applying the expensive full 3-D calculations.

Further simplifications were then applied. Kalkwijk and DeVriend assumed dealing with rivers of which the ratios of depth to width and width to curvature are small and the flow is controlled by friction. A final set of differential equations which accounted for the bottom friction, the flow curvature and the transverse convection of momentum by the secondary flow was derived. The influence of the secondary flow was analyzed and the results were compared with experimental data. The results from their simplified model tended to underestimate the effect of secondary flow, though.

Harrington et al. (1978) used the depth-averaged model, without including necessary extra terms to compute secondary flows or transverse motion, to predict the flow in 180° bend. The results were underestimated because of the lack of the secondary flow effect (Jin and Steffler 1993).

Shimizu and Itakura (1990) made an attempt to calculate 3-D flow and bed deformation with bed load as well as suspended load. A new 3-D model was developed to improve the defects of the 2-D shallow water flow model proposed by Shimizu and Itakura (1986). The model was tested for an experimental flume having

a 180° bend with fixed bed. A hydrostatic pressure distribution was assumed. The 3-D model seemed to predict the flow field more precisely than the 2-D model. Shimizu and Itakura found that the evaluation of the transport of momentum caused by the secondary flow, which was not considered in the 2-D model, is necessary to predict the flow field precisely.

A simplification of the full 3-D model was made to reduce the computational time and effort, in which the vertical distribution of the longitudinal velocity was assumed to be logarithmic. The simplified model was tested in a meandering channel experiment with movable bed. The simplified 3D model was also applied to the computation of bed deformation by bed load as well as suspended load transport in meandering channels. The agreements were found to be good when compared with experimental results. Shimizu and Itakura explained that appropriate estimation of the secondary flow is very important for the bed deformation of meandering channels because it is necessary to predict the direction as well as the magnitude of the flow velocities at the channel bed.

Molls and Chaudhry (1995) developed a general 2-D mathematical model to solve unsteady, depth-averaged equations. Boundary fitted coordinates were used and effective stresses were included. The 2-D depth-averaged equations were obtained by integrating the Navier-Stokes equations from the channel bottom to the water surface. Uniform velocity in the vertical direction, incompressible flow, hydrostatic pressure distribution, small-channel slope, negligible wind shear at the water surface, and negligible Coriolis acceleration were assumed to make it possible to derive the

equations. The depth-averaged stresses were neglected. A constant eddy-viscosity turbulence model was incorporated to approximate the turbulent Reynolds stresses. The time differencing was discretized using a second-order accurate Beam and Warming (1978), while the spatial derivatives were approximated by second-order accurate central differencing approximation. The model was tested to simulate the flow in a 180° channel bend.

Ye and McCorquodale (1997) developed a 2-D depth-averaged free-surface mathematical model in a boundary-fitted curvilinear coordinate system. The convective terms of their model were discretized by a second-order finite volume scheme. A collocated grid system was used in the simulation. The time marching technique was used to reach a steady state solution. The model was applied to a meandering channel. The computed results were compared with experimental data and the agreement was good.

Attention was rather concerned in the previous work on the semiempirical and analytical description of flow features by adopting simplified assumptions that did not show more information regarding, for example, the streamwise development and secondary circulation. This would become more pronounced on dealing with strongly curved bends. In addition, an accurate representation of turbulence models hasn't received much concern in their work. Application of a 3-D model would be sufficient to account for the transverse motion caused by secondary flow. Recently, Ghanmi et al. (1997) formulated a 3-D finite element hydrodynamic model to simulate

secondary flows and their damping in channel bends and flow around obstacles. They focused on the formulation of the viscous terms responsible for developing the secondary flows. Comparisons of experimental and numerical results were presented.

However, the computational effort involved, the additional non-linearity caused by the free surface flow and the complexity of the applied equations make the application of a 3-D model not an easy task. Alternatively, application of 2-D depth-averaged models with extra degrees of freedom or more vertical details would be more reasonable and less expensive from accuracy and computational points of view respectively.

Falcon Ascanio (1979) employed the principle of dealing with the moment of momentum equation in his mathematical model to axisymmetric flow situations (Jin and Steffler, 1993). Odgaard (1986a) developed an analytical model to simulate the flow and bed topography in a meandering alluvial channel or a natural bend with nonuniform approach flow and non-constant radius of curvature. The basis was a solution to the equations for conservation of mass and momentum and for lateral stability of the streambed to account for net lateral mass shift. The bed-stability equation used related the transverse bed slope to primary flow variables. A simple mass-flux balance was used to relate the bed stability equation to the momentum one. Relations for depth and depth-averaged mean velocity were developed. Predefined velocity distributions were substituted into the momentum equations. The analyses showed that the behavior of the transverse bed slope depended on the secondary flow

component as well as the transverse mass shift due to the change in channel curvature. The model was tested with both experimental and field data (Odgaard, 1986b). The main important feature of the model was its account for the net lateral mass shift in relation to streamwise variations.

Johannesson and Parker (1989) developed an analytical model for calculating the lateral distribution of the depth-averaged primary flow velocity in meandering rivers with laterally flat or sloping inerodible beds. They used a small perturbation method to linearize the governing equations. They also used the moment method to make it possible to take into account the convective transport of primary flow momentum by the secondary flow. Johannesson and Parker believed that the convective transport of primary flow momentum by the secondary flow leads to a significant outward redistribution of primary flow velocity. Several researchers (Kalkwijk and De Vriend 1980; and Leschziner and Rodi 1979) have also emphasized on the importance of the same mechanism. Johannesson and Parker explained and quantified the phenomenon of redistribution of primary momentum by secondary flow at a linear level, in the simplest possible fashion to the case of uniform bend flow. The bed topography was assumed to be horizontal in the transverse direction. The model was tested with experimental data.

Yeh and Kennedy (1993a) derived a hybrid integral-differential formulation of free-surface nonuniform, fixed boundary, channel-bend flow in constant-radius open channels. Conservation of flux of moment of momentum and depth-integrated momentum and continuity equations were developed. The integrated equations for the flux of moment of momentum were utilized to formulate the secondary flow and the effects of curvature on the primary-flow velocity profile. Boundary shear stresses were related to the primary-flow shear stress and the primary and secondary velocities. The channel section was treated as rectangular and fixed.

Yeh and Kennedy explained that the consideration of moment formulation is necessary to elucidate the interplay among the secondary and primary flows, particularly the observed flattening of primary velocity profiles and radial redistribution of the depth-averaged primary velocity. By considering conservation of moment of momentum, the phenomenon of the change of the primary flow passing along a long bend was observed by their model. The equations were solved numerically and the results were tested with laboratory data. The analysis was extended in Yeh and Kennedy (1993b) to the case of erodible-bed and fixed wall channels.

Jin and Steffler (1993) introduced a depth-averaged 2-D mathematical model in the Cartesian coordinate for simulating the velocity distribution in curved open channels. The mathematical model consisted of the depth-averaged continuity equation, the momentum equations, and two moment of momentum equations. Parabolic similarity profiles were assumed for the longitudinal as well as the transverse velocities and

were substituted into the moment of momentum equations. A hydrostatic pressure distribution was assumed to simplify the 3-D Reynolds equations into 2-D ones by integrating them over the depth. The effect of secondary flows was included in these profiles.

Jin and Steffler extended the commonly used Chezy bed shear formula to account for the effect of secondary flow on the bed shear stress. The finite element method was used in the numerical simulation as it is more flexible in case of dealing with channels of varying plan curvature. Two experimental data sets from the literature were selected to test and verify the model. Generally, the numerical analysis predicted reasonable secondary flow calculations as well as satisfactory depth-averaged longitudinal and transverse velocities. The characteristic features of the curved channel such as the longitudinal velocity redistribution and longitudinal and transverse velocity profiles seemed to be satisfactorily preserved.

This study uses the derived proposed model, the vertically averaged and moment model derived in chapter 2, with assumed linear and/or quadratic distributions of horizontal velocity components and quadratic vertical velocity and pressure distributions (the VAM linear and/or quadratic models). The proposed model is used to simulate the secondary flow variation in curved channels and the effects of the secondary flow on the depth-averaged flow field. One of these effects is longitudinal velocity redistribution. Curved channels with rigid beds and regular patterns are considered in this study.

The objectives of this study may be stated as follows:

1. To verify and test the validity of the vertically averaged and moment (VAM) equation model for modeling curved open channel flows. In other words, the improvement provided by the proposed model over depth averaged de St. Venant model in simulating the main characteristic features involved in curved channels is to be tested. These features include water surface super-elevation, secondary flow and longitudinal velocity redistribution.
2. To evaluate the sensitivity of the attained results or solutions to different approximations of the pre-assumed velocity and pressure distribution shapes. Comparison between linear and quadratic distributions of horizontal velocity components is to be made. Hydrostatic and quadratic distributions of pressure will also be compared.
3. To evaluate the sensitivity of the attained results or solutions to different approximations of numerical discretizations of the generated finite element meshes.

4. To compare the computational effort and time necessary for different approximations of the pre-assumed velocity and pressure distribution shapes. The question to be answered is whether it would be worthwhile to go from one level of approximation of the pre-assumed velocity and pressure distribution shape to another in terms of attained accuracy, computational effort and time consumed.

The hybrid Petrov-Galerkin and Bubnov-Galerkin finite element schemes are used in the simulation. Five curved channel laboratory scale experimental tests and a field test case are selected for validation and comparison purposes. The experiments include flow in a 180° channel bend with mild curvature (DeVriend, 1976), flow in a 90° channel bend with a variable and irregular cross section (DeVriend, 1980), flow in a 270° channel bend (Steffler, 1984), flow in a 180° channel bend with very strong curvature (Rozovskii, 1961) and flow in two reversing 90° channel bends respectively (Chang, 1971). Coarse and fine finite element meshes are applied in this study. Comparisons of various numerical predictions and the corresponding experimental results are made.

4.2 Experimental Verifications and Comparisons

Comparisons of the model predictions are made with the experimental results obtained by Rozovskii's (1961) run 1, DeVriend (1976 and 1980), Steffler's (1984) run1, and Chang (1971) in curved flumes. Jin and Steffler (1993) used the DeVriend (1976 and 1980) and Steffler's (1984) run1 experiments to test the numerical predictions of their model. The same experiments are selected here to see if the

proposed model gives improved results. Rozovskii's (1961) run 1 experiment is selected as it has been used extensively by other investigators for verification of their numerical and analytical results. The experiment is interesting because the relative curvature is very strong. Chang's (1971) experiment is chosen to check the suitability of the proposed model to predict the features of a reversing flow. Moreover, the most important factor in selecting these experiments is the availability of good detailed data.

In most cases, the finite element grid intensities are designed primarily to meet the requirements of a reasonable execution time. As a result, caution should be exercised in attributing the observed difference between measured and computed results to differences in formulations as numerical discretization errors may not be negligible.

The R2D_VAM program, with both the VAM linear and VAM quadratic models, is run till a steady state solution is obtained. The 10, 5 and 3 equation models are used in these simulations.

4.2.1 Experimental Errors

On comparing predicted and measured velocity distributions consideration must be given to the expected experimental errors. Two kinds of velocity measurement errors can be expected in curved channels. The first one is in measuring the velocity magnitudes, whereas the second one is in measuring the velocity angles or directions. Usually, the relative error in velocity magnitude measurements is estimated to be

fairly small (typically 2%). On the contrary, the relative error in velocity angle measurements may be quite large (typically 20% or higher). As a result, the longitudinal velocity measurements are typically more accurate than the transverse velocity measurements. This may be explained as follows. Consider dealing with the s - n system of coordinates, s and n being the longitudinal and normal to the longitudinal axis respectively. Consider $|V|$ is the velocity magnitude. The longitudinal (V_s) and transverse velocity (V_n) components are then given by:

$$V_s = |V| \cos \theta \dots\dots\dots(4.1)$$

$$V_n = |V| \sin \theta \dots\dots\dots(4.2)$$

Where θ is defined as the angle between the velocity vector and the longitudinal direction. For small θ , equations (4.1)-(4.2) are approximated as:

$$V_s = |V| \dots\dots\dots(4.3)$$

$$V_n = |V| \theta \dots\dots\dots(4.4)$$

If the estimated error in the transverse velocity, V_n , is ε_{V_n} , then ε_{V_n} may be approximately calculated from:

$$V_n + \varepsilon_{V_n} = |V|(\theta + \varepsilon_\theta) \dots\dots\dots(4.5)$$

Where ε_θ is the estimated error in measuring the velocity angle. The relative estimated error in transverse velocity is then given by:

$$\frac{\varepsilon_{V_n}}{V_n} = \frac{\varepsilon_\theta}{\theta} \dots\dots\dots(4.6)$$

Assuming, for example, an estimating error in measuring the velocity angle of $\varepsilon_\theta = 1$ degree and $\theta = 5^\circ$ the expected relative error in measuring the transverse velocity, V_n ,

is estimated from equation (4.6) as $\frac{\varepsilon_{V_n}}{V_n} = \frac{\varepsilon_\theta}{\theta} = \frac{1}{5} \cdot 100 = 20\%$.

Similarly, it can be concluded from equation (4.3) that the expected relative error in measuring the longitudinal velocity magnitude, V_s , is of the same order of that of the velocity (2% as mentioned above).

4.2.2 DeVriend's (1976) experiment

De Vriend (1976) conducted a series of experiments in a 180° rectangular open channel curved flume at the fluid mechanics laboratory of the Civil Engineering Department, Delft University of Technology. One of these experiments is chosen to test the ability of the present model to simulate the flow in curved channel with moderate curvature ($R_c/2b = 2.5$). R_c and $2b$ are the centerline radius and the width of

the flume respectively. The flume had a width of $2b = 1.7$ m with the centerline radius of $R_c = 4.25$ m. Figure 4.1 shows the plan view of the flume.

Total discharge Q of 0.19 m³/s, Froude number of 0.215 and Chezy coefficient C of 57 m^{1/2}/s were used. The downstream water surface elevation was kept constant at a value of 0.18 m.

Neither measurements of the transverse velocity nor the method of measuring could be found in the collected materials of the literature for this case. The error estimates in measuring the velocity magnitude and direction could not be found either.

The simulation is performed using a finite element mesh composed of 1488 triangular elements and 876 nodes (Figure 4.2). The designed mesh, shown in Figure 4.2, is considered the coarsest mesh that could be expected to give reasonably accurate answers. It can be seen that additional nodes are added along the measured cross sections to facilitate the extraction of the cross section data for comparison purposes. In order to preserve the curvature of the boundary domain, the boundary points are set at one-degree intervals around the bend. This can be observed from the relatively small elements along the inside bank.

The boundary conditions are specified as subcritical inflow, subcritical outflow and no-flow across the vertical side walls. The boundary conditions specified at the inflow section on bottom left are total discharge = 0.19 m³/s, $u_l = 0.0$, and $v_l = 0.0$. The boundary condition specified at the outflow section on bottom right is flow depth = 0.18 m. The initial depth h is set to 0.18 m. The rest of the variables (q_x , q_y , u_l , v_l , \bar{w} , w_b , w_h , h_l and h_2) are set to zero. Based on the measured Chezy coefficient, the corresponding roughness height is estimated to be $k_s = 0.0015$ m. (obtained from $\frac{C}{\sqrt{g}} = 6.2 + 5.75 \log\left(\frac{h}{k_s}\right)$). The program is run till a steady state solution is obtained.

The results are shown in Figures 4.3-4.16. Figures 4.3-4.9 compare the experimental and numerically predicted depth averaged longitudinal velocity distributions across the flume at different cross sections. Figures 4.10-4.13 show the predicted surface, mean and bed velocity distributions by the VAM model and mean velocity distribution by the VA model respectively. Figures 4.14-4.15 show the simulated results of mean velocity contours by the VAM quadratic and VA models respectively. Figure 4.16 shows the simulated results of water surface elevation contours by the VAM quadratic model.

It can be seen from Figures 4.3-4.9 that the proposed models, VAM linear and/or VAM quadratic, simulate the longitudinal velocity distributions across the flume at different locations very well and behave significantly better than the VA model.

It is evident from Figures 4.3-4.9, 4.10-4.12 and 4.14 that the longitudinal velocity, as the water enters the curve, is accelerated near the inner bank and retarded near the outer bank. The situation is reversed at the exit of the bend (i.e., the inner bank velocity is smaller than the outer bank velocity at the downstream). The predicted flow velocity distribution by the VAM model is uniform before entering the bend, then the maximum velocity first occurs at the inner bank of the entrance to the bend, then the velocity distribution tends to be uniform. The maximum velocity then starts to shift to the outer bank till it reaches a maximum at the exit.

Such velocity variations are typical of bend flows and were experimentally observed by Ippen et al. (1962), Yen (1965) and Rozovskii (1957). That means the phenomenon of the velocity redistribution is well simulated. This is not the case by the VA model, though (Figures 4.3-4.9, 4.13 and 4.15).

This is due to the fact that the VAM model contains more terms and more equations, which are responsible for generating longitudinal velocity redistribution. Mainly the momentum convection terms ($\frac{\partial hu_1 v_1}{\partial x}$ and $\frac{\partial hu_1 v_1}{\partial y}$), appearing in the momentum equations of the VAM model, are the key factors responsible for such phenomenon. As these important factors are shown in the 5-equation model, then the effect of the 10-equation model, as a preliminary conclusion, would be expected to be small.

The results of the numerical predictions of the water surface elevation by the VA and VAM models appeared to be virtually identical and thus only the results of the VAM quadratic predictions are plotted in Figure 4.16.

A comparison between the full VAM 10-equation and 5-equation models is made. The comparison is carried out in terms of degree of accuracy obtained. This comparison is shown in Figures 4.17-4.19. These figures show clearly that the higher accuracy attained on applying the full VAM 10-equation model is insignificant compared to the VAM 5-equation model. It should be mentioned that this observation substantiates the above preliminary conclusion.

A comparison between the VAM 10-equation, 5-equation and the conventional 3-equation de St. Venant (VA) models in terms of computational effort and time necessary for simulation is made. It is found that the time required for the VAM 10-equation model to converge to a final steady state solution is approximately 2.5 times larger than that of the 5-equation model and 3.4 times larger than that of the VA model. In addition, the memory allocated for the VAM 10-equation model is found to be four times larger than that of the 5-equation model and eleven times larger than that of the VA model.

4.2.3 DeVriend's (1980) experiment

To test the ability of the present model to simulate the flow in a 90° curved flume with uneven bed configuration or with varying cross-sectional area, the experiment

results conducted by DeVriend (1980) are invoked. De Vriend conducted his experiments at the Delft University of Technology and the Delft Hydraulics Laboratories in a hydraulic flume model. The flume had a small depth to width and width to radius of curvature ratios ($R_c/2b = 8.3$). The flume consisted of a 39 m straight part with a symmetric parabolic cross-section followed by a curved part (radius $R_c = 50$ m), in which the deepest point of the bottom gradually shifted from the middle of the channel to the outer bank. The length of the curved part was about 80 m. Figure 4.20 shows the plan view of the flume. The channel had a width of $2b = 6$ m and the cross sections A_0 to B_0 were parabolic with zero longitudinal bed slope, whereas the cross sections C_1 to E_0 were skewed with an average slope of 0.0003. The cross sections B_0 and C_1 formed a smooth transition zone. The geometry of channel sections is plotted in Figure 4.21. The areas of the wet cross-sections in the straight and curved parts of the channel were about the same. Figure 4.22 illustrates the bottom configuration in detail.

The flow was mainly friction controlled, the longitudinal component of the velocity was predominant and the Froude number was small. The Chezy coefficient = $60 \text{ m}^{1/2}/\text{s}$ was used. The bed of the channel had a small inclination to compensate for the friction losses. The experiment with discharge of $0.463 \text{ m}^3/\text{s}$ is chosen to test the numerical predictions. A non-uniform slope varying from 0.0 up to 0.0003 is used in the numerical simulation.

The degree of accuracy in measuring the magnitude and the direction of the velocities was not recorded in the literature for this case. The method of measuring wasn't found either.

The simulation is performed using a finite element mesh composed of 1260 triangular elements and 796 nodes (Figure 4.23). The designed mesh, shown in Figure 4.23, is similar in characteristics to the mesh of the previous case.

The boundary conditions are specified as subcritical inflow, subcritical outflow and no-flow across the vertical side walls. The boundary conditions specified at the inflow section on the bottom are total discharge = $0.463 \text{ m}^3/\text{s}$, $u_I = 0.0$, and $v_I = 0.0$. The boundary condition specified at the outflow section on the top is flow depth = 0.32 m . Initial values for the depth h are assumed while the rest of the variables (q_x , q_y , u_I , v_I , \bar{w} , w_b , w_h , h_I and h_2) are set to zero. The corresponding roughness height to the measured Chezy coefficient is estimated to be $k_s = 0.0015 \text{ m}$. The program is run till a steady state solution is obtained.

The results are shown in Figures 4.24-4.45. Figures 4.24-4.32 compare the experimental and numerically predicted depth averaged longitudinal velocity distributions across the flume at different cross sections. Figures 4.33-4.41 compare the experimental and numerically predicted transverse velocity distributions across the flume at different cross sections. Figures 4.42-4.45 show the predicted surface,

mean and bed velocity distributions by the VAM model and mean velocity distribution by the VA model respectively.

It can be observed from Figures 4.24-4.32 that the proposed models, VAM linear and/or VAM quadratic, simulate the longitudinal velocity distributions across the flume at different locations very reasonably. This is not true near the walls as might be expected, though, as a slip velocity condition is used and the wall friction effects are not well treated or included in the proposed model. Also, it can be seen that the predicted values are overestimated near the inner bank at sections D_o-E_o. It can be noticed that both VAM models behave almost the same and predict very slightly more accurate results than the VA model.

Figures 4.42-4.44 show that the phenomenon of the velocity redistribution (as mentioned before) is well predicted by the proposed model. The difference, in this case, between the VAM predicted results (Figure 4.43) and those of VA (Figure 4.45) is in fact very small.

Figures 4.34-4.41 suggest that the proposed numerical model simulation the secondary flow is quite reasonable, particularly away from the walls, as the trends or tendencies of the secondary flow are well preserved. The predicted values are, however, underestimated at sections A₁-B_o and E_o. This discrepancy is expected at sections A₁-B_o as they represent the non-curved uniform part of the flume. As a result, the secondary flow is expected to be too small or non-existent at these sections.

Locating the downstream boundary a bit further might adjust the underestimated predicted values at section E_o. In addition, these discrepancies in the results could be due to the difficulty in measuring very small values of secondary flow in the laboratory, particularly in a flume with such complicated bed topography. These figures also suggest that both the VAM models give better results than the VA model and the VAM linear model gives results slightly closer to the measurements than the VAM quadratic model, though.

Despite the aforementioned discrepancies, the overall quality of the VAM simulated solutions compare reasonably well with the measured data.

A comparison between the full VAM 10-equation and 5-equation models is made. This comparison is shown in Figures 4.46-4.50. From these figures, it can be easily seen that the attained higher accuracy on applying the full VAM 10-equation model is insignificant compared to the VAM 5-equation model.

A comparison between the VAM 10-equation, 5-equation and the conventional 3-equation de St. Venant (VA) models in terms of computational effort and time necessary for simulation is made. It is found that the time required for the VAM 10-equation model to converge to a final steady state solution is approximately 2.2 times larger than that of the 5-equation model and 3 times larger than that of the VA model. In addition, the memory allocated for the VAM 10-equation model is found to be four

times larger than that of the 5-equation model and eleven times larger than that of the VA model.

4.2.4 Steffler's (1984) experiment

The experimental results conducted by Steffler (1984) at the Hydraulic Laboratory of the University of Alberta in Edmonton are employed herein. The key reason behind selecting these experiments is that detailed data of the longitudinal and transverse velocity profile measurements are found for comparison purposes. Experiment run 1 is selected to test the predictions of the numerical model. Steffler performed his experiments in a 270° curved rectangular flume, with a moderate curvature ($R_c/2b = 3.4$). The flume was 1.07 m in width, 0.21 m in depth, and the radius of curvature to the centerline of the section was $R_c = 3.66$ m. Figure 4.51 illustrates the flume and the locations of measurement stations used in his experiment. Cross sections at 0° , 90° , 180° , and 270° stations are chosen for comparison with the numerical simulation, though.

The experiments were run for two different flow conditions: run 1 with a velocity = 0.36 m/s, a depth = 0.061 m and a Froude number = 0.491; and run 2 with a velocity = 0.42 m/s, a depth = 0.085 m and a Froude number = 0.460. The bed slope was kept constant at a value of 0.00083 and the dimensionless Chezy coefficient C_* was equal to 16.

Measurements of velocity and turbulence were made and recorded in Steffler's (1984) thesis by using the Laser Doppler Anemometer (LDA). The error estimates in measuring the velocity magnitude and direction were not recorded, though.

The simulation is performed using a finite element mesh composed of 1226 triangular elements and 748 nodes (Figure 4.52). Similar criteria, as before, are applied on designing the mesh shown in Figure 4.52.

The boundary conditions are specified as subcritical inflow, subcritical outflow and no-flow across the vertical side walls. The boundary conditions specified at the inflow section at the entrance on the right are total discharge = $0.0235 \text{ m}^3/\text{s}$, $u_I = 0.0$, and $v_I = 0.0$. The boundary condition specified at the outflow section is flow depth = 0.061 m . Initial values for the depth h are assumed while the rest of the variables (q_x , q_y , u_I , v_I , \bar{w} , w_b , w_h , h_1 and h_2) are set to zero. The corresponding roughness height to the measured Chezy coefficient is estimated to be $k_s = 0.0013 \text{ m}$. The program is run till a steady state solution is obtained.

The results are shown in Figures 4.53-4.110. Figures 4.53-4.56 compare the experimental and numerically predicted flow surface elevation across the flume at the selected cross sections. Figures 4.57-4.60 compare the experimental and numerically predicted depth averaged longitudinal velocity distributions across the flume at the selected cross sections. Figures 4.61-4.80 compare the experimental and numerically predicted longitudinal velocity profiles over the vertical direction. Figures 4.81-4.84

show the experimental and numerically predicted transverse velocity distributions across the flume at the selected cross sections. Figures 4.85-4.104 compare the experimental and numerically predicted transverse surface velocity profiles over the vertical direction. Figures 4.105-4.108 show the predicted surface, mean and bed velocity distributions by the VAM model and mean velocity distribution by the VA model respectively. Figures 4.109-4.110 show the simulated results of mean velocity contours by the VAM quadratic and VA models respectively.

It can be clearly seen from Figures 4.53-4.56 that the proposed VAM models predict identical values of the water depths across the flume at the selected locations. That implies that the super-elevation phenomenon is very well preserved.

It can be noticed from Figures 4.57-4.60 that the proposed models, VAM linear and/or VAM quadratic, simulate very accurately the longitudinal velocity distributions across the flume at the selected locations and behave significantly better than the VA model.

Figures 4.57-4.60, 4.105-4.107 and 4.109 illustrates that the phenomenon of velocity redistribution, mentioned earlier, is well simulated. This is not the case by the VA model, though (Figures 4.57-4.60, 4.108 and 4.110).

From Figures 4.61-4.80, it can be seen that the VAM models simulate the longitudinal velocity profiles at different locations across the channel very

satisfactorily and give significantly better results than the VA model. The surface velocities close the inside wall (for example at $y/b = -0.8$ at sections 180° and 270° respectively) are slightly overestimated, though. These discrepancies near the wall are to be expected, though. This can be explained as a consequence of the lack of numerical resolution near the wall and the omission of the physical mechanism of the boundary layer near the walls. Figures 4.61-4.80 don't only suggest that the VAM models predict the depth-averaged flow significantly better than the VA model but they also show that the VAM models simulate measured profile data accurately. The VAM quadratic model seems to capture the shape of the longitudinal velocity profiles much better than the VAM linear model.

As can be seen from Figures 4.81-4.84 that the VAM linear model simulates quite well the secondary flow, while the results predicted by VAM quadratic model are fairly good, particularly away from the wall. Apparently, the VAM models behave significantly better than the VA model.

From Figures 4.85-4.104, it can be said that the agreement between the measured and the VAM predicted results is fairly good. The main characteristic features of the secondary flow such as the slope, the tendency of the velocity profile and the development and decay mechanisms are well preserved at most of the compared locations. The VAM linear model seems to simulate the slope of the secondary flow profiles slightly better than the VAM quadratic model away from the side walls. Noticeably, the VAM quadratic model simulates the secondary flow much better than

the VAM linear model near the walls ($y/b = -0.8$ and 0.8). Obviously, the VAM models behave significantly better than the VA model.

As a result, the overall quality of the VAM simulated solutions compare very well with the measured values and the VAM model seem to predict the flow significantly better than the VA model.

A comparison between the full VAM 10-equation and 5-equation models is made. This comparison is shown in Figures 4.111-4.122. From these figures, it can be easily noticed that the difference between the two solutions suggested by the full VAM 10-equation and the VAM 5-equation models is insignificant (as mentioned earlier).

A comparison between the VAM 10-equation, 5-equation and the conventional 3-equation de St. Venant (VA) models in terms of computational effort and time necessary for simulation is made. It is found that the time required for the VAM 10-equation model to converge to a final steady state solution is approximately 2.3 times larger than that of the 5-equation model and 3 times larger than that of the VA model. In addition, the memory allocated for the VAM 10-equation model is found to be four times larger than that of the 5-equation model and eleven times larger than that of the VA model.

4.2.5 Rozovskii's (1961) experiment

Another set of experiments data that is suited for validating the capability of the present model to simulate the flow field and predict the secondary flows in a bend that exhibits strongly three dimensional characteristics is due to Rozovskii (1961). Rozovskii performed his experiments in a 180° curved rectangular flume with a very strong degree of curvature or a very sharp bend ($R_c/2b = 1$). Rozovskii's experiments have been used extensively by other investigators (e.g., Leschziner and Rodi (1979), Johannesson (1988), Shimizu et al. (1990)) for verification of their analytical and numerical models. The secondary velocities produced in his experiments were very strong due to the sharp curvature of the channel used. Only the results of run 1 are presented here to test the numerical predictions of the proposed model. Rozovskii's channel consisted of a 180° bend with a 6-m-long straight approach and a 3-m-long straight exit. The width of the channel was $2b = 0.8$ m, and the radius of the channel centerline was $R_c = 0.8$ m for the circular reach. Figure 4.123 shows the plan view of the flume.

The entire channel was set on a horizontal bed. The flow depth at entrance was 0.063 m, the flow rate was 0.0123 m³/s and the mean entry velocity was 0.25 m/s. The flow depth at the downstream end was 0.053 m. The channel bottom was smooth and Chezy coefficient was 60 m^{1/2}/s.

Rozovskii obtained and presented results for surface elevation contours as well as for depth averaged tangential velocities. In addition, he presented results for vertical

profiles of tangential and transverse velocity components. The degree of accuracy in measuring the magnitude and the direction of the velocities could not be found in the collected materials of the literature for this case. The method of measuring was not found either.

The simulation is performed using a finite element mesh composed of 2060 triangular elements and 1332 nodes (Figure 4.124). The mesh is designed such that additional nodes are added to the curved part of the flume to accommodate the expected high velocity gradients in this area. Conversely, fewer nodes are placed in the straight parts of the flume as more uniform flow is to be expected in these areas. It can also be seen in Figure 4.124 that additional more nodes are added along the measured cross sections to facilitate the extraction of the cross section data for comparison purposes.

The boundary conditions are specified as subcritical inflow, subcritical outflow and no-flow across the vertical side walls. The boundary conditions specified at the inflow section at the entrance on the left are total discharge = $0.0123 \text{ m}^3/\text{s}$, $u_I = 0.0$, and $v_I = 0.0$. The boundary condition specified at the outflow section at the exit on the left is flow depth = 0.053 m . Initial values for the depth h are assumed while the rest of the variables (q_x , q_y , u_I , v_I , \bar{w} , w_b , w_h , h_I and h_2) are set to zero. Based on the measured Chezy coefficient, the corresponding roughness height is estimated to be $k_s = 0.0004 \text{ m}$. The program is run till a steady state solution is obtained.

The results are shown in Figures 4.125-4.184. Figures 4.125-4.127 compare the water surface elevation along the left side, the center and the right side of the channel respectively. Figures 4.128-4.137 compare the experimental and numerically predicted depth averaged longitudinal velocity distributions across the flume at different cross sections. Figures 4.138-4.158 compare the experimental and numerically predicted longitudinal velocity profiles over the vertical direction. Figures 4.159-4.177 compare the experimental and numerically predicted transverse velocity profiles over the vertical direction. Figures 4.178-4.181 show the predicted surface, mean and bed velocity distributions by the VAM model and mean velocity distribution by the VA model respectively. Figures 4.182-4.183 show the simulated results of mean velocity contours by the VAM quadratic and the VA models respectively. Figure 4.184 shows the simulated results of water surface elevation contours by the VAM quadratic model.

It can be obviously seen from Figures 4.125-4.127 that the proposed VAM models predict favorably the water surface elevations along the flume at different locations. It can be observed from Figures 4.128-4.137 that the proposed models, VAM linear and/or VAM quadratic, simulate the longitudinal velocity distributions across the flume at different locations very well and behave significantly better than the VA model, particularly inside the bend, as to be expected. This is not true near the walls, though. The reason for this discrepancy was mentioned earlier. Both VAM models seem to behave almost the same.

Figures 4.128-4.137, 4.178-4.180 and 4.182 show clearly that the phenomenon of the velocity redistribution, mentioned earlier, is well simulated. This is not quite the case by the VA model, though (Figures 4.128-4.137, 4.181 and 4.183). Figure 4.184 clearly shows that the super-elevation phenomenon is well predicted.

From Figures 4.138-4.158, it can be clearly seen that the predicted longitudinal velocity profiles reveal very satisfactory agreement with the observed ones. The surface velocity at cross-section 8 (at $y/b = -0.5$) is slightly overestimated, though. The VAM quadratic model appears to predict better results than the VAM linear model at most of the locations, except at cross-section 3 ($y/b = 0.5$), cross-section 6 ($y/b = -0.25$), cross-section 8 ($y/b = -0.5$) and cross-section 12 ($y/b = -0.5$ and -1) where the reverse is obviously true. It is clear that the VAM models predict the flow significantly better than the VA model.

From Figures 4.159-4.177, it can be said that the agreement between the measured and the VAM predicted results are good in general. The predicted results by the VAM models at cross-section 3 are said to be only fair (Figures 4.159-4.163). That could be expected, as cross-section 3 is located at the uniform part of the flume where the measured secondary flow is expected to be too small. As a result, any error in measuring could lead to such discrepancy. From Figures 4.164-4.172 (cross section 6), it can be seen that the VAM linear model gives better results than the VAM quadratic model, except near the wall where the reverse is obviously true. This is not the case at cross-section 8, however, as the VAM quadratic model seems to give

better results particularly near the walls ($y/b = -1$ and 1). These observations suggest that there is not much difference in the results for different assumed distribution shapes for the velocities. Obviously, it can be observed that the accuracy attained by the VAM models is significantly better than that of the VA model.

Despite the above discrepancies, the main characteristic features of the secondary flow such as the slope, the tendency of the profiles, and the development and decay mechanisms are still well preserved. It should be mentioned, herein, that Yeh and Kennedy (1993a) recommended that circumspection must be evaluated on comparing any predicted or calculated secondary flow results with those measured by Rozovskii (1961). They believed that some uncertainty surrounded the interpretation of Rozovskii's reported secondary velocities, as their translational and rotational components could not be separated.

Despite the aforementioned discrepancies, the overall quality of the VAM simulated solutions compare reasonably well with the measured values and the VAM model seems to predict the flow significantly better than the VA model.

A comparison between the VAM 10-equation, 5-equation and the conventional 3-equation de St. Venant (VA) models in terms of computational effort and time necessary for simulation is made. It is found that the time required for the VAM 10-equation model to converge to a final steady state solution is approximately 3.2 times larger than that of the 5-equation model and 5 times larger than that of the VA model.

In addition, the memory allocated for the VAM 10-equation model is found to be four times larger than that of the 5-equation model and eleven times larger than that of the VA model.

4.2.6 Chang's (1971) experiment

Chang (1971) performed a series of experiments in rectangular meandering channels measuring with both flow and pollutant concentration. One of his channels with a single meander, which consists of two reversing 90° channel bends, is used to test the reliability of the proposed model to predict the features of a reversing flow. Chang performed his experiments in a channel with moderate curvature ($R_c/2b = 3.6$). The channel had a smooth bed and uniform 90° bends in alternating directions interconnected by a straight reach. The channel was 2.34 m wide, the radius of the channel centerline was $R_c = 8.53$ m, the interconnected straight part was 4.27 m, and the straight inlet and outlet reaches was 2.13 m each. Figure 4.185 shows the plan view of this channel.

The water depth was 0.115 m and the velocity was 0.366 m/s. The measurements were carried out along the second bend of the channel.

Measurements of the longitudinal and secondary flow profiles, the surface transverse velocity or the method of measuring could not be found in the collected materials of the literature for this case. The error estimates in measuring the velocity magnitude and direction could not be found either.

The simulation is performed using a finite element mesh composed of 1955 triangular elements and 1200 nodes (Figure 4.186). The designed mesh, shown in Figure 4.186, is similar in characteristics to the first three experimental cases.

The boundary conditions are specified as subcritical inflow, subcritical outflow and no-flow across the vertical side walls. The boundary conditions specified at the inflow section on the left are total discharge = $0.0985 \text{ m}^3/\text{s}$, $u_I = 0.0$, and $v_I = 0.0$. The boundary condition specified at the outflow section on the right is flow depth = 0.115 m . Initial values for the depth h are assumed while the rest of the variables (q_x , q_y , u_I , v_I , \bar{w} , w_b , w_h , h_1 and h_2) are set to zero. The roughness height is estimated to be $k_s = 0.0015 \text{ m}$. The program is run till a steady state solution is obtained.

The results are shown in Figures 4.187-4.199. Figures 4.187-4.193 compare the experimental and numerically predicted depth averaged longitudinal velocity distributions across the flume at different cross sections. Figures 4.194-4.197 show the predicted surface, mean and bed velocity distributions by the VAM model and mean velocity distribution by the VA model respectively. Figures 4.198-4.199 show the simulated results of mean velocity contours by the VAM quadratic and VA models respectively.

It can be observed from Figures 4.187-4.193 that the proposed models, VAM linear and/or VAM quadratic, simulate the longitudinal velocity distributions across the

flume at different location very well and behave significantly better than the VA model. This is not, however, quite true near the walls. It can be also observed that the VAM quadratic model simulates the flow slightly more accurately than the VAM linear model.

Figures 4.187-4.193, 4.194-4.196 and 4.198 reveal that the phenomenon of the velocity redistribution is well predicted. This is not the case by the VA model, though (Figures 4.187-4.193, 4.197 and 4.199).

A comparison between the full VAM 10-equation and 5-equation models is made. The comparison is carried out in terms of degree of accuracy obtained. This comparison is shown in Figures 4.200-4.201. These figures show clearly that the attained higher accuracy on applying the full VAM 10-equation model is insignificant compared to the VAM 5-equation model.

A comparison between the VAM 10-equation, 5-equation and the conventional 3-equation de St. Venant (VA) models in terms of computational effort and time necessary for simulation is made. It is found that the time required for the VAM 10-equation model to converge to a final steady state solution is approximately 2.6 times larger than that of the 5-equation model and 3.6 times larger than that of the VA model. In addition, the memory allocated for the VAM 10-equation model is found to be four times larger than that of the 5-equation model and eleven times larger than that of the VA model.

4.3 Effect of Numerical Discretization on the Accuracy of the Results

The finite element meshes generated for De Vriend (1976), Steffler (1984) and Chang's (1971) experiments are refined to test the effect of numerical discretization on the accuracy of the results. These refinements are limited only by the available computer memory. The refined finite element meshes for these three cases are shown in Figures 4.202-4.204 (the applied numerical discretizations Δx and Δy are of the order of h). The program is run till a steady state solution is obtained.

The results are shown in Figures 4.205-4.235. Figures 4.205-4.216 compare the experimental and numerically predicted depth averaged longitudinal velocity distributions, by the coarse and fine meshes, across the flume. Figures 4.217-4.224 compare the experimental and numerically predicted longitudinal velocity profiles, by the coarse and fine meshes, over the vertical direction. Figures 4.225-4.232 compare the experimental and numerically predicted transverse velocity profiles, by the coarse and fine meshes, over the vertical direction. Figures 4.233-4.234 show the distributions of the extra non-hydrostatic terms h_1 and h_2 across the flume for Steffler's (1984) run 1 at cross section 180 degrees. Figure 4.235 shows the distribution of the vertical velocity, w , across the flume for Steffler's (1984) run 1 at cross section 180 degrees.

From Figures 4.205-4.232, it can be seen that the results obtained by the fine meshes are generally more accurate, particularly near the wall, than those obtained by the

coarse meshes. It can be noticed from Figures 4.205-4.224 that the improvement of the results obtained by the fine meshes over those by the coarse meshes is small particularly away from the wall. This is not however the case for the secondary flow profiles (Figures 4.225-4.232). It can be clearly observed from Figures 4.225-4.232 that the results obtained by the fine meshes are significantly more accurate than those of the coarse meshes. In addition, it can be observed from Figures 4.233-4.235 that the extra non-hydrostatic pressure terms h_1 and h_2 and the vertical velocity, w , become of more importance near the wall and are only captured by the refined mode.

A comparison between the model with fine and coarse meshes in terms of computational effort and time necessary for simulation is made. The number of nodes for the coarser meshes of DeVriend (1976), Steffler (1984) and Chang (1972) reads 876, 748 and 1200 nodes respectively, while for the finer meshes it reads 5738, 5872 and 5881 nodes respectively. It is found that the time required for the model with a finer mesh to converge to a final steady state solution is approximately 6.5 times larger than that of the model with coarser mesh. In addition, the memory allocated for the model with finer mesh is found to be 14 times larger than that of the model with coarser mesh.

As a result, this study recommends the use of very fine finite element meshes, in which the applied numerical discretizations Δx and Δy are of the order of h , when a high degree of accuracy of the predicted secondary flows near the channel walls is sought.

A comparison between the full VAM 10-equation and 5-equation models, for the finer meshes, is further made. The comparison is carried out in terms of degree of accuracy obtained. This comparison is shown in Figures 4.236-4.243. These figures show clearly that the attained higher accuracy on applying the full VAM 10-equation model is insignificant compared to the VAM 5-equation model. This is may be due to the fact that even though the non-hydrostatic extra terms h_1 and h_2 become more significant near the wall their values are still small such that no significant improvements are obtained over the 5-equation model.

4.4 A Field Test Case

De Vriend and Geldof (1983) compared the results of an intensive numerical study with measured field data in two consecutive sharply curved short bends in the river Dommel, The Netherlands. They studied a 285 m long reach of the river Dommel, approximately 3 km downstream of its crossing with the border between Belgium and The Netherlands. The same reach is chosen in this study to test the applicability of the proposed model to simulate real flow cases in channels of rather simple configuration. This reach contained two opposite bends of almost 90° with a short straight reach in between and almost straight reaches upstream and downstream. The location and the layout of the study area are shown in Figure 4.244.

Measurements of the bed geometry as well as flow velocity were performed. A contour map of bed level in central part of the study area is shown in Figure 4.245.

The derived discharge from the velocity measurements varied from 1.21 to 1.53 m³/s. For a discharge of 1.27 m³/s, a water surface width of 6.1 m and an average water depth of 0.5 m were recorded. That corresponded to a Chezy factor of about 30 m^{1/2}/s.

The simulation is performed using a finite element mesh composed of 6487 triangular elements and 3561 nodes (Figure 4.246). Similar criteria, as before, are used to design the mesh shown in Figure 4.246.

The boundary conditions are specified as subcritical inflow, subcritical outflow and no-flow across the vertical side walls. The boundary conditions specified at the inflow section on the bottom right are total discharge = 1.27 m³/s, $u_I = 0.0$, and $v_I = 0.0$. The boundary condition specified at the outflow section on the top left is water surface elevation = 26.75 m. Initial values for the depth h are assumed while the rest of the variables (q_x , q_y , u_I , v_I , \bar{w} , w_b , w_h , h_I and h_2) are set to zero. The roughness height is estimated for the given Chezy to be $k_s = 0.129$ m. The program is run till a steady state solution is obtained.

The results are shown in Figures 4.247-4.254, d_o being the reference depth and is equal to 0.5 m. Figures 4.247-4.254 compare the measured and numerically predicted depth averaged longitudinal velocity distributions across the study section of the river Dommel at different locations.

It can be observed from Figures 4.247-4.254 that the proposed model, VAM linear, simulates the longitudinal velocity distributions across the river at different locations reasonably well. The model seems however to underestimate the velocities near the wall at most of the cross sections particularly in the deeper parts (for example sections 21 and 33). It can be also noticed that the VAM model simulates the flow only slightly more accurately than the VA model.

4.5 Summary and Conclusions

In this study the developed vertically averaged and moment (VAM) equation model is investigated for modeling curved open channel flows. The VAM with assumed linear and/or quadratic distributions of horizontal velocity components and quadratic vertical velocity and pressure distributions are used in the simulations.

The vertically averaged and moment equations are discretized and modeled using a hybrid Petrov-Galerkin and Bubnov-Galerkin finite element schemes. The vertically averaged continuity, longitudinal and transverse momentum, and moment of longitudinal and transverse momentum equations are upwinded using a two-dimensional Characteristic-Dissipative Galerkin finite element scheme. The rest of the equations are modeled using the Bubnov-Galerkin finite element scheme.

Triangular elements with linear basis functions for all variables are used. The time derivatives are approximated using a weighted-implicit finite difference formulation. For the resulting implicit set of non-linear algebraic equations a Newton-Raphson

technique is used to advance the solution to the next time level and to reach a steady state solution as well.

The proposed model is tested for simulating the main as well as the secondary flow features in curved open channels with encouraging success. Five experimental data sets and a field case from the literature are selected. One of the merits of the proposed VAM model, that should be mentioned herein, is that the evaluation of the secondary flow obtained by applying the moment of momentum equations only and no further assumption or experimental constant is required for the prediction of the secondary flow field.

Coarse and fine generated finite element meshes are used in this study. A comparison between the VAM 10-equation, 5-equation and the conventional 3-equation de St. Venant (VA) models in terms of computational effort, time necessary for simulation and degree of accuracy obtained is made.

The conclusions of this study are stated as follows:

1. This study suggests the validity of the proposed vertically averaged and moment model for predicting the flow features in curved open channels. Mainly, the characteristic features of the flow in curved channels such as water surface super-elevation, secondary flow and longitudinal velocity redistribution are well represented. This study explains that not only does the proposed model represent

the depth-averaged flow velocities significantly better than the conventional VA model, but it also captures the shape of the longitudinal velocity profiles and the tendency of the secondary flow profiles over the vertical direction. The satisfactory performance of the VAM equations in these cases may be attributed to the fact that a higher degree of vertical detail incorporated in the model. This is not however true for the field case used in this study as the two models seem to behave almost the same.

2. The VAM quadratic model seems to behave somewhat better than the VAM linear model in simulating the vertical distribution of longitudinal velocity, whereas it seems to behave almost the same in predicting the secondary flow. Predictions of overall flow characteristics are very close, though. These observations suggest that the results are not very sensitive to different approximations of the pre-assumed velocity distribution shapes.
3. More accurate results are obtained by the finer meshes compared to those of the coarser meshes. This is to be expected as the numerical discretization errors become smaller (Δx and Δy are of the order of h).
4. It is found that the time required for the VAM 10-equation model to converge to a final steady state solution is approximately 2.5 times larger than that of the 5-equation model and 3.4 times larger than that of the VA model. In addition, the memory allocated for the VAM 10-equation model is found to be four times

larger than that of the 5-equation model and eleven times larger than that of the VA model.

5. It is found that the attained higher accuracy on applying the full VAM 10-equation model is insignificant compared to the VAM 5-equation model. This is may be due to the fact that even though the non-hydrostatic extra terms become more significant near the wall their values are still small such that no significant improvements are obtained over the 5-equation model.

As a result, this study suggests that the VAM 5-equation model should be adequate to be applied for cases involving calculation of secondary flow. Thus computational effort and computer memory are conserved while remaining the similar accuracy.

Finally, this study recommends the replacement of the standard conventional de St. Venant model by the vertically averaged and moment 5-equation model (VAM linear or quadratic) in terms of depth or vertically averaged modeling on simulating curved open channels where the secondary flow and its effects are important. This should be however true for large-scale models where the generated numerical meshes are not very fine. In addition, this study recommends the use of very fine finite element meshes when a high degree of accuracy of the predicted secondary flows near the walls is sought. The applied numerical discretizations in this case should be of the order of the flow depth.

4.6 References

- Beam, R. M. and Warming, R. F. (1978), "An implicit factored scheme for the compressible Navier-Stokes equations." *Am. Inst. Aero. Astro. J.*, 16(4), 393-402.
- Chang, Y. C. (1971), "Lateral mixing in meandering channels." Ph.D. thesis, Univ. of Iowa, Iowa City, Iowa.
- De Vriend, H. J. (1976), "A mathematical model of steady flow in curved shallow channels." Report No. 76-1, Department of Civil Engineering, Delft University of Technology.
- De Vriend, H. J. and Geldof, H. J. (1983). "Main flow velocity in short river bends." *Journal of Hydraulic Engineering*, ASCE, Vol. 109, No. 7, pp. 991-1011.
- DeVriend, H. J. and Kalkwijk, J. P. Th. (1980), "Computation of the flow in shallow river bends." *Journal of Hydraulic Research*, Vol. 18(4), pp. 327-341.
- Engelund, F. (1974), "Flow and bed topography in channel bends." *Journal of Hydraulic Division*, ASCE, Vol. 100(11), pp. 1631-1648.
- Falcon Ascanio, M. A. (1979), "Analysis of flow in alluvial channel bends." Ph.D. thesis, University of Iowa, Iowa City, Iowa.
- Ghanem, A., Steffler, P. M., Hicks, F. E. and Katopodis, 1995. "Two-Dimensional Finite Element Modeling of Flow in Aquatic Habitats". Water resources Engineering Report No. 95-S1, Department of Civil Engineering, University of Alberta.

- Ghanmi-Ahmed, Robert-Jean-Loup and Khelifi-Mohamed (1997), "Three-dimensional finite element model to simulate secondary flows: development and validation." *Journal of Hydraulic Research*, Vol. 35(3), pp. 291-300.
- Harrington, R. A., Kouwen, N. and Farquhar, G. J. (1978), "Behavior of hydrodynamic finite element model." *Finite elements in Water Resources*.
- Hicks, F. E. and Steffler, P. M., 1990. "Finite Element Modeling of Open Channel Flow." Department of Civil Engineering, University of Alberta, Technical Report (WRE 90-6).
- Hicks, F. E. and Steffler, P. M., 1992. "Characteristic Dissipative Galerkin Scheme for Open-Channel Flow." *Journal of Hydraulic Engineering*. ASCE, Vol. 118, No. 2, pp. 337-352.
- Ippen, A.T. and Drinker, P. A. (1962), "Boundary shear stress in curved trapezoidal channel." *Journal of Hydraulic Division*, ASCE, Vol. 88(5), pp. 143-179.
- Ishikawa, T. Suzuki, K. and Tanaka, M. (1986), "Efficient numerical analysis of an open channel flow with secondary calculations." *Proc. JSCE*, 375(II-6), 181-189 (in Japanese).
- Itakura, T. and Shimizu, Y. (1986), "Model study of the Ishikari River." *Proc. of IAHR '86 Symp. On Scale Effects in Modeling Sediment Transport Phenomena*, 85-98.
- Jin, Y. C. and Steffler, P. M. (1993), "Predicting Flow in Curved Open Channel by Depth-Averaged Method." *Journal of Hydraulic Engineering*, ASCE, Vol. 119, No. 1, January, pp. 109-124.

- Johannesson, H. (1988), "Theory of river meanders." Ph.D. thesis, University of Minnesota, Minneapolis, Minnesota.
- Johannesson, H. and Parker, G. (1989), "Secondary flow in mildly sinuous channel." *Journal of Hydraulic Engineering*, ASCE, 115(3), 289-308.
- Kupiers, J. and Vreugdenhil, C. B. (1973), "Calculation of two-dimensional horizontal flow." Delft Hydraulics Laboratory, Report S 163, part I.
- Leopold, L. B. and Wolman, M. G. (1960), "River Meanders." *Bull. Geol. Soc. America*, 71, June, 769-794.
- Leschziner, A., and Rodi, W. (1979), "Calculation of strongly curved open channel flow." *Journal of Hydraulic Division*, ASCE, Vol. 105(10), pp. 1297-1314.
- Molls, T. and Chaudhry, M. H. (1995), "Depth-averaged open-channel flow model." *Journal of Hydraulic Engineering*, ASCE, 121(6), 453-465.
- Mori, A. and Kishi, T. (1982), "A study on bed topography in channel bend." *Proc. of Japanese Conf. On Hydr.*, 26, 63-68 (in Japanese).
- Odgaard, A. J. (1986a), "Meander flow model. I: development." *Journal of Hydraulic Engineering*, ASCE, 112(12), 1117-1136.
- Odgaard, A. J. (1986b), "Meander flow model. I: applications." *Journal of Hydraulic Engineering*, ASCE, 112(12), 1137-1150.
- Rozovskii, I. L. (1957), "Flow of water in bends of open channels." Israel Program for Scientific Translations.
- Rozovskii, I. L. (1961), "Flow of water in bends of open channels." Academy of Science of Ukrainian S. S. R., Translated from Russian, Israel Program for Science Translation, 1-233.

- Shimizu, Y., Yamaguchi, H. and Itakura, T. (1990), "Three-dimensional computation of flow and bed deformation." *Journal of Hydraulic Engineering*, ASCE, 116(9), 1090-1108.
- Steffler, P. M. (1984), "Turbulent flow in curved rectangular channel." Ph.D. thesis, University of Alberta, Edmonton, Alberta, Canada.
- Ye, J. and McCorquodale, J. A. (1997), "Depth-averaged hydrodynamic model in curvilinear collected grid." *Journal of Hydraulic Engineering*, ASCE, 123(5), 380-388.
- Yeh, K. C. and Kennedy, J. K. (1993a), "Moment model of non-uniform channel bend flow. II: Fixed beds." *Journal of Hydraulic Engineering*, ASCE, 119(7), 776-795.
- Yeh, K. C. and Kennedy, J. K. (1993b), "Moment model of non-uniform channel bend flow. II: Erodible beds." *Journal of Hydraulic Engineering*, ASCE, 119(7), 796-815.
- Yen, B. C. (1965), "Characteristics of subcritical flow in a meandering channel." Institute of Hydraulic Research, University of Iowa, Iowa City, Iowa.

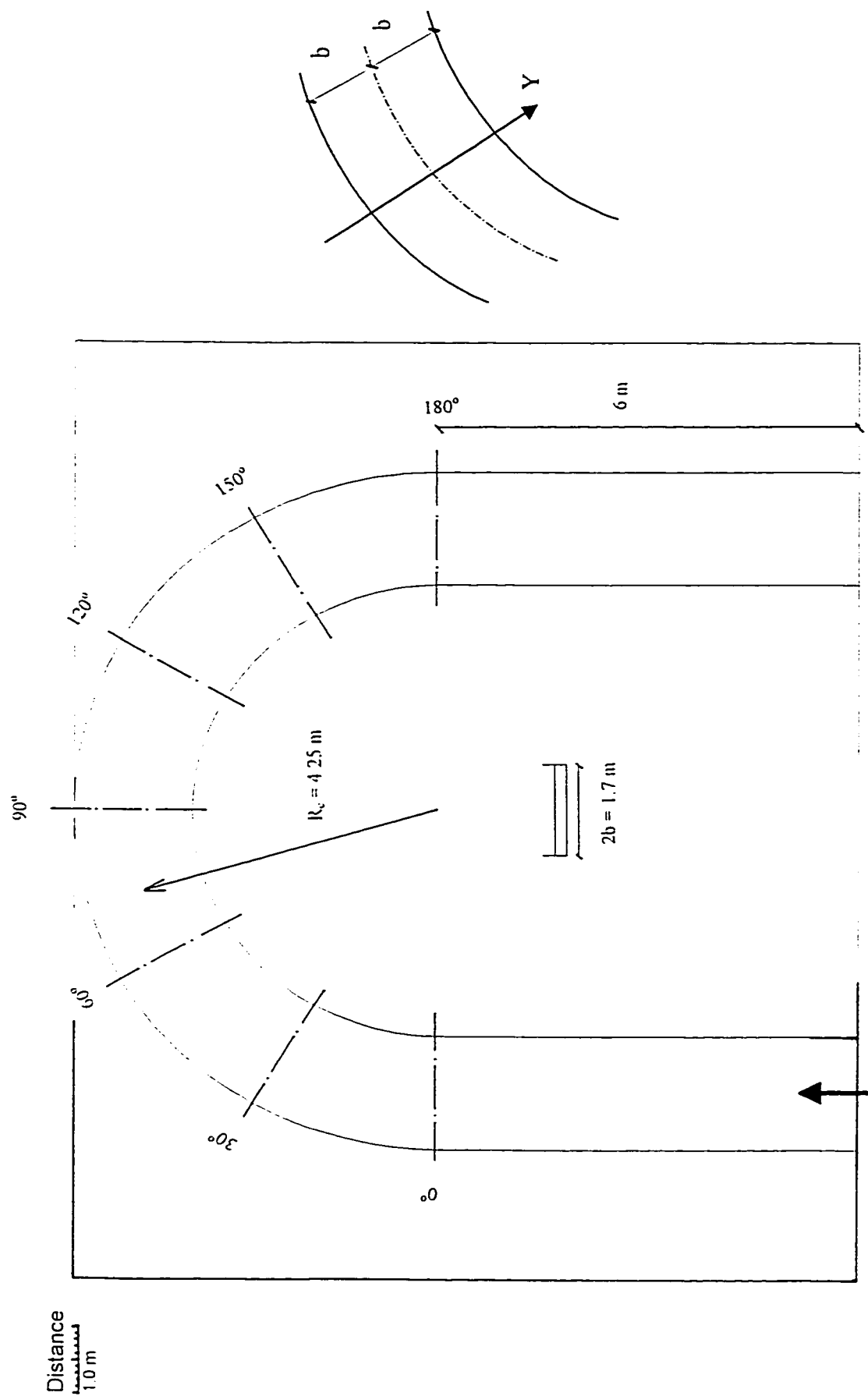
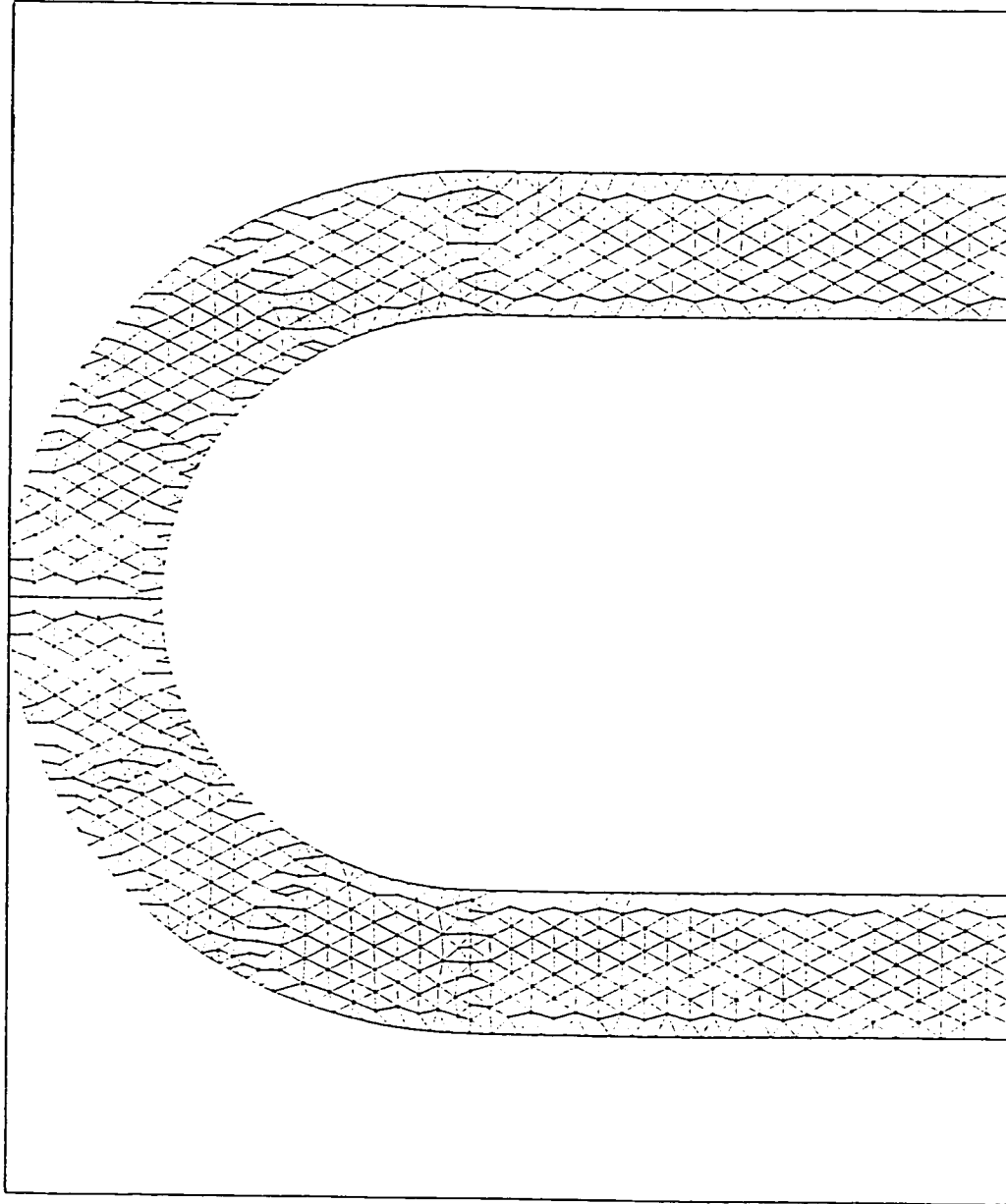


Figure 4.1 The layout of DeVriend's (1976) experiment

Distance
1.0 m



The generated mesh

Number of nodes = 876

Number of elements = 1488

Figure 4.2 Finite element mesh for DeVriend's (1976) experiment

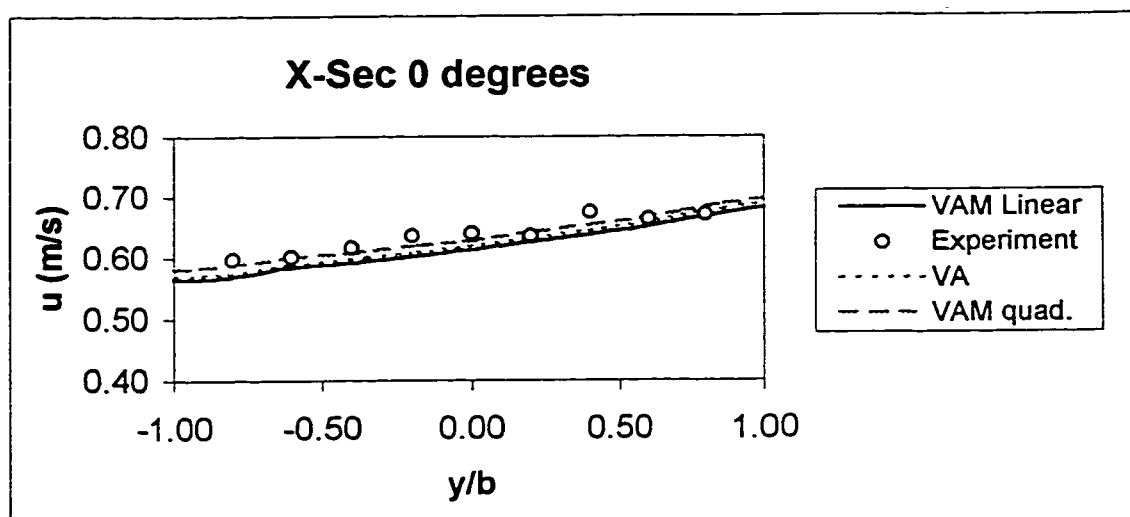


Figure 4.3 The comparison of the longitudinal velocity distribution across the flume for DeVriend (1976) at cross-section 0 degrees

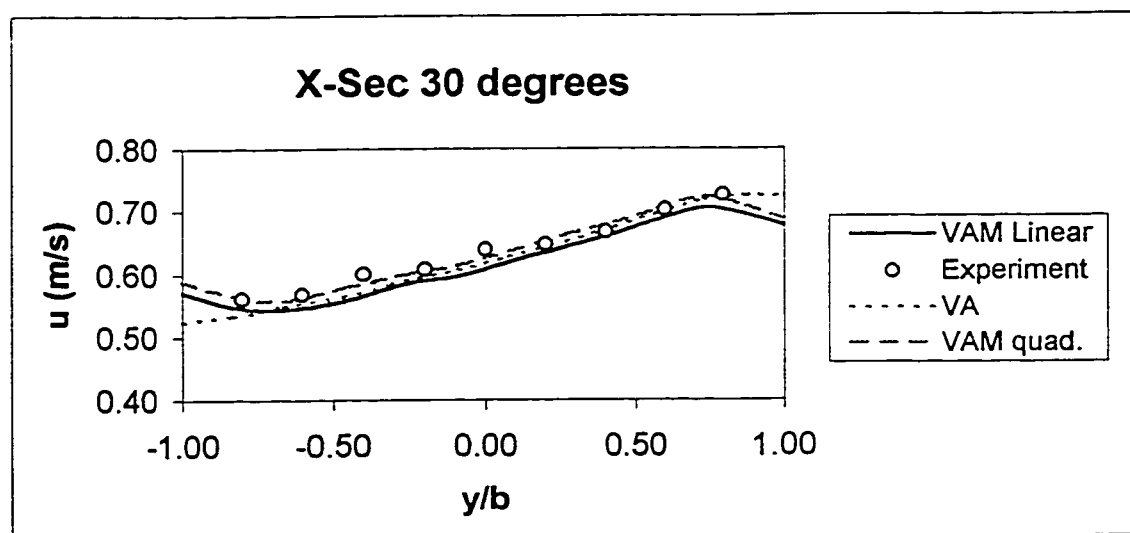


Figure 4.4 The comparison of the longitudinal velocity distribution across the flume for DeVriend (1976) at cross-section 30 degrees

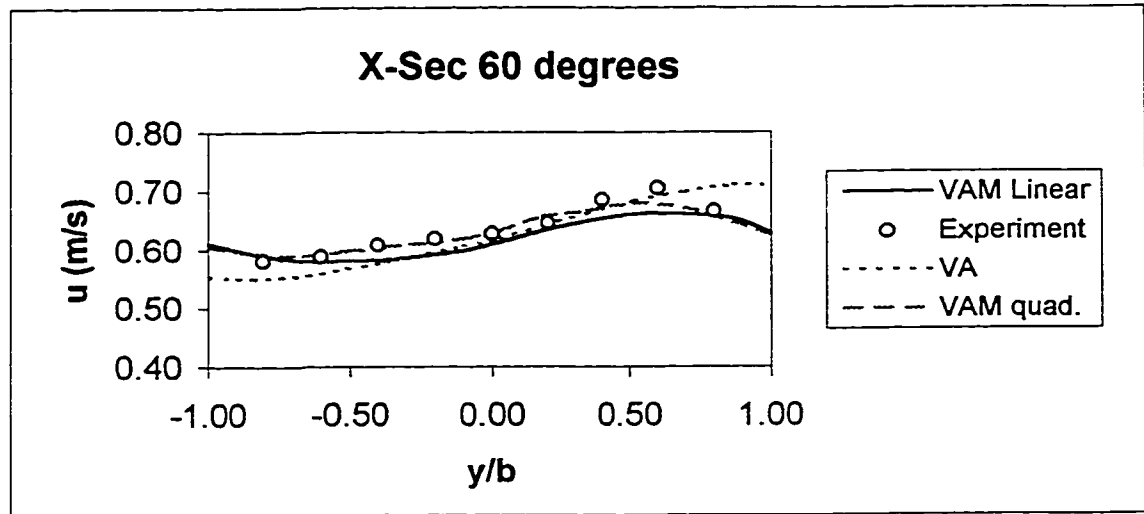


Figure 4.5 The comparison of the longitudinal velocity distribution across the flume for DeVriend (1976) at cross-section 60 degrees

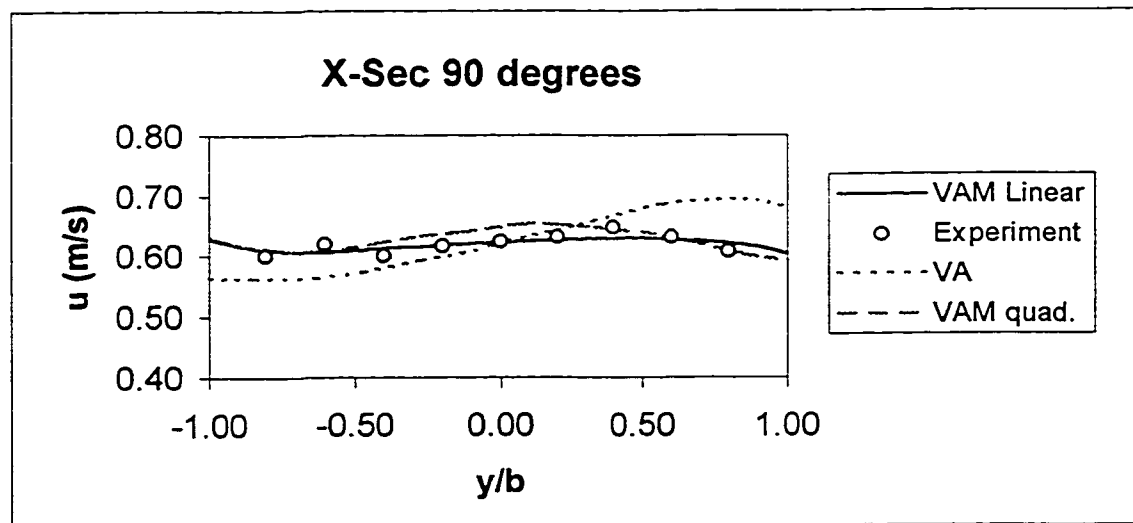


Figure 4.6 The comparison of the longitudinal velocity distribution across the flume for DeVriend (1976) at cross-section 90 degrees

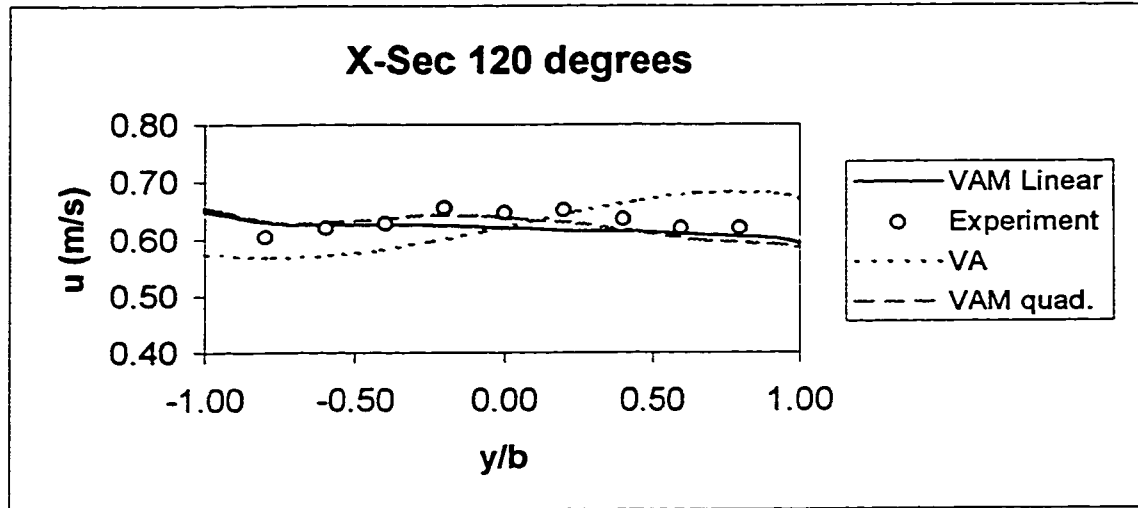


Figure 4.7 The comparison of the longitudinal velocity distribution across the flume for DeVriend (1976) at cross-section 120 degrees

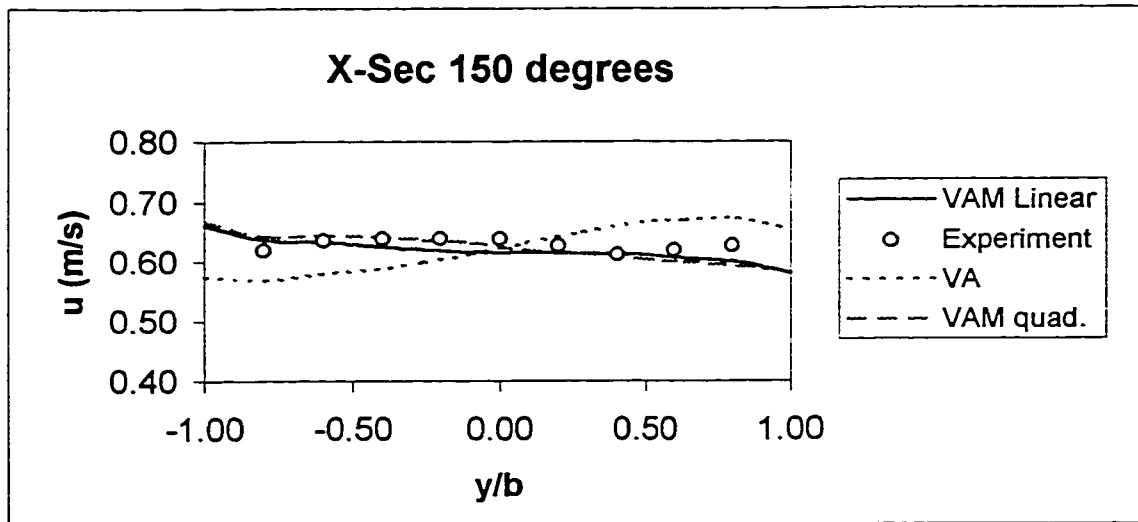


Figure 4.8 The comparison of the longitudinal velocity distribution across the flume for DeVriend (1976) at cross-section 150 degrees

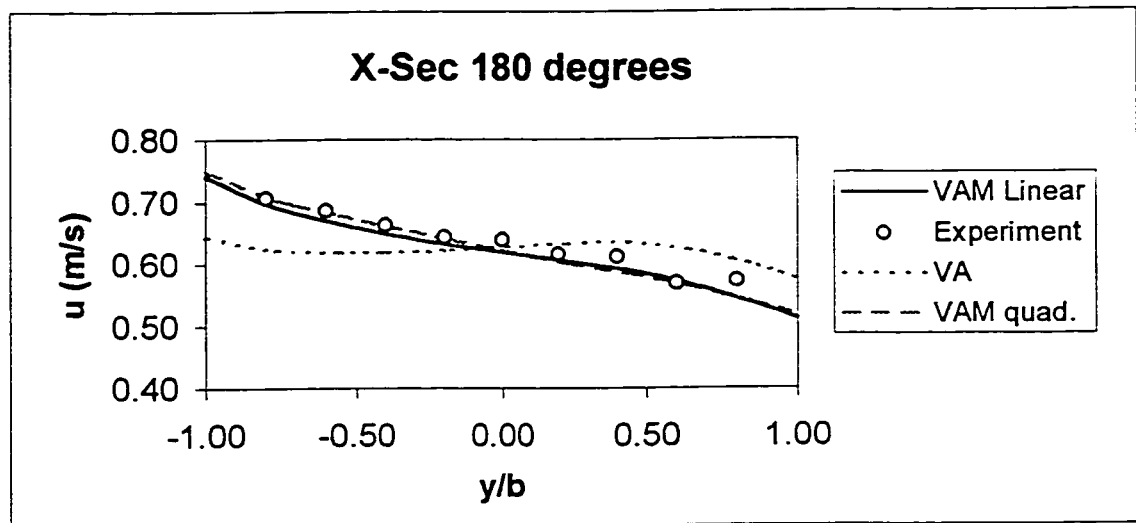


Figure 4.9 The comparison of the longitudinal velocity distribution across the flume for DeVriend (1976) at cross-section 180 degrees

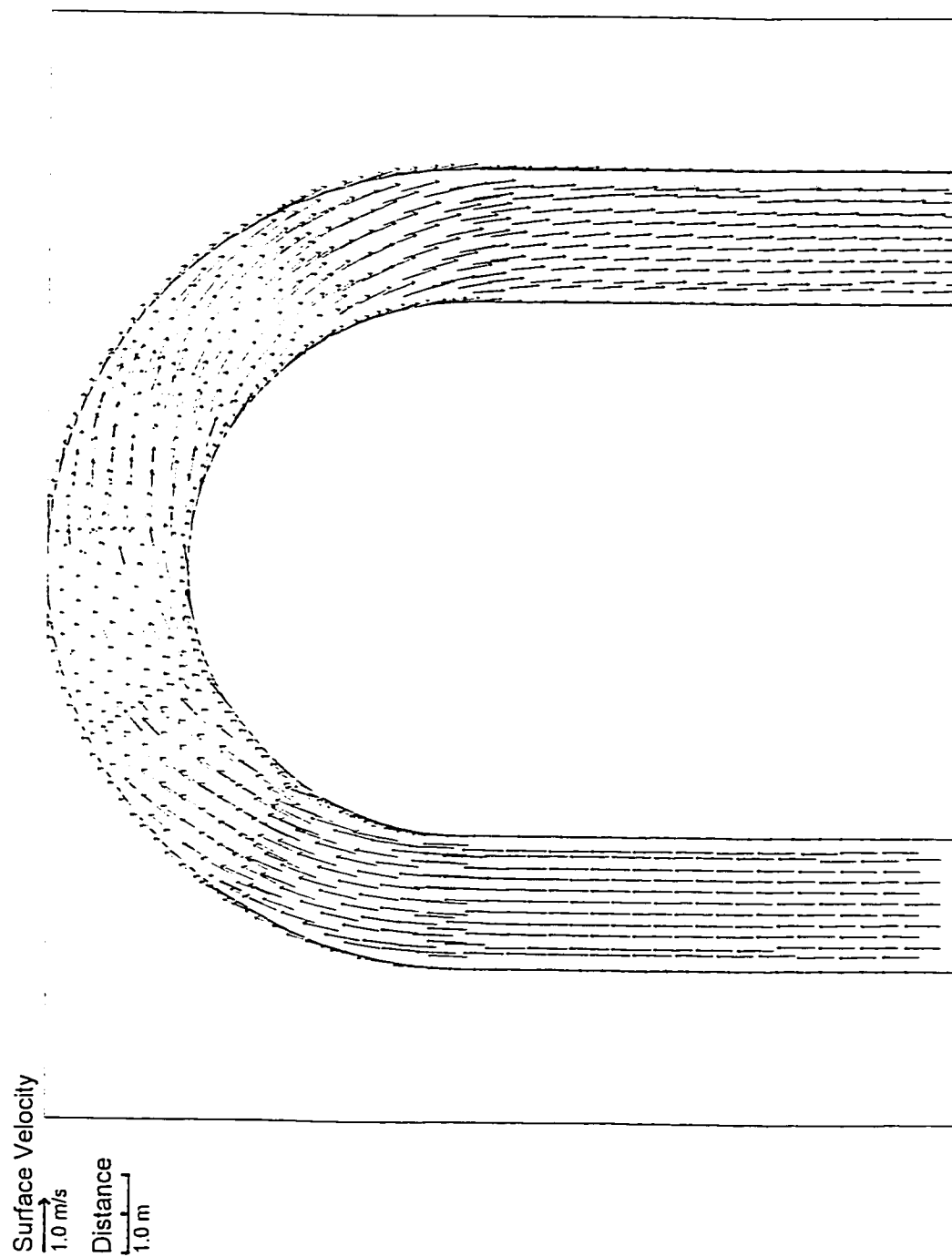


Figure 4.10 Numerical prediction of surface velocity distribution for DeVriend's (1976) experiment (VAM model)

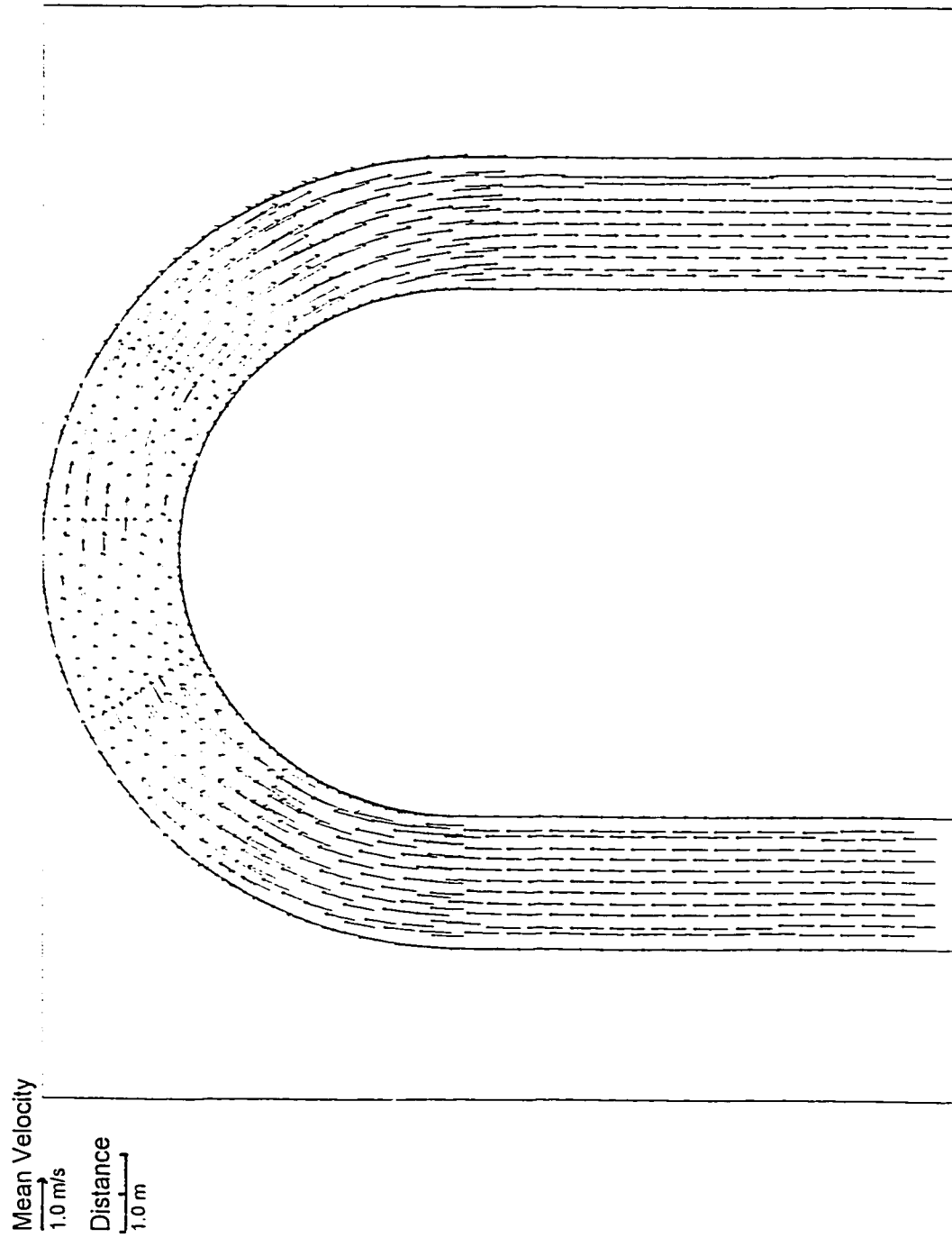


Figure 4.11 Numerical prediction of mean velocity distribution for DeVriend's (1976) experiment (VAM model)

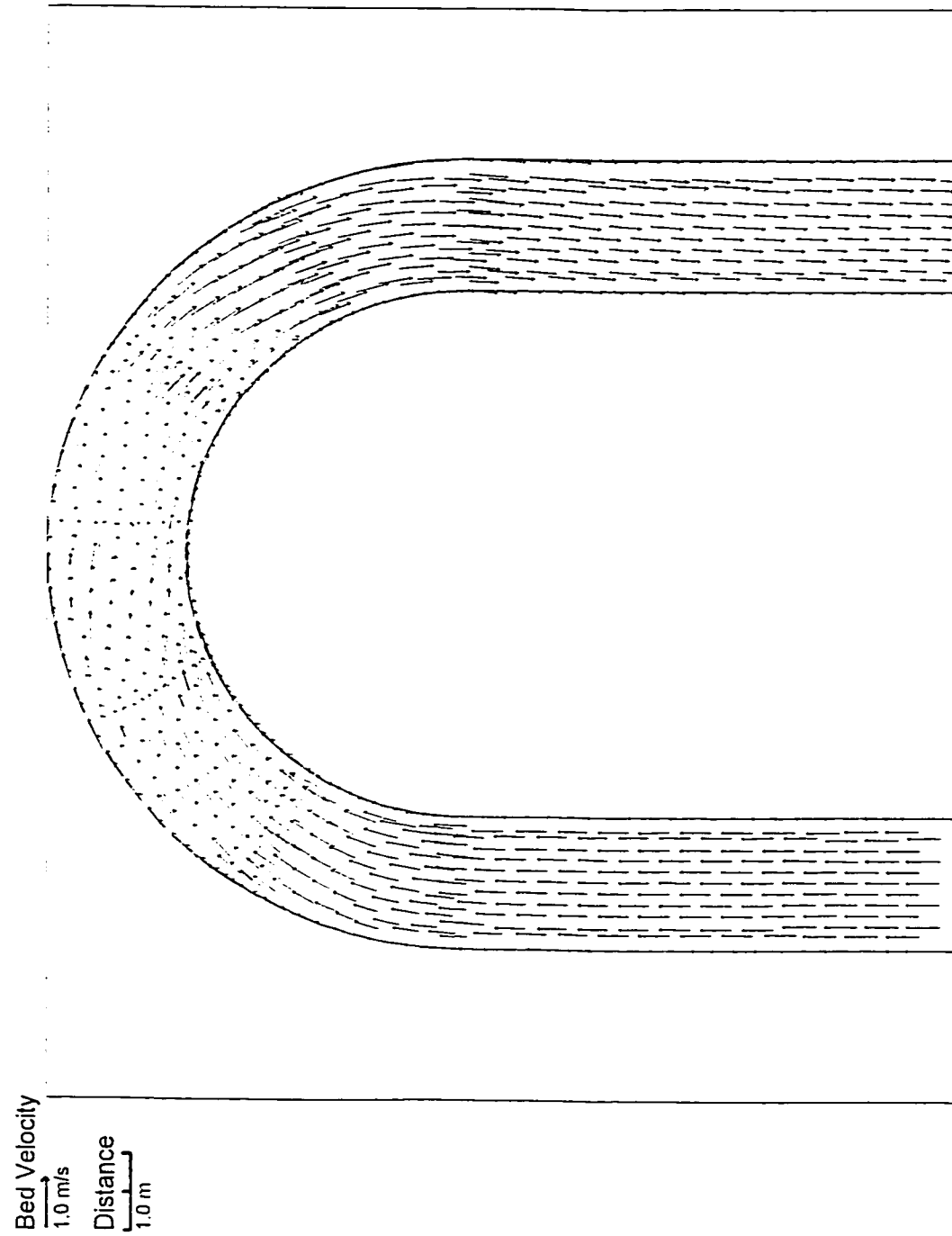


Figure 4.12 Numerical prediction of bed velocity distribution for DeVriend's (1976) experiment (VAM model)

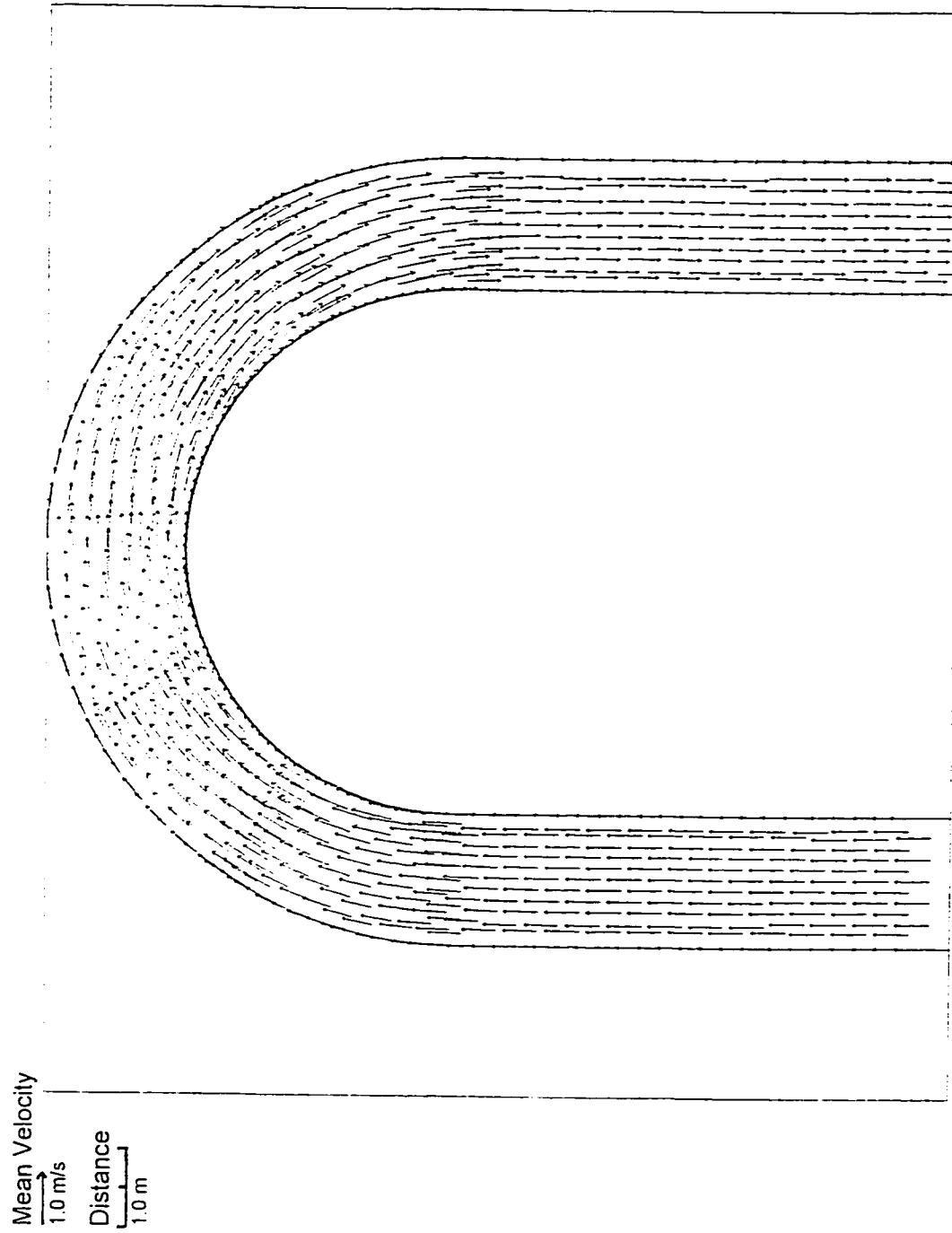
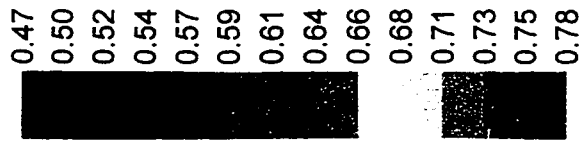


Figure 4.13 Numerical prediction of mean velocity distribution for DeVriend's (1976) experiment (VA model)

Velocity Magnitude (m/s)



Distance

1.0 m



Figure 4.14 Numerical prediction of mean velocity contours for DeVriend's (1976) experiment (VAM model)

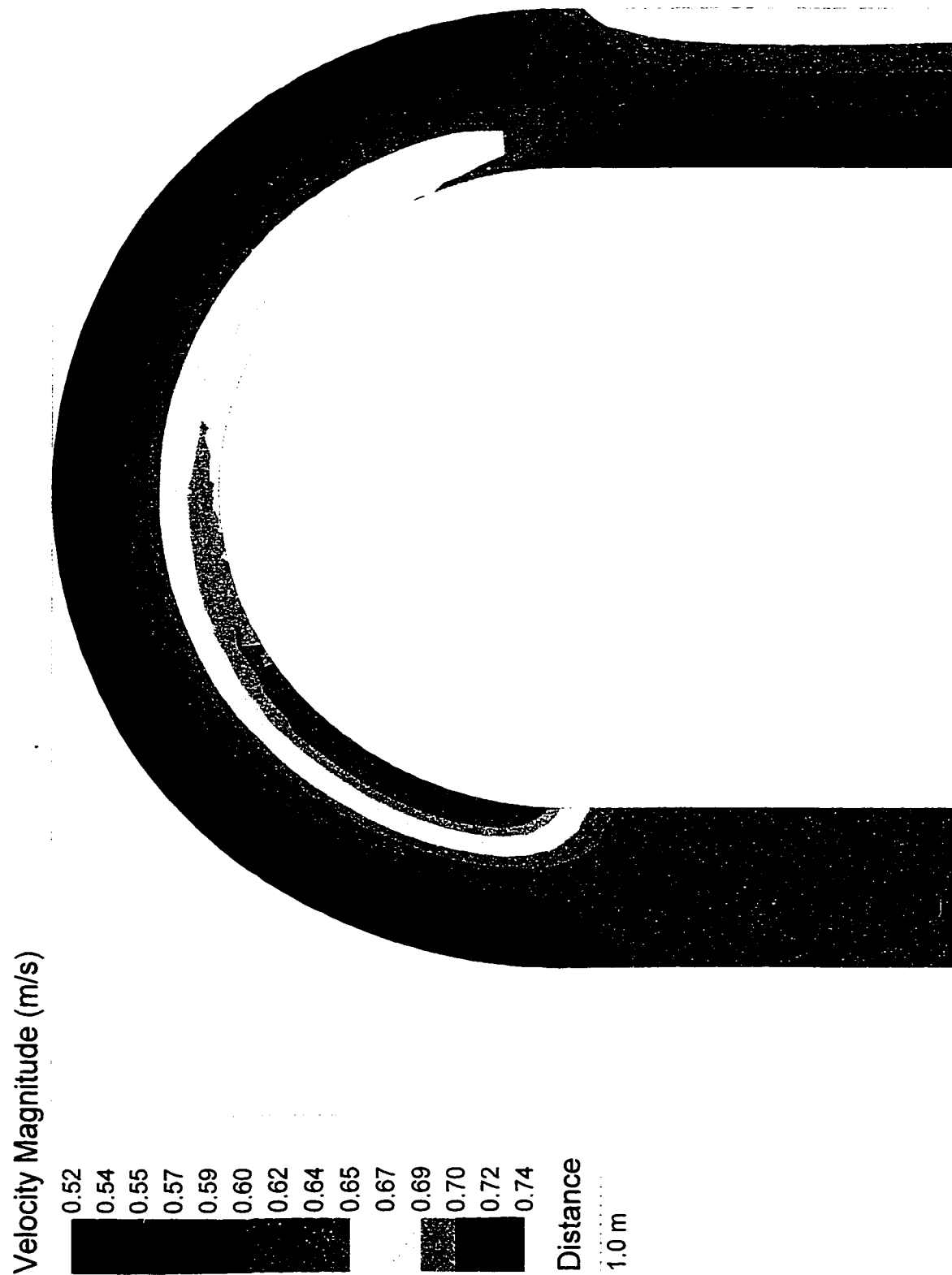


Figure 4.15 Numerical prediction of mean velocity contours for DeVriend's (1976) experiment (VA model)

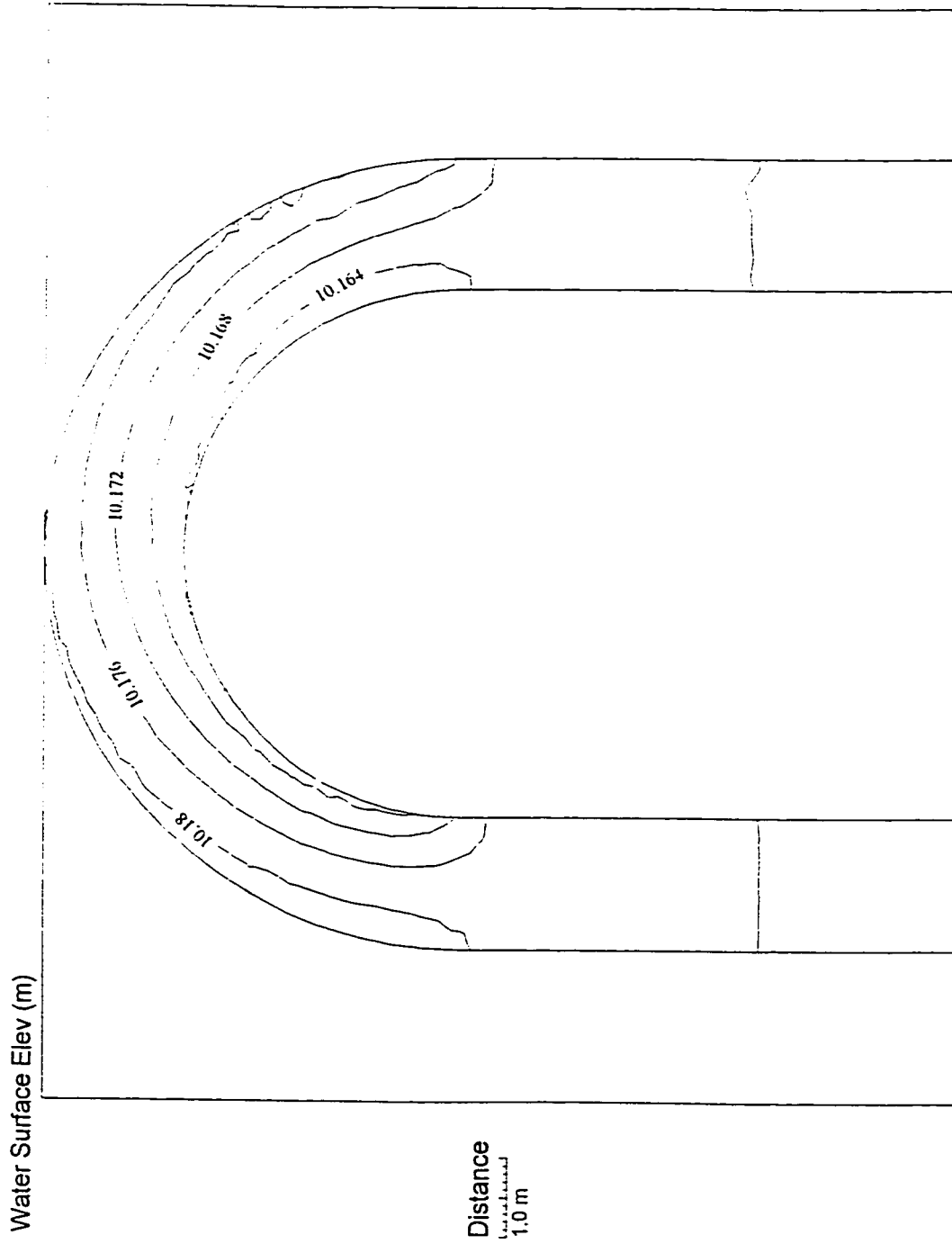


Figure 4.16 Numerical prediction of water surface elevation contours for DeVriend's (1976) experiment (VAM model)

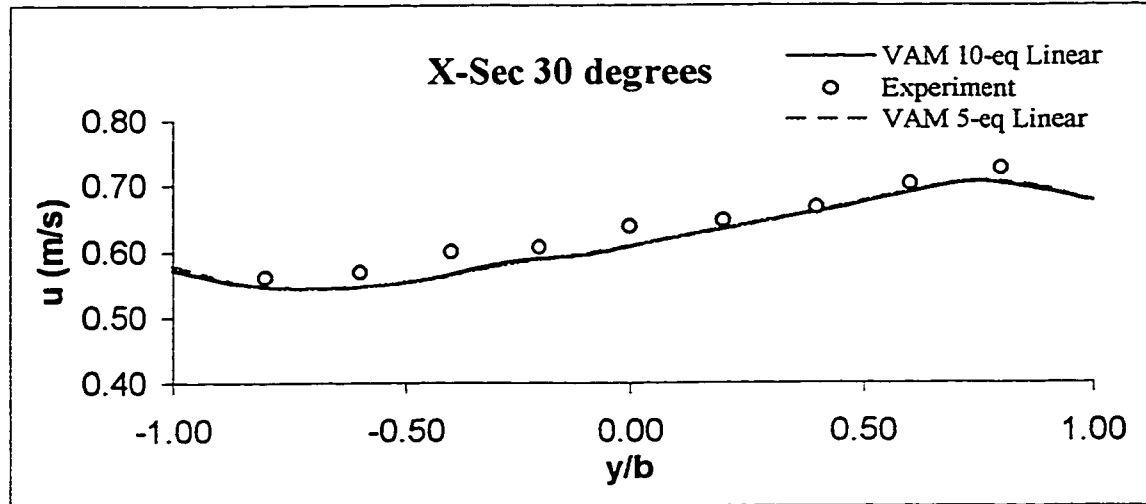


Figure 4.17 The comparison of applying VAM 5- against 10-equation models for longitudinal velocity distribution across the flume for DeVriend's (1976) at cross-section 30 degrees

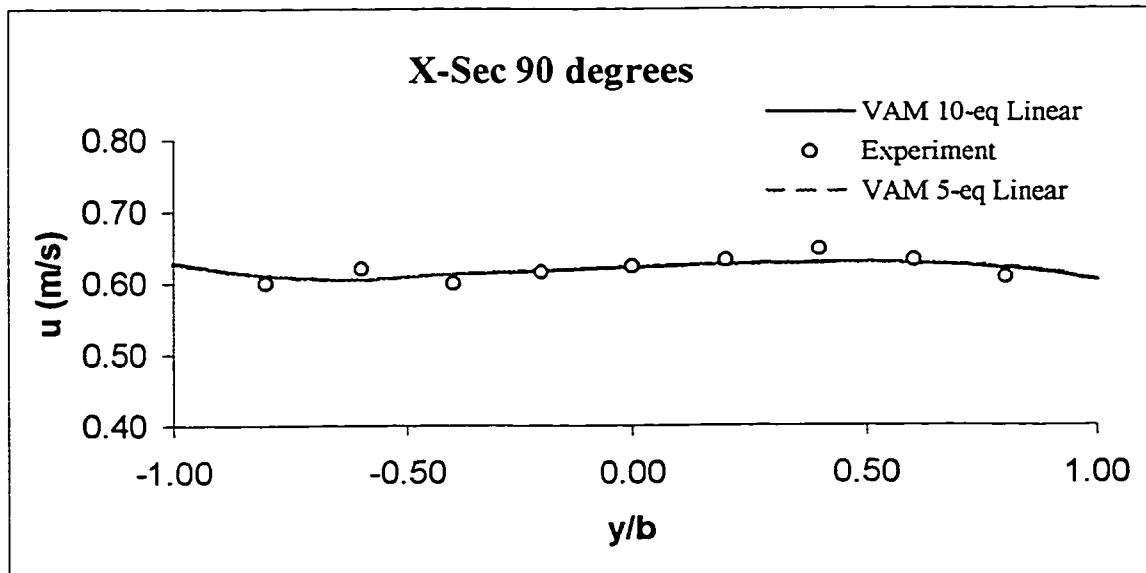


Figure 4.18 The comparison of applying VAM 5- against 10-equation models for longitudinal velocity distribution across the flume for DeVriend's (1976) at cross-section 90 degrees

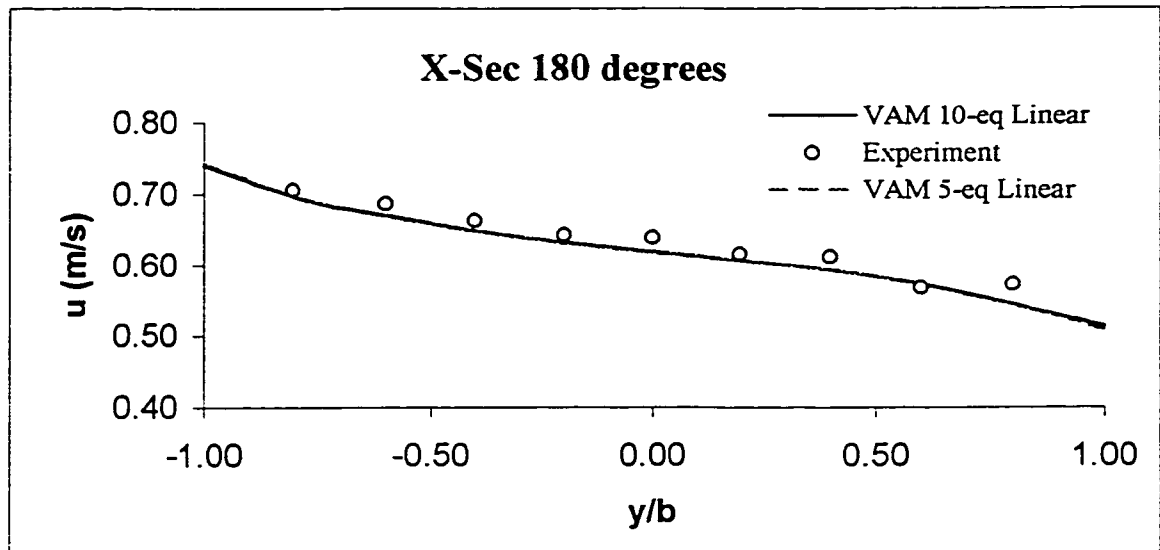


Figure 4.19 The comparison of applying VAM 5- against 10-equation models for longitudinal velocity distribution across the flume for DeVriend's (1976) at cross-section 180 degrees

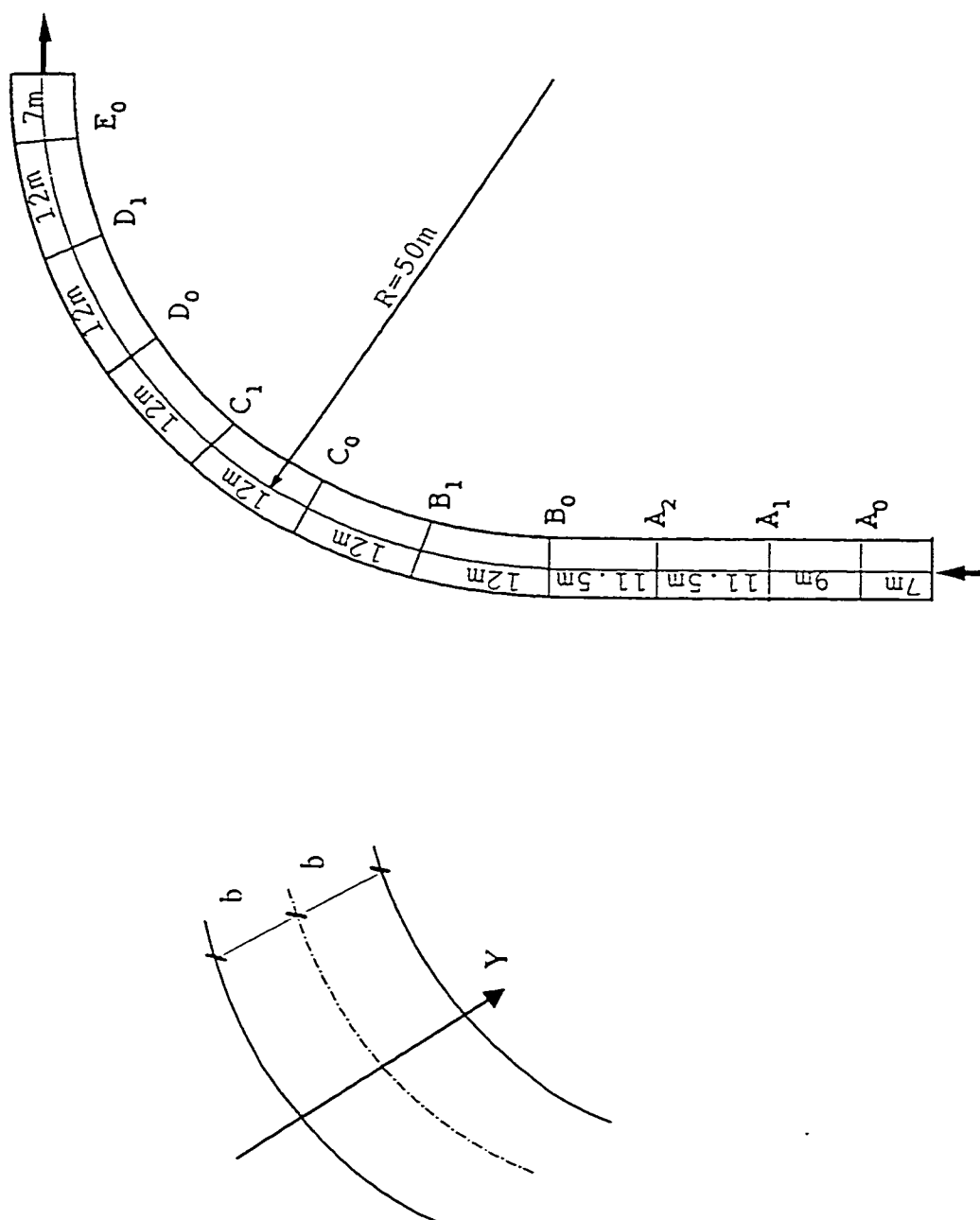


Figure 4.20 The layout of DeVriend's (1980) experiment (adapted from DeVriend, 1980)

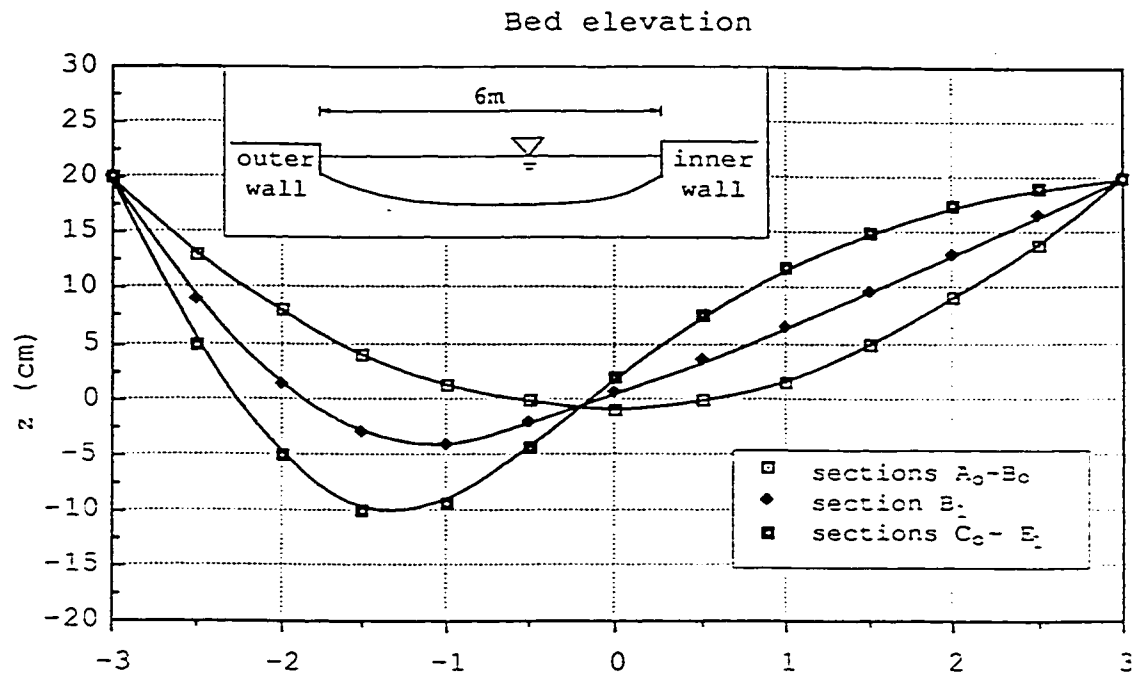


Figure 4.21 Cross-sections geometry of DeVriend's (1980) experiment (adapted from DeVriend, 1980)

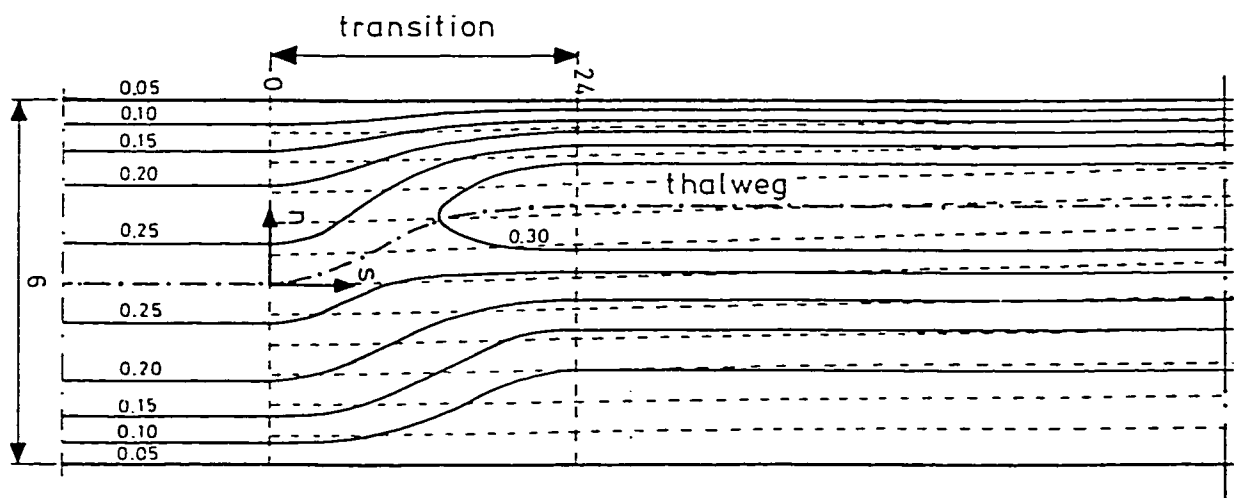
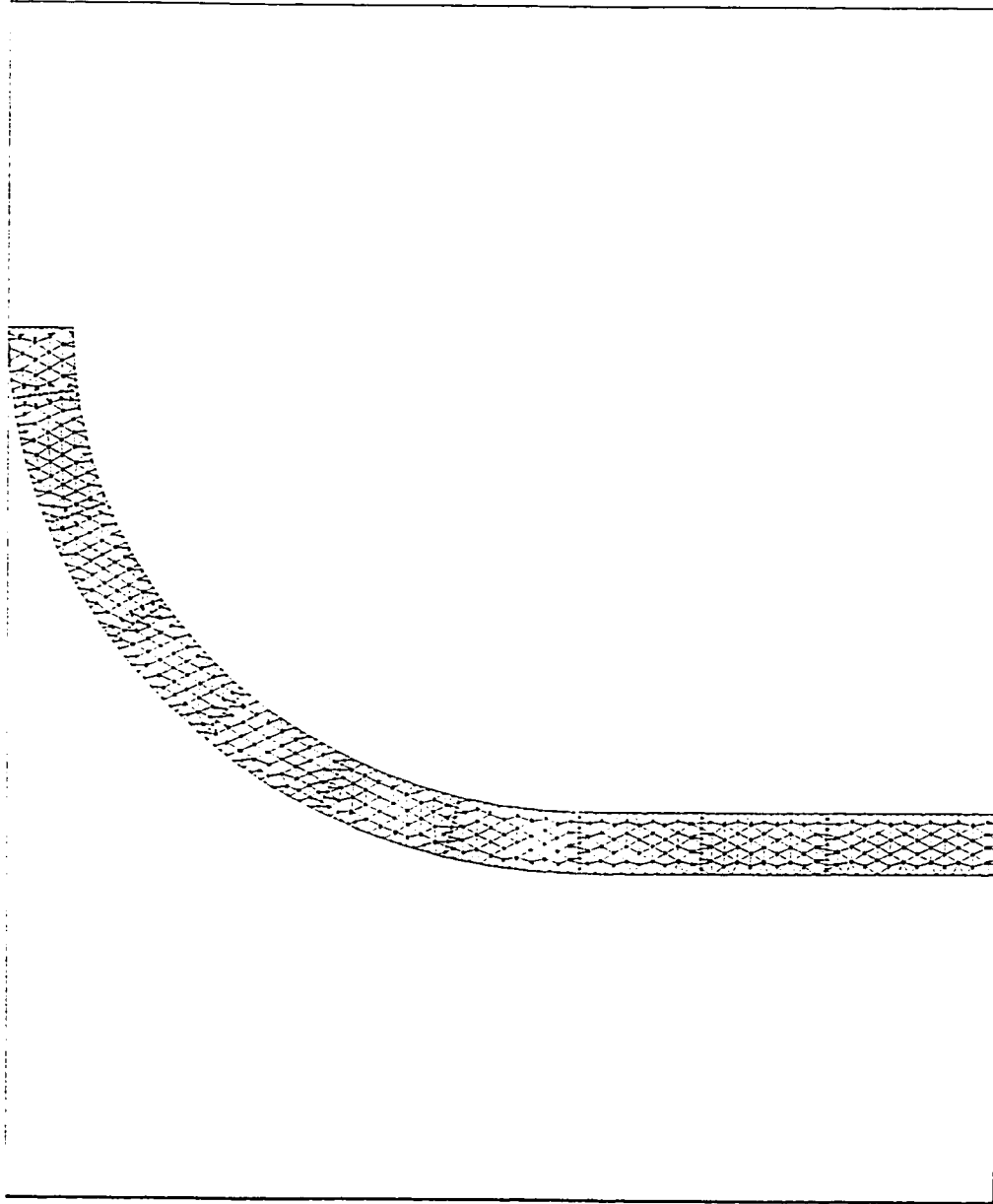


Figure 4.22 Depth contours and characteristics of DeVriend's (1980) experiment (adapted from DeVriend, 1980)

Distance
10.0 m



The generated mesh

Number of nodes = 796

Number of elements = 1260

Figure 4.23 Finite element mesh for DeVriend's (1980) experiment

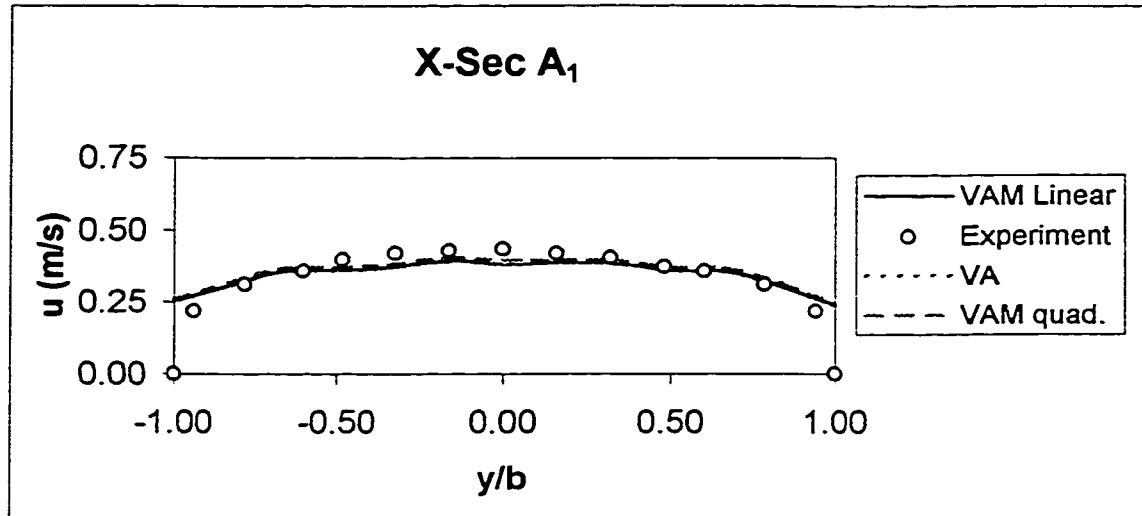


Figure 4.24 The comparison of the longitudinal velocity distribution across the flume for DeVriend (1980) at cross-section A₁

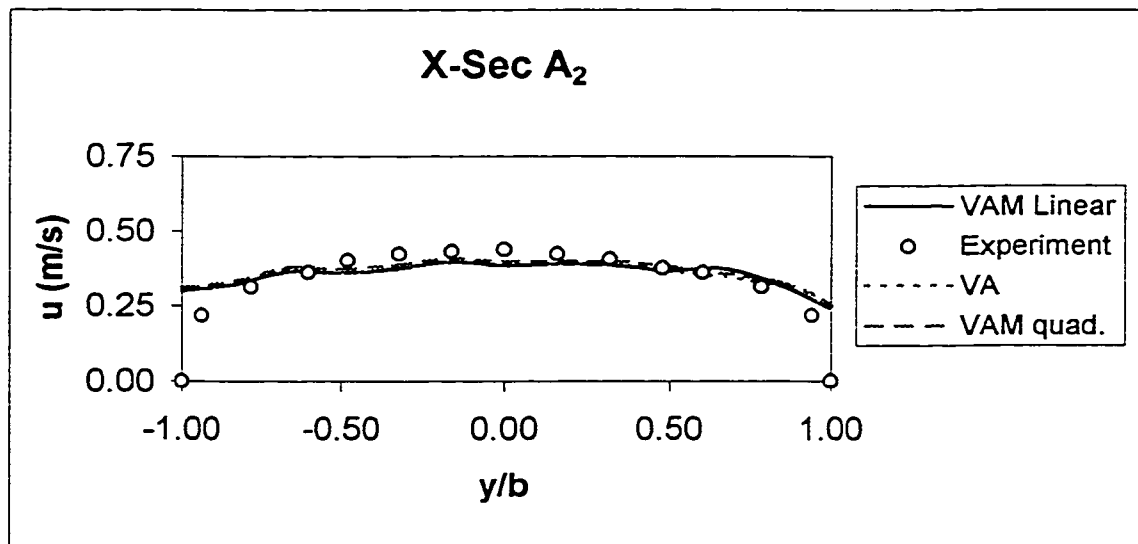


Figure 4.25 The comparison of the longitudinal velocity distribution across the flume for DeVriend (1980) at cross-section A₂

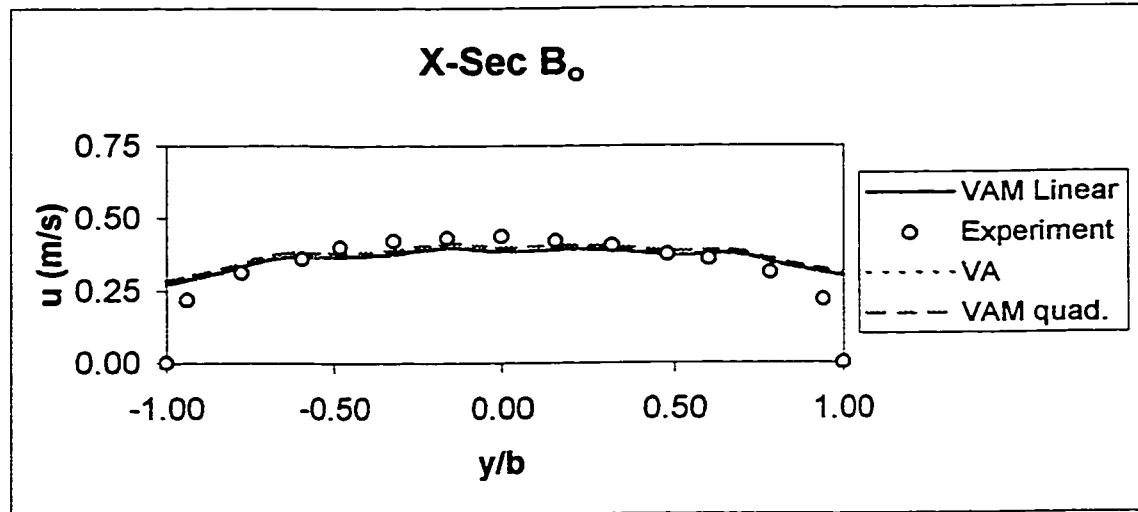


Figure 4.26 The comparison of the longitudinal velocity distribution across the flume for DeVriend (1980) at cross-section B₀

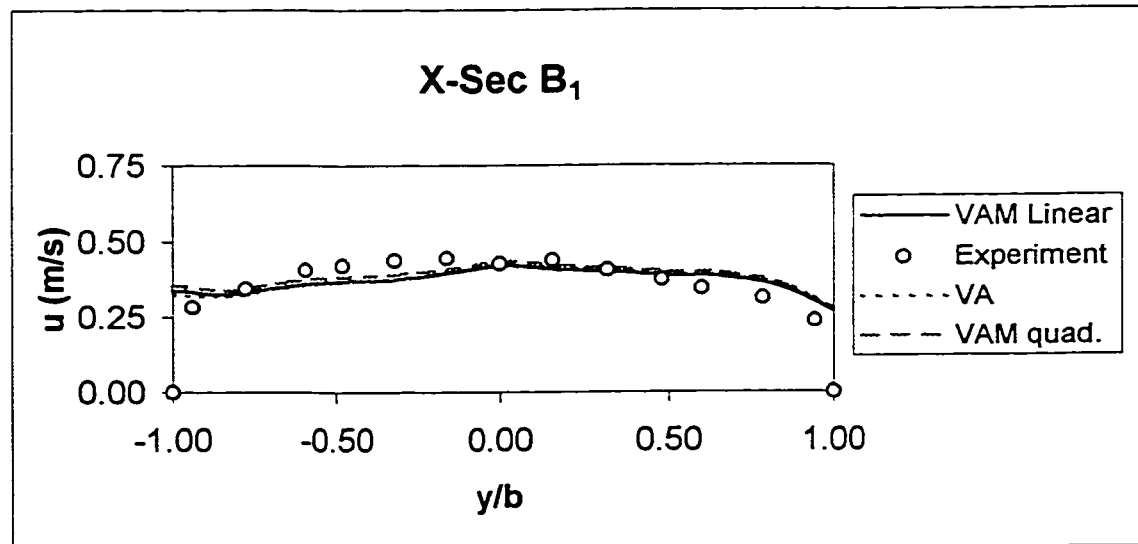


Figure 4.27 The comparison of the longitudinal velocity distribution across the flume for DeVriend (1980) at cross-section B₁

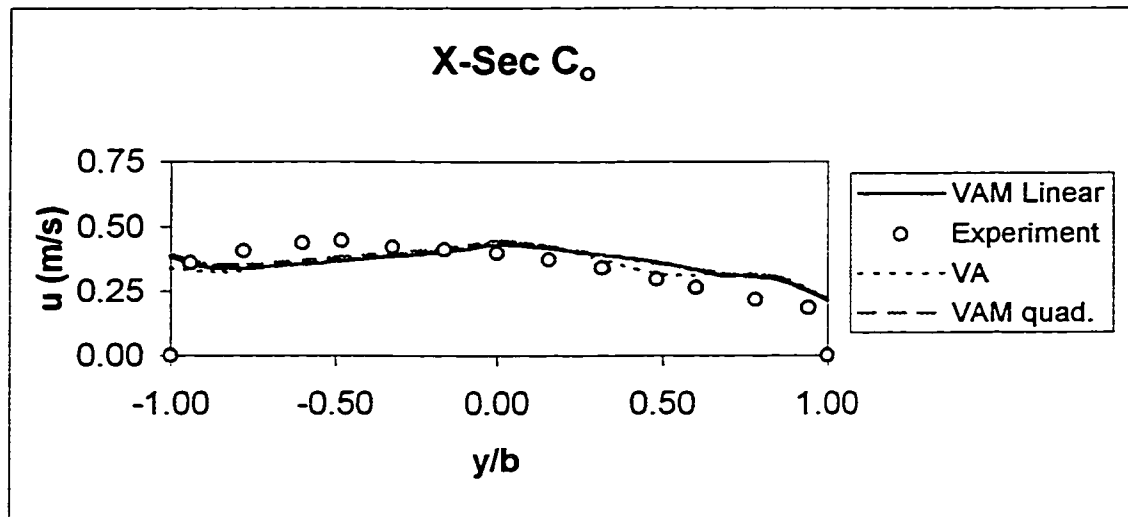


Figure 4.28 The comparison of the longitudinal velocity distribution across the flume for DeVriend (1980) at cross-section C_0

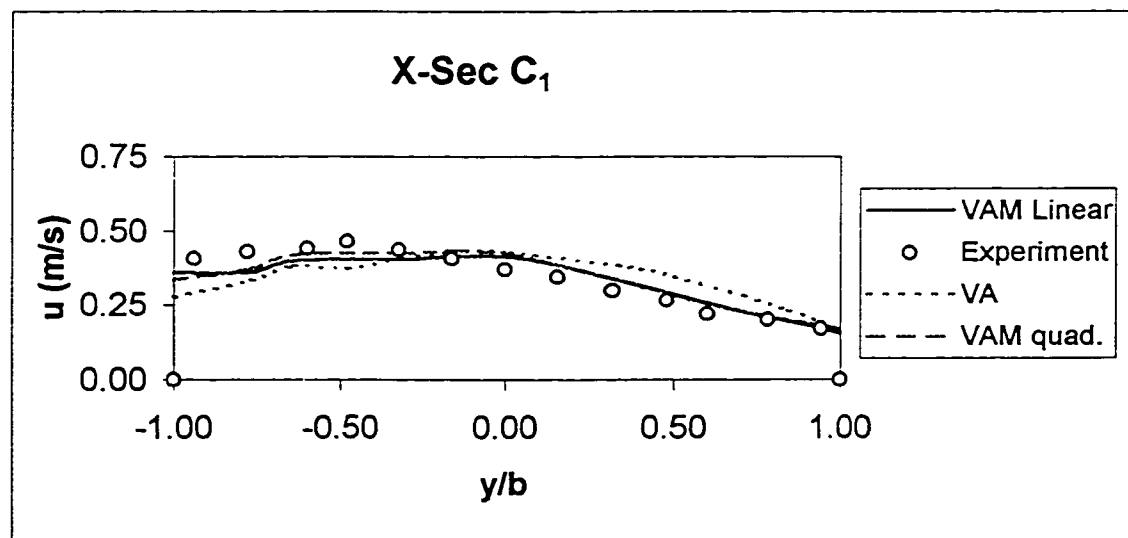


Figure 4.29 The comparison of the longitudinal velocity distribution across the flume for DeVriend (1980) at cross-section C_1

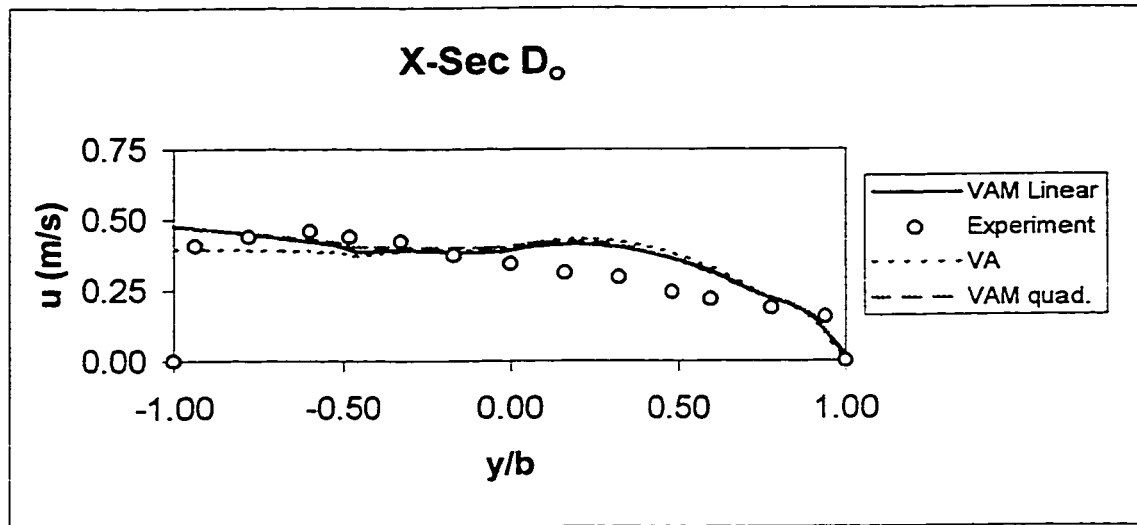


Figure 4.30 The comparison of the longitudinal velocity distribution across the flume for DeVriend (1980) at cross-section D₀

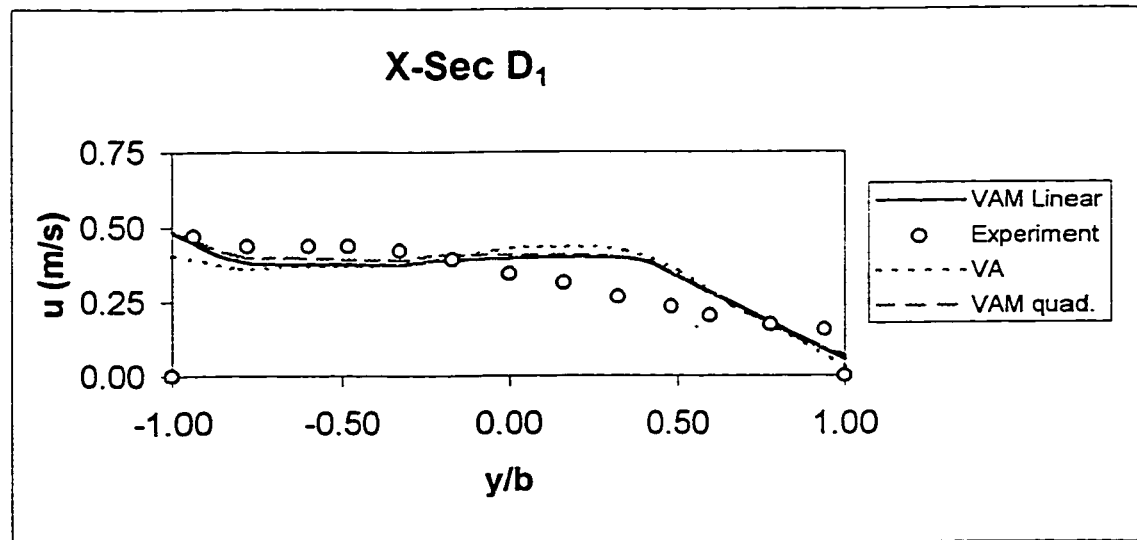


Figure 4.31 The comparison of the longitudinal velocity distribution across the flume for DeVriend (1980) at cross-section D₁

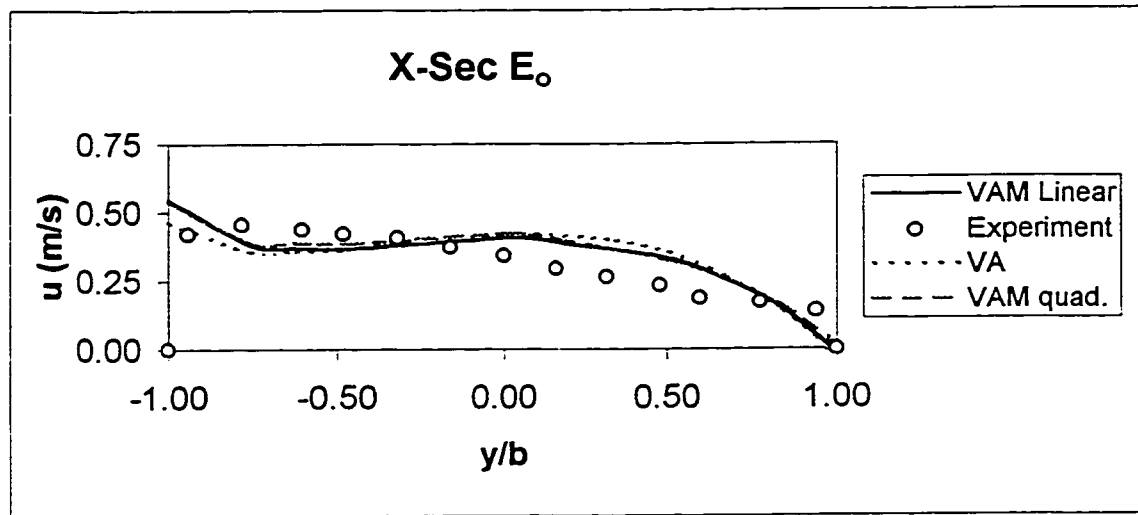


Figure 4.32 The comparison of the longitudinal velocity distribution across the flume for DeVriend (1980) at cross-section E_o

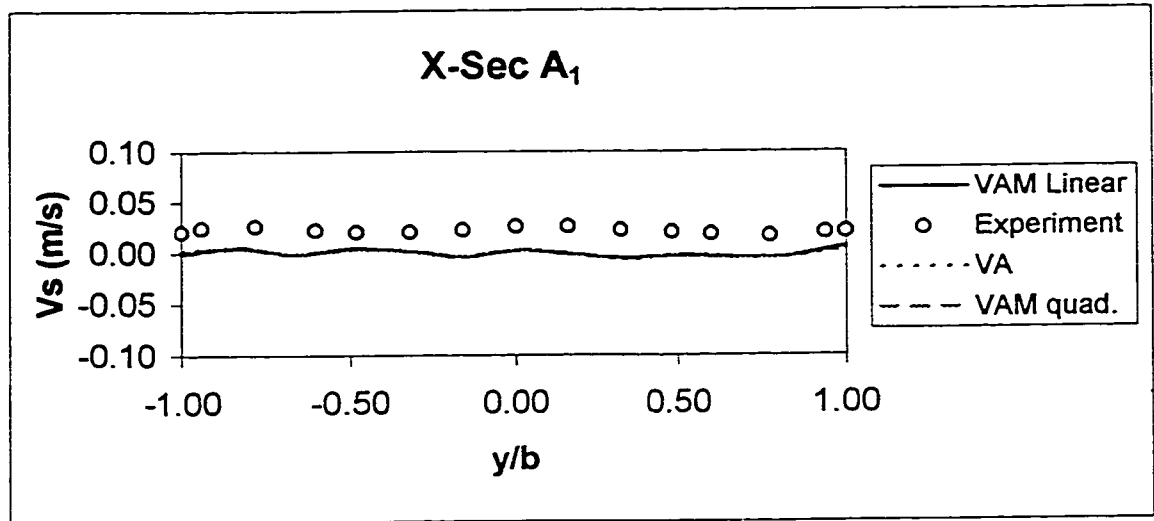


Figure 4.33 The comparison of the transverse surface velocity distribution across the flume for DeVriend (1980) at cross-section A₁

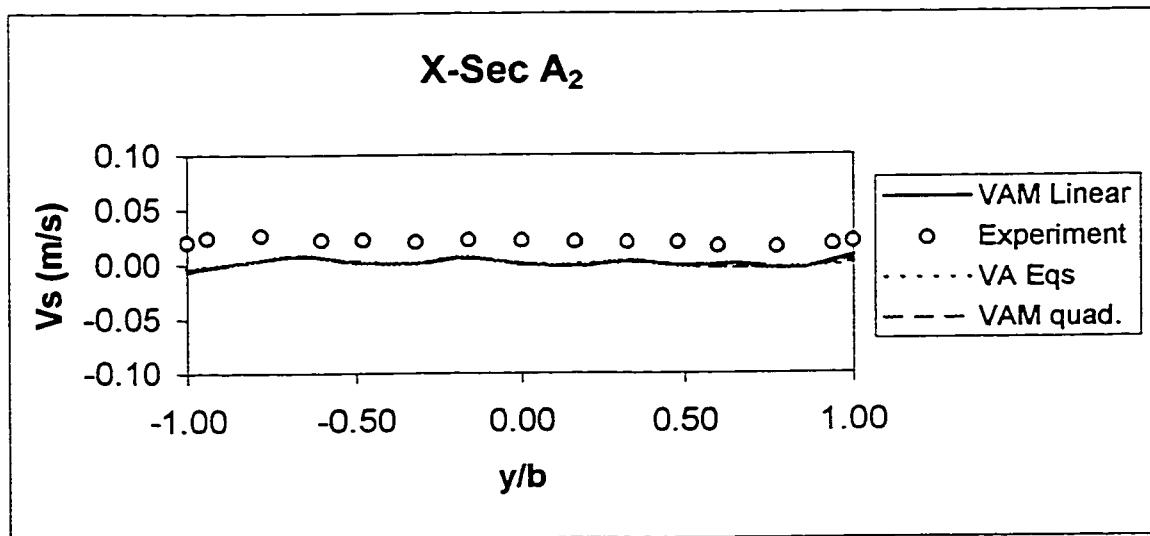


Figure 4.34 The comparison of the transverse surface velocity distribution across the flume for DeVriend (1980) at cross-section A₂

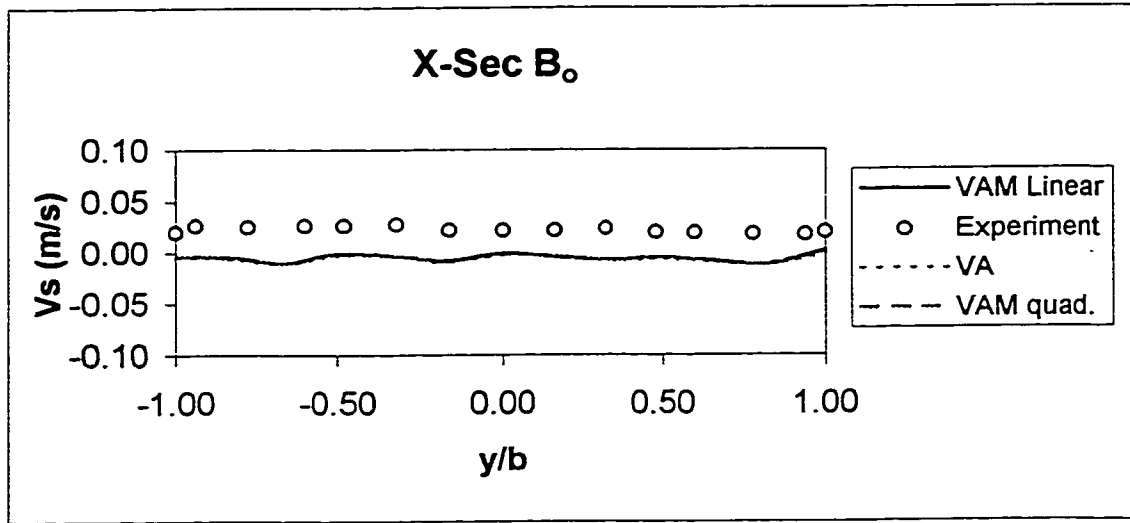


Figure 4.35 The comparison of the transverse surface velocity distribution across the flume for DeVriend (1980) at cross-section B₀

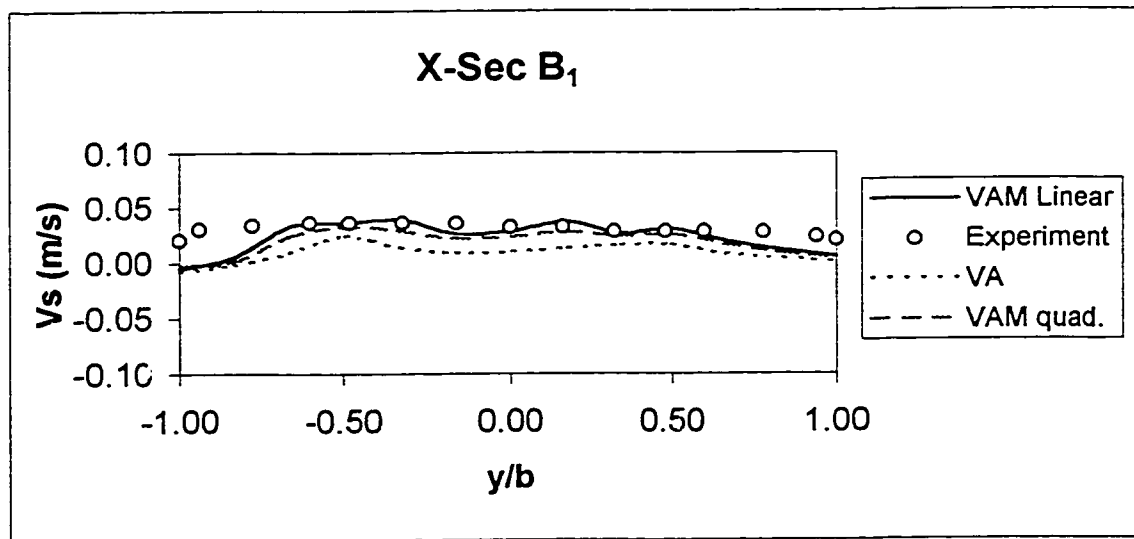


Figure 4.36 The comparison of the transverse surface velocity distribution across the flume for DeVriend (1980) at cross-section B₁

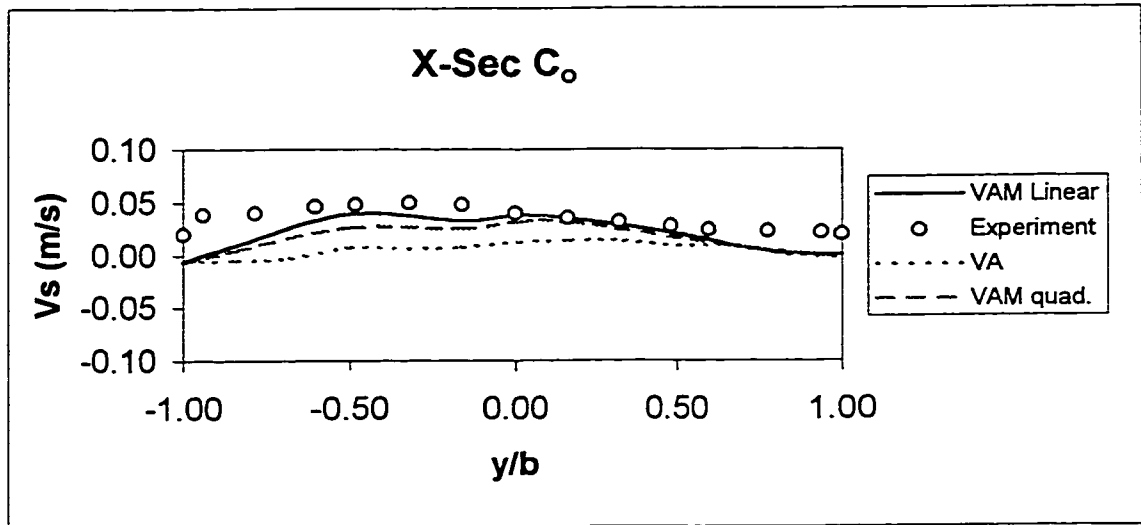


Figure 4.37 The comparison of the transverse surface velocity distribution across the flume for DeVriend (1980) at cross-section C_0

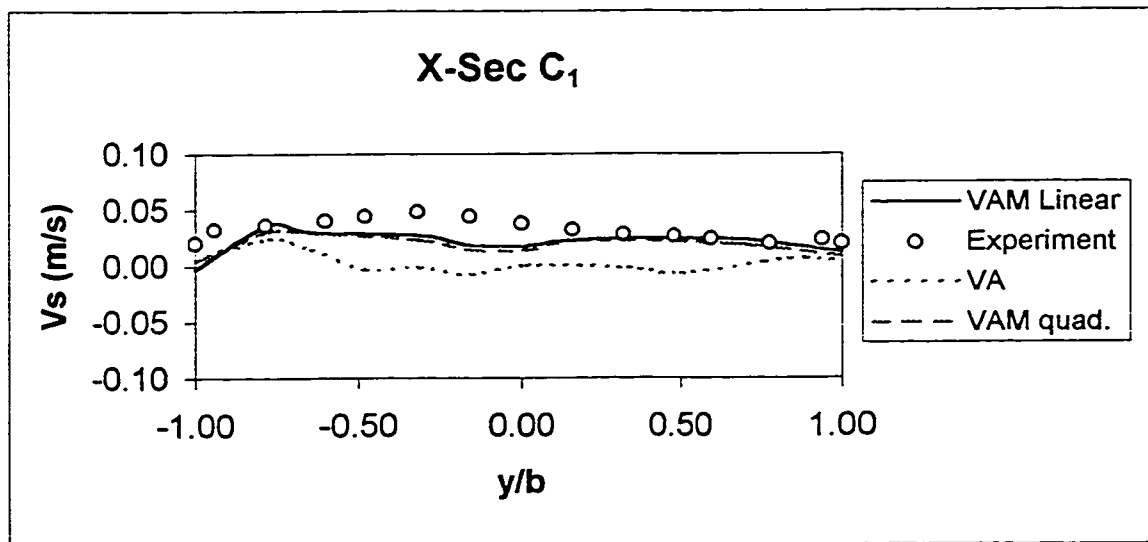


Figure 4.38 The comparison of the transverse surface velocity distribution across the flume for DeVriend (1980) at cross-section C_1

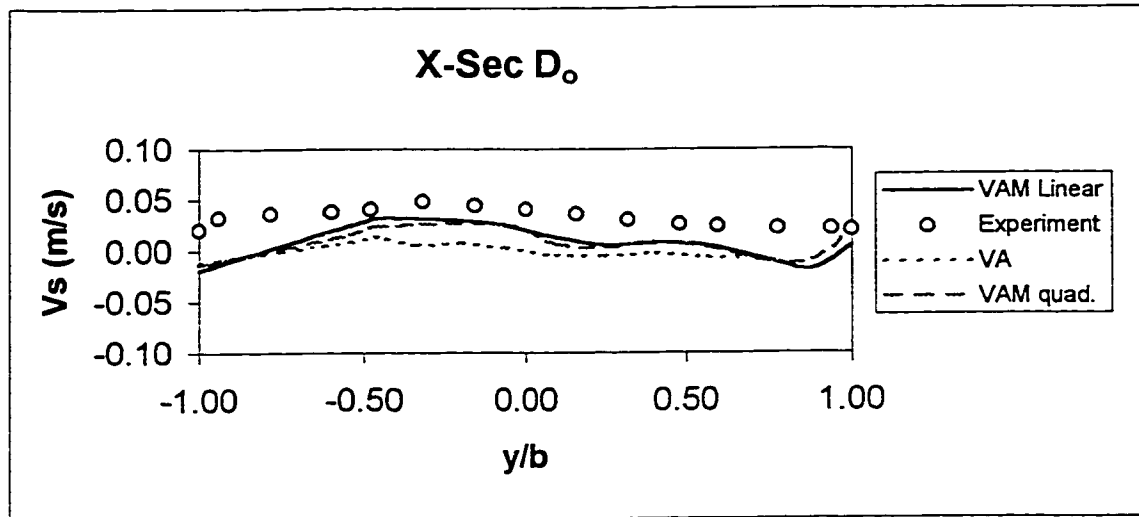


Figure 4.39 The comparison of the transverse surface velocity distribution across the flume for DeVriend (1980) at cross-section D_0 .

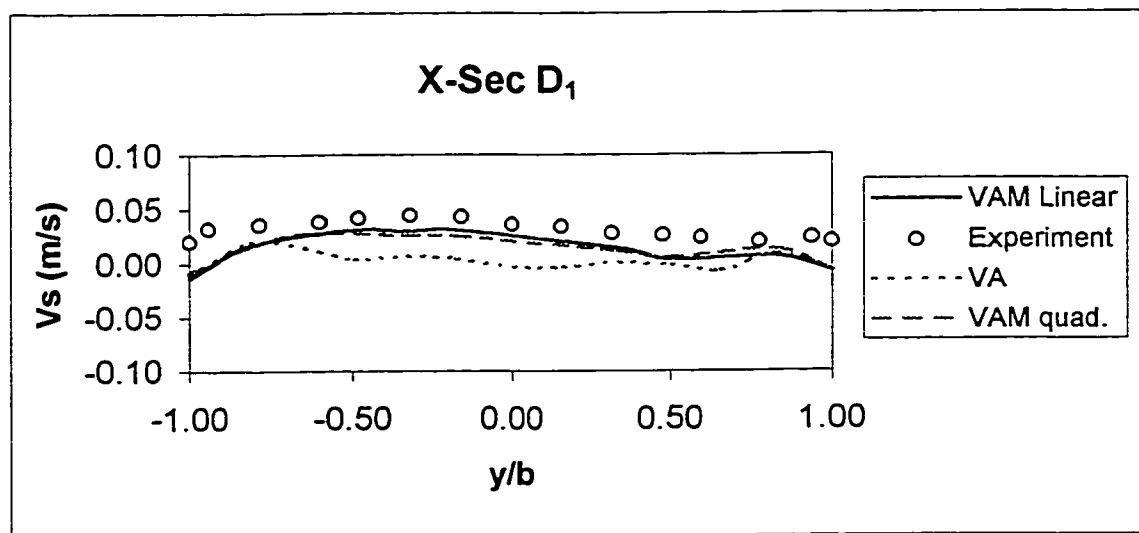


Figure 4.40 The comparison of the transverse surface velocity distribution across the flume for DeVriend (1980) at cross-section D_1 .

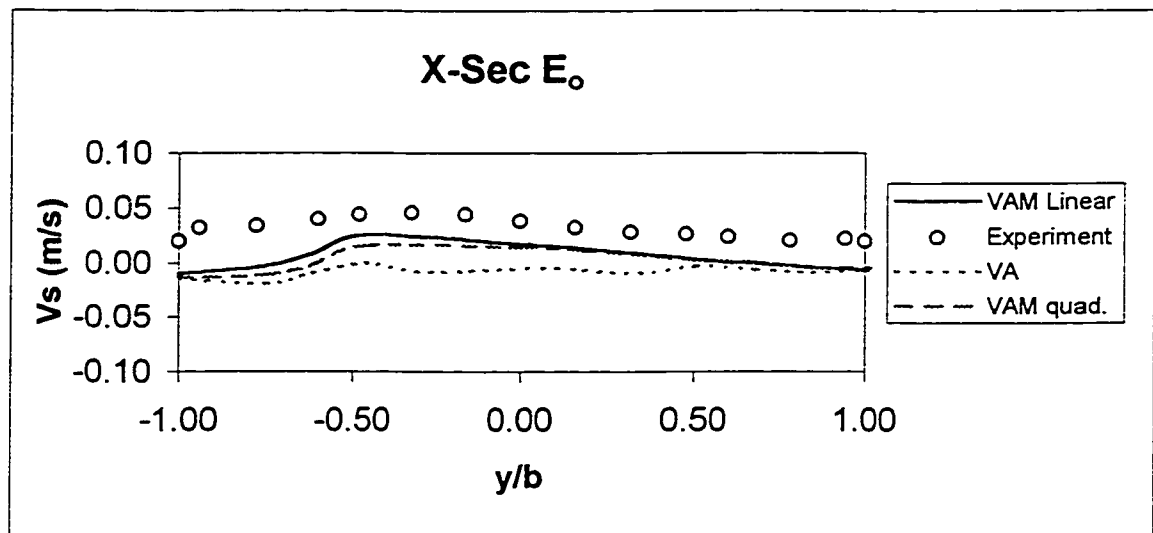


Figure 4.41 The comparison of the transverse surface velocity distribution across the flume for DeVriend (1980) at cross-section E_o

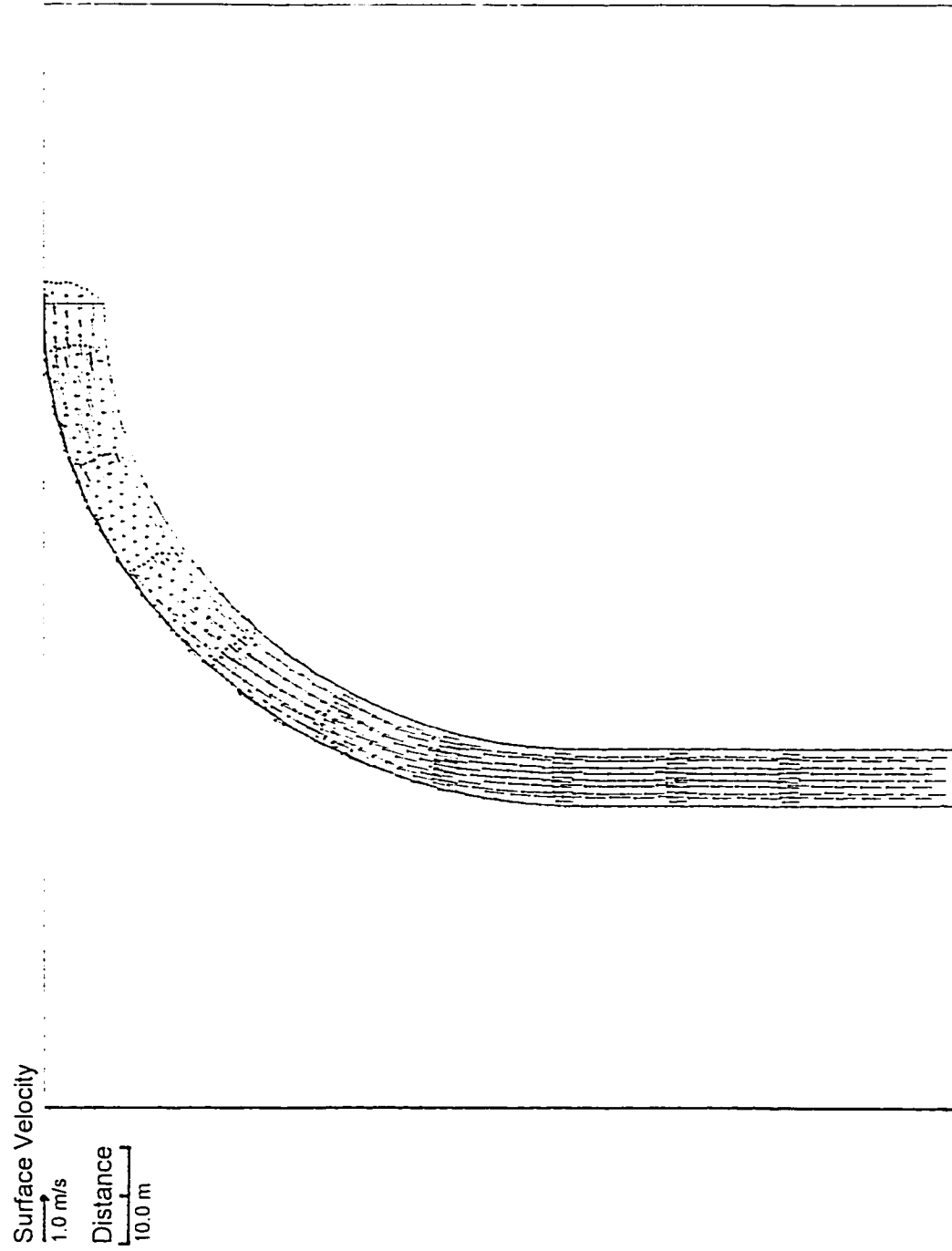


Figure 4.42 Numerical prediction of surface velocity distribution for DeVriend's (1980) experiment (VAM model)

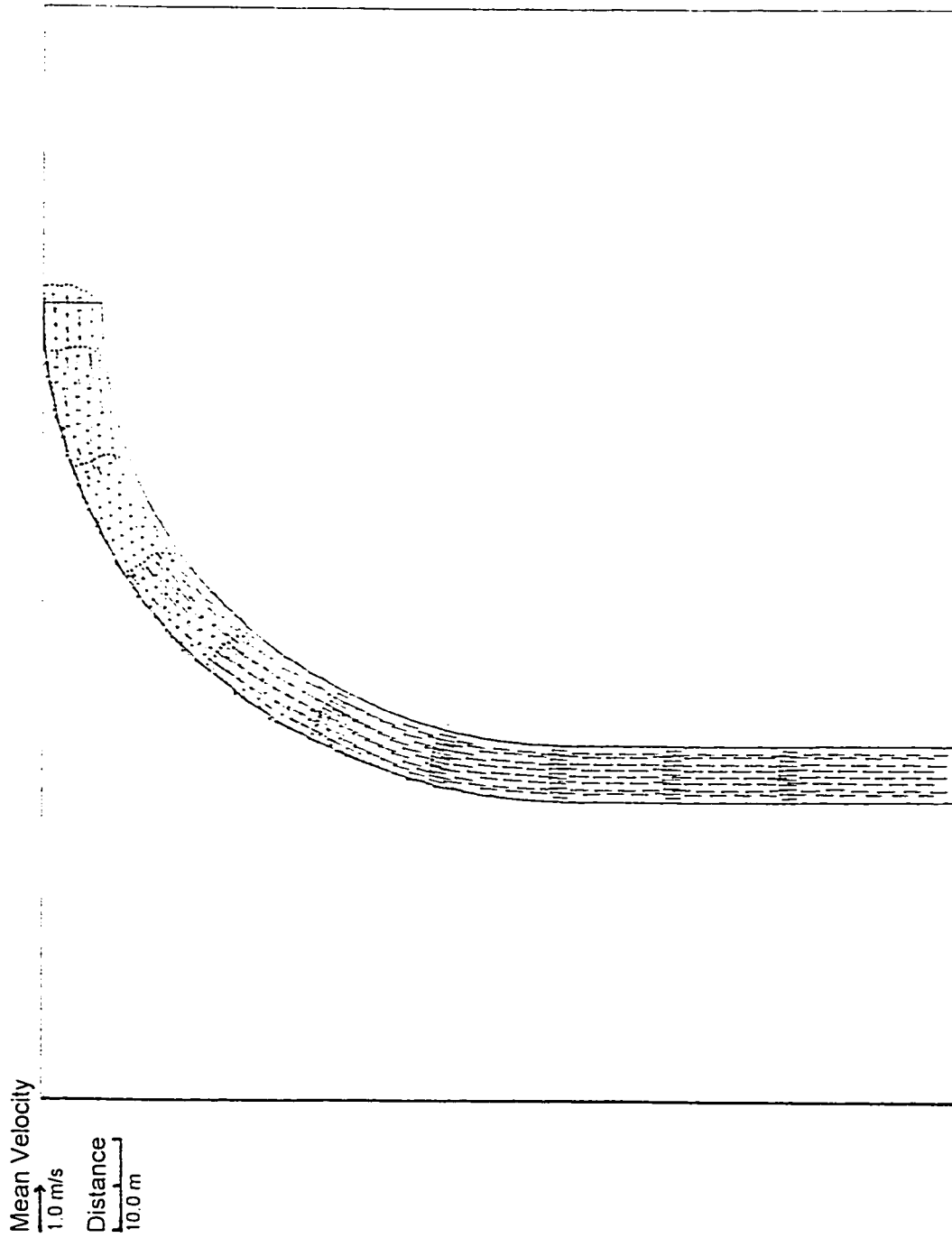


Figure 4.43 Numerical prediction of mean velocity distribution for DeVriend's (1980) experiment (VAM model)

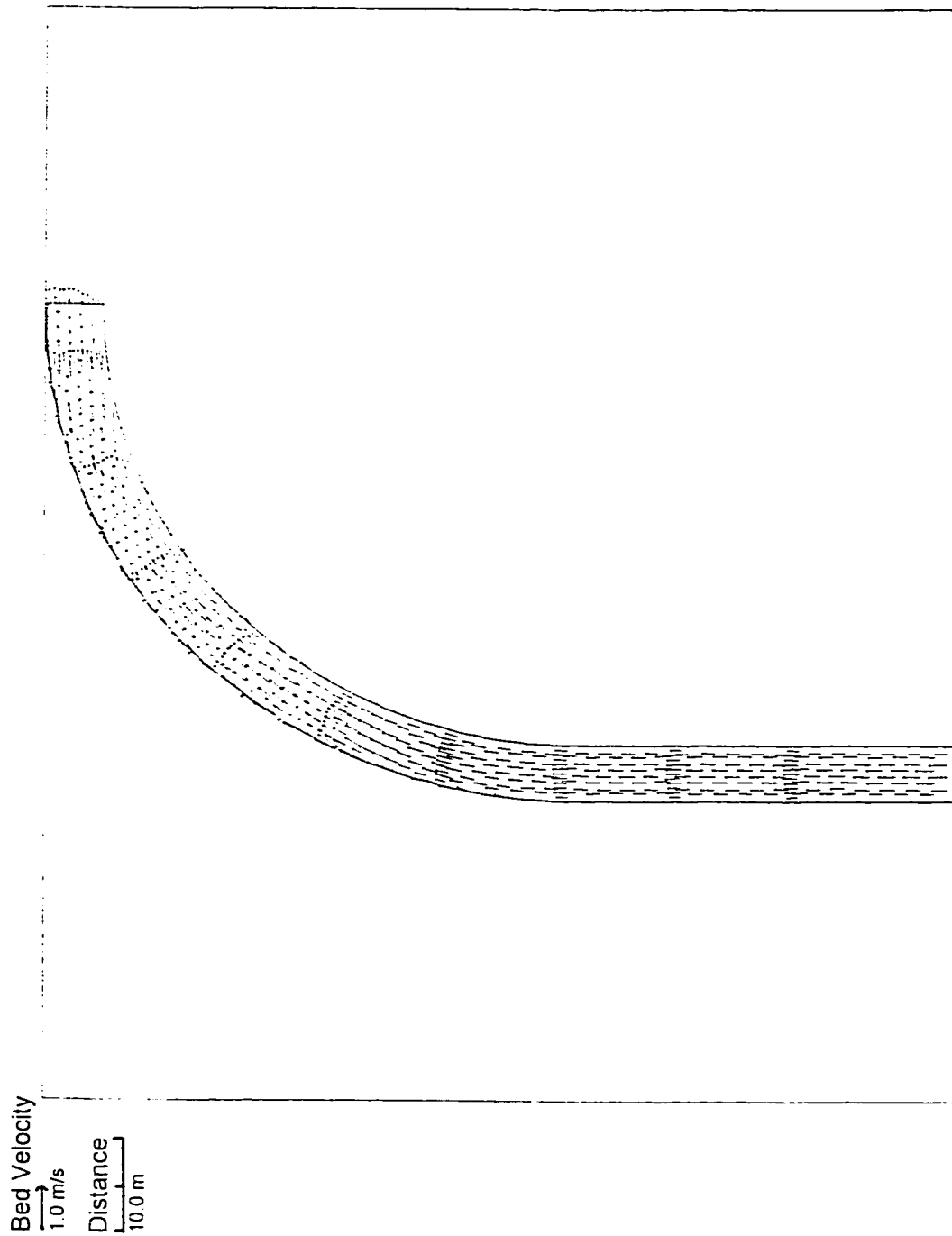


Figure 4.44 Numerical prediction of bed velocity distribution for De Vriend's (1980) experiment (VAM model)

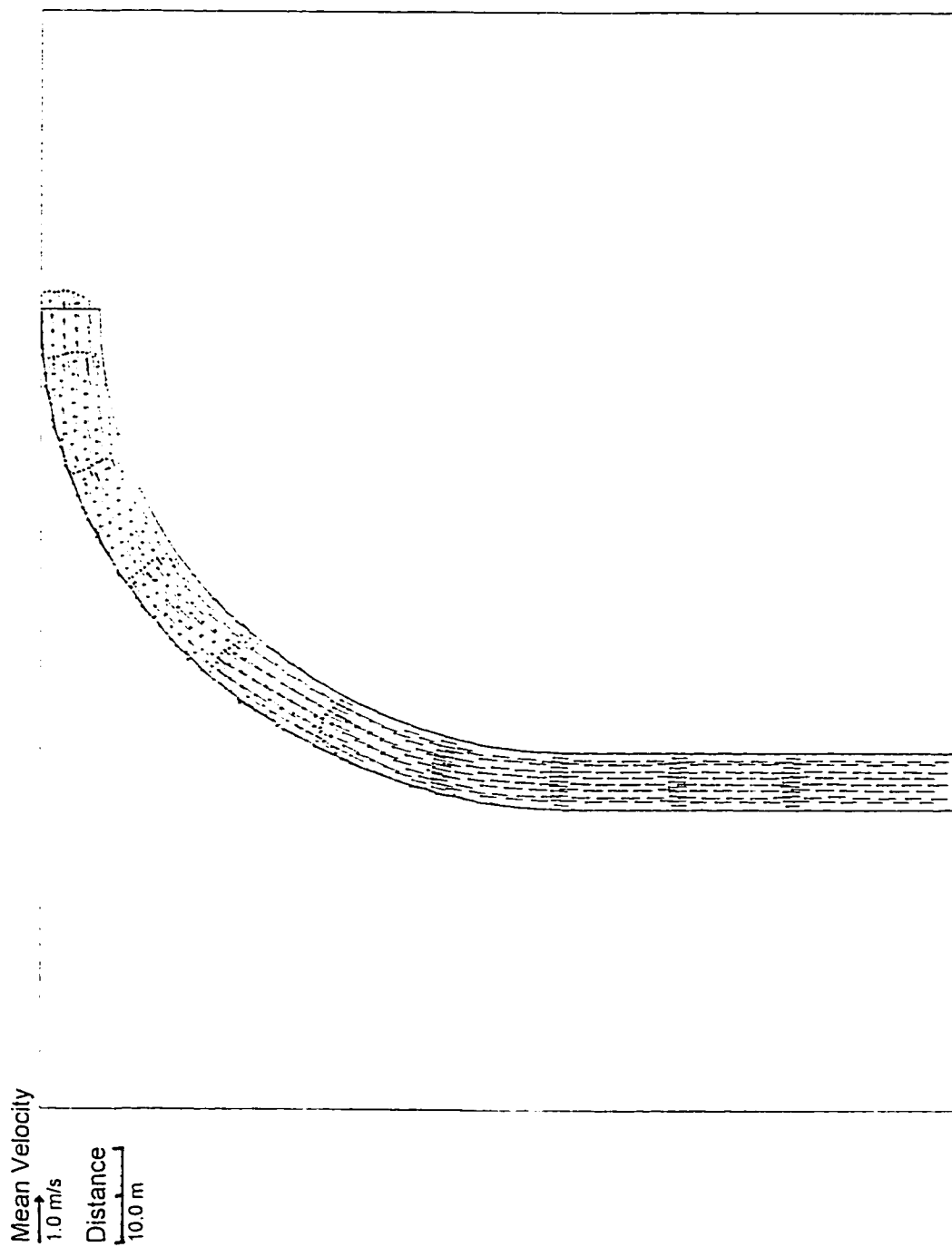


Figure 4.45 Numerical prediction of mean velocity distribution for DeVriend's (1980) experiment (VA model)

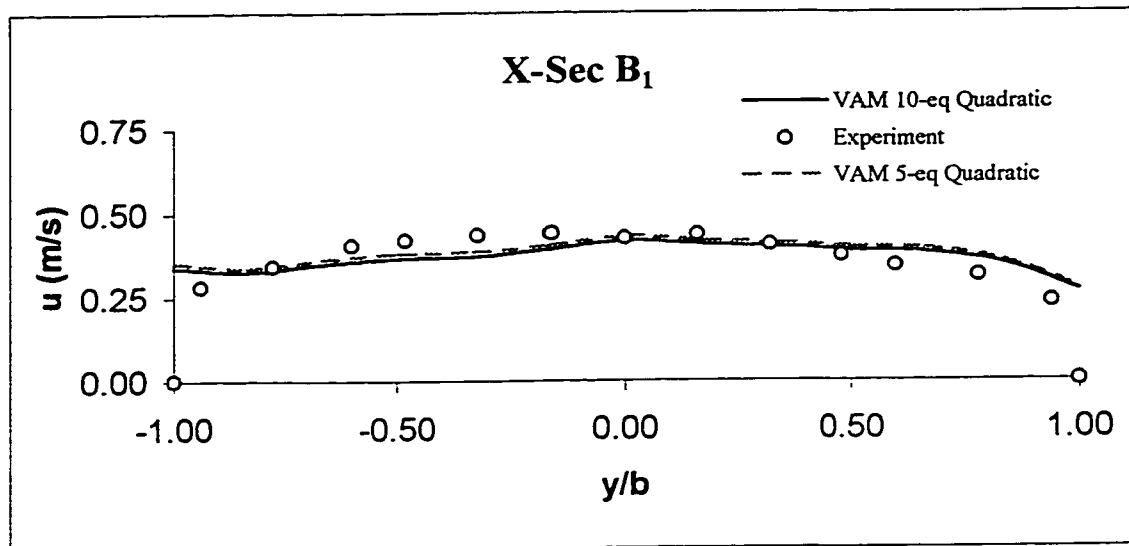


Figure 4.46 The comparison of applying VAM 5- against 10-equation models for longitudinal velocity distribution across the flume for DeVriend's (1980) at cross-section B₁

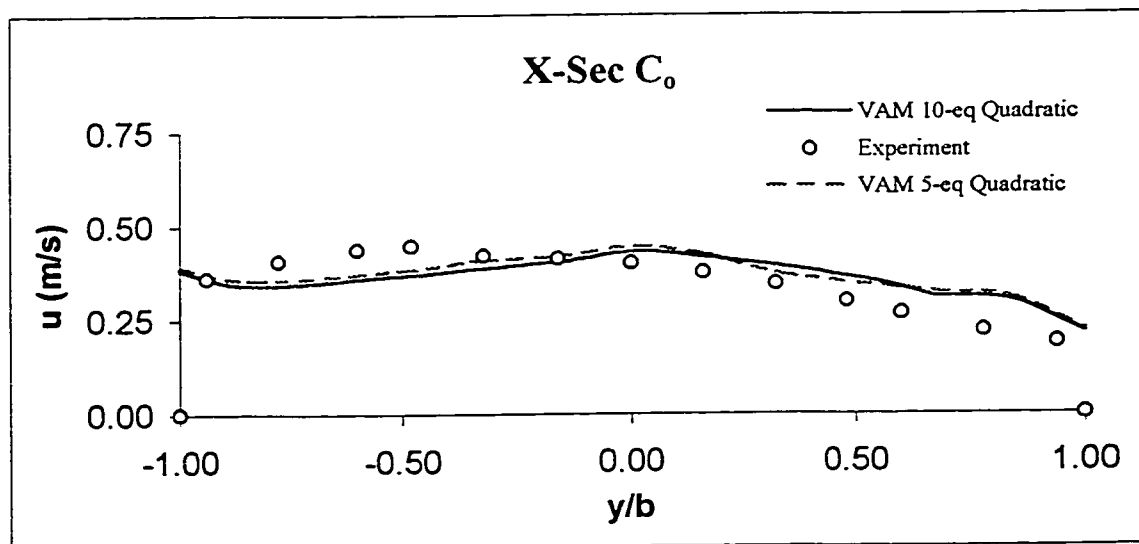


Figure 4.47 The comparison of applying VAM 5- against 10-equation models for longitudinal velocity distribution across the flume for DeVriend's (1980) at cross-section C₀

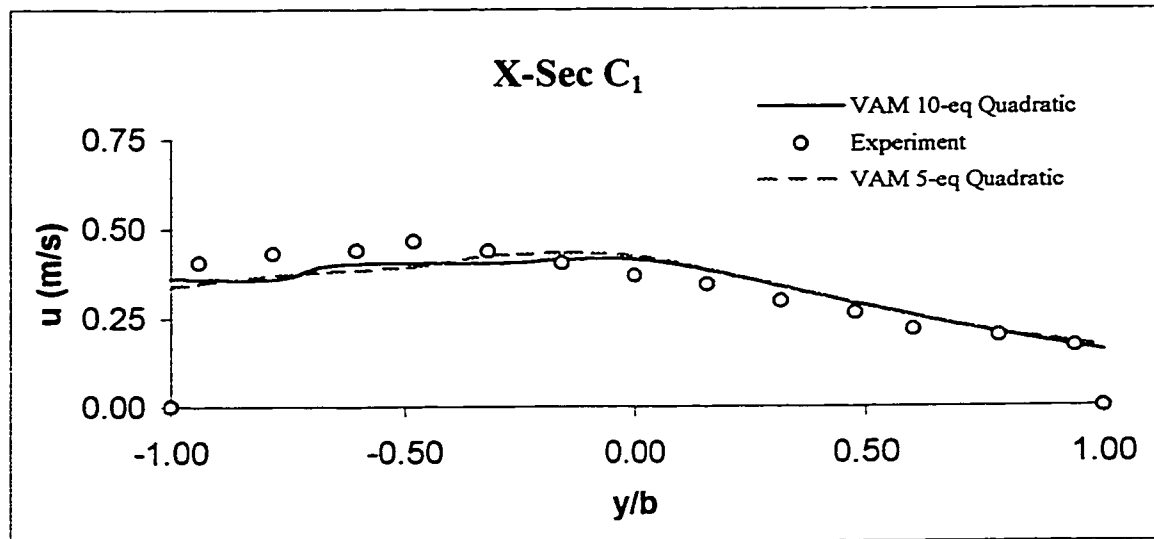


Figure 4.48 The comparison of applying VAM 5- against 10-equation models for longitudinal velocity distribution across the flume for DeVriend's (1980) at cross-section C₁

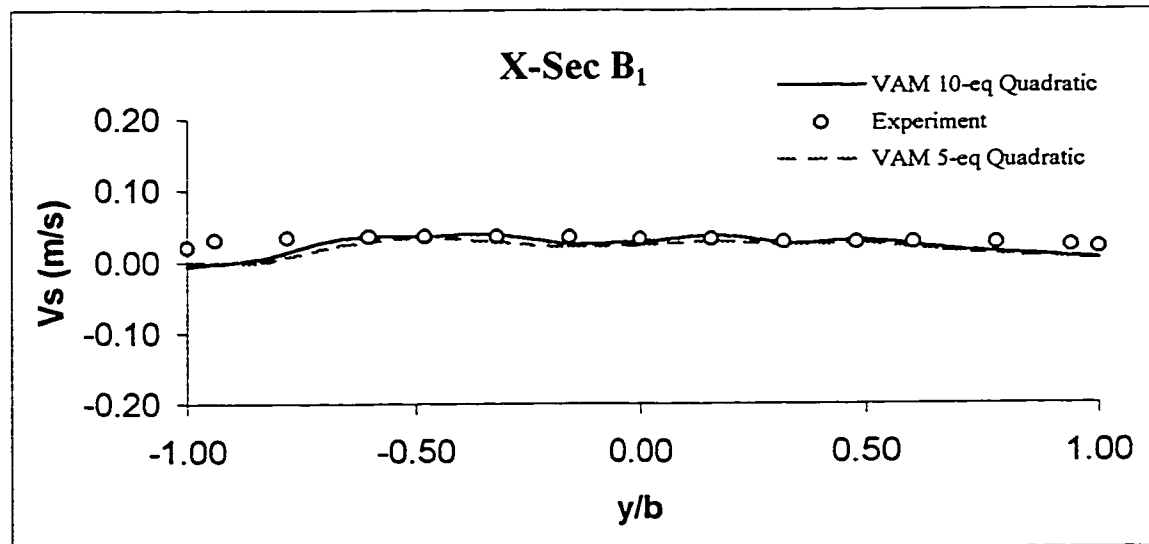


Figure 4.49 The comparison of applying VAM 5- against 10-equation models for transverse velocity distribution across the flume for DeVriend's (1980) at cross-section B₁

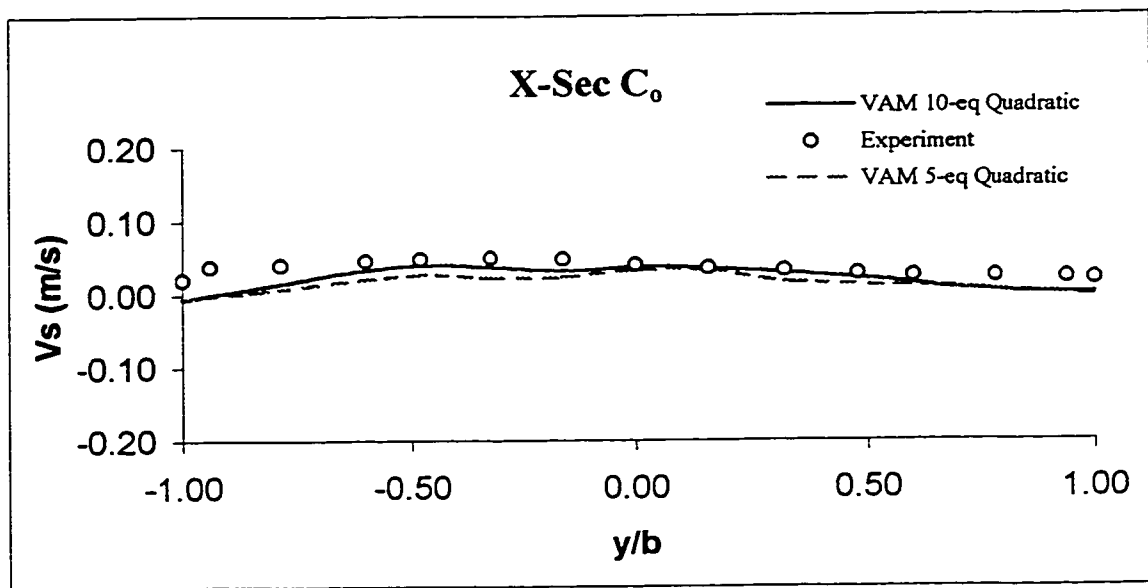
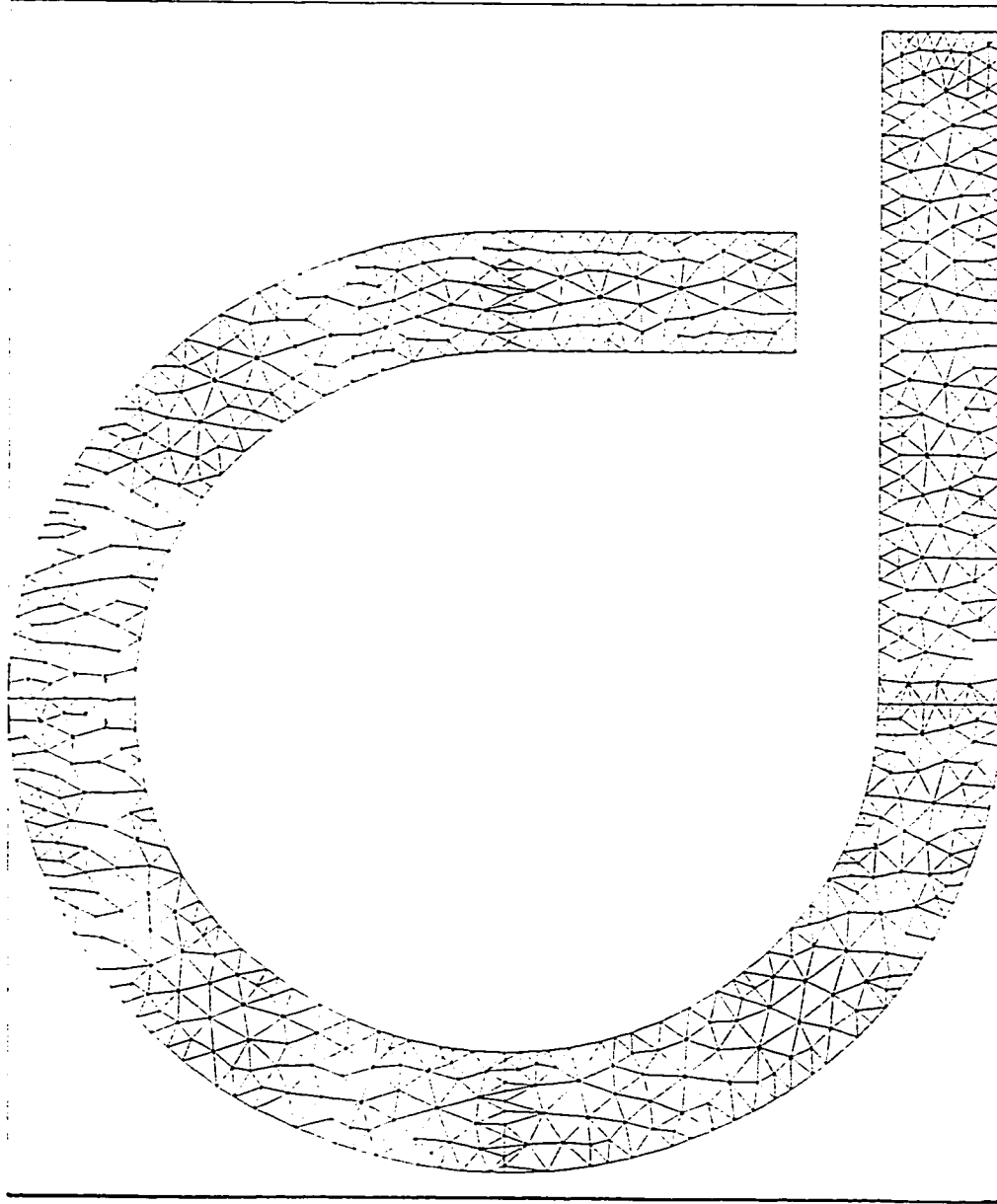


Figure 4.50 The comparison of applying VAM 5- against 10-equation models for transverse velocity distribution across the flume for DeVriend's (1980) at cross-section C_o .

Distance
1.0 m



The generated mesh

Number of nodes = 748

Number of elements = 1226

Figure 4.52 Finite element mesh for Steffler's (1984) experiment

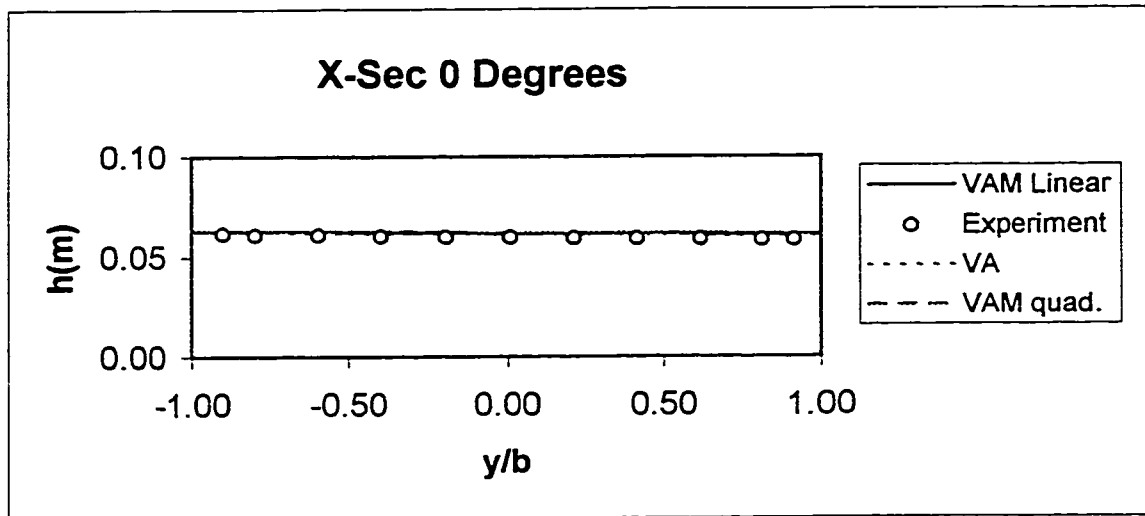


Figure 4.53 The comparison of surface elevation across the flume for Steffler's (1984) run 1 at cross-section 0 degrees

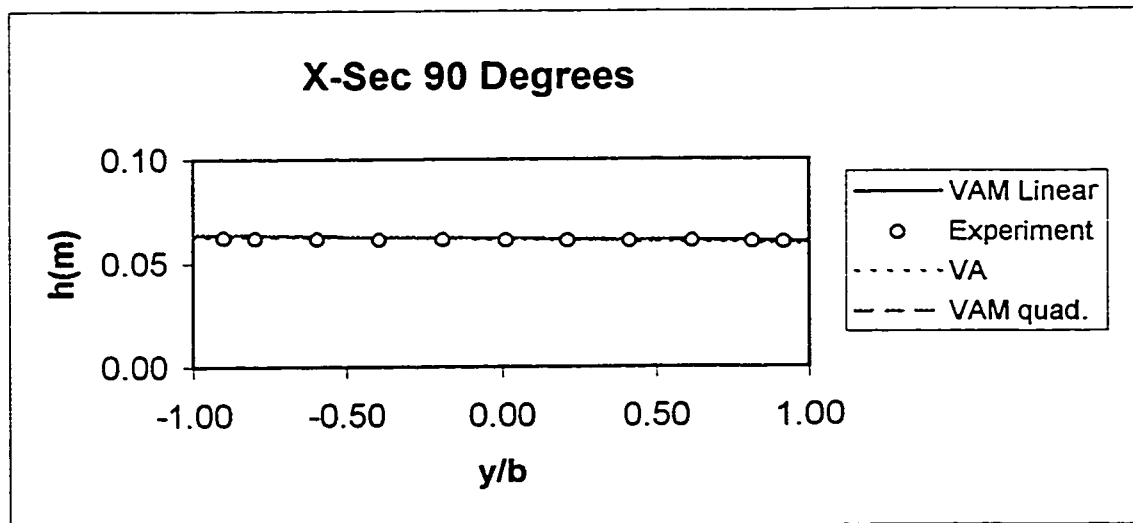


Figure 4.54 The comparison of surface elevation across the flume for Steffler's (1984) run 1 at cross-section 90 degrees

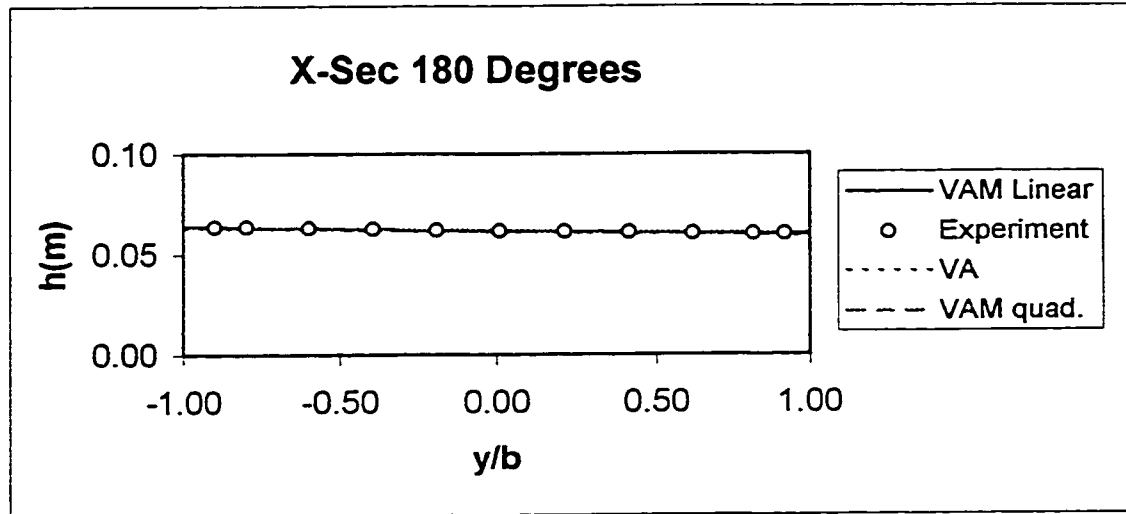


Figure 4.55 The comparison of surface elevation across the flume for Steffler's (1984) run 1 at cross-section 180 degrees

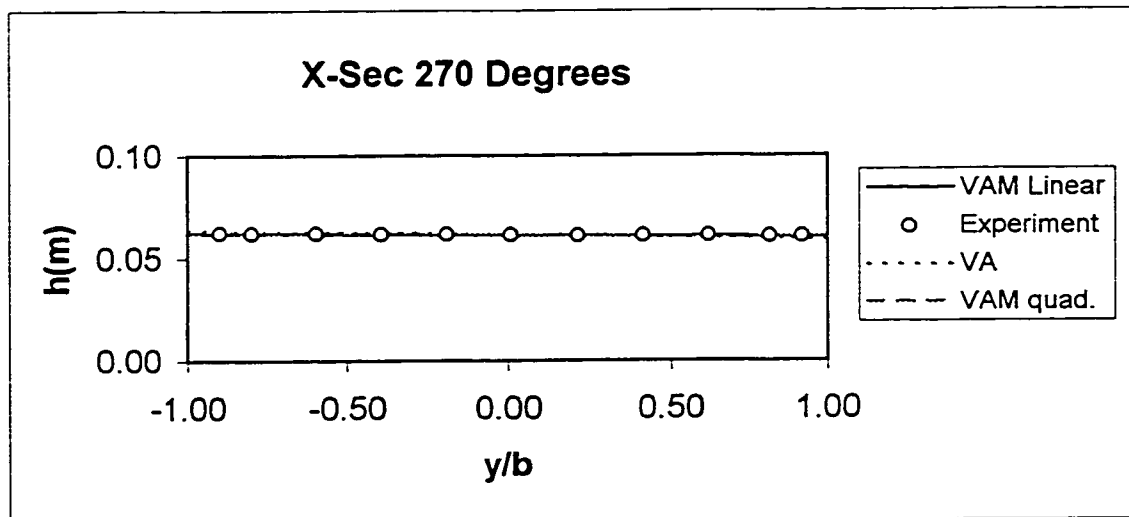


Figure 4.56 The comparison of surface elevation across the flume for Steffler's (1984) run 1 at cross-section 270 degrees

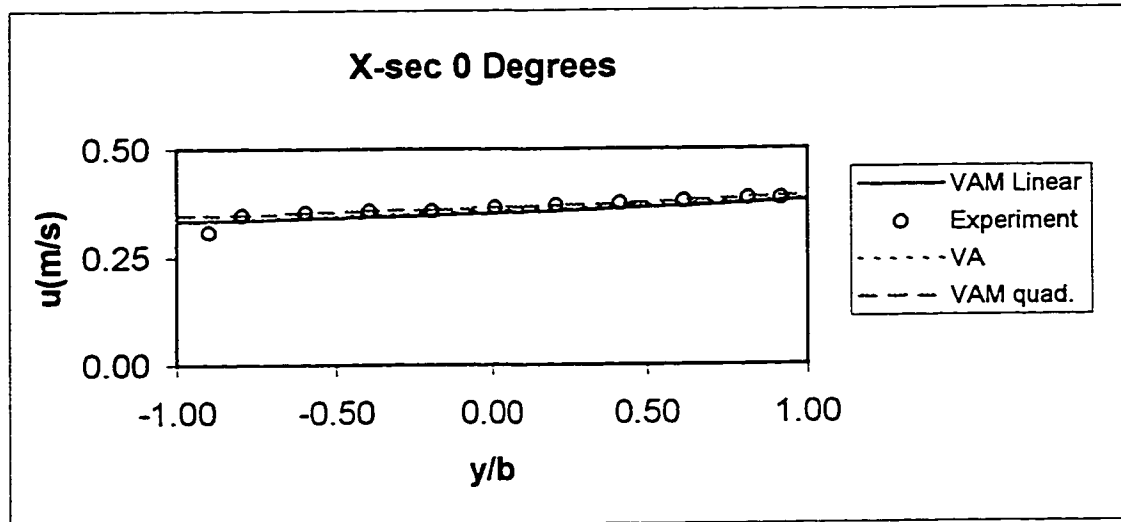


Figure 4.57 The comparison of longitudinal velocity distribution across the flume for Steffler's (1984) run 1 at cross-section 0 degrees

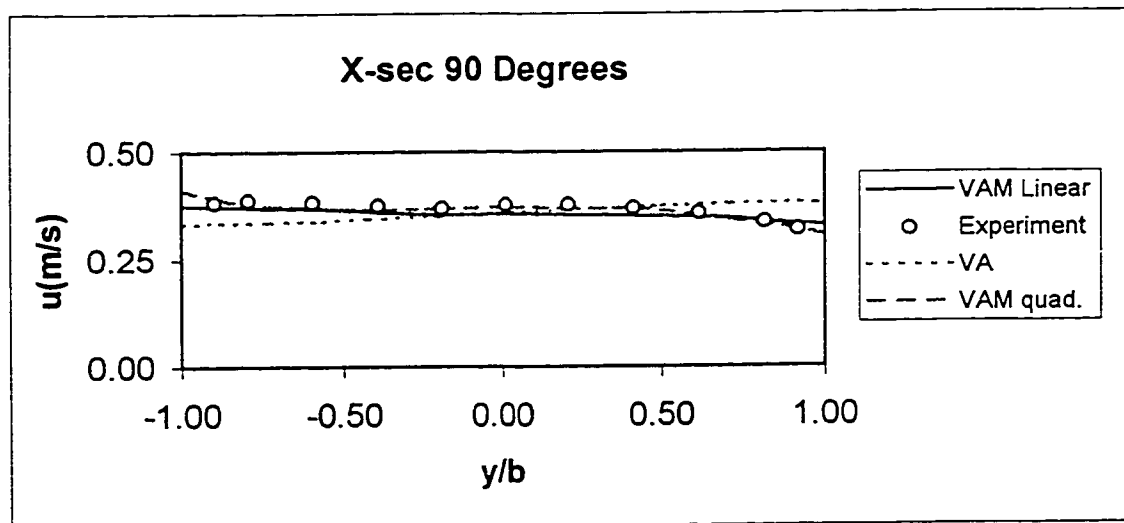


Figure 4.58 The comparison of longitudinal velocity distribution across the flume for Steffler's (1984) run 1 at cross-section 90 degrees

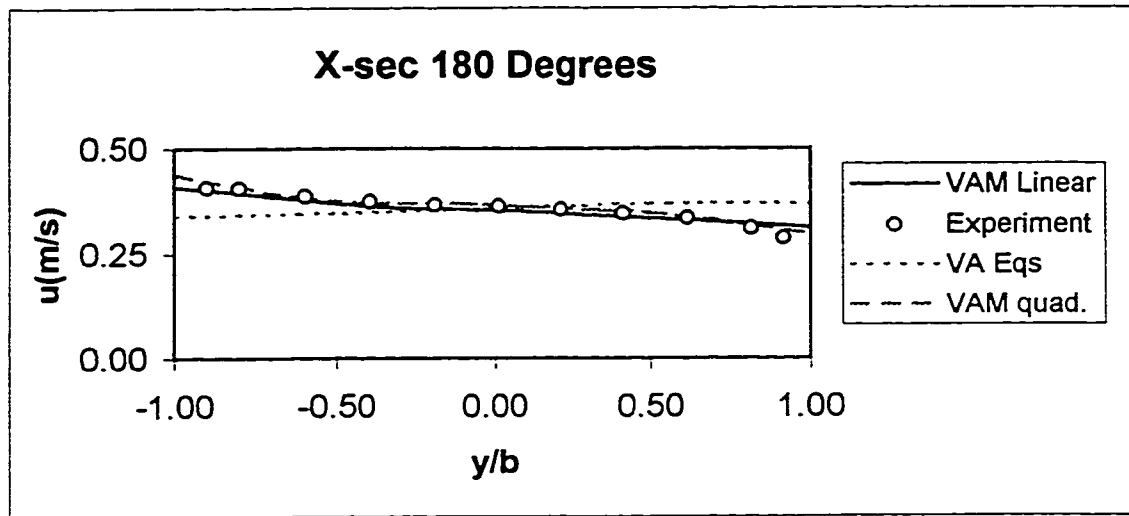


Figure 4.59 The comparison of longitudinal velocity distribution across the flume for Steffler's (1984) run 1 at cross-section 180 degrees

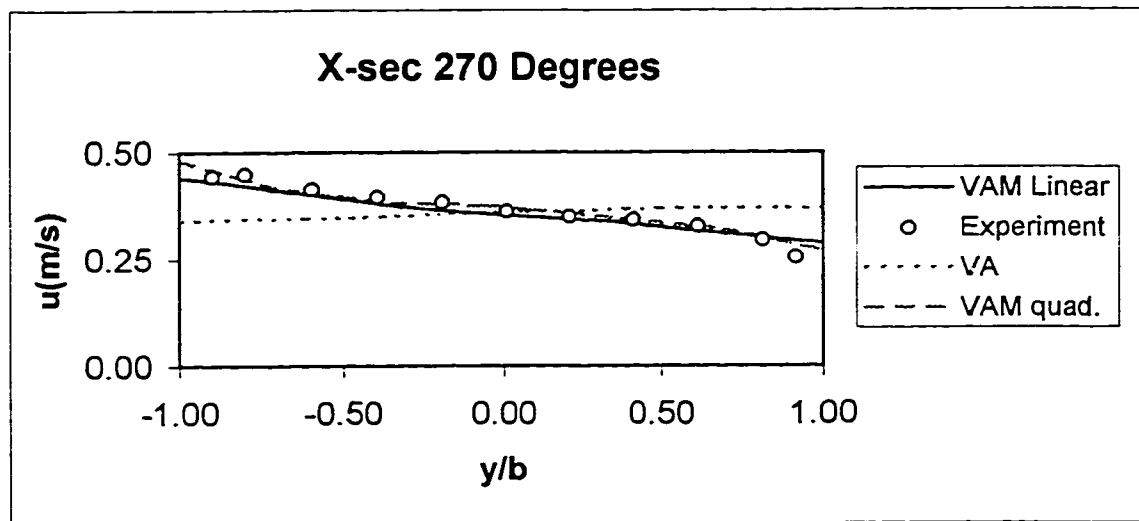


Figure 4.60 The comparison of longitudinal velocity distribution across the flume for Steffler's (1984) run 1 at cross-section 270 degrees

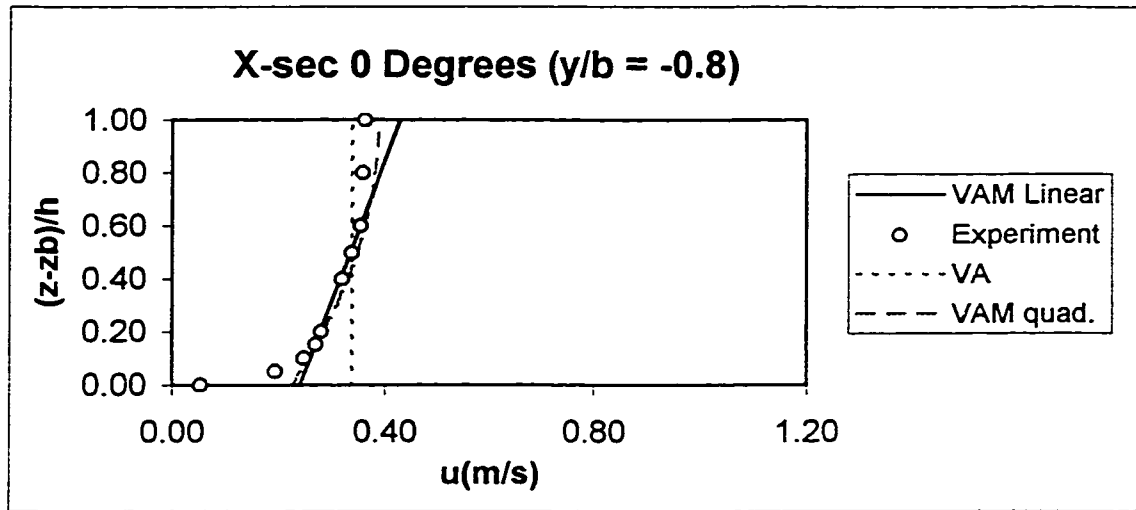


Figure 4.61 The comparison of longitudinal velocity profile for Steffler's (1984) run 1 at cross-section 0 degrees and $y/b = -0.8$

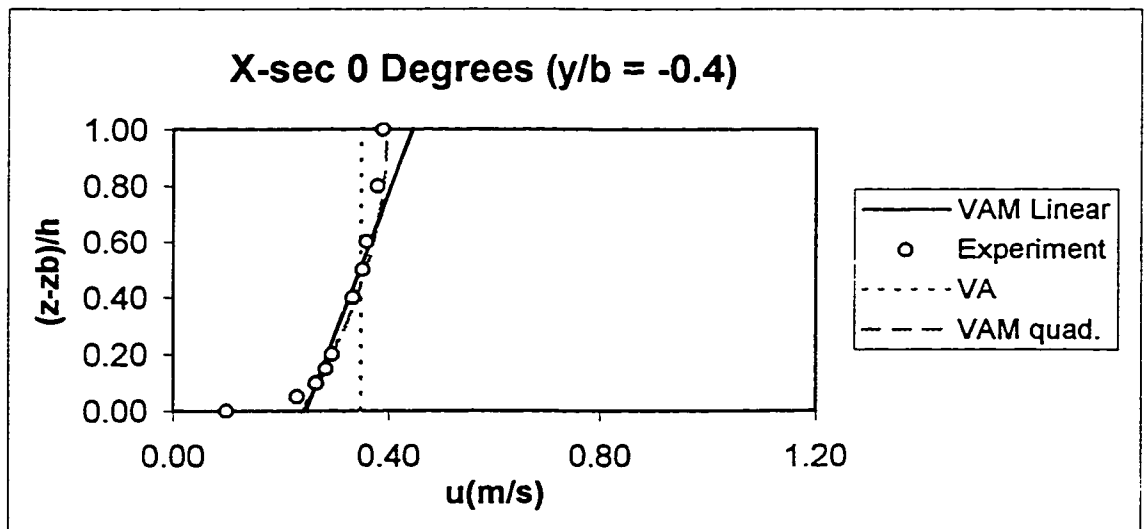


Figure 4.62 The comparison of longitudinal velocity profile for Steffler's (1984) run 1 at cross-section 0 degrees and $y/b = -0.4$

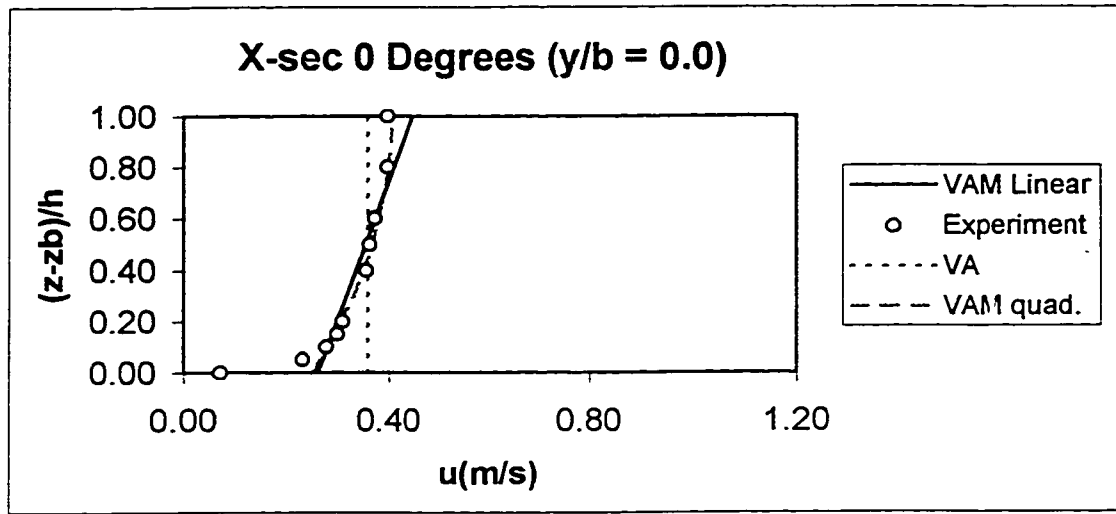


Figure 4.63 The comparison of longitudinal velocity profile for Steffler's (1984) run 1 at cross-section 0 degrees and $y/b = 0$

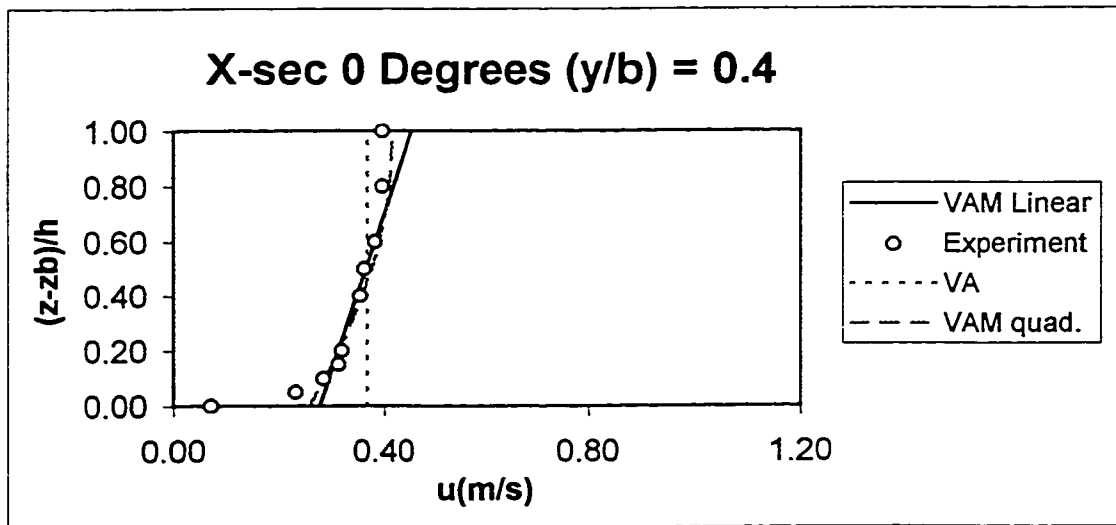


Figure 4.64 The comparison of longitudinal velocity profile for Steffler's (1984) run 1 at cross-section 0 degrees and $y/b = 0.4$

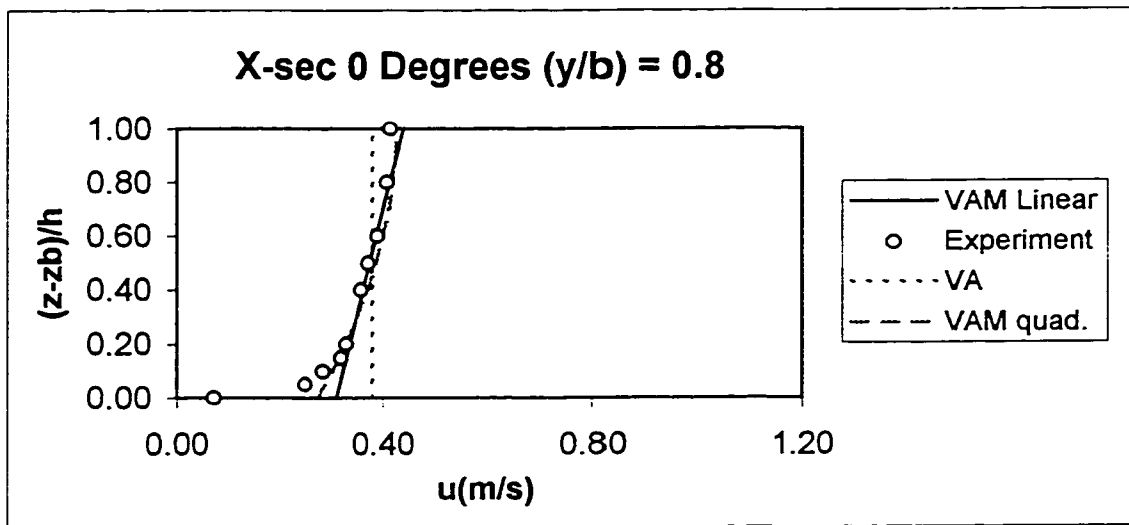


Figure 4.65 The comparison of longitudinal velocity profile for Steffler's (1984) run 1 at cross-section 0 degrees and $y/b = 0.8$

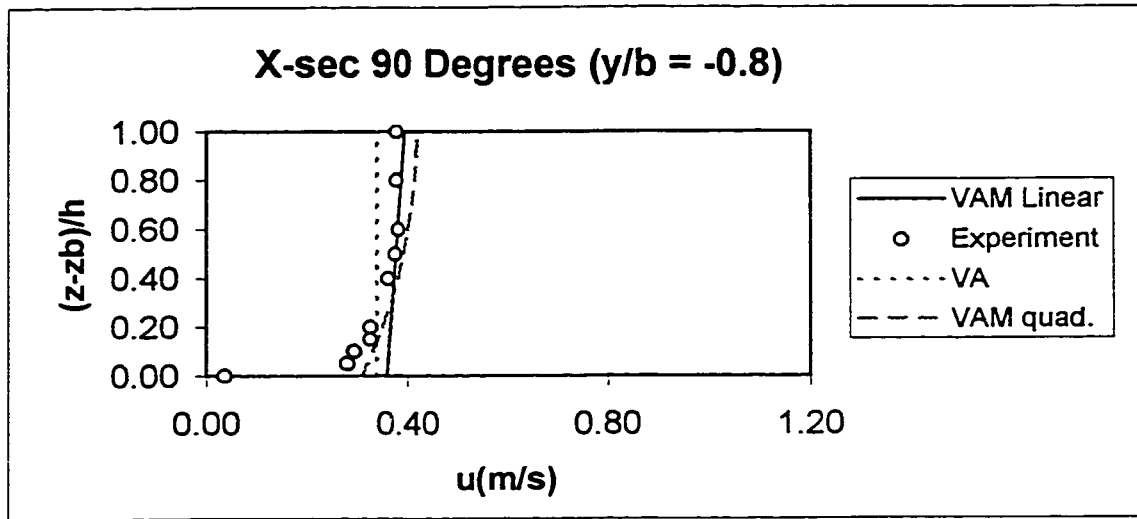


Figure 4.66 The comparison of longitudinal velocity profile for Steffler's (1984) run 1 at cross-section 90 degrees and $y/b = -0.8$

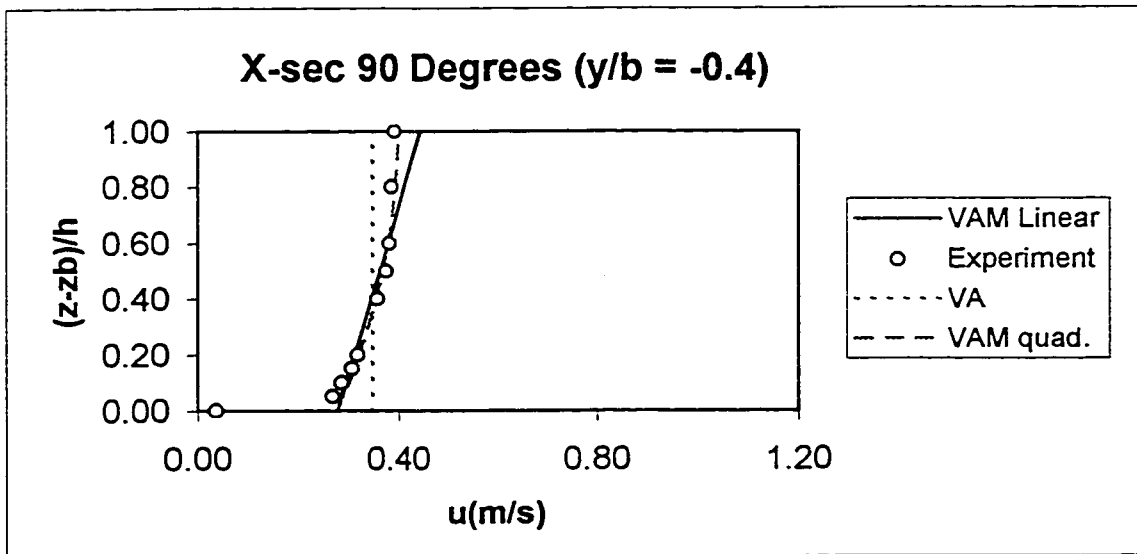


Figure 4.67 The comparison of longitudinal velocity profile for Steffler's (1984) run 1 at cross-section 90 degrees and $y/b = -0.4$

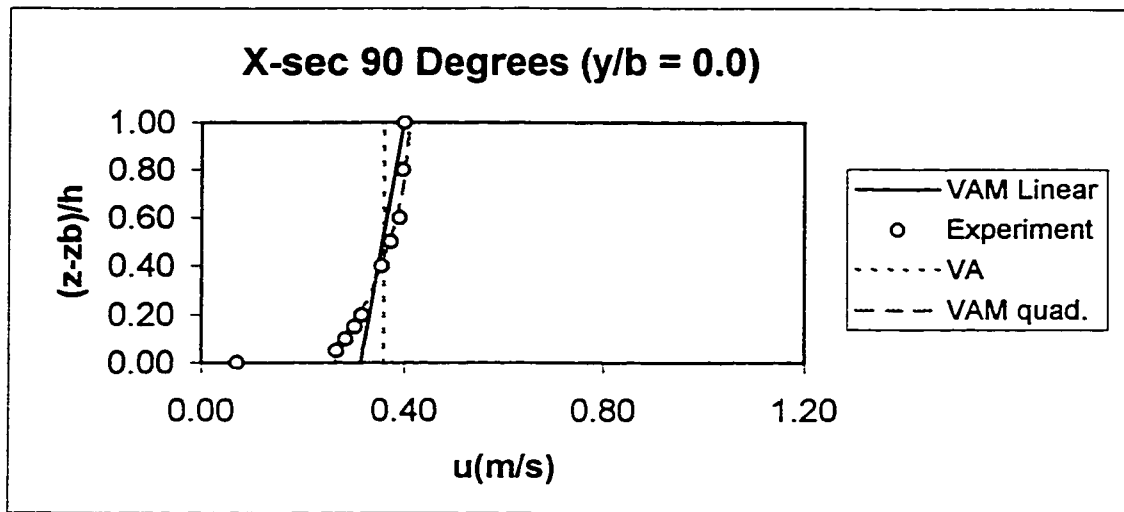


Figure 4.68 The comparison of longitudinal velocity profile for Steffler's (1984) run 1 at cross-section 90 degrees and $y/b = 0$

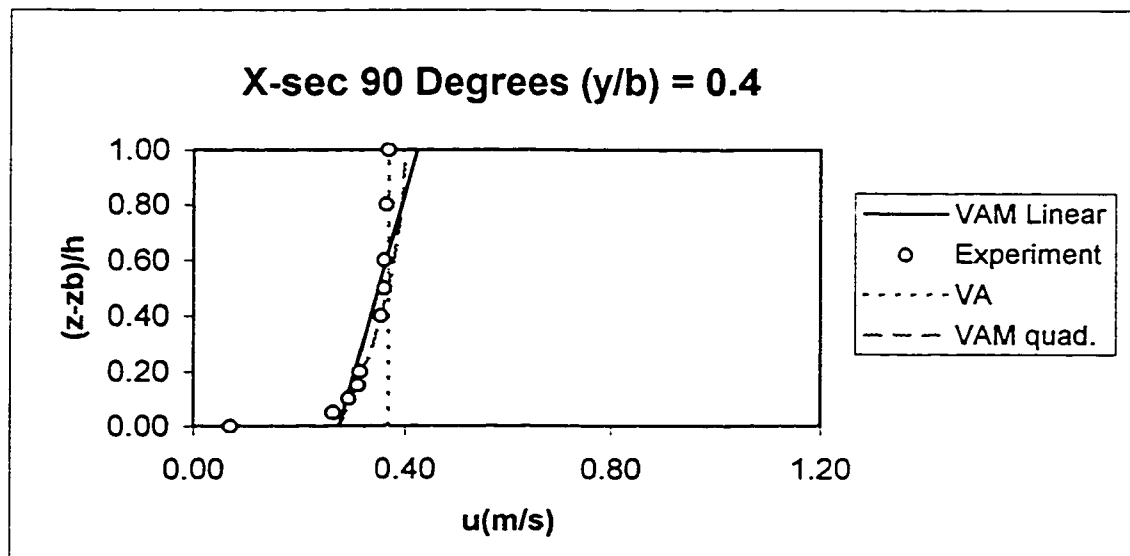


Figure 4.69 The comparison of longitudinal velocity profile for Steffler's (1984) run 1 at cross-section 90 degrees and $y/b = 0.4$

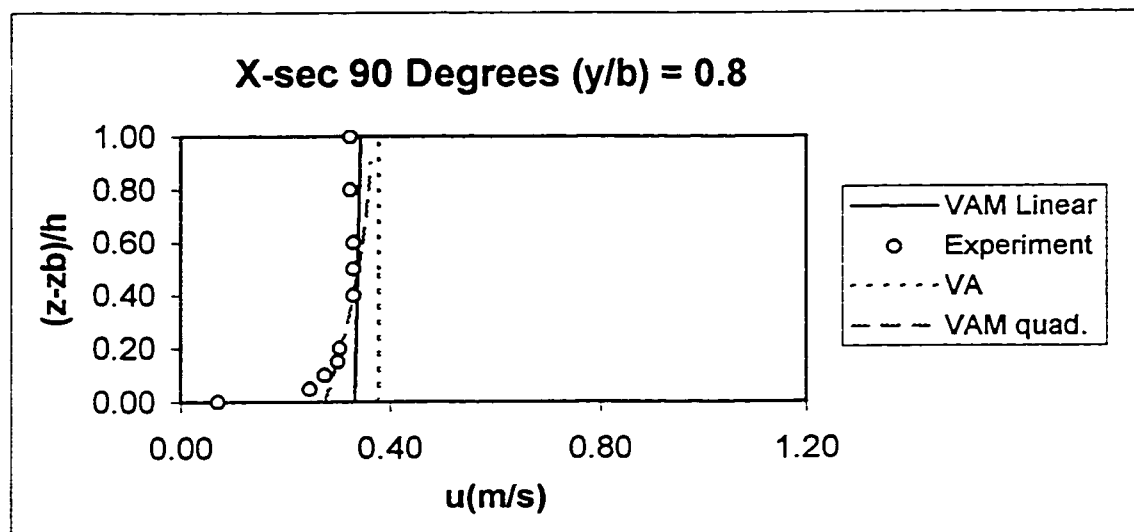


Figure 4.70 The comparison of longitudinal velocity profile for Steffler's (1984) run 1 at cross-section 90 degrees and $y/b = 0.8$

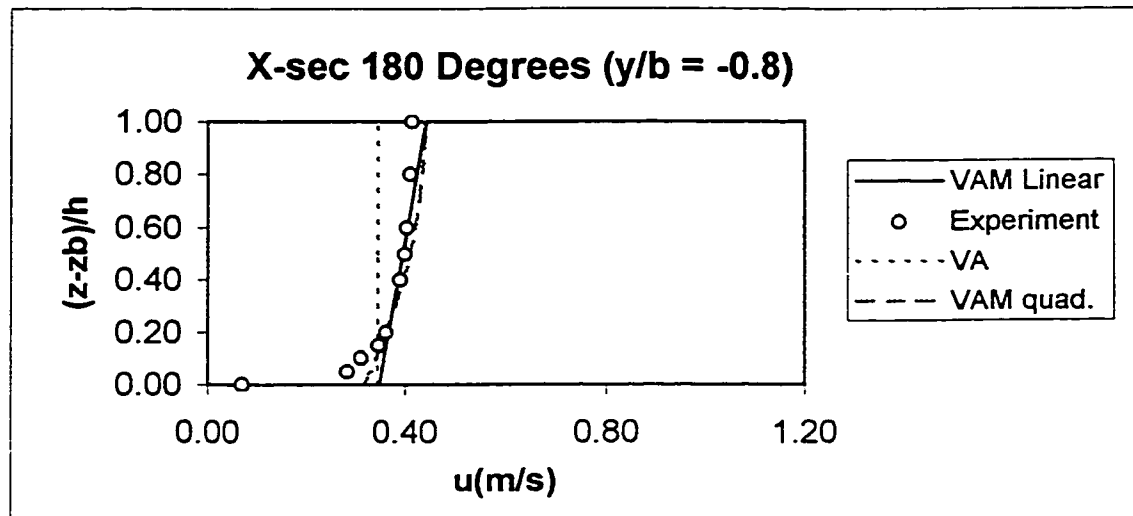


Figure 4.71 The comparison of longitudinal velocity profile for Steffler's (1984) run 1 at cross-section 180 degrees and $y/b = -0.8$

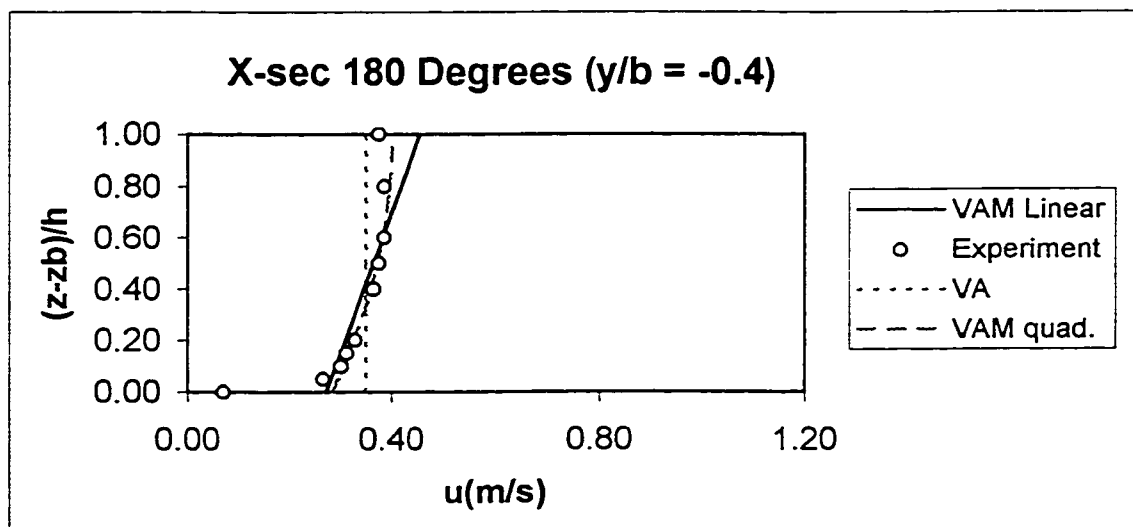


Figure 4.72 The comparison of longitudinal velocity profile for Steffler's (1984) run 1 at cross-section 180 degrees and $y/b = -0.4$

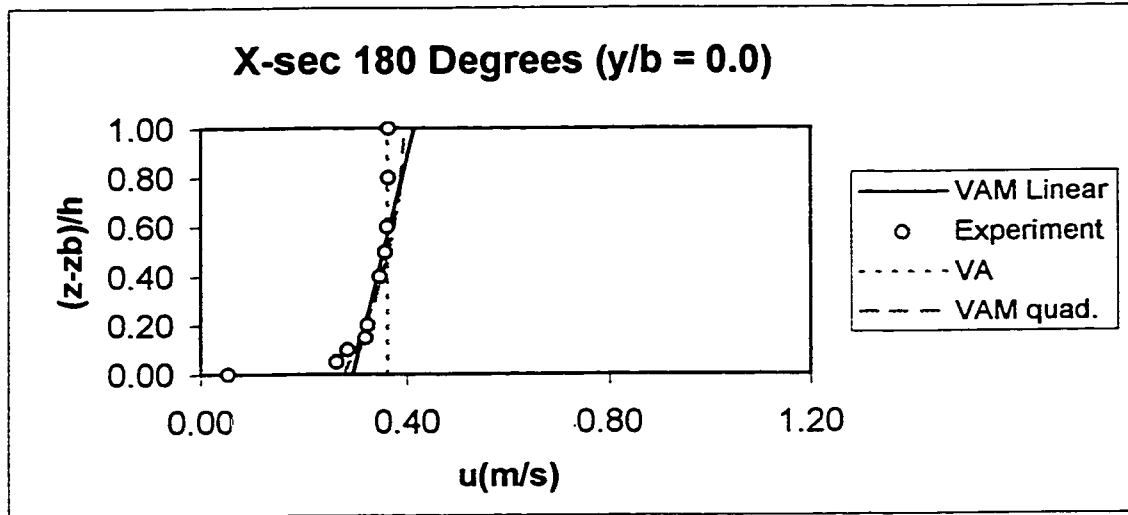


Figure 4.73 The comparison of longitudinal velocity profile for Steffler's (1984) run 1 at cross-section 180 degrees and $y/b = 0$

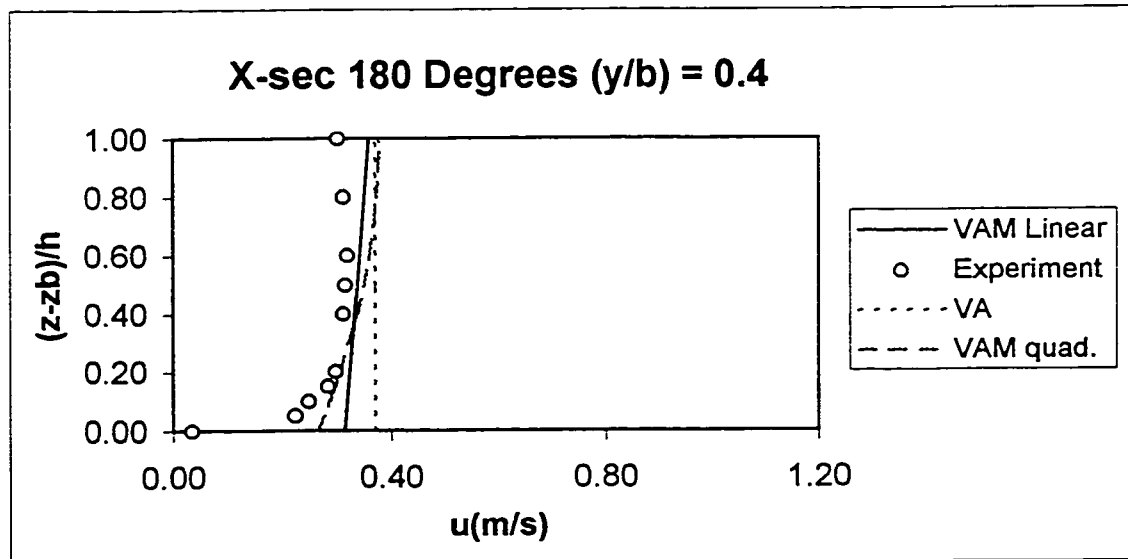


Figure 4.74 The comparison of longitudinal velocity profile for Steffler's (1984) run 1 at cross-section 180 degrees and $y/b = 0.4$

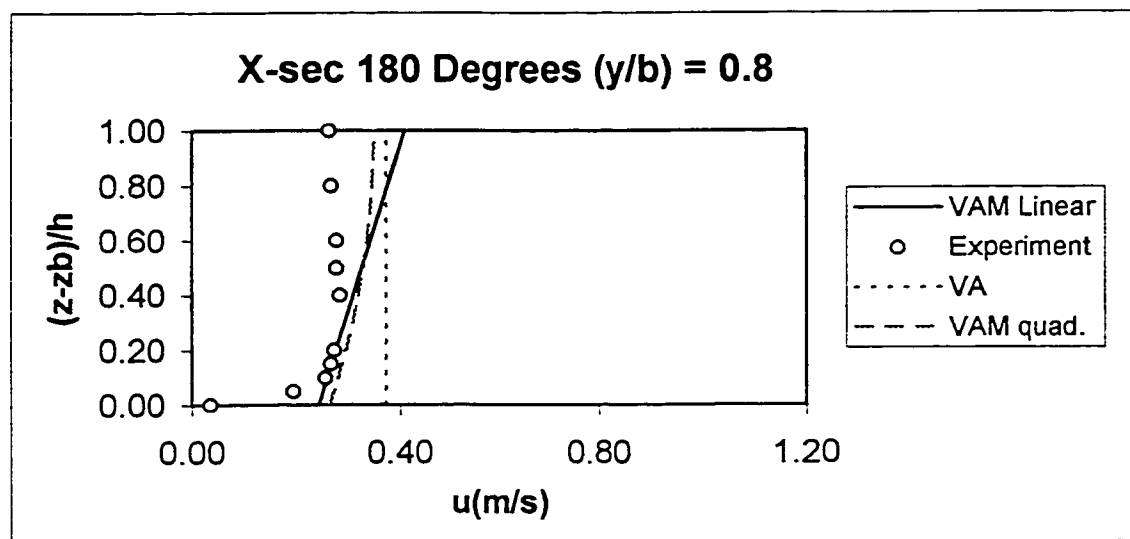


Figure 4.75 The comparison of longitudinal velocity profile for Steffler's (1984) run 1 at cross-section 180 degrees and $y/b = 0.8$

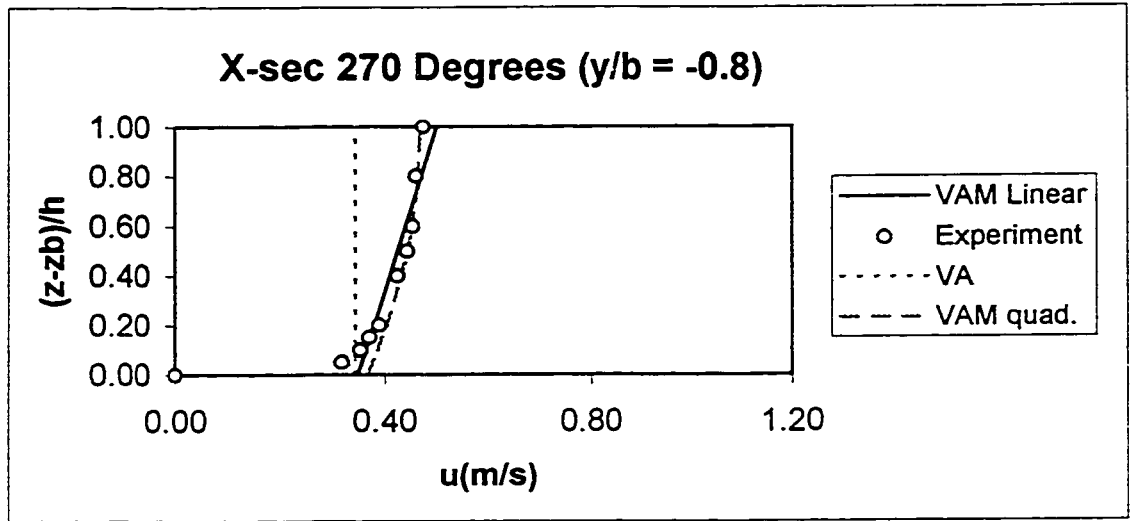


Figure 4.76 The comparison of longitudinal velocity profile for Steffler's (1984) run 1 at cross-section 270 degrees and $y/b = -0.8$

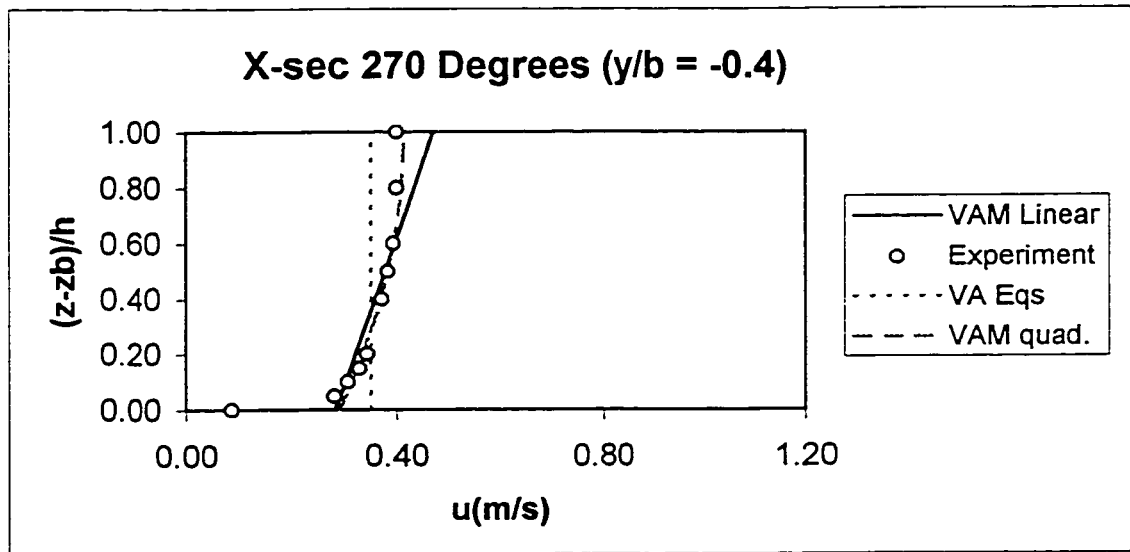


Figure 4.77 The comparison of longitudinal velocity profile for Steffler's (1984) run 1 at cross-section 270 degrees and $y/b = -0.4$

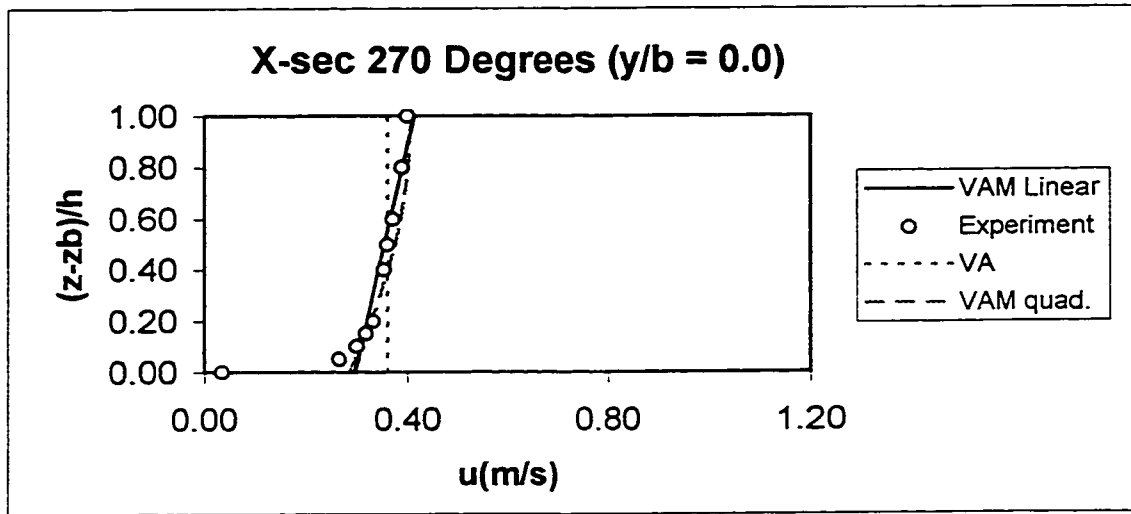


Figure 4.78 The comparison of longitudinal velocity profile for Steffler's (1984) run 1 at cross-section 270 degrees and $y/b = 0$

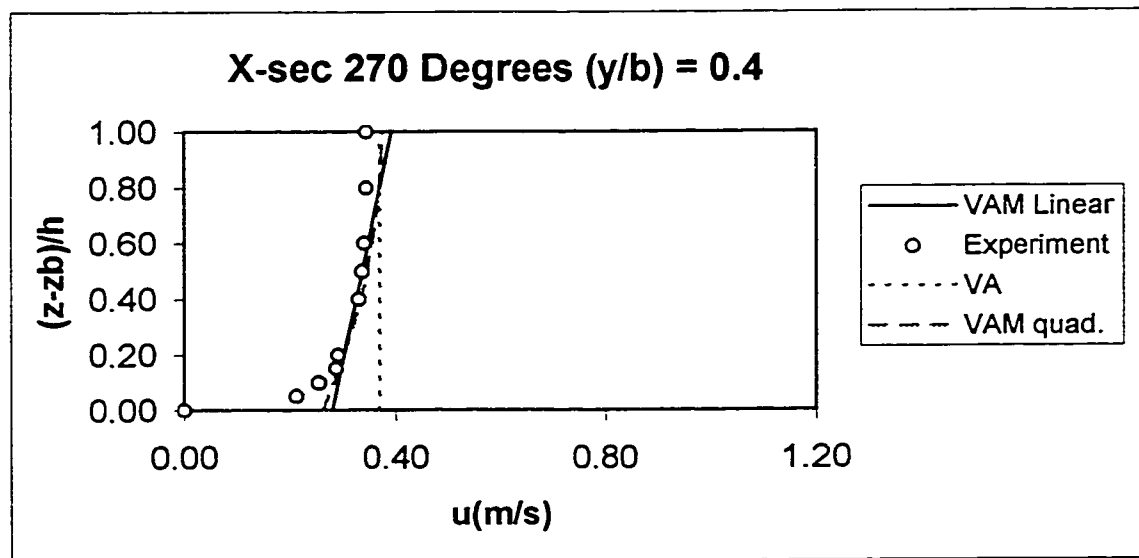


Figure 4.79 The comparison of longitudinal velocity profile for Steffler's (1984) run 1 at cross-section 270 degrees and $y/b = 0.4$

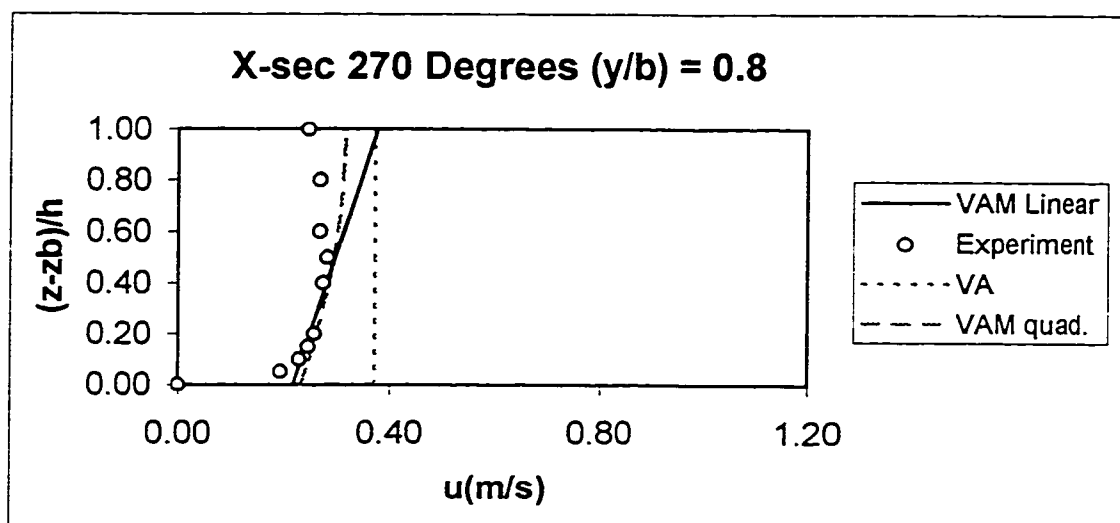


Figure 4.80 The comparison of longitudinal velocity profile for Steffler's (1984) run 1 at cross-section 270 degrees and $y/b = 0.8$

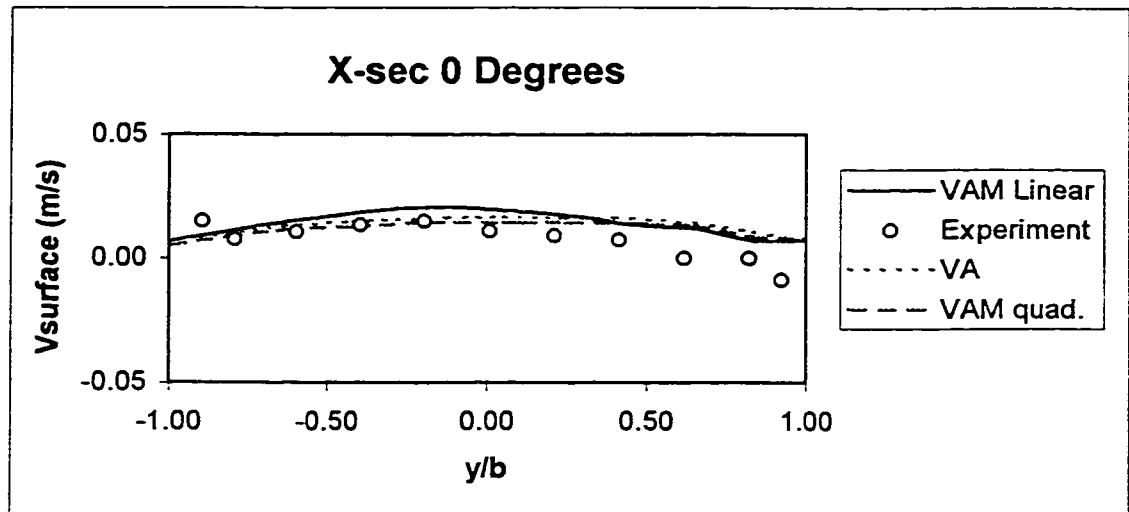


Figure 4.81 The comparison of transverse surface velocity distribution across the flume for Steffler's (1984) run 1 at cross-section 0 degrees

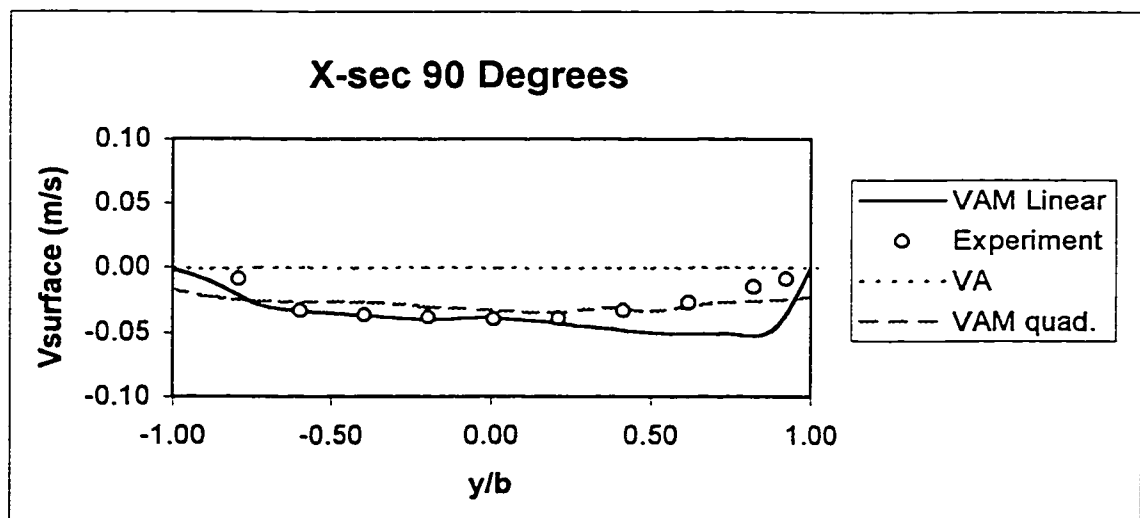


Figure 4.82 The comparison of transverse surface velocity distribution across the flume for Steffler's (1984) run 1 at cross-section 90 degrees

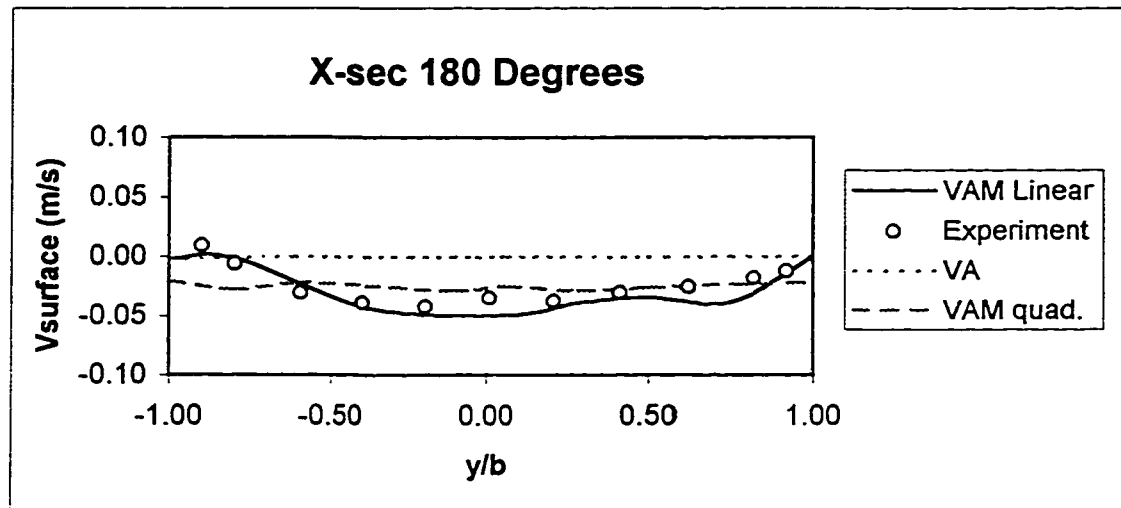


Figure 4.83 The comparison of transverse surface velocity distribution across the flume for Steffler's (1984) run 1 at cross-section 180 degrees

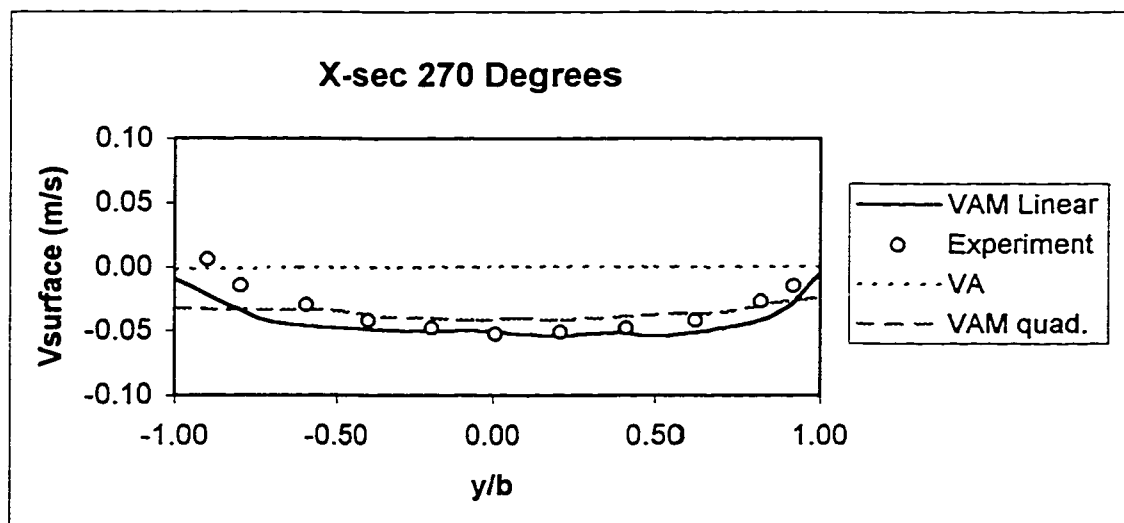


Figure 4.84 The comparison of transverse surface velocity distribution across the flume for Steffler's (1984) run 1 at cross-section 270 degrees

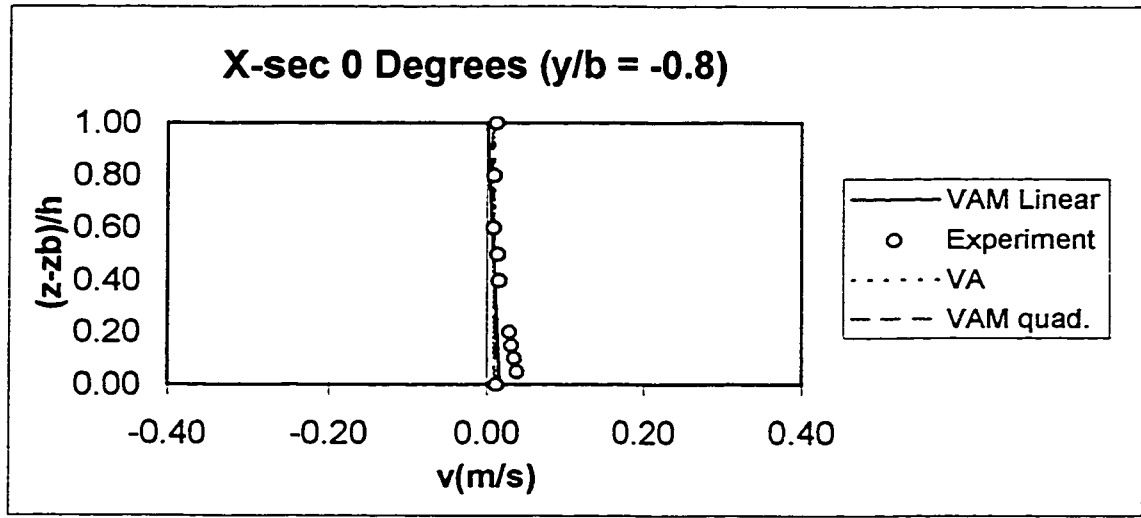


Figure 4.85 The comparison of transverse velocity profile for Steffler's (1984) run 1 at cross-section 0 degrees and $y/b = -0.8$

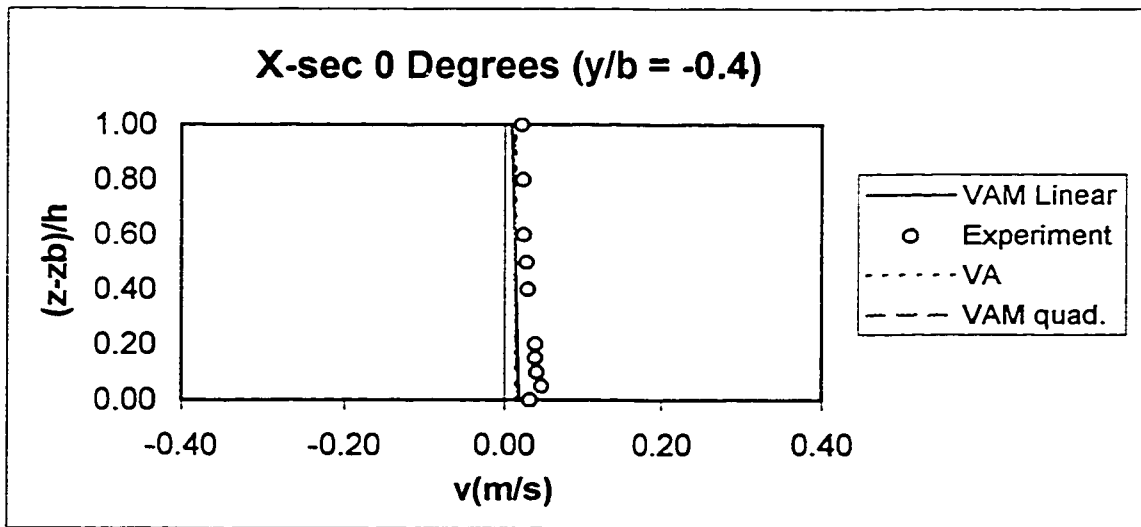


Figure 4.86 The comparison of transverse velocity profile for Steffler's (1984) run 1 at cross-section 0 degrees and $y/b = -0.4$

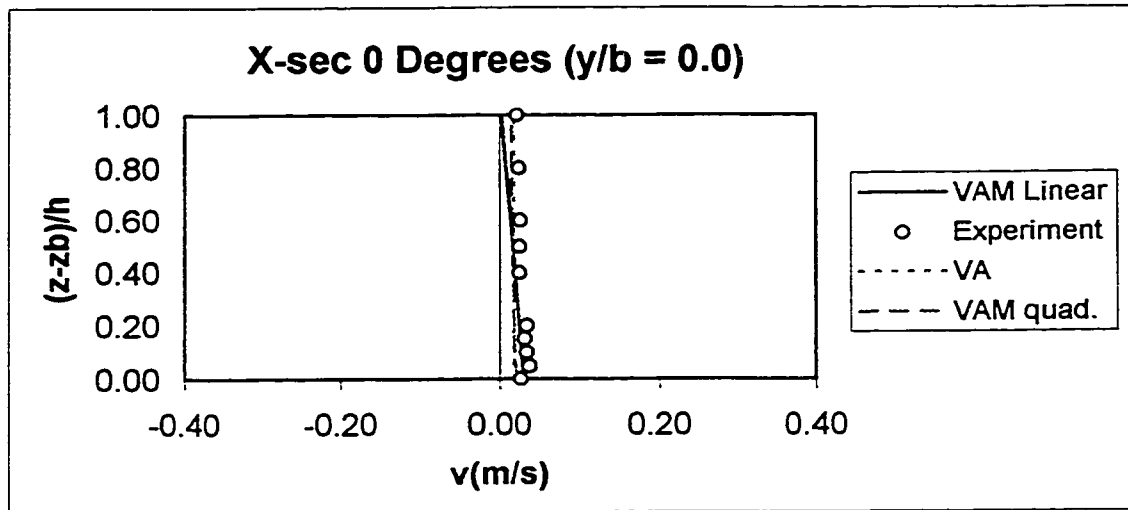


Figure 4.87 The comparison of transverse velocity profile for Steffler's (1984) run 1 at cross-section 0 degrees and $y/b = 0$

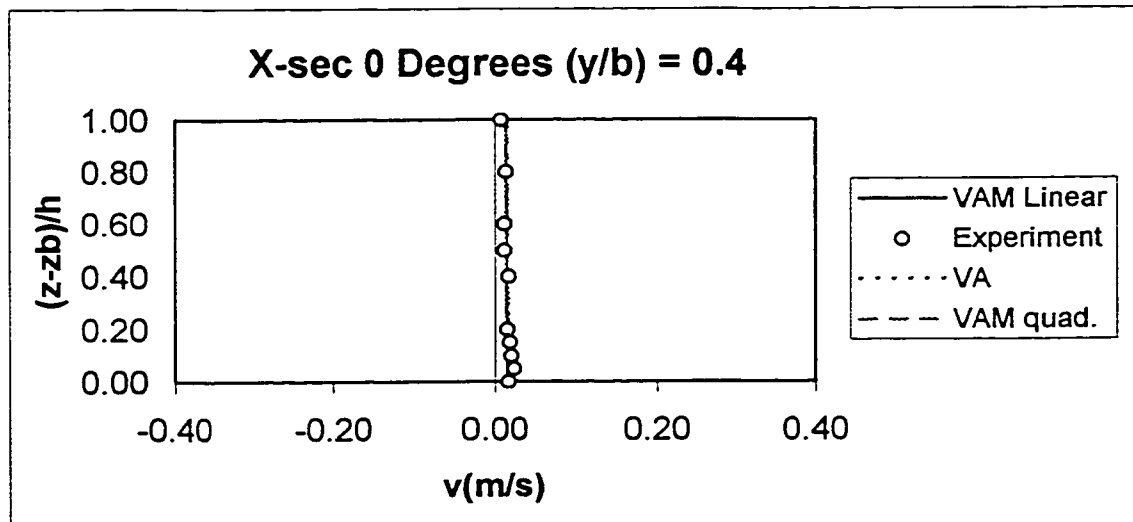


Figure 4.88 The comparison of transverse velocity profile for Steffler's (1984) run 1 at cross-section 0 degrees and $y/b = 0.4$

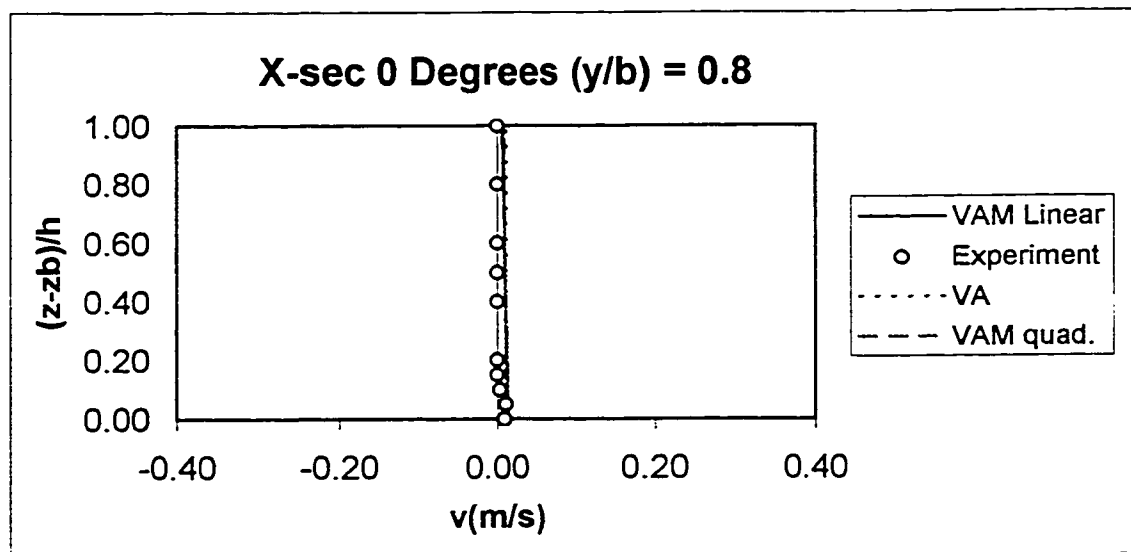


Figure 4.89 The comparison of transverse velocity profile for Steffler's (1984) run 1 at cross-section 0 degrees and $y/b = 0.8$

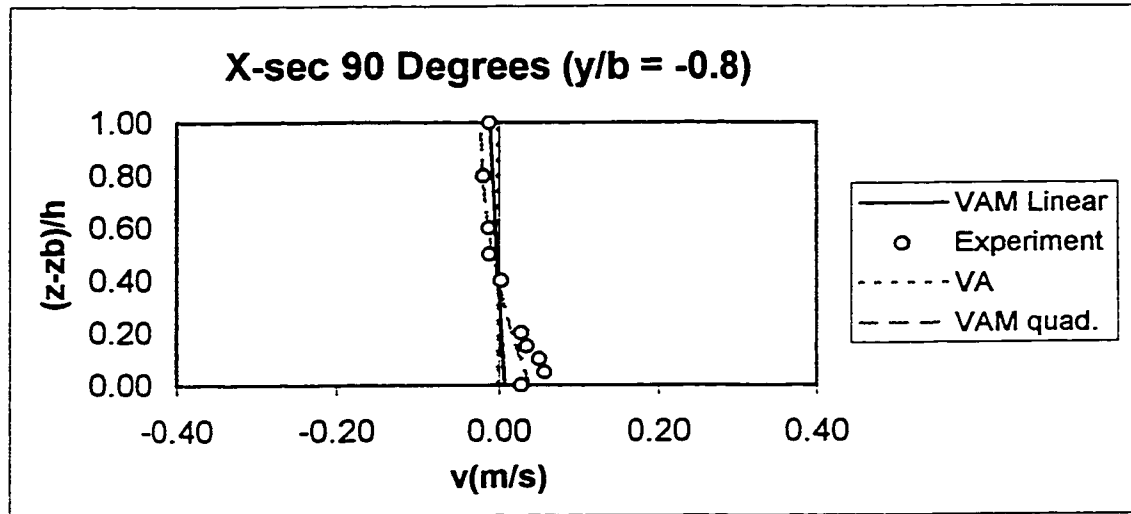


Figure 4.90 The comparison of transverse velocity profile for Steffler's (1984) run 1 at cross-section 90 degrees and $y/b = -0.8$

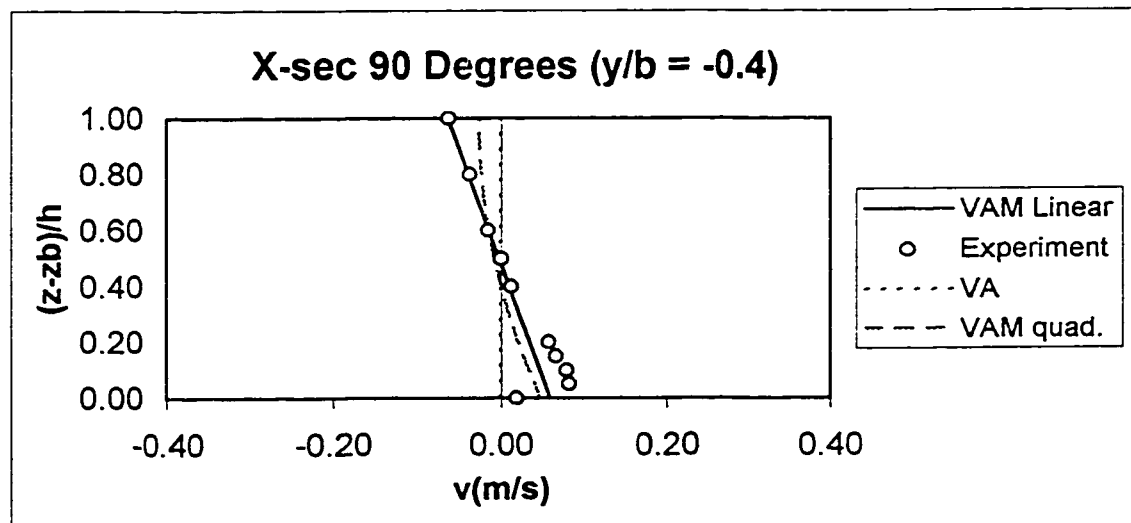


Figure 4.91 The comparison of transverse velocity profile for Steffler's (1984) run 1 at cross-section 90 degrees and $y/b = -0.4$

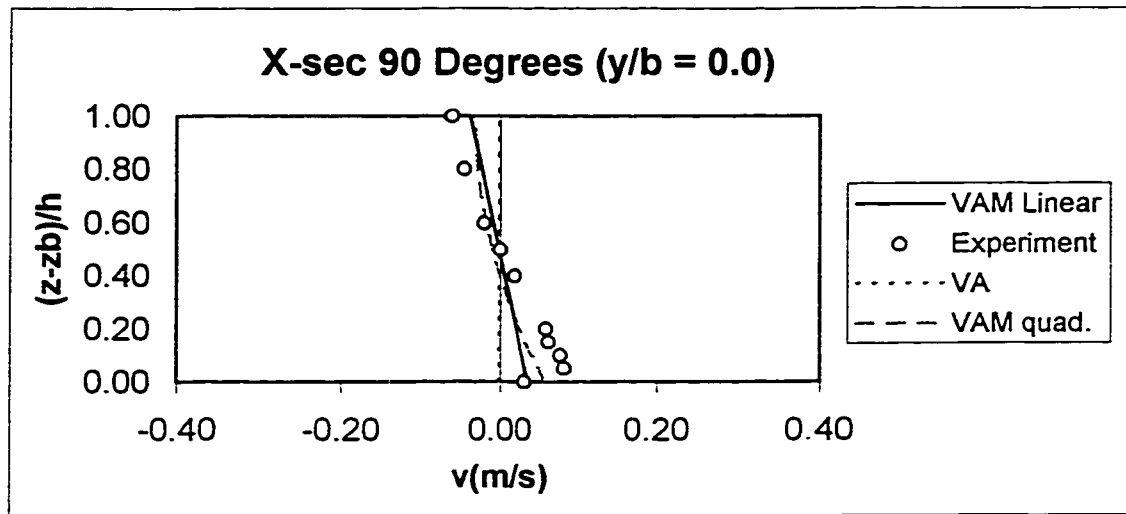


Figure 4.92 The comparison of transverse velocity profile for Steffler's (1984) run 1 at cross-section 90 degrees and $y/b = 0$

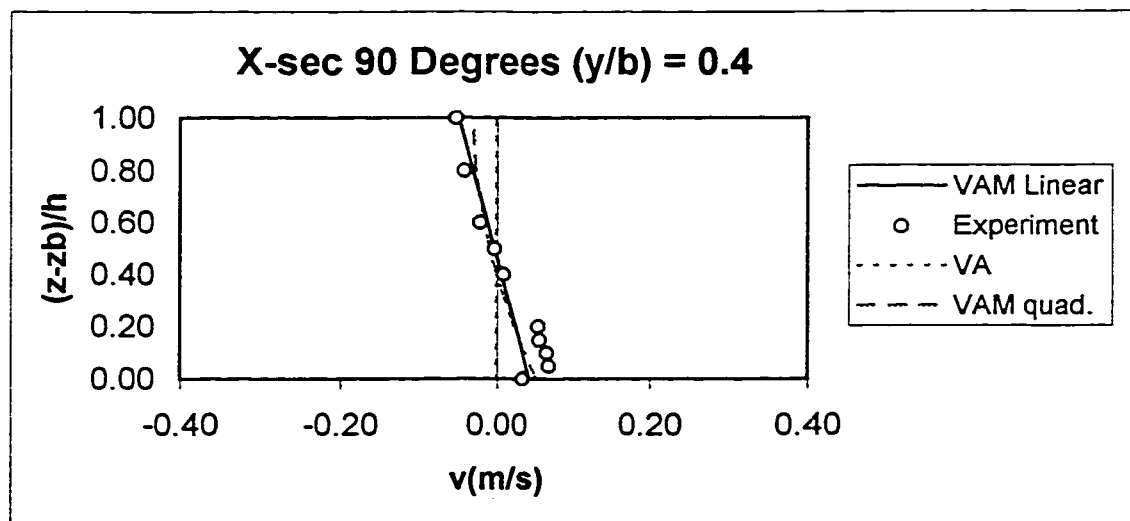


Figure 4.93 The comparison of transverse velocity profile for Steffler's (1984) run 1 at cross-section 90 degrees and $y/b = 0.4$

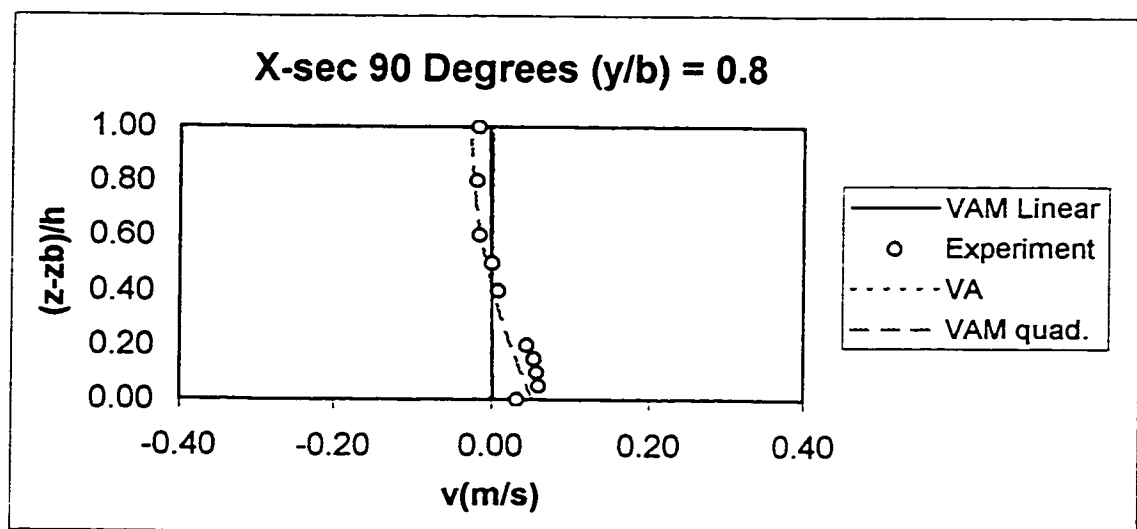


Figure 4.94 The comparison of transverse velocity profile for Steffler's (1984) run 1 at cross-section 90 degrees and $y/b = 0.8$

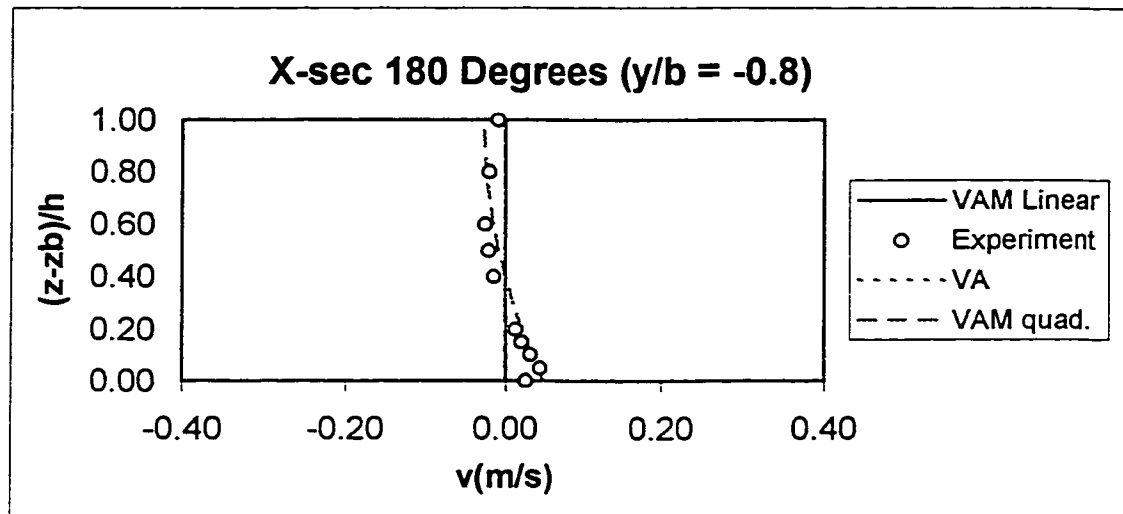


Figure 4.95 The comparison of transverse velocity profile for Steffler's (1984) run 1 at cross-section 180 degrees and $y/b = -0.8$

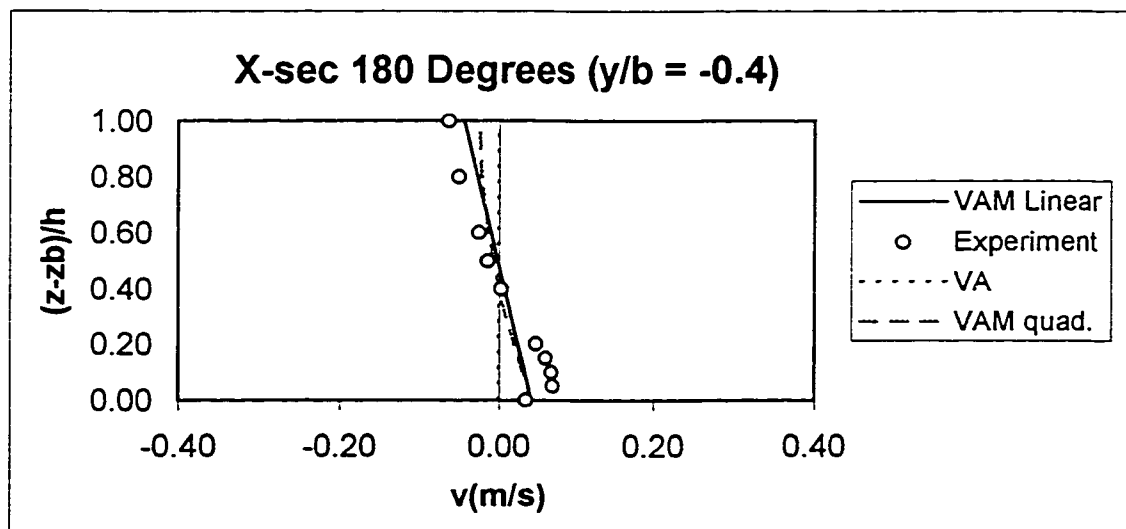


Figure 4.96 The comparison of transverse velocity profile for Steffler's (1984) run 1 at cross-section 180 degrees and $y/b = -0.4$

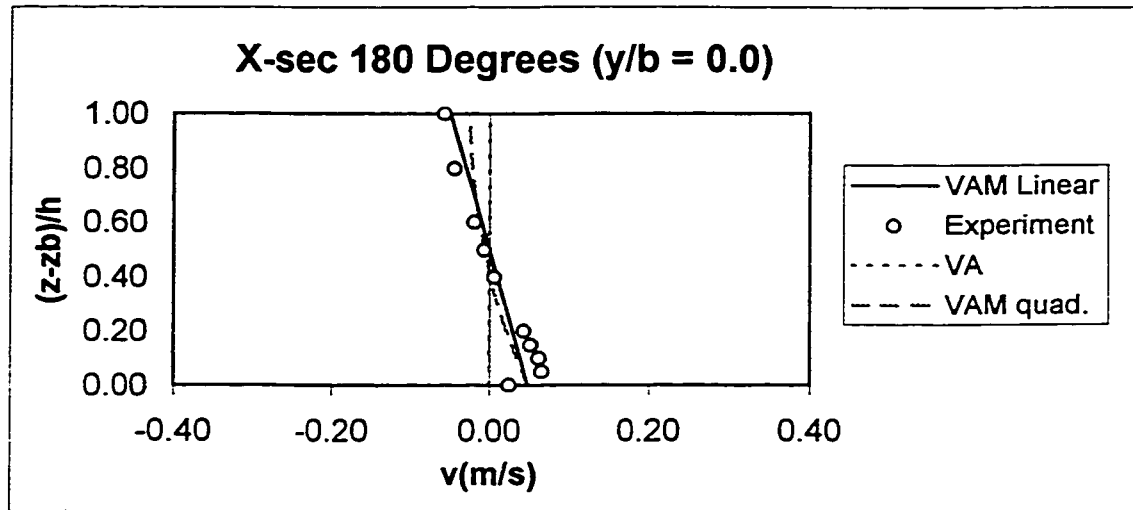


Figure 4.97 The comparison of transverse velocity profile for Steffler's (1984) run 1 at cross-section 180 degrees and $y/b = 0$

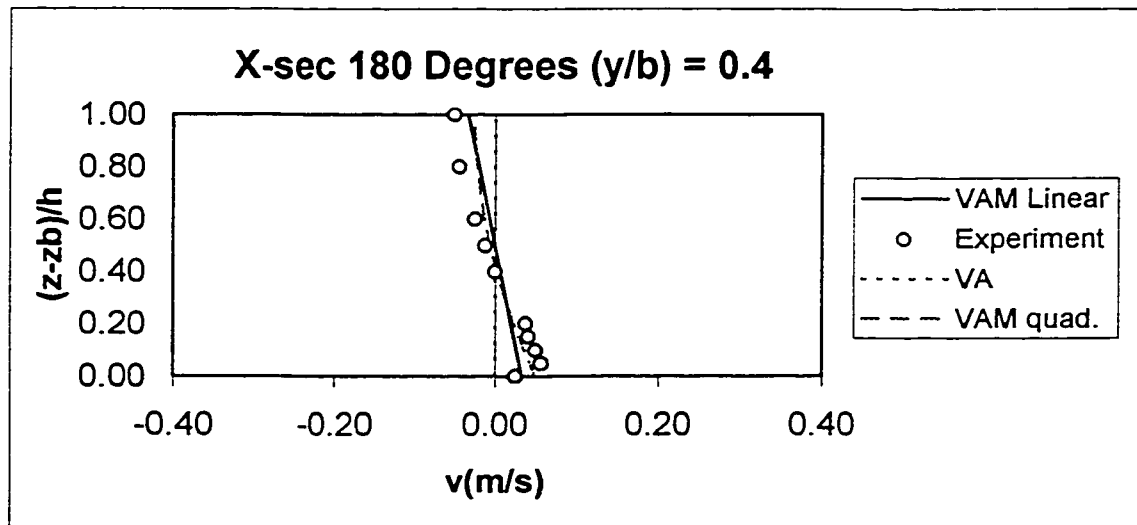


Figure 4.98 The comparison of transverse velocity profile for Steffler's (1984) run 1 at cross-section 180 degrees and $y/b = 0.4$

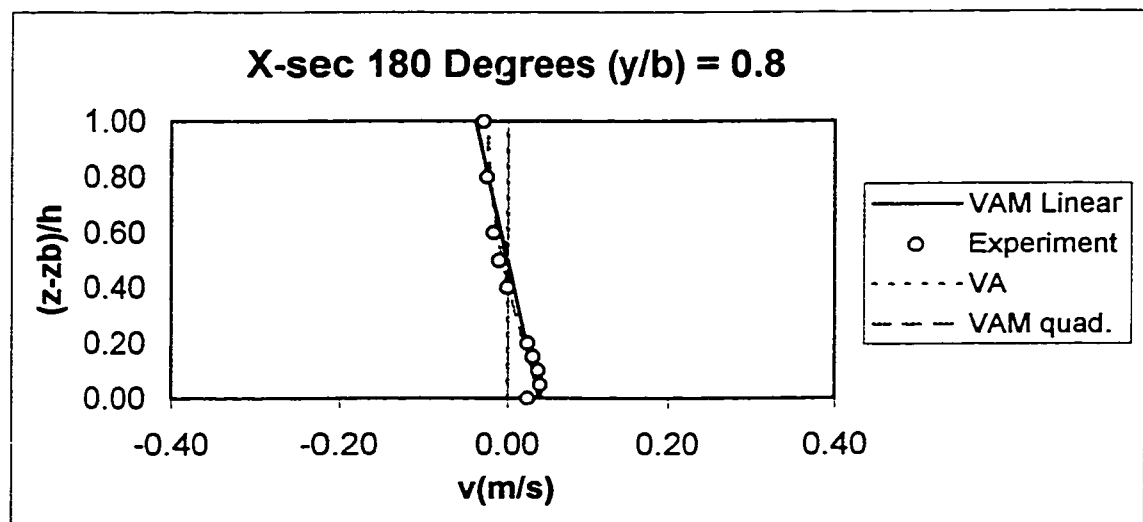


Figure 4.99 The comparison of transverse velocity profile for Steffler's (1984) run 1 at cross-section 180 degrees and $y/b = 0.8$

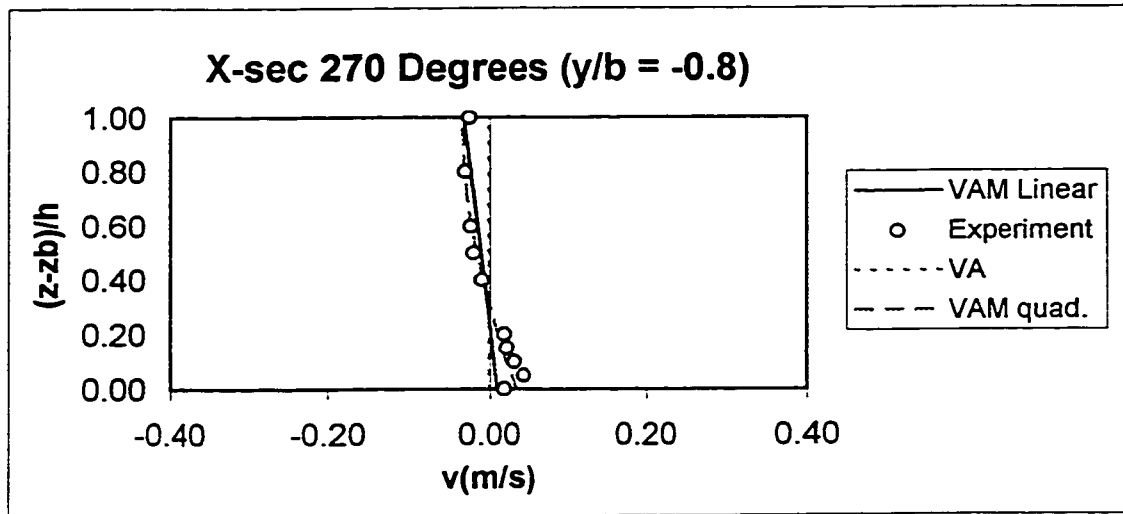


Figure 4.100 The comparison of transverse velocity profile for Steffler's (1984) run 1 at cross-section 270 degrees and $y/b = -0.8$

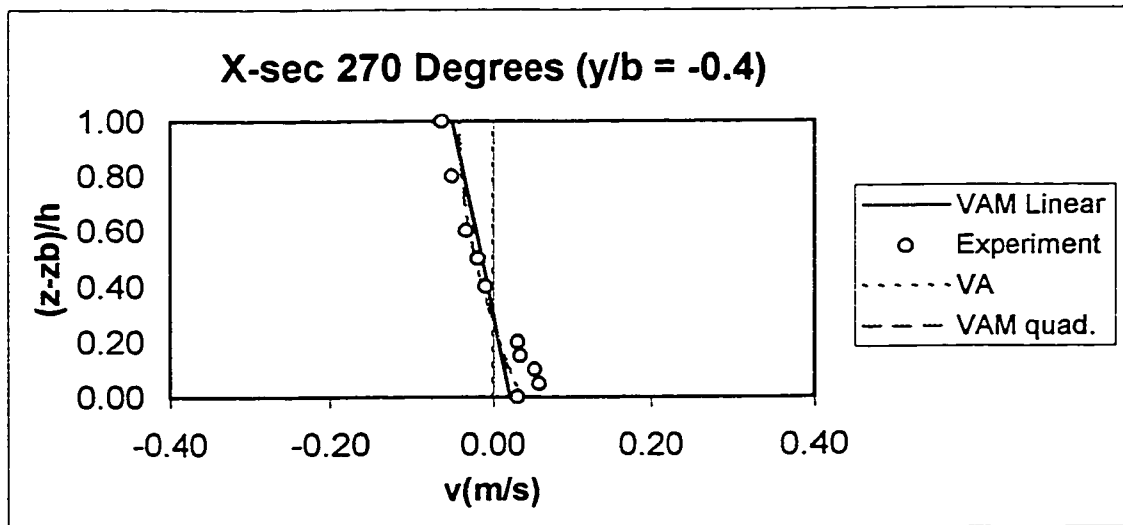


Figure 4.101 The comparison of transverse velocity profile for Steffler's (1984) run 1 at cross-section 270 degrees and $y/b = -0.4$

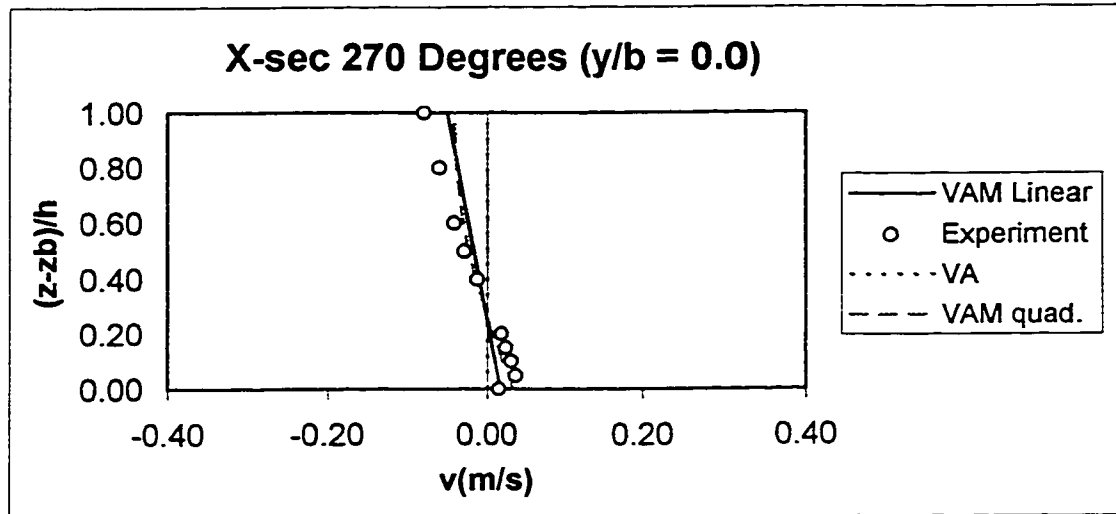


Figure 4.102 The comparison of transverse velocity profile for Steffler's (1984) run 1 at cross-section 270 degrees and $y/b = 0$

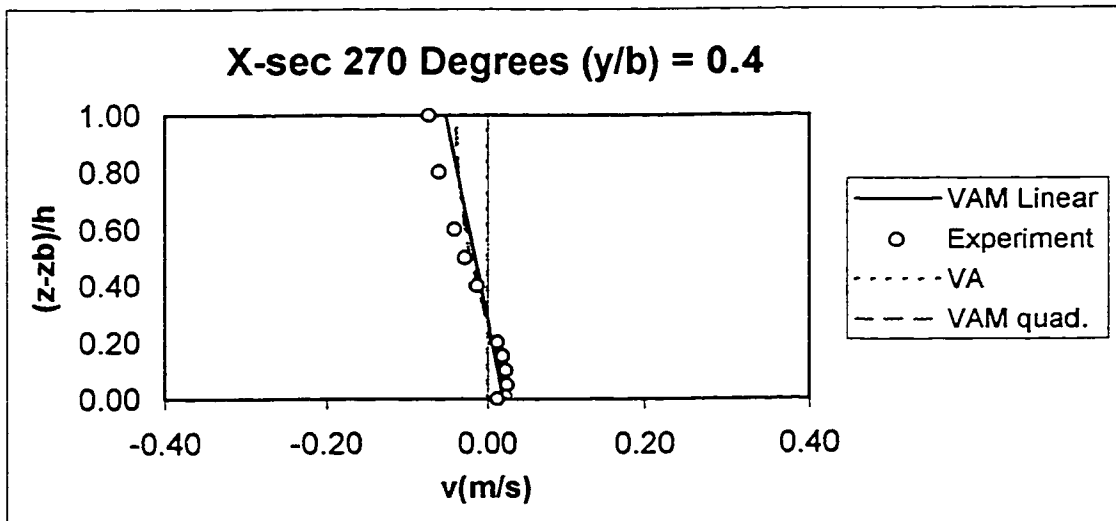


Figure 4.103 The comparison of transverse velocity profile for Steffler's (1984) run 1 at cross-section 270 degrees and $y/b = 0.4$

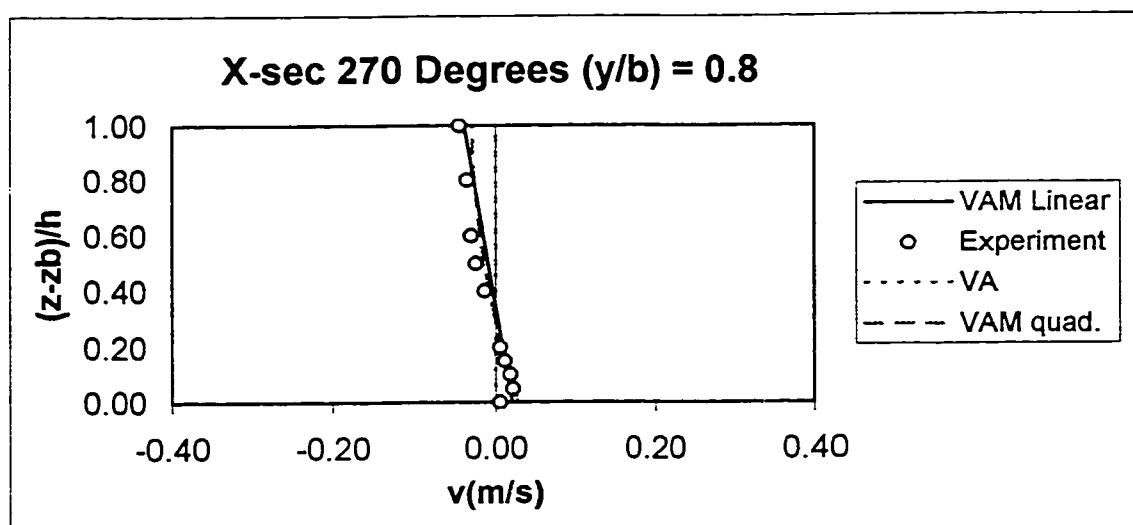


Figure 4.104 The comparison of transverse velocity profile for Steffler's (1984) run 1 at cross-section 270 degrees and $y/b = 0.8$

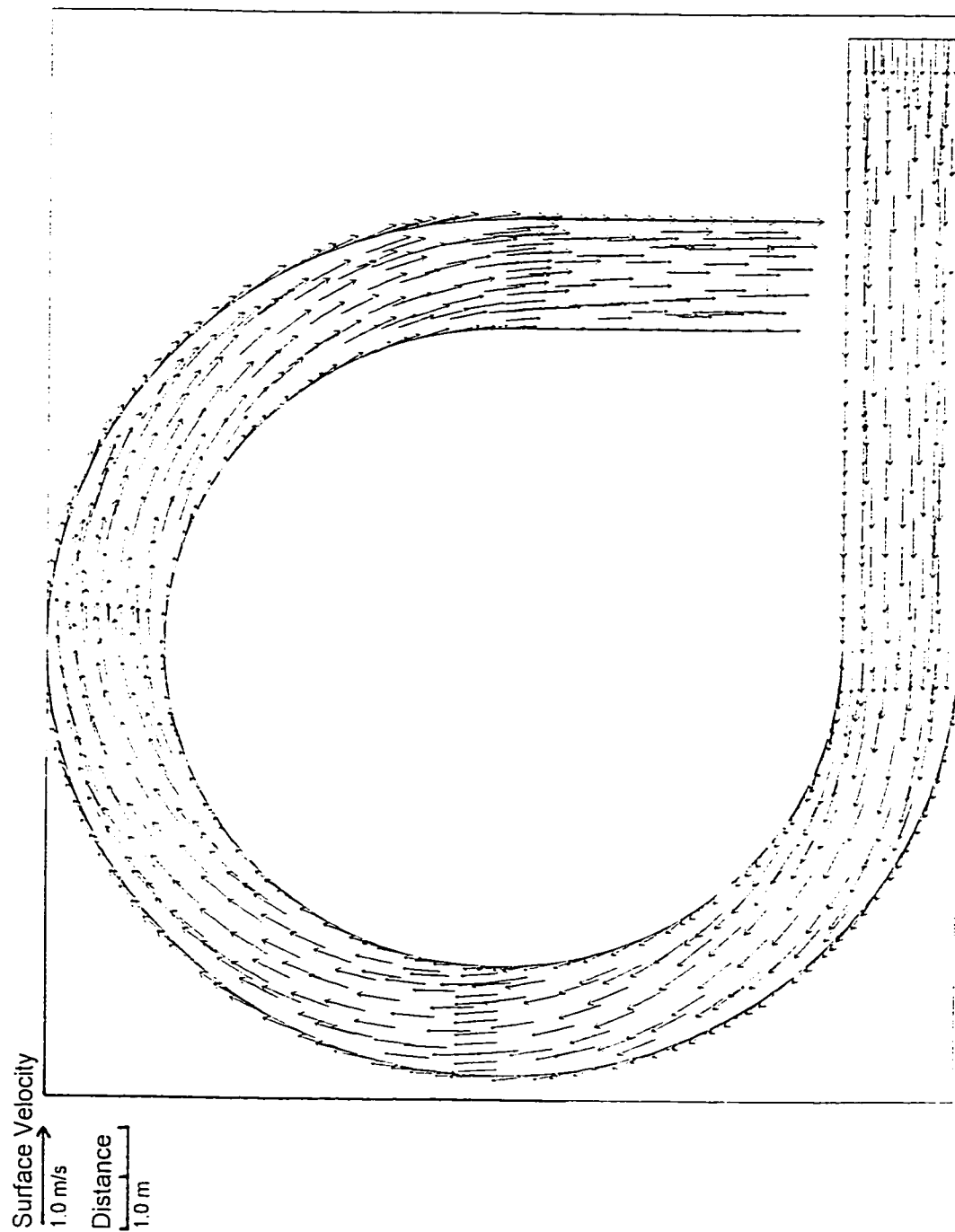


Figure 4.105 Numerical prediction of surface velocity distribution for Steffler's (1984) experiment (VAM model)

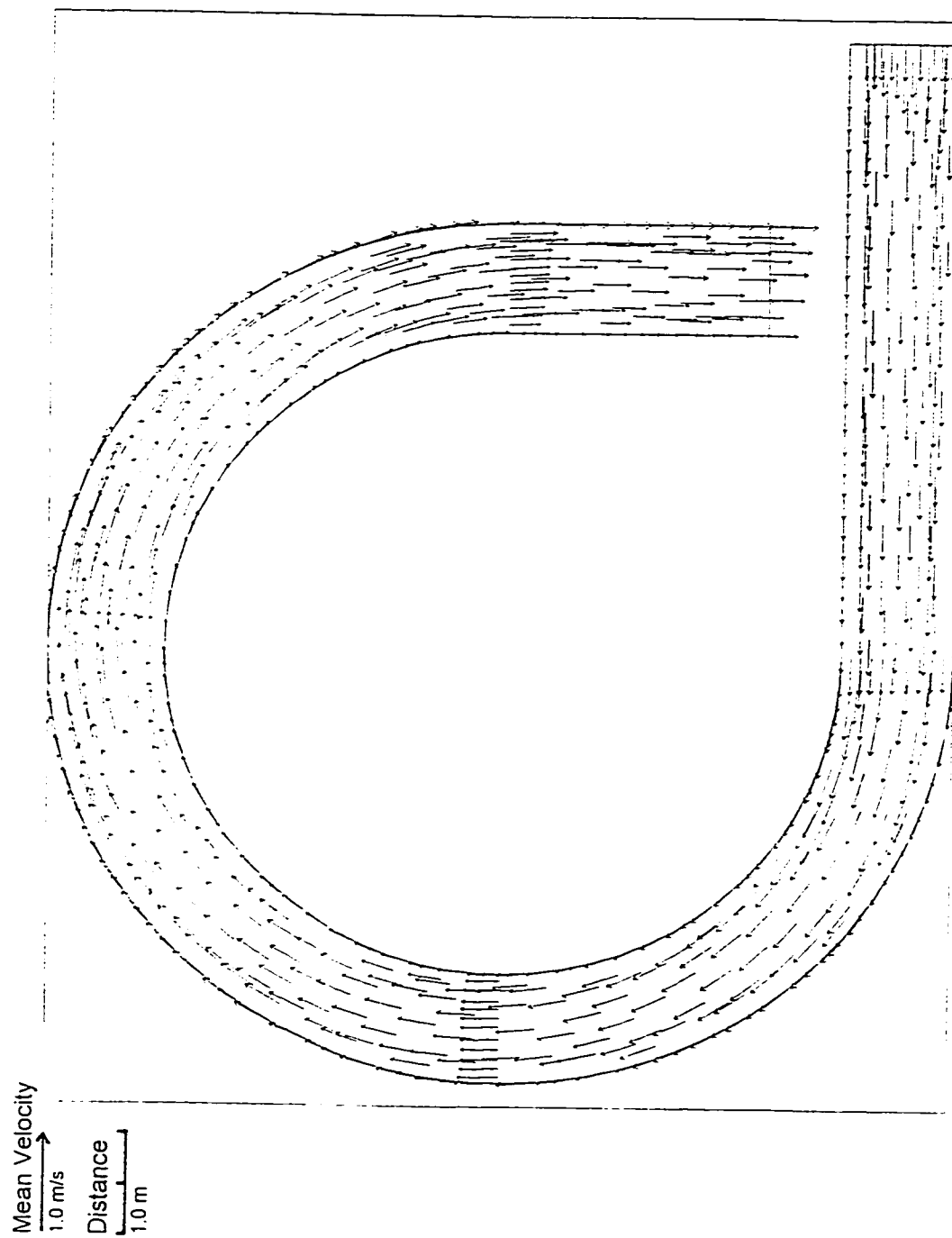


Figure 4.106 Numerical prediction of mean velocity distribution for Steffler's (1984) experiment (VAM model)

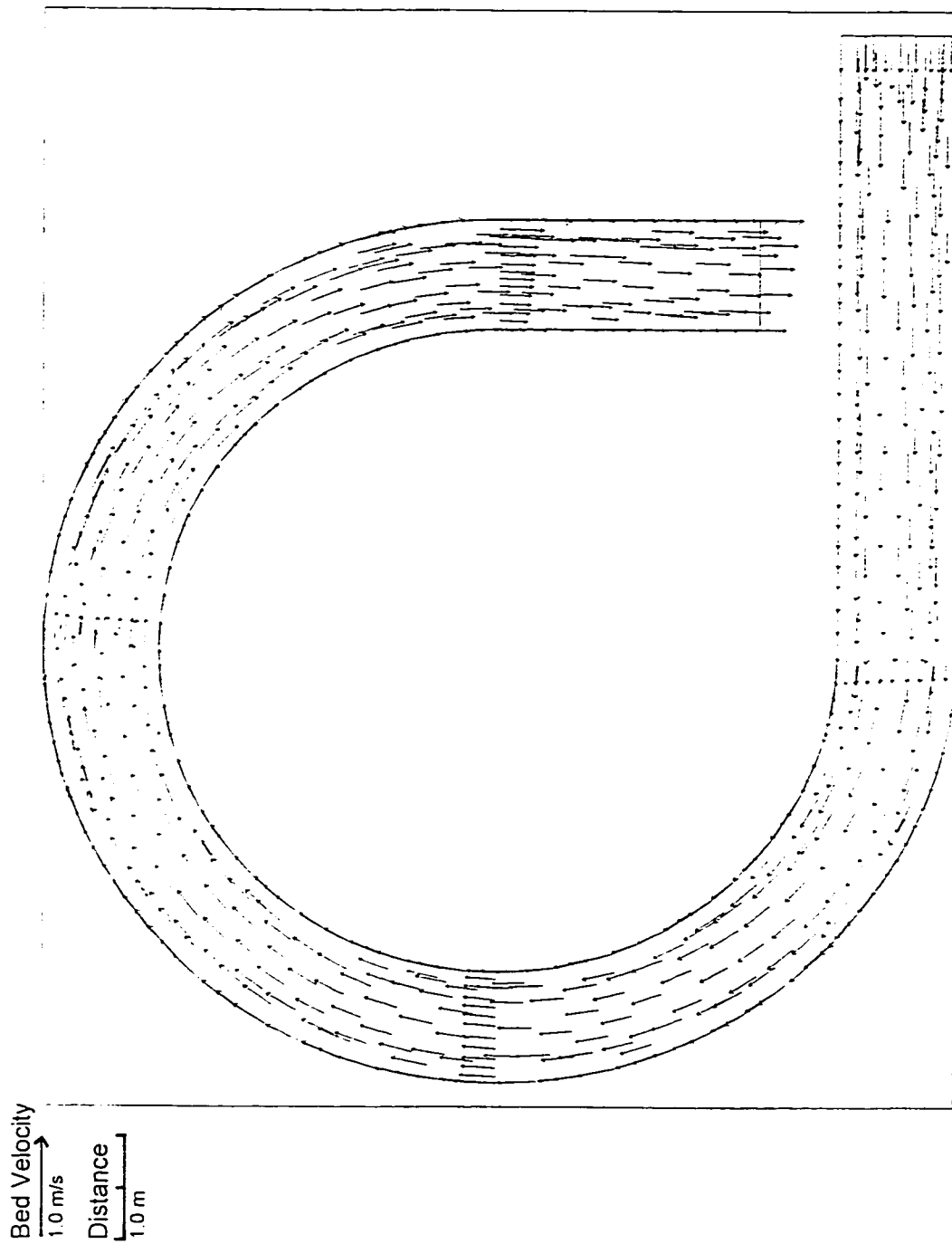


Figure 4.107 Numerical prediction of bed velocity distribution for Steffler's (1984) experiment (VAM model)

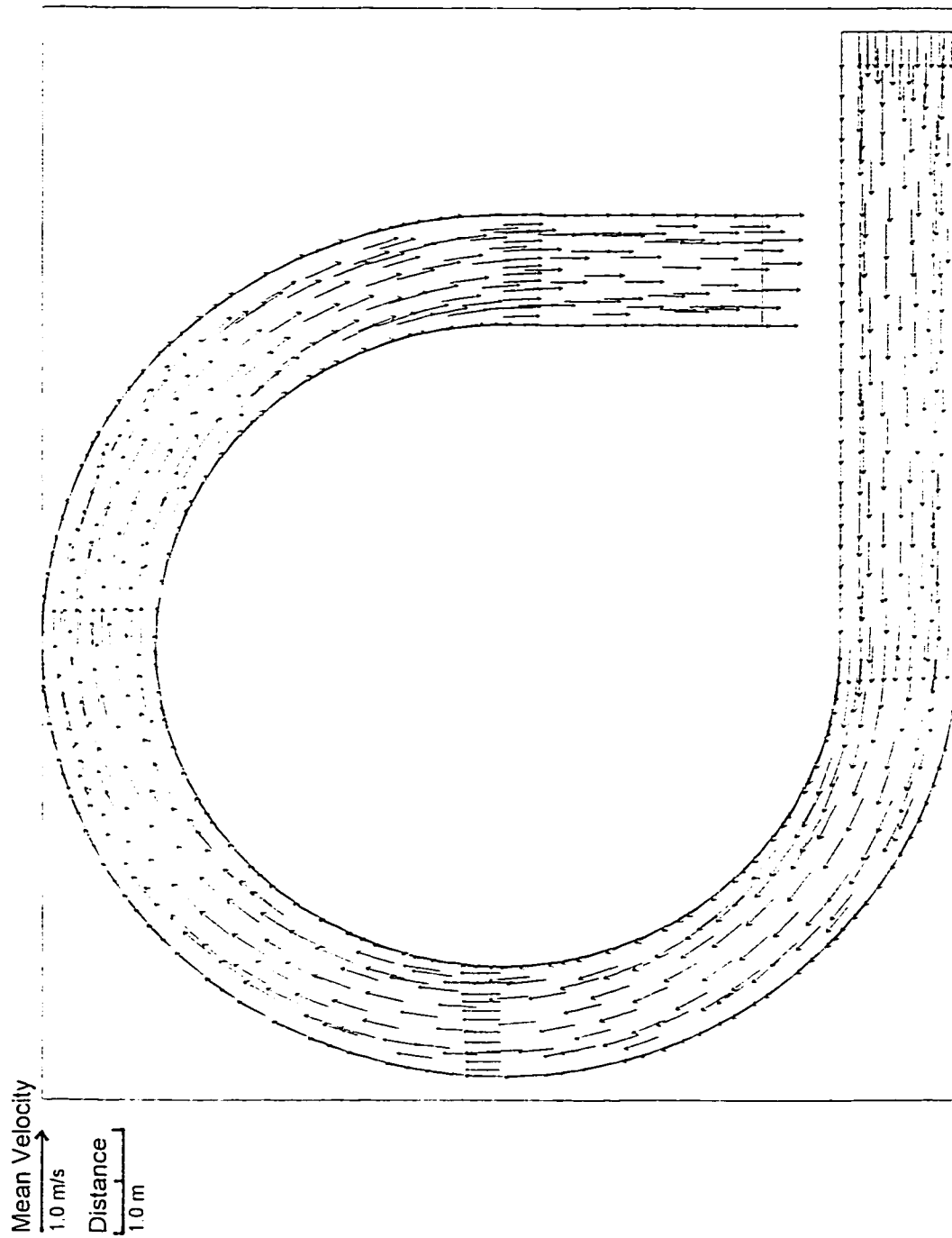


Figure 4.108 Numerical prediction of mean velocity distribution for Steffler's (1984) experiment (VA model)

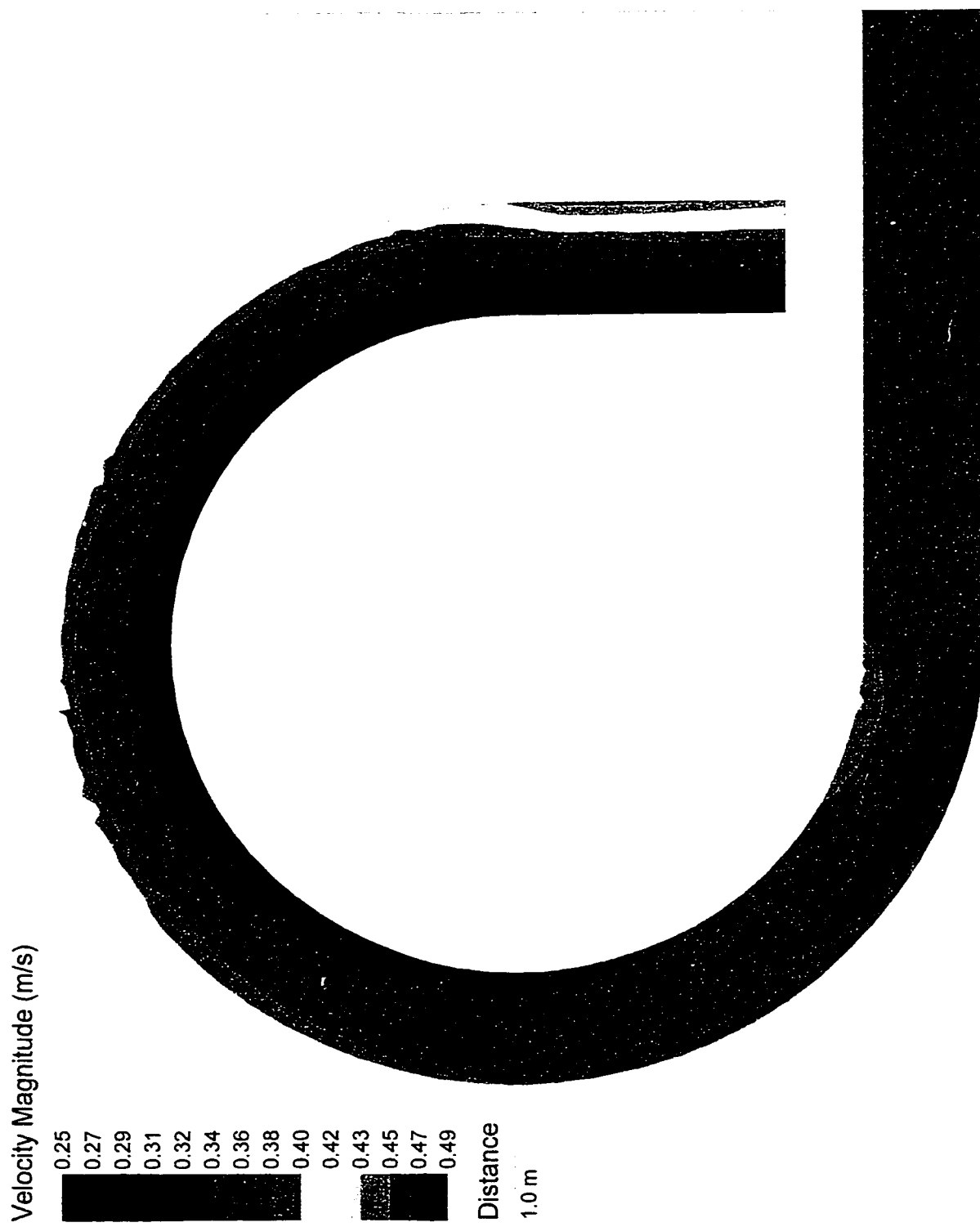


Figure 4.109 Numerical prediction of mean velocity contours for Steffler's (1984) experiment (VAM model)

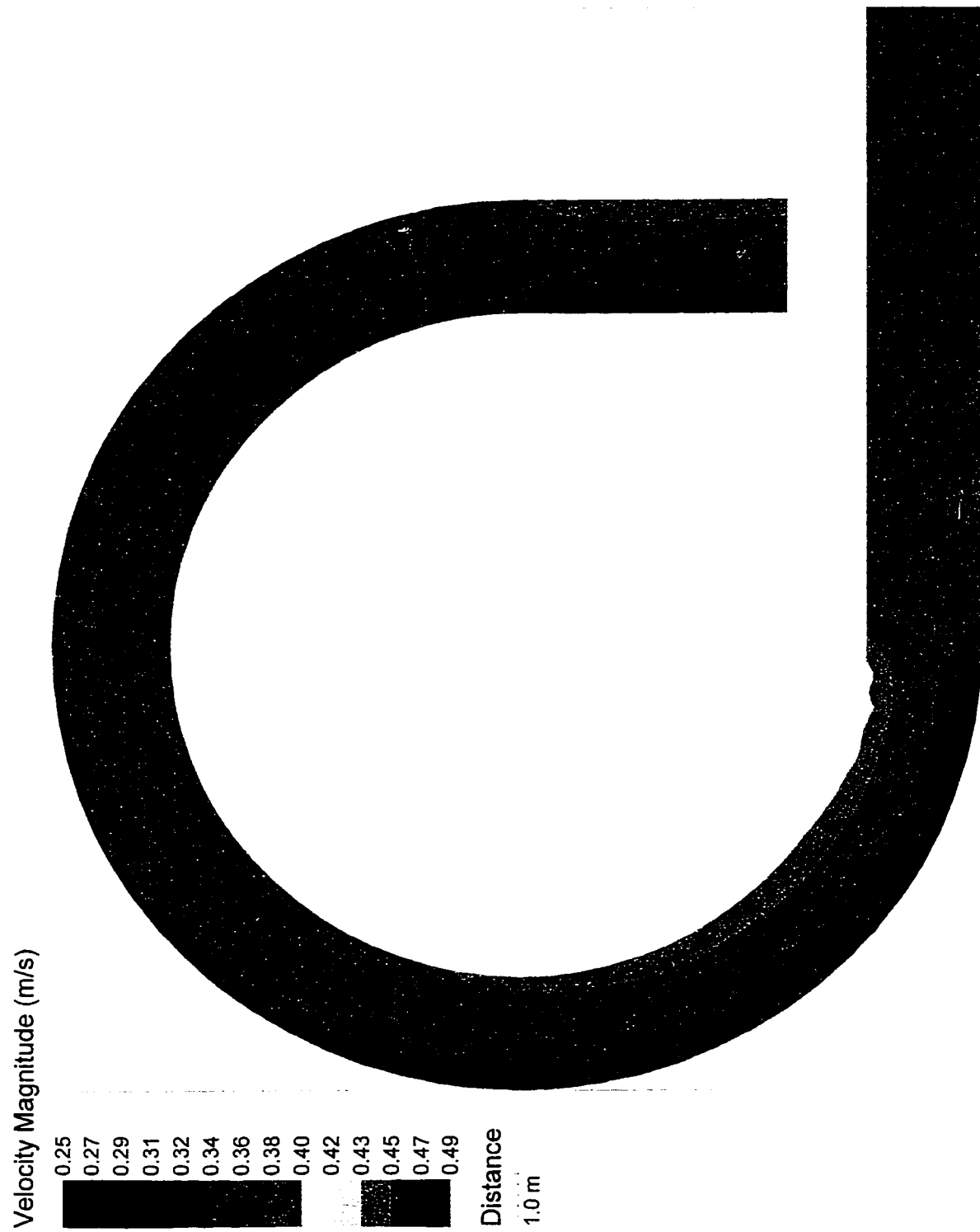


Figure 4.110 Numerical prediction of mean velocity contours for Steffler's (1984) experiment (VA model)

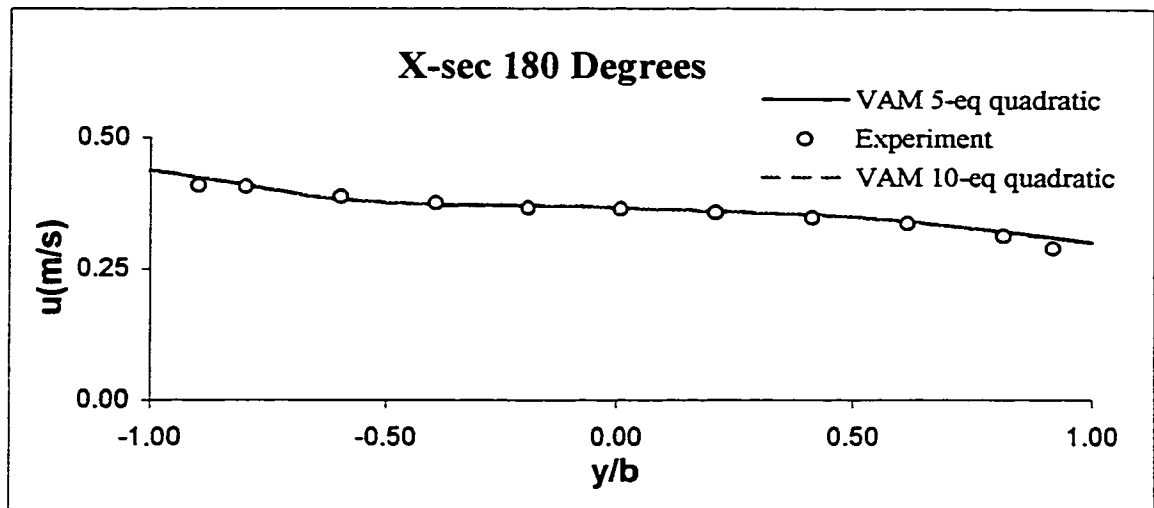


Figure 4.111 The comparison of applying VAM 5- against 10-equation models for longitudinal velocity distribution across the flume for Steffler's (1984) run 1 at cross-section 180 degrees

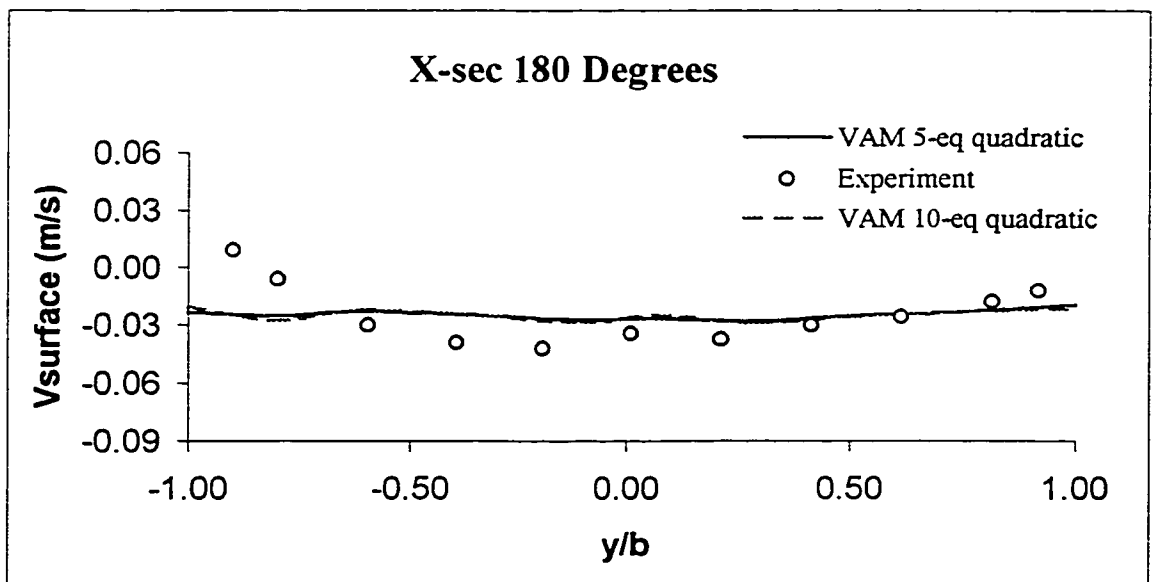


Figure 4.112 The comparison of applying VAM 5- against 10-equation models for transverse velocity distribution across the flume for Steffler's (1984) run 1 at cross-section 180 degrees

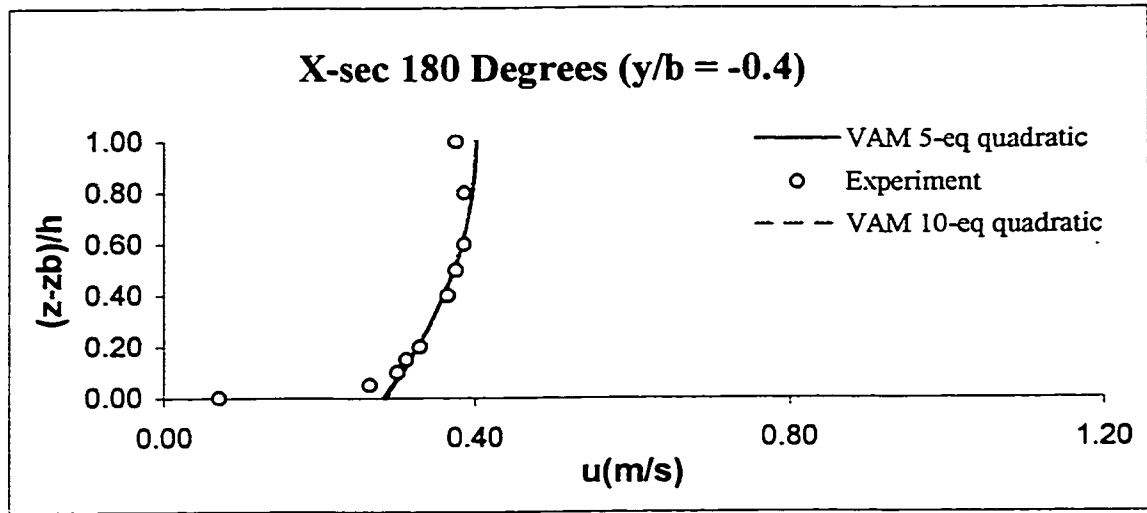


Figure 4.113 The comparison of applying VAM 5- against 10-equation models for longitudinal velocity profile for Steffler's (1984) run 1 at cross-section 180 degrees and $y/b = -0.4$

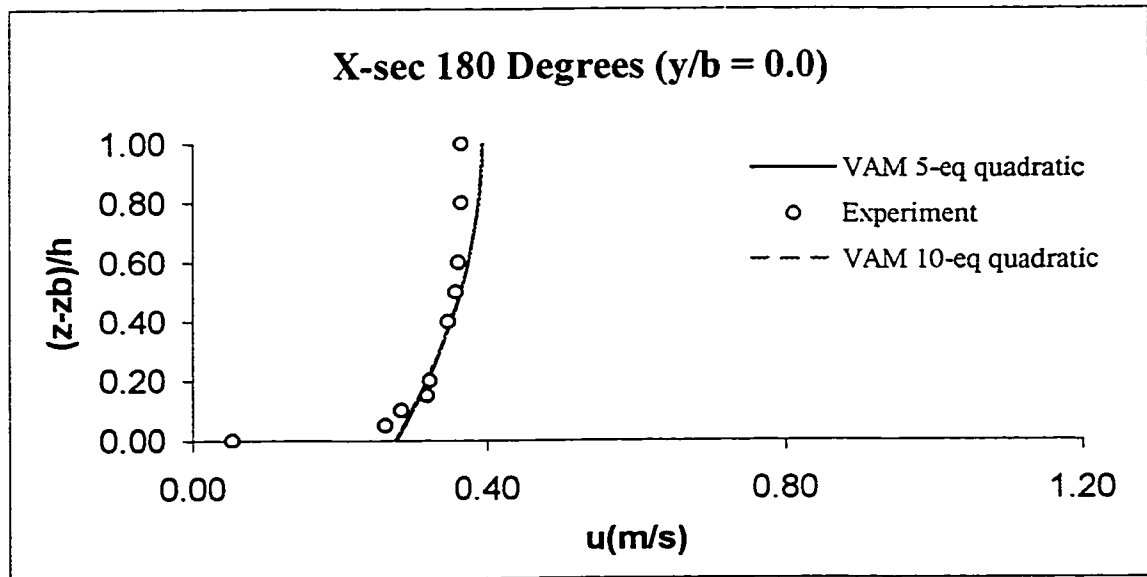


Figure 4.114 The comparison of applying VAM 5- against 10-equation models for longitudinal velocity profile for Steffler's (1984) run 1 at cross-section 180 degrees and $y/b = 0$

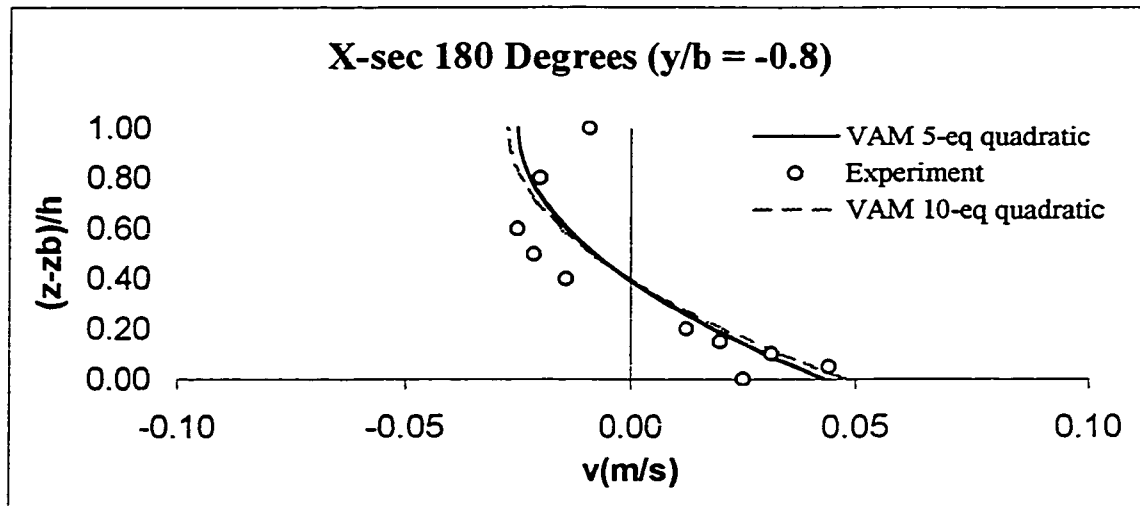


Figure 4.115 The comparison of applying VAM 5- against 10-equation models for transverse velocity profile for Steffler's (1984) run 1 at cross-section 180 degrees and $y/b = -0.8$

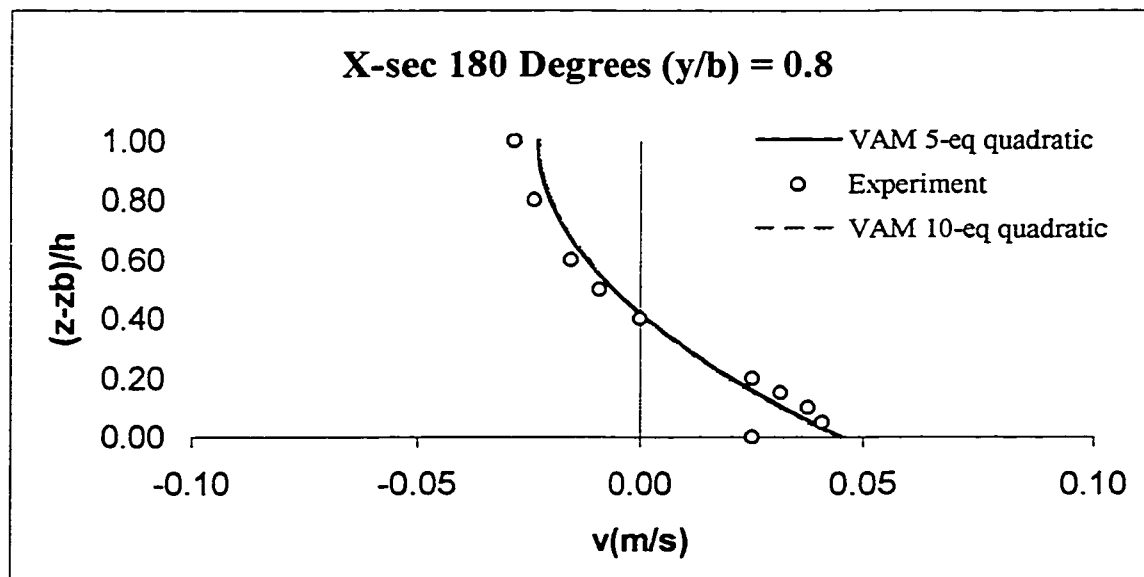


Figure 4.116 The comparison of applying VAM 5- against 10-equation models for transverse velocity profile for Steffler's (1984) run 1 at cross-section 180 degrees and $y/b = 0.8$

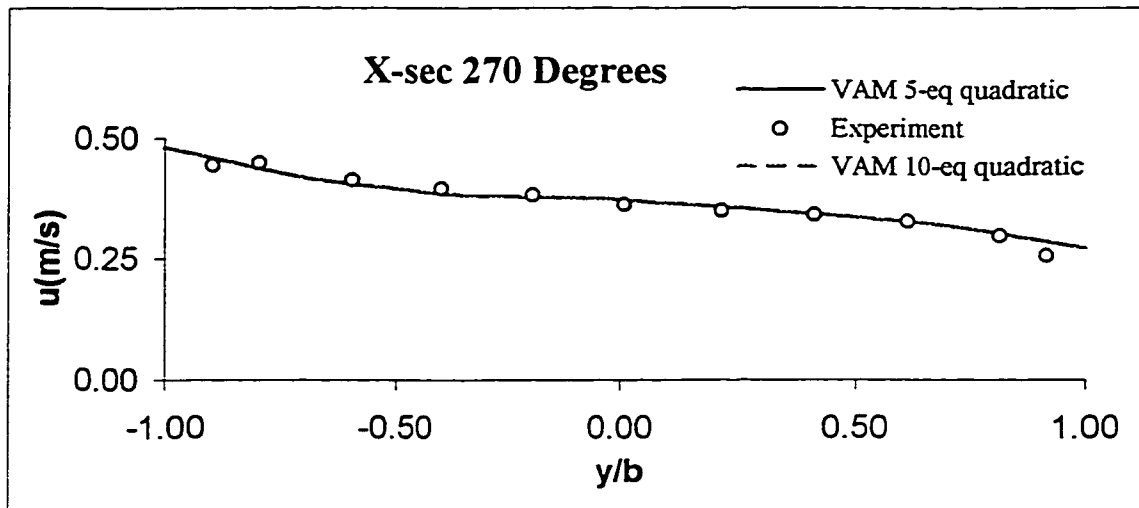


Figure 4.117 The comparison of applying VAM 5- against 10-equation models for longitudinal velocity distribution across the flume for Steffler's (1984) run 1 at cross-section 270 degrees

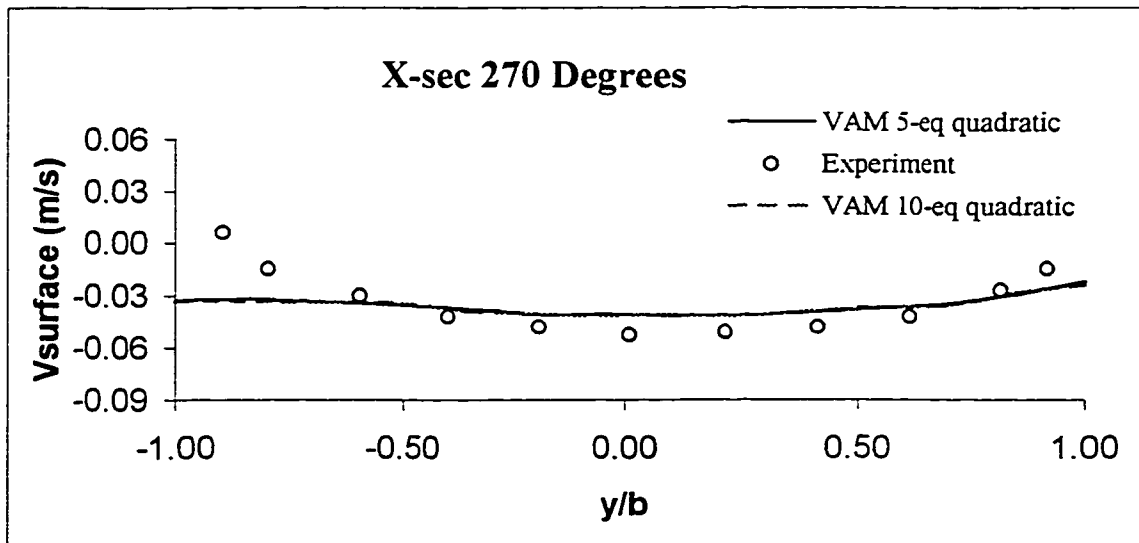


Figure 4.118 The comparison of applying VAM 5- against 10-equation models for transverse velocity distribution across the flume for Steffler's (1984) run 1 at cross-section 270 degrees

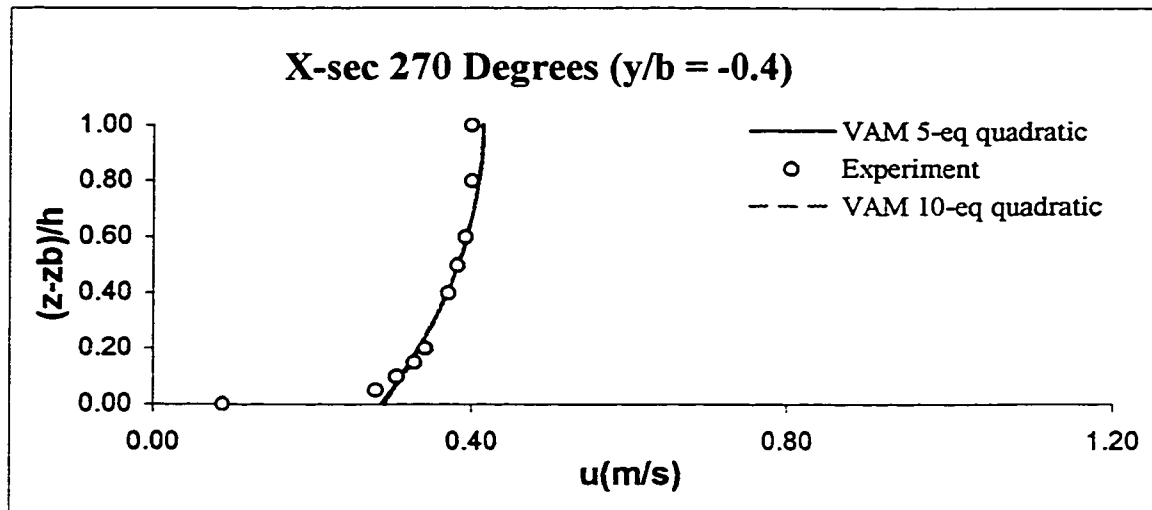


Figure 4.119 The comparison of applying VAM 5- against 10-equation models for longitudinal velocity profile for Steffler's (1984) run 1 at cross-section 270 degrees and $y/b = -0.4$

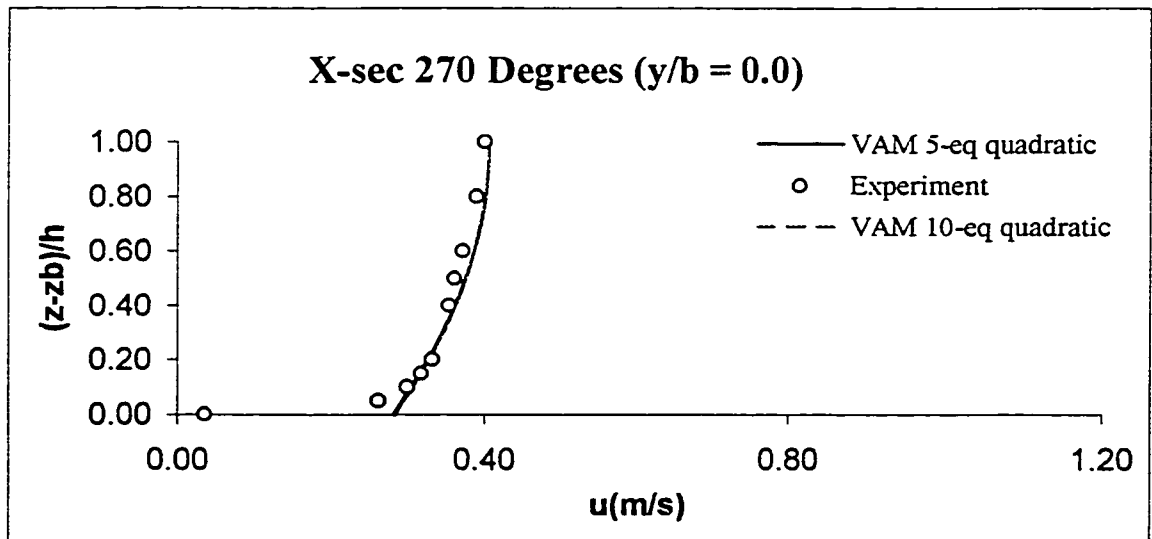


Figure 4.120 The comparison of applying VAM 5- against 10-equation models for longitudinal velocity profile for Steffler's (1984) run 1 at cross-section 270 degrees and $y/b = 0$

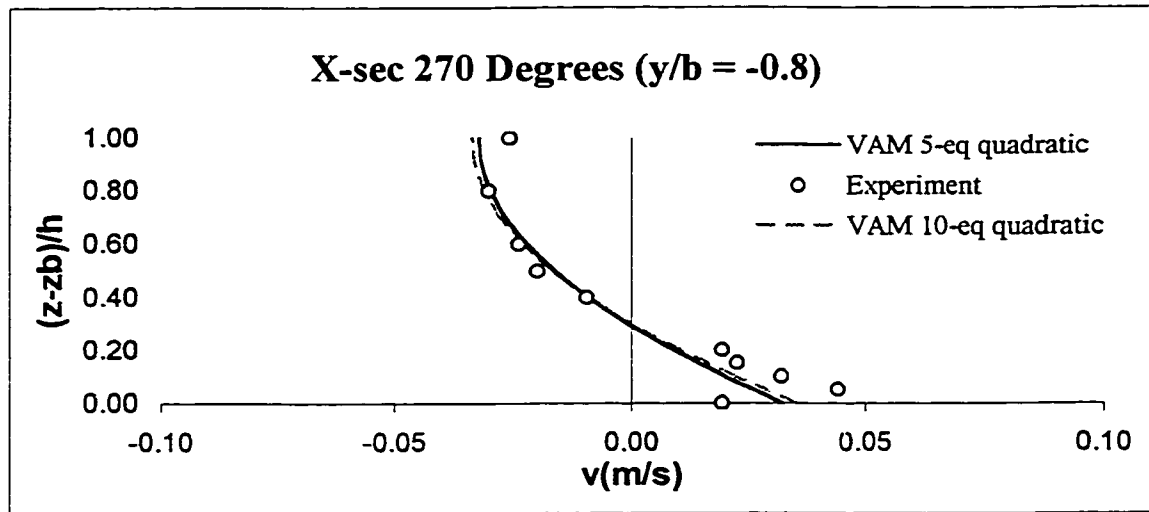


Figure 4.121 The comparison of applying VAM 5- against 10-equation models for transverse velocity profile for Steffler's (1984) run 1 at cross-section 270 degrees and $y/b = -0.8$

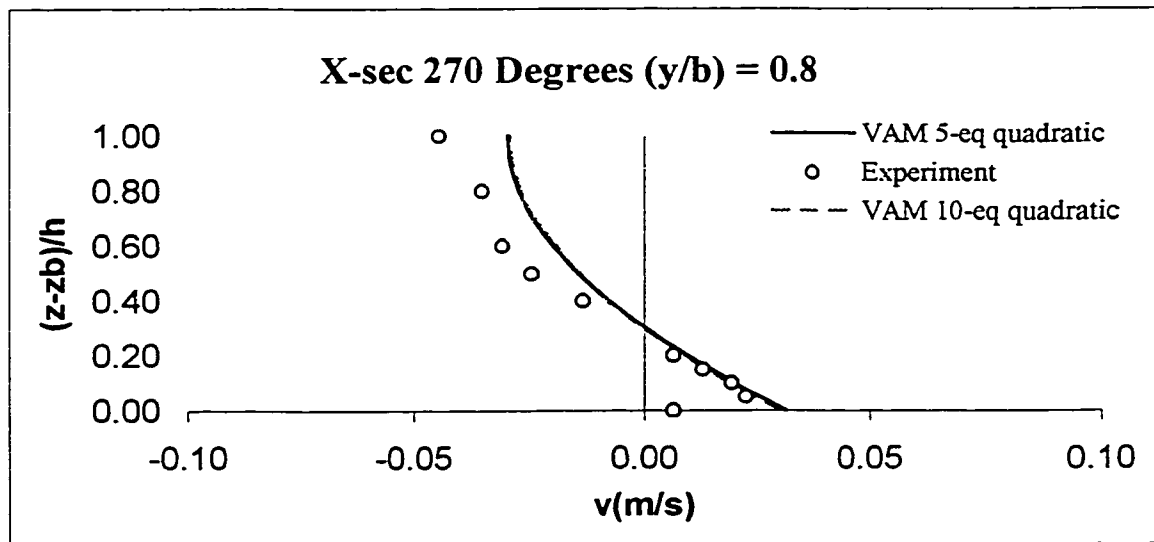


Figure 4.122 The comparison of applying VAM 5- against 10-equation models for transverse velocity profile for Steffler's (1984) run 1 at cross-section 270 degrees and $y/b = 0.8$

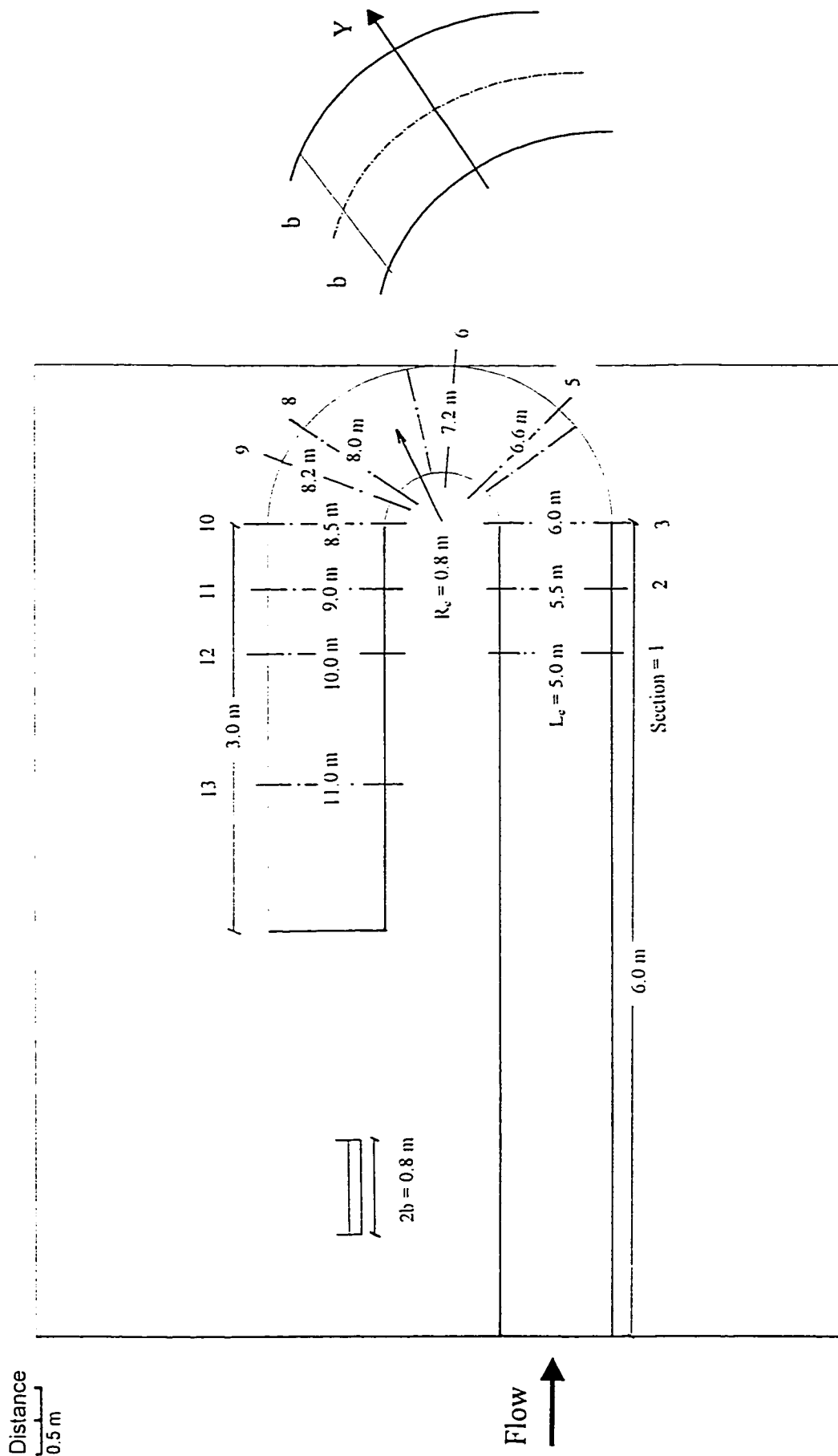
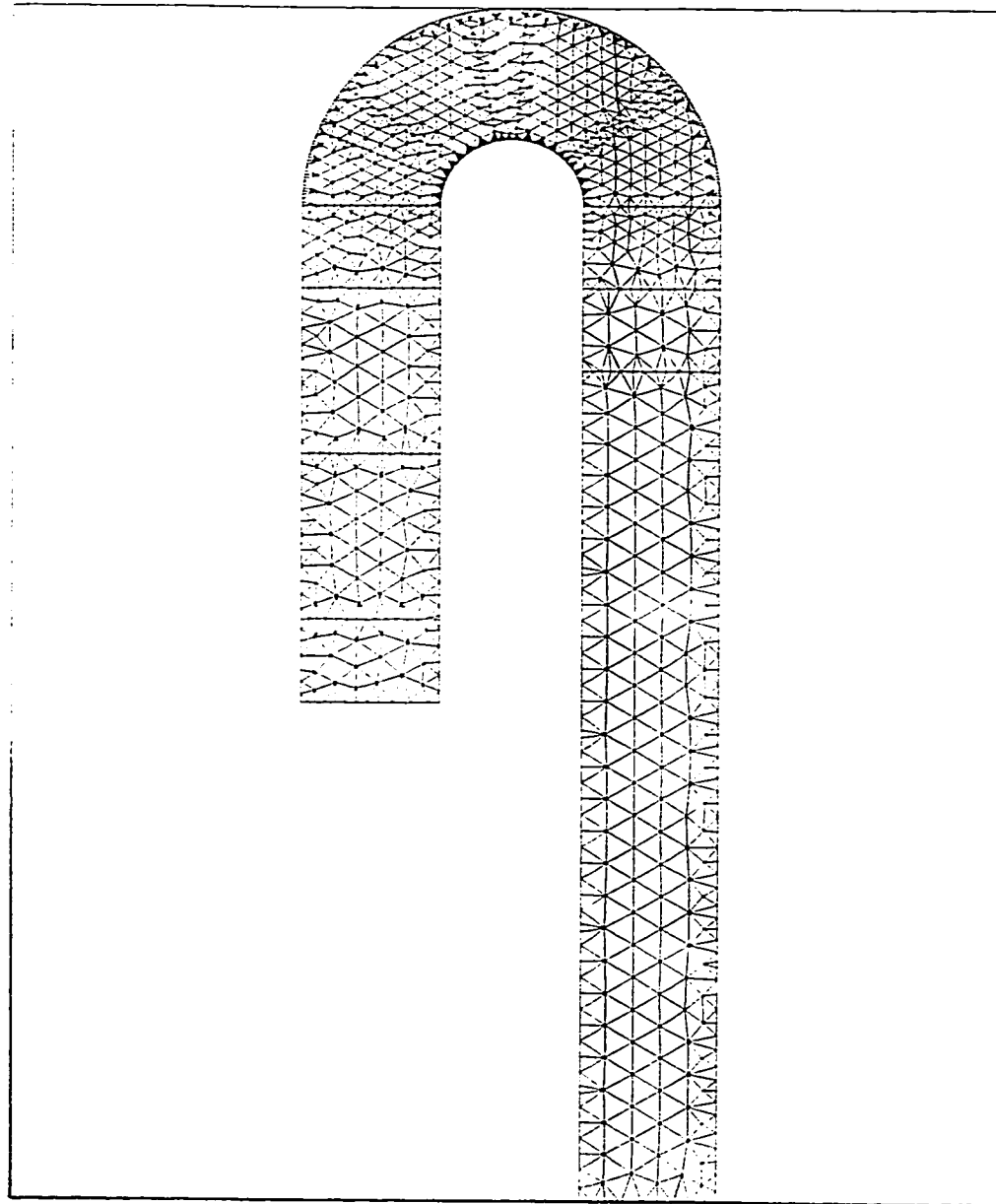


Figure 4.123 The layout of Rozovskii's (1961) experiment

Distance
0.5 m



The generated mesh

Number of nodes = 1332

Number of elements = 2060

Figure 4.124 Finite element mesh for Rozovskii's (1961) experiment

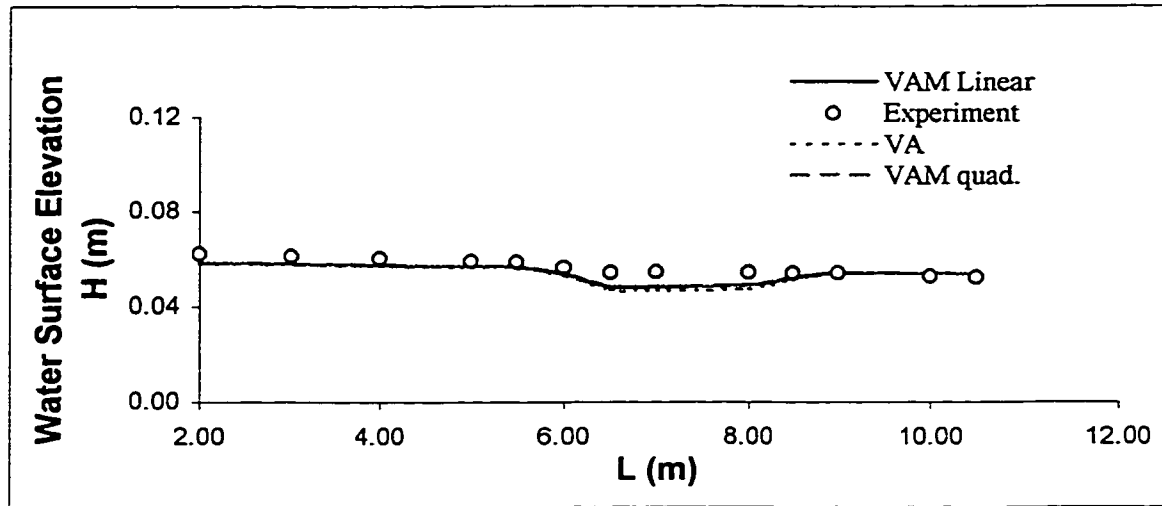


Figure 4.125 The comparison of surface elevation for Rozovskii's (1961) run 1 along the left side of the channel

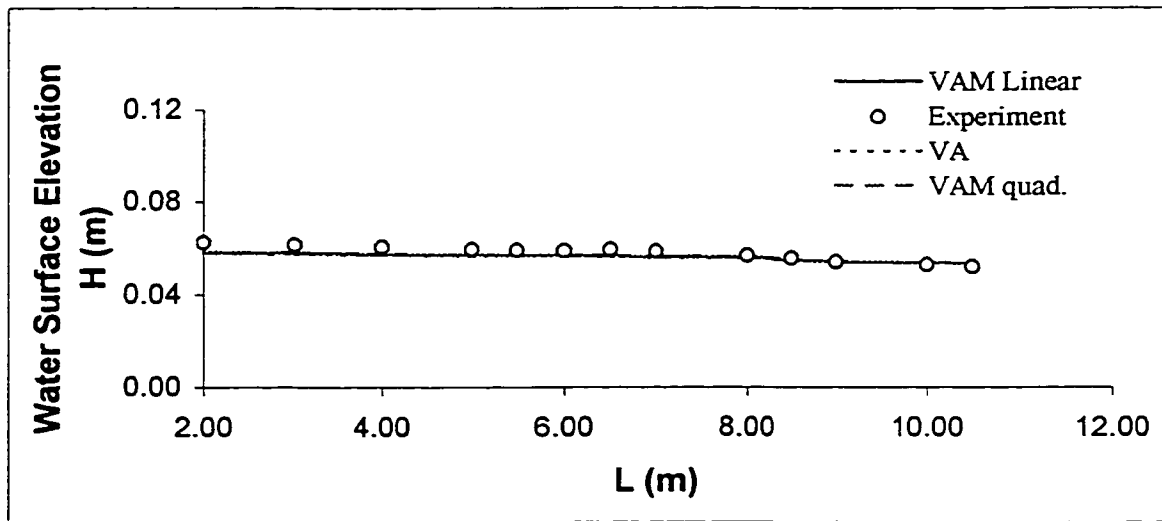


Figure 4.126 The comparison of surface elevation for Rozovskii's (1961) run 1 along the center line of the channel

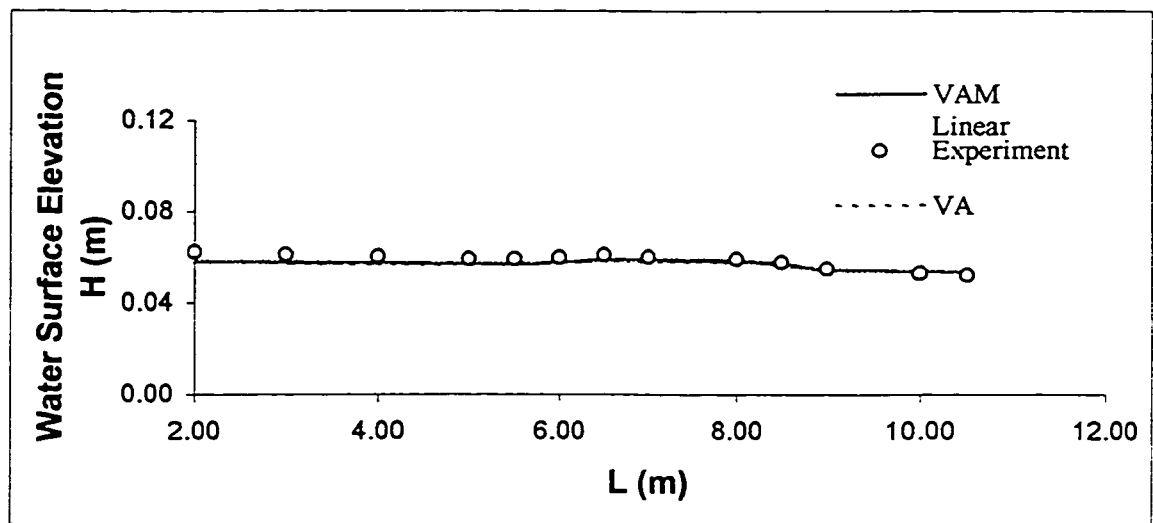


Figure 4.127 The comparison of surface elevation for Rozovskii's (1961) run 1 along the right side of the channel

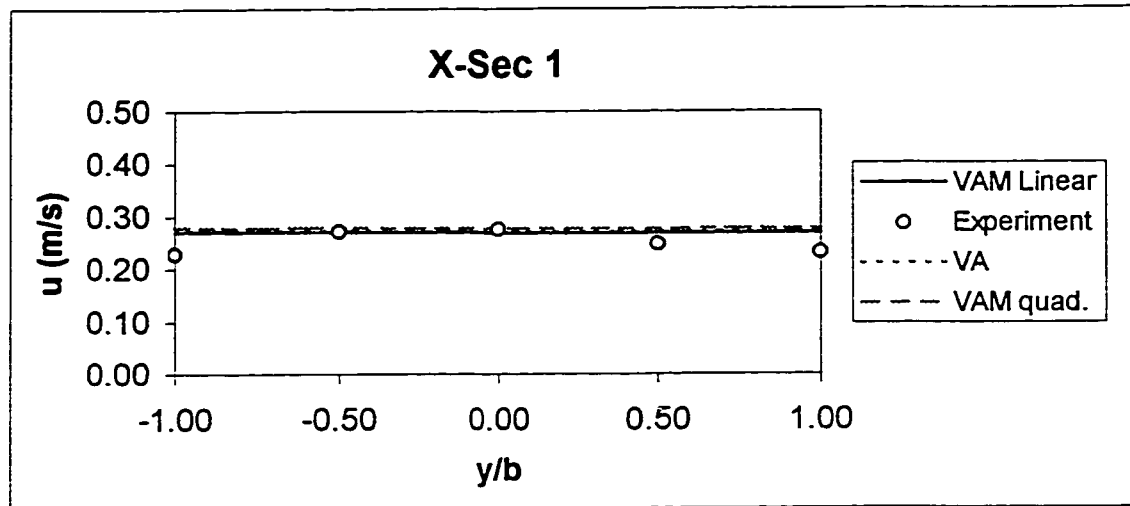


Figure 4.128 The comparison of longitudinal velocity distribution across the flume for Rozovskii's (1961) run 1 at cross-section 1

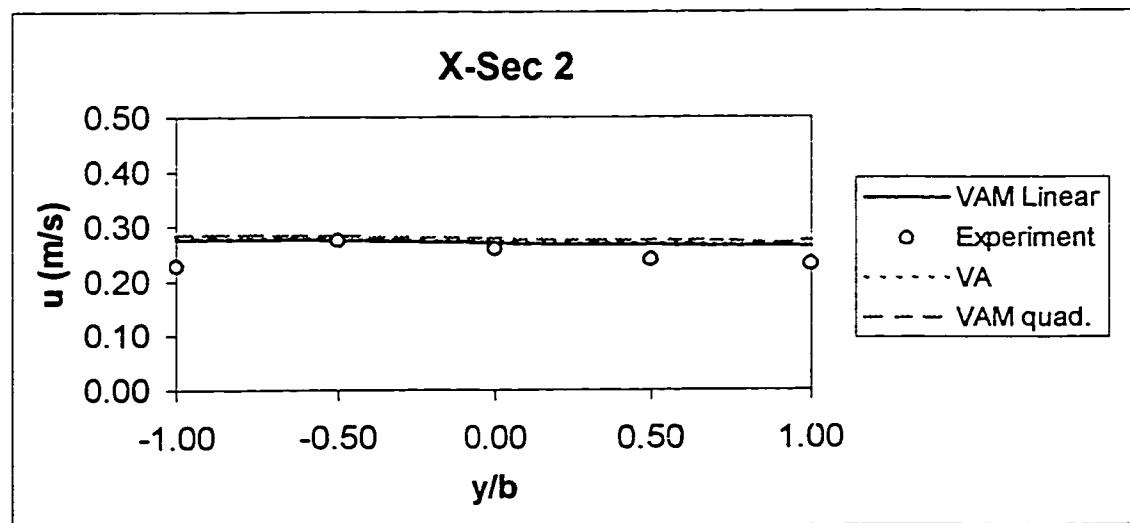


Figure 4.129 The comparison of longitudinal velocity distribution across the flume for Rozovskii's (1961) run 1 at cross-section 2

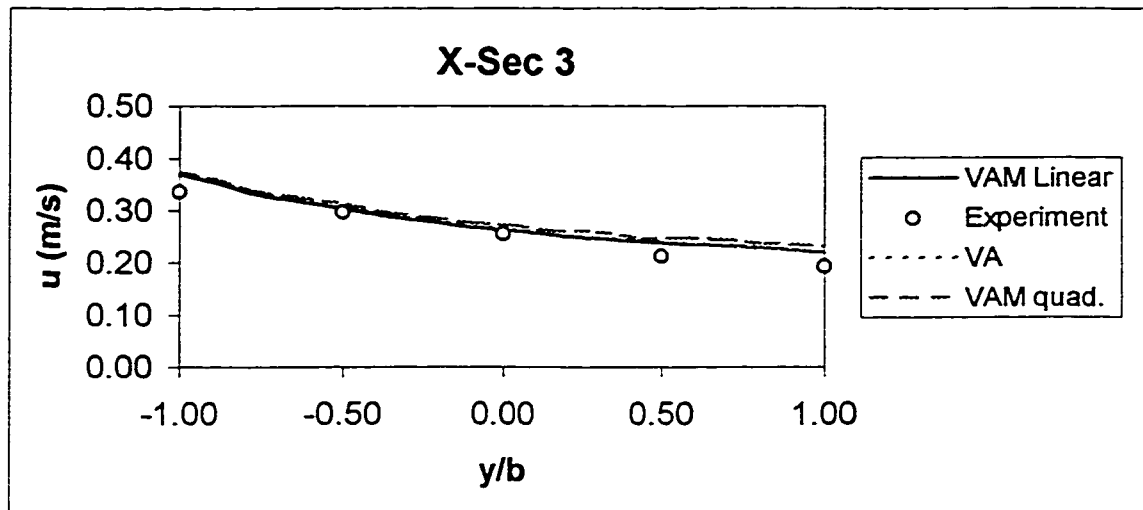


Figure 4.130 The comparison of longitudinal velocity distribution across the flume for Rozovskii's (1961) run 1 at cross-section 3

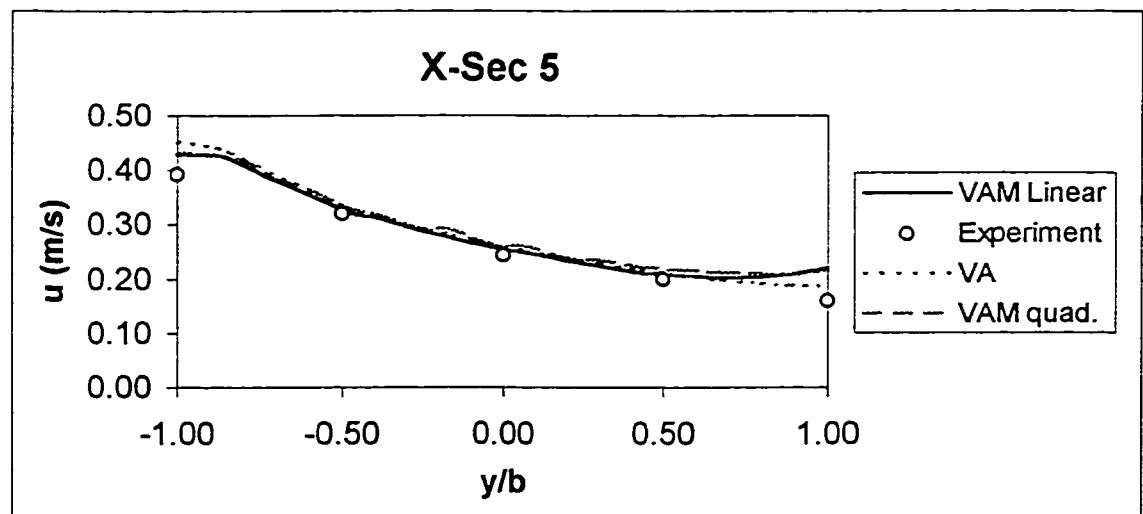


Figure 4.131 The comparison of longitudinal velocity distribution across the flume for Rozovskii's (1961) run 1 at cross-section 5

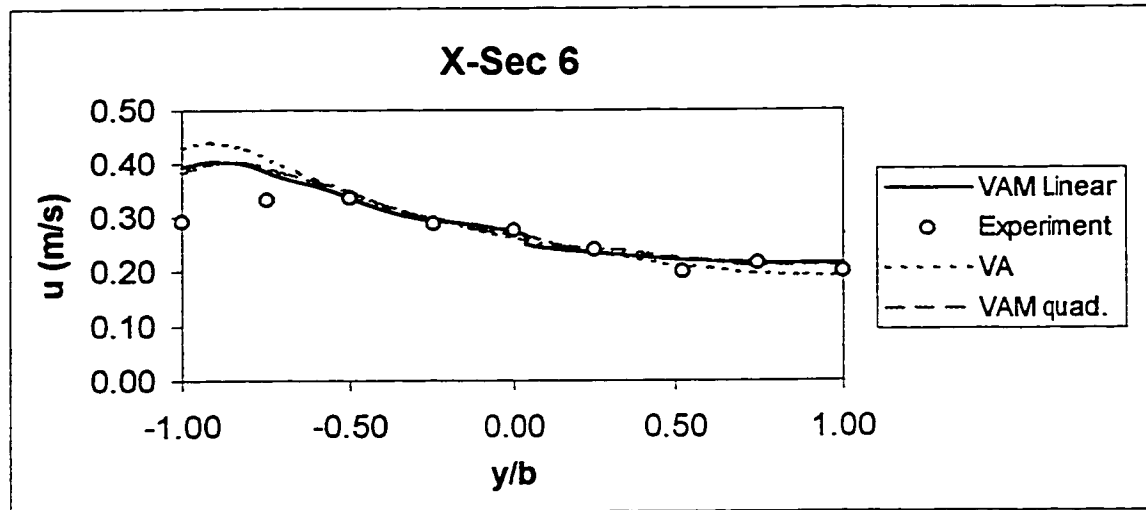


Figure 4.132 The comparison of longitudinal velocity distribution across the flume for Rozovskii's (1961) run 1 at cross-section 6

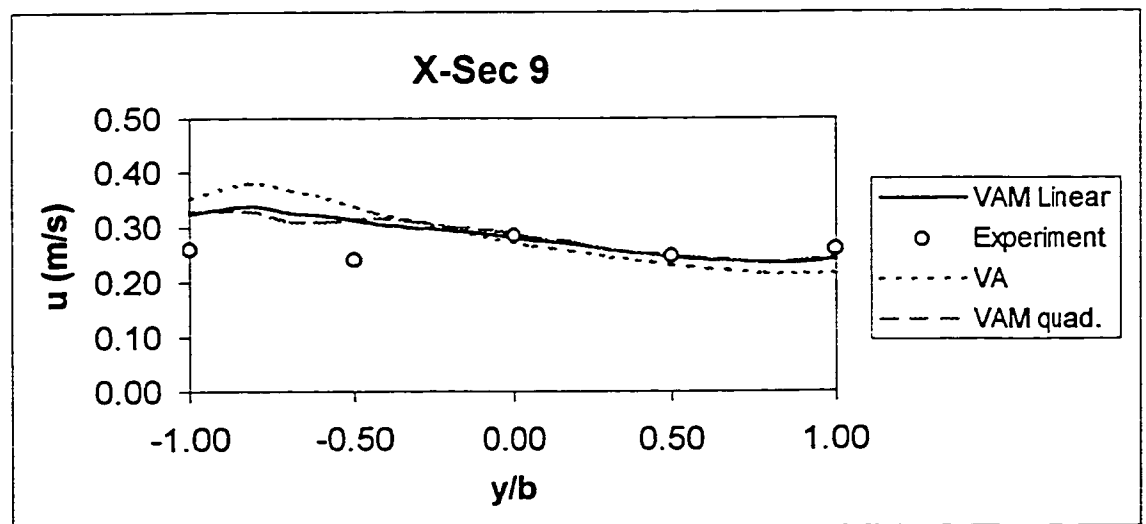


Figure 4.133 The comparison of longitudinal velocity distribution across the flume for Rozovskii's (1961) run 1 at cross-section 9

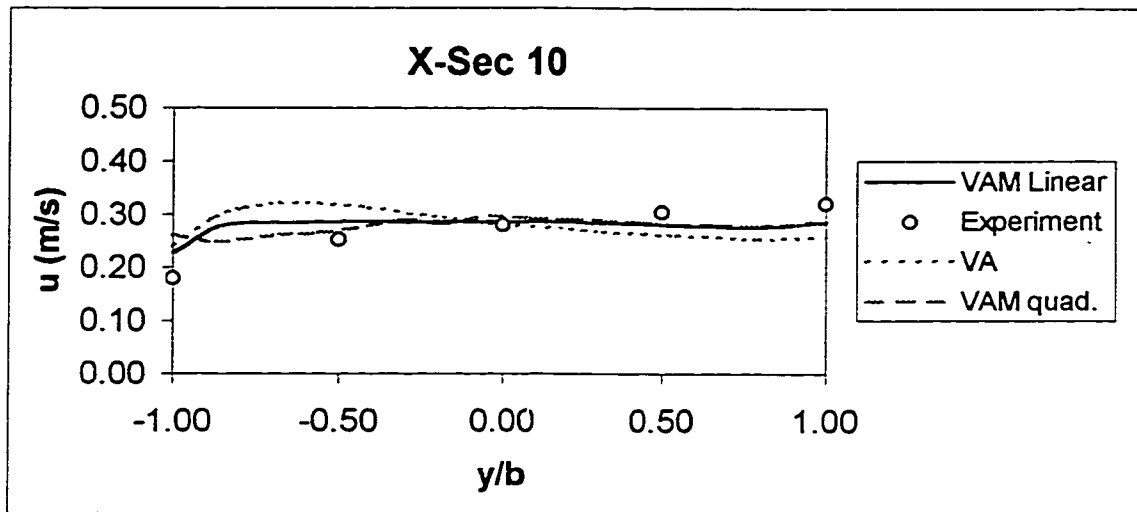


Figure 4.134 The comparison of longitudinal velocity distribution across the flume for Rozovskii's (1961) run 1 at cross-section 10

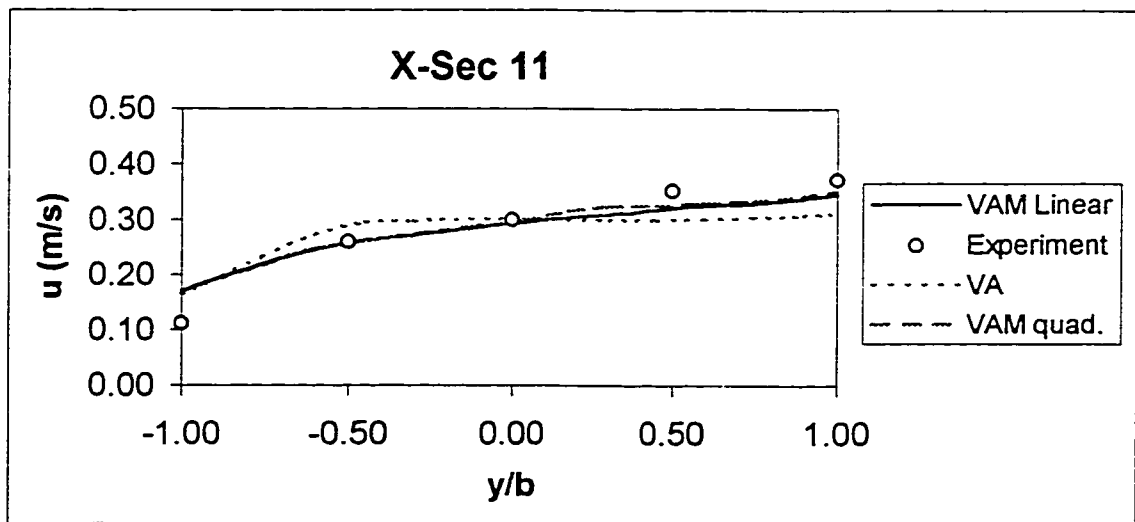


Figure 4.135 The comparison of longitudinal velocity distribution across the flume for Rozovskii's (1961) run 1 at cross-section 11

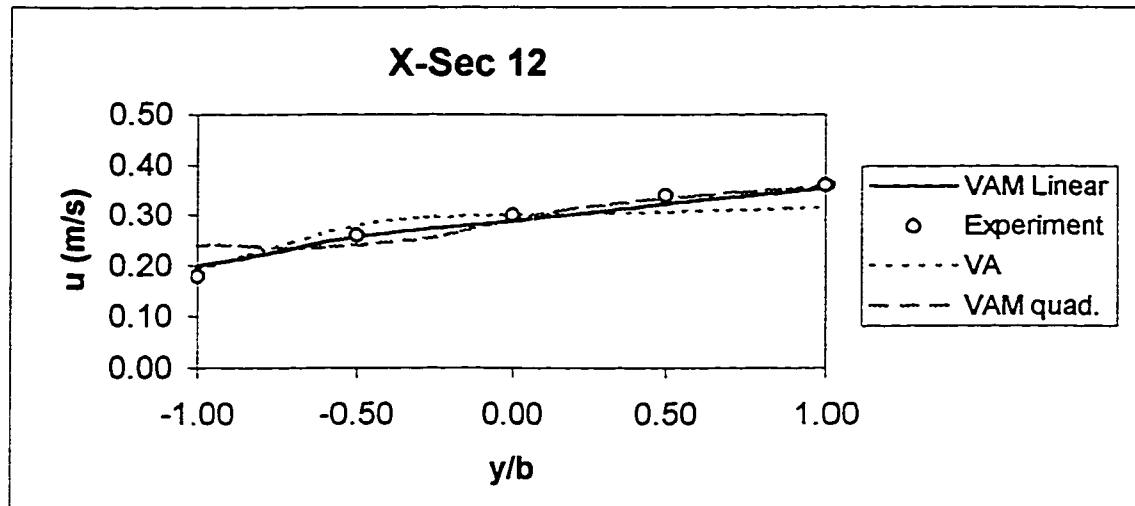


Figure 4.136 The comparison of longitudinal velocity distribution across the flume for Rozovskii's (1961) run 1 at cross-section 12

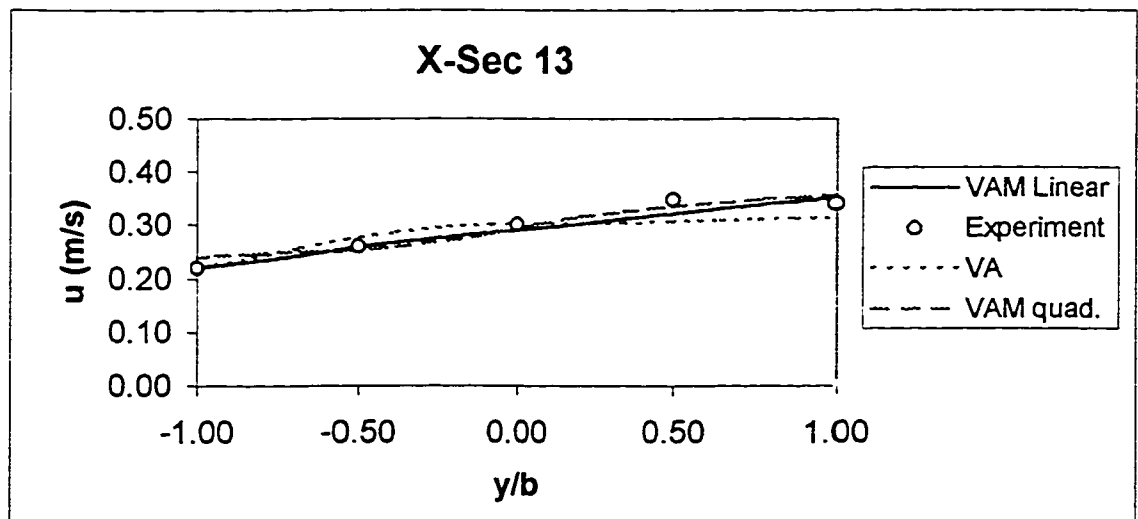


Figure 4.137 The comparison of longitudinal velocity distribution across the flume for Rozovskii's (1961) run 1 at cross-section 13

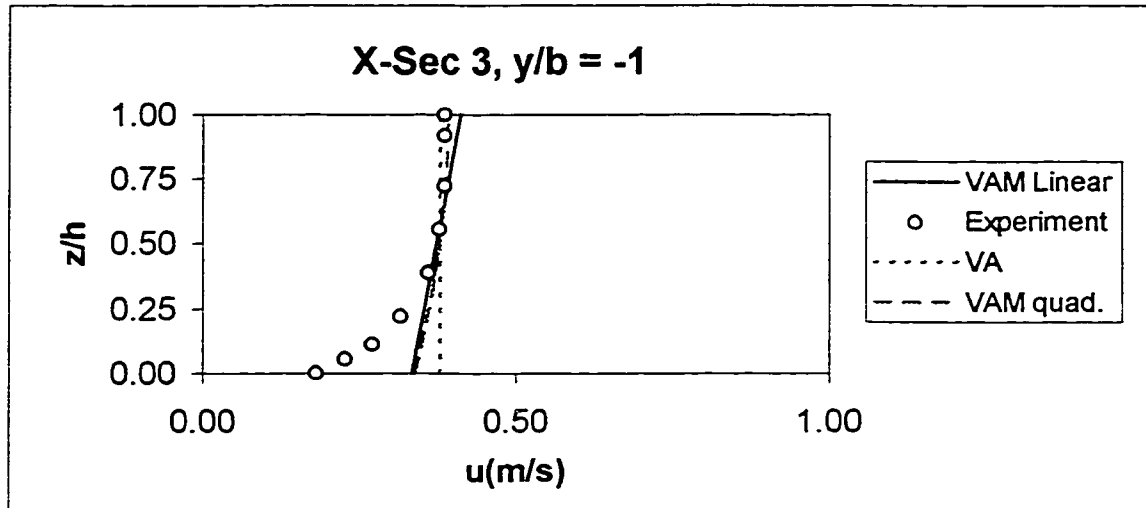


Figure 4.138 The comparison of longitudinal velocity profile for Rozovskii's (1961) run 1 at cross-section 3 and $y/b = -1$

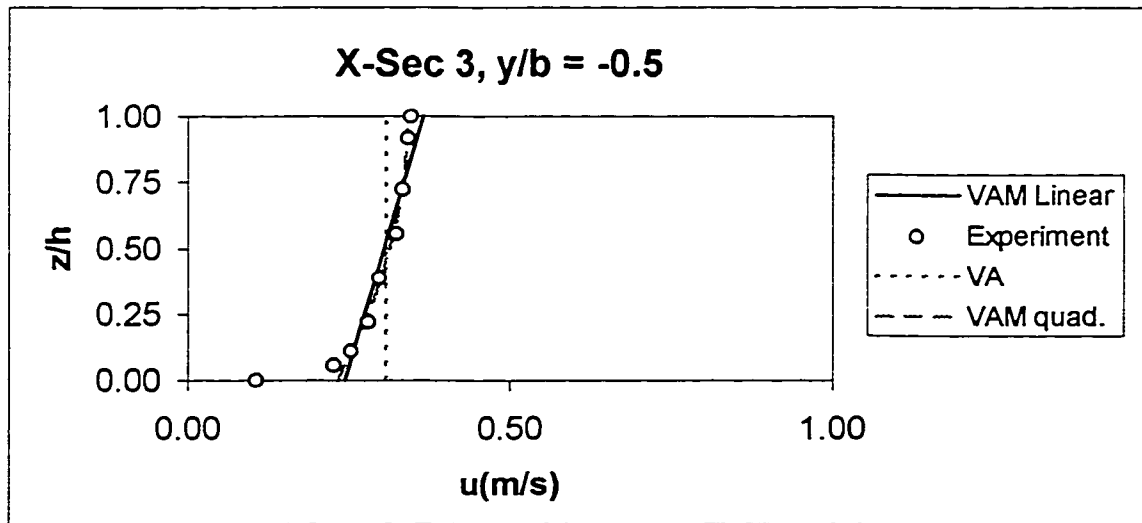


Figure 4.139 The comparison of longitudinal velocity profile for Rozovskii's (1961) run 1 at cross-section 3 and $y/b = -0.5$

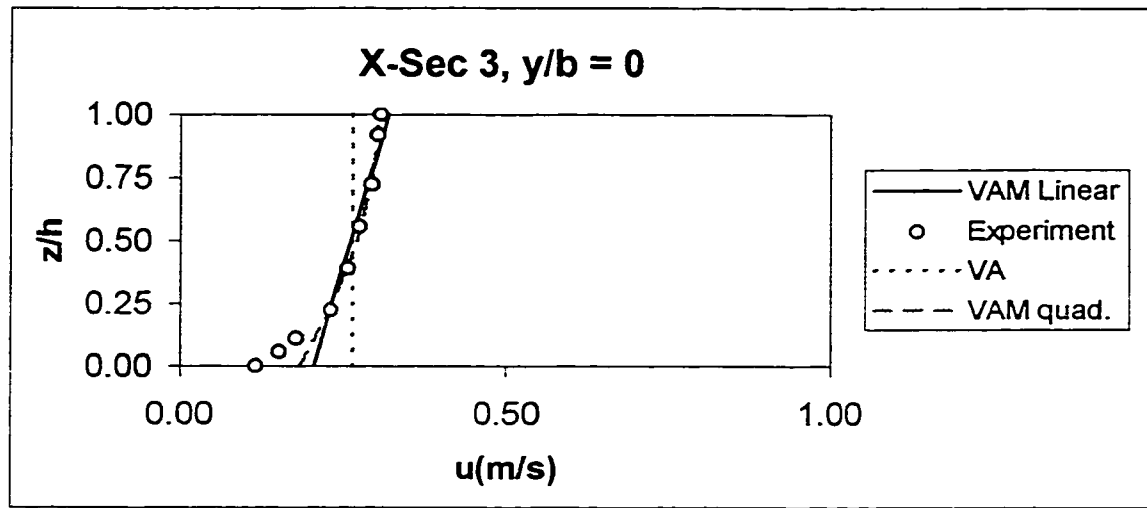


Figure 4.140 The comparison of longitudinal velocity profile for Rozovskii's (1961) run 1 at cross-section 3 and $y/b = 0$

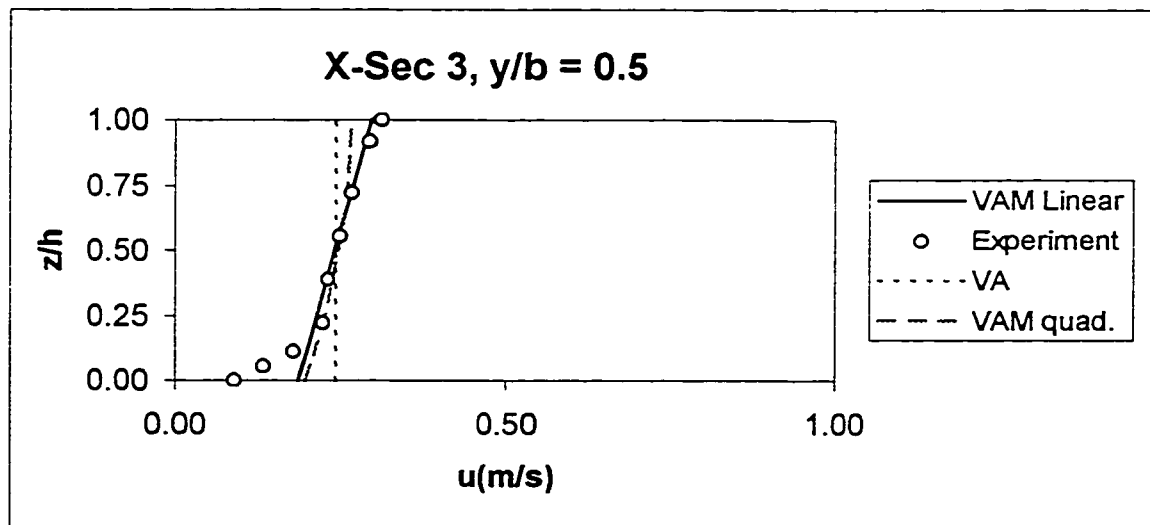


Figure 4.141 The comparison of longitudinal velocity profile for Rozovskii's (1961) run 1 at cross-section 3 and $y/b = 0.5$

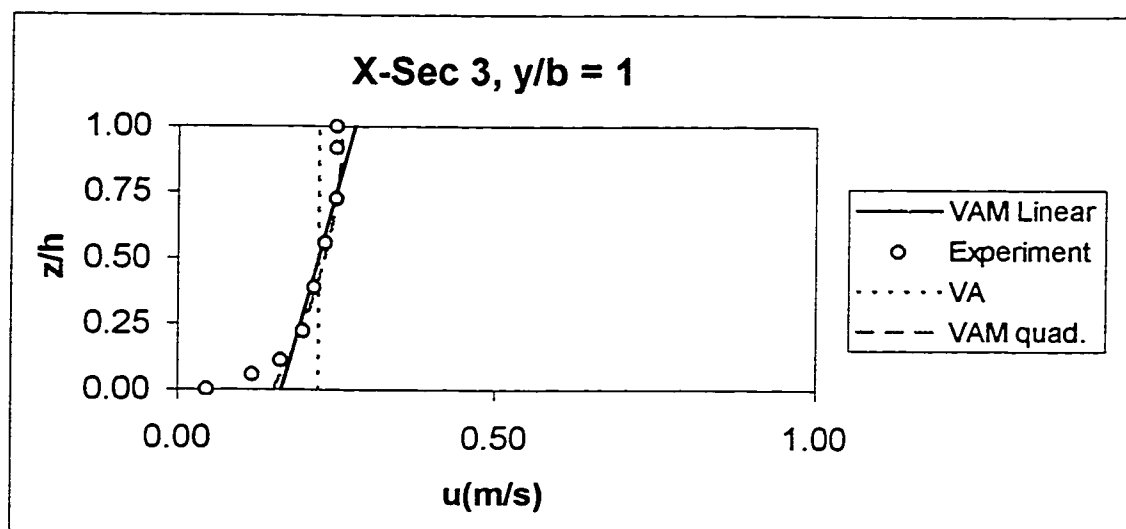


Figure 4.142 The comparison of longitudinal velocity profile for Rozovskii's (1961) run 1 at cross-section 3 and $y/b = 1$

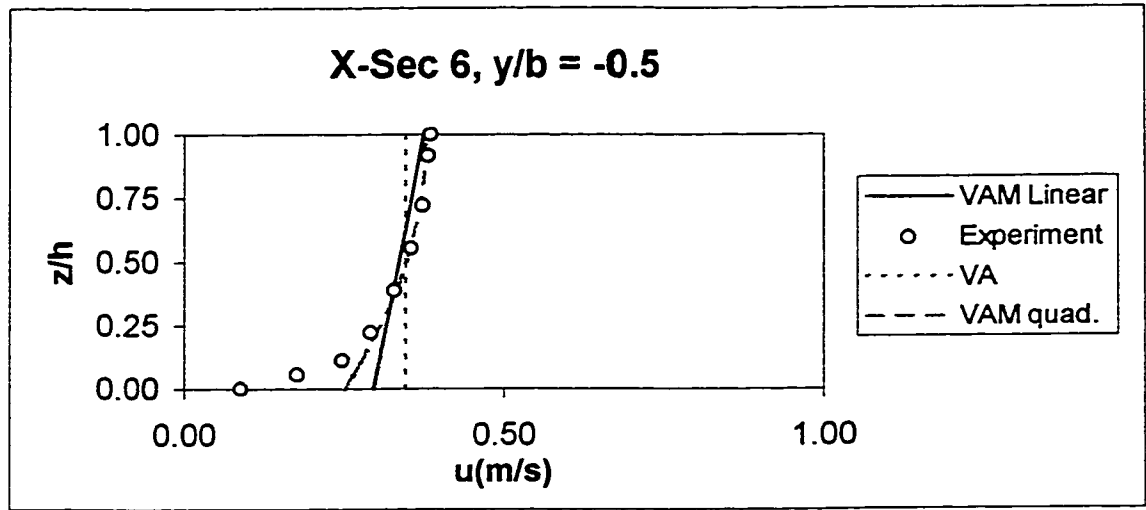


Figure 4.143 The comparison of longitudinal velocity profile for Rozovskii's (1961) run 1 at cross-section 6 and $y/b = -0.5$

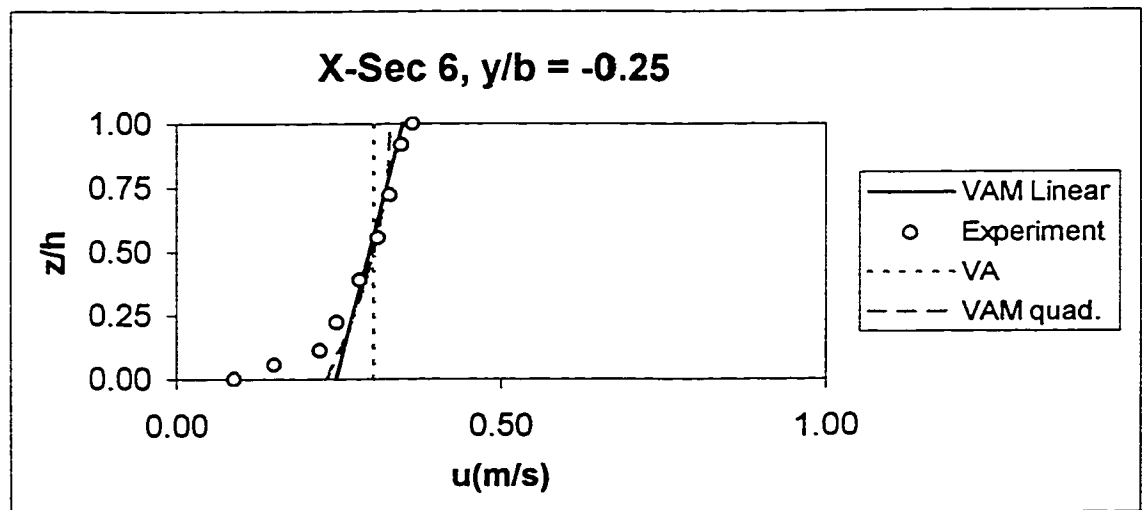


Figure 4.144 The comparison of longitudinal velocity profile for Rozovskii's (1961) run 1 at cross-section 6 and $y/b = -0.25$

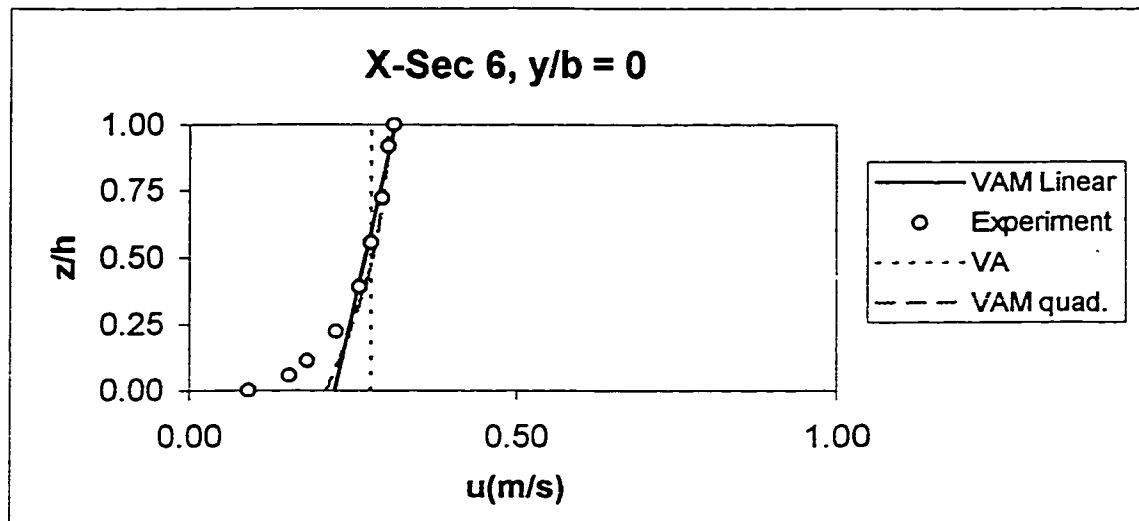


Figure 4.145 The comparison of longitudinal velocity profile for Rozovskii's (1961) run 1 at cross-section 6 and $y/b = 0$

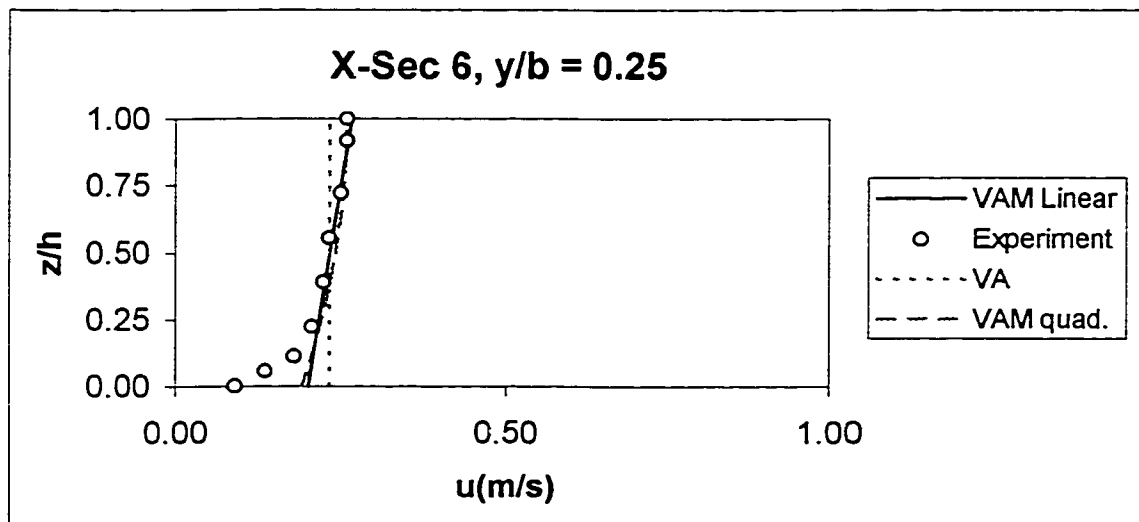


Figure 4.146 The comparison of longitudinal velocity profile for Rozovskii's (1961) run 1 at cross-section 6 and $y/b = 0.25$

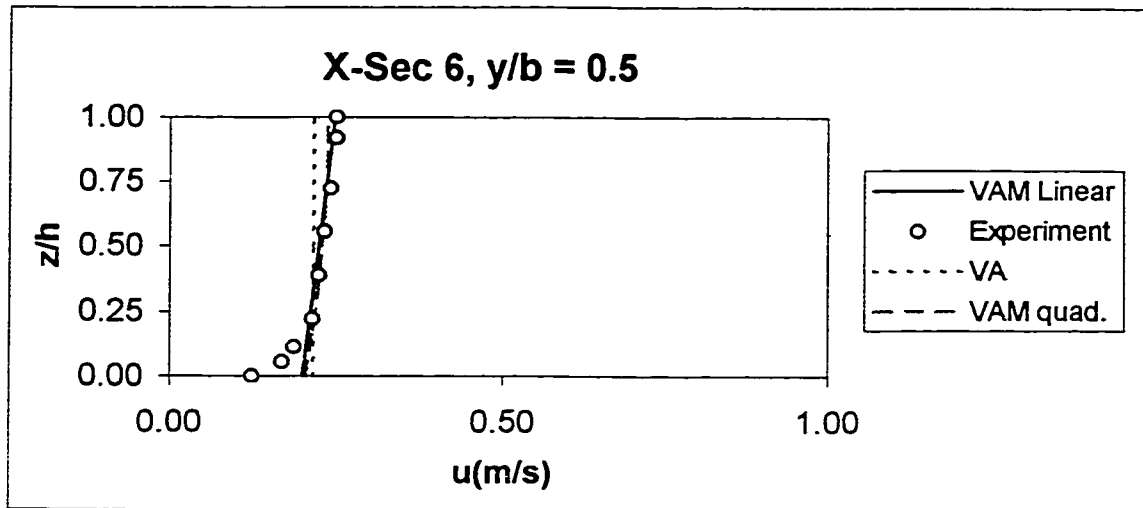


Figure 4.147 The comparison of longitudinal velocity profile for Rozovskii's (1961) run 1 at cross-section 6 and $y/b = 0.5$

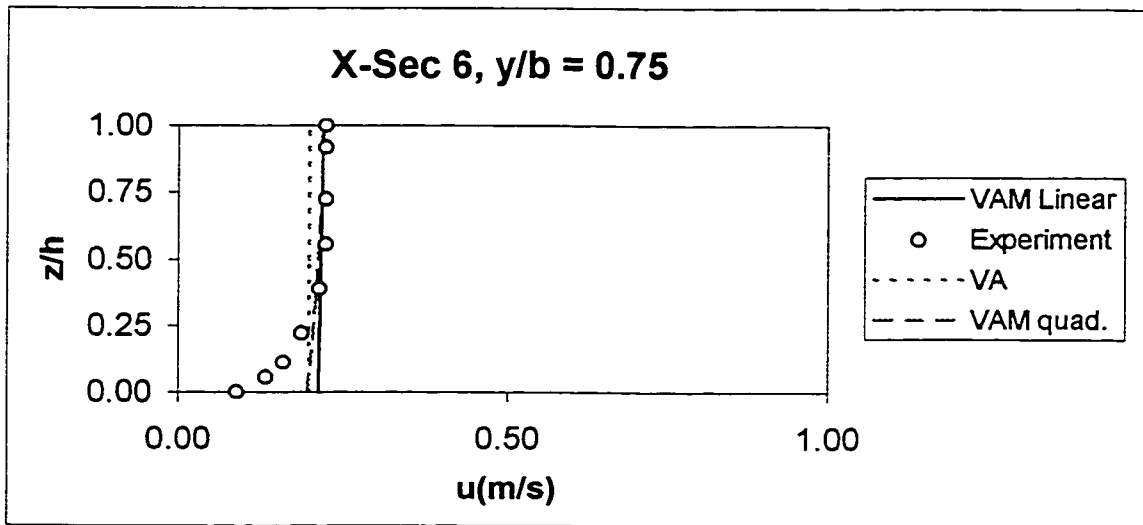


Figure 4.148 The comparison of longitudinal velocity profile for Rozovskii's (1961) run 1 at cross-section 6 and $y/b = 0.75$

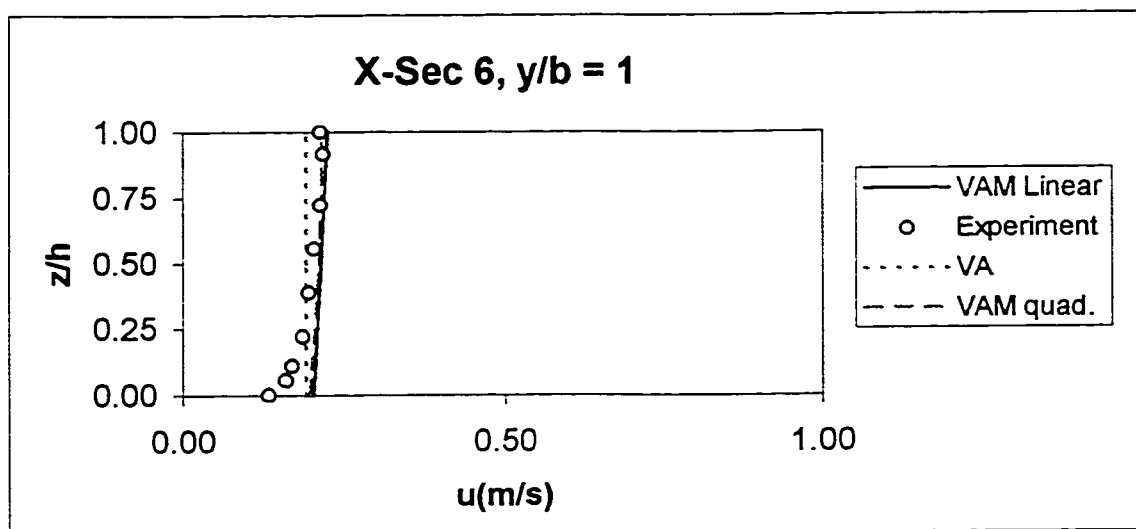


Figure 4.149 The comparison of longitudinal velocity profile for Rozovskii's (1961) run 1 at cross-section 6 and $y/b = 1$

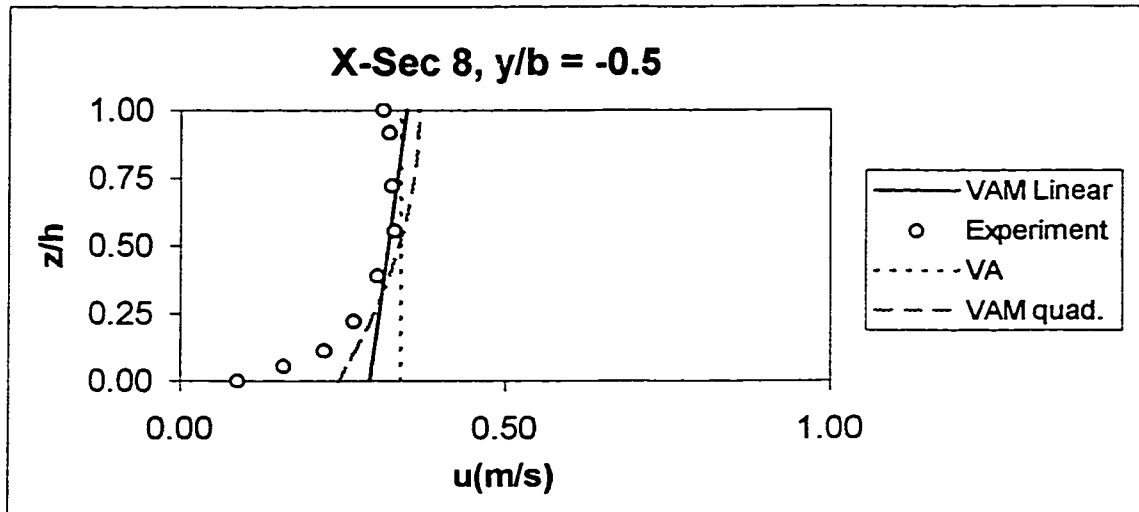


Figure 4.150 The comparison of longitudinal velocity profile for Rozovskii's (1961) run 1 at cross-section 8 and $y/b = -0.5$

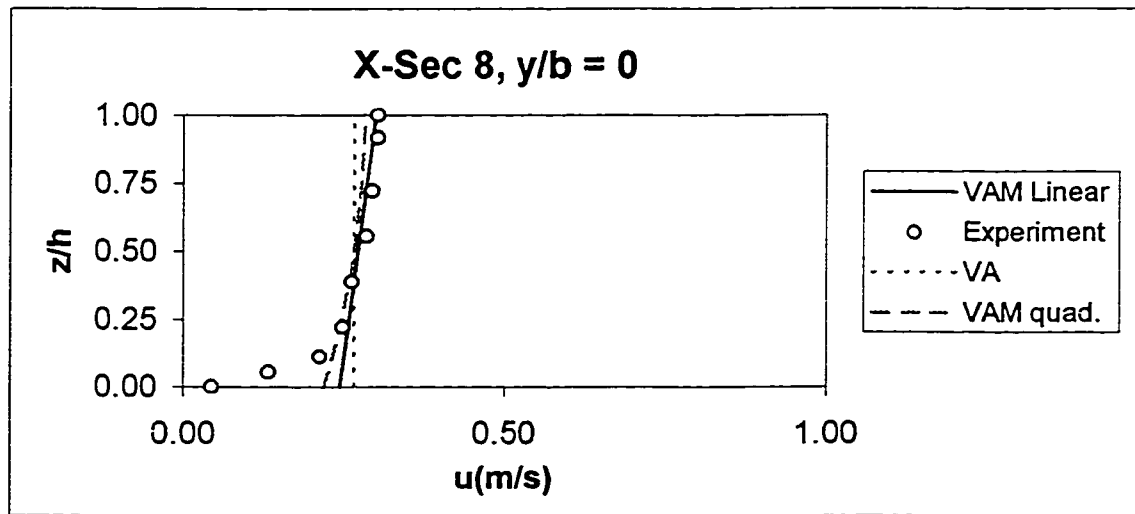


Figure 4.151 The comparison of longitudinal velocity profile for Rozovskii's (1961) run 1 at cross-section 8 and $y/b = 0$

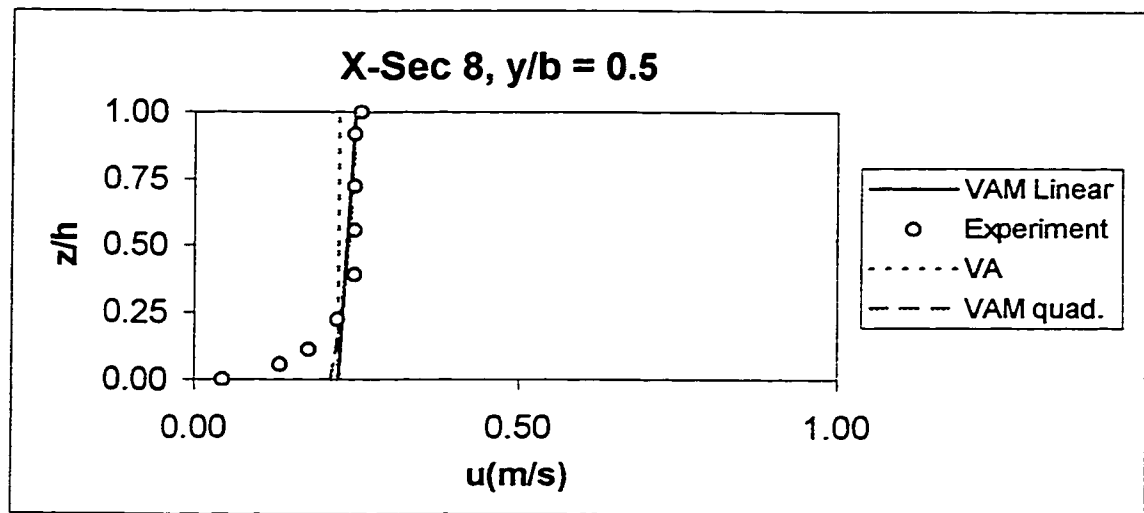


Figure 4.152 The comparison of longitudinal velocity profile for Rozovskii's (1961) run 1 at cross-section 8 and $y/b = 0.5$

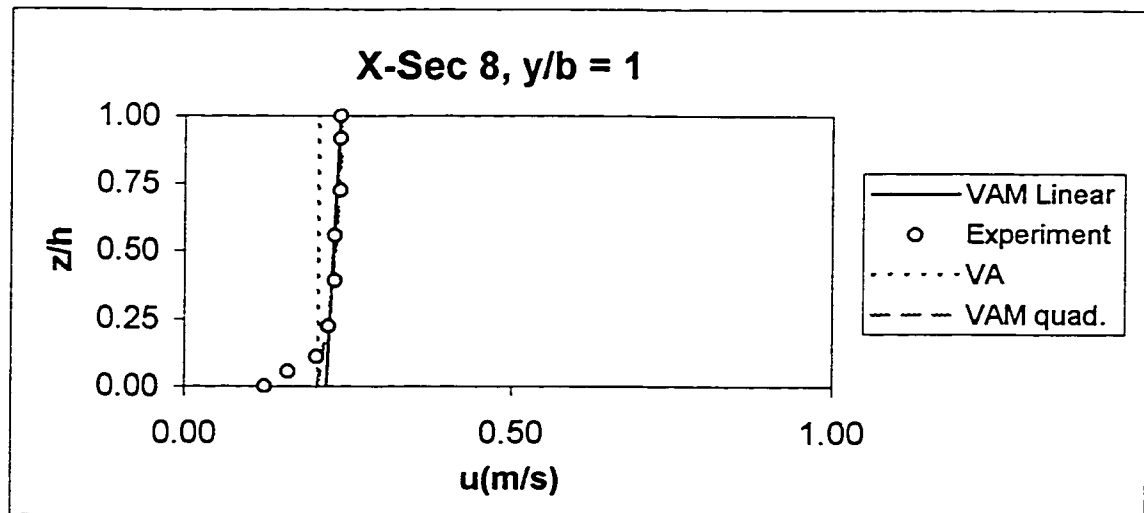


Figure 4.153 The comparison of longitudinal velocity profile for Rozovskii's (1961) run 1 at cross-section 8 and $y/b = 1$

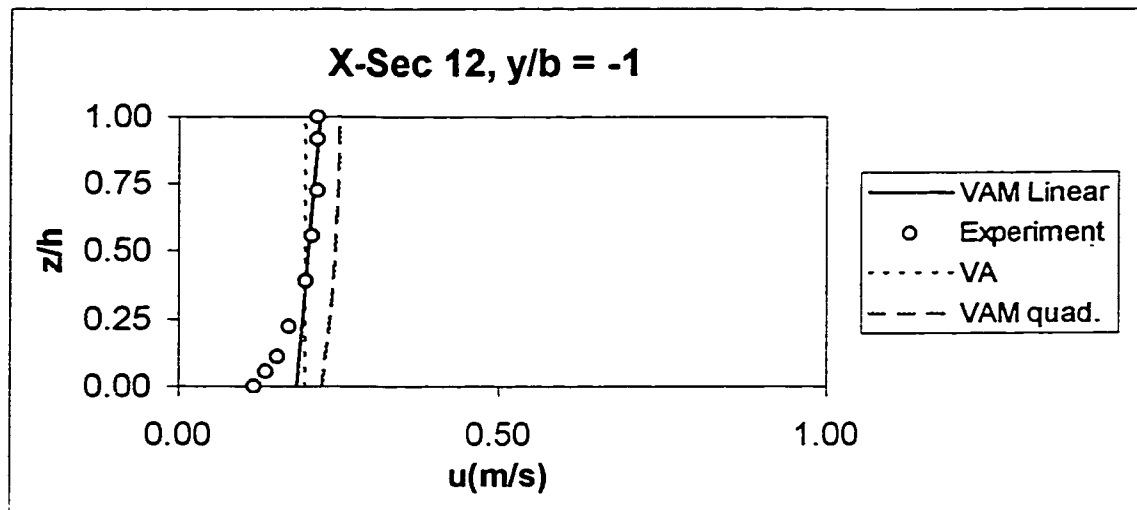


Figure 4.154 The comparison of longitudinal velocity profile for Rozovskii's (1961) run 1 at cross-section 12 and $y/b = -1$

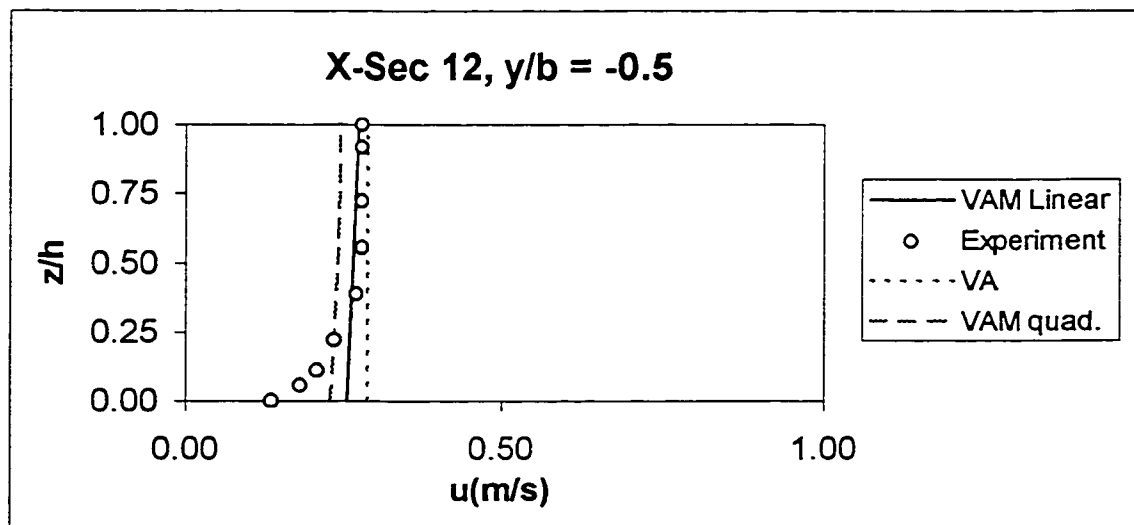


Figure 4.155 The comparison of longitudinal velocity profile for Rozovskii's (1961) run 1 at cross-section 12 and $y/b = -0.5$

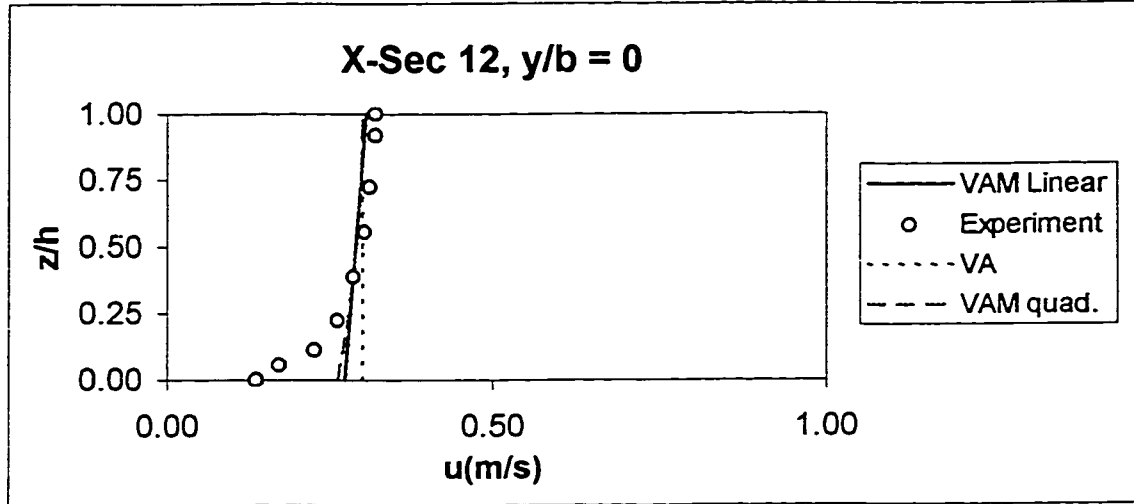


Figure 4.156 The comparison of longitudinal velocity profile for Rozovskii's (1961) run 1 at cross-section 12 and $y/b = 0$

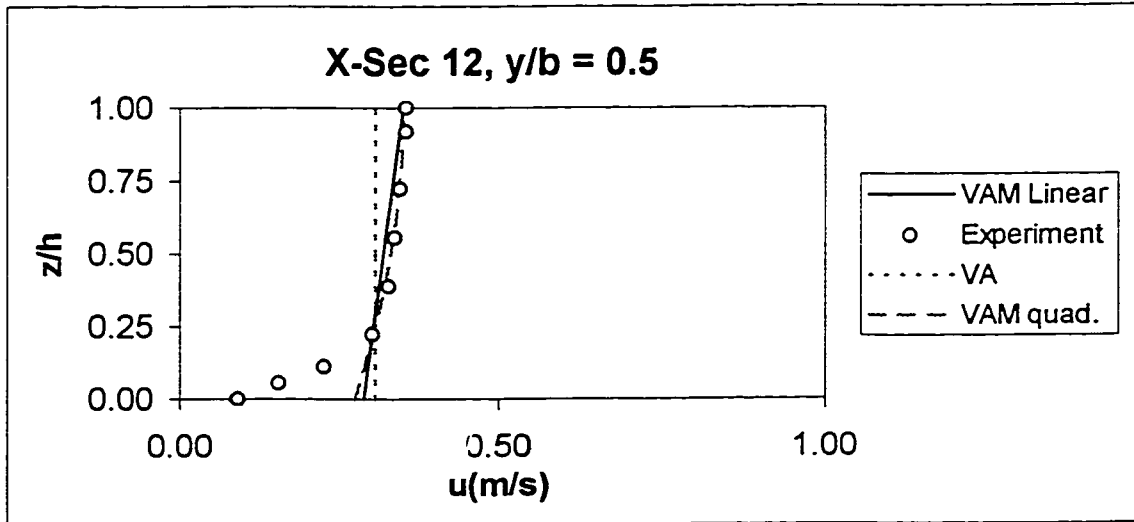


Figure 4.157 The comparison of longitudinal velocity profile for Rozovskii's (1961) run 1 at cross-section 12 and $y/b = 0.5$

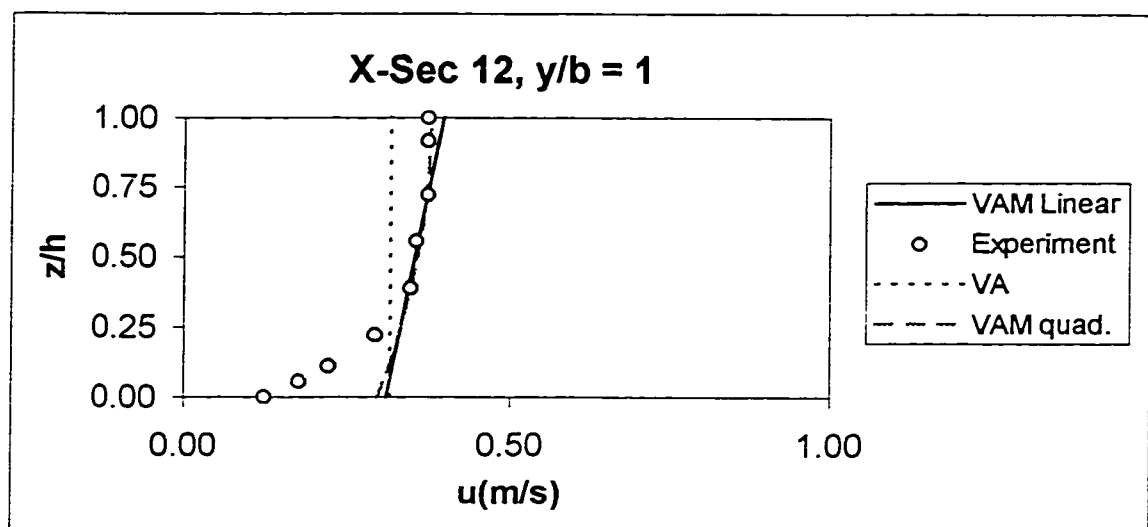


Figure 4.158 The comparison of longitudinal velocity profile for Rozovskii's (1961) run 1 at cross-section 12 and $y/b = 1$

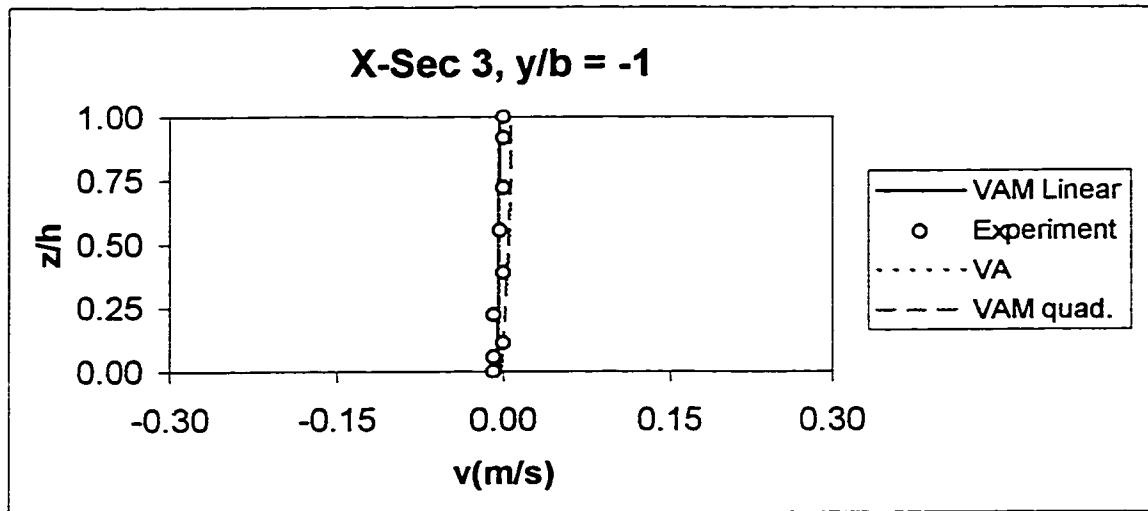


Figure 4.159 The comparison of transverse velocity profile for Rozovskii's (1961) run 1 at cross-section 3 and $y/b = -1$

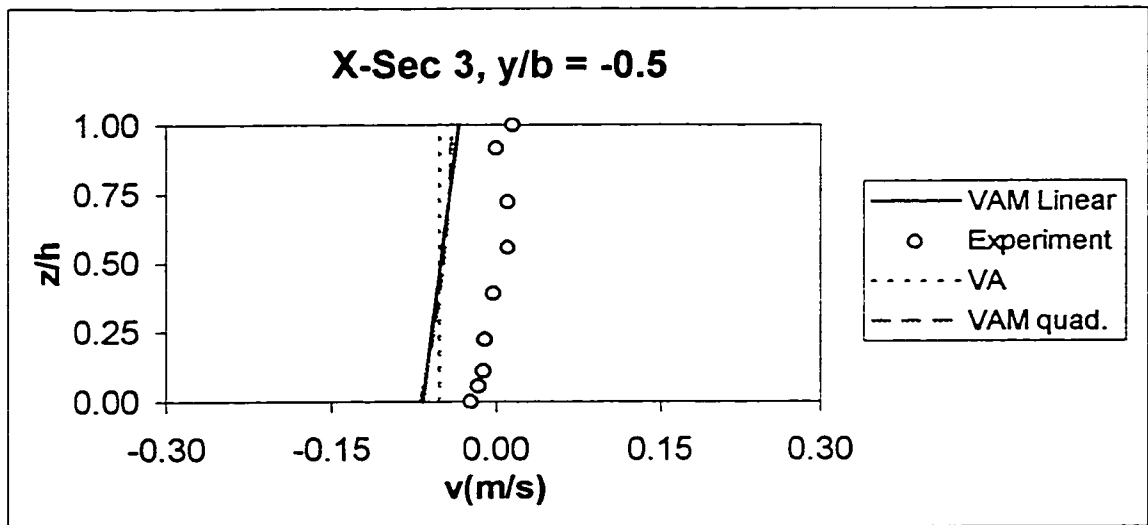


Figure 4.160 The comparison of transverse velocity profile for Rozovskii's (1961) run 1 at cross-section 3 and $y/b = -0.5$

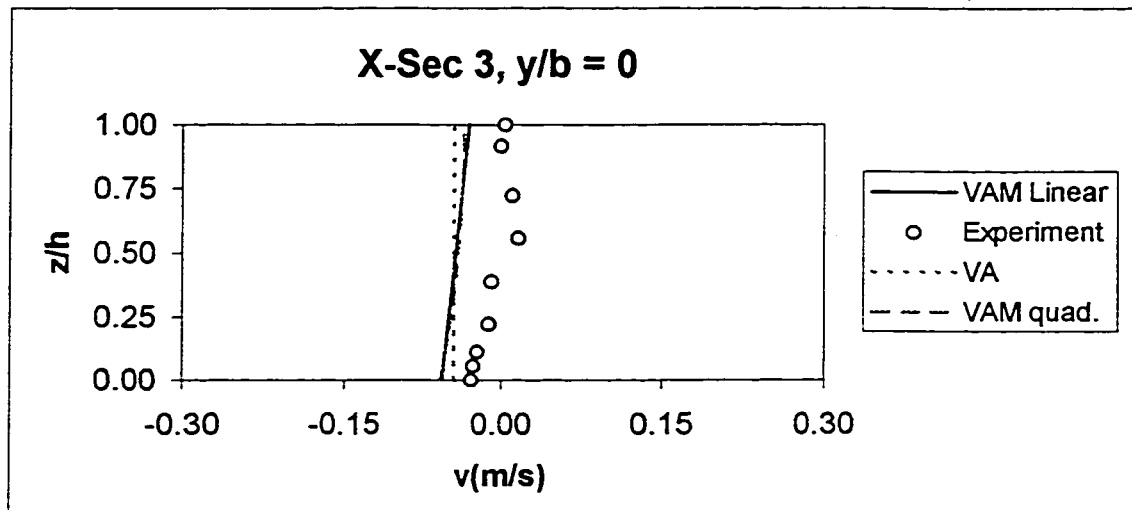


Figure 4.161 The comparison of transverse velocity profile for Rozovskii's (1961) run 1 at cross-section 3 and $y/b = 0$

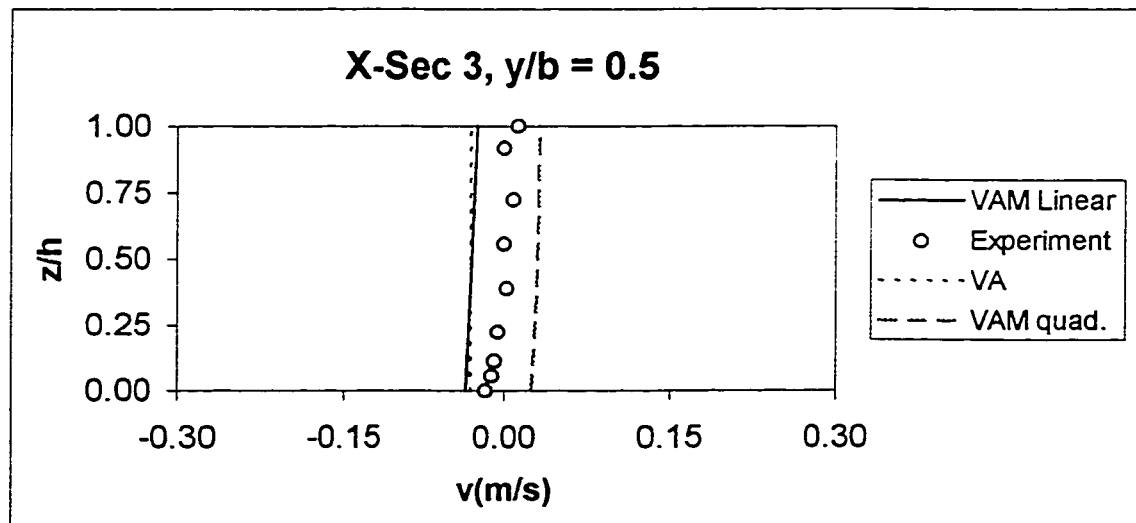


Figure 4.162 The comparison of transverse velocity profile for Rozovskii's (1961) run 1 at cross-section 3 and $y/b = 0.5$

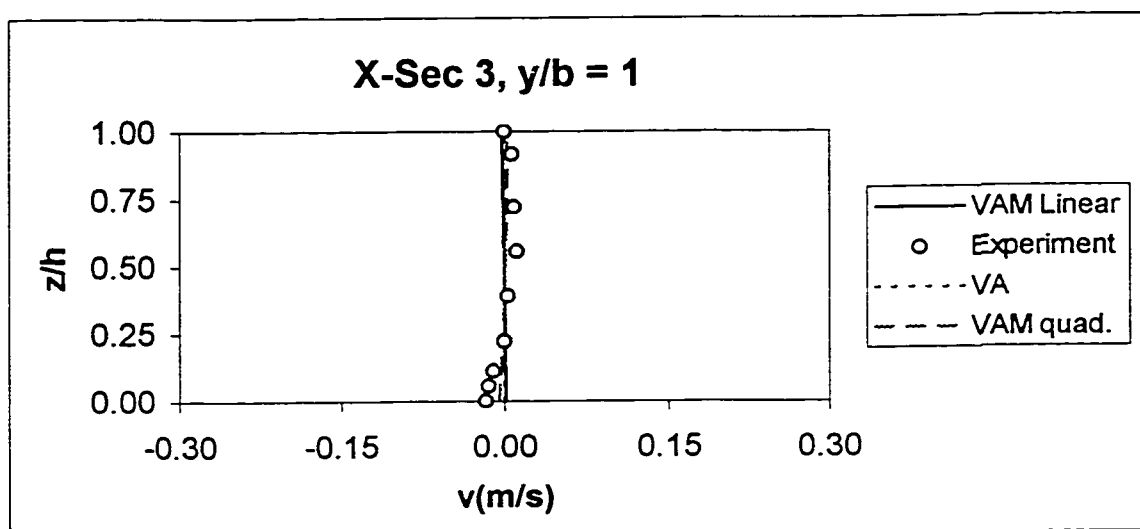


Figure 4.163 The comparison of transverse velocity profile for Rozovskii's (1961) run 1 at cross-section 3 and $y/b = 1$

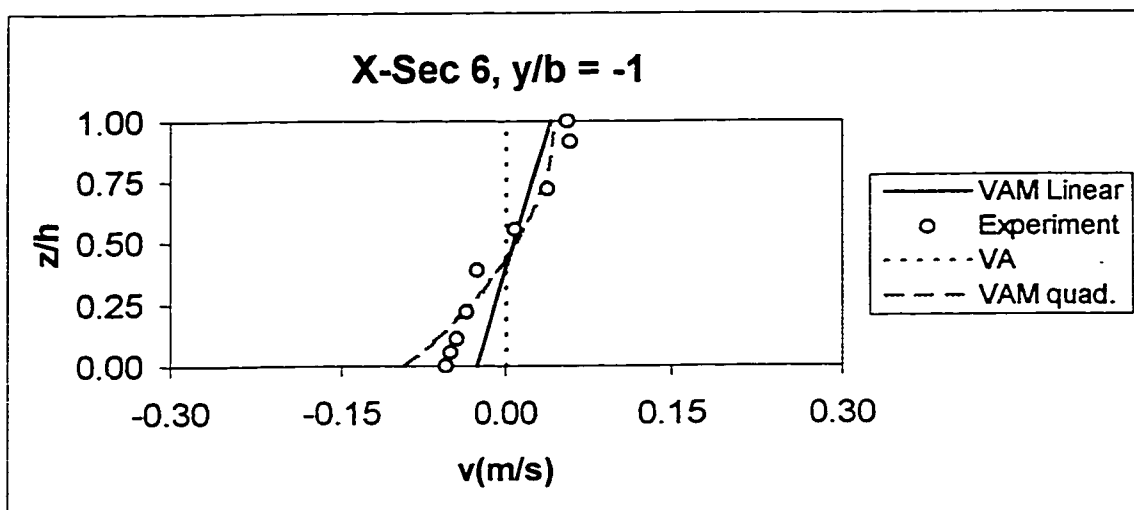


Figure 4.164 The comparison of transverse velocity profile for Rozovskii's (1961) run 1 at cross-section 6 and $y/b = -1$

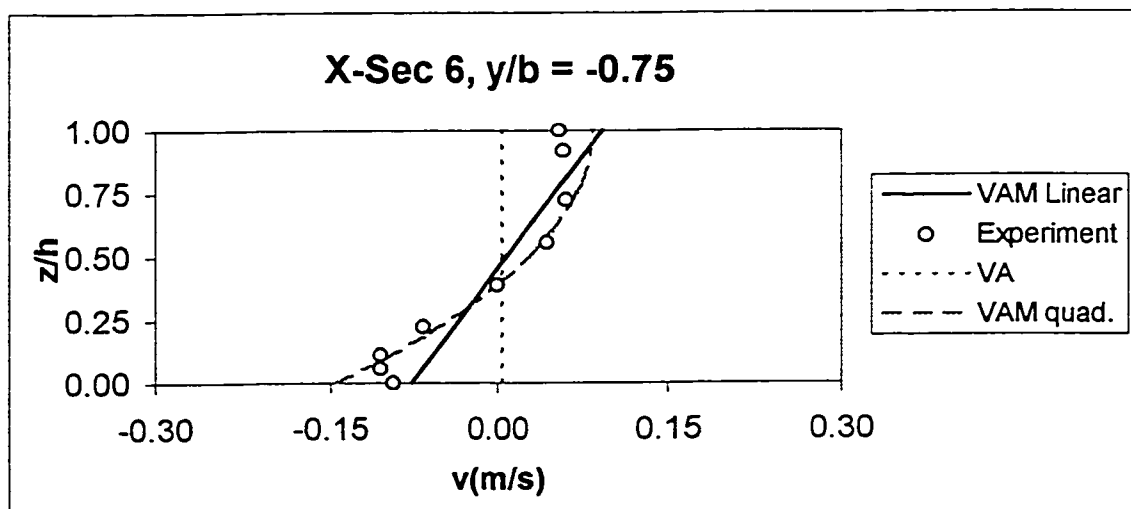


Figure 4.165 The comparison of transverse velocity profile for Rozovskii's (1961) run 1 at cross-section 6 and $y/b = -0.75$

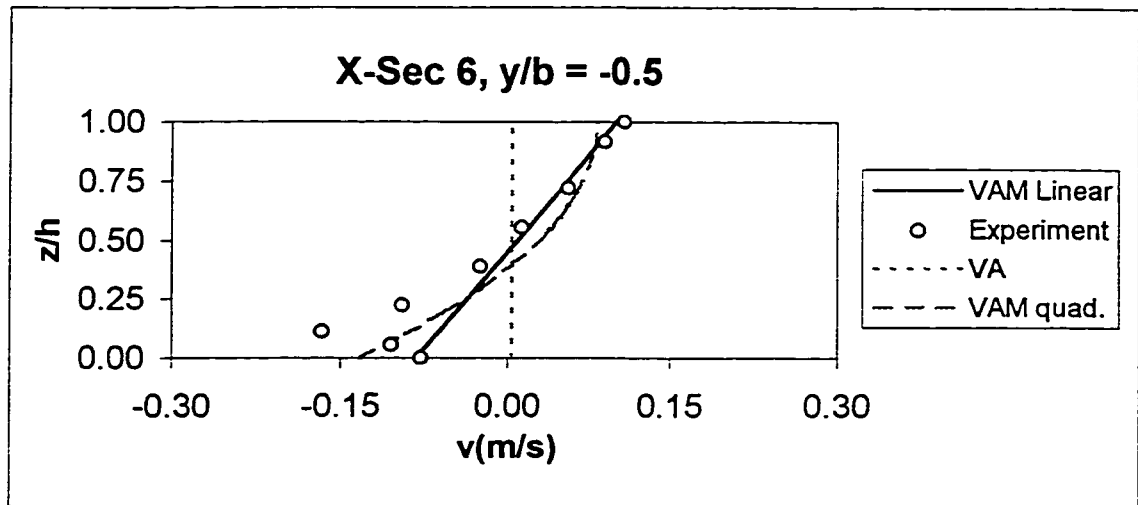


Figure 4.166 The comparison of transverse velocity profile for Rozovskii's (1961) run 1 at cross-section 6 and $y/b = -0.5$

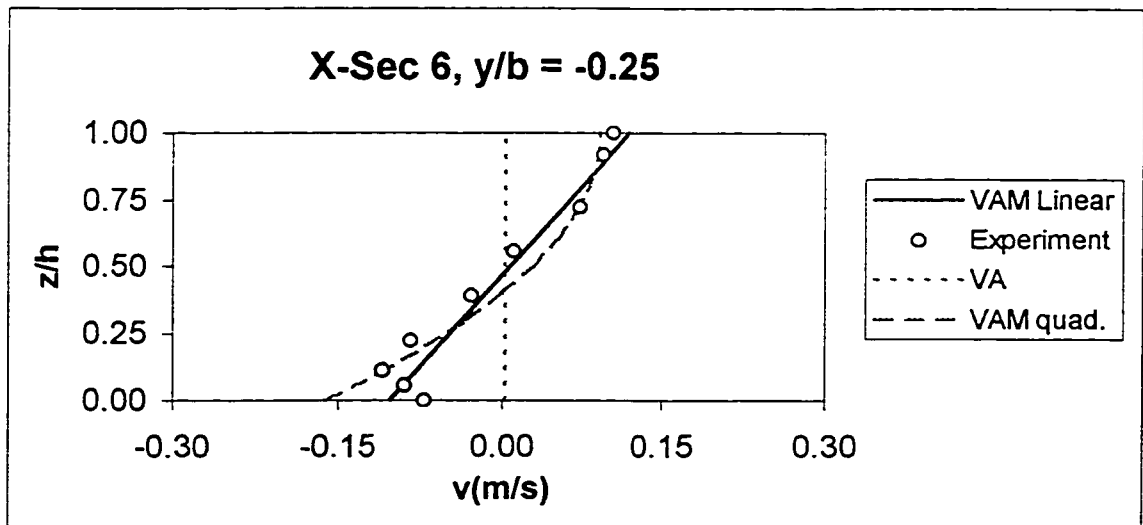


Figure 4.167 The comparison of transverse velocity profile for Rozovskii's (1961) run 1 at cross-section 6 and $y/b = -0.25$

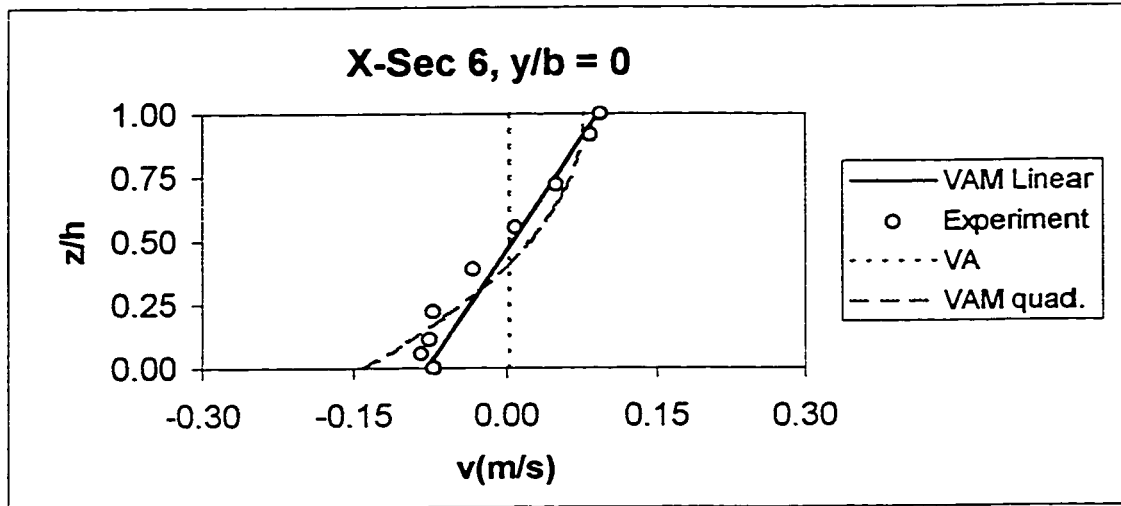


Figure 4.168 The comparison of transverse velocity profile for Rozovskii's (1961) run 1 at cross-section 6 and $y/b = 0$

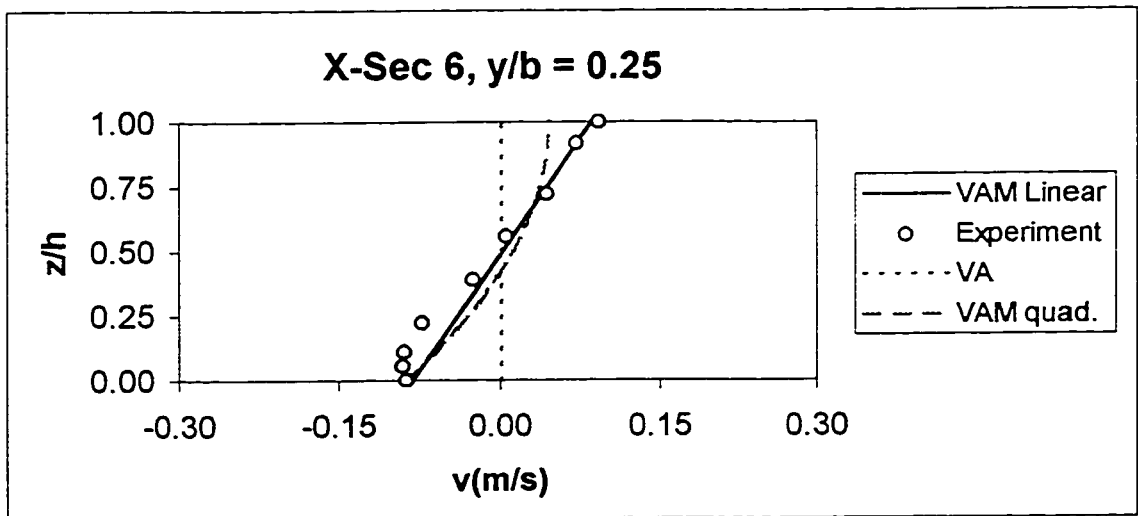


Figure 4.169 The comparison of transverse velocity profile for Rozovskii's (1961) run 1 at cross-section 6 and $y/b = 0.25$

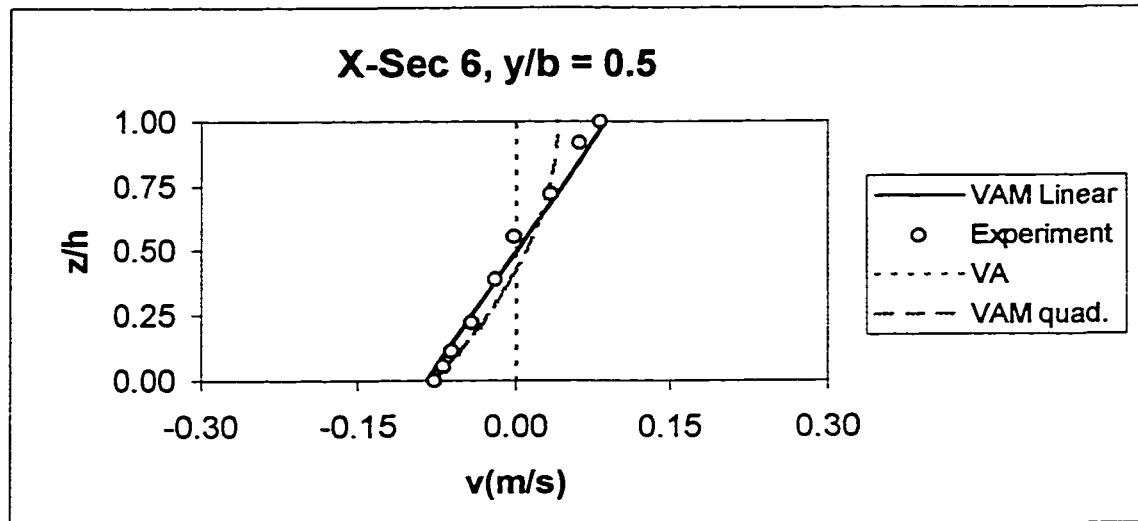


Figure 4.170 The comparison of transverse velocity profile for Rozovskii's (1961) run 1 at cross-section 6 and $y/b = 0.5$

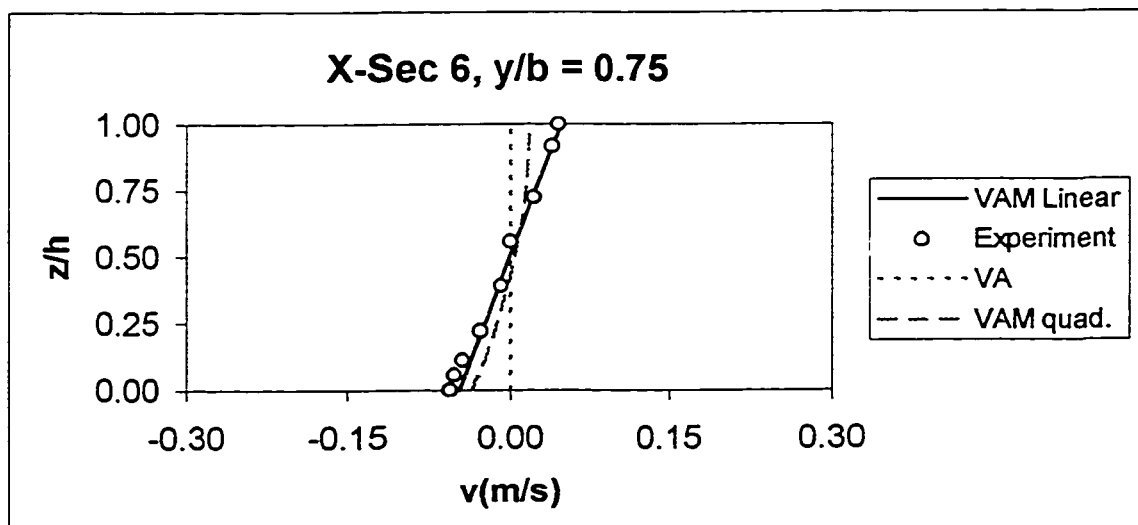


Figure 4.171 The comparison of transverse velocity profile for Rozovskii's (1961) run 1 at cross-section 6 and $y/b = 0.75$

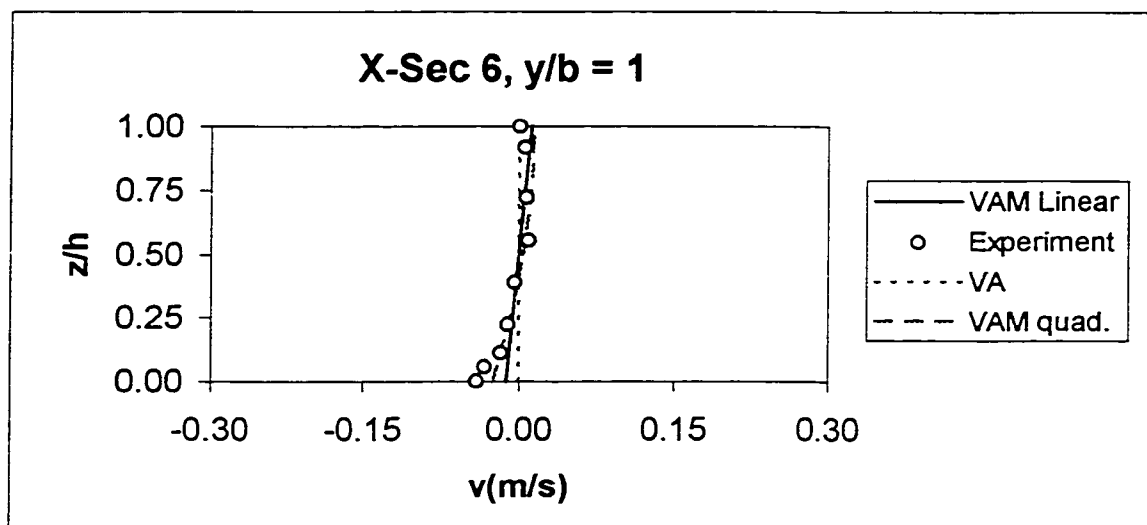


Figure 4.172 The comparison of transverse velocity profile for Rozovskii's (1961) run 1 at cross-section 6 and $y/b = 1$

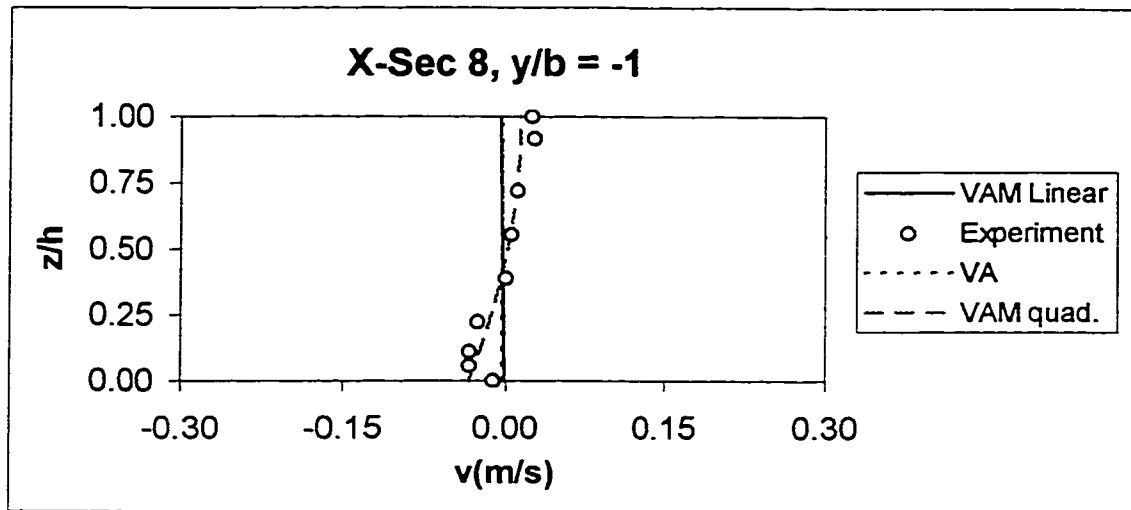


Figure 4.173 The comparison of transverse velocity profile for Rozovskii's (1961) run 1 at cross-section 8 and $y/b = -1$

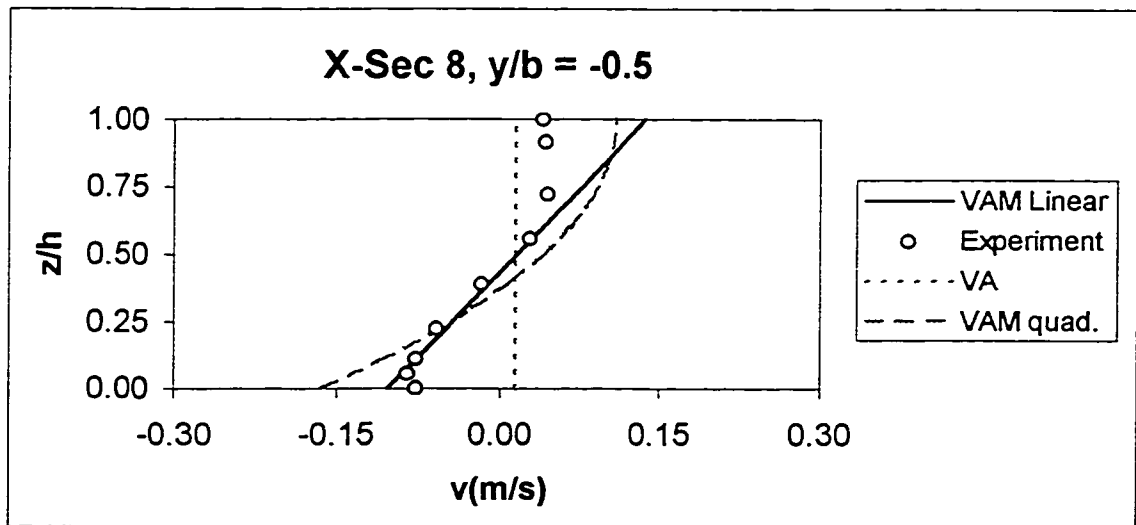


Figure 4.174 The comparison of transverse velocity profile for Rozovskii's (1961) run 1 at cross-section 8 and $y/b = -0.5$

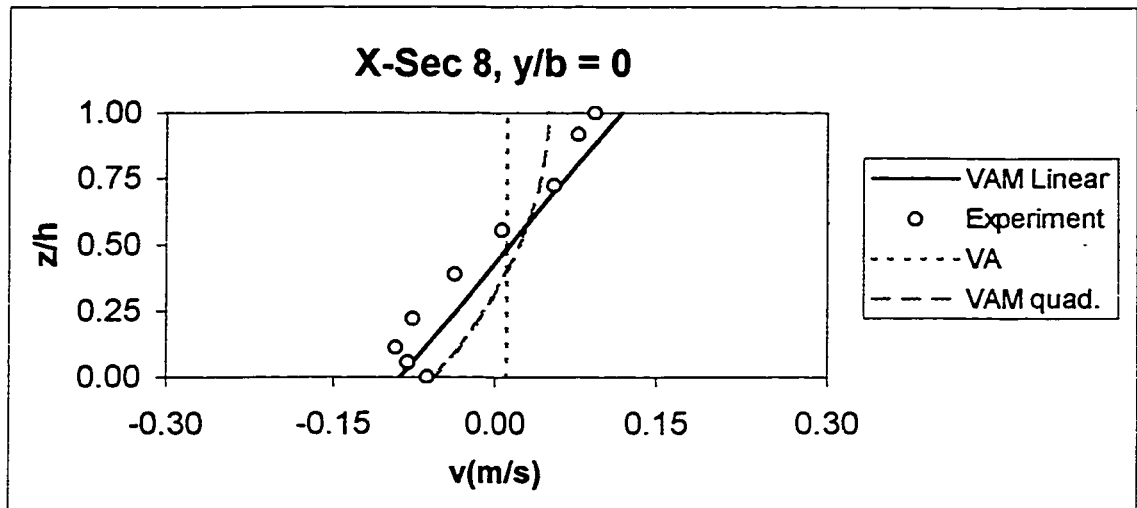


Figure 4.175 The comparison of transverse velocity profile for Rozovskii's (1961) run 1 at cross-section 8 and $y/b = 0$

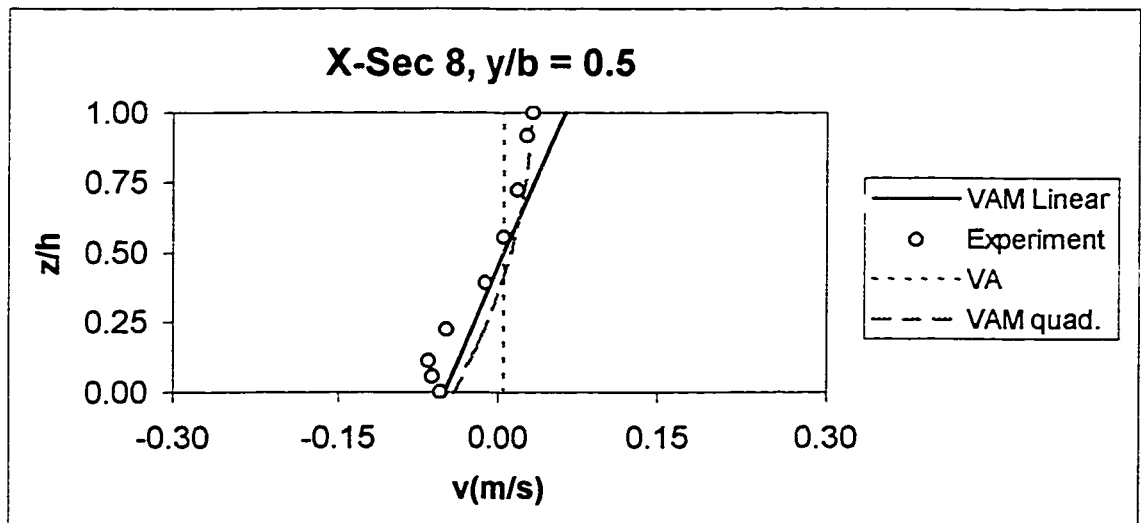


Figure 4.176 The comparison of transverse velocity profile for Rozovskii's (1961) run 1 at cross-section 8 and $y/b = 0.5$

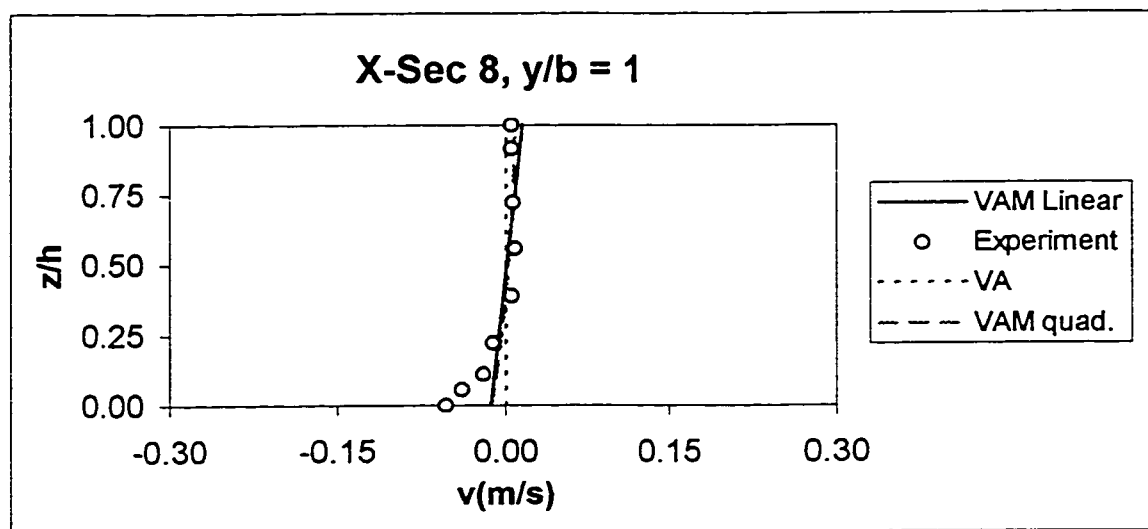


Figure 4.177 The comparison of transverse velocity profile for Rozovskii's (1961) run 1 at cross-section 8 and $y/b = 1$

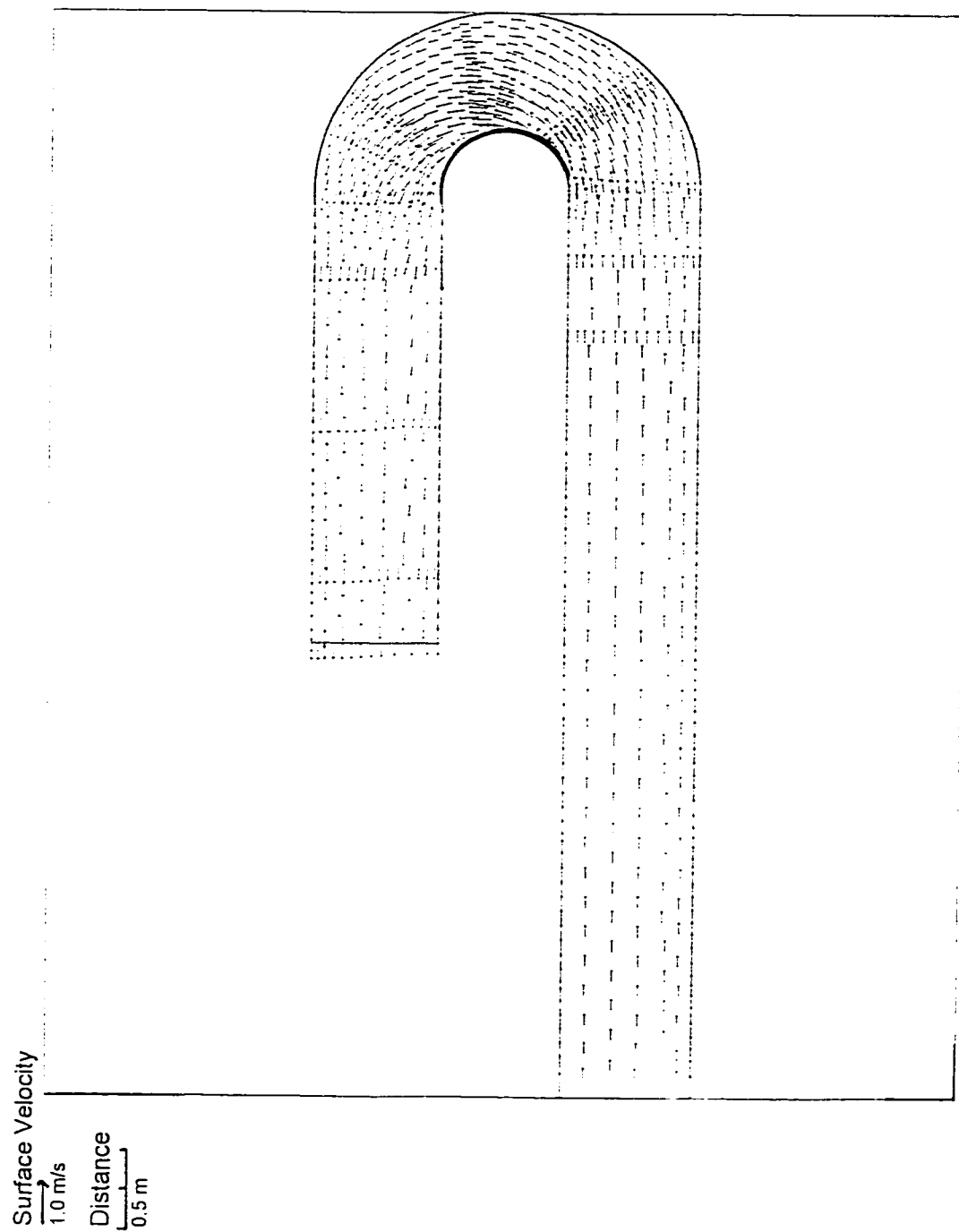


Figure 4.178 Numerical prediction of surface velocity distribution for Rozovskii's (1961) experiment (VAM model)

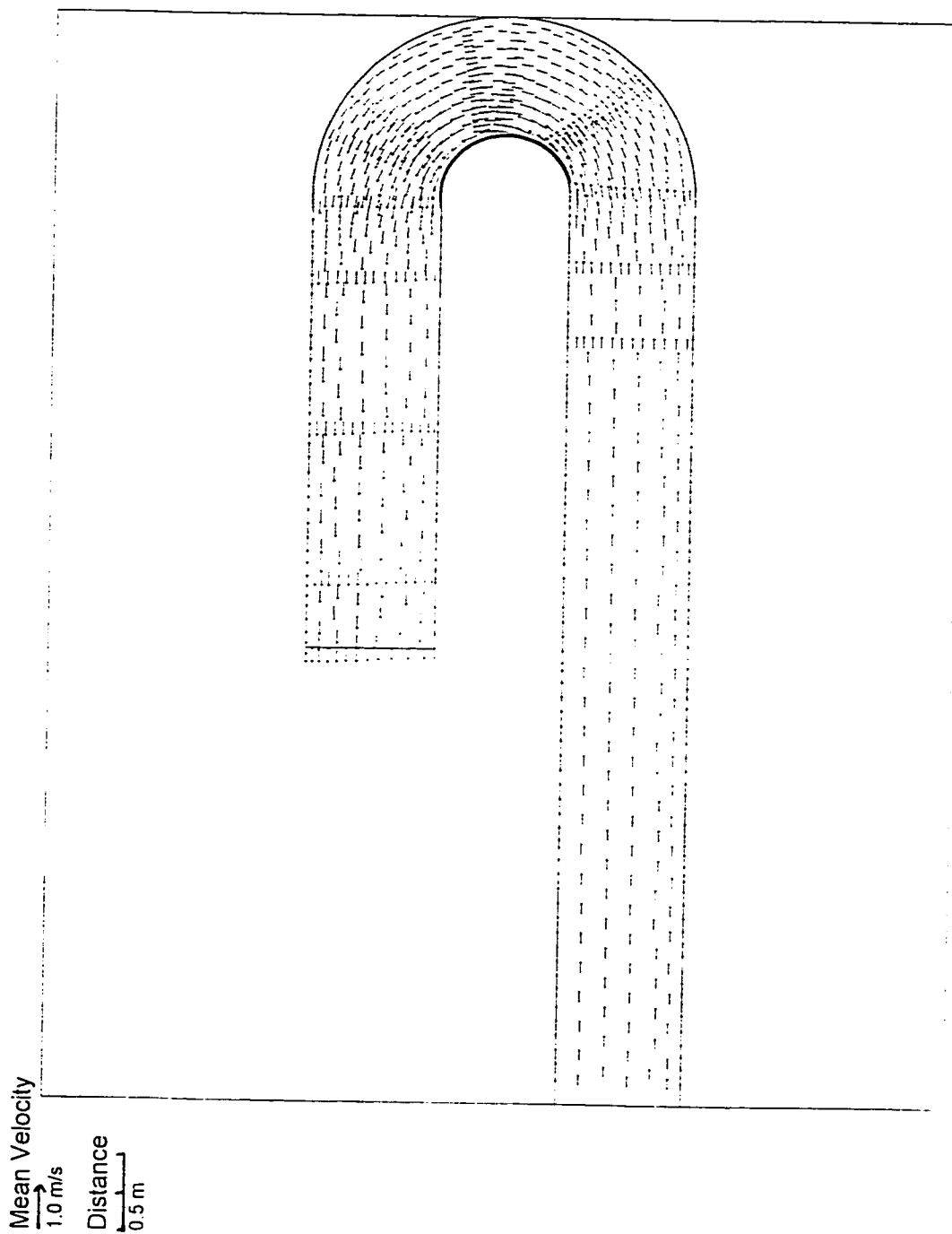


Figure 4.179 Numerical prediction of mean velocity distribution for Rozovskii's (1961) experiment (VAM model)

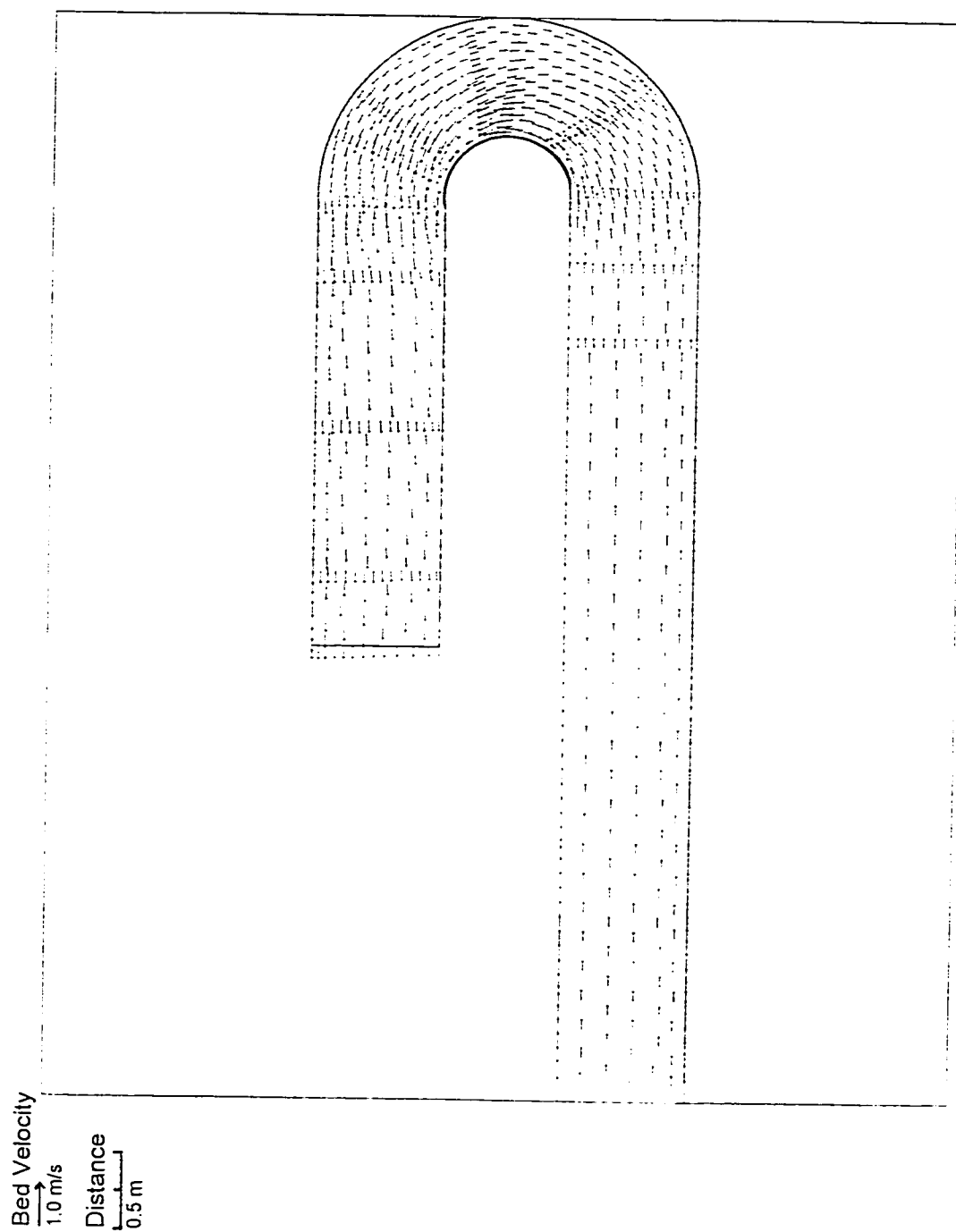


Figure 4.180 Numerical prediction of bed velocity distribution for Rozovskii's (1961) experiment (VAM model)

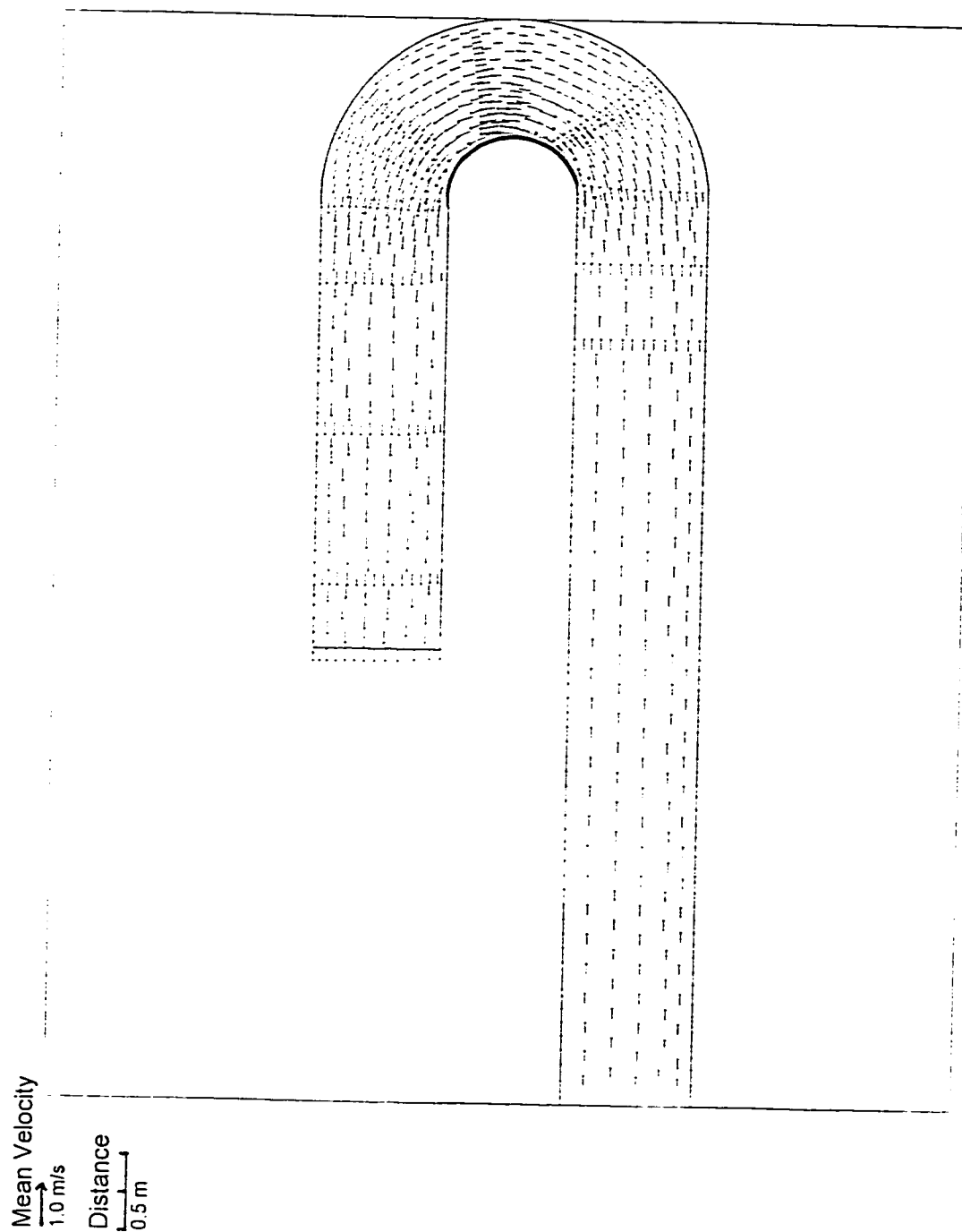


Figure 4.181 Numerical prediction of mean velocity distribution for Rozovskii's (1961) experiment (VA model)

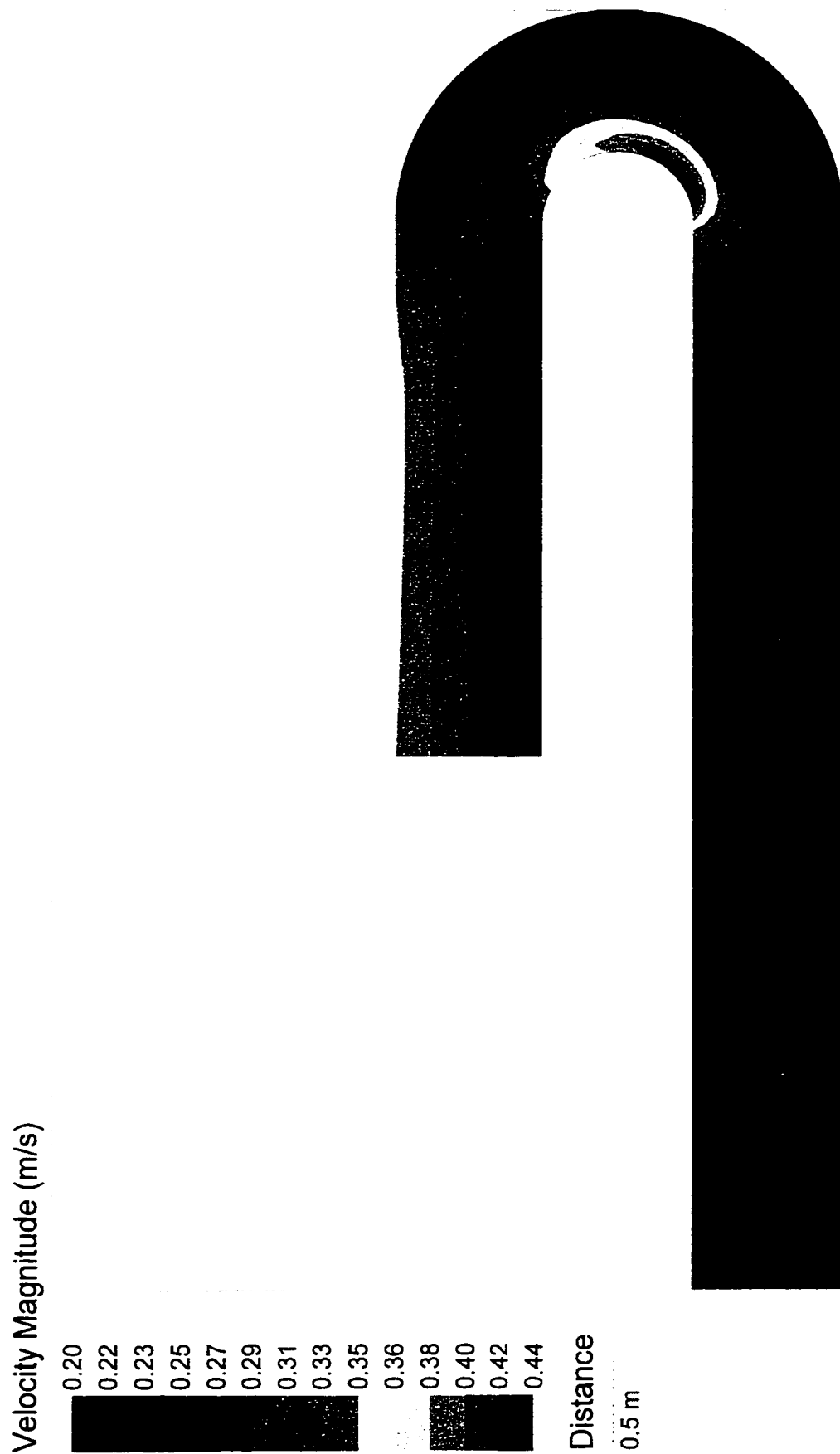


Figure 4.182 Numerical prediction of mean velocity contours for Rozovskii's (1961) experiment (VAM model)

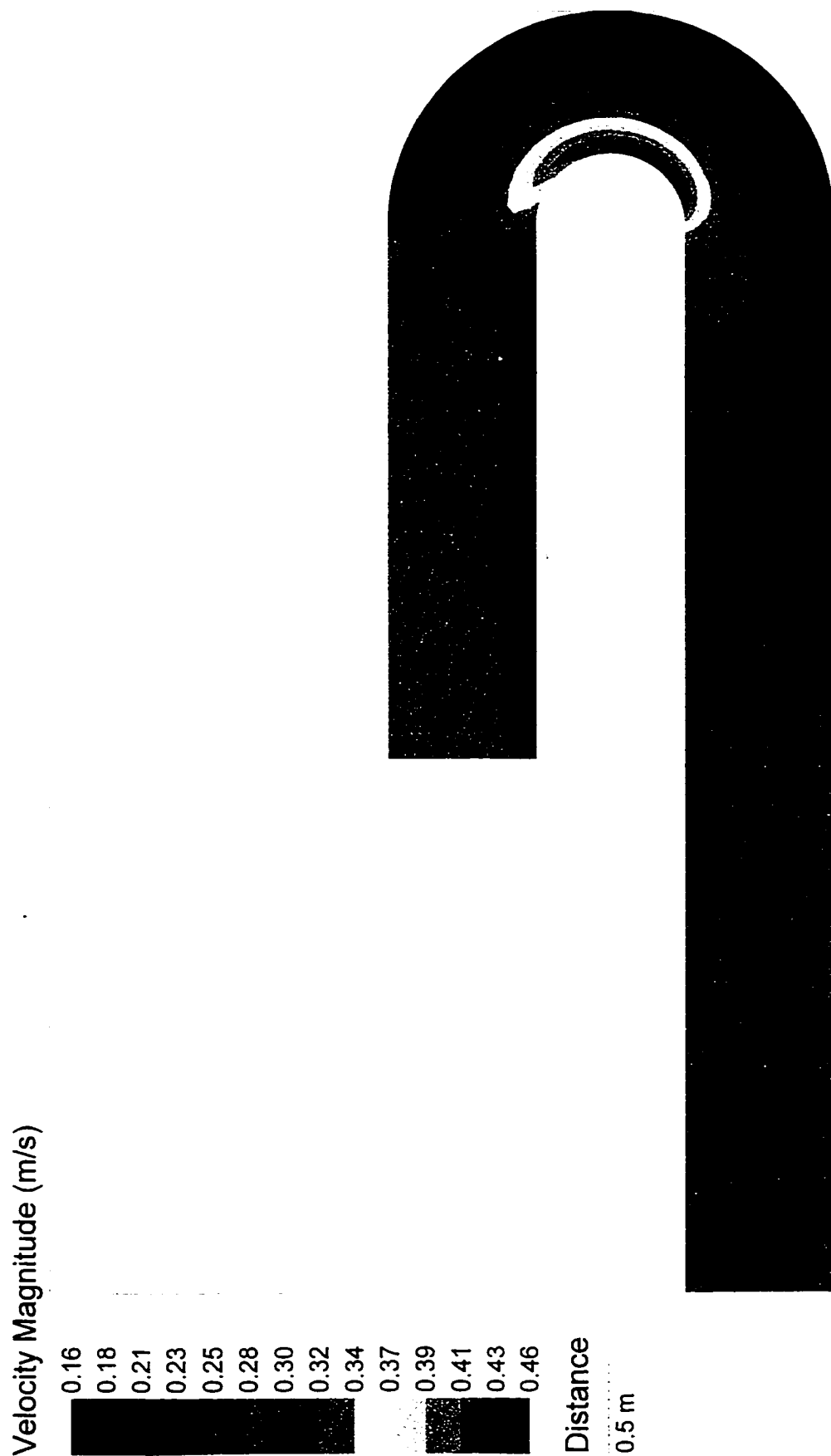


Figure 4.183 Numerical prediction of mean velocity contours for Rozovskii's (1961) experiment (VA model)

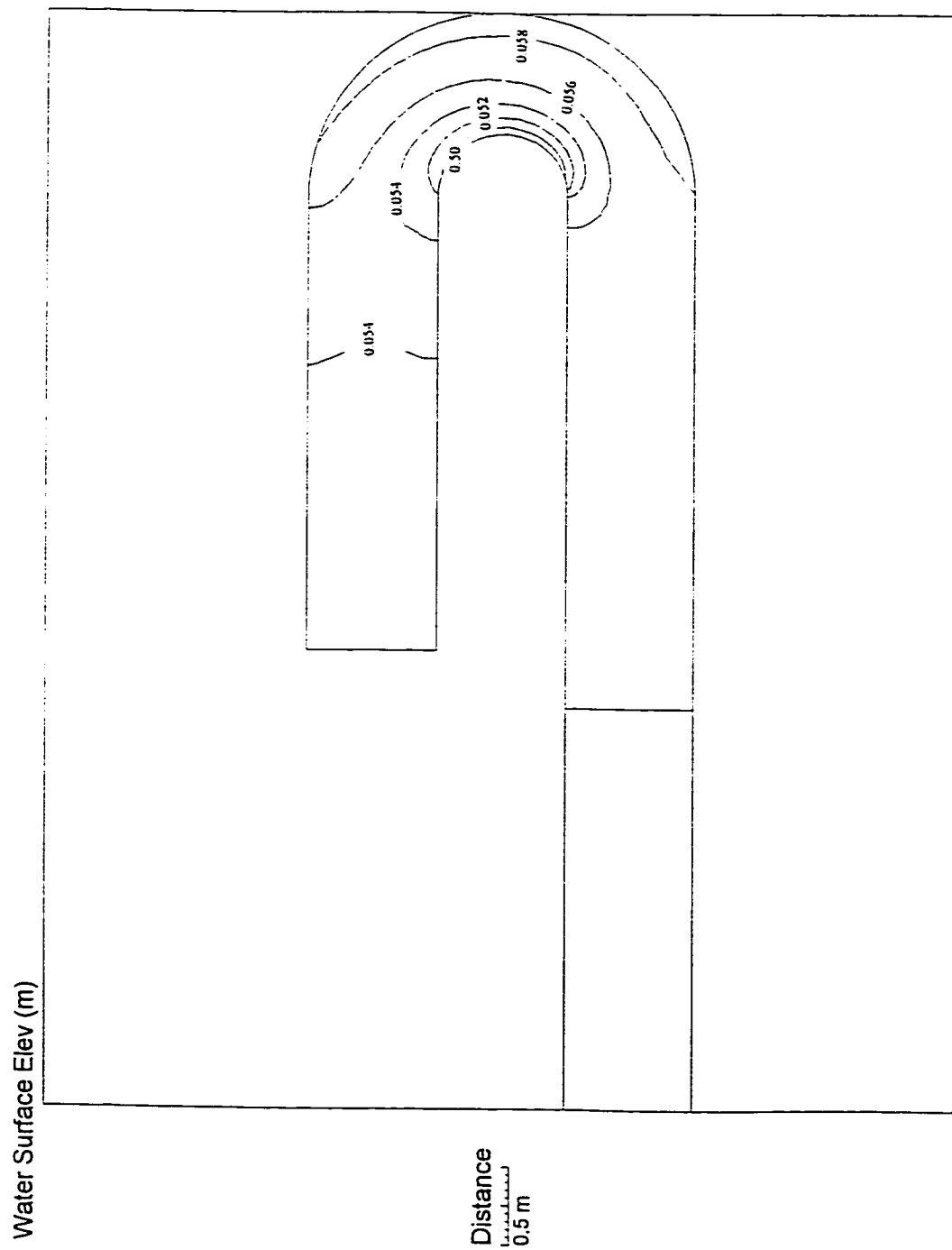


Figure 4.184 Numerical prediction of water surface elevation contours for Rozovskii's (1961) experiment (VAM model)

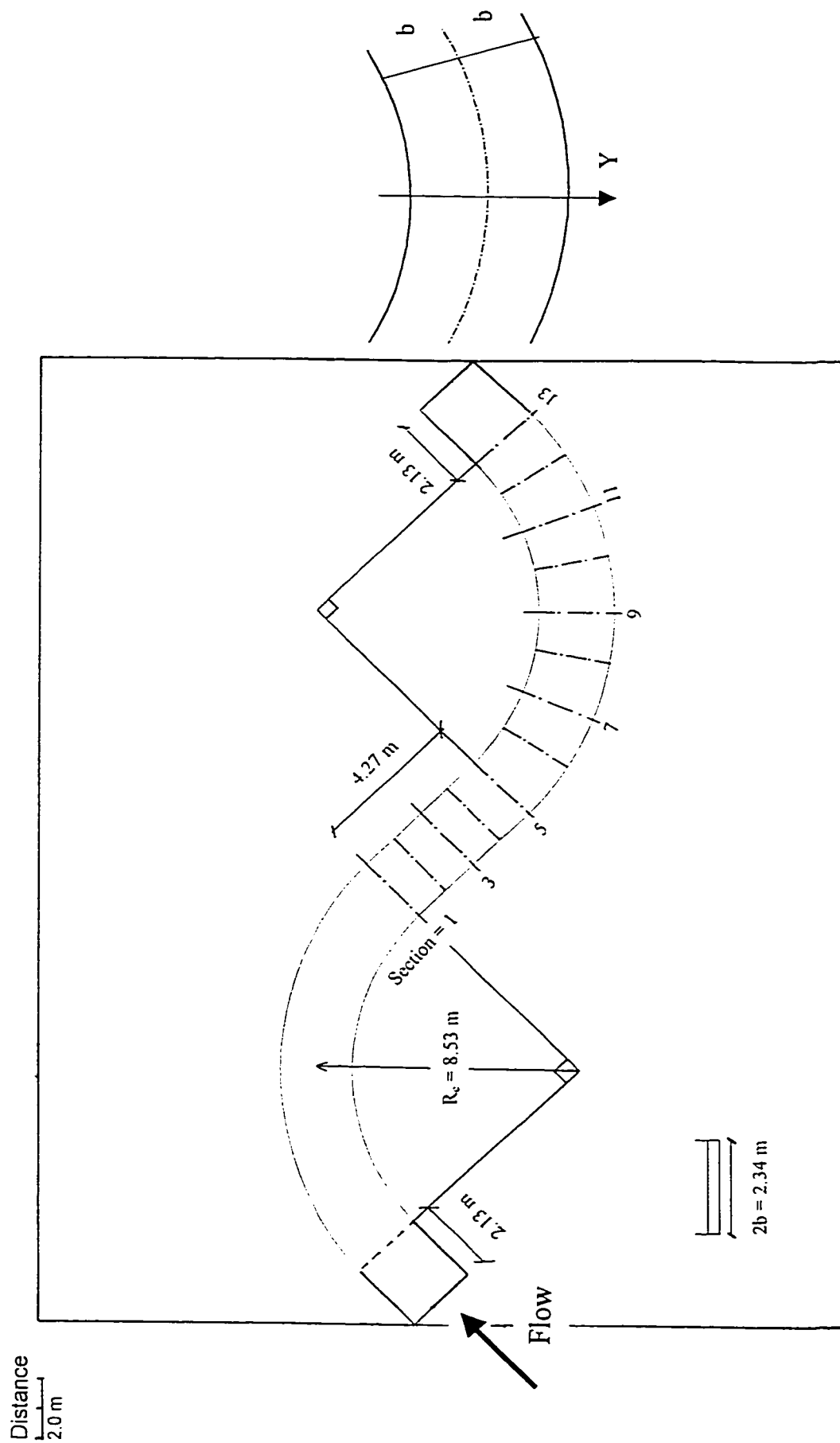
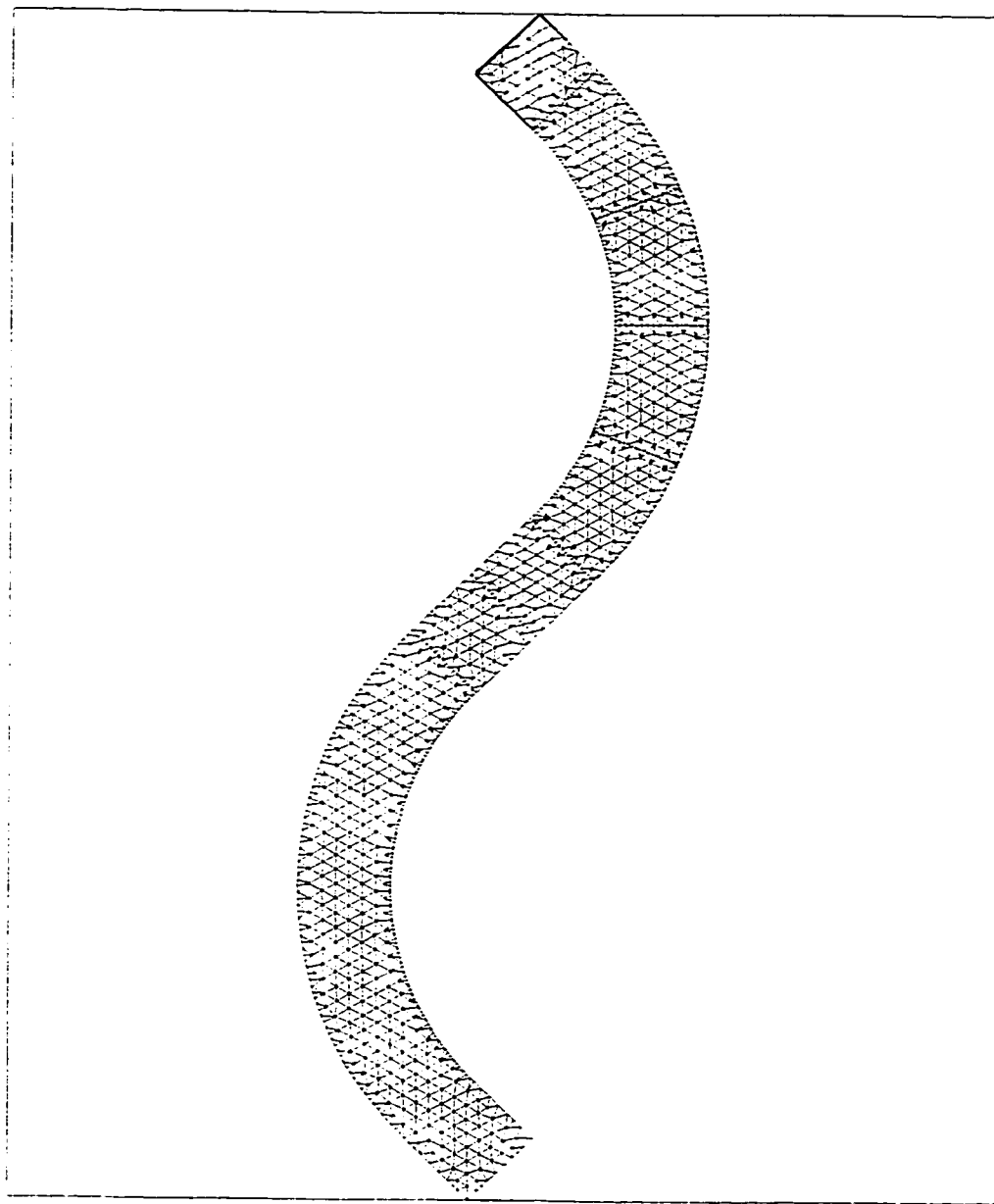


Figure 4.185 The layout of Chang's (1971) experiment

Distance
2.0 m



The generated mesh

Number of nodes = 1200

Number of elements = 1955

Figure 4.186 Finite element mesh for Chang's (1971) experiment

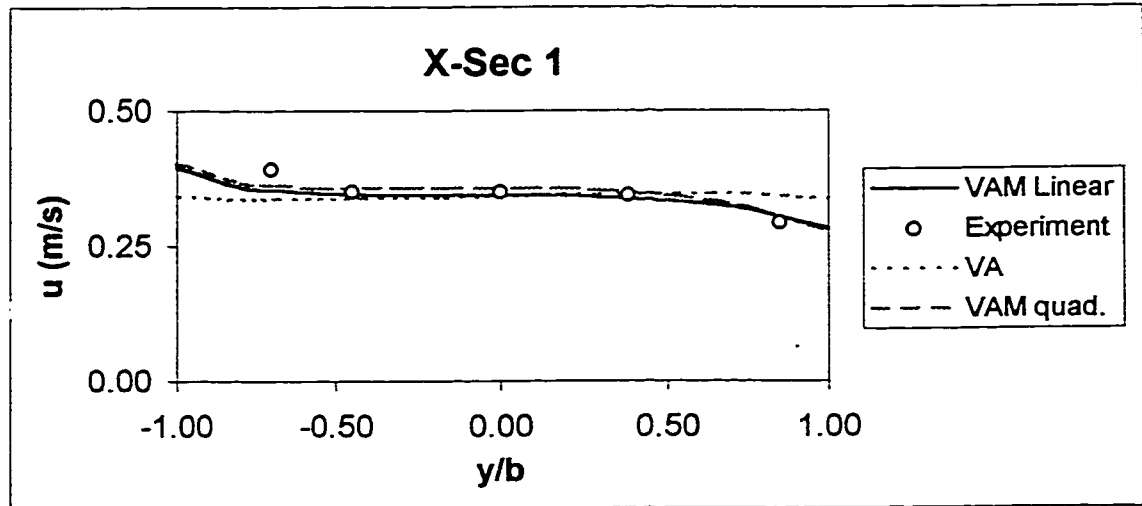


Figure 4.187 The comparison of longitudinal velocity distribution across the flume for Chang (1971) at cross-section 1

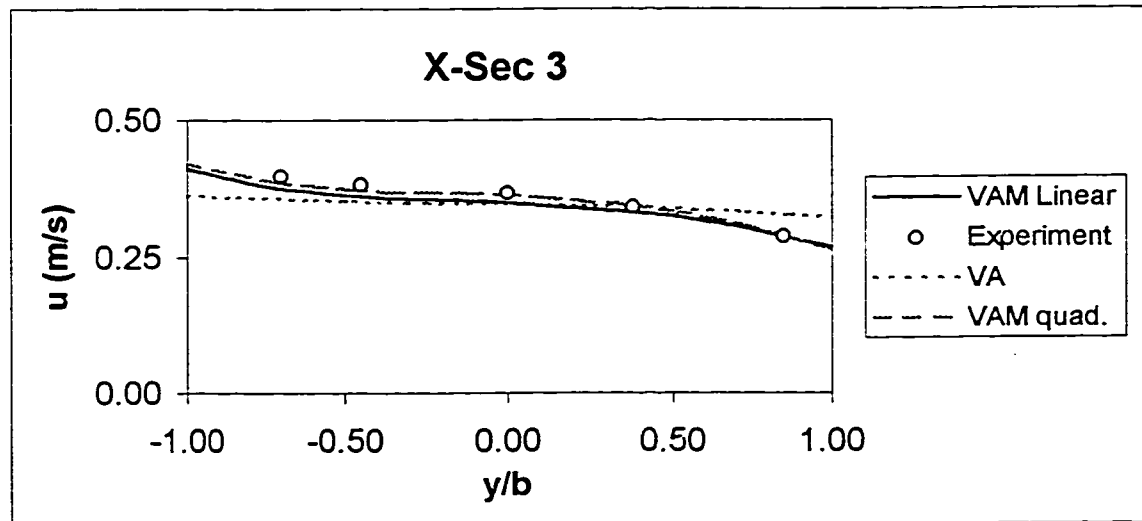


Figure 4.188 The comparison of longitudinal velocity distribution across the flume for Chang (1971) at cross-section 3

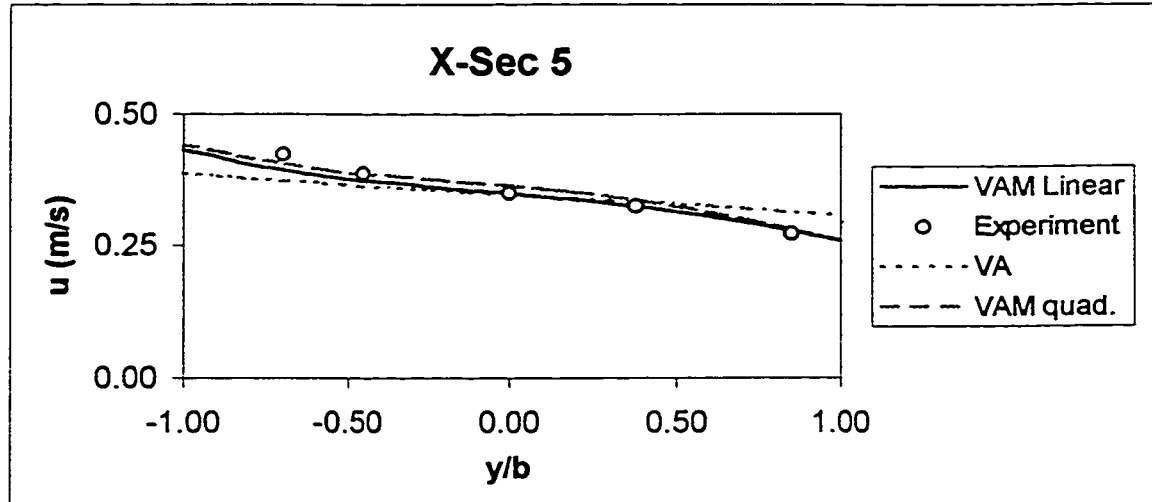


Figure 4.189 The comparison of longitudinal velocity distribution across the flume for Chang (1971) at cross-section 5

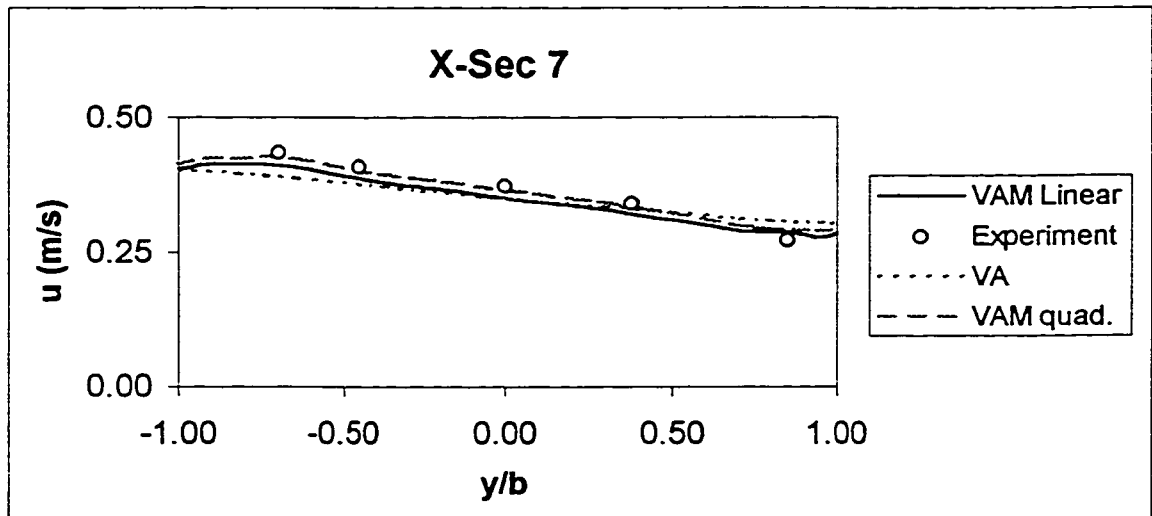


Figure 4.190 The comparison of longitudinal velocity distribution across the flume for Chang (1971) at cross-section 7

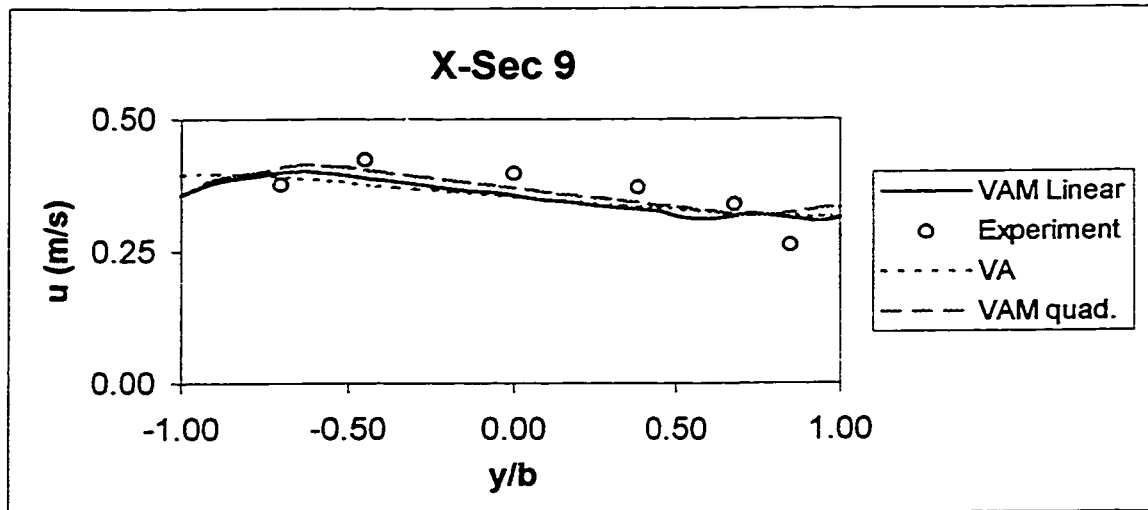


Figure 4.191 The comparison of longitudinal velocity distribution across the flume for Chang (1971) at cross-section 9

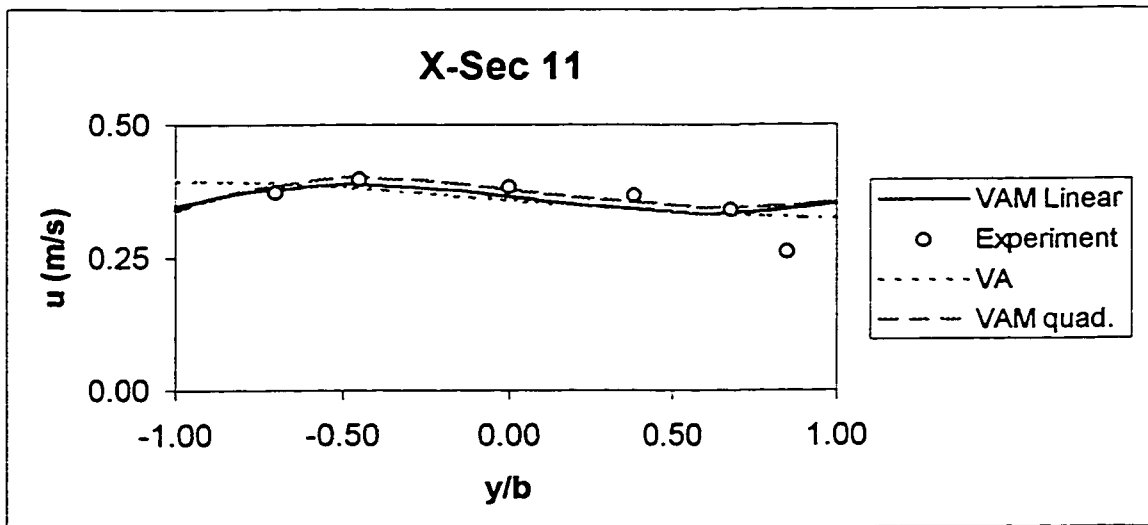


Figure 4.192 The comparison of longitudinal velocity distribution across the flume for Chang (1971) at cross-section 11

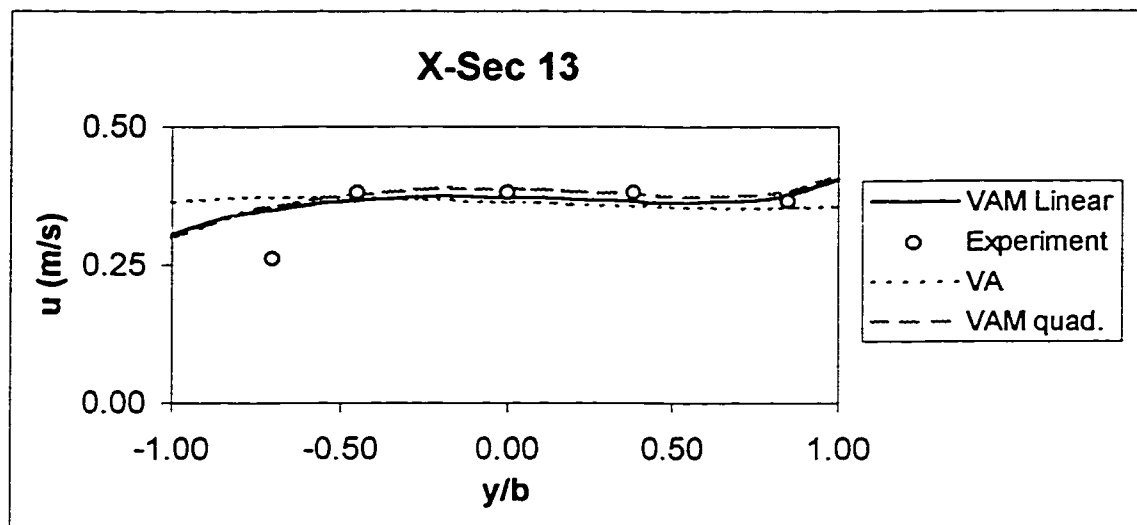


Figure 4.193 The comparison of longitudinal velocity distribution across the flume for Chang (1971) at cross-section 13

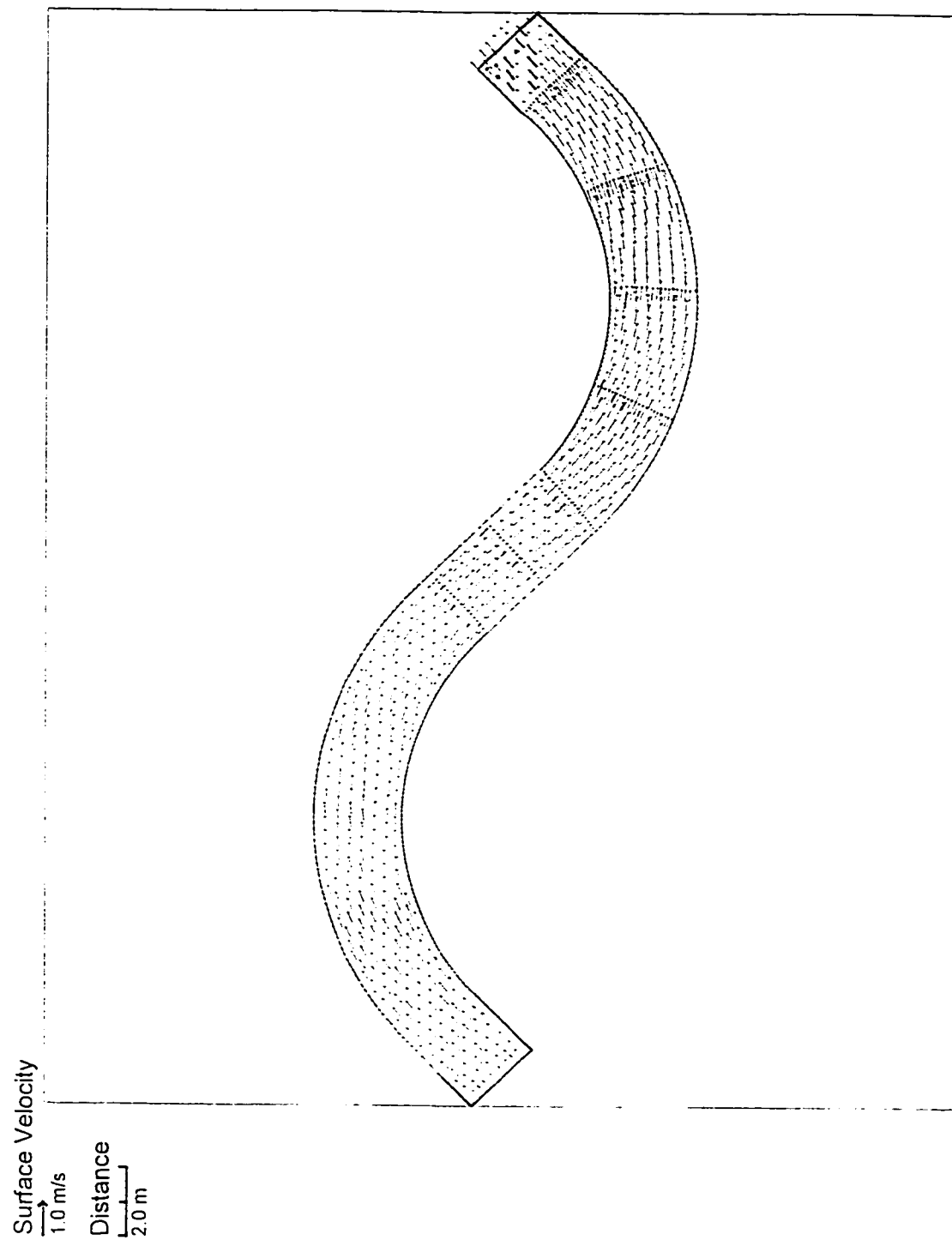


Figure 4.194 Numerical prediction of surface velocity distribution for Chang's (1971) experiment (VAM model)

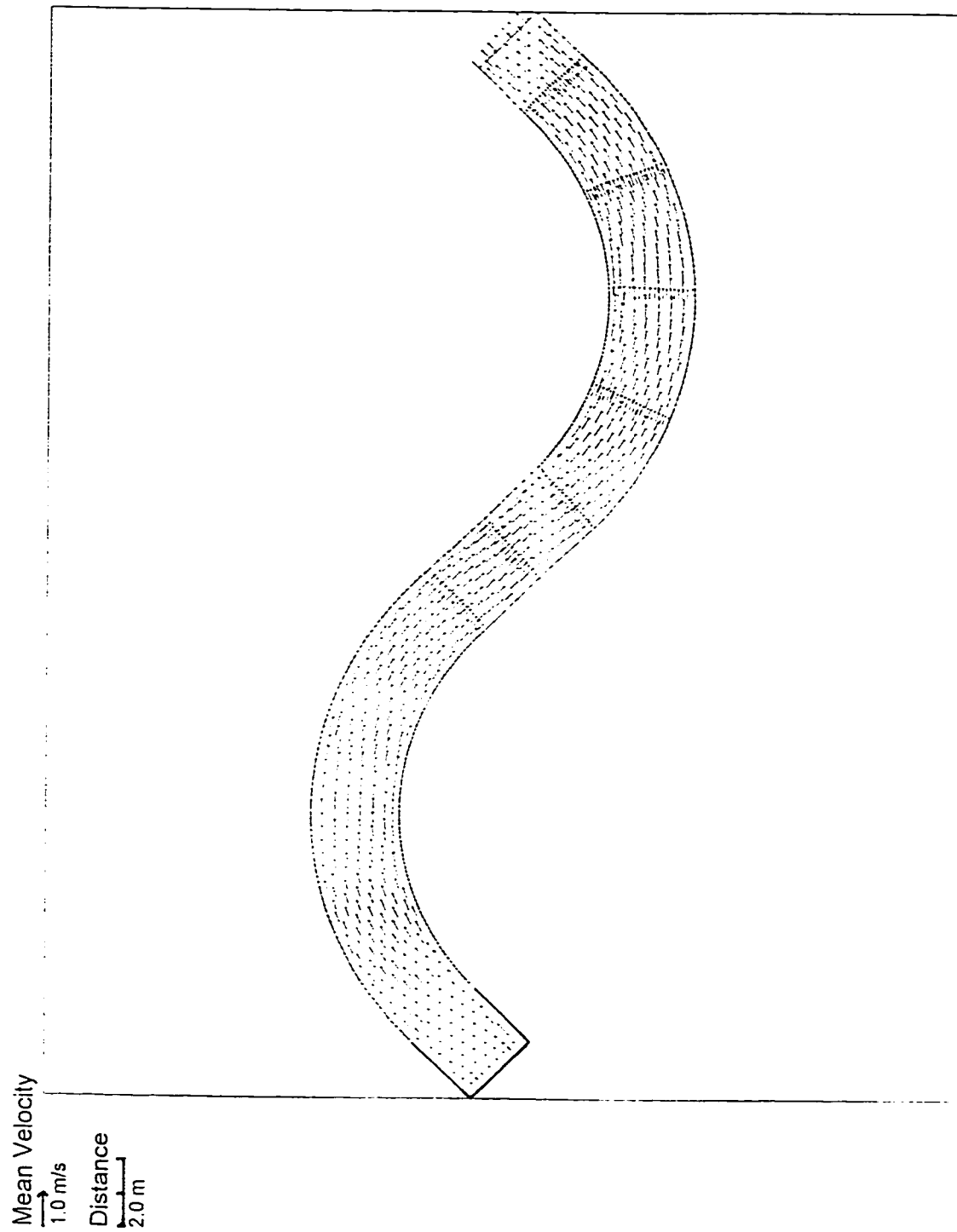


Figure 4.195 Numerical prediction of mean velocity distribution for Chang's (1971) experiment (VAM model)

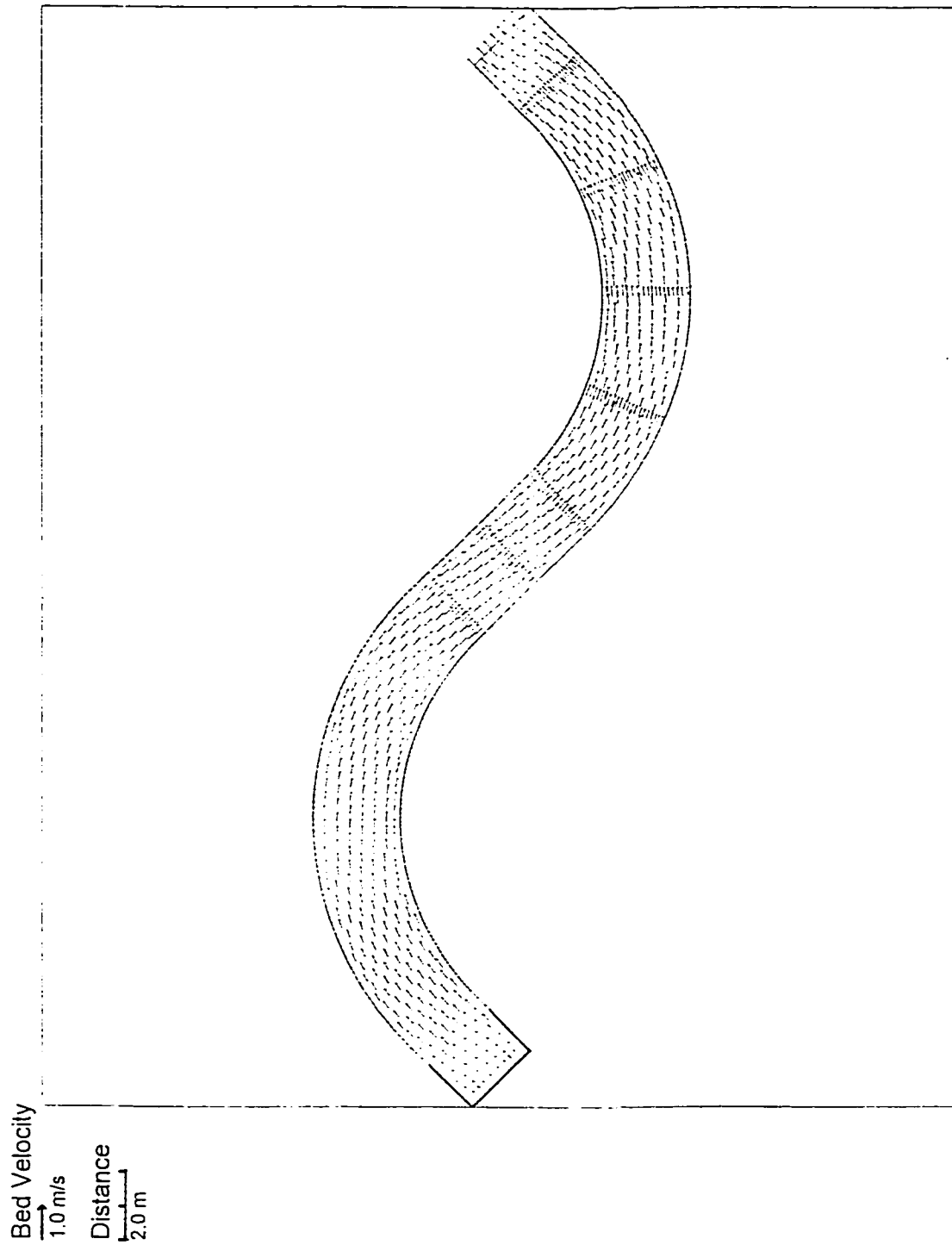


Figure 4.196 Numerical prediction of bed velocity distribution for Chang's (1971) experiment (VAM model)

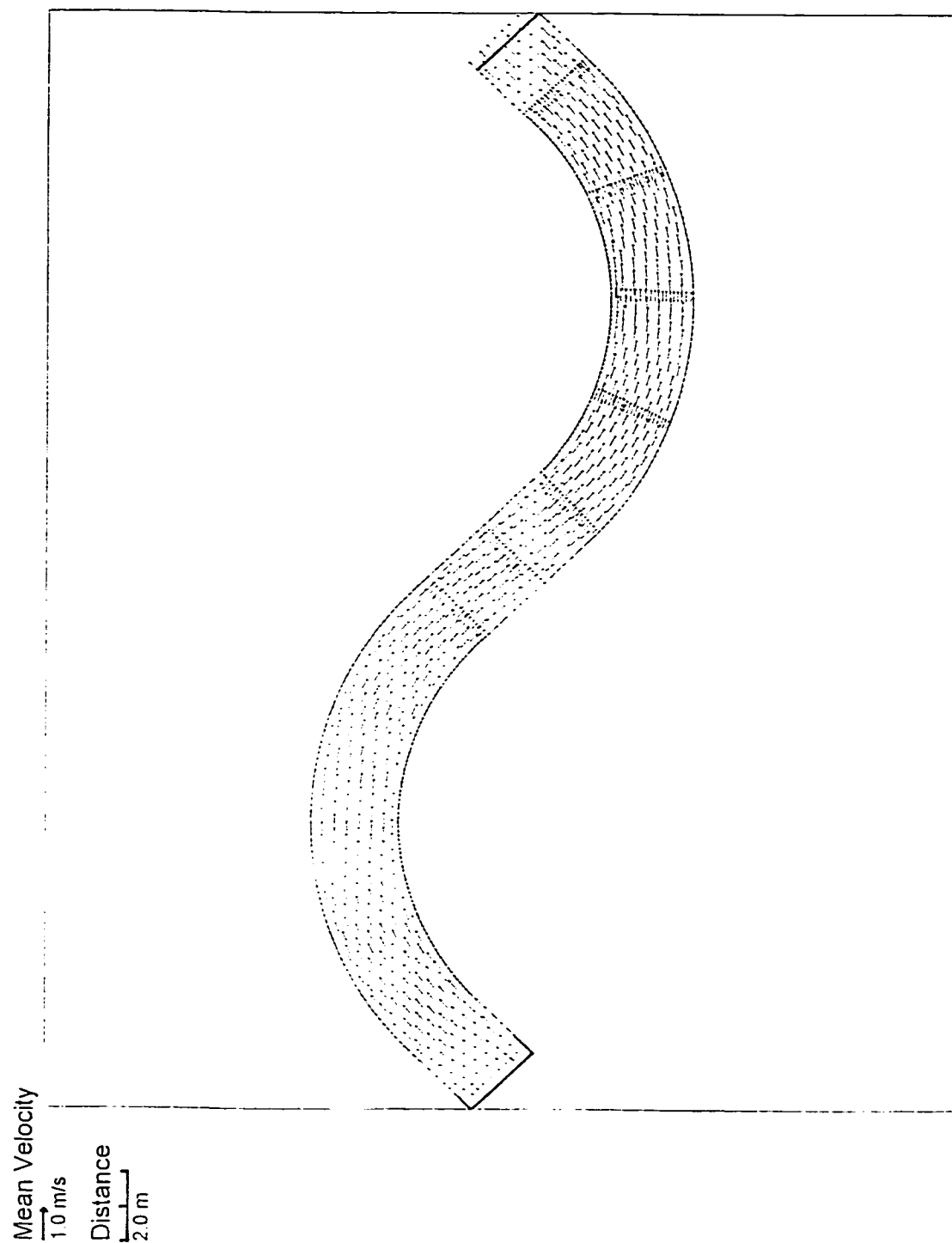


Figure 4.197 Numerical prediction of mean velocity distribution for Chang's (1971) experiment (VA model)

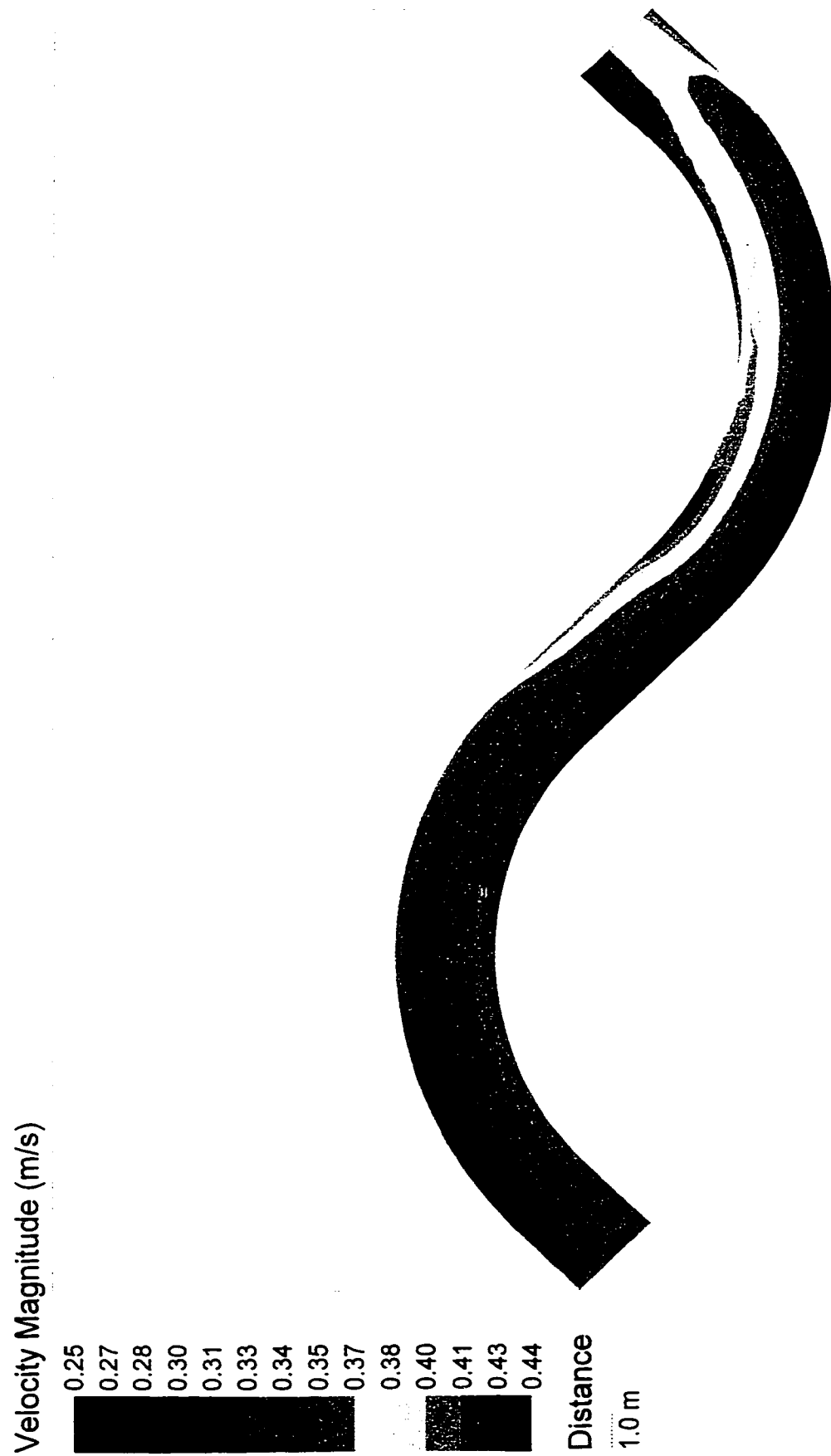


Figure 4.198 Numerical prediction of mean velocity contours for Chang's (1971) experiment (VAM model)

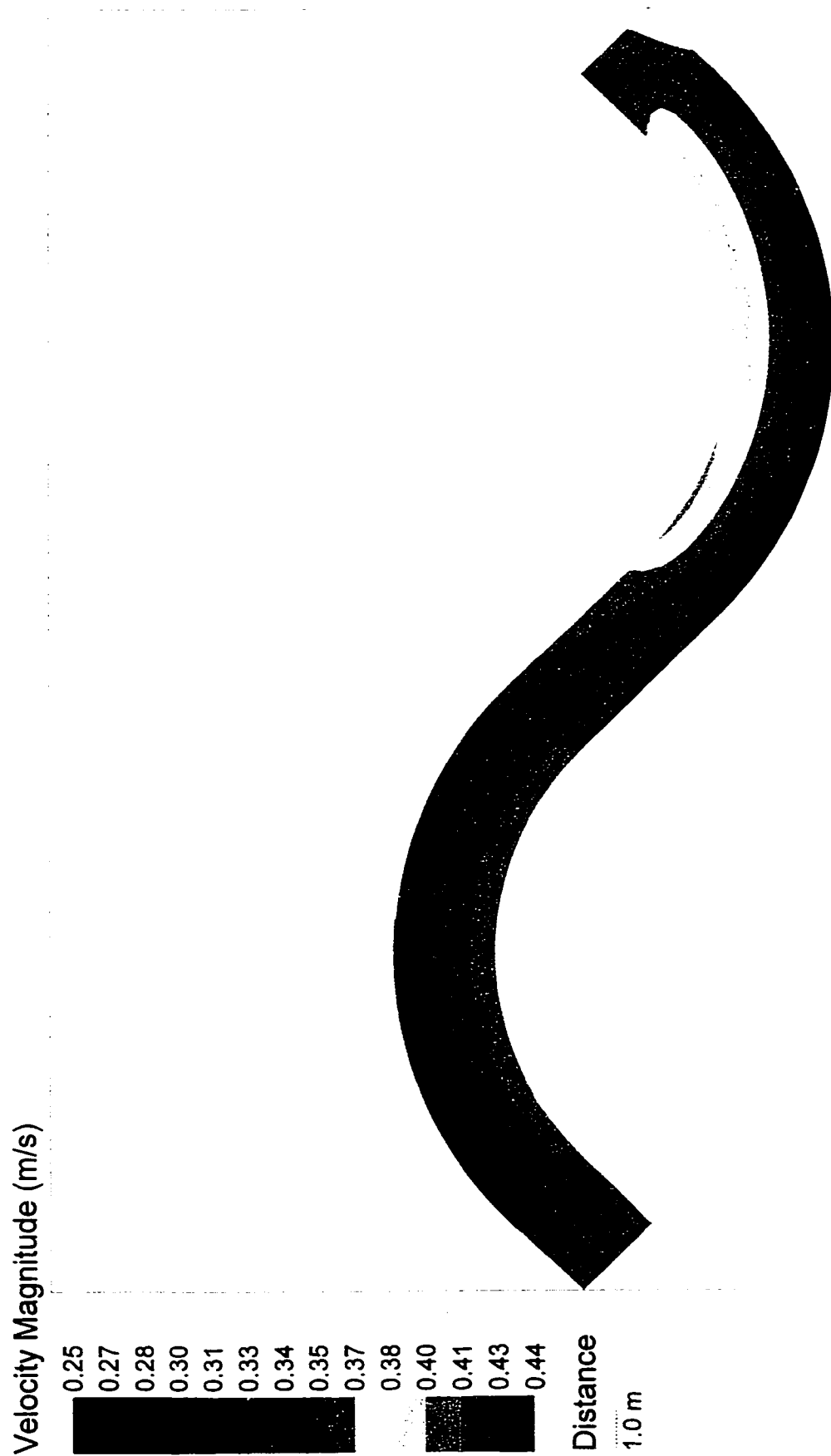


Figure 4.199 Numerical prediction of mean velocity contours for Chang's (1971) experiment (VA model)

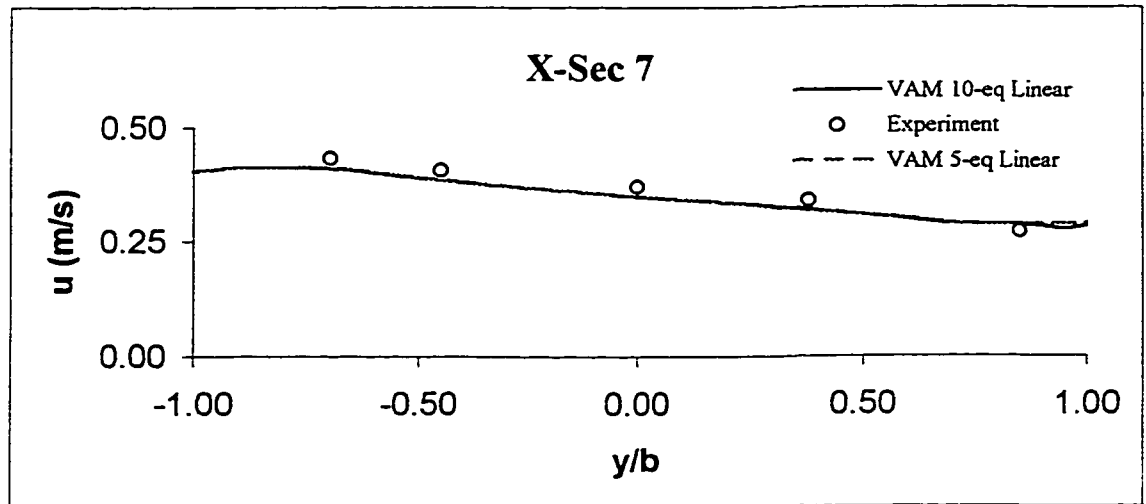


Figure 4.200 The comparison of applying VAM 5- against 10-equation models for longitudinal velocity distribution across the flume for Chang's (1971) at cross-section 7

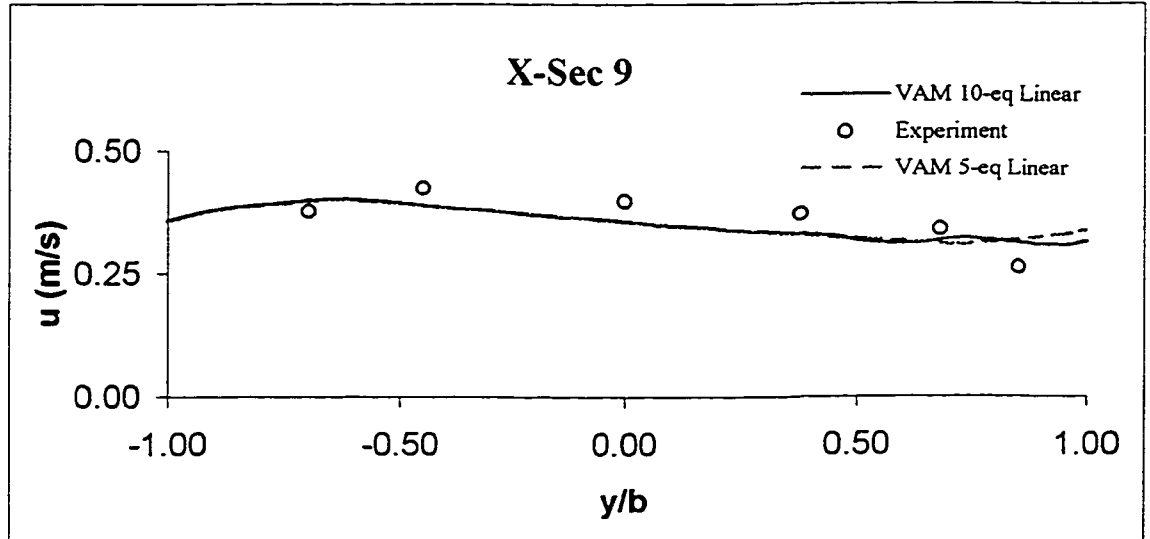


Figure 4.201 The comparison of applying VAM 5- against 10-equation models for longitudinal velocity distribution across the flume for Chang's (1971) at cross-section 9

Distance
1.0 m

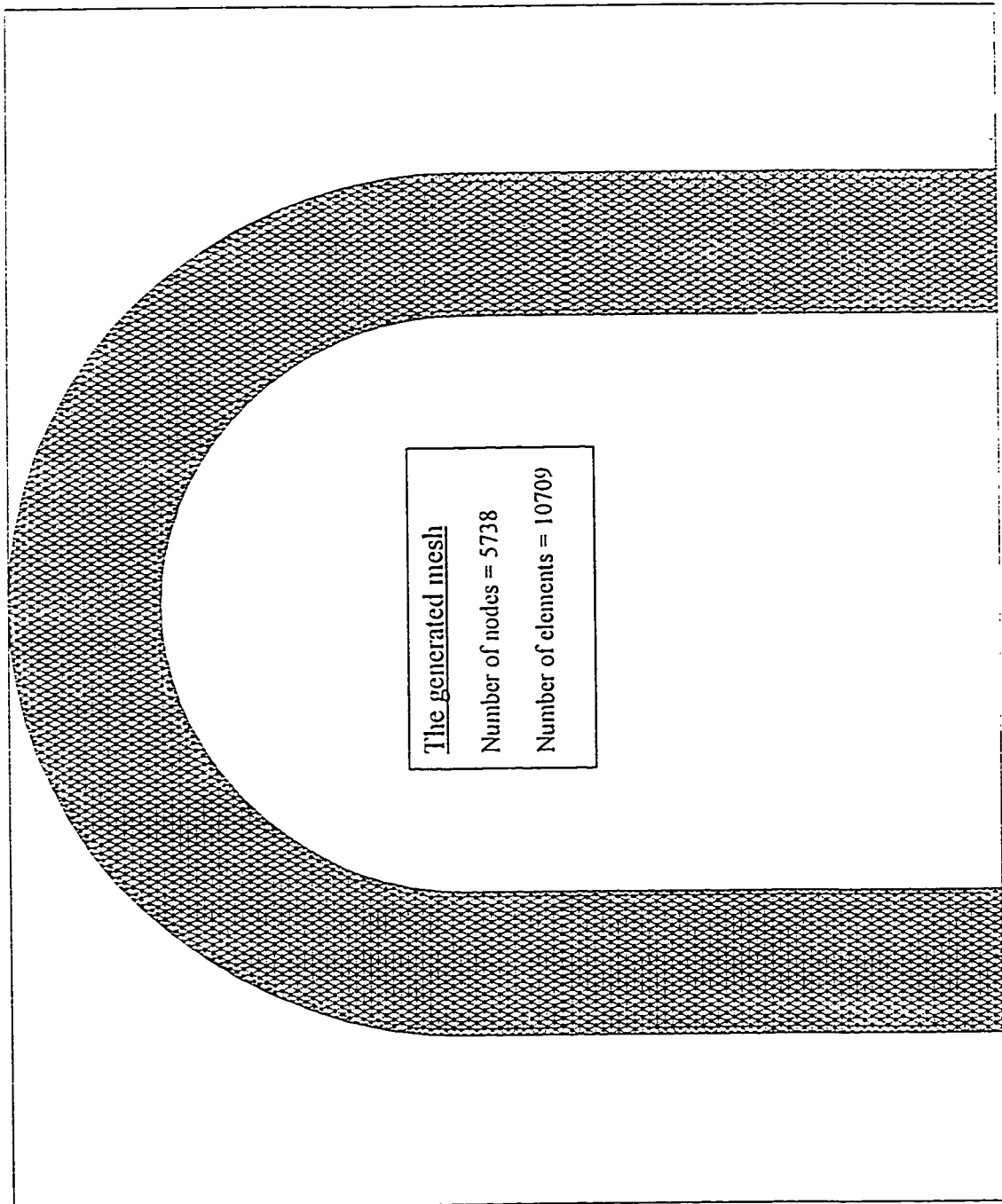


Figure 4.202 Refined generated finite element mesh for DeVriend's (1976) experiment

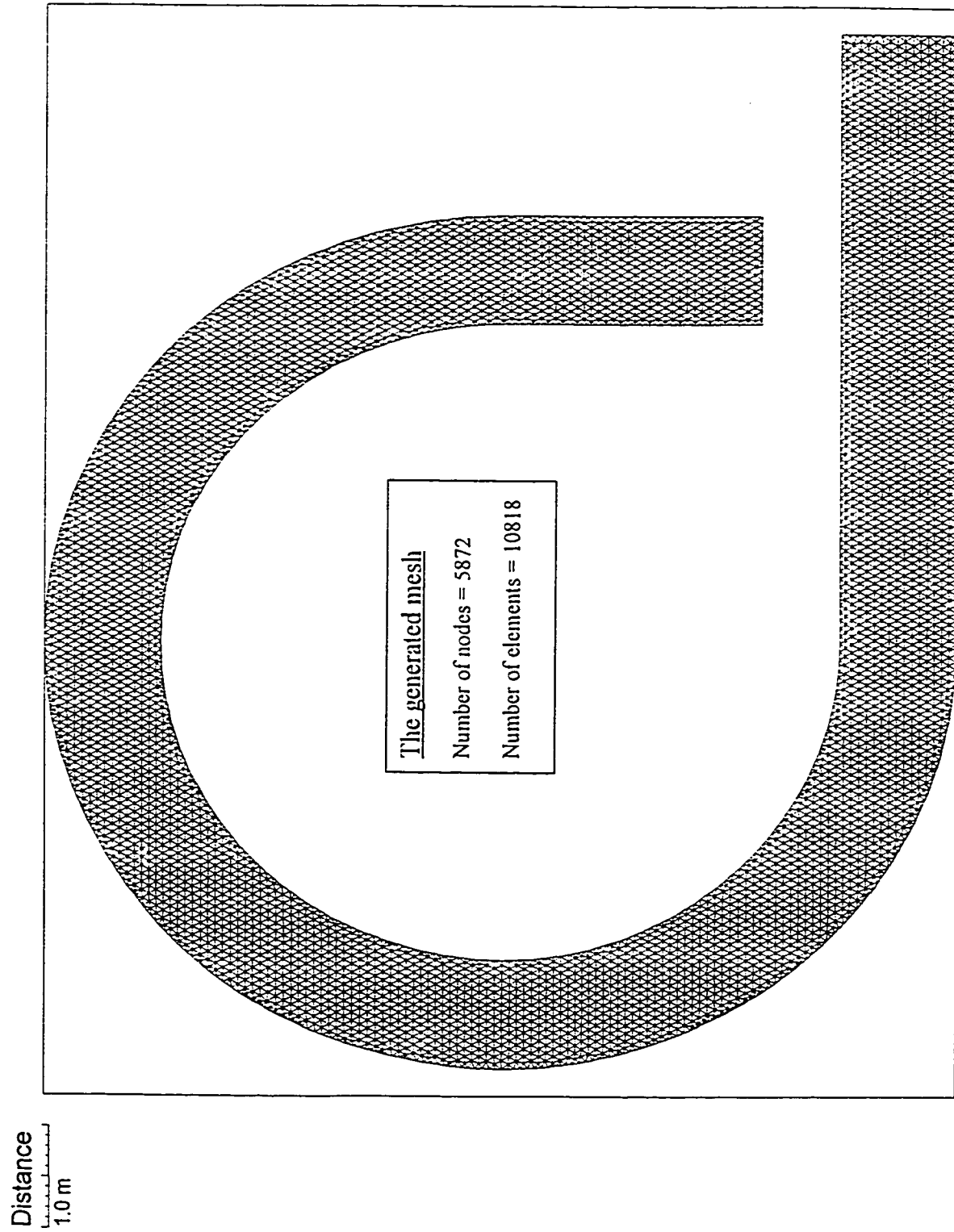


Figure 4.203 Refined generated finite element mesh for Steffler's (1984) experiment

Distance
2.0 m

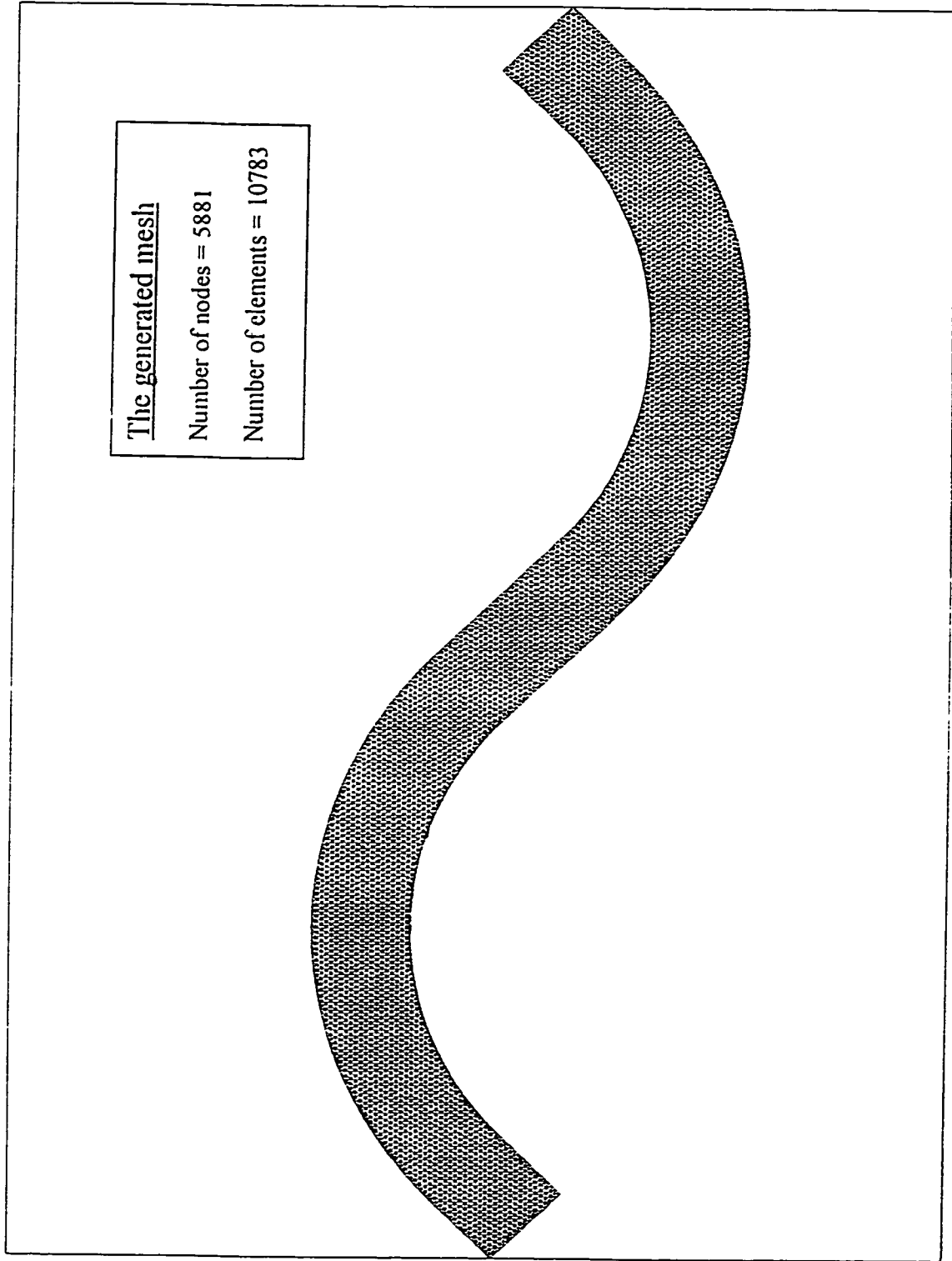


Figure 4.204 Refined generated finite element mesh for Chang's (1971) experiment

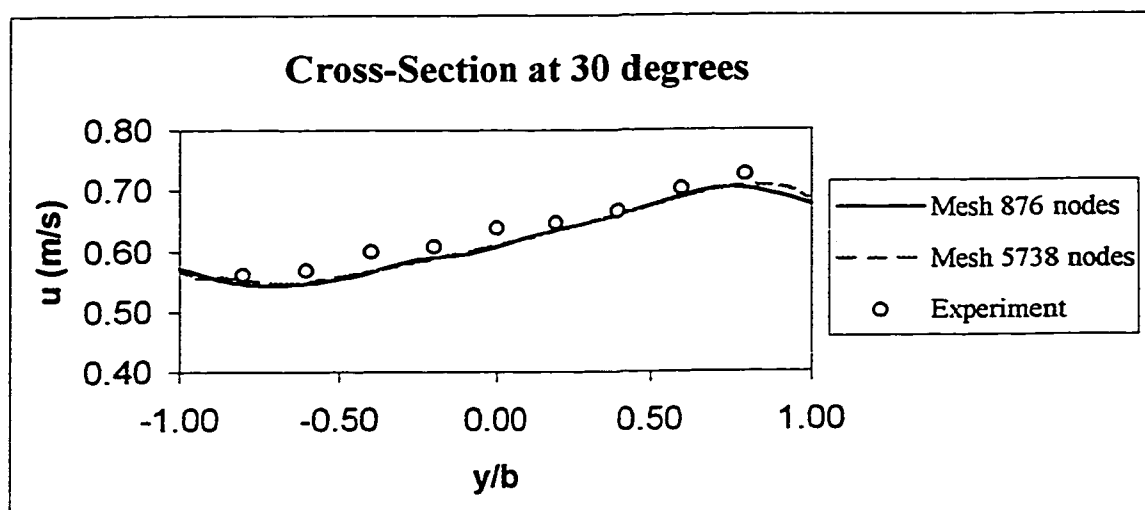


Figure 4.205 The comparison of the longitudinal velocity distribution across the flume for DeVriend (1976) at cross-section 30 degrees for two different generated finite element meshes

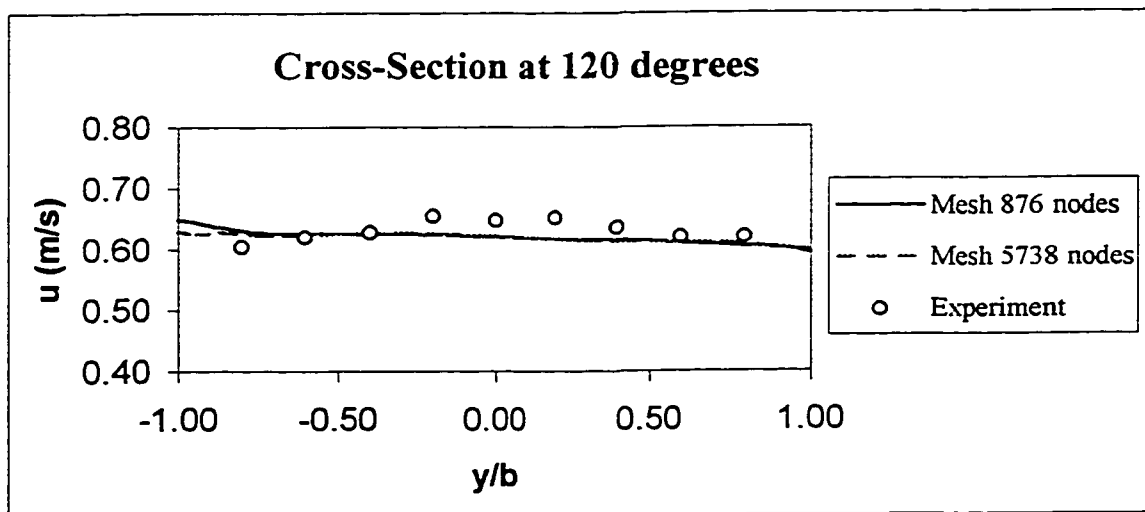


Figure 4.206 The comparison of the longitudinal velocity distribution across the flume for DeVriend (1976) at cross-section 120 degrees for two different generated finite element meshes

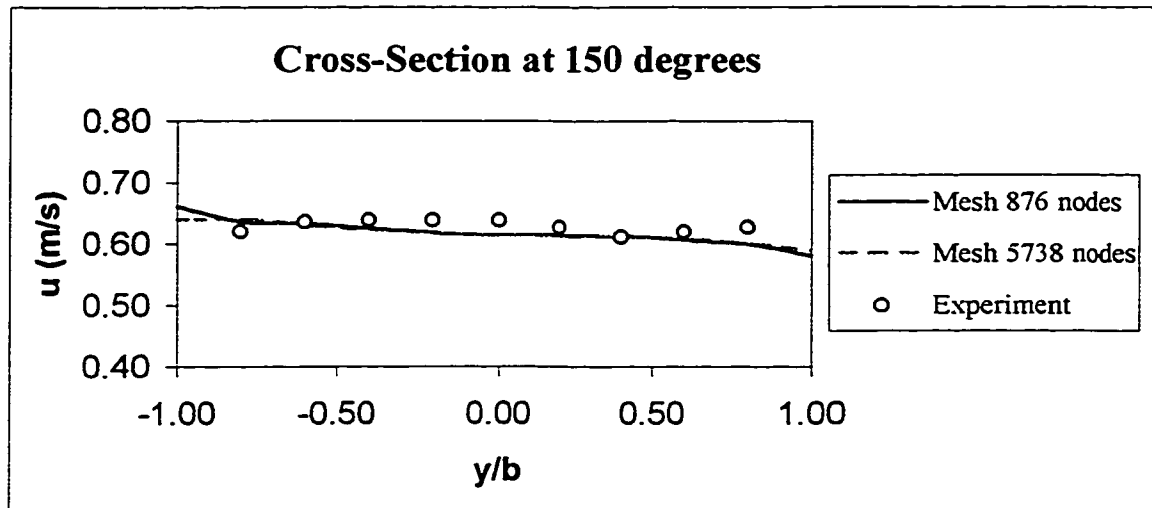


Figure 4.207 The comparison of the longitudinal velocity distribution across the flume for DeVriend (1976) at cross-section 150 degrees for two different generated finite element meshes

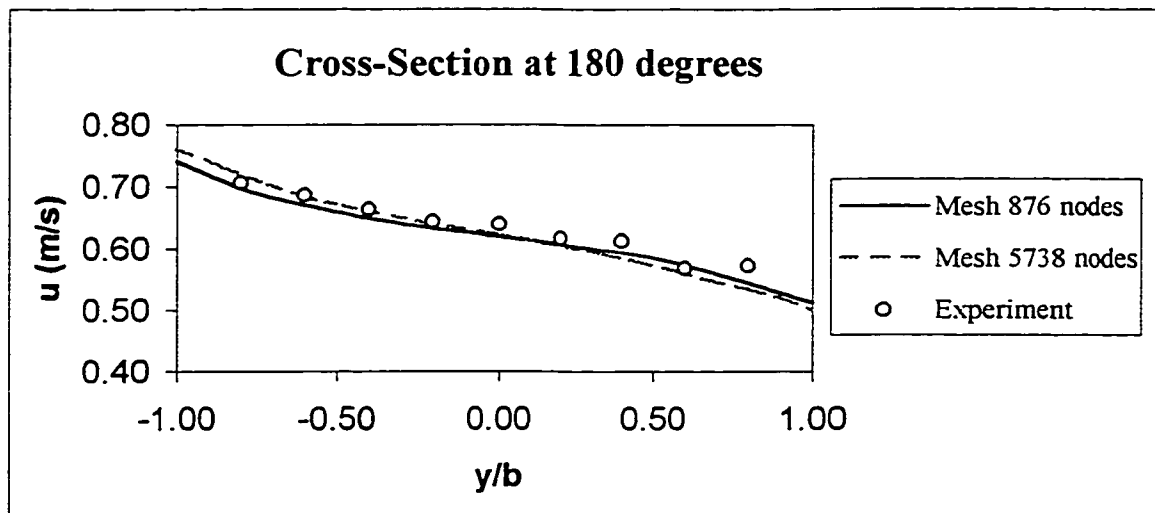


Figure 4.208 The comparison of the longitudinal velocity distribution across the flume for DeVriend (1976) at cross-section 180 degrees for two different generated finite element meshes

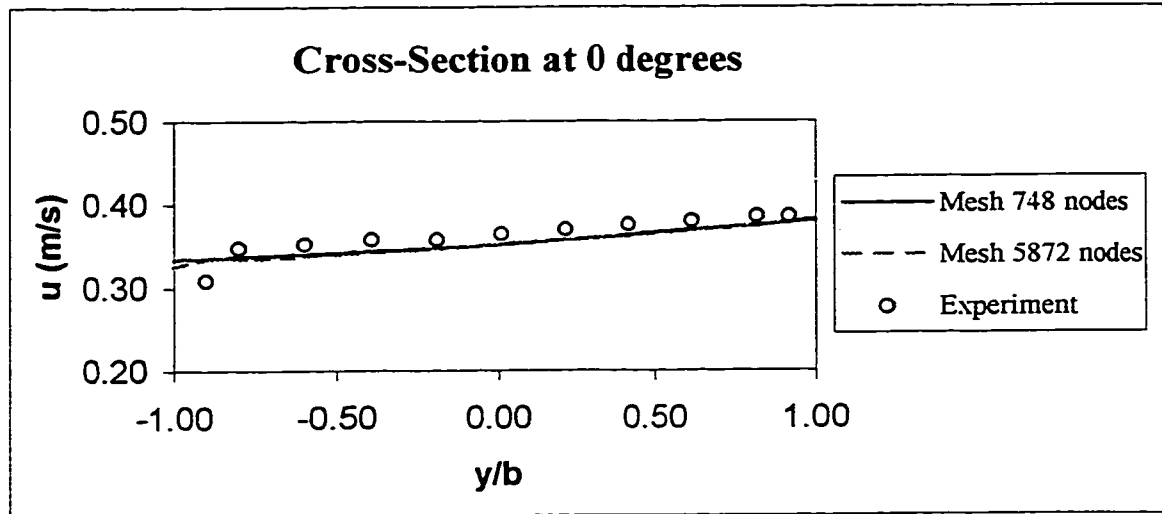


Figure 4.209 The comparison of longitudinal velocity distribution across the flume for Steffler's (1984) run 1 at cross-section 0 degrees for two different generated finite element meshes

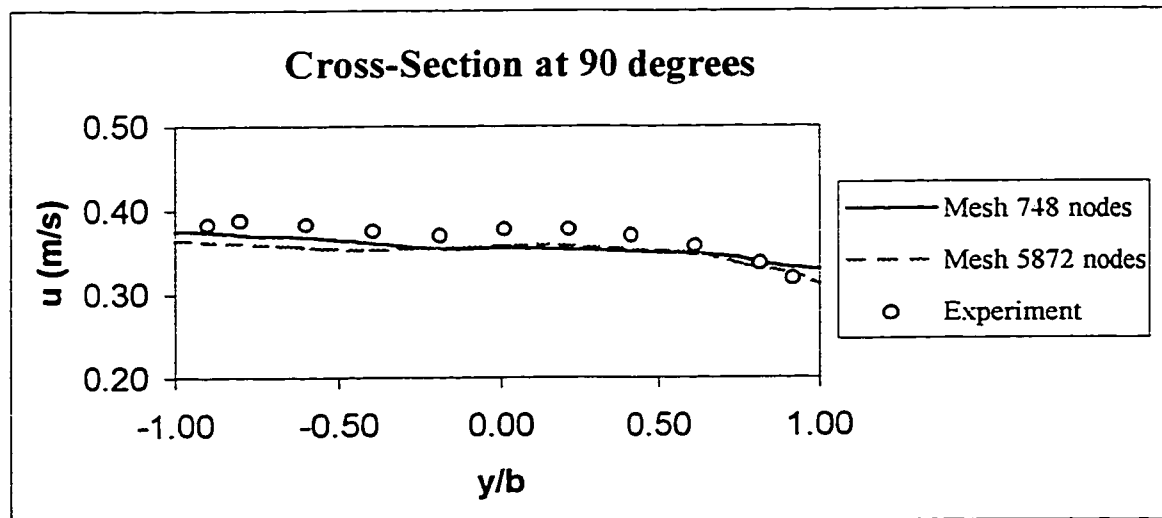


Figure 4.210 The comparison of longitudinal velocity distribution across the flume for Steffler's (1984) run 1 at cross-section 90 degrees for two different generated finite element meshes

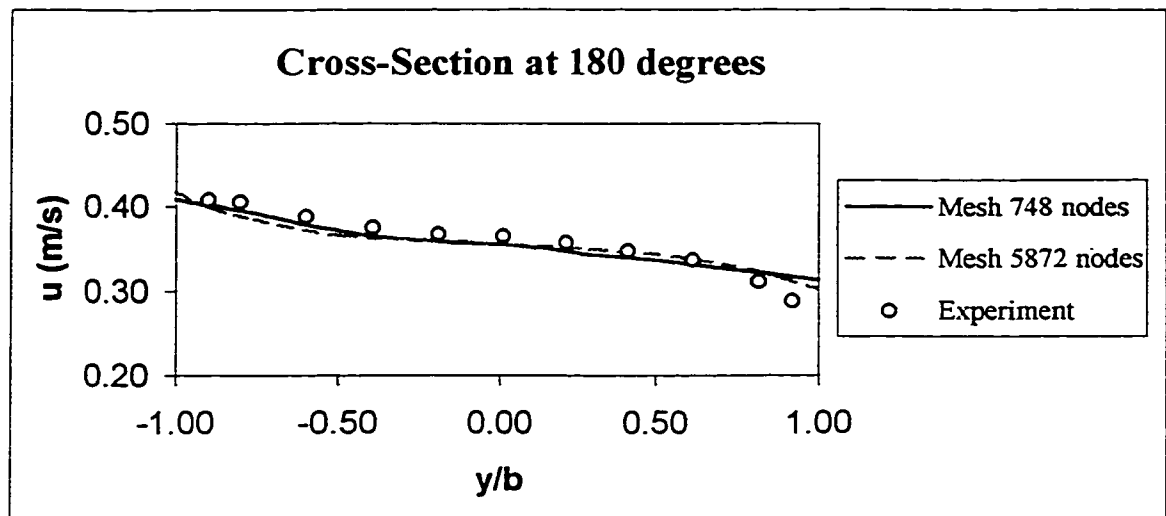


Figure 4.211 The comparison of longitudinal velocity distribution across the flume for Steffler's (1984) run 1 at cross-section 180 degrees for two different generated finite element meshes

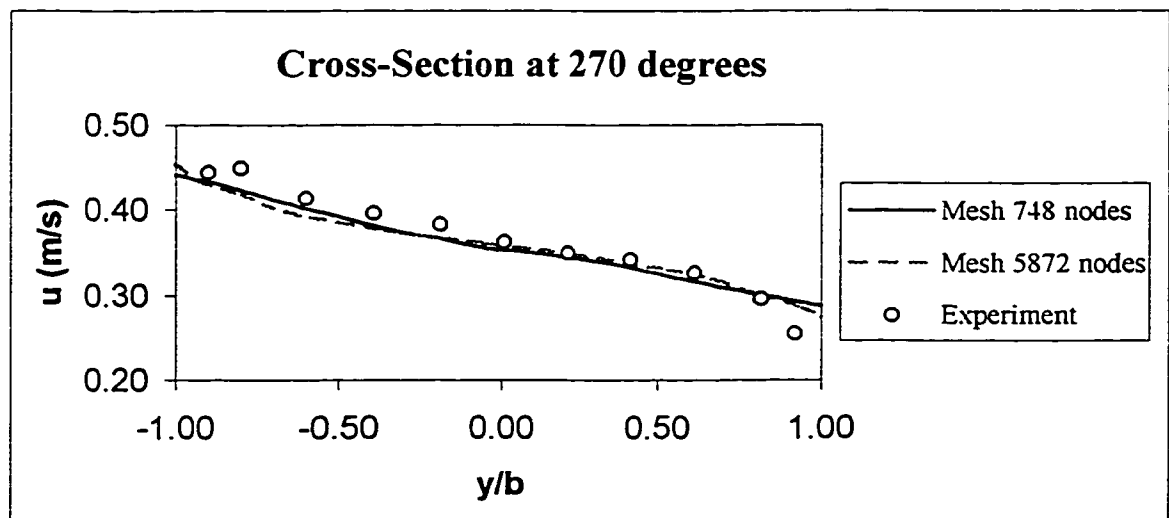


Figure 4.212 The comparison of longitudinal velocity distribution across the flume for Steffler's (1984) run 1 at cross-section 270 degrees for two different generated finite element meshes

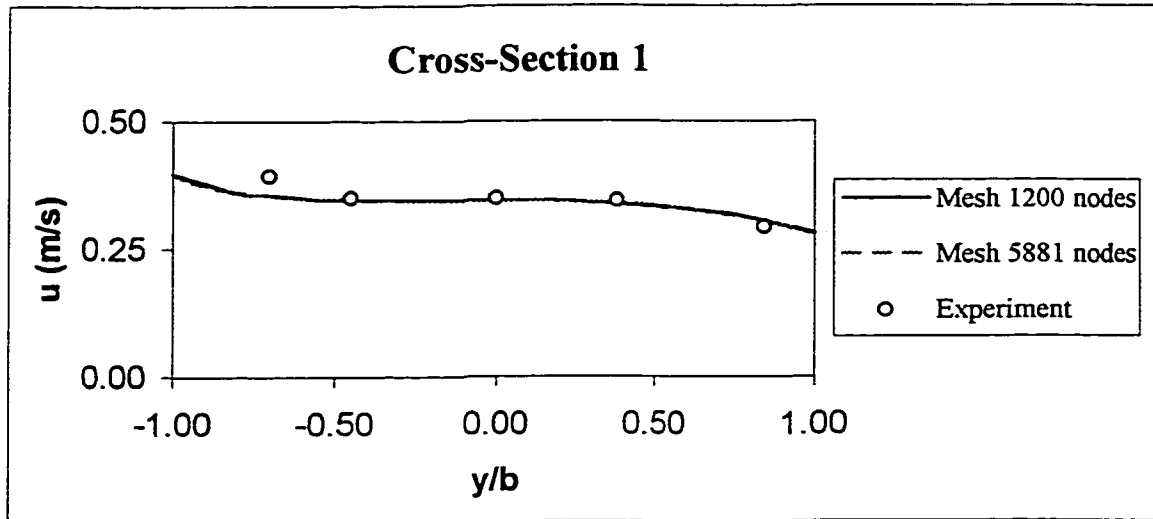


Figure 4.213 The comparison of longitudinal velocity distribution across the flume for Chang (1971) at cross-section 1 for two different generated finite element meshes

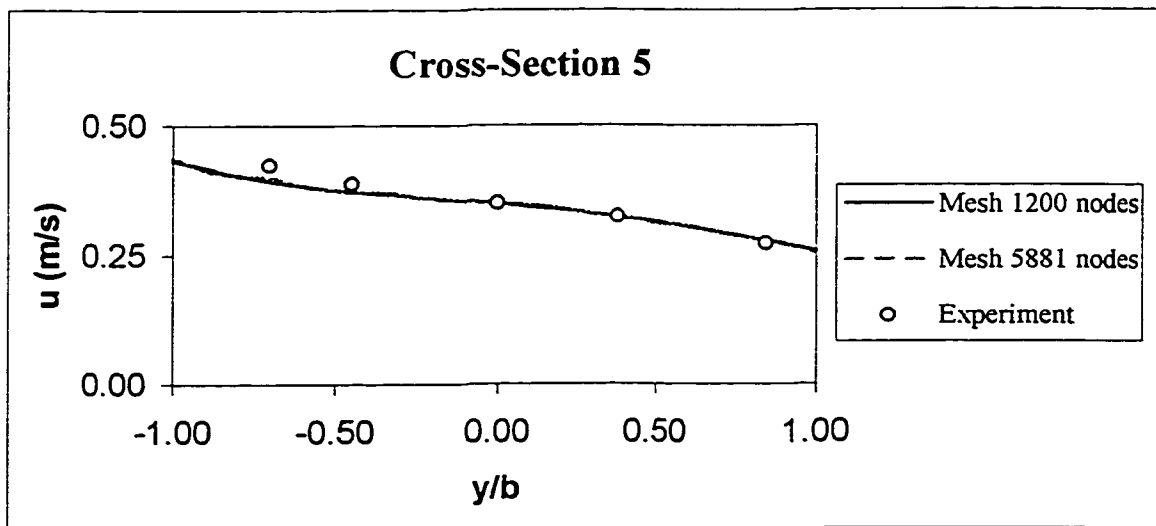


Figure 4.214 The comparison of longitudinal velocity distribution across the flume for Chang (1971) at cross-section 5 for two different generated finite element meshes

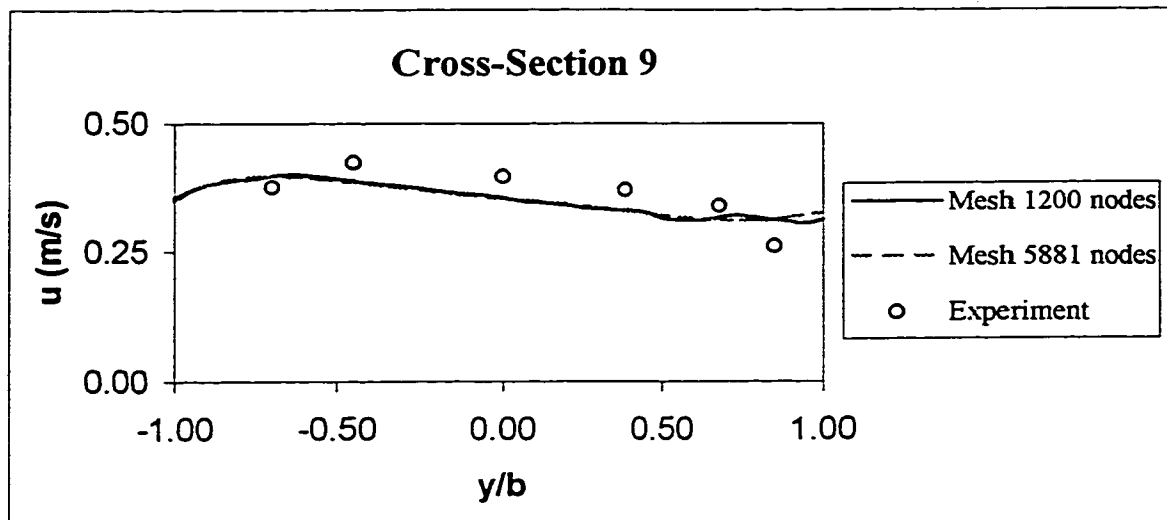


Figure 4.215 The comparison of longitudinal velocity distribution across the flume for Chang (1971) at cross-section 9 for two different generated finite element meshes

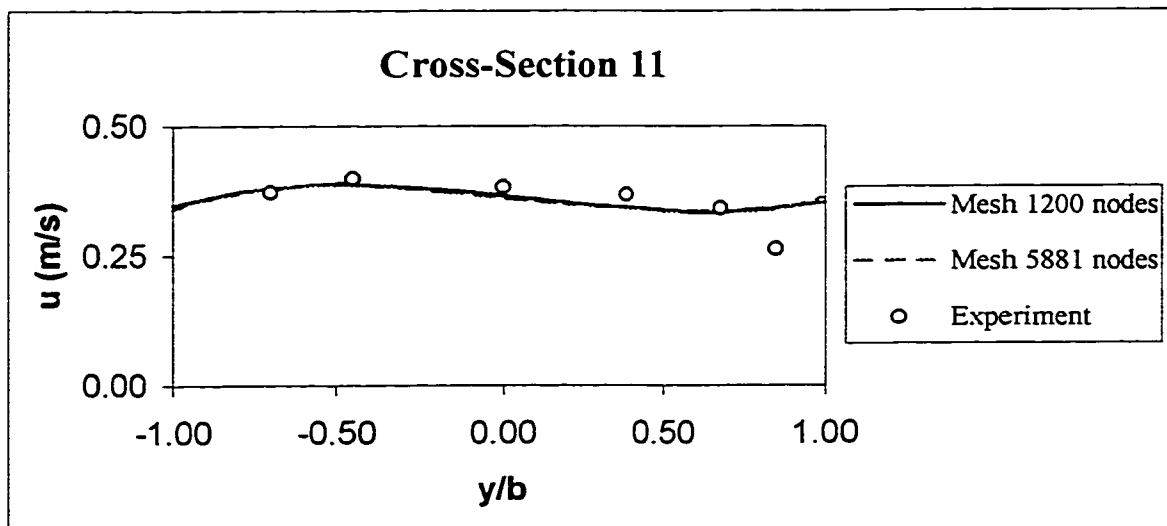


Figure 4.216 The comparison of longitudinal velocity distribution across the flume for Chang (1971) at cross-section 11 for two different generated finite element meshes

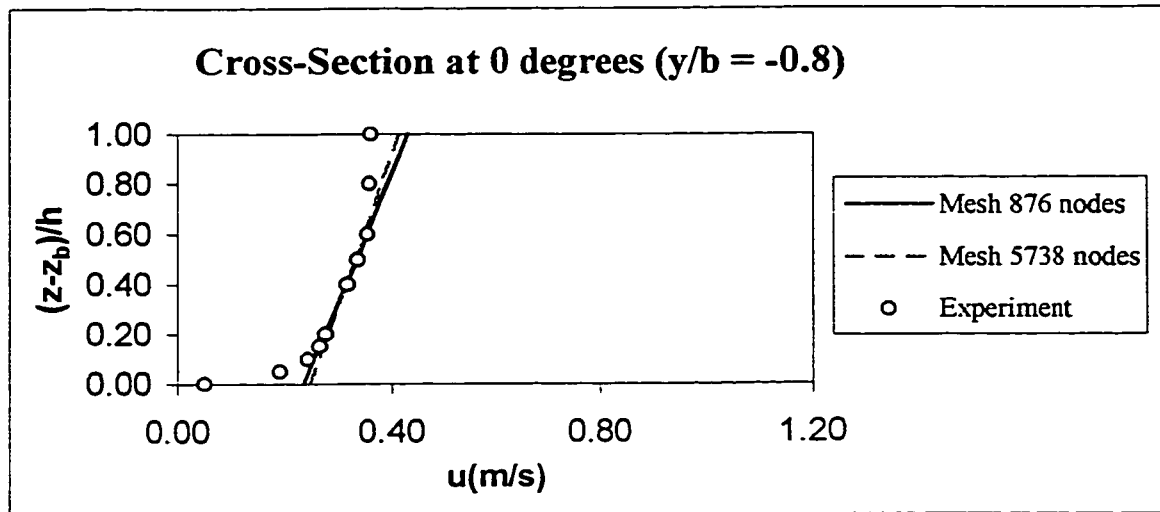


Figure 4.217 The comparison of longitudinal velocity profile for Steffler's (1984) run 1 at cross-section 0 degrees and $y/b = -0.8$ for two different generated finite element meshes

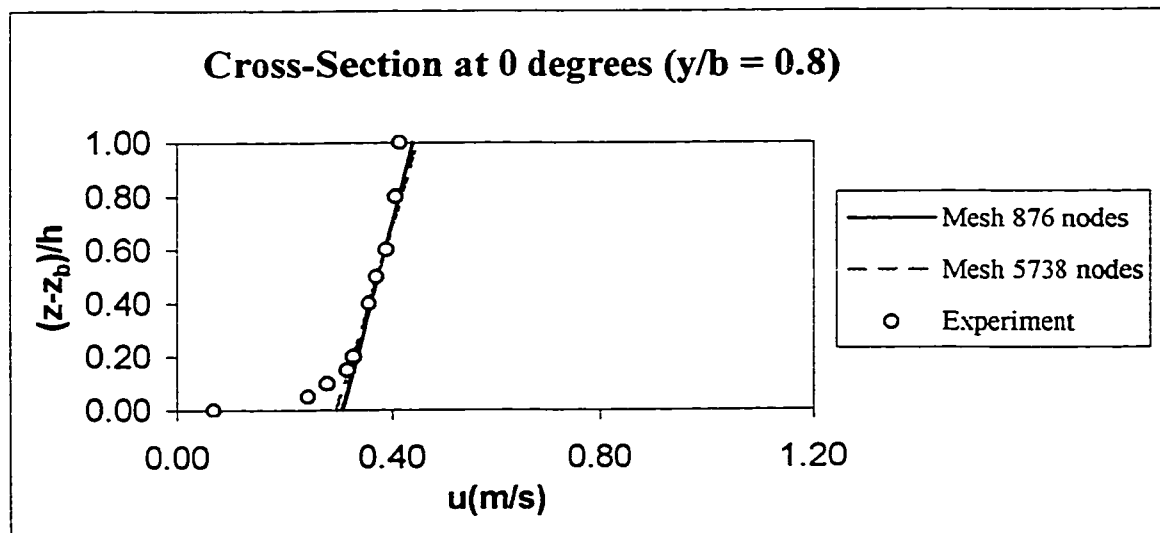


Figure 4.218 The comparison of longitudinal velocity profile for Steffler's (1984) run 1 at cross-section 0 degrees and $y/b = 0.8$ for two different generated finite element meshes

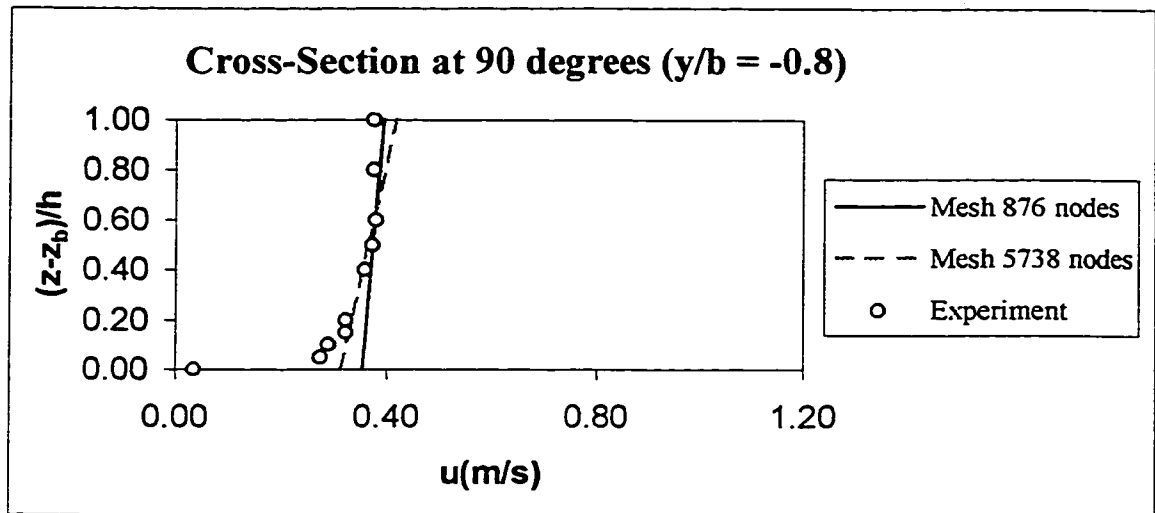


Figure 4.219 The comparison of longitudinal velocity profile for Steffler's (1984) run 1 at cross-section 90 degrees and $y/b = -0.8$ for two different generated finite element meshes

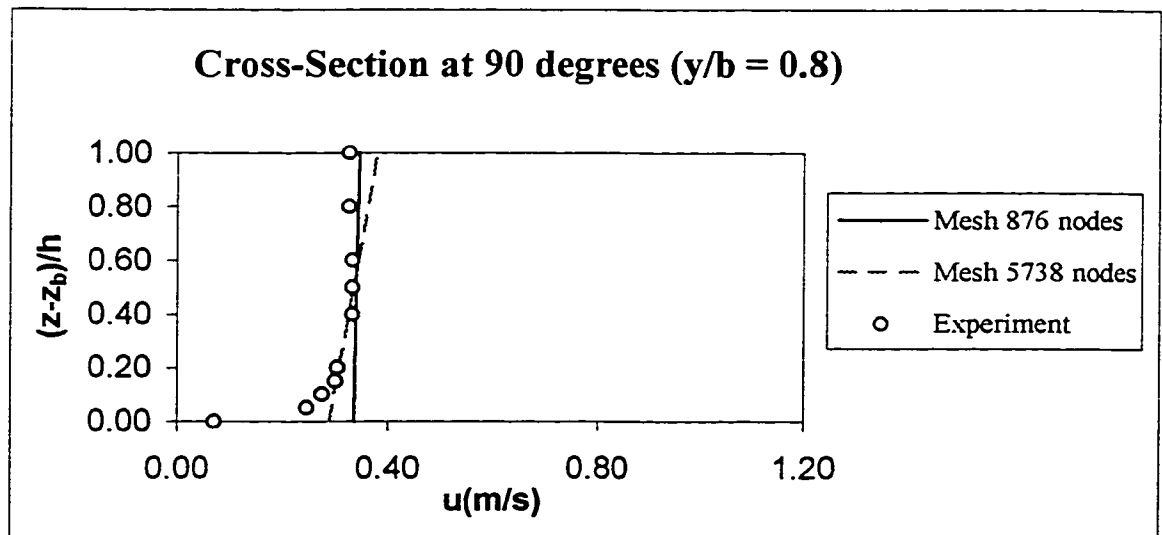


Figure 4.220 The comparison of longitudinal velocity profile for Steffler's (1984) run 1 at cross-section 90 degrees and $y/b = 0.8$ for two different generated finite element meshes

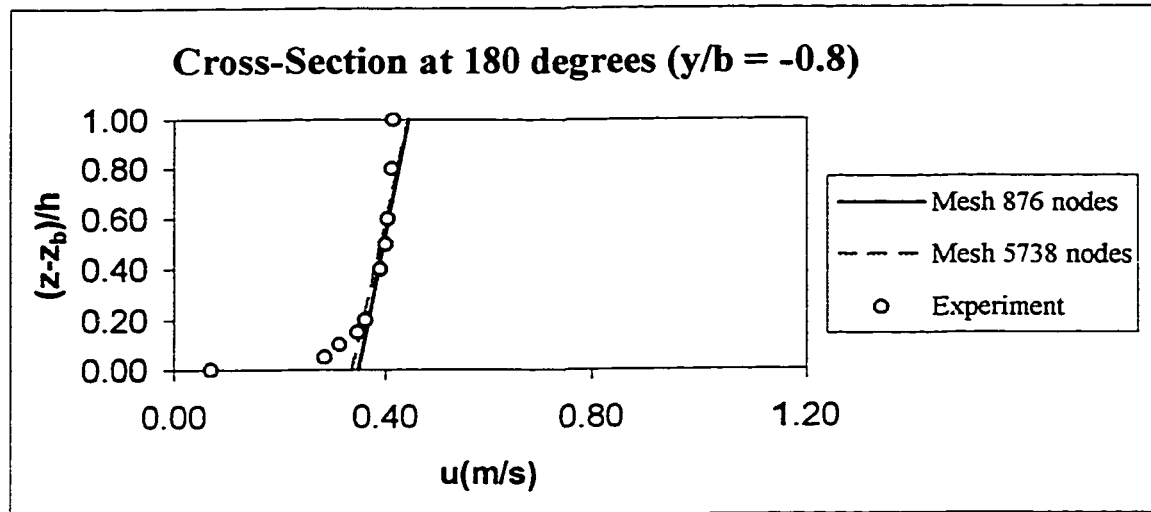


Figure 4.221 The comparison of longitudinal velocity profile for Steffler's (1984) run 1 at cross-section 180 degrees and $y/b = -0.8$ for two different generated finite element meshes

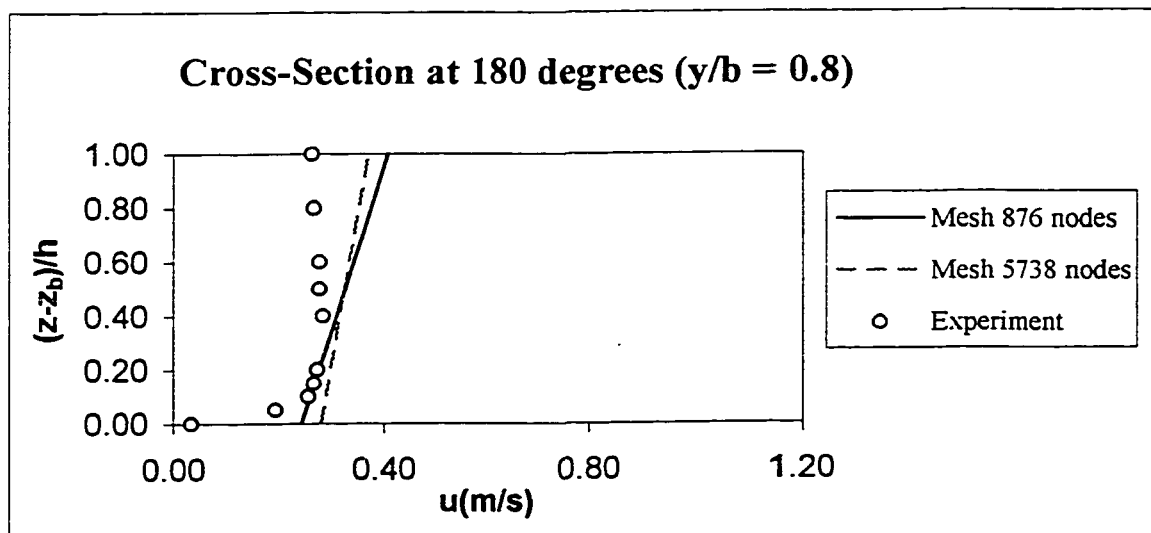


Figure 4.222 The comparison of longitudinal velocity profile for Steffler's (1984) run 1 at cross-section 180 degrees and $y/b = 0.8$ for two different generated finite element meshes

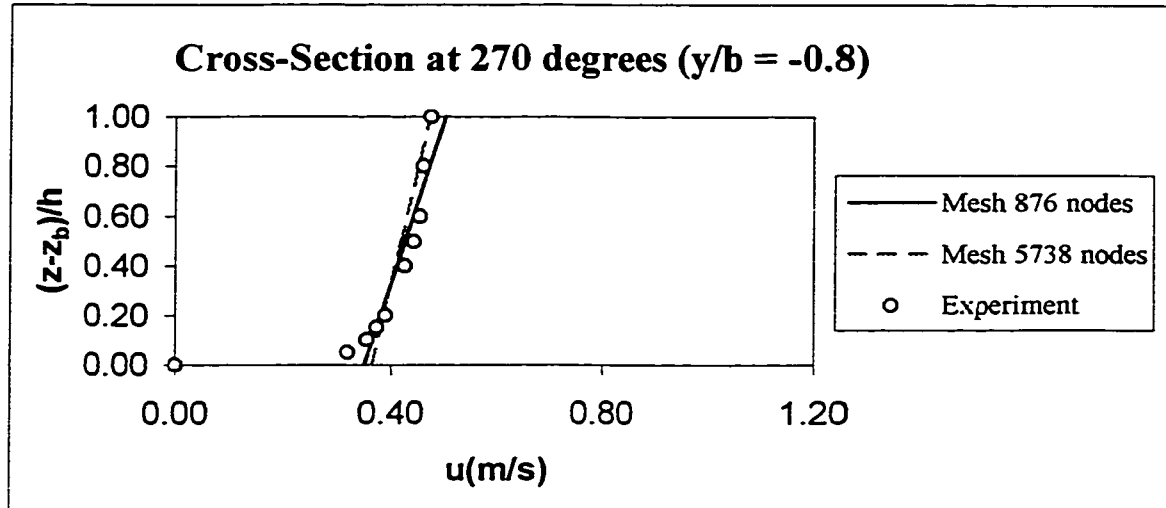


Figure 4.223 The comparison of longitudinal velocity profile for Steffler's (1984) run 1 at cross-section 270 degrees and $y/b = -0.8$ for two different generated finite element meshes

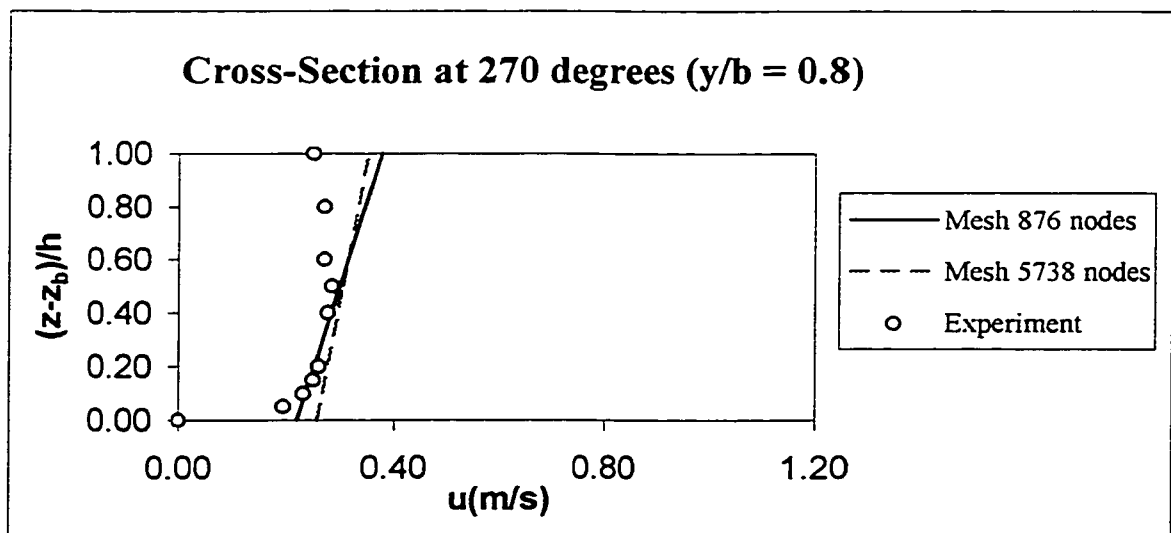


Figure 4.224 The comparison of longitudinal velocity profile for Steffler's (1984) run 1 at cross-section 270 degrees and $y/b = 0.8$ for two different generated finite element meshes

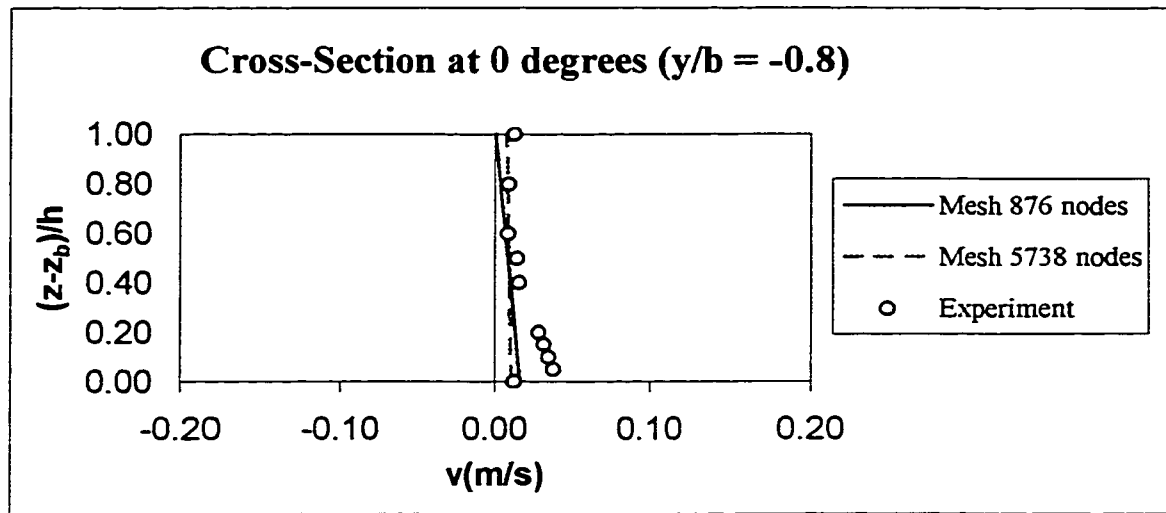


Figure 4.225 The comparison of transverse velocity profile for Steffler's (1984) run 1 at cross-section 0 degrees and $y/b = -0.8$ for two different generated finite element meshes

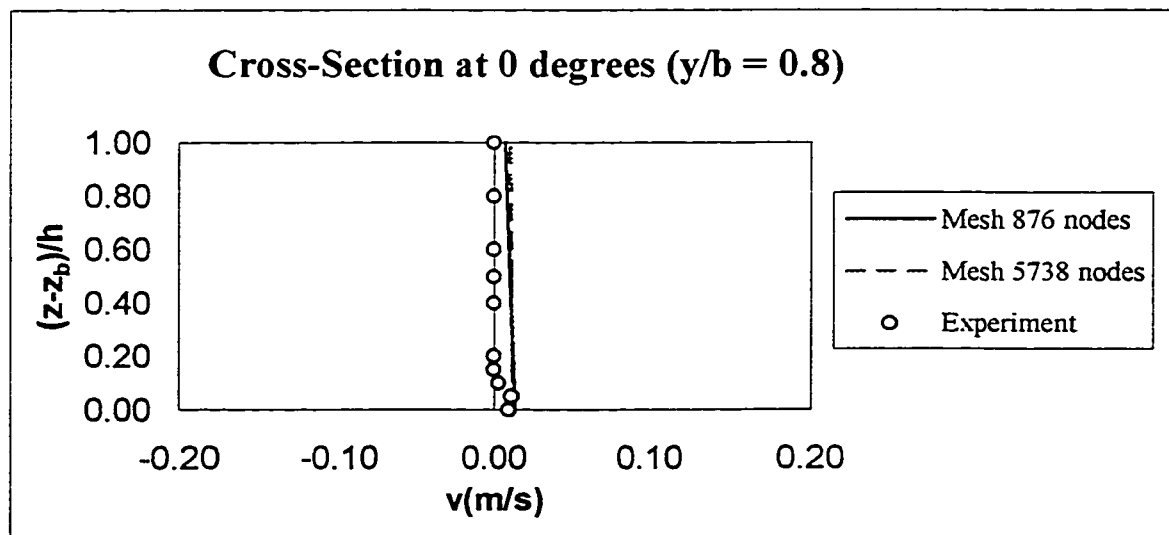


Figure 4.226 The comparison of transverse velocity profile for Steffler's (1984) run 1 at cross-section 0 degrees and $y/b = 0.8$ for two different generated finite element meshes

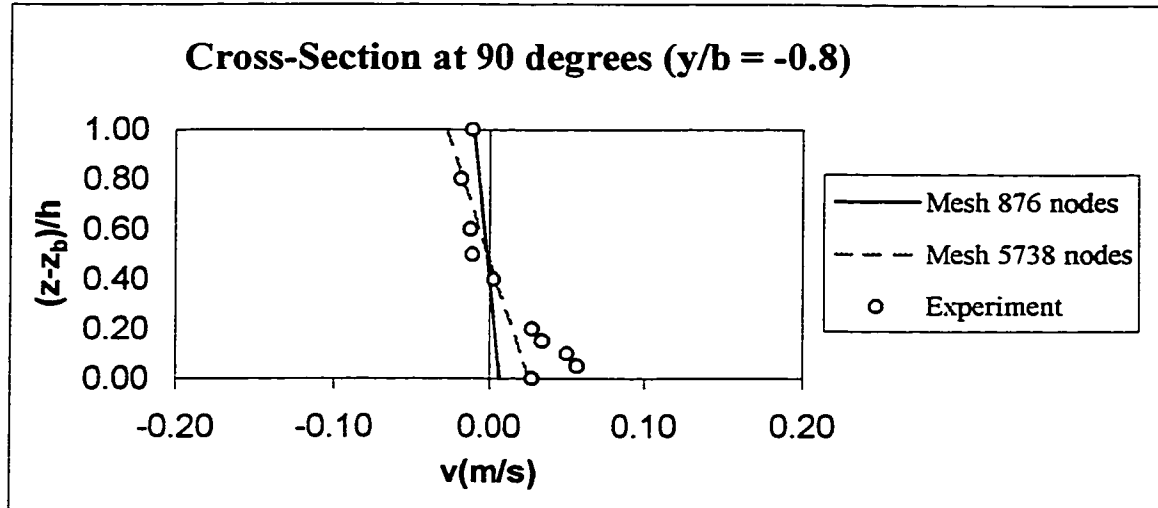


Figure 4.227 The comparison of transverse velocity profile for Steffler's (1984) run 1 at cross-section 90 degrees and $y/b = -0.8$ for two different generated finite element meshes

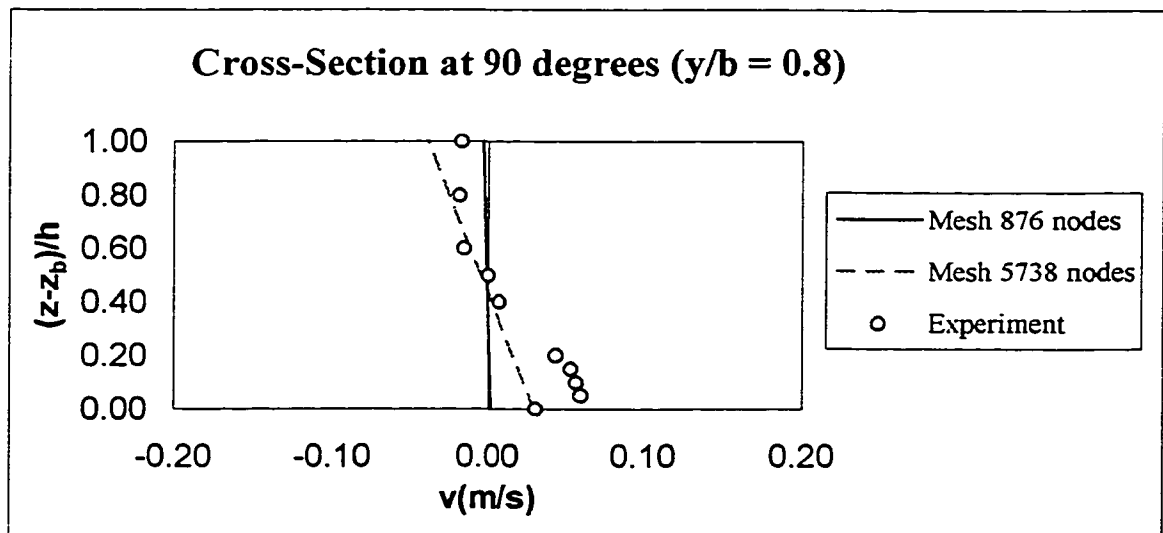


Figure 4.228 The comparison of transverse velocity profile for Steffler's (1984) run 1 at cross-section 90 degrees and $y/b = 0.8$ for two different generated finite element meshes

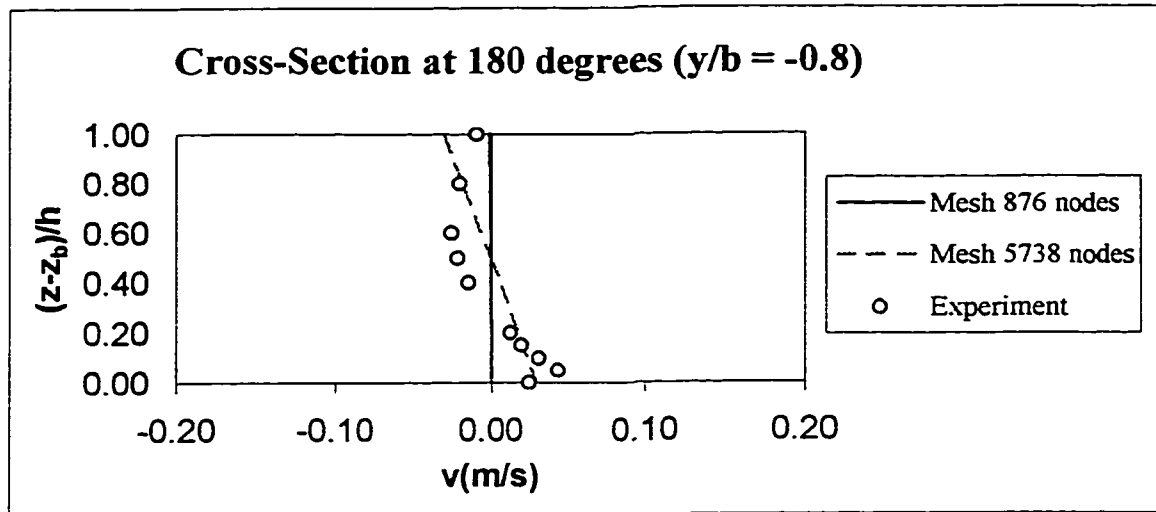


Figure 4.229 The comparison of transverse velocity profile for Steffler's (1984) run 1 at cross-section 180 degrees and $y/b = -0.8$ for two different generated finite element meshes

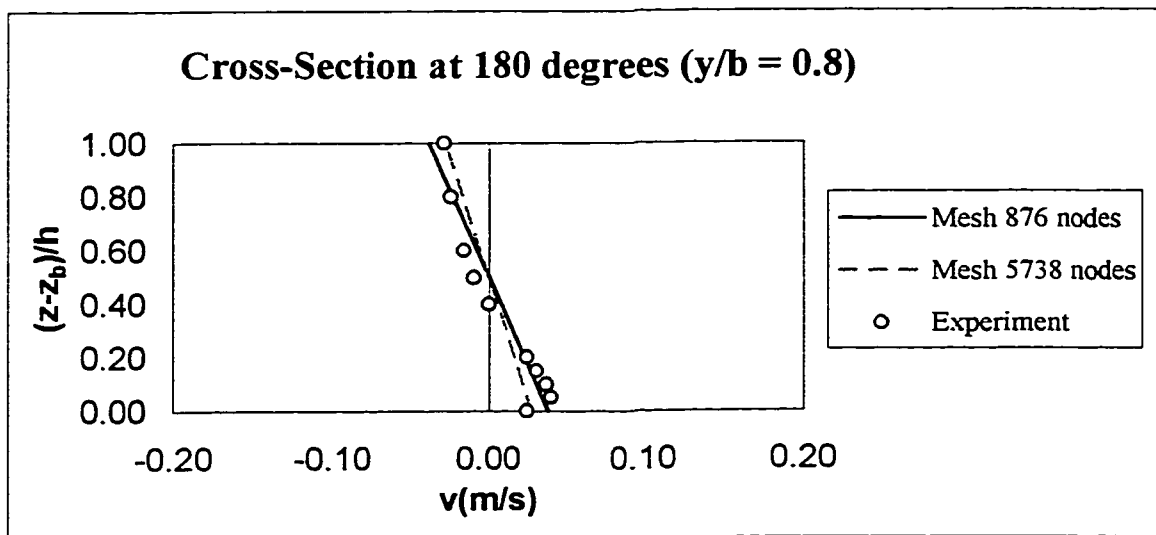


Figure 4.230 The comparison of transverse velocity profile for Steffler's (1984) run 1 at cross-section 180 degrees and $y/b = 0.8$ for two different generated finite element meshes

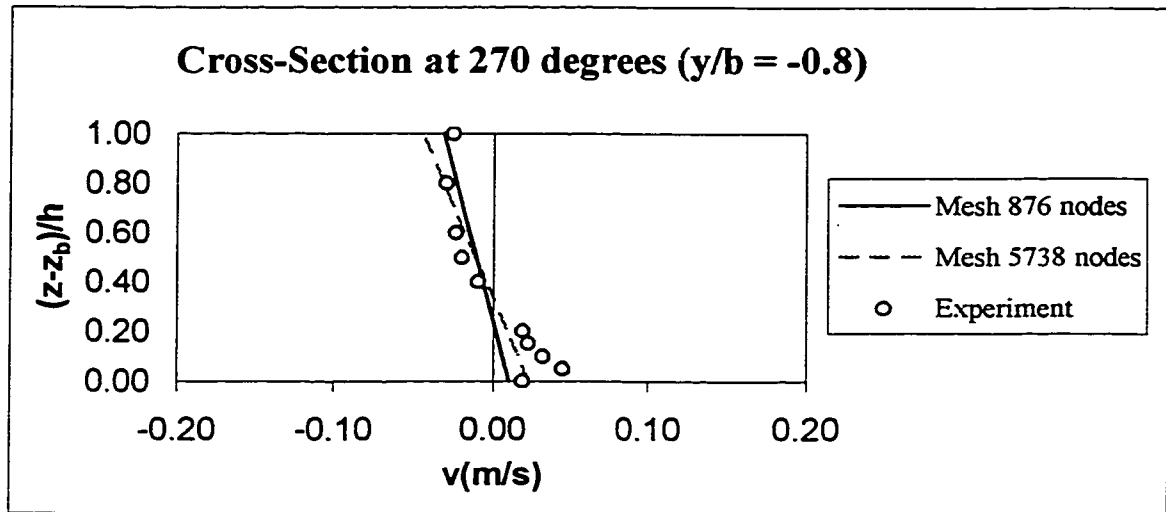


Figure 4.231 The comparison of transverse velocity profile for Steffler's (1984) run 1 at cross-section 270 degrees and $y/b = -0.8$ for two different generated finite element meshes

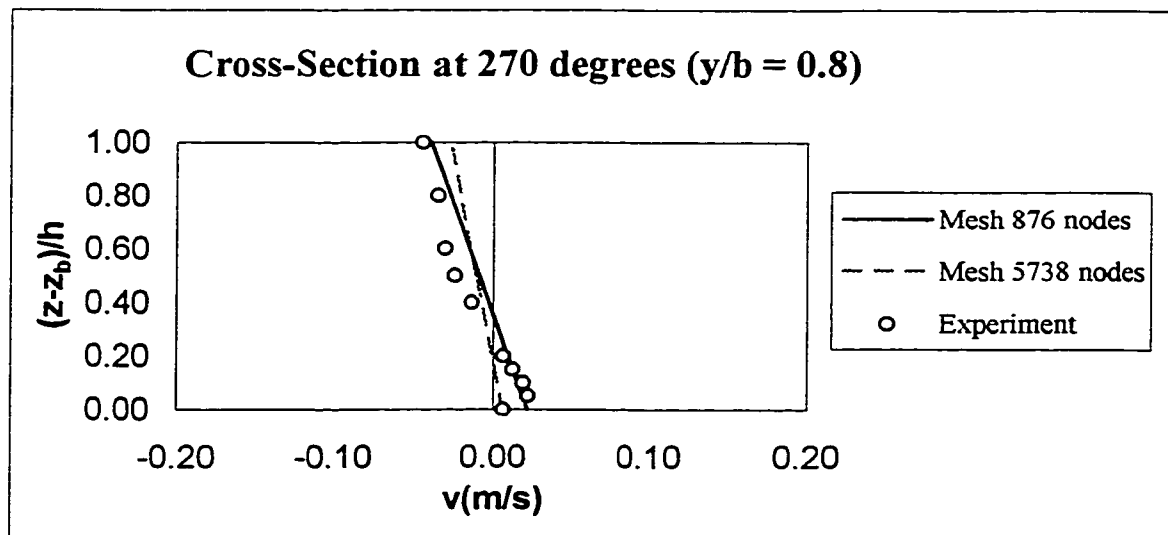


Figure 4.232 The comparison of transverse velocity profile for Steffler's (1984) run 1 at cross-section 270 degrees and $y/b = 0.8$ for two different generated finite element meshes

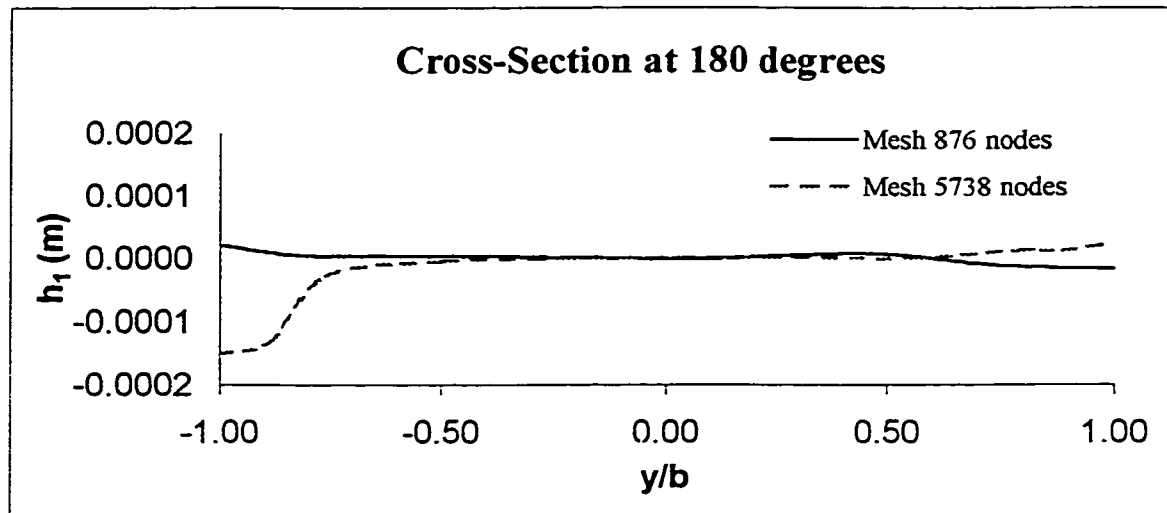


Figure 4.233 The comparison of extra non-hydrostatic pressure head (h_1) distribution across the flume for Steffler's (1984) run 1 at cross-section 180 degrees for two different generated finite element meshes

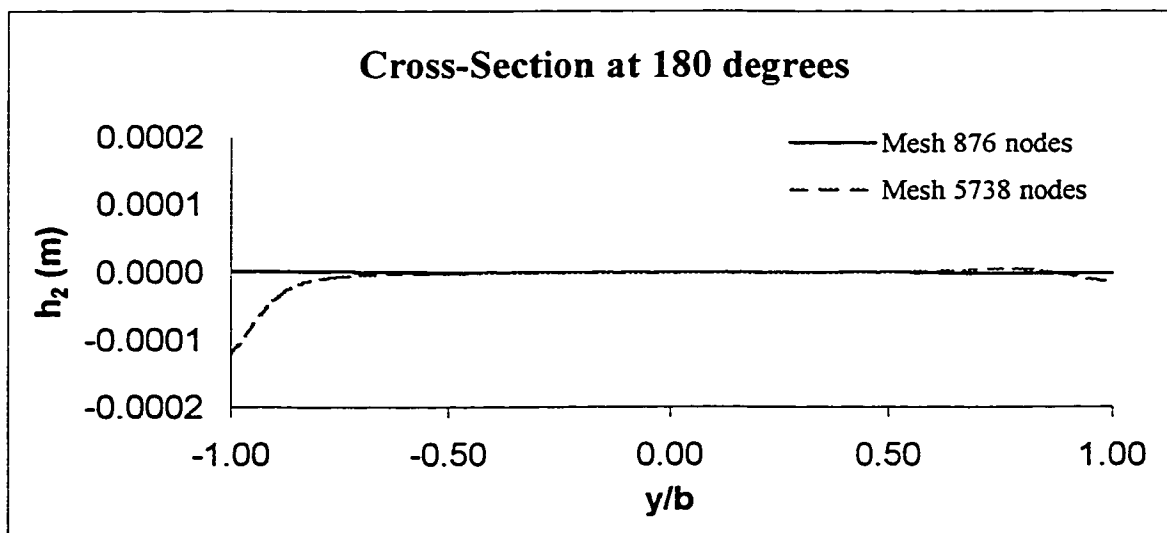


Figure 4.234 The comparison of extra non-hydrostatic pressure head (h_2) distribution across the flume for Steffler's (1984) run 1 at cross-section 180 degrees for two different generated finite element

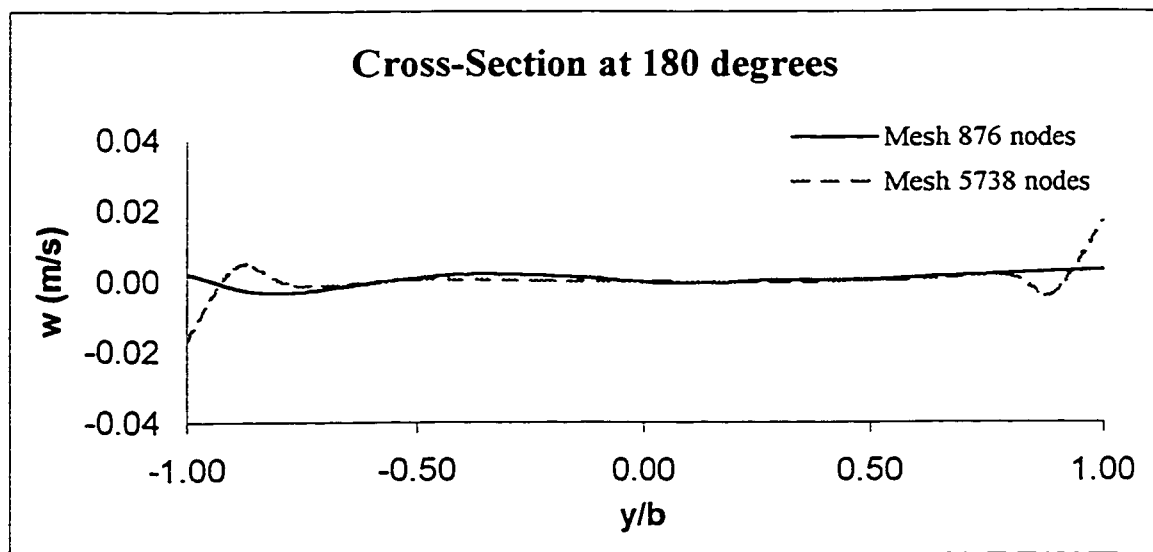


Figure 4.235 The comparison of average vertical velocity distribution across the flume for Steffler's (1984) run 1 at cross-section 180 degrees for two different generated finite element meshes

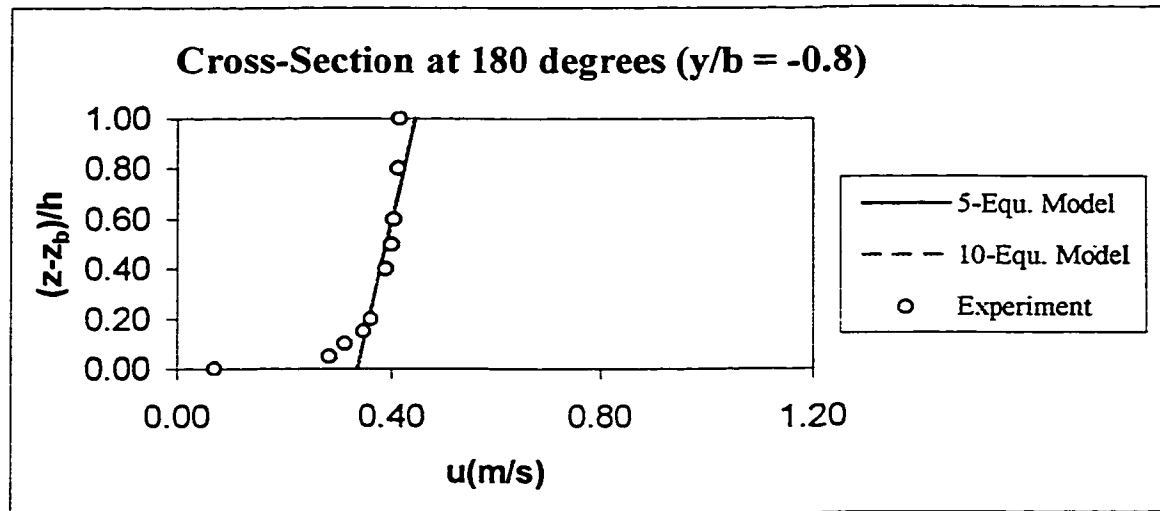


Figure 4.236 The comparison of applying VAM 5- against 10-equation models for longitudinal velocity profile for Steffler's (1984) run 1 at cross-section 180 degrees and $y/b = -0.8$ for the finer finite element mesh

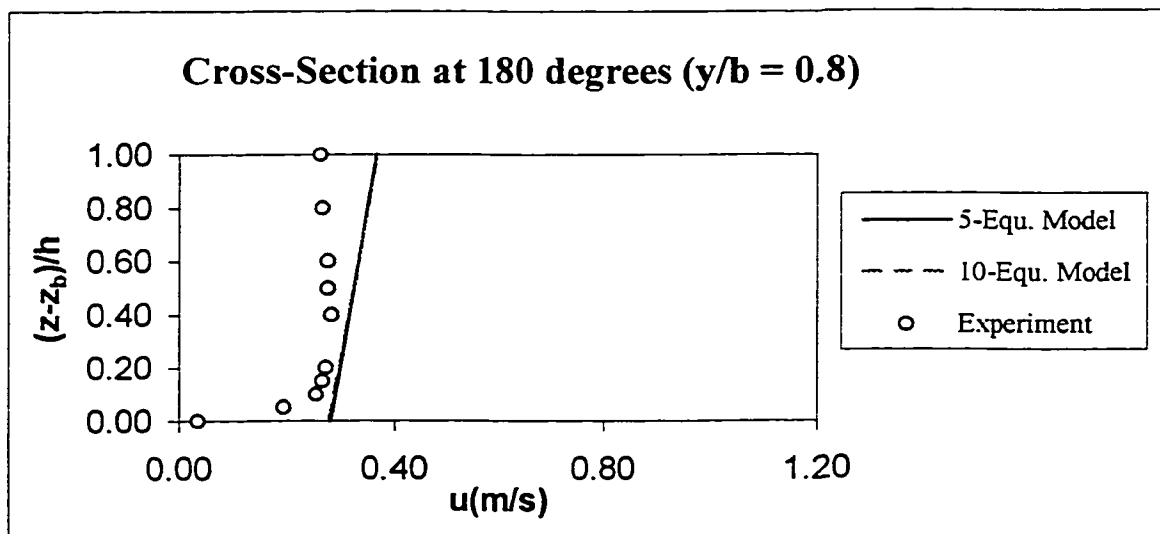


Figure 4.237 The comparison of applying VAM 5- against 10-equation models for longitudinal velocity profile for Steffler's (1984) run 1 at cross-section 180 degrees and $y/b = 0.8$ for the finer finite element mesh

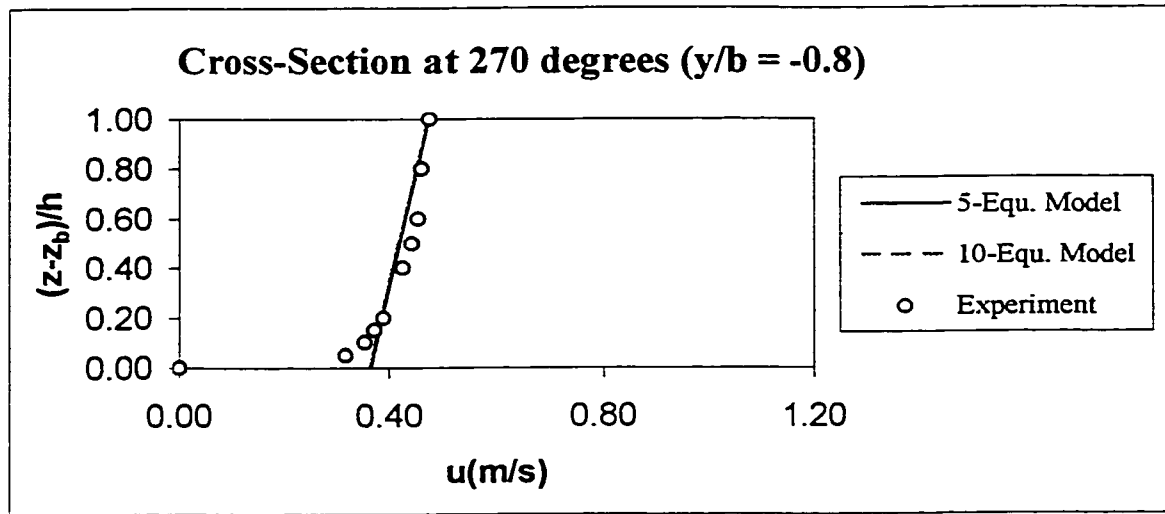


Figure 4.238 The comparison of applying VAM 5- against 10-equation models for longitudinal velocity profile for Steffler's (1984) run 1 at cross-section 270 degrees and $y/b = -0.8$ for the finer finite element mesh

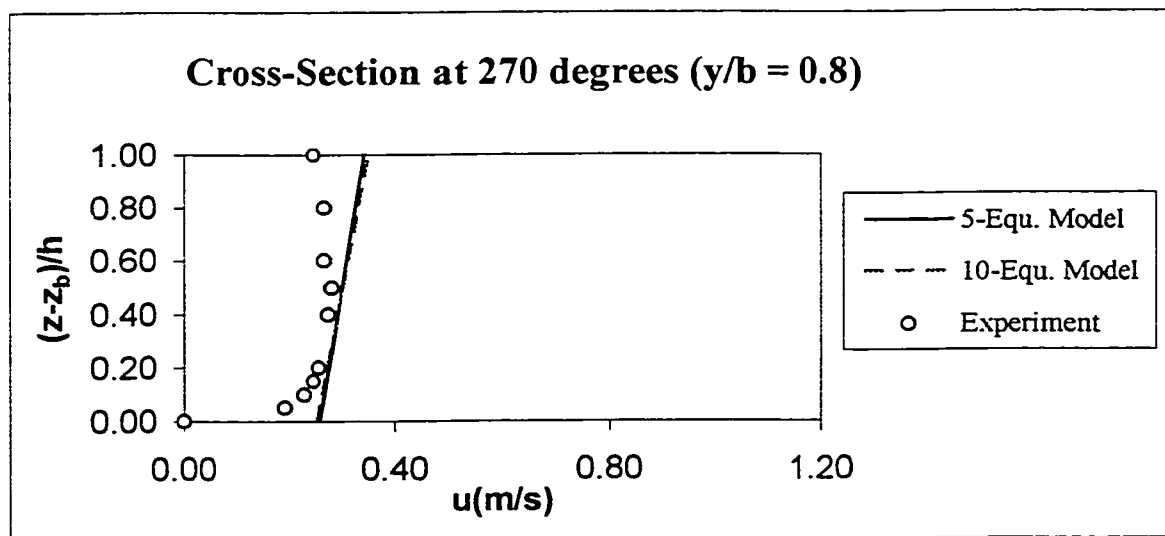


Figure 4.239 The comparison of applying VAM 5- against 10-equation models for longitudinal velocity profile for Steffler's (1984) run 1 at cross-section 270 degrees and $y/b = 0.8$ for the finer finite element mesh

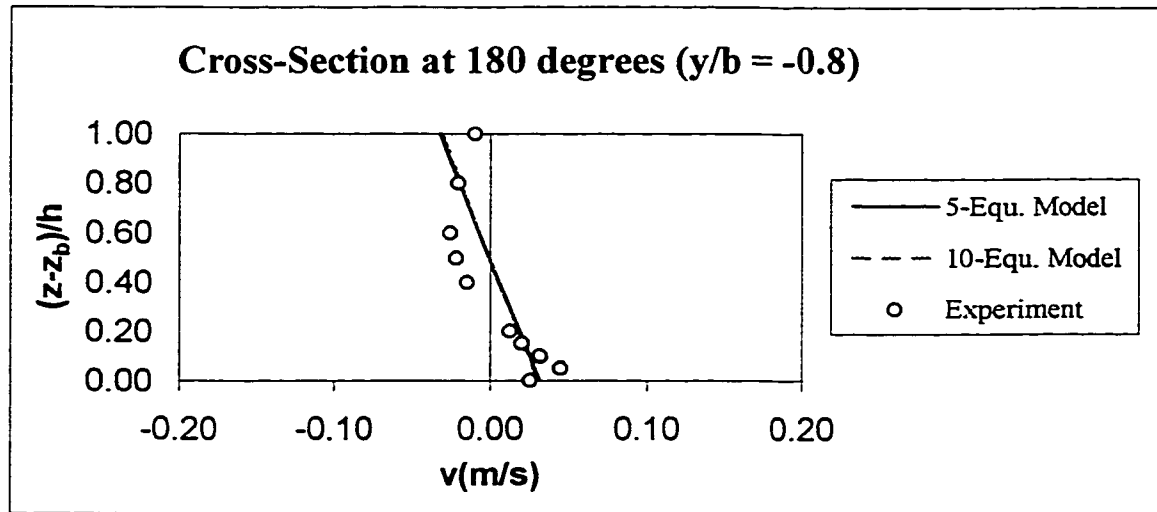


Figure 4.240 The comparison of applying VAM 5- against 10-equation models for transverse velocity profile for Steffler's (1984) run 1 at cross-section 180 degrees and $y/b = -0.8$ for the finer finite element mesh

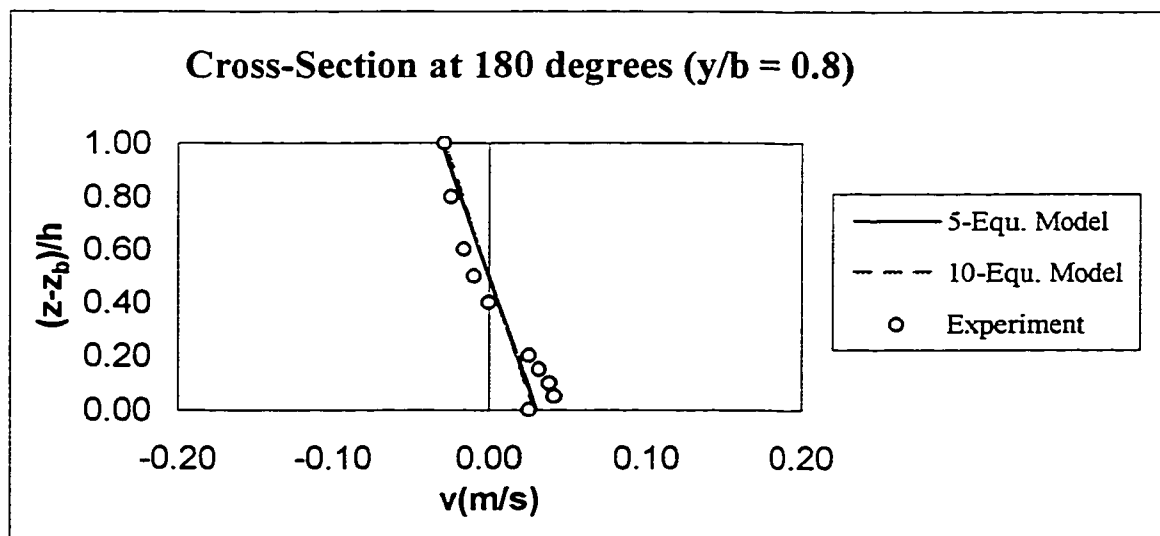


Figure 4.241 The comparison of applying VAM 5- against 10-equation models for transverse velocity profile for Steffler's (1984) run 1 at cross-section 180 degrees and $y/b = 0.8$ for the finer finite element mesh

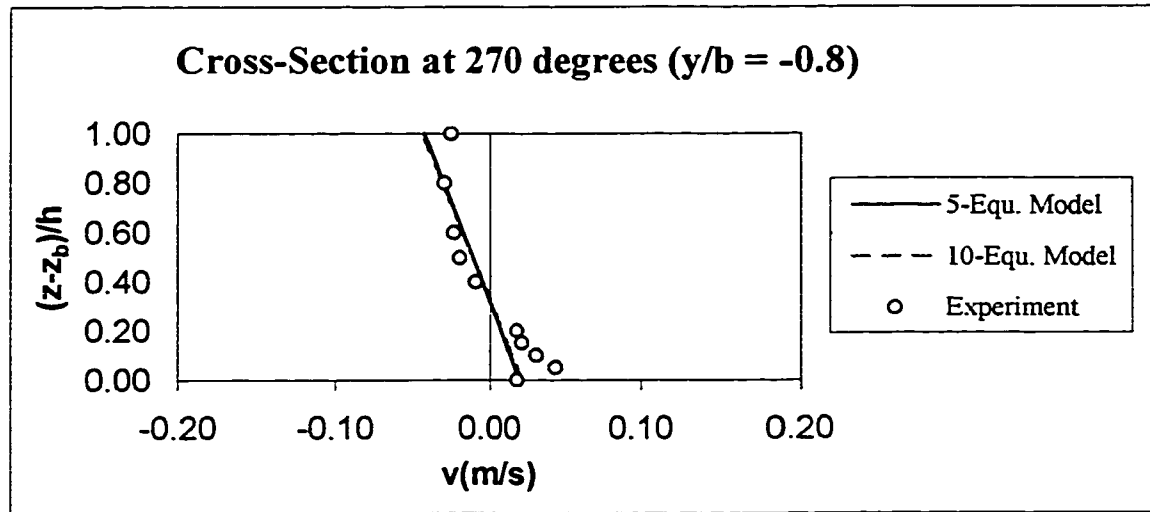


Figure 4.242 The comparison of applying VAM 5- against 10-equation models for transverse velocity profile for Steffler's (1984) run 1 at cross-section 270 degrees and $y/b = -0.8$ for the finer finite element mesh

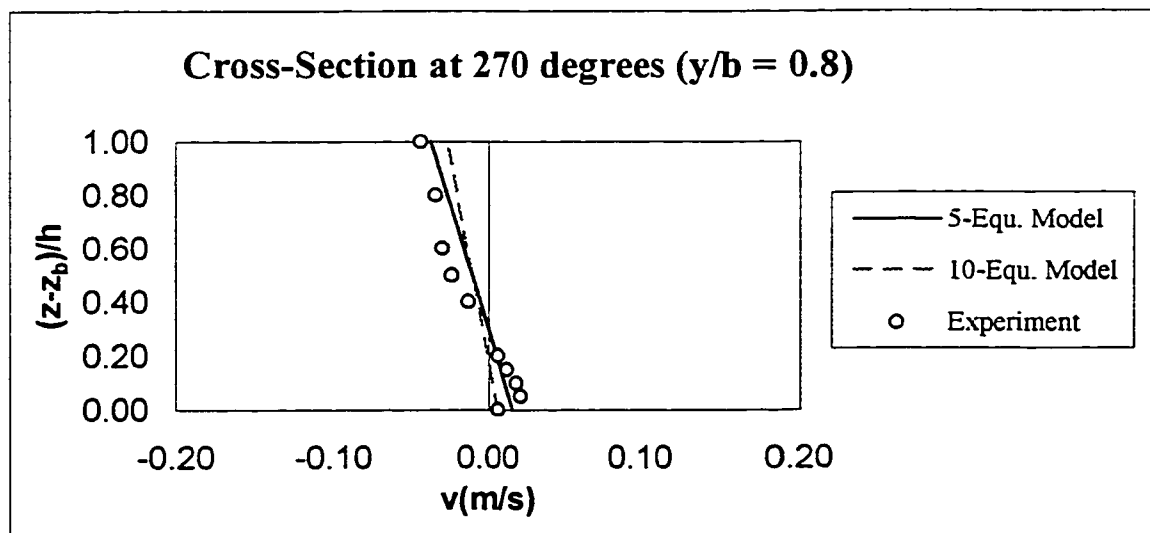


Figure 4.243 The comparison of applying VAM 5- against 10-equation models for transverse velocity profile for Steffler's (1984) run 1 at cross-section 270 degrees and $y/b = 0.8$ for the finer finite element mesh

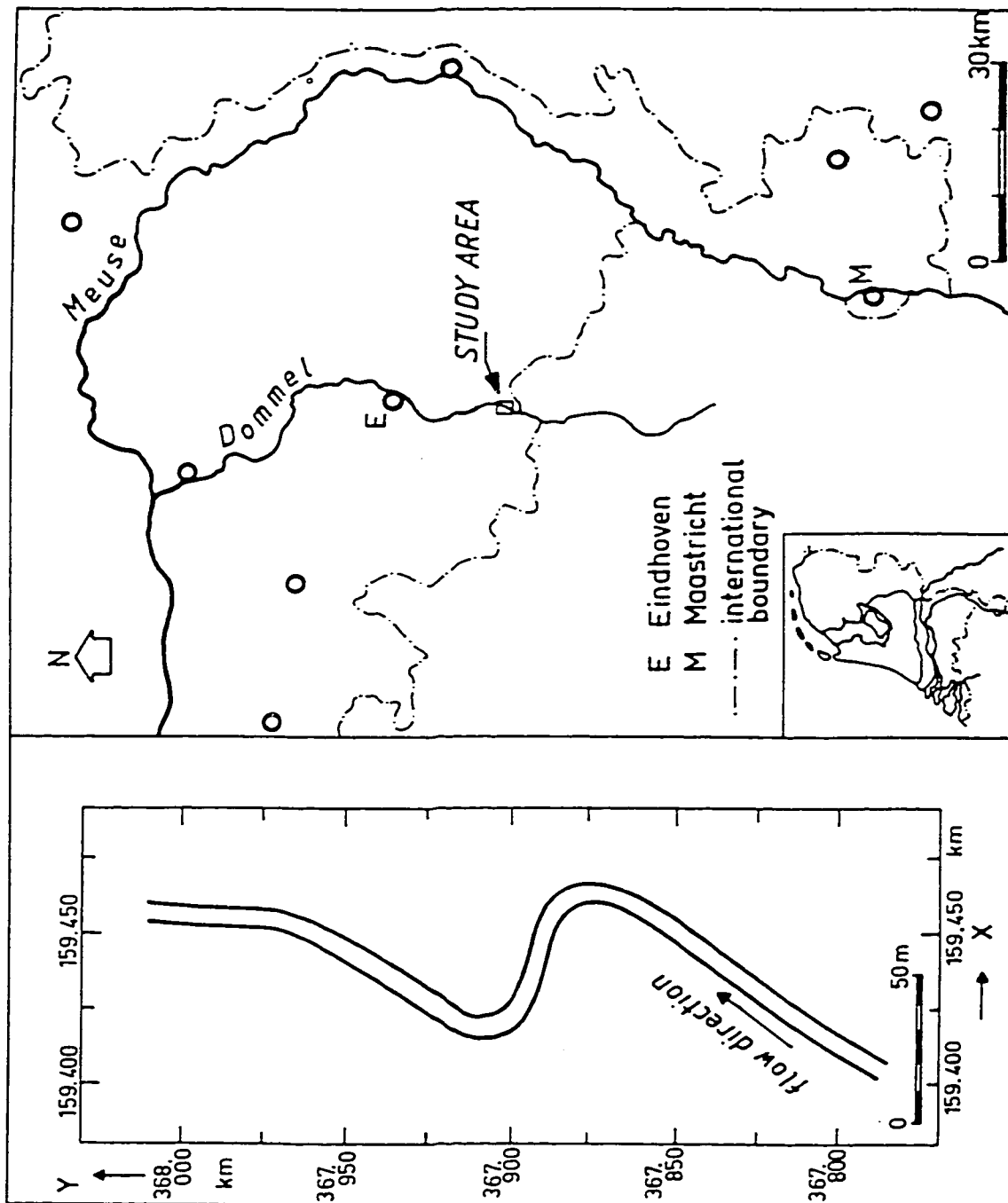


Figure 4.244 Location of the study reach of the river Dommel (adapted from De Vriend and Geldof, 1983)

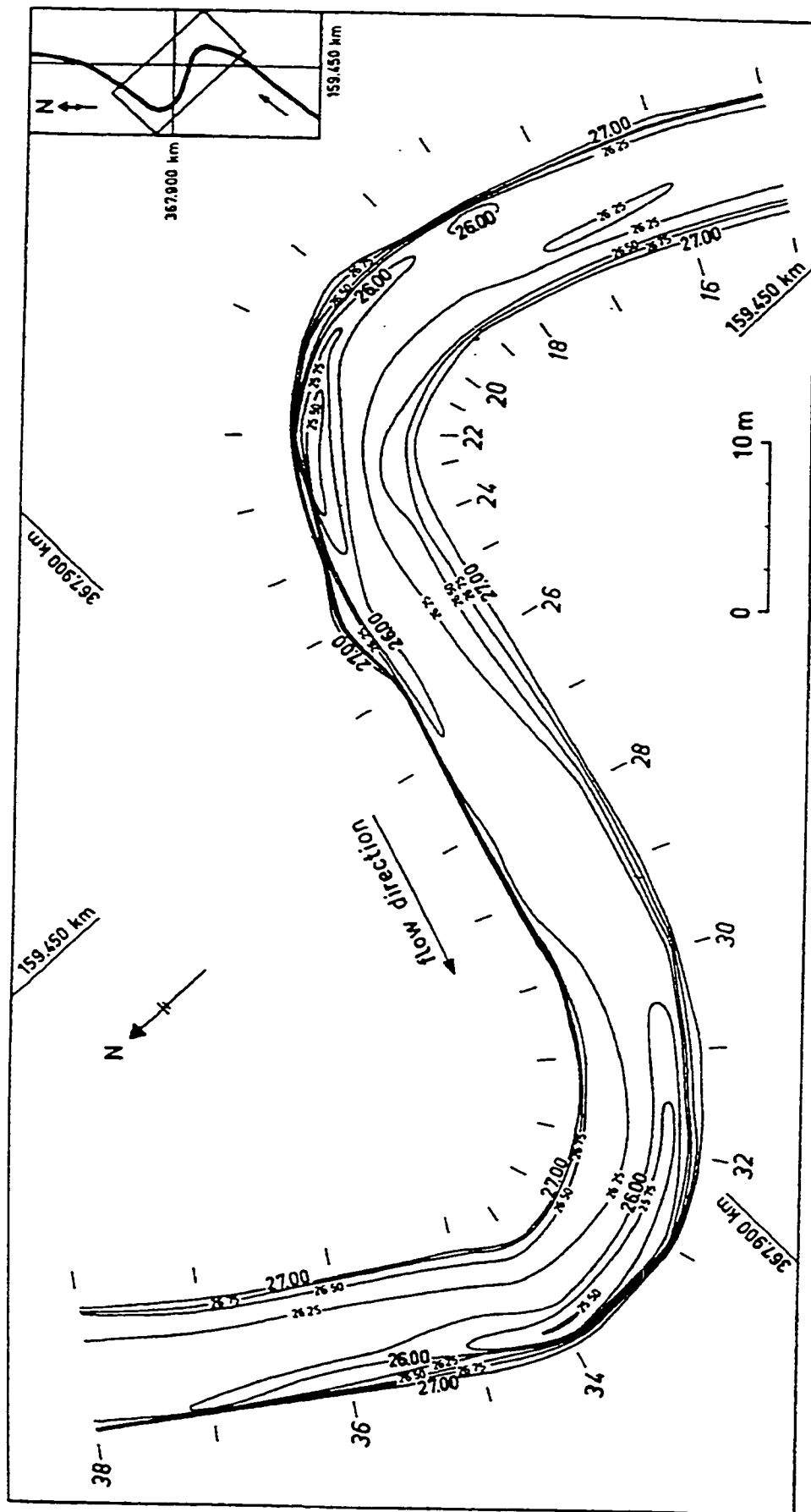


Figure 4.245 Contour map of bed level in central part of the study reach of the river Dommel (adapted from De Vriend and Geldof, 1983)

Distance
2.0 m

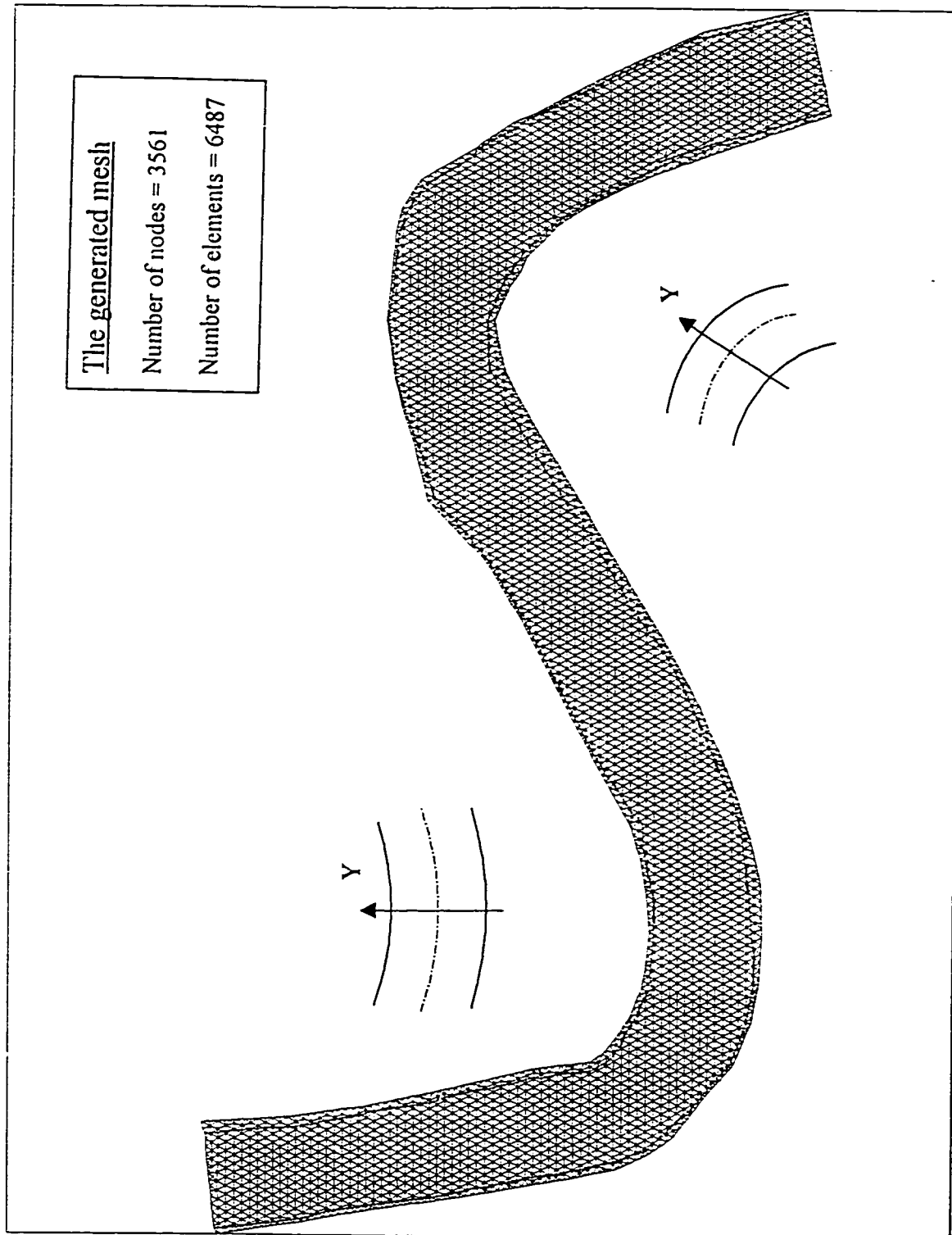


Figure 4.246 Finite element mesh for the study reach of the river Dommel

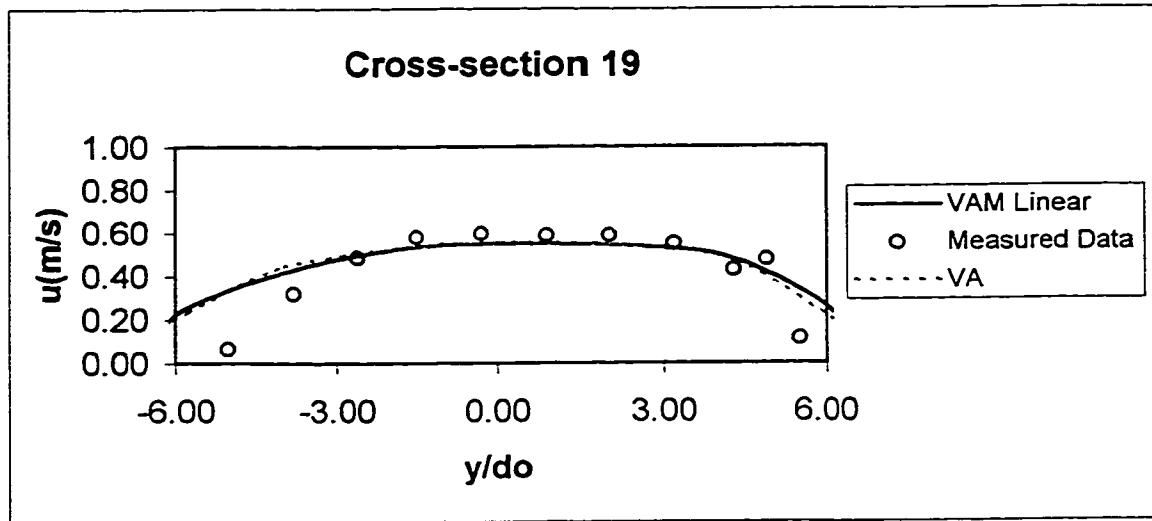


Figure 4.247 The comparison of longitudinal velocity distribution across the river Dommel at cross-section 19

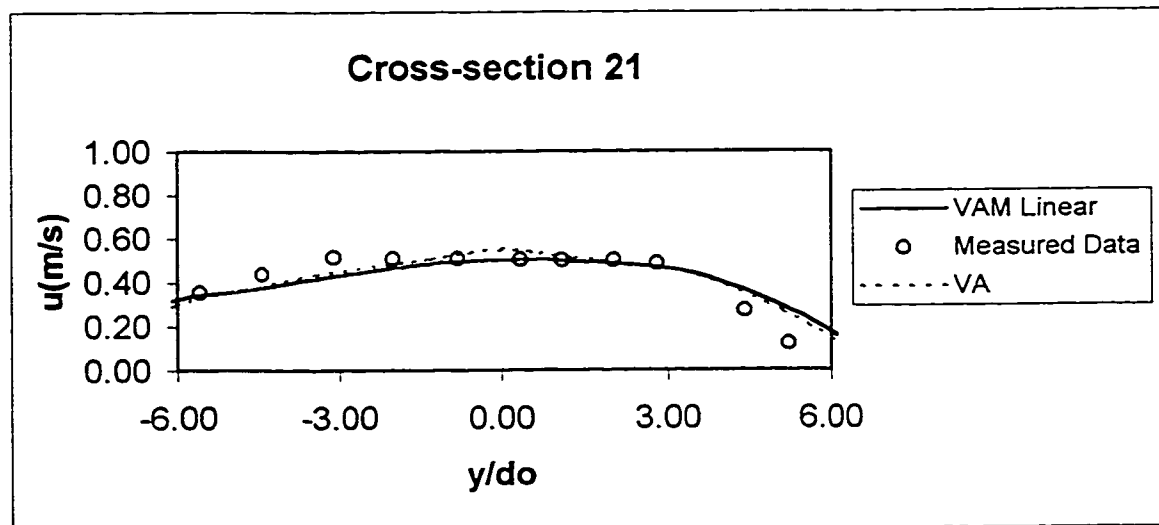


Figure 4.248 The comparison of longitudinal velocity distribution across the river Dommel at cross-section 21

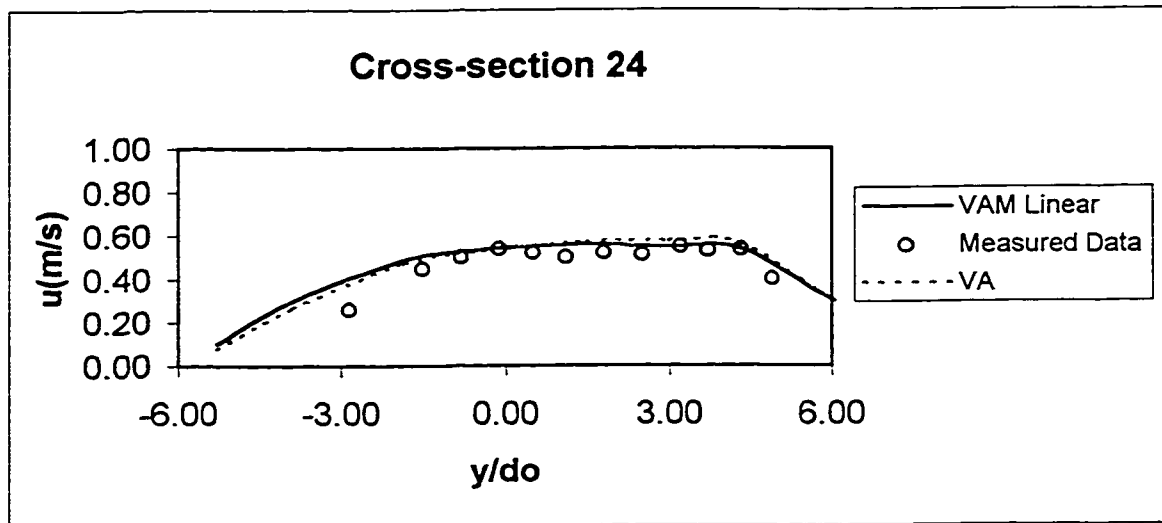


Figure 4.249 The comparison of longitudinal velocity distribution across the river Dommel at cross-section 24

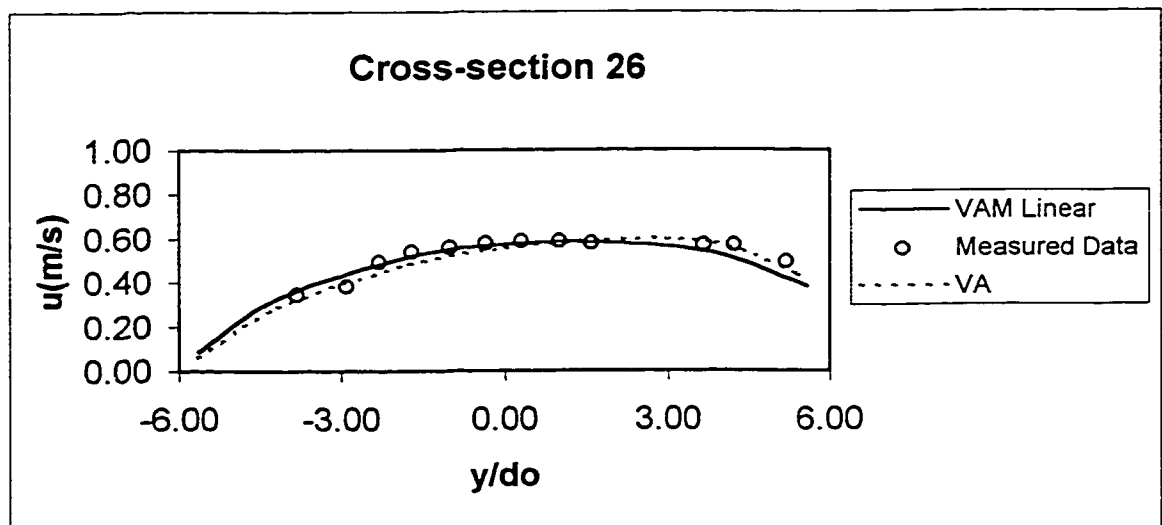


Figure 4.250 The comparison of longitudinal velocity distribution across the river Dommel at cross-section 26

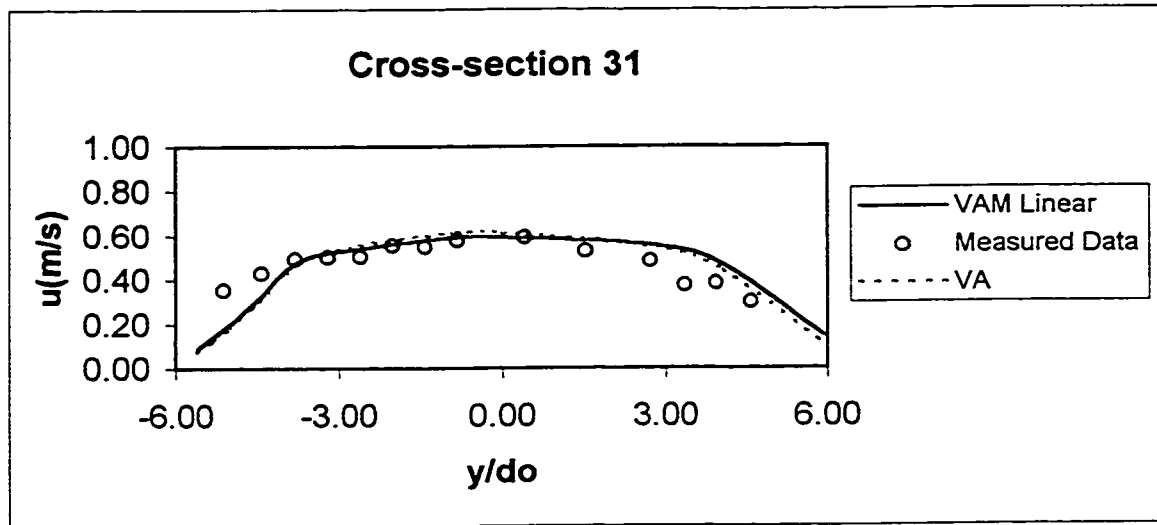


Figure 4.251 The comparison of longitudinal velocity distribution across the river Dommel at cross-section 31

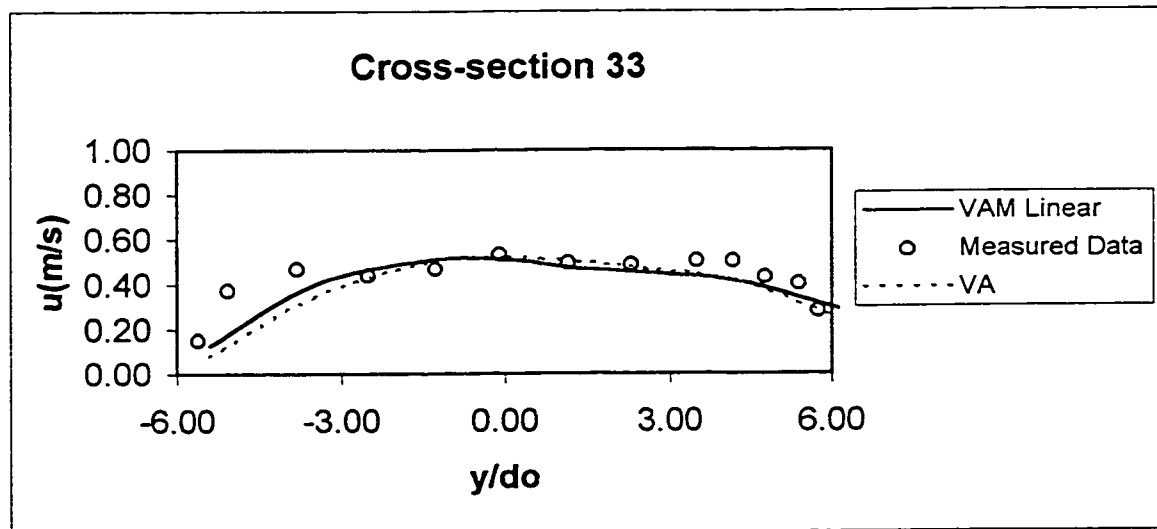


Figure 4.252 The comparison of longitudinal velocity distribution across the river Dommel at cross-section 33

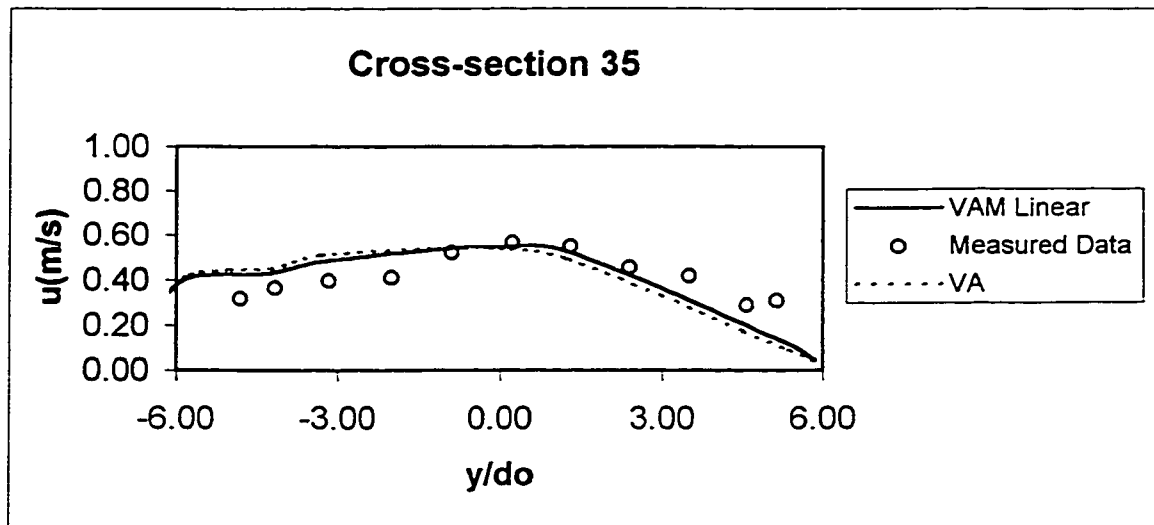


Figure 4.253 The comparison of longitudinal velocity distribution across the river Dommel at cross-section 35

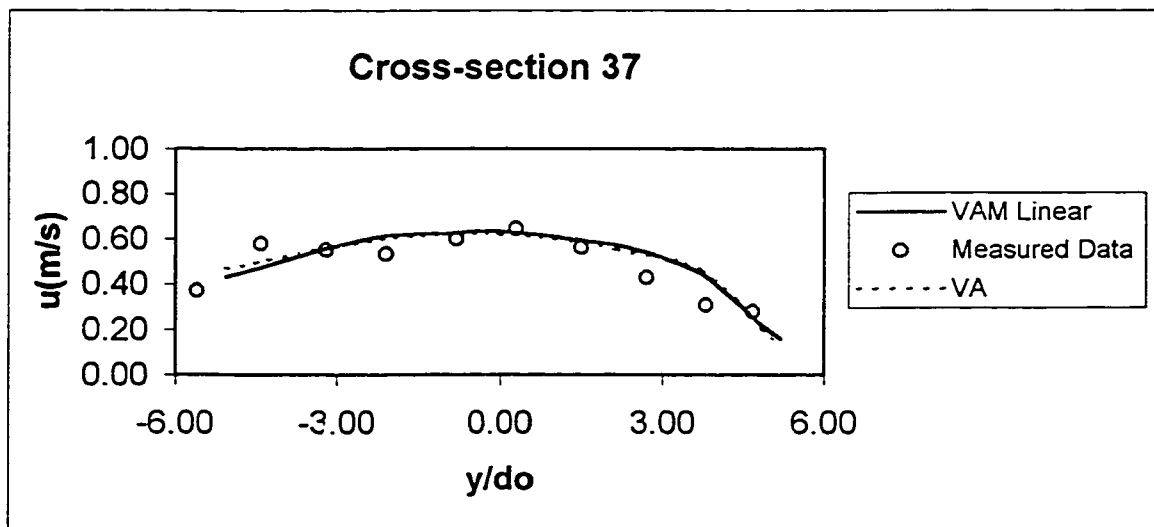


Figure 4.254 The comparison of longitudinal velocity distribution across the river Dommel at cross-section 37

Chapter 5

Summary and Conclusions

A two-dimensional (2-D) model framework, in which some vertical detail is included, is established. The new equations, called the vertically averaged and moment equations, are derived by a moment weighted residual method from the fundamental three-dimensional (3-D) Reynolds equations. The equations are developed in a general way that can accommodate different shapes of velocity and pressure distributions.

The vertically averaged and moment equations are discretized and modeled using a hybrid Petrov-Galerkin and Bubnov-Galerkin finite element scheme. The vertically averaged continuity, longitudinal and transverse momentum, and moment of longitudinal and transverse momentum equations are upwinded using a two-dimensional Characteristic-Dissipative Petrov-Galerkin finite element scheme. The rest of the equations are modeled using the Bubnov-Galerkin finite element scheme.

Triangular elements with linear basis functions for all variables are used. The time derivatives are approximated using a weighted-implicit finite difference formulation. For the resulting implicit set of non-linear algebraic equations a Newton-Raphson technique is used to advance the solution to the next time level and to reach a steady state solution as well.

The developed general equations are then adapted, for convenience and comparison purposes, to allow for the use of linear or quadratic distributions of horizontal velocity components. An existing finite element model is modified to suit these equations.

As a first application, the proposed model is tested for a uniform steady state case. A preliminary numerical test is then carried out to check if the equations are derived and coded correctly. A one-dimensional channel laboratory scale experimental test is selected for this purpose.

The results show that the derivation and the coding of the proposed equations are correctly done. In addition, the VAM model seems to behave significantly better than the VA model.

Next, the obtained vertically averaged and moment equations are investigated for modeling rapidly varied flow transitions with relatively small wavelength to depth ratios ($\lambda/h \approx 7$) where non-hydrostatic pressure and non-uniform velocity distributions might be expected to be significant. The proposed model with assumed linear distributions of horizontal velocity components and quadratic vertical velocity and pressure distributions (the VAM linear model) is used. Two experimental hydraulic problems, from the literature, are selected. In each case the simulated results are compared with the measured data.

Generally, a satisfactory agreement is obtained between the numerical predictions and the experimental measured data. The obtained solutions show that better results are gained regarding the water surface profile by the proposed model compared to the conventional depth or vertically averaged de St. Venant model (the VA model). In addition, this study suggests that the wavelengths involved in the applied test are not short enough for the non-hydrostatic pressure and non-uniform velocity effects to be of significance.

The proposed model is then investigated for modeling curved open channel flows. The VAM with assumed linear and/or quadratic distributions of horizontal velocity components and quadratic vertical velocity and pressure distributions are used in the simulations (the VAM linear and quadratic models). The proposed model is tested for simulating the main as well as the secondary flow features in curved open channels. Five experimental data sets and a field case situation from the literature are selected. The predicted results are compared with the measured data for each case.

A comparison between coarse and fine finite element meshes is considered. A comparison between the VAM 10-equation, 5-equation and the conventional 3-equation de St. Venant (VA) models in terms of computational effort, time necessary for simulation and degree of accuracy obtained is made.

A satisfactory agreement is generally obtained between the numerical predictions and the experimental measured data. The proposed model predicts flow depths and

vertically averaged longitudinal and transverse velocities very favorably as well as reasonable secondary flows. Mainly, the characteristic features of the flow in curved channels such as water surface super-elevation, secondary flow and longitudinal velocity redistribution are well represented. One of the merits of the proposed VAM model is that the evaluation of the secondary flow is obtained by applying the moment of momentum equations only and no further assumptions or experimental constants are required.

This study shows that not only does the proposed model represent the depth averaged flow velocities significantly better than the conventional VA model, but it also captures the shape of the longitudinal velocity profiles and the tendency of the secondary flow profiles over the vertical direction. Predictions of the overall flow characteristics obtained from the VAM linear and quadratic models are seemingly very close. These results suggest that the results are not very sensitive to different approximations of the pre-assumed velocity distribution shapes.

More accurate results are obtained by the finer meshes compared to the coarser meshes. This is to be expected as the numerical discretization errors become smaller (Δx and Δy are of the order of h).

It is found that the time required for the VAM 10-equation model to converge to a final steady state solution is approximately 2.5 times larger than that of the 5-equation model and 3.7 times larger than that of the VA model. In addition, the memory

allocated for the VAM 10-equation model is found to be four times larger than that of the 5-equation model and eleven times larger than that of the VA model.

It is also found that the attained higher accuracy on applying the full VAM 10-equation model is insignificant compared to the VAM 5-equation model. This is may be due to the fact that even though the non-hydrostatic extra terms become more significant near the wall their values are still small such that no significant improvements are obtained over the 5-equation model.

As a result, this study recommends the replacement of the conventional de St. Venant model by the vertically averaged and moment 5-equation model (VAM linear or quadratic), in terms of depth or vertically averaged modeling, on simulating curved open channels where the secondary flow and its effects are important. This should be true for large-scale models where the generated numerical meshes are not very fine. In addition, this study recommends that very fine meshes, in which the applied numerical discretizations are of the order of the flow depth, be applied when a high degree of accuracy of the predicted secondary flows near the channel walls is sought.

It should be mentioned that the proposed model was also tested for 2-D applications with drying areas.

The satisfactory performance of the VAM equations in the previous cases may be attributed to the fact that a higher degree of vertical detail incorporated in the model

compared to the VA model. The new model thus extends the application of the depth averaged open channel flow models to cases where non-uniform velocity and non-hydrostatic pressure distributions are significant. Compared with the full application of a three dimensional model, the new approach would require less computational effort.

This model suffers, however, from the crudeness and arbitrariness of the assumed distributions. The long and complex equations that result are difficult to derive and model correctly.

Recommendations

The present model could be used for fish habitat studies because of its ability to predict approximate near bed velocity and its high flexibility of accommodating different sets of assumed velocity and pressure distributions.

More tests with very short wavelengths to depth ratios ($\lambda/h \approx 1-3$) are recommended to be investigated.

More work is needed in the development of this new model or method. For example, the extension of the development of the new proposed two dimensional model to accommodate for situations that require consideration of sediment transport, e.g. scour around piers and aggradation/degradation of a river regime, should be worked out. Also, a full extension of the derived two dimensional model to accommodate for

flow cases that deals with dispersion is required. More accurate methods to resolve the boundary layer near the bed as well as near the walls (no slip boundary conditions) are needed.

Appendix A

Model Development

In this section, details of the numerical model applied are presented. The derived vertically averaged and moment (VAM) equations are:

$$\frac{\partial h}{\partial t} + \frac{\partial}{\partial x}(q_x i_1 + u_1 h i_2) + \frac{\partial}{\partial y}(q_y i_3 + v_1 h i_4) = 0 \dots\dots\dots(\text{A.1})$$

$$\begin{aligned} & \frac{\partial}{\partial t}(q_x i_1 + u_1 h i_2) + \frac{\partial}{\partial x} \left(\frac{q_x^2}{h} i_5 + q_x u_1 i_6 + u_1^2 h i_7 + g h^2 i_{30} \right) \\ & + \frac{\partial}{\partial y} \left(\frac{q_x q_y}{h} i_{11} + q_x v_1 i_{12} + u_1 q_y i_{13} + u_1 v_1 h i_{14} \right) + \frac{\partial}{\partial x} \left(\frac{p_1 h i_{30}}{\rho} + \frac{p_2 h i_{31}}{\rho} - \frac{h \bar{\sigma}_x}{\rho} \right) \dots\dots(\text{A.2}) \\ & + \frac{\partial}{\partial y} \left(\frac{-h \bar{\tau}_{xy}}{\rho} \right) + \frac{1}{\rho} \left\{ (\rho g h + p_1) \frac{\partial z_b}{\partial x} + \tau_{x_b} \right\} = 0 \end{aligned}$$

$$\begin{aligned} & \frac{\partial}{\partial t}(q_y i_3 + v_1 h i_4) + \frac{\partial}{\partial x} \left(\frac{q_x q_y}{h} i_{11} + q_x v_1 i_{12} + u_1 q_y i_{13} + u_1 v_1 h i_{14} \right) \\ & + \frac{\partial}{\partial y} \left(\frac{q_y^2}{h} i_8 + q_y v_1 i_9 + v_1^2 h i_{10} + g h^2 i_{30} \right) + \frac{\partial}{\partial y} \left(\frac{p_1 h i_{30}}{\rho} + \frac{p_2 h i_{31}}{\rho} - \frac{h \bar{\sigma}_y}{\rho} \right) \dots\dots\dots(\text{A.3}) \\ & + \frac{\partial}{\partial x} \left(\frac{-h \bar{\tau}_{yx}}{\rho} \right) + \frac{1}{\rho} \left\{ (\rho g h + p_1) \frac{\partial z_b}{\partial y} + \tau_{y_b} \right\} = 0 \end{aligned}$$

$$\begin{aligned}
& \frac{\partial}{\partial t} [q_x(h.i_{32} + z_b.i_1) + u_1 h(h.i_{33} + z_b.i_2)] \\
& + \frac{\partial}{\partial x} \left[\frac{q_x^2}{h} (h.i_{36} + z_b.i_5) + q_x u_1 (h.i_{37} + z_b.i_6) + u_1^2 h(h.i_{38} + z_b.i_7) \right] \\
& + \frac{\partial}{\partial y} \left[\frac{q_x q_y}{h} (h.i_{44} + z_b.i_{11}) + q_x v_1 (h.i_{46} + z_b.i_{12}) \right. \\
& \quad \left. + q_y u_1 (h.i_{45} + z_b.i_{13}) + v_1 u_1 h(h.i_{47} + z_b.i_{14}) \right] \\
& + \frac{\partial}{\partial x} \left[g h^2 (h.i_{39} + z_b.i_{30}) + \frac{p_1 h(h.i_{39} + z_b.i_{30})}{\rho} + \frac{p_2 h(h.i_{40} + z_b.i_{31})}{\rho} \right] \\
& - \bar{z} \left[\frac{\partial}{\partial t} (q_x.i_1 + u_1 h.i_2) + \frac{\partial}{\partial x} \left(\frac{q_x^2}{h} .i_5 + q_x u_1 h.i_6 + u_1^2 h.i_7 \right) \right. \\
& \quad \left. + \frac{\partial}{\partial y} \left(\frac{q_x q_y}{h} .i_{11} + q_x v_1 .i_{12} + q_y u_1 .i_{13} + v_1 u_1 h.i_{14} \right) \right] \\
& - [w_b(q_x.i_{18} + u_1 h.i_{19}) + w_2(q_x.i_{20} + u_1 h.i_{21}) + w_h(q_x.i_{22} + u_1 h.i_{23})] \dots\dots\dots(\text{A.4})
\end{aligned}$$

$$+ \frac{1}{\rho} \left\{ \rho g \left[-\bar{z} \frac{\partial h^2.i_{30}}{\partial x} - \frac{h^2}{2} \frac{\partial z_b}{\partial x} \right] - \bar{z} \frac{\partial p_1 h.i_{30}}{\partial x} - \frac{p_1 h}{2} \frac{\partial z_b}{\partial x} \right. \\
\left. - \bar{z} \frac{\partial p_2 h.i_{31}}{\partial x} - h \bar{\sigma}_x \frac{\partial \bar{z}}{\partial x} - h \bar{\tau}_{xy} \frac{\partial \bar{z}}{\partial y} - \frac{h}{2} \tau_{\kappa_b} + h \bar{\tau}_{\kappa} \right\} = 0$$

$$\begin{aligned}
& \frac{\partial}{\partial t} [q_y(hi_{34} + z_b.i_3) + v_1 h(hi_{35} + z_b.i_4)] \\
& + \frac{\partial}{\partial x} \left[\frac{q_x q_y}{h} (hi_{44} + z_b.i_{11}) + q_x v_1 (hi_{46} + z_b.i_{12}) \right. \\
& \quad \left. + q_y u_1 (hi_{45} + z_b.i_{13}) + v_1 u_1 h(hi_{47} + z_b.i_{14}) \right] \\
& + \frac{\partial}{\partial y} \left[\frac{q_y^2}{h} (hi_{41} + z_b.i_8) + q_y v_1 (hi_{42} + z_b.i_9) + v_1^2 h(hi_{43} + z_b.i_{10}) \right] \\
& + \frac{\partial}{\partial y} \left[gh^2(hi_{39} + z_b.i_{30}) + \frac{p_1 h(hi_{39} + z_b.i_{30})}{\rho} + \frac{p_2 h(hi_{40} + z_b.i_{31})}{\rho} \right] \\
& - \bar{z} \left[\frac{\partial}{\partial t} (q_y.i_3 + v_1 h i_4) + \frac{\partial}{\partial x} \left(\frac{q_x q_y}{h} .i_{11} + q_x v_1 .i_{12} + q_y u_1 .i_{13} + v_1 u_1 h i_{14} \right) \right. \\
& \quad \left. + \frac{\partial}{\partial y} \left(\frac{q_y^2}{h} .i_8 + q_y v_1 .i_9 + v_1^2 h i_{10} \right) \right] \\
& - [w_b(q_y.i_{24} + v_1 h i_{25}) + w_2(q_y.i_{26} + v_1 h i_{27}) + w_h(q_y.i_{28} + v_1 h i_{29})] \dots\dots\dots(A.5) \\
& + \frac{1}{\rho} \left\{ \rho g \left[-\bar{z} \frac{\partial h^2 .i_{30}}{\partial y} - \frac{h^2}{2} \frac{\partial z_b}{\partial y} \right] - \bar{z} \frac{\partial p_1 h i_{30}}{\partial y} - \frac{p_1 h}{2} \frac{\partial z_b}{\partial y} \right. \\
& \quad \left. - \bar{z} \frac{\partial p_2 h i_{31}}{\partial y} - h \bar{\sigma}_y \frac{\partial \bar{z}}{\partial y} - h \bar{\tau}_{yx} \frac{\partial \bar{z}}{\partial x} - \frac{h}{2} \tau_{y\bar{z}} + h \bar{\tau}_{y\bar{z}} \right\} = 0
\end{aligned}$$

$$\begin{aligned}
& \frac{\partial}{\partial t} \left(\frac{h^2}{4} \right) + \frac{\partial}{\partial x} [q_x(hi_{32} + z_b i_1) + u_1 h(hi_{33} + z_b i_2)] \\
& + \frac{\partial}{\partial y} [q_y(hi_{34} + z_b i_3) + v_1 h(hi_{35} + z_b i_4)] \\
& \dots\dots\dots (A.6)
\end{aligned}$$

$$\begin{aligned}
& -\bar{z} \left[\frac{\partial}{\partial x} (q_x i_1 + u_1 h i_2) + \frac{\partial}{\partial y} (q_y i_3 + v_1 h i_4) \right] \\
& - (w_b h i_{15} + w_2 h i_{16} + w_h h i_{17}) = 0
\end{aligned}$$

$$-\left(\frac{q_x}{h} - D_1 u_1 \right) \frac{\partial z_b}{\partial x} - \left(\frac{q_y}{h} - D_1 v_1 \right) \frac{\partial z_b}{\partial y} + w_b = 0 \dots\dots\dots (A.7)$$

$$\frac{\partial(-h)}{\partial t} - \left(\frac{q_x}{h} + u_1 \right) \frac{\partial}{\partial x} (h + z_b) - \left(\frac{q_y}{h} + v_1 \right) \frac{\partial}{\partial y} (h + z_b) + w_h = 0 \dots\dots\dots (A.8)$$

$$\begin{aligned}
& \frac{\partial}{\partial t} (w_b h i_{15} + w_2 h i_{16} + w_h h i_{17}) \\
& + \frac{\partial}{\partial x} [w_b (q_x i_{18} + u_1 h i_{19}) + w_2 (q_x i_{20} + u_1 h i_{21}) + w_h (q_x i_{22} + u_1 h i_{23})] \\
& \dots\dots\dots (A.9)
\end{aligned}$$

$$\begin{aligned}
& + \frac{\partial}{\partial y} [w_b (q_y i_{24} + v_1 h i_{25}) + w_2 (q_y i_{26} + v_1 h i_{27}) + w_h (q_y i_{28} + v_1 h i_{29})] \\
& + \frac{\partial}{\partial x} \left(\frac{-h \bar{\tau}_x}{\rho} \right) + \frac{\partial}{\partial y} \left(\frac{-h \bar{\tau}_y}{\rho} \right) - \frac{1}{\rho} \left\{ p_1 + \tau_{y z_b} \frac{\partial z_b}{\partial y} + \tau_{z_b x} \frac{\partial z_b}{\partial x} \right\} = 0
\end{aligned}$$

$$\begin{aligned}
& \frac{\partial}{\partial t} [w_b h(hi_{48} + z_b i_{15}) + w_2 h(hi_{49} + z_b i_{16}) + w_h h(hi_{50} + z_b i_{17})] \\
& + \frac{\partial}{\partial x} \left\{ \begin{aligned} & w_b [q_x (hi_{51} + z_b i_{18}) + u_1 h(hi_{54} + z_b i_{19})] \\ & + w_2 [q_x (hi_{52} + z_b i_{20}) + u_1 h(hi_{55} + z_b i_{21})] \\ & + w_h [q_x (hi_{53} + z_b i_{22}) + u_1 h(hi_{56} + z_b i_{23})] \end{aligned} \right\} \\
& + \frac{\partial}{\partial y} \left\{ \begin{aligned} & w_b [q_y (hi_{57} + z_b i_{24}) + v_1 h(hi_{60} + z_b i_{25})] \\ & + w_2 [q_y (hi_{58} + z_b i_{26}) + v_1 h(hi_{61} + z_b i_{27})] \\ & + w_h [q_y (hi_{59} + z_b i_{28}) + v_1 h(hi_{62} + z_b i_{29})] \end{aligned} \right\} \\
& - \bar{z} \left\{ \begin{aligned} & \frac{\partial}{\partial t} (w_b hi_{15} + w_2 hi_{16} + w_h hi_{17}) \\ & + \frac{\partial}{\partial x} [w_b (q_x i_{18} + u_1 hi_{19}) + w_2 (q_x i_{20} + u_1 hi_{21}) + w_h (q_x i_{22} + u_1 hi_{23})] \\ & + \frac{\partial}{\partial y} [w_b (q_y i_{24} + v_1 hi_{25}) + w_2 (q_y i_{26} + v_1 hi_{27}) + w_h (q_y i_{28} + v_1 hi_{29})] \end{aligned} \right\} \\
& - (w_b^2 hi_{63} + w_b w_2 hi_{64} + w_b w_h hi_{65} + w_2^2 hi_{66} + w_2 w_h hi_{67} + w_h^2 hi_{68}) \dots\dots\dots (A.10)
\end{aligned}$$

$$+ \frac{1}{\rho} \left\{ \begin{aligned} & -h\bar{\tau}_x \frac{\partial \bar{z}}{\partial x} - h\bar{\tau}_{xy} \frac{\partial \bar{z}}{\partial y} + \left(\frac{h}{2} - hi_{30} \right) (\rho gh + p_1) - p_2 hi_{31} \\ & + \frac{h}{2} \left[\tau_{yz} \frac{\partial z_b}{\partial y} + \tau_{xz} \frac{\partial z_b}{\partial y} \right] + h\bar{\sigma}_z \end{aligned} \right\} = 0$$

Where

$$\bar{z} = z_b + \frac{h}{2} \dots\dots\dots (A.11)$$

To obtain the previous equations, the following general distributions are used for horizontal velocity components, vertical velocity and pressure respectively:

$$u = u_o f_1 (\eta) + u_l g_1 (\eta) \dots\dots\dots (A.12)$$

$$v = v_o f_2 (\eta) + v_l g_2 (\eta) \dots\dots\dots (A.13)$$

$$w = w_b f_3 (\eta) + w_2 g_3 (\eta) + w_h H_3 (\eta) \dots\dots\dots (A.14)$$

$$p = \rho g h f_4 (\eta) + p_l f_4 (\eta) + p_2 g_4 (\eta) \dots\dots\dots (A.15)$$

Where u_l is the velocity at the surface in excess of the mean velocity u_o ; v_l is the velocity at the surface in excess of the mean velocity v_o ; w_b and w_h indicate the vertical velocities at the bottom and at the surface respectively; w_2 is the mid-depth vertical velocity in excess of the average of the vertical velocities at the surface and bed; p_l is the pressure intensity in excess of the hydrostatic at bed; p_2 is the mid-depth pressure in excess of the average of pressure at the bed and surface; η is non-

dimensional vertical coordinate and given by $\eta = (z-z_b)/h$; $f_1(\eta)$, $g_1(\eta)$, $f_2(\eta)$, $g_2(\eta)$, $f_3(\eta)$, $g_3(\eta)$, $H_3(\eta)$, $f_4(\eta)$ and $g_4(\eta)$ are functions defining the different distributions of the velocities as well as the pressure; D_I is a constant that depends on the pre-assumed distribution shapes of the horizontal velocity components and i 's represent integral constants and given in Appendix B.

It should be mentioned that the functions $f_1(\eta)$ and $f_2(\eta)$ are kept constant and equal to one. In addition, the integrals $\int_0^1 g_1(\eta) d\eta$ and $\int_0^1 g_2(\eta) d\eta$ should vanish, i.e. they should be equal to zeros.

Equations (A.1)-(A.10) represent VA continuity, VA x-momentum, VA y-momentum, VAM x-momentum, VAM y-momentum, VAM continuity, " w_b ", " w_h ", VA z-momentum and VAM z-momentum equations respectively.

The vertically averaged turbulent shear and normal stresses appearing in equations (A.1)-(A.10) are approximated according to Boussinesq model and given by:

$$\bar{\sigma}_x = \bar{\tau}_{xx} = 2\rho\nu_h \frac{\partial u_o}{\partial x} \dots\dots\dots (A.16)$$

$$\bar{\sigma}_y = \bar{\tau}_{yy} = 2\rho\nu_h \frac{\partial v_o}{\partial y} \dots\dots\dots (A.17)$$

$$\bar{\sigma}_z = \bar{\tau}_z = 2\rho\nu_z \frac{w_h - w_b}{h} \dots\dots\dots(\text{A.18})$$

$$\bar{\tau}_{xy} = \bar{\tau}_{yx} = \rho\nu_h \left(\frac{\partial u_o}{\partial y} + \frac{\partial v_o}{\partial x} \right) \dots\dots\dots(\text{A.19})$$

$$\bar{\tau}_{xz} = \bar{\tau}_{zx} = \rho\nu_z \left(\frac{D_2 u_1}{h} + \frac{\partial \bar{w}}{\partial x} \right) \dots\dots\dots(\text{A.20})$$

$$\bar{\tau}_{yz} = \bar{\tau}_{zy} = \rho\nu_z \left(\frac{D_2 v_1}{h} + \frac{\partial \bar{w}}{\partial y} \right) \dots\dots\dots(\text{A.21})$$

Where ν_h is the vertically averaged turbulent exchange coefficient or eddy viscosity in the horizontal direction (x-y plane), and ν_z is the vertically averaged turbulent eddy viscosity in the vertical direction. For simplicity, the case of bed-dominated turbulence is assumed and values of the order of $\nu_h = 0.5 u_* h$ and $\nu_z = 0.07 u_* h$ are

used (Fisher et al., 1979). u_* being the shear velocity and equal to $\sqrt{\left(\frac{\tau_{bx}}{\rho}\right)^2 + \left(\frac{\tau_{by}}{\rho}\right)^2}$.

D_2 is a constant that depends on the pre-assumed distribution shapes of the horizontal velocity components.

The bed shear stresses, appearing in equations (A.1)-(A.10), are approximated according to:

$$\tau_{xz_b} = \frac{\rho}{C_*^2} u_o \sqrt{u_o^2 + v_o^2 + \bar{w}^2} \dots\dots\dots (A.22)$$

$$\tau_{yz_b} = \frac{\rho}{C_*^2} v_o \sqrt{u_o^2 + v_o^2 + \bar{w}^2} \dots\dots\dots (A.23)$$

C_* being the dimensionless Chezy Coefficient and is related to the effective roughness height, k_s , through:

$$C_* = 5.75 \log \left(12 \frac{h}{k_s} \right) \dots\dots\dots (A.24)$$

For small depth to roughness ratios ($h/k_s < e/12$), e being the natural logarithmic constant and equal to 2.71828, equation (A.24) is replaced by:

$$C_* = \frac{30}{e} \left(\frac{h}{k_s} \right) \dots\dots\dots (A.25)$$

For practical purposes, the following approach to boundary condition seems to work: the first three equations ((A.1)-(A.3)) are essentially the shallow water equations and use the appropriate set of boundary conditions for sub- and supercritical inflow,

outflow and no flow cases. For case of subcritical flow, a given total flow is specified at the upstream cross-section as an inflow boundary, whereas a fixed water surface elevation is specified at the downstream cross-section as an outflow boundary. For case of supercritical flow, both the flow and the water surface elevation are given at the upstream cross-section as inflow boundaries, whereas no conditions are applied at the outflow boundary. A no cross-flow condition is specified at the walls.

The equations of moment of momentum in horizontal and transverse directions ((A.4.)-(A.5)) appear to have the characteristic of transport equations. As a result, values for the velocities in excess of the means at the surface, u_I and v_I , are given at the upstream cross-section for inflow boundary case, whereas they are left free at the outflow boundary case. At the walls, a slip velocity condition is specified for u_I and v_I . That means the velocities in excess of the means at the surface, u_I and v_I , may have a component parallel to the wall, but not perpendicular to the wall.

The rest of the equations ((A.6)-(A.10)) are mostly reactive type of equations; that is, the dependent variables being evaluated from each of these equations do not involve the temporal or spatial derivative of that variable. As a result, the rest of the variables: \bar{w} , w_b , w_h , p_1 , and p_2 are left free at all boundaries.

At time $t = 0$, all variables are defined to have initial values at each point of the domain of interest. Having defined the initial values of the variables and specified the boundary conditions, we are left with a closed system which defines a 'model' for

2-D or a quasi 3-D flow in open channels (equations (A.1)-(A.10)). This model solves for “ h ”, “ q_x ”, “ q_y ”, “ u_l ”, “ v_l ”, “ \bar{w} or w_2 ”, “ w_b ”, “ w_h ”, “ h_l or p_l ” and “ h_2 or p_2 ” dependent variables respectively, h_l and h_2 being $p_l/\rho g$ and $p_2/\rho g$ respectively. Essentially, equation (A.1) solves for “ h ”, equation (A.2) solves for “ q_x ”, equation (A.3) solves for “ q_y ”, equation (A.4) solves for “ u_l ”, equation (A.5) solves for “ v_l ”, equation (A.6) solves for “ \bar{w} ”, equation (A.7) solves for “ w_b ”, equation (A.8) solves for “ w_h ”, equation (A.9) solves for “ h_l or p_l ”, and equation (A.10) solves for “ h_2 or p_2 ”.

It should be mentioned that all the extra degrees of freedom, introduced by the proposed VAM model, are perturbations to those of de St. Venant and Boussinesq. Thus the above system of equations can easily be reduced to the de St. Venant or Boussinesq equations by forcing the appropriate perturbations to zero and eliminating the corresponding equations.

The vertically averaged and moment equations are discretized and modeled using a hybrid Petrov-Galerkin and Bubnov-Galerkin finite element scheme. The vertically averaged continuity, longitudinal and transverse momentum, and moment of longitudinal and transverse momentum equations are upwinded using the two-dimensional Characteristic Dissipative Petrov-Galerkin finite element scheme recently used by Ghanem et al. (1995). This scheme has the ability of providing selective artificial dissipation for shock capturing and modeling both progressive and regressive waves accurately (Hicks and Steffler, 1990, 1992 and Ghanem et al.,

1995). The rest of the equations are modeled using the Bubnov-Galerkin finite element scheme. This may be explained in the following sections.

Equations (A.1)-(A.10) may be written in the form:

$$\frac{\partial \psi(\phi)}{\partial t} + \frac{\partial \mathbf{F}_x(\phi)}{\partial x} + \frac{\partial \mathbf{F}_y(\phi)}{\partial y} + \mathbf{G}(\phi) = 0.0 \quad \text{.....(A.26)}$$

Where bold letters represent vectors and matrices. ϕ represents $N_u \times 1$ vector per element, N_u being the total number of unknowns. For example ϕ is equal to $(h, q_x, q_y, u_l, v_l, \bar{w} \text{ or } w_2, w_b, w_h, p_l, p_2)^T$ for the 10-equation model ($N_u=10$). Ω is the solution domain.

$$\psi(\phi) = \left\{ \begin{array}{c} \psi_1(\phi) \\ \psi_2(\phi) \\ \psi_3(\phi) \\ \psi_4(\phi) \\ \psi_5(\phi) \\ \psi_6(\phi) \\ \psi_7(\phi) \\ \psi_8(\phi) \\ \psi_9(\phi) \\ \psi_{10}(\phi) \end{array} \right\}_{N_u \times 1} \quad \text{.....(A.27)}$$

$$\psi_1(\phi) = h \quad \text{.....(A.28)}$$

$$\psi_2(\phi) = q_x.i_1 + u_1.hi_2 \dots\dots\dots (A.29)$$

$$\psi_3(\phi) = q_y.i_3 + v_1.hi_4 \dots\dots\dots (A.30)$$

$$\psi_4(\phi) = q_x(hi_{32} + z_b.i_1) + u_1.h(hi_{33} + z_b.i_2) \dots\dots\dots (A.31)$$

$$\psi_5(\phi) = q_y(hi_{34} + z_b.i_3) + v_1.h(hi_{35} + z_b.i_4) \dots\dots\dots (A.32)$$

$$\psi_6(\phi) = \frac{h^2}{4} \dots\dots\dots (A.33)$$

$$\psi_7(\phi) = 0 \dots\dots\dots (A.34)$$

$$\psi_8(\phi) = -h \dots\dots\dots (A.35)$$

$$\psi_9(\phi) = w_b.hi_{15} + w_2.hi_{16} + w_h.hi_{17} \dots\dots\dots (A.36)$$

$$\psi_{10}(\phi) = w_b.h(hi_{48} + z_b.i_{15}) + w_2.h(hi_{49} + z_b.i_{16}) + w_h.h(hi_{50} + z_b.i_{17}) \dots\dots\dots (A.37)$$

$$\mathbf{F}_x(\phi) = \begin{Bmatrix} F_{x_1}(\phi) \\ F_{x_2}(\phi) \\ F_{x_3}(\phi) \\ F_{x_4}(\phi) \\ F_{x_5}(\phi) \\ F_{x_6}(\phi) \\ F_{x_7}(\phi) \\ F_{x_8}(\phi) \\ F_{x_9}(\phi) \\ F_{x_{10}}(\phi) \end{Bmatrix}_{N_u \times 1} \dots\dots\dots (A.38)$$

$$F_{x_1}(\phi) = q_x i_1 + u_1 h i_2 \dots\dots\dots (A.39)$$

$$F_{x_2}(\phi) = \frac{q_x^2}{h} i_5 + q_x u_1 i_6 + u_1^2 h i_7 + g h^2 i_{30} + \frac{p_1 h i_{30}}{\rho} + \frac{p_2 h i_{31}}{\rho} - \frac{h \bar{\sigma}_x}{\rho} \dots\dots\dots (A.40)$$

$$F_{x_3}(\phi) = \frac{q_x q_y}{h} i_{11} + q_x v_1 i_{12} + u_1 q_y i_{13} + u_1 v_1 h i_{14} - \frac{h \bar{\tau}_{yx}}{\rho} \dots\dots\dots (A.41)$$

$$F_{x_4}(\phi) = \frac{q_x^2}{h} (h i_{36} + z_b i_5) + q_x u_1 (h i_{37} + z_b i_6) + u_1^2 h (h i_{38} + z_b i_7) \\ + g h^2 (h i_{39} + z_b i_{30}) + \frac{p_1 h (h i_{39} + z_b i_{30})}{\rho} + \frac{p_2 h (h i_{40} + z_b i_{31})}{\rho} \dots\dots\dots (A.42)$$

$$F_{x_5}(\phi) = \frac{q_x q_y}{h} (h i_{44} + z_b i_{11}) + q_x v_1 (h i_{46} + z_b i_{12}) + q_y u_1 (h i_{45} + z_b i_{13}) \\ + v_1 u_1 h (h i_{47} + z_b i_{14}) \dots\dots\dots (A.43)$$

$$F_{x_6}(\phi) = q_x(hi_{32} + z_b i_1) + u_1 h(hi_{33} + z_b i_2) \dots\dots\dots (A.44)$$

$$F_{x_7}(\phi) = 0 \dots\dots\dots (A.45)$$

$$F_{x_8}(\phi) = 0 \dots\dots\dots (A.46)$$

$$F_{x_9}(\phi) = w_b(q_x i_{18} + u_1 h i_{19}) + w_2(q_x i_{20} + u_1 h i_{21}) + w_h(q_x i_{22} + u_1 h i_{23}) - \frac{h\bar{\tau}_x}{\rho} \dots\dots (A.47)$$

$$\begin{aligned} F_{x_{10}}(\phi) = & w_b[q_x(hi_{51} + z_b i_{18}) + u_1 h(hi_{54} + z_b i_{19})] \\ & + w_2[q_x(hi_{52} + z_b i_{20}) + u_1 h(hi_{55} + z_b i_{21})] \dots\dots\dots (A.48) \\ & + w_h[q_x(hi_{53} + z_b i_{22}) + u_1 h(hi_{56} + z_b i_{23})] \end{aligned}$$

$$\mathbf{F}_y(\phi) = \left\{ \begin{array}{c} F_{y_1}(\phi) \\ F_{y_2}(\phi) \\ F_{y_3}(\phi) \\ F_{y_4}(\phi) \\ F_{y_5}(\phi) \\ F_{y_6}(\phi) \\ F_{y_7}(\phi) \\ F_{y_8}(\phi) \\ F_{y_9}(\phi) \\ F_{y_{10}}(\phi) \end{array} \right\}_{N_y \times 1} \dots\dots\dots (A.49)$$

$$F_{y_1}(\phi) = q_y i_3 + v_1 h i_4 \dots\dots\dots (A.50)$$

$$F_{y_2}(\phi) = \frac{q_x q_y}{h} i_{11} + q_x v_1 i_{12} + u_1 q_y i_{13} + u_1 v_1 h i_{14} - \frac{h \bar{\tau}_{xy}}{\rho} \dots\dots\dots (A.51)$$

$$F_{y_3}(\phi) = \frac{q_y^2}{h} i_8 + q_y v_1 i_9 + v_1^2 h i_{10} + g h^2 i_{30} + \frac{p_1 h i_{30}}{\rho} + \frac{p_2 h i_{31}}{\rho} - \frac{h \bar{\sigma}_y}{\rho} \dots\dots\dots (A.52)$$

$$F_{y_4}(\phi) = \frac{q_x q_y}{h} (h i_{44} + z_b i_{11}) + q_x v_1 (h i_{46} + z_b i_{12}) + q_y u_1 (h i_{45} + z_b i_{13}) \\ + v_1 u_1 h (h i_{47} + z_b i_{14}) \dots\dots\dots (A.53)$$

$$F_{y_5}(\phi) = \frac{q_x^2}{h} (h i_{41} + z_b i_8) + q_y v_1 (h i_{42} + z_b i_9) + v_1^2 h (h i_{43} + z_b i_{10}) \\ + g h^2 (h i_{39} + z_b i_{30}) + \frac{p_1 h (h i_{39} + z_b i_{30})}{\rho} + \frac{p_2 h (h i_{40} + z_b i_{31})}{\rho} \dots\dots\dots (A.54)$$

$$F_{y_6}(\phi) = q_y (h i_{34} + z_b i_3) + v_1 h (h i_{35} + z_b i_4) \dots\dots\dots (A.55)$$

$$F_{y_7}(\phi) = 0 \dots\dots\dots (A.56)$$

$$F_{y_8}(\phi) = 0 \dots\dots\dots (A.57)$$

$$F_{y_9}(\phi) = w_b (q_y i_{24} + v_1 h i_{25}) + w_2 (q_y i_{26} + v_1 h i_{27}) + w_h (q_y i_{28} + v_1 h i_{29}) - \frac{h \bar{\tau}_{xy}}{\rho} \dots\dots (A.58)$$

$$\begin{aligned}
F_{y_{10}}(\phi) = & w_b \left[q_y (h i_{57} + z_b i_{24}) + v_1 h (h i_{60} + z_b i_{25}) \right] \\
& + w_2 \left[q_y (h i_{58} + z_b i_{26}) + v_1 h (h i_{61} + z_b i_{27}) \right] \dots \dots \dots (A.59) \\
& + w_h \left[q_y (h i_{59} + z_b i_{28}) + v_1 h (h i_{62} + z_b i_{29}) \right]
\end{aligned}$$

$$\mathbf{G}(\phi) = \left\{ \begin{array}{c} G_1(\phi) \\ G_2(\phi) \\ G_3(\phi) \\ G_4(\phi) \\ G_5(\phi) \\ G_6(\phi) \\ G_7(\phi) \\ G_8(\phi) \\ G_9(\phi) \\ G_{10}(\phi) \end{array} \right\}_{N_u \times 1} \dots \dots \dots (A.60)$$

$$G_1(\phi) = 0 \dots \dots \dots (A.61)$$

$$G_2(\phi) = \frac{1}{\rho} \left\{ (\rho g h + p_1) \frac{\partial z_b}{\partial x} + \tau_{xz_b} \right\} \dots \dots \dots (A.62)$$

$$G_3(\phi) = \frac{1}{\rho} \left\{ (\rho g h + p_1) \frac{\partial z_b}{\partial y} + \tau_{yz_b} \right\} \dots \dots \dots (A.63)$$

$$G_4(\phi) = -\bar{z} \left[\frac{\partial}{\partial t} (q_x i_1 + u_1 h i_2) + \frac{\partial}{\partial x} \left(\frac{q_x^2}{h} i_5 + q_x u_1 h i_6 + u_1^2 h i_7 \right) \right] \\ + \frac{\partial}{\partial y} \left(\frac{q_x q_y}{h} i_{11} + q_x v_1 i_{12} + q_y u_1 i_{13} + v_1 u_1 h i_{14} \right) \\ - [w_b (q_x i_{18} + u_1 h i_{19}) + w_2 (q_x i_{20} + u_1 h i_{21}) + w_h (q_x i_{22} + u_1 h i_{23})] \dots\dots\dots (A.64)$$

$$+ \frac{1}{\rho} \left\{ \rho g \left[-\bar{z} \frac{\partial h^2 i_{30}}{\partial x} - \frac{h^2}{2} \frac{\partial z_b}{\partial x} \right] - \bar{z} \frac{\partial p_1 h i_{30}}{\partial x} - \frac{p_1 h}{2} \frac{\partial z_b}{\partial x} \right. \\ \left. - \bar{z} \frac{\partial p_2 h i_{31}}{\partial x} - h \bar{\sigma}_x \frac{\partial \bar{z}}{\partial x} - h \bar{\tau}_{xy} \frac{\partial \bar{z}}{\partial y} - \frac{h}{2} \tau_{x_b} + h \bar{\tau}_x \right\}$$

$$G_5(\phi) = -\bar{z} \left[\frac{\partial}{\partial t} (q_y i_3 + v_1 h i_4) + \frac{\partial}{\partial x} \left(\frac{q_x q_y}{h} i_{11} + q_x v_1 i_{12} + q_y u_1 i_{13} + v_1 u_1 h i_{14} \right) \right] \\ + \frac{\partial}{\partial y} \left(\frac{q_y^2}{h} i_8 + q_y v_1 i_9 + v_1^2 h i_{10} \right) \\ - [w_b (q_y i_{24} + v_1 h i_{25}) + w_2 (q_y i_{26} + v_1 h i_{27}) + w_h (q_y i_{28} + v_1 h i_{29})] \dots\dots (A.65)$$

$$+ \frac{1}{\rho} \left\{ \rho g \left[-\bar{z} \frac{\partial h^2 i_{30}}{\partial y} - \frac{h^2}{2} \frac{\partial z_b}{\partial y} \right] - \bar{z} \frac{\partial p_1 h i_{30}}{\partial y} - \frac{p_1 h}{2} \frac{\partial z_b}{\partial y} \right. \\ \left. - \bar{z} \frac{\partial p_2 h i_{31}}{\partial y} - h \bar{\sigma}_y \frac{\partial \bar{z}}{\partial y} - h \bar{\tau}_{yx} \frac{\partial \bar{z}}{\partial x} - \frac{h}{2} \tau_{y_b} + h \bar{\tau}_{yz} \right\}$$

$$G_6(\phi) = -\bar{z} \left[\frac{\partial}{\partial x} (q_x i_1 + u_1 h i_2) + \frac{\partial}{\partial y} (q_y i_3 + v_1 h i_4) \right] - (w_b h i_{15} + w_2 h i_{16} + w_h h i_{17}). (A.66)$$

$$G_7(\phi) = - \left(\frac{q_x}{h} - u_1 \right) \frac{\partial z_b}{\partial x} - \left(\frac{q_y}{h} - v_1 \right) \frac{\partial z_b}{\partial y} + w_b \dots\dots\dots (A.67)$$

$$G_8(\phi) = -\left(\frac{q_x}{h} + u_1\right) \frac{\partial}{\partial x}(h + z_b) - \left(\frac{q_y}{h} + v_1\right) \frac{\partial}{\partial y}(h + z_b) + w_h \dots\dots\dots (A.68)$$

$$G_9(\phi) = -\frac{1}{\rho} \left\{ p_1 + \tau_{yz} \frac{\partial z_b}{\partial y} + \tau_{xz} \frac{\partial z_b}{\partial x} \right\} \dots\dots\dots (A.69)$$

$$\begin{aligned} G_{10}(\phi) = & -\bar{z} \left\{ \frac{\partial}{\partial t}(w_b h i_{15} + w_2 h i_{16} + w_h h i_{17}) \right. \\ & + \frac{\partial}{\partial x} [w_b (q_x i_{18} + u_1 h i_{19}) + w_2 (q_x i_{20} + u_1 h i_{21}) + w_h (q_x i_{22} + u_1 h i_{23})] \\ & \left. + \frac{\partial}{\partial y} [w_b (q_y i_{24} + v_1 h i_{25}) + w_2 (q_y i_{26} + v_1 h i_{27}) + w_h (q_y i_{28} + v_1 h i_{29})] \right\} \\ & - (w_b^2 h i_{63} + w_b w_2 h i_{64} + w_b w_h h i_{65} + w_2^2 h i_{66} + w_2 w_h h i_{67} + w_h^2 h i_{68}) \dots\dots\dots \\ & + \frac{1}{\rho} \left\{ -h \bar{\tau}_x \frac{\partial \bar{z}}{\partial x} - h \bar{\tau}_y \frac{\partial \bar{z}}{\partial y} + \left(\frac{h}{2} - h i_{30} \right) (\rho g h + p_1) - p_2 h i_{31} \right. \\ & \left. + \frac{h}{2} \left[\tau_{yz} \frac{\partial z_b}{\partial y} + \tau_{xz} \frac{\partial z_b}{\partial x} \right] + h \bar{\sigma}_z \right\} \dots\dots\dots (A.70) \end{aligned}$$

The application of the Petrov-Galerkin (Streamline Upwind) finite element scheme to (A.1)-(A.3) equations (VA continuity, momentum in the x-direction and momentum in the y-direction) in the form of equation (A.26) results in the following weak statement equation:

$$\int_{\Omega} \hat{\mathbf{B}} \left(\frac{\partial \psi(\tilde{\phi})}{\partial t} + \frac{\partial \mathbf{F}_x(\tilde{\phi})}{\partial x} + \frac{\partial \mathbf{F}_y(\tilde{\phi})}{\partial y} + \mathbf{G}(\tilde{\phi}) \right) d\Omega = 0 \dots\dots\dots (\text{A.71})$$

where:

$$\hat{\mathbf{B}} = \mathbf{B} + \omega \Delta x \mathbf{W}_x \frac{\partial \mathbf{B}}{\partial x} + \omega \Delta y \mathbf{W}_y \frac{\partial \mathbf{B}}{\partial y} \dots\dots\dots (\text{A.72})$$

$\hat{\mathbf{B}}$ is the matrix of test functions. \mathbf{B} is the matrix of basis functions. ω is an upwinding coefficient set equal to 0.5 for this study (Ghanem et al., 1995). \mathbf{W}_x and \mathbf{W}_y are the upwinding matrix coefficients in x and y directions respectively which control both the amount and the direction of the numerical diffusion. $\Delta x = \Delta y = \frac{\sqrt{A}}{2}$ is used, A being the element area (Ghanem et al., 1995). The approximation, $\tilde{\phi}$, to the unknown vector is defined as:

$$\tilde{\phi} = \mathbf{B}^T \Phi \dots\dots\dots (\text{A.73})$$

Where \mathbf{B} are the shape function matrices and are of size $N_u \times (N_u \times NS)$, NS being the total number of shape functions, and Φ is the nodal-value vector of the unknowns and is of length $(N_u \times NS) \times 1$. Φ is equal to $\{h_j, q_{xj}, q_{yj}, u_{lj}, v_{lj}, w_{2j}, w_{bj}, w_{hj}, p_{lj}, p_{2j}\}^T$. The subscript j refers to a specific node number.

Making the use of equation (A.72) into equation (A.71) results in:

$$\int_{\Omega} \left(\mathbf{B} + \omega \Delta x \mathbf{W}_x(\tilde{\phi}) \frac{\partial \mathbf{B}}{\partial x} + \omega \Delta y \mathbf{W}_y(\tilde{\phi}) \frac{\partial \mathbf{B}}{\partial y} \right) \left(\frac{\partial \psi(\tilde{\phi})}{\partial t} + \frac{\partial \mathbf{F}_x(\tilde{\phi})}{\partial x} + \frac{\partial \mathbf{F}_y(\tilde{\phi})}{\partial y} + \mathbf{G}(\tilde{\phi}) \right) d\Omega = 0 \dots$$

.....(A.74)

Expanding equation (A.74) yields:

$$\int_{\Omega} \left(\mathbf{B} + \omega \Delta x \mathbf{W}_x(\tilde{\phi}) \frac{\partial \mathbf{B}}{\partial x} + \omega \Delta y \mathbf{W}_y(\tilde{\phi}) \frac{\partial \mathbf{B}}{\partial y} \right) \frac{\partial \psi(\tilde{\phi})}{\partial t} d\Omega$$

$$+ \int_{\Omega} \mathbf{B} \left(\frac{\partial \mathbf{F}_x(\tilde{\phi})}{\partial x} + \frac{\partial \mathbf{F}_y(\tilde{\phi})}{\partial y} + \mathbf{G}(\tilde{\phi}) \right) d\Omega \dots\dots\dots(\text{A.75})$$

$$\int_{\Omega} \left(\omega \Delta x \mathbf{W}_x(\tilde{\phi}) \frac{\partial \mathbf{B}}{\partial x} + \omega \Delta y \mathbf{W}_y(\tilde{\phi}) \frac{\partial \mathbf{B}}{\partial y} \right) \left(\frac{\partial \mathbf{F}_x(\tilde{\phi})}{\partial x} + \frac{\partial \mathbf{F}_y(\tilde{\phi})}{\partial y} + \mathbf{G}(\tilde{\phi}) \right) d\Omega = 0$$

Integrating the underlined part in equation (A.75) by parts results in:

$$\int_{\Omega} \left(\mathbf{B} + \omega \Delta x \mathbf{W}_x(\tilde{\phi}) \frac{\partial \mathbf{B}}{\partial x} + \omega \Delta y \mathbf{W}_y(\tilde{\phi}) \frac{\partial \mathbf{B}}{\partial y} \right) \frac{\partial \psi(\tilde{\phi})}{\partial t} d\Omega$$

$$- \int_{\Omega} \left(\mathbf{F}_x(\tilde{\phi}) \frac{\partial \mathbf{B}}{\partial x} + \mathbf{F}_y(\tilde{\phi}) \frac{\partial \mathbf{B}}{\partial y} \right) d\Omega + \int_{\Omega} \mathbf{B} \left(\frac{\partial \mathbf{F}_x(\tilde{\phi})}{\partial x} + \frac{\partial \mathbf{F}_y(\tilde{\phi})}{\partial y} + \mathbf{G}(\tilde{\phi}) \right) d\Omega \dots\dots\dots(\text{A.76})$$

$$+ \int_{\Omega} \left(\omega \Delta x \mathbf{W}_x(\tilde{\phi}) \frac{\partial \mathbf{B}}{\partial x} + \omega \Delta y \mathbf{W}_y(\tilde{\phi}) \frac{\partial \mathbf{B}}{\partial y} \right) \left(\frac{\partial \mathbf{F}_x(\tilde{\phi})}{\partial x} + \frac{\partial \mathbf{F}_y(\tilde{\phi})}{\partial y} + \mathbf{G}(\tilde{\phi}) \right) d\Omega$$

$$+ \int_{\Gamma} \mathbf{B} [\mathbf{F}_x(\tilde{\phi}) n_x + \mathbf{F}_y(\tilde{\phi}) n_y] d\Gamma = 0$$

Where $\int_{\Gamma} \mathbf{B}[\mathbf{F}_x(\tilde{\phi})n_x + \mathbf{F}_y(\tilde{\phi})n_y]d\Gamma$ represents natural convective fluxes across the

boundaries and are defined as:

$$\int_{\Gamma} \mathbf{B}[\mathbf{F}_x(\tilde{\phi})n_x + \mathbf{F}_y(\tilde{\phi})n_y]d\Gamma = \int_{\Gamma} \mathbf{B}[\tilde{\mathbf{F}}_n(\tilde{\phi})\tilde{n}]d\Gamma = \int_y \mathbf{B}\mathbf{F}_x(\tilde{\phi})dy - \int_x \mathbf{B}\mathbf{F}_y(\tilde{\phi})dx \dots\dots(A.77)$$

Γ is the boundary domain. n_x and n_y are the x and y components of the unit normal vector n . \tilde{n} is the unit inward vector normal to Γ .

The boundary integral (equation (A.77)) represents natural convective fluxes across the boundaries. This provides an accurate and easy means for specifying boundary conditions. For example, the boundary integral term for the continuity equation is

$$\int_{\Gamma} -\mathbf{B}(\mathbf{q} \cdot \mathbf{n})d\Gamma.$$

To specify a no-flow boundary condition (wall condition), \mathbf{q}_n ($=\mathbf{q} \cdot \mathbf{n}$) is set equal to zero, and the term is simply not computed. In addition, specified boundary conditions are implemented directly by specifying given values in that term. For example, for an inflow boundary \mathbf{q}_n has a specified distribution and the integral term is evaluated and the contributions summed to the appropriate residuals. For an outflow boundary \mathbf{q}_n has an unknown value and thus the integral boundary term is treated as an unknown term in the equations.

Triangular elements with linear basis functions for all variables are used. The time derivatives are approximated using a weighted-implicit finite difference formulation.

As a result, equation (A.76) becomes:

$$\begin{aligned}
 & \int_{\Omega} \left\{ \theta \left(\mathbf{B} + \omega \Delta x \mathbf{W}_x(\tilde{\phi}) \frac{\partial \mathbf{B}}{\partial x} + \omega \Delta y \mathbf{W}_y(\tilde{\phi}) \frac{\partial \mathbf{B}}{\partial y} \right)^{n+1} \right. \\
 & \quad \left. + (1-\theta) \left(\mathbf{B} + \omega \Delta x \mathbf{W}_x(\tilde{\phi}) \frac{\partial \mathbf{B}}{\partial x} + \omega \Delta y \mathbf{W}_y(\tilde{\phi}) \frac{\partial \mathbf{B}}{\partial y} \right)^n \right\} \frac{[\psi(\tilde{\phi})^{n+1} - \psi(\tilde{\phi})^n]}{\Delta t} d\Omega \\
 & + \left\{ \begin{aligned} & - \int_{\Omega} \left(\mathbf{F}_x(\tilde{\phi}) \frac{\partial \mathbf{B}}{\partial x} + \mathbf{F}_y(\tilde{\phi}) \frac{\partial \mathbf{B}}{\partial y} \right) d\Omega + \int_{\Omega} \mathbf{B} \left(\frac{\partial \mathbf{F}_x(\tilde{\phi})}{\partial x} + \frac{\partial \mathbf{F}_y(\tilde{\phi})}{\partial y} + \mathbf{G}(\tilde{\phi}) \right) d\Omega \\ & + \int_{\Omega} \left(\omega \Delta x \mathbf{W}_x(\tilde{\phi}) \frac{\partial \mathbf{B}}{\partial x} + \omega \Delta y \mathbf{W}_y(\tilde{\phi}) \frac{\partial \mathbf{B}}{\partial y} \right) \left(\frac{\partial \mathbf{F}_x(\tilde{\phi})}{\partial x} + \frac{\partial \mathbf{F}_y(\tilde{\phi})}{\partial y} + \mathbf{G}(\tilde{\phi}) \right) d\Omega \\ & + \int_{\Gamma} \mathbf{B} [\mathbf{F}_x(\tilde{\phi}) n_x + \mathbf{F}_y(\tilde{\phi}) n_y] d\Gamma \end{aligned} \right\}^{n+1} \\
 & + (1-\theta) \left\{ \begin{aligned} & - \int_{\Omega} \left(\mathbf{F}_x(\tilde{\phi}) \frac{\partial \mathbf{B}}{\partial x} + \mathbf{F}_y(\tilde{\phi}) \frac{\partial \mathbf{B}}{\partial y} \right) d\Omega + \int_{\Omega} \mathbf{B} \left(\frac{\partial \mathbf{F}_x(\tilde{\phi})}{\partial x} + \frac{\partial \mathbf{F}_y(\tilde{\phi})}{\partial y} + \mathbf{G}(\tilde{\phi}) \right) d\Omega \\ & + \int_{\Omega} \left(\omega \Delta x \mathbf{W}_x(\tilde{\phi}) \frac{\partial \mathbf{B}}{\partial x} + \omega \Delta y \mathbf{W}_y(\tilde{\phi}) \frac{\partial \mathbf{B}}{\partial y} \right) \left(\frac{\partial \mathbf{F}_x(\tilde{\phi})}{\partial x} + \frac{\partial \mathbf{F}_y(\tilde{\phi})}{\partial y} + \mathbf{G}(\tilde{\phi}) \right) d\Omega \\ & + \int_{\Gamma} \mathbf{B} [\mathbf{F}_x(\tilde{\phi}) n_x + \mathbf{F}_y(\tilde{\phi}) n_y] d\Gamma \end{aligned} \right\}^n = 0
 \end{aligned}
 \tag{A.78}$$

Where superscript n refers to evaluation of the quantity at the n^{th} time step (assumed known) and $n+1$ represents evaluation at a time Δt later (generally unknown).

The upwinding matrices, \mathbf{W}_x and \mathbf{W}_y , are calculated according to Hughes and Mallet (1986a and 1986b) and Hughes et al. (1986), these are:

$$\mathbf{W}_x = \frac{\mathbf{A}_x}{\sqrt{\mathbf{A}_x^2 + \mathbf{A}_y^2}} = \mathbf{A}_x \left(\sqrt{\mathbf{A}_x^2 + \mathbf{A}_y^2} \right)^{-1} \dots\dots\dots(\text{A.79})$$

$$\mathbf{W}_y = \frac{\mathbf{A}_y}{\sqrt{\mathbf{A}_x^2 + \mathbf{A}_y^2}} = \mathbf{A}_y \left(\sqrt{\mathbf{A}_x^2 + \mathbf{A}_y^2} \right)^{-1} \dots\dots\dots(\text{A.80})$$

Where \mathbf{A}_x and \mathbf{A}_y are the advection matrices of (A.1)-(A.3) system of equations in x and y directions respectively and are given by:

$$\mathbf{A}_x = \begin{bmatrix} \frac{\partial F_{x_1}}{\partial h} & \frac{\partial F_{x_1}}{\partial q_x} & \frac{\partial F_{x_1}}{\partial q_y} \\ \frac{\partial F_{x_2}}{\partial h} & \frac{\partial F_{x_2}}{\partial q_x} & \frac{\partial F_{x_2}}{\partial q_y} \\ \frac{\partial F_{x_3}}{\partial h} & \frac{\partial F_{x_3}}{\partial q_x} & \frac{\partial F_{x_3}}{\partial q_y} \end{bmatrix} \dots\dots\dots(\text{A.81})$$

$$\mathbf{A}_y = \begin{bmatrix} \frac{\partial F_{y_1}}{\partial h} & \frac{\partial F_{y_1}}{\partial q_x} & \frac{\partial F_{y_1}}{\partial q_y} \\ \frac{\partial F_{y_2}}{\partial h} & \frac{\partial F_{y_2}}{\partial q_x} & \frac{\partial F_{y_2}}{\partial q_y} \\ \frac{\partial F_{y_3}}{\partial h} & \frac{\partial F_{y_3}}{\partial q_x} & \frac{\partial F_{y_3}}{\partial q_y} \end{bmatrix} \dots\dots\dots (\text{A.82})$$

As a result:

$$\mathbf{A}_x = \begin{bmatrix} 0 & 1 & 0 \\ \frac{-q_x^2}{h^2}i_5 + u_1^2i_7 + 2ghi_{30} & \frac{2q_x}{h}i_5 + u_1i_6 & 0 \\ \frac{-q_xq_y}{h^2}i_{11} + u_1v_1i_{14} & \frac{q_y}{h}i_{11} + v_1i_{12} & \frac{q_x}{h}i_{11} + u_1i_{13} \end{bmatrix} \dots\dots\dots (\text{A.83})$$

$$\mathbf{A}_y = \begin{bmatrix} 0 & 0 & 1 \\ \frac{-q_xq_y}{h^2}i_{11} + u_1v_1i_{14} & \frac{q_y}{h}i_{11} + v_1i_{12} & \frac{q_x}{h}i_{11} + u_1i_{13} \\ \frac{-q_y^2}{h^2}i_8 + v_1^2i_{10} + 2ghi_{30} & 0 & \frac{2q_y}{h}i_8 + v_1i_9 \end{bmatrix} \dots\dots\dots (\text{A.84})$$

The inverse of the matrix $\left(\sqrt{\mathbf{A}_x^2 + \mathbf{A}_y^2}\right)$ is calculated numerically using the Cayley-Hamilton theorem (Hoger and Carlson 1984). The details of these calculations are found in Appendix C. The upwinding matrices \mathbf{W}_x and \mathbf{W}_y are then obtained numerically from (A.78)-(A.79) equations respectively. The obtained upwinding matrices may be written in the form:

$$\mathbf{W}_x = \begin{bmatrix} W_{x11} & W_{x12} & W_{x13} \\ W_{x21} & W_{x22} & W_{x23} \\ W_{x31} & W_{x32} & W_{x33} \end{bmatrix} \dots\dots\dots (A.85)$$

$$\mathbf{W}_y = \begin{bmatrix} W_{y11} & W_{y12} & W_{y13} \\ W_{y21} & W_{y22} & W_{y23} \\ W_{y31} & W_{y32} & W_{y33} \end{bmatrix} \dots\dots\dots (A.86)$$

Substituting of equations (A.85)-(A.86) into equation (A.78) and multiplying and expanding through, results in:

$$\begin{aligned}
& \int_{\Omega_e} \left\{ \theta \left[(b_i + W_{11})^{n+1} (\psi_1(\tilde{\phi})^{n+1} - \psi_1(\tilde{\phi})^n) + W_{12}^{n+1} (\psi_2(\tilde{\phi})^{n+1} - \psi_2(\tilde{\phi})^n) + W_{13}^{n+1} (\psi_3(\tilde{\phi})^{n+1} - \psi_3(\tilde{\phi})^n) \right] \right. \\
& \quad \left. + (1-\theta) \left[(b_i + W_{11})^n (\psi_1(\tilde{\phi})^{n+1} - \psi_1(\tilde{\phi})^n) + W_{12}^n (\psi_2(\tilde{\phi})^{n+1} - \psi_2(\tilde{\phi})^n) + W_{13}^n (\psi_3(\tilde{\phi})^{n+1} - \psi_3(\tilde{\phi})^n) \right] \right\} d\Omega_e \\
& + \theta \Delta t \left\{ - \int_{\Omega_e} \left(F_{x_1}(\tilde{\phi}) \frac{\partial b_i}{\partial x} + F_{y_1}(\tilde{\phi}) \frac{\partial b_i}{\partial y} \right) d\Omega_e + \int_{\Omega} b_i \left(\frac{\partial F_{x_1}(\tilde{\phi})}{\partial x} + \frac{\partial F_{y_1}(\tilde{\phi})}{\partial y} + G_1(\tilde{\phi}) \right) d\Omega_e \right. \\
& \quad + \int_{\Omega_e} \left[W_{11} \left(\frac{\partial F_{x_1}(\tilde{\phi})}{\partial x} + \frac{\partial F_{y_1}(\tilde{\phi})}{\partial y} + G_1(\tilde{\phi}) \right) + W_{12} \left(\frac{\partial F_{x_2}(\tilde{\phi})}{\partial x} + \frac{\partial F_{y_2}(\tilde{\phi})}{\partial y} + G_2(\tilde{\phi}) \right) \right. \\
& \quad \left. \left. + W_{13} \left(\frac{\partial F_{x_3}(\tilde{\phi})}{\partial x} + \frac{\partial F_{y_3}(\tilde{\phi})}{\partial y} + G_3(\tilde{\phi}) \right) \right] d\Omega_e \right. \\
& \quad \left. + \int_{dy_e} b_i F_{x_1} dy_e - \int_{dx_e} b_i F_{y_1} dx_e \right\}^{n+1} \\
& + (1-\theta) \Delta t \left\{ - \int_{\Omega_e} \left(F_{x_1}(\tilde{\phi}) \frac{\partial b_i}{\partial x} + F_{y_1}(\tilde{\phi}) \frac{\partial b_i}{\partial y} \right) d\Omega_e + \int_{\Omega} b_i \left(\frac{\partial F_{x_1}(\tilde{\phi})}{\partial x} + \frac{\partial F_{y_1}(\tilde{\phi})}{\partial y} + G_1(\tilde{\phi}) \right) d\Omega_e \right. \\
& \quad + \int_{\Omega_e} \left[W_{11} \left(\frac{\partial F_{x_1}(\tilde{\phi})}{\partial x} + \frac{\partial F_{y_1}(\tilde{\phi})}{\partial y} + G_1(\tilde{\phi}) \right) + W_{12} \left(\frac{\partial F_{x_2}(\tilde{\phi})}{\partial x} + \frac{\partial F_{y_2}(\tilde{\phi})}{\partial y} + G_2(\tilde{\phi}) \right) \right. \\
& \quad \left. \left. + W_{13} \left(\frac{\partial F_{x_3}(\tilde{\phi})}{\partial x} + \frac{\partial F_{y_3}(\tilde{\phi})}{\partial y} + G_3(\tilde{\phi}) \right) \right] d\Omega_e \right. \\
& \quad \left. + \int_{dy_e} b_i F_{x_1} dy_e - \int_{dx_e} b_i F_{y_1} dx_e \right\}^n = 0
\end{aligned}$$

.....(A.87)

$$\begin{aligned}
& \int_{\Omega_e} \left\{ \theta \left[W_{21}^{n+1} (\psi_1(\tilde{\Phi})^{n+1} - \psi_1(\tilde{\Phi})^n) + (b_i + W_{22})^{n+1} (\psi_2(\tilde{\Phi})^{n+1} - \psi_2(\tilde{\Phi})^n) + W_{23}^{n+1} (\psi_3(\tilde{\Phi})^{n+1} - \psi_3(\tilde{\Phi})^n) \right] \right. \\
& \quad \left. + (1-\theta) \left[W_{21}^n (\psi_1(\tilde{\Phi})^{n+1} - \psi_1(\tilde{\Phi})^n) + (b_i + W_{22})^n (\psi_2(\tilde{\Phi})^{n+1} - \psi_2(\tilde{\Phi})^n) + W_{23}^n (\psi_3(\tilde{\Phi})^{n+1} - \psi_3(\tilde{\Phi})^n) \right] \right\} d\Omega_e \\
& + \theta \Delta t \left\{ \int_{\Omega_e} \left[- \int_{\Omega_e} \left(F_{x_1}(\tilde{\Phi}) \frac{\partial b_i}{\partial x} + F_{y_1}(\tilde{\Phi}) \frac{\partial b_i}{\partial y} \right) d\Omega_e + \int_{\Omega} b_i \left(\frac{\partial F_{x_1}(\tilde{\Phi})}{\partial x} + \frac{\partial F_{y_1}(\tilde{\Phi})}{\partial y} + G_2(\tilde{\Phi}) \right) d\Omega_e \right. \right. \\
& \quad \left. \left. + \int_{\Omega_e} \left[W_{21} \left(\frac{\partial F_{x_1}(\tilde{\Phi})}{\partial x} + \frac{\partial F_{y_1}(\tilde{\Phi})}{\partial y} + G_1(\tilde{\Phi}) \right) + W_{22} \left(\frac{\partial F_{x_2}(\tilde{\Phi})}{\partial x} + \frac{\partial F_{y_2}(\tilde{\Phi})}{\partial y} + G_2(\tilde{\Phi}) \right) \right] \right. \right. \\
& \quad \left. \left. + W_{23} \left(\frac{\partial F_{x_3}(\tilde{\Phi})}{\partial x} + \frac{\partial F_{y_3}(\tilde{\Phi})}{\partial y} + G_3(\tilde{\Phi}) \right) \right] d\Omega_e \right. \\
& \quad \left. + \int_{dy_e} b_i F_{x_2} dy_e - \int_{dx_e} b_i F_{y_2} dx_e \right\}^{n+1} \\
& + (1-\theta) \Delta t \left\{ \int_{\Omega_e} \left[- \int_{\Omega_e} \left(F_{x_1}(\tilde{\Phi}) \frac{\partial b_i}{\partial x} + F_{y_1}(\tilde{\Phi}) \frac{\partial b_i}{\partial y} \right) d\Omega_e + \int_{\Omega} b_i \left(\frac{\partial F_{x_1}(\tilde{\Phi})}{\partial x} + \frac{\partial F_{y_1}(\tilde{\Phi})}{\partial y} + G_2(\tilde{\Phi}) \right) d\Omega_e \right. \right. \\
& \quad \left. \left. + \int_{\Omega_e} \left[W_{21} \left(\frac{\partial F_{x_1}(\tilde{\Phi})}{\partial x} + \frac{\partial F_{y_1}(\tilde{\Phi})}{\partial y} + G_1(\tilde{\Phi}) \right) + W_{23} \left(\frac{\partial F_{x_2}(\tilde{\Phi})}{\partial x} + \frac{\partial F_{y_2}(\tilde{\Phi})}{\partial y} + G_2(\tilde{\Phi}) \right) \right] \right. \right. \\
& \quad \left. \left. + W_{22} \left(\frac{\partial F_{x_3}(\tilde{\Phi})}{\partial x} + \frac{\partial F_{y_3}(\tilde{\Phi})}{\partial y} + G_3(\tilde{\Phi}) \right) \right] d\Omega_e \right. \\
& \quad \left. + \int_{dy_e} b_i F_{x_2} dy_e - \int_{dx_e} b_i F_{y_2} dx_e \right\}^n = 0
\end{aligned}$$

.....(A.88)

$$\begin{aligned} & \int_{\Omega_e} \left\{ \theta \left[W_{31}^{n+1} (\psi_1(\tilde{\Phi})^{n+1} - \psi_1(\tilde{\Phi})^n) + W_{32}^{n+1} (\psi_2(\tilde{\Phi})^{n+1} - \psi_2(\tilde{\Phi})^n) + (b_i + W_{33})^{n+1} (\psi_3(\tilde{\Phi})^{n+1} - \psi_3(\tilde{\Phi})^n) \right] \right. \\ & \quad \left. + (1-\theta) \left[W_{31}^n (\psi_1(\tilde{\Phi})^{n+1} - \psi_1(\tilde{\Phi})^n) + W_{32}^n (\psi_2(\tilde{\Phi})^{n+1} - \psi_2(\tilde{\Phi})^n) + (b_i + W_{33})^n (\psi_3(\tilde{\Phi})^{n+1} - \psi_3(\tilde{\Phi})^n) \right] \right\} d\Omega_e \\ & + \theta \Delta t \left\{ \int_{\Omega_e} \left[- \left(F_{x_1}(\tilde{\Phi}) \frac{\partial b_i}{\partial x} + F_{y_1}(\tilde{\Phi}) \frac{\partial b_i}{\partial y} \right) d\Omega_e + \int_{\Omega} b_i \left(\frac{\partial F_{x_1}(\tilde{\Phi})}{\partial x} + \frac{\partial F_{y_1}(\tilde{\Phi})}{\partial y} + G_1(\tilde{\Phi}) \right) d\Omega_e \right. \right. \\ & \quad \left. \left. + W_{31} \left(\frac{\partial F_{x_1}(\tilde{\Phi})}{\partial x} + \frac{\partial F_{y_1}(\tilde{\Phi})}{\partial y} + G_1(\tilde{\Phi}) \right) + W_{32} \left(\frac{\partial F_{x_2}(\tilde{\Phi})}{\partial x} + \frac{\partial F_{y_2}(\tilde{\Phi})}{\partial y} + G_2(\tilde{\Phi}) \right) \right] d\Omega_e \right. \\ & \quad \left. + \int_{dy_e} b_i F_{x_1} dy_e - \int_{dx_e} b_i F_{y_1} dx_e \right\}^{n+1} \\ & + (1-\theta) \Delta t \left\{ \int_{\Omega_e} \left[- \left(F_{x_1}(\tilde{\Phi}) \frac{\partial b_i}{\partial x} + F_{y_1}(\tilde{\Phi}) \frac{\partial b_i}{\partial y} \right) d\Omega_e + \int_{\Omega} b_i \left(\frac{\partial F_{x_1}(\tilde{\Phi})}{\partial x} + \frac{\partial F_{y_1}(\tilde{\Phi})}{\partial y} + G_1(\tilde{\Phi}) \right) d\Omega_e \right. \right. \\ & \quad \left. \left. + W_{31} \left(\frac{\partial F_{x_1}(\tilde{\Phi})}{\partial x} + \frac{\partial F_{y_1}(\tilde{\Phi})}{\partial y} + G_1(\tilde{\Phi}) \right) + W_{32} \left(\frac{\partial F_{x_2}(\tilde{\Phi})}{\partial x} + \frac{\partial F_{y_2}(\tilde{\Phi})}{\partial y} + G_2(\tilde{\Phi}) \right) \right] d\Omega_e \right. \\ & \quad \left. + \int_{dy_e} b_i F_{x_1} dy_e - \int_{dx_e} b_i F_{y_1} dx_e \right\}^n = 0 \end{aligned} \quad \dots\dots\dots (A.89)$$

Equations (A.87)-(A.89) represent the equivalent Petrov Galerkin finite element model for VA continuity, VA momentum in the x -direction and VA momentum in the y -direction equations respectively (equations (A.1)-(A.3)). The subscript e refers to an element and implies integration over the element. b_i is one of the entries of the test

function matrix **B**. For example, the test function matrix **B** for the 3-equation model (equations (A.87)-(A.89)) is defined, over the element, as:

$$\mathbf{B}_e = \begin{bmatrix} b_1 & 0 & 0 \\ 0 & b_1 & 0 \\ 0 & 0 & b_1 \\ b_2 & 0 & 0 \\ 0 & b_2 & 0 \\ 0 & 0 & b_2 \\ b_3 & 0 & 0 \\ 0 & b_3 & 0 \\ 0 & 0 & b_3 \end{bmatrix} \dots\dots\dots(\text{A.90})$$

The subscript *i* refers to a specific test function number and has the value, over an element, of 1, 2 or 3 for triangular finite elements.

The different parts of equations ((A.87)-(A.89)) are defined as follows:

$$\mathbf{W} = \begin{bmatrix} W_{11} & W_{12} & W_{13} \\ W_{21} & W_{22} & W_{23} \\ W_{31} & W_{32} & W_{33} \end{bmatrix}$$

$$= \begin{bmatrix} \omega\Delta x W_{x_{11}} \frac{\partial B}{\partial x} + \omega\Delta y W_{y_{11}} \frac{\partial B}{\partial y} & \omega\Delta x W_{x_{12}} \frac{\partial B}{\partial x} + \omega\Delta y W_{y_{12}} \frac{\partial B}{\partial y} & \omega\Delta x W_{x_{13}} \frac{\partial B}{\partial x} + \omega\Delta y W_{y_{13}} \frac{\partial B}{\partial y} \\ \omega\Delta x W_{x_{21}} \frac{\partial B}{\partial x} + \omega\Delta y W_{y_{21}} \frac{\partial B}{\partial y} & \omega\Delta x W_{x_{22}} \frac{\partial B}{\partial x} + \omega\Delta y W_{y_{22}} \frac{\partial B}{\partial y} & \omega\Delta x W_{x_{23}} \frac{\partial B}{\partial x} + \omega\Delta y W_{y_{23}} \frac{\partial B}{\partial y} \\ \omega\Delta x W_{x_{31}} \frac{\partial B}{\partial x} + \omega\Delta y W_{y_{31}} \frac{\partial B}{\partial y} & \omega\Delta x W_{x_{32}} \frac{\partial B}{\partial x} + \omega\Delta y W_{y_{32}} \frac{\partial B}{\partial y} & \omega\Delta x W_{x_{33}} \frac{\partial B}{\partial x} + \omega\Delta y W_{y_{33}} \frac{\partial B}{\partial y} \end{bmatrix} \dots\dots\dots(\text{A.91})$$

$$\psi_1(\tilde{\Phi}) = \tilde{h} \dots\dots\dots (A.92)$$

$$\psi_2(\tilde{\Phi}) = \tilde{q}_x i_1 + \tilde{u}_1 \tilde{h} i_2 \dots\dots\dots (A.93)$$

$$\psi_3(\tilde{\Phi}) = \tilde{q}_y i_3 + \tilde{v}_1 \tilde{h} i_4 \dots\dots\dots (A.94)$$

$$F_{x_1}(\tilde{\Phi}) = \tilde{q}_x i_1 + \tilde{u}_1 \tilde{h} i_2 \dots\dots\dots (A.95)$$

$$F_{x_2}(\tilde{\Phi}) = \frac{\tilde{q}_x^2}{\tilde{h}} i_5 + \tilde{q}_x \tilde{u}_1 i_6 + \tilde{u}_1^2 \tilde{h} i_7 + g \tilde{h}^2 i_{30} + \frac{\tilde{p}_1 \tilde{h} i_{30}}{\rho} + \frac{\tilde{p}_2 \tilde{h} i_{31}}{\rho} - \frac{\tilde{h} \tilde{\sigma}_x}{\rho} \dots\dots\dots (A.96)$$

$$F_{x_3}(\tilde{\Phi}) = \frac{\tilde{q}_x \tilde{q}_y}{\tilde{h}} i_{11} + \tilde{q}_x \tilde{v}_1 i_{12} + \tilde{u}_1 \tilde{q}_y i_{13} + \tilde{u}_1 \tilde{v}_1 \tilde{h} i_{14} - \frac{\tilde{h} \tilde{\tau}_{yx}}{\rho} \dots\dots\dots (A.97)$$

$$F_{y_1}(\tilde{\Phi}) = \tilde{q}_y i_3 + \tilde{v}_1 \tilde{h} i_4 \dots\dots\dots (A.98)$$

$$F_{y_2}(\tilde{\Phi}) = \frac{\tilde{q}_x \tilde{q}_y}{\tilde{h}} i_{11} + \tilde{q}_x \tilde{v}_1 i_{12} + \tilde{u}_1 \tilde{q}_y i_{13} + \tilde{u}_1 \tilde{v}_1 \tilde{h} i_{14} - \frac{\tilde{h} \tilde{\tau}_{xy}}{\rho} \dots\dots\dots (A.99)$$

$$F_{y_3}(\tilde{\Phi}) = \frac{\tilde{q}_y^2}{\tilde{h}} i_8 + \tilde{q}_y \tilde{v}_1 i_9 + \tilde{v}_1^2 \tilde{h} i_{10} + g \tilde{h}^2 i_{30} + \frac{\tilde{p}_1 \tilde{h} i_{30}}{\rho} + \frac{\tilde{p}_2 \tilde{h} i_{31}}{\rho} - \frac{\tilde{h} \tilde{\sigma}_y}{\rho} \dots\dots\dots (A.100)$$

$$\frac{\partial F_{x_1}(\tilde{\phi})}{\partial x} = \frac{\partial \tilde{q}_x}{\partial x} \dots\dots\dots (A.101)$$

$$\begin{aligned} \frac{\partial F_{x_2}(\tilde{\phi})}{\partial x} = & 2 g \tilde{h} i_{30} \frac{\partial \tilde{h}}{\partial x} + \left(2 i_5 \frac{\partial \tilde{q}_x}{\partial x} \tilde{q}_x \right) / \tilde{h} \\ & + i_6 \frac{\partial \tilde{u}_1}{\partial x} \tilde{q}_x - \left(i_5 \frac{\partial \tilde{h}}{\partial x} \tilde{q}_x \tilde{q}_x \right) / (\tilde{h}^2) \\ & + i_6 \frac{\partial \tilde{q}_x}{\partial x} \tilde{u}_1 + 2 \tilde{h} i_7 \frac{\partial \tilde{u}_1}{\partial x} \tilde{u}_1 + i_7 \frac{\partial \tilde{h}}{\partial x} \tilde{u}_1 \tilde{u}_1 \\ & + \left(i_{30} \tilde{p}_1 \frac{\partial \tilde{h}}{\partial x} + i_{31} \tilde{p}_2 \frac{\partial \tilde{h}}{\partial x} + \tilde{h} \right. \\ & \left. i_{30} \frac{\partial \tilde{p}_1}{\partial x} + \tilde{h} i_{31} \frac{\partial \tilde{p}_2}{\partial x} - \frac{\partial \tilde{h}}{\partial x} \tilde{\sigma}_x \right) / \rho \end{aligned}$$

..... (A.102)

$$\begin{aligned} \frac{\partial F_{x_3}(\tilde{\phi})}{\partial x} = & \left(i_{11} \frac{\partial \tilde{q}_y}{\partial x} \tilde{q}_x \right) / \tilde{h} + i_{12} \frac{\partial v_1}{\partial x} \tilde{q}_x + \left(i_{11} \frac{\partial \tilde{q}_x}{\partial x} \tilde{q}_y \right) / \tilde{h} \\ & + i_{13} \frac{\partial \tilde{u}_1}{\partial x} \tilde{q}_y - \left(i_{11} \frac{\partial \tilde{h}}{\partial x} \tilde{q}_x \tilde{q}_y \right) / (\tilde{h}^2) - \left(\frac{\partial \tilde{h}}{\partial x} \tilde{\tau}_{yx} \right) / \rho \\ & + i_{13} \frac{\partial \tilde{q}_y}{\partial x} \tilde{u}_1 + \tilde{h} i_{14} \frac{\partial v_1}{\partial x} \tilde{u}_1 + i_{12} \frac{\partial \tilde{q}_x}{\partial x} \tilde{v}_1 \\ & + \tilde{h} i_{14} \frac{\partial \tilde{u}_1}{\partial x} \tilde{v}_1 + i_{14} \frac{\partial \tilde{h}}{\partial x} \tilde{u}_1 \tilde{v}_1 \end{aligned}$$

..... (A.103)

$$\frac{\partial F_{y_1}(\vec{\phi})}{\partial y} = \frac{\partial \tilde{q}_y}{\partial y} \dots \dots \dots (A.104)$$

$$\begin{aligned} \frac{\partial F_{y_2}(\vec{\phi})}{\partial y} = & \left(i_{11} \frac{\partial \tilde{q}_y}{\partial y} \tilde{q}_x \right) / \hbar + i_{12} \frac{\partial \tilde{v}_1}{\partial y} \tilde{q}_x + \left(i_{11} \frac{\partial \tilde{q}_x}{\partial y} \tilde{q}_y \right) / \hbar \\ & + i_{13} \frac{\partial \tilde{u}_1}{\partial y} \tilde{q}_y - \left(i_{11} \frac{\partial \hbar}{\partial y} \tilde{q}_x \tilde{q}_y \right) / (\hbar^2) - \left(\frac{\partial \hbar}{\partial y} \tilde{z}_{xy} \right) / \rho \\ & + i_{13} \frac{\partial \tilde{q}_y}{\partial y} \tilde{u}_1 + \hbar i_{14} \frac{\partial \tilde{v}_1}{\partial y} \tilde{u}_1 + i_{12} \frac{\partial \tilde{q}_x}{\partial y} \tilde{v}_1 \\ & + \hbar i_{14} \frac{\partial \tilde{u}_1}{\partial y} \tilde{v}_1 + i_{14} \frac{\partial \hbar}{\partial y} \tilde{u}_1 \tilde{v}_1 \\ & \dots \dots \dots (A.105) \end{aligned}$$

$$\begin{aligned} \frac{\partial F_{y_3}(\vec{\phi})}{\partial y} = & 2 g \hbar i_{30} \frac{\partial \hbar}{\partial y} + \left(2 i_8 \frac{\partial \tilde{q}_y}{\partial y} \tilde{q}_y \right) / \hbar + i_9 \frac{\partial \tilde{v}_1}{\partial y} \tilde{q}_y \\ & - \left(i_8 \frac{\partial \hbar}{\partial y} \tilde{q}_y \tilde{q}_y \right) / (\hbar^2) \\ & + i_9 \frac{\partial \tilde{q}_y}{\partial y} \tilde{v}_1 + 2 \hbar i_{10} \frac{\partial \tilde{v}_1}{\partial y} \tilde{v}_1 + i_{10} \frac{\partial \hbar}{\partial y} \tilde{v}_1 \tilde{v}_1 \\ & + \left(i_{30} \tilde{p}_1 \frac{\partial \hbar}{\partial y} + i_{31} \tilde{p}_2 \frac{\partial \hbar}{\partial y} + \right. \\ & \left. \hbar i_{30} \frac{\partial \tilde{p}_1}{\partial y} + \hbar i_{31} \frac{\partial \tilde{p}_2}{\partial y} - \frac{\partial \hbar}{\partial y} \tilde{\sigma}_y \right) / \rho \\ & \dots \dots \dots (A.106) \end{aligned}$$

$$G_1(\tilde{\Phi}) = 0 \dots\dots\dots (A.107)$$

$$G_2(\tilde{\Phi}) = \frac{1}{\rho} \left\{ (\rho g \tilde{h} + \tilde{p}_1) \frac{\partial z_b}{\partial x} + \tilde{\tau}_{x_b} \right\} \dots\dots\dots (A.108)$$

$$G_3(\tilde{\Phi}) = \frac{1}{\rho} \left\{ (\rho g \tilde{h} + \tilde{p}_1) \frac{\partial z_b}{\partial y} + \tilde{\tau}_{y_b} \right\} \dots\dots\dots (A.109)$$

$$\tilde{\sigma}_x = \tilde{\tau}_{xx} = 2\rho\nu_h \frac{\partial}{\partial x} \left(\frac{\tilde{q}_x}{\tilde{h}} \right) \dots\dots\dots (A.110)$$

$$\tilde{\sigma}_y = \tilde{\tau}_{yy} = 2\rho\nu_h \frac{\partial}{\partial y} \left(\frac{\tilde{q}_y}{\tilde{h}} \right) \dots\dots\dots (A.111)$$

$$\tilde{\tau}_{xy} = \tilde{\tau}_{yx} = \rho\nu_h \left(\frac{\partial}{\partial y} \left(\frac{\tilde{q}_x}{\tilde{h}} \right) + \frac{\partial}{\partial x} \left(\frac{\tilde{q}_y}{\tilde{h}} \right) \right) \dots\dots\dots (A.112)$$

$$\tilde{\tau}_{x_b} = \frac{\rho}{C_*^2} \left(\frac{\tilde{q}_x}{\tilde{h}} \right) \sqrt{\left(\frac{\tilde{q}_x}{\tilde{h}} \right)^2 + \left(\frac{\tilde{q}_y}{\tilde{h}} \right)^2 + \tilde{w}^2} \dots\dots\dots (A.113)$$

$$\tilde{\tau}_{y_b} = \frac{\rho}{C_*^2} \left(\frac{\tilde{q}_y}{\tilde{h}} \right) \sqrt{\left(\frac{\tilde{q}_x}{\tilde{h}} \right)^2 + \left(\frac{\tilde{q}_y}{\tilde{h}} \right)^2 + \tilde{w}^2} \dots\dots\dots (A.114)$$

$$\tilde{w} = i_{15} \tilde{w}_b + i_{16} \tilde{w}_2 + i_{17} \tilde{w}_h \dots\dots\dots (A.115)$$

The quantities $\tilde{\varphi}$, $\frac{\partial \tilde{\varphi}}{\partial x}$ and $\frac{\partial \tilde{\varphi}}{\partial y}$ are respectively given by:

$$\tilde{h} = \sum_{j=1}^3 b_j h_j \dots\dots\dots(\text{A.116})$$

$$\tilde{q}_x = \sum_{j=1}^3 b_j q_{x_j} \dots\dots\dots(\text{A.117})$$

$$\tilde{q}_y = \sum_{j=1}^3 b_j q_{y_j} \dots\dots\dots(\text{A.118})$$

$$\tilde{u}_1 = \sum_{j=1}^3 b_j u_{1_j} \dots\dots\dots(\text{A.119})$$

$$\tilde{v}_1 = \sum_{j=1}^3 b_j v_{1_j} \dots\dots\dots(\text{A.120})$$

$$\tilde{w}_2 = \sum_{j=1}^3 b_j w_{2_j} \dots\dots\dots(\text{A.121})$$

$$\tilde{w}_b = \sum_{j=1}^3 b_j w_{b_j} \dots\dots\dots(\text{A.122})$$

$$\tilde{w}_h = \sum_{j=1}^3 b_j h_j \dots\dots\dots(\text{A.123})$$

$$\tilde{p}_1 = \sum_{j=1}^3 b_j p_{1j} \dots\dots\dots(\text{A.124})$$

$$\tilde{p}_2 = \sum_{j=1}^3 b_j p_{2j} \dots\dots\dots(\text{A.125})$$

$$\frac{\partial \tilde{h}}{\partial x} = \sum_{j=1}^3 \frac{\partial b_j}{\partial x} \cdot h_j \dots\dots\dots(\text{A.126})$$

$$\frac{\partial \tilde{q}_x}{\partial x} = \sum_{j=1}^3 \frac{\partial b_j}{\partial x} \cdot q_{x_j} \dots\dots\dots(\text{A.127})$$

$$\frac{\partial \tilde{q}_y}{\partial x} = \sum_{j=1}^3 \frac{\partial b_j}{\partial x} \cdot q_{y_j} \dots\dots\dots(\text{A.128})$$

$$\frac{\partial \tilde{u}_1}{\partial x} = \sum_{j=1}^3 \frac{\partial b_j}{\partial x} \cdot u_{1j} \dots\dots\dots(\text{A.129})$$

$$\frac{\partial \tilde{v}_1}{\partial x} = \sum_{j=1}^3 \frac{\partial b_j}{\partial x} \cdot v_{1j} \dots\dots\dots(\text{A.130})$$

$$\frac{\partial \tilde{w}_2}{\partial x} = \sum_{j=1}^3 \frac{\partial b_j}{\partial x} \cdot w_{2_j} \dots\dots\dots (A.131)$$

$$\frac{\partial \tilde{w}_b}{\partial x} = \sum_{j=1}^3 \frac{\partial b_j}{\partial x} \cdot w_{b_j} \dots\dots\dots (A.132)$$

$$\frac{\partial \tilde{w}_h}{\partial x} = \sum_{j=1}^3 \frac{\partial b_j}{\partial x} \cdot w_{h_j} \dots\dots\dots (A.133)$$

$$\frac{\partial \tilde{p}_1}{\partial x} = \sum_{j=1}^3 \frac{\partial b_j}{\partial x} \cdot p_{1_j} \dots\dots\dots (A.134)$$

$$\frac{\partial \tilde{p}_2}{\partial x} = \sum_{j=1}^3 \frac{\partial b_j}{\partial x} \cdot p_{2_j} \dots\dots\dots (A.135)$$

$$\frac{\partial \tilde{h}}{\partial y} = \sum_{j=1}^3 \frac{\partial b_j}{\partial y} \cdot h_j \dots\dots\dots (A.136)$$

$$\frac{\partial \tilde{q}_x}{\partial y} = \sum_{j=1}^3 \frac{\partial b_j}{\partial y} \cdot q_{x_j} \dots\dots\dots (A.137)$$

$$\frac{\partial \tilde{q}_y}{\partial y} = \sum_{j=1}^3 \frac{\partial b_j}{\partial y} \cdot q_{y_j} \dots\dots\dots (A.138)$$

$$\frac{\partial \tilde{u}_1}{\partial y} = \sum_{j=1}^3 \frac{\partial b_j}{\partial y} \cdot u_{1,j} \dots\dots\dots (A.139)$$

$$\frac{\partial \tilde{v}_1}{\partial y} = \sum_{j=1}^3 \frac{\partial b_j}{\partial y} \cdot v_{1,j} \dots\dots\dots (A.140)$$

$$\frac{\partial \tilde{w}_2}{\partial y} = \sum_{j=1}^3 \frac{\partial b_j}{\partial y} \cdot w_{2,j} \dots\dots\dots (A.141)$$

$$\frac{\partial \tilde{w}_b}{\partial y} = \sum_{j=1}^3 \frac{\partial b_j}{\partial y} \cdot w_{b,j} \dots\dots\dots (A.142)$$

$$\frac{\partial \tilde{w}_h}{\partial y} = \sum_{j=1}^3 \frac{\partial b_j}{\partial y} \cdot w_{h,j} \dots\dots\dots (A.143)$$

$$\frac{\partial \tilde{p}_1}{\partial y} = \sum_{j=1}^3 \frac{\partial b_j}{\partial y} \cdot p_{1,j} \dots\dots\dots (A.144)$$

$$\frac{\partial \tilde{p}_2}{\partial y} = \sum_{j=1}^3 \frac{\partial b_j}{\partial y} \cdot p_{2,j} \dots\dots\dots (A.145)$$

b_j is one of the entries of the basis function matrix **B**. The subscript j refers to a specific node number and has the value, over an element, of 1, 2 or 3 for triangular finite elements.

The application of the Petrov-Galerkin (Streamline Upwind) finite element scheme to (A.4)-(A.5) equations (VAM momentum in the x - and y -directions respectively) in the form of equation (A.26) results in the following weak statement equation:

$$\int_{\Omega} \hat{\mathbf{B}} \left(\frac{\partial \psi(\tilde{\phi})}{\partial t} + \frac{\partial \mathbf{F}_x(\tilde{\phi})}{\partial x} + \frac{\partial \mathbf{F}_y(\tilde{\phi})}{\partial y} + \mathbf{G}(\tilde{\phi}) \right) d\Omega = 0 \dots\dots\dots (\text{A.146})$$

where:

$$\hat{\mathbf{B}} = \mathbf{B} + \omega \Delta x W_{ux} \frac{\partial \mathbf{B}}{\partial x} + \omega \Delta y W_{uy} \frac{\partial \mathbf{B}}{\partial y} \dots\dots\dots (\text{A.147})$$

W_{ux} and W_{uy} are calculated according to Hughes and Mallet (1986a and 1986b) and Hughes et al. (1986) and are defined as:

$$W_{ux} = \frac{u}{\sqrt{u^2 + v^2}} \dots\dots\dots (\text{A.148})$$

$$W_{uy} = \frac{v}{\sqrt{u^2 + v^2}} \dots\dots\dots (\text{A.149})$$

Substituting of equations (A.122)-(A.123) into equation (A.120) and multiplying and expanding through, results in:

$$\begin{aligned}
& \int_{\Omega_e} \left[\theta (b_i + W_{wx})^{n+1} (\psi_4(\tilde{\Phi})^{n+1} - \psi_4(\tilde{\Phi})^n) + (1-\theta) (b_i + W_{wx})^n (\psi_4(\tilde{\Phi})^{n+1} - \psi_4(\tilde{\Phi})^n) \right] d\Omega_e \\
& + \theta \Delta t \left\{ - \int_{\Omega_e} \left(F_{x_i}(\tilde{\Phi}) \frac{\partial b_i}{\partial x} + F_{y_i}(\tilde{\Phi}) \frac{\partial b_i}{\partial y} \right) d\Omega_e + \int_{\Omega} b_i \left(\frac{\partial F_{x_i}(\tilde{\Phi})}{\partial x} + \frac{\partial F_{y_i}(\tilde{\Phi})}{\partial y} + G_i(\tilde{\Phi}) \right) d\Omega_e \right. \\
& \quad + \int_{\Omega_e} W_{wx} \left(\frac{\partial F_{x_i}(\tilde{\Phi})}{\partial x} + \frac{\partial F_{y_i}(\tilde{\Phi})}{\partial y} + G_i(\tilde{\Phi}) \right) d\Omega_e \\
& \quad \left. + \int_{dy_e} b_i F_{x_i} dy_e - \int_{dx_e} b_i F_{y_i} dx_e \right\}^{n+1} \\
& + (1-\theta) \Delta t \left\{ - \int_{\Omega_e} \left(F_{x_i}(\tilde{\Phi}) \frac{\partial b_i}{\partial x} + F_{y_i}(\tilde{\Phi}) \frac{\partial b_i}{\partial y} \right) d\Omega_e + \int_{\Omega} b_i \left(\frac{\partial F_{x_i}(\tilde{\Phi})}{\partial x} + \frac{\partial F_{y_i}(\tilde{\Phi})}{\partial y} + G_i(\tilde{\Phi}) \right) d\Omega_e \right. \\
& \quad + \int_{\Omega_e} W_{wx} \left(\frac{\partial F_{x_i}(\tilde{\Phi})}{\partial x} + \frac{\partial F_{y_i}(\tilde{\Phi})}{\partial y} + G_i(\tilde{\Phi}) \right) d\Omega_e \\
& \quad \left. + \int_{dy_e} b_i F_{x_i} dy_e - \int_{dx_e} b_i F_{y_i} dx_e \right\}^n = 0 \quad \dots
\end{aligned}$$

.....(A.150)

$$\begin{aligned}
& \int_{\Omega_e} \left[\theta (b_i + W_{wy})^{n+1} (\psi_s(\tilde{\phi})^{n+1} - \psi_s(\tilde{\phi})^n) + (1-\theta) (b_i + W_{wy})^n (\psi_s(\tilde{\phi})^{n+1} - \psi_s(\tilde{\phi})^n) \right] d\Omega_e \\
& + \theta \Delta t \left\{ \begin{aligned} & - \int_{\Omega_e} \left(F_{x_i}(\tilde{\phi}) \frac{\partial b_i}{\partial x} + F_{y_i}(\tilde{\phi}) \frac{\partial b_i}{\partial y} \right) d\Omega_e + \int_{\Omega_e} b_i \left(\frac{\partial F_{x_i}(\tilde{\phi})}{\partial x} + \frac{\partial F_{y_i}(\tilde{\phi})}{\partial y} + G_s(\tilde{\phi}) \right) d\Omega_e \\ & + \int_{\Omega_e} W_{wy} \left(\frac{\partial F_{x_i}(\tilde{\phi})}{\partial x} + \frac{\partial F_{y_i}(\tilde{\phi})}{\partial y} + G_s(\tilde{\phi}) \right) d\Omega_e \\ & + \int_{dy_e} b_i F_{x_i} dy_e - \int_{dx_e} b_i F_{y_i} dx_e \end{aligned} \right\}^{n+1} \\
& + (1-\theta) \Delta t \left\{ \begin{aligned} & - \int_{\Omega_e} \left(F_{x_i}(\tilde{\phi}) \frac{\partial b_i}{\partial x} + F_{y_i}(\tilde{\phi}) \frac{\partial b_i}{\partial y} \right) d\Omega_e + \int_{\Omega_e} b_i \left(\frac{\partial F_{x_i}(\tilde{\phi})}{\partial x} + \frac{\partial F_{y_i}(\tilde{\phi})}{\partial y} + G_s(\tilde{\phi}) \right) d\Omega_e \\ & + \int_{\Omega_e} W_{wy} \left(\frac{\partial F_{x_i}(\tilde{\phi})}{\partial x} + \frac{\partial F_{y_i}(\tilde{\phi})}{\partial y} + G_s(\tilde{\phi}) \right) d\Omega_e \\ & + \int_{dy_e} b_i F_{x_i} dy_e - \int_{dx_e} b_i F_{y_i} dx_e \end{aligned} \right\}^n = 0 \quad \dots
\end{aligned}
\tag{A.151}$$

Equations (A.150)-(A.151) represent the equivalent Petrov Galerkin finite element model for VAM momentum in the x -direction and VAM momentum in the y -direction equations respectively (equations (A.4)-(A.5)).

The different parts of equations ((A.150)-(A.151)) are defined as follows:

$$\psi_4(\tilde{\phi}) = \tilde{q}_x (\tilde{h} i_{32} + z_b i_1) + \tilde{u}_1 \tilde{h} (\tilde{h} i_{33} + z_b i_2) \dots \tag{A.152}$$

$$\psi_5(\tilde{\Phi}) = \tilde{q}_y(\tilde{h}i_{34} + z_b i_3) + \tilde{v}_1 \tilde{h}(\tilde{h}i_{35} + z_b i_4) \dots\dots\dots (A.153)$$

$$\begin{aligned} F_{x_4}(\tilde{\Phi}) = & \frac{\tilde{q}_x^2}{\tilde{h}}(\tilde{h}i_{36} + z_b i_5) + \tilde{q}_x \tilde{u}_1(\tilde{h}i_{37} + z_b i_6) + \tilde{u}_1^2 \tilde{h}(\tilde{h}i_{38} + z_b i_7) \\ & + g\tilde{h}^2(\tilde{h}i_{39} + z_b i_{30}) + \frac{\tilde{p}_1 \tilde{h}(\tilde{h}i_{39} + z_b i_{30})}{\rho} + \frac{\tilde{p}_2 \tilde{h}(\tilde{h}i_{40} + z_b i_{31})}{\rho} \dots\dots\dots (A.154) \end{aligned}$$

$$\begin{aligned} F_{x_5}(\tilde{\Phi}) = & \frac{\tilde{q}_x \tilde{q}_y}{\tilde{h}}(\tilde{h}i_{44} + z_b i_{11}) + \tilde{q}_x \tilde{v}_1(\tilde{h}i_{46} + z_b i_{12}) + \tilde{q}_y \tilde{u}_1(\tilde{h}i_{45} + z_b i_{13}) \\ & + \tilde{v}_1 \tilde{u}_1 \tilde{h}(\tilde{h}i_{47} + z_b i_{14}) \dots\dots\dots (A.155) \end{aligned}$$

$$\begin{aligned} F_{y_4}(\tilde{\Phi}) = & \frac{\tilde{q}_x \tilde{q}_y}{\tilde{h}}(\tilde{h}i_{44} + z_b i_{11}) + \tilde{q}_x \tilde{v}_1(\tilde{h}i_{46} + z_b i_{12}) + \tilde{q}_y \tilde{u}_1(\tilde{h}i_{45} + z_b i_{13}) \\ & + \tilde{v}_1 \tilde{u}_1 \tilde{h}(\tilde{h}i_{47} + z_b i_{14}) \dots\dots\dots (A.156) \end{aligned}$$

$$\begin{aligned} F_{y_5}(\tilde{\Phi}) = & \frac{\tilde{q}_x^2}{\tilde{h}}(\tilde{h}i_{41} + z_b i_8) + \tilde{q}_y \tilde{v}_1(\tilde{h}i_{42} + z_b i_9) + \tilde{v}_1^2 \tilde{h}(\tilde{h}i_{43} + z_b i_{10}) \\ & + g\tilde{h}^2(\tilde{h}i_{39} + z_b i_{30}) + \frac{\tilde{p}_1 \tilde{h}(\tilde{h}i_{39} + z_b i_{30})}{\rho} + \frac{\tilde{p}_2 \tilde{h}(\tilde{h}i_{40} + z_b i_{31})}{\rho} \dots\dots\dots (A.157) \end{aligned}$$

$$\begin{aligned}
G_4(\vec{\phi}) = & -(i_{20} \tilde{q}_x + \hbar i_{21} \tilde{u}_1) \tilde{w}_2 \\
& - (i_{18} \tilde{q}_x + \hbar i_{19} \tilde{u}_1) \tilde{w}_b - (i_{22} \tilde{q}_x + \hbar i_{23} \tilde{u}_1) \tilde{w}_h \\
& - \left(\left(2 i_5 \frac{\partial \tilde{q}_x}{\partial x} \tilde{q}_x \right) / \hbar + i_6 \frac{\partial \tilde{u}_1}{\partial x} \tilde{q}_x - \left(i_5 \frac{\partial \hbar}{\partial x} \tilde{q}_x \tilde{q}_x \right) / (\hbar^2) \right. \\
& \quad \left. + i_6 \frac{\partial \tilde{q}_x}{\partial x} \tilde{u}_1 + 2 \hbar i_7 \frac{\partial \tilde{u}_1}{\partial x} \tilde{u}_1 + i_7 \frac{\partial \hbar}{\partial x} \tilde{u}_1 \tilde{u}_1 \right) \\
& \left. \right) (\hbar / 2. + z_b) \\
& - \left(\left(i_{11} \frac{\partial \tilde{q}_y}{\partial y} \tilde{q}_x \right) / \hbar + i_{12} \frac{\partial \tilde{v}_1}{\partial y} \tilde{q}_x + \left(i_{11} \frac{\partial \tilde{q}_x}{\partial y} \tilde{q}_y \right) / \hbar \right. \\
& \quad \left. + i_{13} \frac{\partial \tilde{u}_1}{\partial y} \tilde{q}_y - \left(i_{11} \frac{\partial \hbar}{\partial y} \tilde{q}_x \tilde{q}_y \right) / (\hbar^2) + i_{13} \frac{\partial \tilde{q}_y}{\partial y} \tilde{u}_1 \right. \\
& \quad \left. + \hbar i_{14} \frac{\partial \tilde{v}_1}{\partial y} \tilde{u}_1 \right. \\
& \quad \left. + i_{12} \frac{\partial \tilde{q}_x}{\partial y} \tilde{v}_1 + \hbar i_{14} \frac{\partial \tilde{u}_1}{\partial y} \tilde{v}_1 + i_{14} \frac{\partial \hbar}{\partial y} \tilde{u}_1 \tilde{v}_1 \right) \\
& \left. \right) (\hbar / 2. + z_b) \\
& + \left(- \left(\hbar \tilde{p}_1 \frac{\partial z_b}{\partial x} \right) / 2. \right. \\
& \quad - \hbar \left(\frac{\partial \hbar}{\partial x} / 2. + \frac{\partial z_b}{\partial x} \right) \tilde{\sigma}_x - \hbar \left(\frac{\partial \hbar}{\partial y} / 2. + \frac{\partial z_b}{\partial y} \right) \tilde{\tau}_{xy} \\
& \quad - \left(\hbar \tilde{\tau}_{xz_b} \right) / 2. + \hbar \tilde{\tau}_{xz} \\
& \quad - \left(i_{30} \tilde{p}_1 \frac{\partial \hbar}{\partial x} + \hbar i_{30} \frac{\partial \tilde{p}_1}{\partial x} \right) (\hbar / 2. + z_b) \\
& \quad - \left(i_{31} \tilde{p}_2 \frac{\partial \hbar}{\partial x} + \hbar i_{31} \frac{\partial \tilde{p}_2}{\partial x} \right) (\hbar / 2. + z_b) \\
& \quad \left. + g \rho \left(- \left(\hbar^2 \frac{\partial z_b}{\partial x} \right) / 2. - 2 \hbar i_{30} \frac{\partial \hbar}{\partial x} (\hbar / 2. + z_b) \right) \right) \\
& \left. \right) / \rho
\end{aligned}$$

..... (A.158)

$$\begin{aligned}
G_5(\bar{\phi}) = & -(i_{26} \bar{q}_y + \hbar i_{27} \bar{v}_1) \bar{w}_2 \\
& - (i_{24} \bar{q}_y + \hbar i_{25} \bar{v}_1) \bar{w}_b - (i_{28} \bar{q}_y + \hbar i_{29} \bar{v}_1) \bar{w}_h \\
& - \left(\left(i_{11} \frac{\partial \bar{q}_y}{\partial x} \bar{q}_x \right) / \hbar + i_{12} \frac{\partial v_1}{\partial x} \bar{q}_x + \left(i_{11} \frac{\partial \bar{q}_x}{\partial x} \bar{q}_y \right) / \hbar \right. \\
& + i_{13} \frac{\partial \bar{u}_1}{\partial x} \bar{q}_y - \left(i_{11} \frac{\partial \hbar}{\partial x} \bar{q}_x \bar{q}_y \right) / (\hbar^2) + i_{13} \frac{\partial \bar{q}_y}{\partial x} \bar{u}_1 \\
& + \hbar i_{14} \frac{\partial v_1}{\partial x} \bar{u}_1 + i_{12} \frac{\partial \bar{q}_x}{\partial x} \bar{v}_1 \\
& + \hbar i_{14} \frac{\partial \bar{u}_1}{\partial x} \bar{v}_1 + i_{14} \frac{\partial \hbar}{\partial x} \bar{u}_1 \bar{v}_1 \\
& \left. \right) (\hbar / 2. + z_b) \\
& - \left(\left(2 i_8 \frac{\partial \bar{q}_y}{\partial y} \bar{q}_y \right) / \hbar + i_9 \frac{\partial \bar{v}_1}{\partial y} \bar{q}_y \right. \\
& - \left(i_8 \frac{\partial \hbar}{\partial y} \bar{q}_y \bar{q}_y \right) / (\hbar^2) + i_9 \frac{\partial \bar{q}_y}{\partial y} \bar{v}_1 \\
& + 2 \hbar i_{10} \frac{\partial \bar{v}_1}{\partial y} \bar{v}_1 + i_{10} \frac{\partial \hbar}{\partial y} \bar{v}_1 \bar{v}_1 \left. \right) (\hbar / 2. + z_b) \\
& + \left(- \left(\hbar \bar{p}_1 \frac{\partial z_b}{\partial y} \right) / 2. \right. \\
& - \hbar \left(\frac{\partial \hbar}{\partial y} / 2. + \frac{\partial z_b}{\partial y} \right) \bar{\sigma}_y - \hbar \left(\frac{\partial \hbar}{\partial x} / 2. + \frac{\partial z_b}{\partial x} \right) \bar{\tau}_{yx} \\
& - (\hbar \bar{\tau}_{yz_b}) / 2. + \hbar \bar{\tau}_{yz} \\
& + \left(- \left(i_{30} \bar{p}_1 \frac{\partial \hbar}{\partial y} \right) - \hbar i_{30} \frac{\partial \bar{p}_1}{\partial y} \right) (\hbar / 2. + z_b) \\
& - \left(i_{31} \bar{p}_2 \frac{\partial \hbar}{\partial y} + \hbar i_{31} \frac{\partial \bar{p}_2}{\partial y} \right) (\hbar / 2. + z_b) \\
& + g \rho \left(- \left((\hbar^2) \frac{\partial z_b}{\partial y} \right) / 2. - 2 \hbar i_{30} \frac{\partial \hbar}{\partial y} (\hbar / 2. + z_b) \right) \\
& \left. \right) / \rho
\end{aligned}$$

..... (A.159)

$$\tilde{\tau}_x = \rho v_z \left(\frac{D_2 \tilde{u}_1}{\tilde{h}} + \frac{\partial \tilde{w}}{\partial x} \right) \dots \dots \dots (\text{A.160})$$

$$\tilde{\tau}_{yz} = \rho v_z \left(\frac{D_2 \tilde{v}_1}{\tilde{h}} + \frac{\partial \tilde{w}}{\partial y} \right) \dots \dots \dots (\text{A.161})$$

The application of the Bubnov-Galerkin Scheme to the rest of the equations (A.6)-(A.10) (VAM continuity, w_b , w_h , VA momentum in the z -direction and VAM momentum in the z -direction respectively) in the form of equation (A.26) results in the following weak statement equation:

$$\int_{\Omega} \mathbf{B} \left(\frac{\partial \psi(\tilde{\Phi})}{\partial t} + \frac{\partial \mathbf{F}_x(\tilde{\Phi})}{\partial x} + \frac{\partial \mathbf{F}_y(\tilde{\Phi})}{\partial y} + \mathbf{G}(\tilde{\Phi}) \right) d\Omega = 0 \dots \dots \dots (\text{A.162})$$

Multiplying and expanding through equation (A.136) results in:

$$\begin{aligned} & \int_{\Omega_e} \left[\theta (b_i)^{n-1} (\psi_{\epsilon}(\tilde{\Phi})^{n-1} - \psi_{\epsilon}(\tilde{\Phi})^n) + (1-\theta) (b_i)^n (\psi_{\epsilon}(\tilde{\Phi})^{n-1} - \psi_{\epsilon}(\tilde{\Phi})^n) \right] d\Omega_e \\ & + \theta \Delta t \left\{ - \int_{\Omega_e} \left(F_{x_{\epsilon}}(\tilde{\Phi}) \frac{\partial b_i}{\partial x} + F_{y_{\epsilon}}(\tilde{\Phi}) \frac{\partial b_i}{\partial y} \right) d\Omega_e + \int_{\Omega} b_i \left(\frac{\partial F_{x_{\epsilon}}(\tilde{\Phi})}{\partial x} + \frac{\partial F_{y_{\epsilon}}(\tilde{\Phi})}{\partial y} + G_{\epsilon}(\tilde{\Phi}) \right) d\Omega_e \right\}^{n+1} \\ & + (1-\theta) \Delta t \left\{ - \int_{\Omega_e} \left(F_{x_{\epsilon}}(\tilde{\Phi}) \frac{\partial b_i}{\partial x} + F_{y_{\epsilon}}(\tilde{\Phi}) \frac{\partial b_i}{\partial y} \right) d\Omega_e + \int_{\Omega} b_i \left(\frac{\partial F_{x_{\epsilon}}(\tilde{\Phi})}{\partial x} + \frac{\partial F_{y_{\epsilon}}(\tilde{\Phi})}{\partial y} + G_{\epsilon}(\tilde{\Phi}) \right) d\Omega_e \right\}^n \\ & + \int_{dy_{\epsilon}} b_i F_{x_{\epsilon}} dy_{\epsilon} - \int_{dx_{\epsilon}} b_i F_{y_{\epsilon}} dx_{\epsilon} \end{aligned} \dots \dots \dots (\text{A.163})$$

$$\begin{aligned}
& \int_{\Omega_e} \left[\theta (b_i)^{n+1} (\psi_7(\tilde{\Phi})^{n+1} - \psi_7(\tilde{\Phi})^n) + (1-\theta) (b_i)^n (\psi_7(\tilde{\Phi})^{n+1} - \psi_7(\tilde{\Phi})^n) \right] d\Omega_e \\
& + \theta \Delta t \left\{ \begin{aligned} & - \int_{\Omega_e} \left(F_{x_7}(\tilde{\Phi}) \frac{\partial b_i}{\partial x} + F_{y_7}(\tilde{\Phi}) \frac{\partial b_i}{\partial y} \right) d\Omega_e + \int_{\Omega} b_i \left(\frac{\partial F_{x_7}(\tilde{\Phi})}{\partial x} + \frac{\partial F_{y_7}(\tilde{\Phi})}{\partial y} + G_7(\tilde{\Phi}) \right) d\Omega_e \\ & + \int_{dy_e} b_i F_{x_7} dy_e - \int_{dx_e} b_i F_{y_7} dx_e \end{aligned} \right\}^{n+1} \\
& + (1-\theta) \Delta t \left\{ \begin{aligned} & - \int_{\Omega_e} \left(F_{x_7}(\tilde{\Phi}) \frac{\partial b_i}{\partial x} + F_{y_7}(\tilde{\Phi}) \frac{\partial b_i}{\partial y} \right) d\Omega_e + \int_{\Omega} b_i \left(\frac{\partial F_{x_7}(\tilde{\Phi})}{\partial x} + \frac{\partial F_{y_7}(\tilde{\Phi})}{\partial y} + G_7(\tilde{\Phi}) \right) d\Omega_e \\ & + \int_{dy_e} b_i F_{x_7} dy_e - \int_{dx_e} b_i F_{y_7} dx_e \end{aligned} \right\}^n = 0 \dots
\end{aligned}$$

.....(A.164)

$$\begin{aligned}
& \int_{\Omega_e} \left[\theta (b_i)^{n+1} (\psi_8(\tilde{\Phi})^{n+1} - \psi_8(\tilde{\Phi})^n) + (1-\theta) (b_i)^n (\psi_8(\tilde{\Phi})^{n+1} - \psi_8(\tilde{\Phi})^n) \right] d\Omega_e \\
& + \theta \Delta t \left\{ \begin{aligned} & - \int_{\Omega_e} \left(F_{x_8}(\tilde{\Phi}) \frac{\partial b_i}{\partial x} + F_{y_8}(\tilde{\Phi}) \frac{\partial b_i}{\partial y} \right) d\Omega_e + \int_{\Omega} b_i \left(\frac{\partial F_{x_8}(\tilde{\Phi})}{\partial x} + \frac{\partial F_{y_8}(\tilde{\Phi})}{\partial y} + G_8(\tilde{\Phi}) \right) d\Omega_e \\ & + \int_{dy_e} b_i F_{x_8} dy_e - \int_{dx_e} b_i F_{y_8} dx_e \end{aligned} \right\}^{n+1} \\
& + (1-\theta) \Delta t \left\{ \begin{aligned} & - \int_{\Omega_e} \left(F_{x_8}(\tilde{\Phi}) \frac{\partial b_i}{\partial x} + F_{y_8}(\tilde{\Phi}) \frac{\partial b_i}{\partial y} \right) d\Omega_e + \int_{\Omega} b_i \left(\frac{\partial F_{x_8}(\tilde{\Phi})}{\partial x} + \frac{\partial F_{y_8}(\tilde{\Phi})}{\partial y} + G_8(\tilde{\Phi}) \right) d\Omega_e \\ & + \int_{dy_e} b_i F_{x_8} dy_e - \int_{dx_e} b_i F_{y_8} dx_e \end{aligned} \right\}^n = 0 \dots
\end{aligned}$$

.....(A.165)

$$\begin{aligned}
& \int_{\Omega_e} \left[\theta (b_i)^{n+1} (\psi_9(\tilde{\Phi})^{n+1} - \psi_9(\tilde{\Phi})^n) + (1-\theta) (b_i)^n (\psi_9(\tilde{\Phi})^{n+1} - \psi_9(\tilde{\Phi})^n) \right] d\Omega_e \\
& + \theta \Delta t \left\{ - \int_{\Omega_e} \left(F_{x_9}(\tilde{\Phi}) \frac{\partial b_i}{\partial x} + F_{y_9}(\tilde{\Phi}) \frac{\partial b_i}{\partial y} \right) d\Omega_e + \int_{\Omega} b_i \left(\frac{\partial F_{x_9}(\tilde{\Phi})}{\partial x} + \frac{\partial F_{y_9}(\tilde{\Phi})}{\partial y} + G_9(\tilde{\Phi}) \right) d\Omega_e \right\}^{n+1} \\
& \quad + \int_{dy_e} b_i F_{x_9} dy_e - \int_{dx_e} b_i F_{y_9} dx_e \\
& + (1-\theta) \Delta t \left\{ - \int_{\Omega_e} \left(F_{x_9}(\tilde{\Phi}) \frac{\partial b_i}{\partial x} + F_{y_9}(\tilde{\Phi}) \frac{\partial b_i}{\partial y} \right) d\Omega_e + \int_{\Omega} b_i \left(\frac{\partial F_{x_9}(\tilde{\Phi})}{\partial x} + \frac{\partial F_{y_9}(\tilde{\Phi})}{\partial y} + G_9(\tilde{\Phi}) \right) d\Omega_e \right\}^n \\
& \quad + \int_{dy_e} b_i F_{x_9} dy_e - \int_{dx_e} b_i F_{y_9} dx_e \Bigg\} = 0 \dots
\end{aligned}$$

.....(A.166)

$$\begin{aligned}
& \int_{\Omega_e} \left[\theta (b_i)^{n+1} (\psi_{10}(\tilde{\Phi})^{n+1} - \psi_{10}(\tilde{\Phi})^n) + (1-\theta) (b_i)^n (\psi_{10}(\tilde{\Phi})^{n+1} - \psi_{10}(\tilde{\Phi})^n) \right] d\Omega_e \\
& + \theta \Delta t \left\{ - \int_{\Omega_e} \left(F_{x_{10}}(\tilde{\Phi}) \frac{\partial b_i}{\partial x} + F_{y_{10}}(\tilde{\Phi}) \frac{\partial b_i}{\partial y} \right) d\Omega_e + \int_{\Omega} b_i \left(\frac{\partial F_{x_{10}}(\tilde{\Phi})}{\partial x} + \frac{\partial F_{y_{10}}(\tilde{\Phi})}{\partial y} + G_{10}(\tilde{\Phi}) \right) d\Omega_e \right\}^{n+1} \\
& \quad + \int_{dy_e} b_i F_{x_{10}} dy_e - \int_{dx_e} b_i F_{y_{10}} dx_e \\
& + (1-\theta) \Delta t \left\{ - \int_{\Omega_e} \left(F_{x_{10}}(\tilde{\Phi}) \frac{\partial b_i}{\partial x} + F_{y_{10}}(\tilde{\Phi}) \frac{\partial b_i}{\partial y} \right) d\Omega_e + \int_{\Omega} b_i \left(\frac{\partial F_{x_{10}}(\tilde{\Phi})}{\partial x} + \frac{\partial F_{y_{10}}(\tilde{\Phi})}{\partial y} + G_{10}(\tilde{\Phi}) \right) d\Omega_e \right\}^n \\
& \quad + \int_{dy_e} b_i F_{x_{10}} dy_e - \int_{dx_e} b_i F_{y_{10}} dx_e \Bigg\} = 0
\end{aligned}$$

.....(A.167)

Equations (A.137)-(A.141) represent the equivalent Bubnov Galerkin finite element model for VAM continuity, “ w_b ”, “ w_h ”, VA momentum in the z -direction and VAM momentum in the z -direction equations respectively (equations (A.6)-(A.10)).

The different parts of equations ((A.137)-(A.141)) are defined as follows:

$$\psi_6(\tilde{\Phi}) = \frac{\tilde{h}^2}{4} \dots\dots\dots (A.168)$$

$$\psi_7(\tilde{\Phi}) = 0 \dots\dots\dots (A.169)$$

$$\psi_8(\tilde{\Phi}) = -\tilde{h} \dots\dots\dots (A.170)$$

$$\psi_9(\tilde{\Phi}) = \tilde{w}_b \tilde{h} j_{15} + \tilde{w}_2 \tilde{h} j_{16} + \tilde{w}_h \tilde{h} j_{17} \dots\dots\dots (A.171)$$

$$\psi_{10}(\tilde{\Phi}) = \tilde{w}_b \tilde{h} (\tilde{h} j_{48} + z_b j_{15}) + \tilde{w}_2 \tilde{h} (\tilde{h} j_{49} + z_b j_{16}) + \tilde{w}_h \tilde{h} (\tilde{h} j_{50} + z_b j_{17}) \dots\dots\dots (A.172)$$

$$F_{x_6}(\tilde{\Phi}) = \tilde{q}_x (\tilde{h} j_{32} + z_b j_1) + \tilde{u}_1 \tilde{h} (\tilde{h} j_{33} + z_b j_2) \dots\dots\dots (A.173)$$

$$F_{x_7}(\tilde{\Phi}) = 0 \dots\dots\dots (A.174)$$

$$F_{x_8}(\tilde{\phi}) = 0 \dots\dots\dots (A.175)$$

$$F_{x_9}(\tilde{\phi}) = \tilde{w}_b(\tilde{q}_x i_{18} + \tilde{u}_1 \tilde{h} i_{19}) + \tilde{w}_2(\tilde{q}_x i_{20} + \tilde{u}_1 \tilde{h} i_{21}) + \tilde{w}_h(\tilde{q}_x i_{22} + \tilde{u}_1 \tilde{h} i_{23}) - \frac{\tilde{h} \tilde{\tau}_x}{\rho} \dots (A.176)$$

$$\begin{aligned} F_{x_{10}}(\tilde{\phi}) = & \tilde{w}_b[\tilde{q}_x(\tilde{h} i_{51} + z_b i_{18}) + \tilde{u}_1 \tilde{h}(\tilde{h} i_{54} + z_b i_{19})] \\ & + \tilde{w}_2[\tilde{q}_x(\tilde{h} i_{52} + z_b i_{20}) + \tilde{u}_1 \tilde{h}(\tilde{h} i_{55} + z_b i_{21})] \dots\dots\dots (A.177) \\ & + \tilde{w}_h[\tilde{q}_x(\tilde{h} i_{53} + z_b i_{22}) + \tilde{u}_1 \tilde{h}(\tilde{h} i_{56} + z_b i_{23})] \end{aligned}$$

$$F_{y_6}(\tilde{\phi}) = \tilde{q}_y(\tilde{h} i_{34} + z_b i_3) + \tilde{v}_1 \tilde{h}(\tilde{h} i_{35} + z_b i_4) \dots\dots\dots (A.178)$$

$$F_{y_7}(\tilde{\phi}) = 0 \dots\dots\dots (A.179)$$

$$F_{y_8}(\tilde{\phi}) = 0 \dots\dots\dots (A.180)$$

$$F_{y_9}(\tilde{\phi}) = \tilde{w}_b(\tilde{q}_y i_{24} + \tilde{v}_1 \tilde{h} i_{25}) + \tilde{w}_2(\tilde{q}_y i_{26} + \tilde{v}_1 \tilde{h} i_{27}) + \tilde{w}_h(\tilde{q}_y i_{28} + \tilde{v}_1 \tilde{h} i_{29}) - \frac{\tilde{h} \tilde{\tau}_y}{\rho} \dots (A.181)$$

$$\begin{aligned}
F_{y_{10}}(\tilde{\Phi}) = & \tilde{w}_b \left[\tilde{q}_y (\tilde{h}_{j_{57}} + z_b j_{24}) + \tilde{v}_1 \tilde{h} (\tilde{h}_{j_{60}} + z_b j_{25}) \right] \\
& + \tilde{w}_2 \left[\tilde{q}_y (\tilde{h}_{j_{58}} + z_b j_{26}) + \tilde{v}_1 \tilde{h} (\tilde{h}_{j_{61}} + z_b j_{27}) \right] \dots\dots\dots (A.182) \\
& + \tilde{w}_h \left[\tilde{q}_y (\tilde{h}_{j_{59}} + z_b j_{28}) + \tilde{v}_1 \tilde{h} (\tilde{h}_{j_{62}} + z_b j_{29}) \right]
\end{aligned}$$

$$\begin{aligned}
G_6(\tilde{\Phi}) = & -\tilde{z} \left[\frac{\partial}{\partial x} (\tilde{q}_x j_1 + \tilde{u}_1 \tilde{h}_{j_2}) + \frac{\partial}{\partial y} (\tilde{q}_y j_3 + \tilde{v}_1 \tilde{h}_{j_4}) \right] - (\tilde{w}_b \tilde{h}_{j_{15}} + \tilde{w}_2 \tilde{h}_{j_{16}} + \tilde{w}_h \tilde{h}_{j_{17}}) \dots\dots\dots \\
& \dots\dots\dots (A.183)
\end{aligned}$$

$$G_7(\tilde{\Phi}) = - \left(\frac{\tilde{q}_x}{\tilde{h}} - \tilde{u}_1 \right) \frac{\partial z_b}{\partial x} - \left(\frac{\tilde{q}_y}{\tilde{h}} - \tilde{v}_1 \right) \frac{\partial z_b}{\partial y} + \tilde{w}_b \dots\dots\dots (A.184)$$

$$G_8(\tilde{\Phi}) = - \left(\frac{\tilde{q}_x}{\tilde{h}} + \tilde{u}_1 \right) \frac{\partial}{\partial x} (\tilde{h} + z_b) - \left(\frac{\tilde{q}_y}{\tilde{h}} + \tilde{v}_1 \right) \frac{\partial}{\partial y} (\tilde{h} + z_b) + \tilde{w}_h \dots\dots\dots (A.185)$$

$$G_9(\tilde{\Phi}) = -\frac{1}{\rho} \left\{ \tilde{p}_1 + \tilde{\tau}_{y_{z_b}} \frac{\partial z_b}{\partial y} + \tilde{\tau}_{x_b} \frac{\partial z_b}{\partial x} \right\} \dots\dots\dots (A.186)$$

$$\begin{aligned}
G_{10}(\vec{\phi}) = & \left(-(\hbar \ i_{31} \ \vec{p}_z) \right. \\
& + (\hbar / 2. - \hbar \ i_{30}) (\vec{p}_1 + g \ \hbar \ \rho) + \hbar \ \vec{\sigma}_z - \left(\hbar \ \frac{\partial z_b}{\partial x} \ \vec{t}_{xz_b} \right) / 2. \\
& - \left(\hbar \ \frac{\partial z_b}{\partial y} \ \vec{t}_{yz_b} \right) / 2. - \hbar \left(\frac{\partial \hbar}{\partial x} / 2. + \frac{\partial z_b}{\partial x} \right) \vec{t}_{zx} \\
& - \hbar \left(\frac{\partial \hbar}{\partial y} / 2. + \frac{\partial z_b}{\partial y} \right) \vec{t}_{zy} \\
& \left. \right) / \rho \\
& - \hbar \ i_{66} \ \tilde{w}_2 \ \tilde{w}_2 - \hbar \ i_{64} \ \tilde{w}_2 \ \tilde{w}_b - \hbar \ i_{63} \ \tilde{w}_b \ \tilde{w}_b \\
& - \hbar \ i_{67} \ \tilde{w}_2 \ \tilde{w}_h - \hbar \ i_{65} \ \tilde{w}_b \ \tilde{w}_h - \hbar \ i_{68} \ \tilde{w}_h \ \tilde{w}_h \\
& - \left(\frac{\partial \tilde{w}_b}{\partial x} (i_{18} \ \tilde{q}_x + \hbar \ i_{19} \ \tilde{u}_1) \right. \\
& + \frac{\partial \tilde{w}_2}{\partial x} (i_{20} \ \tilde{q}_x + \hbar \ i_{21} \ \tilde{u}_1) + \frac{\partial \tilde{w}_h}{\partial x} (i_{22} \ \tilde{q}_x + \hbar \ i_{23} \ \tilde{u}_1) \\
& + \left(i_{20} \ \frac{\partial \tilde{q}_x}{\partial x} + \hbar \ i_{21} \ \frac{\partial \tilde{u}_1}{\partial x} + i_{21} \ \frac{\partial \hbar}{\partial x} \ \tilde{u}_1 \right) \tilde{w}_2 \\
& + \left(i_{18} \ \frac{\partial \tilde{q}_x}{\partial x} + \hbar \ i_{19} \ \frac{\partial \tilde{u}_1}{\partial x} + i_{19} \ \frac{\partial \hbar}{\partial x} \ \tilde{u}_1 \right) \tilde{w}_b \\
& + \left(i_{22} \ \frac{\partial \tilde{q}_x}{\partial x} + \hbar \ i_{23} \ \frac{\partial \tilde{u}_1}{\partial x} + i_{23} \ \frac{\partial \hbar}{\partial x} \ \tilde{u}_1 \right) \tilde{w}_h \\
& \left. \right) (\hbar / 2. + z_b) \\
& - \left(\frac{\partial \tilde{w}_b}{\partial y} (i_{24} \ \tilde{q}_y + \hbar \ i_{25} \ \tilde{v}_1) \right. \\
& + \frac{\partial \tilde{w}_2}{\partial y} (i_{26} \ \tilde{q}_y + \hbar \ i_{27} \ \tilde{v}_1) + \frac{\partial \tilde{w}_h}{\partial y} (i_{28} \ \tilde{q}_y + \hbar \ i_{29} \ \tilde{v}_1) \\
& + \left(i_{26} \ \frac{\partial \tilde{q}_y}{\partial y} + \hbar \ i_{27} \ \frac{\partial \tilde{v}_1}{\partial y} + i_{27} \ \frac{\partial \hbar}{\partial y} \ \tilde{v}_1 \right) \tilde{w}_2 \\
& + \left(i_{24} \ \frac{\partial \tilde{q}_y}{\partial y} + \hbar \ i_{25} \ \frac{\partial \tilde{v}_1}{\partial y} + i_{25} \ \frac{\partial \hbar}{\partial y} \ \tilde{v}_1 \right) \tilde{w}_b \\
& + \left(i_{28} \ \frac{\partial \tilde{q}_y}{\partial y} + \hbar \ i_{29} \ \frac{\partial \tilde{v}_1}{\partial y} + i_{29} \ \frac{\partial \hbar}{\partial y} \ \tilde{v}_1 \right) \tilde{w}_h \\
& \left. \right) (\hbar / 2. + z_b)
\end{aligned}$$

..... (A.187)

$$\tilde{\sigma}_z = \tilde{\tau}_z = 2\rho\nu_z \frac{\tilde{w}_h - \tilde{w}_b}{\tilde{h}} \dots\dots\dots(\text{A.188})$$

$$\tilde{\tau}_x = \rho\nu_z \left(\frac{D_2 \tilde{u}_1}{\tilde{h}} + \frac{\partial \tilde{w}}{\partial x} \right) \dots\dots\dots(\text{A.189})$$

$$\tilde{\tau}_{xy} = \rho\nu_z \left(\frac{D_2 \tilde{v}_1}{\tilde{h}} + \frac{\partial \tilde{w}}{\partial y} \right) \dots\dots\dots(\text{A.190})$$

It should be mentioned that the turbulent diffusion terms, appearing in the $F_x(\tilde{\phi})$ and $F_y(\tilde{\phi})$ parts, are omitted in those of the boundary integral terms. That means the wall friction effects are not included in the current formulations. Equations (A.87)-(A.89) in the form of equation (A.71), Equations (A.150)-(A.151) in the form of equation (A.146), and Equations (A.163)-(A.167) in the form of equation (A.162) may be generally represented by:

$$\mathbf{R} = 0 \dots\dots\dots(\text{A.191})$$

R represents the vector of the residuals and is of length $(N_u \times NS) \times 1$ and is defined as:

$$\mathbf{R} = \begin{Bmatrix} R_1 \\ R_2 \\ R_3 \\ R_4 \\ R_5 \\ R_6 \\ R_7 \\ R_8 \\ R_9 \\ R_{10} \end{Bmatrix} = \begin{Bmatrix} \text{Equation(A.87)} \\ \text{Equation(A.88)} \\ \text{Equation(A.89)} \\ \text{Equation(A.150)} \\ \text{Equation(A.151)} \\ \text{Equation(A.163)} \\ \text{Equation(A.164)} \\ \text{Equation(A.165)} \\ \text{Equation(A.166)} \\ \text{Equation(A.167)} \end{Bmatrix} \dots\dots\dots(\text{A.192})$$

R actually represents an implicit set of non-linear algebraic equations. Special iterative techniques are thus necessary to solve this system of non-linear equations. This may be explained as follows.

Two methods are used to solve the system of obtained non-linear equations. These methods are transient and steady method solutions. Two techniques, with slight differences, are used in this study to solve the transient and steady problems. This may be briefly explained as follows.

For the transient solution, the objective is to get the correct distributions of the flow at a certain time or to actually map the time history at a certain domain. For the resulting implicit set of non-linear algebraic equations, a Newton-Raphson technique, where the derivatives are evaluated analytically where possible, is used to advance the solution to the next time level. The corrections vector necessary to update the variables after each iteration, or on other words the vector of differences between the Φ vectors at two successive iterations, $\delta\Phi$, are obtained from:

$$\mathbf{J}^{n+1,m} \delta\Phi^{n+1,m} = -\mathbf{R}^{n+1,m} \dots\dots\dots(\text{A.193})$$

Where superscript m refers to evaluation of the quantity at the m^{th} iteration. \mathbf{J} is the Jacobian matrix of size $(N_u \times NS) \times (N_u \times NS)$ and is given by:

$$\mathbf{J}^{n+1,m} = \left[\frac{\partial \mathbf{R}}{\partial \Phi} \right]^{n+1,m} \dots\dots\dots(\text{A.194})$$

Or

$$\left\{ \frac{\partial R_1}{\partial \Phi} \right\}^{n+1,m} = \int_{\Omega_e} \left\{ \theta \left[(b_i + W_{11})^{n+1} \frac{\partial \psi_1(\tilde{\Phi})^{n+1}}{\partial \Phi} + W_{12}^{n+1} \frac{\partial \psi_2(\tilde{\Phi})^{n+1}}{\partial \Phi} + W_{13}^{n+1} \frac{\partial \psi_3(\tilde{\Phi})^{n+1}}{\partial \Phi} \right] \right. \\ \left. + (1-\theta) \left[(b_i + W_{11})^n \frac{\partial \psi_1(\tilde{\Phi})^{n+1}}{\partial \Phi} + W_{12}^n \frac{\partial \psi_2(\tilde{\Phi})^{n+1}}{\partial \Phi} + W_{13}^n \frac{\partial \psi_3(\tilde{\Phi})^{n+1}}{\partial \Phi} \right] \right\}^m d\Omega_e$$

$$+ \int_{\Omega_e} \theta \left\{ \frac{\partial W_{11}^{n+1}}{\partial \Phi} \cdot [\psi_1(\tilde{\Phi})^{n+1} - \psi_1(\tilde{\Phi})^n] + \frac{\partial W_{12}^{n+1}}{\partial \Phi} \cdot [\psi_2(\tilde{\Phi})^{n+1} - \psi_2(\tilde{\Phi})^n] \right\}^m \\ \left\{ + \frac{\partial W_{13}^{n+1}}{\partial \Phi} \cdot [\psi_3(\tilde{\Phi})^{n+1} - \psi_3(\tilde{\Phi})^n] \right\}^m d\Omega_e$$

$$+ \theta \Delta t \int_{\Omega_e} \left\{ - \left(\frac{\partial F_{x_1}(\tilde{\Phi})}{\partial \Phi} \frac{\partial b_i}{\partial x} + \frac{\partial F_{y_1}(\tilde{\Phi})}{\partial \Phi} \frac{\partial b_i}{\partial y} \right) \right. \\ \left. b_i \left[\frac{\partial}{\partial \Phi} \left(\frac{\partial F_{x_1}(\tilde{\Phi})}{\partial x} \right) + \frac{\partial}{\partial \Phi} \left(\frac{\partial F_{y_1}(\tilde{\Phi})}{\partial y} \right) + \frac{\partial G_1(\tilde{\Phi})}{\partial \Phi} \right] \right\}^{n+1,m} d\Omega_e$$

$$+ \theta \Delta t \int_{\Omega_e} \left\{ W_{11} \left[\frac{\partial}{\partial \Phi} \left(\frac{\partial F_{x_1}(\tilde{\Phi})}{\partial x} \right) + \frac{\partial}{\partial \Phi} \left(\frac{\partial F_{y_1}(\tilde{\Phi})}{\partial y} \right) + \frac{\partial G_1(\tilde{\Phi})}{\partial \Phi} \right] \right. \\ \left. + W_{12} \left[\frac{\partial}{\partial \Phi} \left(\frac{\partial F_{x_2}(\tilde{\Phi})}{\partial x} \right) + \frac{\partial}{\partial \Phi} \left(\frac{\partial F_{y_2}(\tilde{\Phi})}{\partial y} \right) + \frac{\partial G_2(\tilde{\Phi})}{\partial \Phi} \right] \right. \\ \left. + W_{13} \left[\frac{\partial}{\partial \Phi} \left(\frac{\partial F_{x_3}(\tilde{\Phi})}{\partial x} \right) + \frac{\partial}{\partial \Phi} \left(\frac{\partial F_{y_3}(\tilde{\Phi})}{\partial y} \right) + \frac{\partial G_3(\tilde{\Phi})}{\partial \Phi} \right] \right\}^{n+1,m} d\Omega_e$$

$$\begin{aligned}
& + \theta \Delta t \left\{ \int_{\Omega_e} \left[\begin{aligned} & \frac{\partial W_{11}}{\partial \Phi} \left(\frac{\partial F_{x_1}(\tilde{\Phi})}{\partial x} + \frac{\partial F_{y_1}(\tilde{\Phi})}{\partial y} + G_1(\tilde{\Phi}) \right) \\ & + \frac{\partial W_{12}}{\partial \Phi} \left(\frac{\partial F_{x_2}(\tilde{\Phi})}{\partial x} + \frac{\partial F_{y_2}(\tilde{\Phi})}{\partial y} + G_2(\tilde{\Phi}) \right) \\ & + \frac{\partial W_{13}}{\partial \Phi} \left(\frac{\partial F_{x_3}(\tilde{\Phi})}{\partial x} + \frac{\partial F_{y_3}(\tilde{\Phi})}{\partial y} + G_3(\tilde{\Phi}) \right) \end{aligned} \right] d\Omega_e \right\}^{n+1,m} \\
& + \int_{\phi_e} b_i \frac{\partial F_{x_i}}{\partial \Phi} dy_e - \int_{dx_e} b_i \frac{\partial F_{y_i}}{\partial \Phi} dx_e
\end{aligned}
\tag{A.196}$$

$\left\{ \frac{\partial R_2}{\partial \Phi} \right\}^{n+1,m}$ is calculated as follows:

$$\begin{aligned}
\left\{ \frac{\partial R_2}{\partial \Phi} \right\}^{n+1,m} &= \int_{\Omega_e} \left\{ \begin{aligned} & \theta \left[W_{21}^{n+1} \frac{\partial \psi_1(\tilde{\Phi})^{n+1}}{\partial \Phi} + (b_i + W_{22})^{n+1} \frac{\partial \psi_2(\tilde{\Phi})^{n+1}}{\partial \Phi} + W_{23}^{n+1} \frac{\partial \psi_3(\tilde{\Phi})^{n+1}}{\partial \Phi} \right] \\ & + (1 - \theta) \left[W_{21}^n \frac{\partial \psi_1(\tilde{\Phi})^{n+1}}{\partial \Phi} + (b_i + W_{22})^n \frac{\partial \psi_2(\tilde{\Phi})^{n+1}}{\partial \Phi} + W_{23}^n \frac{\partial \psi_3(\tilde{\Phi})^{n+1}}{\partial \Phi} \right] \end{aligned} \right\}^m d\Omega_e \\
& + \int_{\Omega_e} \theta \left\{ \begin{aligned} & \frac{\partial W_{21}^{n+1}}{\partial \Phi} \cdot [\psi_1(\tilde{\Phi})^{n+1} - \psi_1(\tilde{\Phi})^n] + \frac{\partial W_{22}^{n+1}}{\partial \Phi} \cdot [\psi_2(\tilde{\Phi})^{n+1} - \psi_2(\tilde{\Phi})^n] \\ & + \frac{\partial W_{23}^{n+1}}{\partial \Phi} \cdot [\psi_3(\tilde{\Phi})^{n+1} - \psi_3(\tilde{\Phi})^n] \end{aligned} \right\}^m d\Omega_e
\end{aligned}$$

$$\begin{aligned}
& + \theta \Delta t \int_{\Omega_e} \left\{ \begin{aligned} & - \left(\frac{\partial F_{x_2}(\tilde{\Phi})}{\partial \Phi} \frac{\partial b_i}{\partial x} + \frac{\partial F_{y_2}(\tilde{\Phi})}{\partial \Phi} \frac{\partial b_i}{\partial y} \right) \\ & \left[b_i \left(\frac{\partial}{\partial \Phi} \left(\frac{\partial F_{x_2}(\tilde{\Phi})}{\partial x} \right) + \frac{\partial}{\partial \Phi} \left(\frac{\partial F_{y_2}(\tilde{\Phi})}{\partial y} \right) + \frac{\partial G_2(\tilde{\Phi})}{\partial \Phi} \right) \right] \end{aligned} \right\}^{n+1,m} d\Omega_e \\
& + \theta \Delta t \int_{\Omega_e} \left\{ \begin{aligned} & W_{21} \left[\frac{\partial}{\partial \Phi} \left(\frac{\partial F_{x_1}(\tilde{\Phi})}{\partial x} \right) + \frac{\partial}{\partial \Phi} \left(\frac{\partial F_{y_1}(\tilde{\Phi})}{\partial y} \right) + \frac{\partial G_1(\tilde{\Phi})}{\partial \Phi} \right] \\ & + W_{22} \left[\frac{\partial}{\partial \Phi} \left(\frac{\partial F_{x_2}(\tilde{\Phi})}{\partial x} \right) + \frac{\partial}{\partial \Phi} \left(\frac{\partial F_{y_2}(\tilde{\Phi})}{\partial y} \right) + \frac{\partial G_2(\tilde{\Phi})}{\partial \Phi} \right] \\ & + W_{23} \left[\frac{\partial}{\partial \Phi} \left(\frac{\partial F_{x_3}(\tilde{\Phi})}{\partial x} \right) + \frac{\partial}{\partial \Phi} \left(\frac{\partial F_{y_3}(\tilde{\Phi})}{\partial y} \right) + \frac{\partial G_3(\tilde{\Phi})}{\partial \Phi} \right] \end{aligned} \right\}^{n+1,m} d\Omega_e \\
& + \theta \Delta t \left\{ \begin{aligned} & \int_{\Omega_e} \left[\begin{aligned} & \frac{\partial W_{21}}{\partial \Phi} \left(\frac{\partial F_{x_1}(\tilde{\Phi})}{\partial x} + \frac{\partial F_{y_1}(\tilde{\Phi})}{\partial y} + G_1(\tilde{\Phi}) \right) \\ & + \frac{\partial W_{22}}{\partial \Phi} \left(\frac{\partial F_{x_2}(\tilde{\Phi})}{\partial x} + \frac{\partial F_{y_2}(\tilde{\Phi})}{\partial y} + G_2(\tilde{\Phi}) \right) \\ & + \frac{\partial W_{23}}{\partial \Phi} \left(\frac{\partial F_{x_3}(\tilde{\Phi})}{\partial x} + \frac{\partial F_{y_3}(\tilde{\Phi})}{\partial y} + G_3(\tilde{\Phi}) \right) \end{aligned} \right] d\Omega_e \\ & + \int_{dy_e} b_i \frac{\partial F_{x_2}}{\partial \Phi} dy_e - \int_{dx_e} b_i \frac{\partial F_{y_2}}{\partial \Phi} dx_e \end{aligned} \right\}^{n+1,m} \\
& \dots\dots\dots (A.197)
\end{aligned}$$

$\left\{ \frac{\partial R_3}{\partial \Phi} \right\}^{n+1,m}$ is calculated as follows:

$$\begin{aligned}
\left\{ \frac{\partial R_3}{\partial \Phi} \right\}^{n+1,m} &= \int_{\Omega_e} \left\{ \theta \left[W_{31}^{n+1} \frac{\partial \psi_1(\tilde{\Phi})^{n+1}}{\partial \Phi} + W_{32}^{n+1} \frac{\partial \psi_2(\tilde{\Phi})^{n+1}}{\partial \Phi} + (b_i + W_{33})^{n+1} \frac{\partial \psi_3(\tilde{\Phi})^{n+1}}{\partial \Phi} \right] \right. \\
&\quad \left. + (1-\theta) \left[W_{31}^n \frac{\partial \psi_1(\tilde{\Phi})^{n+1}}{\partial \Phi} + W_{32}^n \frac{\partial \psi_2(\tilde{\Phi})^{n+1}}{\partial \Phi} + (b_i + W_{33})^n \frac{\partial \psi_3(\tilde{\Phi})^{n+1}}{\partial \Phi} \right] \right\}^m d\Omega_e \\
&\quad + \int_{\Omega_e} \theta \left\{ \frac{\partial W_{31}^{n+1}}{\partial \Phi} \cdot [\psi_1(\tilde{\Phi})^{n+1} - \psi_1(\tilde{\Phi})^n] + \frac{\partial W_{32}^{n+1}}{\partial \Phi} \cdot [\psi_2(\tilde{\Phi})^{n+1} - \psi_2(\tilde{\Phi})^n] \right. \\
&\quad \left. + \frac{\partial W_{33}^{n+1}}{\partial \Phi} \cdot [\psi_3(\tilde{\Phi})^{n+1} - \psi_3(\tilde{\Phi})^n] \right\}^m d\Omega_e \\
&\quad + \theta \Delta t \int_{\Omega_e} \left\{ - \left(\frac{\partial F_{x_3}(\tilde{\Phi})}{\partial \Phi} \frac{\partial b_i}{\partial x} + \frac{\partial F_{y_3}(\tilde{\Phi})}{\partial \Phi} \frac{\partial b_i}{\partial y} \right) \right. \\
&\quad \left. b_i \left[\frac{\partial}{\partial \Phi} \left(\frac{\partial F_{x_3}(\tilde{\Phi})}{\partial x} \right) + \frac{\partial}{\partial \Phi} \left(\frac{\partial F_{y_3}(\tilde{\Phi})}{\partial y} \right) + \frac{\partial G_3(\tilde{\Phi})}{\partial \Phi} \right] \right\}^{n+1,m} d\Omega_e \\
&\quad + \theta \Delta t \int_{\Omega_e} \left\{ W_{31} \left[\frac{\partial}{\partial \Phi} \left(\frac{\partial F_{x_1}(\tilde{\Phi})}{\partial x} \right) + \frac{\partial}{\partial \Phi} \left(\frac{\partial F_{y_1}(\tilde{\Phi})}{\partial y} \right) + \frac{\partial G_1(\tilde{\Phi})}{\partial \Phi} \right] \right. \\
&\quad + W_{32} \left[\frac{\partial}{\partial \Phi} \left(\frac{\partial F_{x_2}(\tilde{\Phi})}{\partial x} \right) + \frac{\partial}{\partial \Phi} \left(\frac{\partial F_{y_2}(\tilde{\Phi})}{\partial y} \right) + \frac{\partial G_2(\tilde{\Phi})}{\partial \Phi} \right] \\
&\quad \left. + W_{33} \left[\frac{\partial}{\partial \Phi} \left(\frac{\partial F_{x_3}(\tilde{\Phi})}{\partial x} \right) + \frac{\partial}{\partial \Phi} \left(\frac{\partial F_{y_3}(\tilde{\Phi})}{\partial y} \right) + \frac{\partial G_3(\tilde{\Phi})}{\partial \Phi} \right] \right\}^{n+1,m} d\Omega_e
\end{aligned}$$

$$\begin{aligned}
& + \theta \Delta t \left\{ \int_{\Omega_e} \left[\frac{\partial W_{31}}{\partial \Phi} \left(\frac{\partial F_{x_1}(\tilde{\Phi})}{\partial x} + \frac{\partial F_{y_1}(\tilde{\Phi})}{\partial y} + G_1(\tilde{\Phi}) \right) \right. \right. \\
& \quad + \frac{\partial W_{32}}{\partial \Phi} \left(\frac{\partial F_{x_2}(\tilde{\Phi})}{\partial x} + \frac{\partial F_{y_2}(\tilde{\Phi})}{\partial y} + G_2(\tilde{\Phi}) \right) \\
& \quad \left. \left. + \frac{\partial W_{33}}{\partial \Phi} \left(\frac{\partial F_{x_3}(\tilde{\Phi})}{\partial x} + \frac{\partial F_{y_3}(\tilde{\Phi})}{\partial y} + G_3(\tilde{\Phi}) \right) \right] d\Omega_e \right\}^{n+1,m} \\
& \quad + \int_{dy_e} b_i \frac{\partial F_{x_3}}{\partial \Phi} dy_e - \int_{dx_e} b_i \frac{\partial F_{y_3}}{\partial \Phi} dx_e
\end{aligned}
\tag{A.198}$$

$\frac{\partial \left\{ \begin{smallmatrix} R_4 \\ R_5 \end{smallmatrix} \right\}}{\partial \Phi} \Big\}^{n+1,m}$ are calculated as follows:

$$\begin{aligned}
& \frac{\partial \left\{ \begin{smallmatrix} R_4 \\ R_5 \end{smallmatrix} \right\}}{\partial \Phi} \Big\}^{n+1,m} = \\
& \int_{\Omega_e} \left\{ \theta \left(b_i + \left\{ \begin{smallmatrix} W_{ux} \\ W_{uy} \end{smallmatrix} \right\} \right)^{n+1} \frac{\partial \left\{ \begin{smallmatrix} \psi_4(\tilde{\Phi})^{n+1} \\ \psi_5(\tilde{\Phi})^{n+1} \end{smallmatrix} \right\}}{\partial \Phi} + (1-\theta) \left(b_i + \left\{ \begin{smallmatrix} W_{ux} \\ W_{uy} \end{smallmatrix} \right\} \right)^n \frac{\partial \left\{ \begin{smallmatrix} \psi_4(\tilde{\Phi})^{n+1} \\ \psi_5(\tilde{\Phi})^{n+1} \end{smallmatrix} \right\}}{\partial \Phi} \right\}^m d\Omega_e \\
& \quad + \int_{\Omega_e} \theta \left\{ \frac{\partial \left\{ \begin{smallmatrix} W_{ux} \\ W_{uy} \end{smallmatrix} \right\}^{n+1}}{\partial \Phi} \cdot \left\{ \begin{smallmatrix} \psi_4(\tilde{\Phi})^{n+1} - \psi_4(\tilde{\Phi})^n \\ \psi_5(\tilde{\Phi})^{n+1} - \psi_5(\tilde{\Phi})^n \end{smallmatrix} \right\} \right\}^m d\Omega_e
\end{aligned}$$

$$\begin{aligned}
& + \theta \Delta t \int_{\Omega_e} \left\{ \begin{aligned} & - \left(\frac{\partial \left\{ \frac{F_{x_4}(\tilde{\Phi})}{F_{x_3}(\tilde{\Phi})} \right\}}{\partial \Phi} \frac{\partial b_i}{\partial x} + \frac{\partial \left\{ \frac{F_{y_4}(\tilde{\Phi})}{F_{y_3}(\tilde{\Phi})} \right\}}{\partial \Phi} \frac{\partial b_i}{\partial y} \right) \\ & b_i \left[\frac{\partial}{\partial \Phi} \left(\frac{\partial \left\{ \frac{F_{x_4}(\tilde{\Phi})}{F_{x_3}(\tilde{\Phi})} \right\}}{\partial x} \right) + \frac{\partial}{\partial \Phi} \left(\frac{\partial \left\{ \frac{F_{y_4}(\tilde{\Phi})}{F_{y_3}(\tilde{\Phi})} \right\}}{\partial y} \right) + \frac{\partial \left\{ \frac{G_4(\tilde{\Phi})}{G_5(\tilde{\Phi})} \right\}}{\partial \Phi} \right] \end{aligned} \right\} d\Omega_e \\
& + \theta \Delta t \int_{\Omega_e} \left\{ \begin{aligned} & \left\{ \frac{W_{ux}}{W_{uy}} \right\} \left[\frac{\partial}{\partial \Phi} \left(\frac{\partial \left\{ \frac{F_{x_4}(\tilde{\Phi})}{F_{x_3}(\tilde{\Phi})} \right\}}{\partial x} \right) + \frac{\partial}{\partial \Phi} \left(\frac{\partial \left\{ \frac{F_{y_4}(\tilde{\Phi})}{F_{y_3}(\tilde{\Phi})} \right\}}{\partial y} \right) + \frac{\partial \left\{ \frac{G_4(\tilde{\Phi})}{G_5(\tilde{\Phi})} \right\}}{\partial \Phi} \right] \end{aligned} \right\} d\Omega_e \\
& + \theta \Delta t \left\{ \begin{aligned} & \int_{\Omega_e} \left[\frac{\partial \left\{ \frac{W_{ux}}{W_{uy}} \right\}}{\partial \Phi} \left(\frac{\partial \left\{ \frac{F_{x_4}(\tilde{\Phi})}{F_{x_3}(\tilde{\Phi})} \right\}}{\partial x} + \frac{\partial \left\{ \frac{F_{y_4}(\tilde{\Phi})}{F_{y_3}(\tilde{\Phi})} \right\}}{\partial y} + \left\{ \frac{G_4(\tilde{\Phi})}{G_5(\tilde{\Phi})} \right\} \right) \right] d\Omega_e \\ & + \int_{dy_e} b_i \frac{\partial \left\{ \frac{F_{x_4}}{F_{x_3}} \right\}}{\partial \Phi} dy_e - \int_{dx_e} b_i \frac{\partial \left\{ \frac{F_{y_4}}{F_{y_3}} \right\}}{\partial \Phi} dx_e \end{aligned} \right\}
\end{aligned}
\tag{A.199}$$

$\left\{ \frac{\partial}{\partial \Phi} \begin{Bmatrix} R_6 \\ R_7 \\ R_8 \\ R_9 \\ R_{10} \end{Bmatrix} \right\}^{n+1,m}$ are calculated as follows:

$$\left\{ \frac{\partial}{\partial \Phi} \begin{Bmatrix} R_6 \\ R_7 \\ R_8 \\ R_9 \\ R_{10} \end{Bmatrix} \right\}^{n+1,m} = \int_{\Omega_e} \left\{ b_i \frac{\partial}{\partial \Phi} \begin{Bmatrix} \psi_6(\tilde{\Phi})^{n+1} \\ \psi_7(\tilde{\Phi})^{n+1} \\ \psi_8(\tilde{\Phi})^{n+1} \\ \psi_9(\tilde{\Phi})^{n+1} \\ \psi_{10}(\tilde{\Phi})^{n+1} \end{Bmatrix} \right\}^m d\Omega_e$$

$$+ \theta \Delta t \int_{\Omega_e} \left\{ - \left(\frac{\partial}{\partial \Phi} \begin{Bmatrix} F_{x_6}(\tilde{\Phi}) \\ F_{x_7}(\tilde{\Phi}) \\ F_{x_8}(\tilde{\Phi}) \\ F_{x_9}(\tilde{\Phi}) \\ F_{x_{10}}(\tilde{\Phi}) \end{Bmatrix} \frac{\partial b_i}{\partial x} + \frac{\partial}{\partial \Phi} \begin{Bmatrix} F_{y_6}(\tilde{\Phi}) \\ F_{y_7}(\tilde{\Phi}) \\ F_{y_8}(\tilde{\Phi}) \\ F_{y_9}(\tilde{\Phi}) \\ F_{y_{10}}(\tilde{\Phi}) \end{Bmatrix} \frac{\partial b_i}{\partial y} \right) \right\}^{n+1,m} d\Omega_e$$

$$+ \theta \Delta t \left\{ \int_{dy_e} b_i \frac{\partial}{\partial \Phi} \begin{Bmatrix} F_{x_6}(\tilde{\Phi}) \\ F_{x_7}(\tilde{\Phi}) \\ F_{x_8}(\tilde{\Phi}) \\ F_{x_9}(\tilde{\Phi}) \\ F_{x_{10}}(\tilde{\Phi}) \end{Bmatrix} dy_e - \int_{dx_e} b_i \frac{\partial}{\partial \Phi} \begin{Bmatrix} F_{y_6}(\tilde{\Phi}) \\ F_{y_7}(\tilde{\Phi}) \\ F_{y_8}(\tilde{\Phi}) \\ F_{y_9}(\tilde{\Phi}) \\ F_{y_{10}}(\tilde{\Phi}) \end{Bmatrix} dx_e \right\}^{n+1,m}$$

.....(A.200)

As a result, the system of equations represented by equation (A.193) becomes linear in $\delta\Phi^{n+1,m}$. A LU decomposition matrix solver, with a skyline matrix storage for the Jacobian \mathbf{J} , is employed to solve this system of linear equations to obtain $\delta\Phi^{n+1}$. After each iteration, the values of the variables are updated through:

$$\Phi^{n+1,m+1} = \Phi^{n+1,m} + \delta\Phi^{n+1,m} \dots\dots\dots(\text{A.201})$$

Where superscript $m+1$ refers to evaluation of the quantity at the $m+1^{\text{th}}$ iteration

Finally, when the error norm $\varepsilon^{n+1,m} = \left(\sqrt{\frac{\sum (\delta\Phi)^2}{\sum \Phi^2}} \right)^{n+1,m}$ is \leq a user specified tolerance

(typically 10^{-6}), the solution proceeds to the next time step.

For the steady state solution, the objective is to reach the final steady state with as few calculations as possible while remaining stable under any flow circumstances. Herein, the 3-equation model is firstly run till a final steady state solution is obtained. This final steady solution is then used as an input file to run the full 10-equation model. It is found that by this way the convergence to a final steady state solution becomes faster.

A special technique is used to accelerate the convergence The equations are solved with $\theta = 1$ (fully implicit) θ being the implicitness factor. To control convergence, the steady state is found to be essentially simulated as an unsteady but with number of iterations equal to 1 per time step. This process is actually a pseudo-transient one. A

time step acceleration procedure speeds the process to final completion by systematically increasing the time increment. The time increment is increased according to:

$$\Delta t^{n+1} = \Delta t^n \frac{\varepsilon_g}{\varepsilon^{n+1,1}} \dots\dots\dots (A.202)$$

where ε_g is a user specified goal relative change of all the variables. Typically a value of ε_g of the order of 0.1 is used. After each time step, the values of the variables are updated through:

$$\Phi^{n+1,1} = \Phi^{n,1} + \delta\Phi^{n+1,1} \dots\dots\dots (A.203)$$

As the solution progresses toward steady state, usually the overall rate of change $\varepsilon / \Delta t$ decreases and longer time steps are possible. The progress toward a final steady state may not be uniform. The program logic proceeds as follows. At the end of each time step the overall relative change ε is calculated and compared to the goal change ε_g . If the actual change is less than 1.25 times the goal change ε_g , then the current iteration is accepted and the increment for the next time step is then calculated according to equation (A.202). If the actual change is greater than 1.25 times the goal change ε_g , then the current iteration is rejected and a new time increment is calculated as half of the result of equation (A.202) and the iteration is retried. This process may

repeat a few times until a small enough time step is achieved to allow the solution to progress.

In most cases, the time step eventually becomes large and the solution converges quickly to steady state. At each successful iteration, the overall change ε and the net outflow discharge ($q_n = q_x \Delta y - q_y \Delta x$) are printed on the screen as indicators of how close the solution is to a final steady. When the net outflow discharge indicates a constant value and the overall change approaches zero (typical value of the order of 10^{-6} is used), the solution is considered to be steady state. More details are found in Steffler (1997a).

It should be mentioned that few of the equations listed beforehand are printed out by Mathematica application package. That is why the shapes of the equation boxes in this Appendix are not consistent.

References

- Fischer et al. (1979), "Mixing in Inland and Coastal Waters." Book, Academic Press.
- Ghanem, A., Steffler, P. M., Hicks, F. E. and Katopodis (1995), "Two-Dimensional Finite Element Modeling of Flow in Aquatic Habitats". Water resources Engineering Report No. 95-S1, Department of Civil Engineering, University of Alberta.

- Hicks, F. E. and Steffler, P. M. (1990), "Finite Element Modeling of Open Channel Flow." Department of Civil Engineering, University of Alberta, Technical Report (WRE 90-6).
- Hicks, F. E. and Steffler, P. M. (1992), "Characteristic Dissipative Galerkin Scheme for Open-Channel Flow." *Journal of Hydraulic Engineering*. ASCE, Vol. 118, No. 2, pp. 337-352.
- Hoger, A. and Carlson, D. E. (1984), "Determination of the stretch and rotation in the polar decomposition of the deformation gradient." *Quarterly of Applied Mathematics*, Vol. 42, No. 1, pp. 113-117.
- Hughes, T. J. R. and Mallet, M. (1986a), "A new finite element formulation for computational fluid dynamics: III. The generalized streamline operator for multidimensional advective-diffusive systems." *Computer Methods in Applied Mechanics and Engineering*, Vol. 58, pp. 305-328.
- Hughes, T. J. R. and Mallet, M. (1986b), "A new finite element formulation for computational fluid dynamics: IV. A discontinuity-capturing operator for multidimensional advective-diffusive systems." *Computer Methods in Applied Mechanics and Engineering*, Vol. 58, pp. 329-336.
- Hughes, T. J. R., Mallet, M. and Mizukami, A. (1986), "A new finite element formulation for computational fluid dynamics: II. Beyond SUPG." *Computer Methods in Applied Mechanics and Engineering*, Vol. 54, pp. 341-355.
- Steffler, P. M. (1997a), "cdg2d depth averaged hydrodynamic model reference manual." Civil Engineering Department, University of Alberta, Edmonton, Canada.

Appendix B

List of the Integral Constants in the Derived Equations

List of the little integral constants i 's appearing in the general derived equations

$$i_1 = \int_0^1 f_1(\eta) d\eta$$

$$i_2 = \int_0^1 g_1(\eta) d\eta$$

$$i_3 = \int_0^1 f_2(\eta) d\eta$$

$$i_4 = \int_0^1 g_2(\eta) d\eta$$

$$i_5 = \int_0^1 f_1(\eta) f_1(\eta) d\eta$$

$$i_6 = \int_0^1 2f_1(\eta) g_1(\eta) d\eta$$

$$i_7 = \int_0^1 g_1(\eta) g_1(\eta) d\eta$$

$$i_8 = \int_0^1 f_2(\eta) f_2(\eta) d\eta$$

$$i_9 = \int_0^1 2f_2(\eta) g_2(\eta) d\eta$$

$$i_{10} = \int_0^1 g_2(\eta) g_2(\eta) d\eta$$

$$i_{11} = \int_0^1 f_1(\eta) f_2(\eta) d\eta$$

$$i_{12} = \int_0^1 f_1(\eta) g_2(\eta) d\eta$$

$$i_{13} = \int_0^1 g_1(\eta) f_2(\eta) d\eta$$

$$i_{14} = \int_0^1 g_1(\eta) g_2(\eta) d\eta$$

$$i_{15} = \int_0^1 f_3(\eta) d\eta$$

$$i_{16} = \int_0^1 g_3(\eta) d\eta$$

$$i_{17} = \int_0^1 H_3(\eta) d\eta$$

$$i_{18} = \int_0^1 f_1(\eta) f_3(\eta) d\eta$$

$$i_{19} = \int_0^1 g_1(\eta) f_3(\eta) d\eta$$

$$i_{20} = \int_0^1 f_1(\eta) g_3(\eta) d\eta$$

$$i_{21} = \int_0^1 g_1(\eta) g_3(\eta) d\eta$$

$$i_{22} = \int_0^1 f_1(\eta) H_3(\eta) d\eta$$

$$i_{23} = \int_0^1 g_1(\eta) H_3(\eta) d\eta$$

$$i_{24} = \int_0^1 f_2(\eta) f_3(\eta) d\eta$$

$$i_{25} = \int_0^1 g_2(\eta) f_3(\eta) d\eta$$

$$i_{26} = \int_0^1 f_2(\eta) g_3(\eta) d\eta$$

$$i_{27} = \int_0^1 g_2(\eta) g_3(\eta) d\eta$$

$$i_{28} = \int_0^1 f_2(\eta) H_3(\eta) d\eta$$

$$i_{29} = \int_0^1 g_2(\eta) H_3(\eta) d\eta$$

$$i_{30} = \int_0^1 f_4(\eta) d\eta$$

$$i_{31} = \int_0^1 g_4(\eta) d\eta$$

$$i_{32} = \int_0^1 \eta f_1(\eta) d\eta$$

$$i_{33} = \int_0^1 \eta g_1(\eta) d\eta$$

$$i_{34} = \int_0^1 \eta f_2(\eta) d\eta$$

$$i_{35} = \int_0^1 \eta g_2(\eta) d\eta$$

$$i_{36} = \int_0^1 \eta f_1(\eta) f_1(\eta) d\eta$$

$$i_{37} = \int_0^1 2\eta f_1(\eta) g_1(\eta) d\eta$$

$$i_{38} = \int_0^1 \eta g_1(\eta) g_1(\eta) d\eta$$

$$i_{39} = \int_0^1 \eta f_4(\eta) d\eta$$

$$i_{40} = \int_0^1 \eta g_4(\eta) d\eta$$

$$i_{41} = \int_0^1 \eta f_2(\eta) f_2(\eta) d\eta$$

$$i_{42} = \int_0^1 2\eta f_2(\eta) g_2(\eta) d\eta$$

$$i_{43} = \int_0^1 \eta g_2(\eta) g_2(\eta) d\eta \quad i_{44} = \int_0^1 \eta f_1(\eta) f_2(\eta) d\eta \quad i_{45} = \int_0^1 \eta g_1(\eta) f_2(\eta) d\eta$$

$$i_{46} = \int_0^1 \eta f_1(\eta) g_2(\eta) d\eta \quad i_{47} = \int_0^1 \eta g_1(\eta) g_2(\eta) d\eta \quad i_{48} = \int_0^1 \eta f_3(\eta) d\eta$$

$$i_{49} = \int_0^1 \eta g_3(\eta) d\eta \quad i_{50} = \int_0^1 \eta H_3(\eta) d\eta \quad i_{51} = \int_0^1 \eta f_1(\eta) f_3(\eta) d\eta$$

$$i_{52} = \int_0^1 \eta f_1(\eta) g_3(\eta) d\eta \quad i_{53} = \int_0^1 \eta f_1(\eta) H_3(\eta) d\eta \quad i_{54} = \int_0^1 \eta g_1(\eta) f_3(\eta) d\eta$$

$$i_{55} = \int_0^1 \eta g_1(\eta) g_3(\eta) d\eta \quad i_{56} = \int_0^1 \eta g_1(\eta) H_3(\eta) d\eta \quad i_{57} = \int_0^1 \eta f_2(\eta) f_3(\eta) d\eta$$

$$i_{58} = \int_0^1 \eta f_2(\eta) g_3(\eta) d\eta \quad i_{59} = \int_0^1 \eta f_2(\eta) H_3(\eta) d\eta \quad i_{60} = \int_0^1 \eta g_2(\eta) f_3(\eta) d\eta$$

$$i_{61} = \int_0^1 \eta g_2(\eta) g_3(\eta) d\eta \quad i_{62} = \int_0^1 \eta g_2(\eta) H_3(\eta) d\eta \quad i_{63} = \int_0^1 f_3(\eta) f_3(\eta) d\eta$$

$$i_{64} = \int_0^1 2 f_3(\eta) g_3(\eta) d\eta \quad i_{65} = \int_0^1 2 f_3(\eta) H_3(\eta) d\eta \quad i_{66} = \int_0^1 g_3(\eta) g_3(\eta) d\eta$$

$$i_{67} = \int_0^1 2g_3(\eta) H_3(\eta) d\eta \qquad i_{68} = \int_0^1 H_3(\eta) H_3(\eta) d\eta$$

Appendix C

Evaluation of the Square Root of the Convection Matrix

The inverse of the matrix $\left(\sqrt{\mathbf{A}_x^2 + \mathbf{A}_y^2}\right)$ is calculated numerically using Hoger and Carlson's (1984) method as follows:

$$\mathbf{A}_2 = \mathbf{A}_x^2 + \mathbf{A}_y^2 = \begin{bmatrix} A_{211} & A_{212} & A_{213} \\ A_{221} & A_{222} & A_{223} \\ A_{231} & A_{232} & A_{233} \end{bmatrix} \dots\dots\dots (C.1)$$

$$\mathbf{C}_2 = \mathbf{A}_2^{-1} = \begin{bmatrix} C_{211} & C_{212} & C_{213} \\ C_{221} & C_{222} & C_{223} \\ C_{231} & C_{232} & C_{233} \end{bmatrix} \dots\dots\dots (C.2)$$

$$I_c = A_{211} + A_{222} + A_{233} \dots\dots\dots (C.3)$$

$$II_c = 0.5 [(A_{211} + A_{222} + A_{233})^2 - (C_{211} + C_{222} + C_{233})] \dots\dots\dots (C.4)$$

$$\begin{aligned} III_c &= \text{Det.} [\mathbf{A}_2] \\ &= -(A_{211} A_{222} A_{233}) + A_{212} A_{223} A_{231} + A_{213} A_{221} A_{232} \dots\dots\dots (C.5) \\ &\quad - A_{211} A_{223} A_{232} - A_{212} A_{221} A_{233} + A_{211} A_{222} A_{233} \end{aligned}$$

$$III_u = \sqrt{III_c} \dots\dots\dots (C.6)$$

$$\xi = \frac{2^5}{27} (2I_c^3 - 9I_c II_c + 27III_c) \dots\dots\dots (C.7)$$

$$\eta = \frac{2^{10}}{27} (4II_c^3 - I_c^2 II_c^2 + 4I_c^3 III_c - 18I_c II_c III_c + 27III_c^2) \dots\dots\dots (C.8)$$

$$\zeta = -\frac{2}{3}I_c + (\xi + \sqrt{\eta})^{1/3} + (\xi - \sqrt{\eta})^{1/3} \dots\dots\dots (C.9)$$

$$I_u = \begin{cases} \frac{1}{2} \left(\sqrt{2I_c + \zeta} + \sqrt{2I_c - \zeta + 16\sqrt{III_c} / \sqrt{2I_c + \zeta}} \right), & \zeta \neq -2I_c \\ \sqrt{I_c + 2\sqrt{III_c}}, & \zeta = -2I_c \end{cases} \dots\dots\dots (C.10)$$

$$II_u = \sqrt{II_c + 2\sqrt{III_c}I_u} \dots\dots\dots (C.11)$$

$$\left(\sqrt{\mathbf{A}_x^2 + \mathbf{A}_y^2} \right)^{-1} = \left\{ III_u^2 (III_u + I_u I_c) + I_u^2 (I_u III_c + III_u II_c) \right\}^{-1} \\ \left\{ \begin{aligned} & I_u (I_u II_u - III_u) \mathbf{C}_2 - (I_u II_u - III_u) (III_u + I_u I_c) \mathbf{A}_2 \\ & + [II_u III_u (III_u + I_u I_c) + I_u^2 (II_u II_c + III_c)] \mathbf{I} \end{aligned} \right\} \dots\dots\dots (C.12)$$

Where **I** is the identity matrix given by:

$$\mathbf{I} = \begin{bmatrix} 1 & 0 & 0 \\ 0 & 1 & 0 \\ 0 & 0 & 1 \end{bmatrix} \dots\dots\dots (C.13)$$

Appendix D

List of the Integral Constant Values in the Derived Linear and Quadratic Models

The list of the values of the integral constants i 's for the VAM linear model:

$$i_1 = 1$$

$$i_2 = 0$$

$$i_3 = 1$$

$$i_4 = 0$$

$$i_5 = 1$$

$$i_6 = 0$$

$$i_7 = 1/3$$

$$i_8 = 1$$

$$i_9 = 0$$

$$i_{10} = 1/3$$

$$i_{11} = 1$$

$$i_{12} = 0$$

$$i_{13} = 0$$

$$i_{14} = 1/3$$

$$i_{15} = 1/2$$

$$i_{16} = 2/3$$

$$i_{17} = 1/2$$

$$i_{18} = 1/2$$

$$i_{19} = -1/6$$

$$i_{20} = 2/3$$

$$i_{21} = 0$$

$$i_{22} = 1/2$$

$$i_{23} = 1/6$$

$$i_{24} = 1/2$$

$$i_{25} = -1/6$$

$$i_{26} = 2/3$$

$$i_{27} = 0$$

$$i_{28} = 1/2$$

$$i_{29} = 1/6$$

$$i_{30} = 1/2$$

$$i_{31} = 2/3$$

$$i_{32} = 1/2$$

$$i_{33} = 1/6$$

$$i_{34} = 1/2$$

$$i_{35} = 1/6$$

$$i_{36} = 1/2$$

$$i_{37} = 1/3$$

$$i_{38} = 1/6$$

$$i_{39} = 1/6$$

$$i_{40} = 1/3$$

$$i_{41} = 1/2$$

$$i_{42} = 1/3$$

$$i_{43} = 1/6$$

$$i_{44} = 1/2$$

$$i_{45} = 1/6$$

$$i_{46} = 1/6$$

$$i_{47} = 1/6$$

$$i_{48} = 1/6$$

$$i_{49} = 1/3$$

$$i_{50} = 1/3$$

$$i_{51} = 1/6$$

$$i_{52} = 1/3$$

$$i_{53} = 1/3$$

$$i_{54} = 0$$

$$i_{55} = 1/15$$

$$i_{56} = 1/6$$

$$i_{57} = 1/6$$

$$i_{58} = 1/3$$

$$i_{59} = 1/3$$

$$i_{60} = 0$$

$$i_{61} = 1/15$$

$$i_{62} = 1/6$$

$$i_{63} = 1/3$$

$$i_{64} = 2/3$$

$$i_{65} = 1/3$$

$$i_{66} = 8/15$$

$$i_{67} = 2/3$$

$$i_{68} = 1/3$$

The list of the values of the integral constants i 's for the VAM quadratic model:

$$i_1 = 1$$

$$i_2 = 0$$

$$i_3 = 1$$

$$i_4 = 0$$

$$i_5 = 1$$

$$i_6 = 0$$

$$i_7 = 4/5$$

$$i_8 = 1$$

$$i_9 = 0$$

$$i_{10} = 4/5$$

$$i_{11} = 1$$

$$i_{12} = 0$$

$$i_{13} = 0$$

$$i_{14} = 4/5$$

$$i_{15} = 1/2$$

$$i_{16} = 2/3$$

$$i_{17} = 1/2$$

$$i_{18} = 1/2$$

$$i_{19} = -1/4$$

$$i_{20} = 2/3$$

$$i_{21} = 1/15$$

$$i_{22} = 1/2$$

$$i_{23} = 1/4$$

$$i_{24} = 1/2$$

$$i_{25} = -1/4$$

$$i_{26} = 2/3$$

$$i_{27} = 1/15$$

$$i_{28} = 1/2$$

$$i_{29} = 1/4$$

$$i_{30} = 1/2$$

$$i_{31} = 2/3$$

$$i_{32} = 1/2$$

$$i_{33} = 1/4$$

$$i_{34} = 1/2$$

$$i_{35} = 1/4$$

$$i_{36} = 1/2$$

$$i_{37} = 1/2$$

$$i_{38} = 3/10$$

$$i_{39} = 1/6$$

$$i_{40} = 1/3$$

$$i_{41} = 1/2$$

$$i_{42} = 1/2$$

$$i_{43} = 3/10$$

$$i_{44} = 1/2$$

$$i_{45} = 1/4$$

$$i_{46} = 1/4$$

$$i_{47} = 3/10$$

$$i_{48} = 1/6$$

$$i_{49} = 1/3$$

$$i_{50} = 1/3$$

$$i_{51} = 1/6$$

$$i_{52} = 1/3$$

$$i_{53} = 1/3$$

$$i_{54} = 1/60$$

$$i_{55} = 2/15$$

$$i_{56} = 7/30$$

$$i_{57} = 1/6$$

$$i_{58} = 1/3$$

$$i_{59} = 1/3$$

$$i_{60} = 1/60$$

$$i_{61} = 2/15$$

$$i_{62} = 7/30$$

$$i_{63} = 1/3$$

$$i_{64} = 2/3$$

$$i_{65} = 1/3$$

$$i_{66} = 8/15$$

$$i_{67} = 2/3$$

$$i_{68} = 1/3$$